frontiers | Research Topics

Condition monitoring for renewable energy systems, volume II

Edited by
Yusen He, Alan Wai Hou Lio, Tinghui Ouyang, Xun Shen and Shuang Zhao

Published in
Frontiers in Energy Research

ISSN 1664-8714
ISBN 978-2-83251-499-3
DOI 10.3389/978-2-83251-499-3

About Frontiers

Frontiers is more than just an open access publisher of scholarly articles: it is a pioneering approach to the world of academia, radically improving the way scholarly research is managed. The grand vision of Frontiers is a world where all people have an equal opportunity to seek, share and generate knowledge. Frontiers provides immediate and permanent online open access to all its publications, but this alone is not enough to realize our grand goals.

Frontiers journal series

The Frontiers journal series is a multi-tier and interdisciplinary set of open-access, online journals, promising a paradigm shift from the current review, selection and dissemination processes in academic publishing. All Frontiers journals are driven by researchers for researchers; therefore, they constitute a service to the scholarly community. At the same time, the *Frontiers journal series* operates on a revolutionary invention, the tiered publishing system, initially addressing specific communities of scholars, and gradually climbing up to broader public understanding, thus serving the interests of the lay society, too.

Dedication to quality

Each Frontiers article is a landmark of the highest quality, thanks to genuinely collaborative interactions between authors and review editors, who include some of the world's best academicians. Research must be certified by peers before entering a stream of knowledge that may eventually reach the public - and shape society; therefore, Frontiers only applies the most rigorous and unbiased reviews. Frontiers revolutionizes research publishing by freely delivering the most outstanding research, evaluated with no bias from both the academic and social point of view. By applying the most advanced information technologies, Frontiers is catapulting scholarly publishing into a new generation.

What are Frontiers Research Topics?

Frontiers Research Topics are very popular trademarks of the *Frontiers journals series*: they are collections of at least ten articles, all centered on a particular subject. With their unique mix of varied contributions from Original Research to Review Articles, Frontiers Research Topics unify the most influential researchers, the latest key findings and historical advances in a hot research area.

Find out more on how to host your own Frontiers Research Topic or contribute to one as an author by contacting the Frontiers editorial office: frontiersin.org/about/contact

Condition monitoring for renewable energy systems, volume II

Topic editors

Yusen He — The University of Iowa, United States
Alan Wai Hou Lio — Technical University of Denmark, Denmark
Tinghui Ouyang — National Institute of Advanced Industrial Science and Technology (AIST), Japan
Xun Shen — Tokyo Institute of Technology, Japan
Shuang Zhao — Hefei University of Technology, China

Citation

He, Y., Lio, A. W. H., Ouyang, T., Shen, X., Zhao, S., eds. (2023). *Condition monitoring for renewable energy systems, volume II*. Lausanne: Frontiers Media SA. doi: 10.3389/978-2-83251-499-3

Table of contents

frontiers | Frontiers in Energy Research

BRIEF RESEARCH REPORT
published: 08 July 2022
doi: 10.3389/fenrg.2022.945327

Ultra-Short-Term Power Prediction of a Photovoltaic Power Station Based on the VMD-CEEMDAN-LSTM Model

Shuaijie Wang, Shu Liu and Xin Guan*

School of Renewable Energy, Shenyang Institute of Engineering, Shenyang, China

The prediction of photovoltaic power generation is helpful to the overall allocation of power planning departments and improves the utilization rate of photovoltaic power generation. Therefore, this study puts forward an ultra-short-term power forecasting model of a photovoltaic power station based on modal decomposition and deep learning. The methodology involved taking the data of a 50 MW photovoltaic power generation system in the Inner Mongolia Autonomous Region as a sample. Furthermore, the weather conditions were classified, and the historical power data were decomposed into multiple VMF subcomponents and residual terms by the VMD method. Then, the residual term was decomposed twice by the CEEMDAN method. All subcomponents were sent to the LSTM network for prediction, and the predicted value of the photovoltaic power station was obtained by superimposing the subcomponent prediction results. ARIMA, SVM, LSTM, and VMD-LSTM models were built to compare the accuracy with the proposed models. The results revealed that the prediction accuracy of a non-combination forecasting model was limited when the weather suddenly changed. The VMD method was used to decompose the residual term twice, which could fully extract the complex data information in the residual term, and when compared with the VMD-LSTM model, the e_{RMSE}, e_{MAPE}, and e_{TIC} of the VMD-CEEMDAN-LSTM model were reduced by 0.104, 16.596, and 0.038, respectively. The second decomposition technology has obvious prediction advantages. The proposed quadratic modal decomposition model effectively improves the precision of ultra-short-term prediction of photovoltaic power plants.

Keywords: photovoltaic power station, quadratic modal decomposition, long-term memory neural network, ultra-short term, power prediction

OPEN ACCESS

Edited by:
Xun Shen,
Tokyo Institute of Technology, Japan

Reviewed by:
Sandeep Kumar Duran,
Lovely Professional University, India
Vikram Kamboj,
Lovely Professional University, India

****Correspondence:***
Shuaijie Wang
D11402027@mail.dlut.edu.cn

Specialty section:
This article was submitted to Smart Grids, a section of the journal Frontiers in Energy Research

Received: *16 May 2022*
Accepted: *30 May 2022*
Published: *08 July 2022*

Citation:
Wang S, Liu S and Guan X (2022) Ultra-Short-Term Power Prediction of a Photovoltaic Power Station Based on the VMD-CEEMDAN-LSTM Model. Front. Energy Res. 10:945327. doi: 10.3389/fenrg.2022.945327

Abbreviations: VMD, variational mode decomposition; VMF, Vienna mapping function; CEEMDAN, complete ensemble empirical mode decomposition with adaptive noise; IMF, intrinsic mode function; LSTM, long short-term memory; ADMM, alternating direction method of multipliers; EEMD, ensemble empirical mode decomposition; CEEMDAN, complete ensemble empirical mode decomposition with adaptive noise; ARIMA, autoregressive integrated moving average model; SVM, support vector machine.

1 INTRODUCTION

The increasing population and modern lifestyle are threatening the traditional energy sources such as coal, oil, and natural gas. In order to meet the world's energy demand, renewable energy must be developed and utilized on a large scale (Wang H. et al., 2020; Sohani et al., 2021). In renewable energy, solar energy occupies a dominant position (Yuan et al., 2021). However, photovoltaic power generation is very sensitive to climate and seasonal factors (Meng et al., 2021). Small changes in photovoltaic power may affect the safe and stable operation of the power grid (Ding, 2021). In order to ensure the stability, reliability, and power dispatching ability of the power system, it is very important to design a true and accurate photovoltaic power forecasting method.

Photovoltaic power forecasting methods are generally divided into physical methods and statistical methods. Physical methods are not suitable in many cases because of their low prediction accuracy and high calculation cost (Ma et al., 2014; Yao, 2014; Hassan et al., 2021). The statistical method optimizes the mapping relationship between historical samples and actual photovoltaic power by minimizing the error, which is proved to be effective in the field of solar energy prediction. At present, the machine learning model (Chiteka and Enweremadu, 2016; Jang et al., 2016; Gao et al., 2019; Ghimire et al., 2019; Ye et al., 2021; Chiang and Young, 2022) has been successfully applied to photovoltaic power prediction. In order to improve the accuracy of power prediction, some combination models (Mellit et al., 2010; Mohammadi et al., 2015; Wang X. et al., 2020; Yang et al., 2020) have also been applied in the field of photovoltaic prediction. However, the prediction of photovoltaic power generation is not only related to the current weather conditions but also related to historical data. Machine learning belongs to the shallow network, which is more suitable for small batch data analysis. With the explosive growth of data, these methods cannot mine the most effective features from massive data, and there are problems such as gradient disappearance and explosion, so the prediction accuracy is limited (Changwei et al., 2019).

In recent years, the deep learning method has been successfully applied in the field of photovoltaic forecasting because of its strong ability of data feature extraction and fitting, which can independently mine the main learning features from massive data (Alzahrani et al., 2017; Abdel-Nasser and Mahmoud, 2019; Chang and Lu, 2018; Zang et al., 2018; Zhou et al., 2019). Zhou et al. (2019) adopted an attention mechanism, that adaptively focuses attention on two important input features, namely, temperature and irradiance, so that more relevant information can be mined. Alzahrani et al. (2017) proposed a recurrent neural network model to predict the solar irradiance level. Abdel-Nasser and Mahmoud (2019) compared long-term and short-term memory networks with three traditional methods: multiple linear regression, regression tree, and ANN. Chang and Lu (2018) compared the depth confidence network with SVR, back propagation neural network, and other methods, and the results show that DBN has the best prediction effect. In the work of Zang et al. (2018), the convolutional neural network is compared with BPNN and SVR models, and it is found that the CNN model has the lowest prediction accuracy.

The above research on photovoltaic power prediction has made some achievements, but the statistical model also has its own limitations. Compared with physical forecasting methods, statistical models are more concise in modeling, but there are also some problems in actual forecasting, such as difficulty in parameter adjustment, stagnation of convergence, etc., and the weather type has a great influence on photovoltaic forecasting, while most statistical models do not classify and analyze different weather conditions. At present, the existing literature uses the VMD decomposition method to decompose the photovoltaic power curve but ignores the important information in the residual term obtained by VMD decomposition. In order to further improve the accuracy of ultra-short-term prediction of photovoltaic power, this paper classified the weather conditions, used the VMD method to decompose the historical power, and used the adaptive noise complete empirical mode decomposition method to decompose the residual term for the second time. By making full use of the information in the residual term, VMF and IMF components were sent to the LSTM network, and the final prediction result was obtained by superimposing the prediction results of each subcomponent. The errors of ARIMA, SVM, LSTM, and VMD-LSTM models were compared, and the results showed the accuracy of the quadratic decomposition model proposed in this paper.

2 INFLUENCE OF WEATHER TYPES ON PHOTOVOLTAIC OUTPUT

Photovoltaic power is affected by many factors such as meteorology, environment, and location. This paper selects the power data of a photovoltaic power station in the Inner Mongolia Autonomous Region from 1 January 2019 to 31 December 2020 as the sample. There are 52 sampling points in the power station, and the sampling interval is 15 min. As the photovoltaic power station only works in daytime, only the data from 08: 00 to 18: 00 are selected for analysis. When there is no sudden change in the weather (sunny, cloudy, rainy, and snowy), the photovoltaic output is relatively stable, and the output curve is approximately parabolic; However, when the weather suddenly changes during the day, the photovoltaic output curve fluctuates greatly, which affects the safe and stable operation of the power system. Therefore, it is necessary to distinguish between the weather types to study the photovoltaic output.

3 DESCRIPTION OF THE MODEL CONCEPT AND MECHANISM

The photovoltaic power series is a non-stationary and nonlinear time series. The VMD method can decompose a photovoltaic series into several VMF components with low complexity and residual terms. In previous studies, only VMF components were studied and the residual terms were discarded, but the residual terms also contained a lot of useful information. If the residual

term is discarded directly, the prediction accuracy of the model will be greatly affected. In order to improve the prediction accuracy, this study uses the CEEMDAN method to decompose the residual term after VMD decomposition for the second time and then sends both the VMF component and IMF component to the LSTM network (Li et al., 2021a; Li et al., 2021b; Le et al., 2021; Toyoda and Wu, 2021; Wu et al., 2021).

3.1 Variable Modal Decomposition

3.1.1 Variable Modal Decomposition Principle

The core of variable modal decomposition is to decompose signals by adaptive and completely non-recursive methods. This method can adaptively match the best frequency and bandwidth and then realize the effective decomposition of VMF components, thus solving the endpoint effect problem of the EMD method. The model expression is as shown in the following equation:

$$\left\{ \begin{array}{ll} \min\limits_{\{u_k\},\{w_k\}} & \left\{ \sum\limits_k \left\| \partial_t \left[\left(\delta(t) + \frac{j}{\pi t} \right) * u_k(t) \right] e^{-jw_k t} \right\|_2^2 \right\} \\ s.t. & \sum\limits_k u_k = f \end{array} \right\}, \tag{1}$$

where k is the number of VMF components; $\{u_k\}: = \{u_1, \cdots, u_k\}$ represents the modal subcomponent VMF; $\{w_k\}: = \{w_1, \cdots, w_k\}$ represents the center frequency value of the VMF component; f is the original data sequence; ∂_t stands for taking partial derivative of time; $\delta(t)$ represents the Dirac function; $e^{-jw_k t}$ the center frequency value of the VMF component can be adjusted.

In order to obtain the optimal solution, the quadratic penalty factor α and Lagrange operator $\lambda(t)$ are introduced.

$$\begin{aligned} L(\{u_k\},\{w_k\},\lambda): = \alpha \sum_k \left\| \partial_t \left[\left(\delta(t) + \frac{j}{\pi t} \right) u_k(t) \right] e^{-jw_k t} \right\|_2^2 + \\ \left\| f(t) - \sum_b u_k(t) \right\|_2^2 + \left(\lambda(t), f(t) - \sum_k u_k(t) \right), \end{aligned} \tag{2}$$

where Lagrange operator $\lambda(t)$ maintains the constraint condition; the quadratic penalty factor α is used to ensure the accuracy of data sequence reconstruction. During iterative search, the ADMM algorithm is used to calculate the saddle point of the Lagrange function. $VMFu_k$ and center frequency w_k are obtained as follows:

$$\hat{u}_k^{n+1}(w) = \frac{\hat{f}(w) - \sum_{i \neq k} \hat{u}_i(w) + \frac{\hat{\lambda}(w)}{2}}{1 + 2\alpha(w - w_k)^2}, \tag{3}$$

$$\hat{w}_k^{n+1} = \frac{\int_0^\infty w |\hat{u}_k(w)|^2 dw}{\int_0^\infty \hat{u}_k|(w)|^2 dw}. \tag{4}$$

1) Set the appropriate component number K, and make the related parameters $\{u_k^1\}\{w_k^1\}$, λ^1, $n = 0$.
2) Update u_k and w_k according to the iterative search method of ADMM algorithm in **Eqs 3**, **4**.
3) Update that $\lambda(t)$ value of Lagrange operator.

$$\hat{\lambda}^{n+1} = \hat{\lambda}^n + \tau \left[f(w) - \sum_k \hat{u}_k^{n+1}(w) \right]. \tag{5}$$

4) Judging the judgment precision.

$$\sum_k \left\| \hat{u}_k^{n+1} - \hat{u}_k^n \right\|_2^2 \Big/ \left\| \hat{u}_k^n \right\|_2^2 < \varepsilon. \tag{6}$$

When condition (6) is satisfied, the iteration stops, otherwise, the process returns to step 2.

In the abovementioned formula, $\hat{u}_k^n(w)$, $\hat{f}(w)$, and $\hat{\lambda}^n(w)$ are Fourier transforms corresponding to $\hat{u}_k^n$, $f(t)$, andλ^n's Fourier transform.

3.1.2 Variational Modal Decomposition Results

When the VMD method is used for modal decomposition of photovoltaic power, if there are many VMF components, modal aliasing will easily occur, but when there are few VMF components, the complexity of the photovoltaic power sequence cannot be effectively reduced, so the number of VMF components needs to be determined according to the change of instantaneous frequency before decomposition. When the number of VMF components is 7, the instantaneous frequency curve is obviously bent and over-decomposed. Therefore, this paper sets the number of VMF components to 6.

3.2 Complete Empirical Mode Decomposition of Adaptive Noise

3.2.1 Principle of Adaptive Noise Complete Empirical Mode Decomposition

Empirical decomposition can decompose a photovoltaic power sequence into several IMF components, but due to the non-stationary and nonlinear characteristics of the photovoltaic power curve, aliasing can easily appear in the decomposition process. The EEMD decomposition method adds white noise to the original sequence and makes use of the frequency equilibrium distribution characteristics of white noise to improve the mode aliasing problem, but the decomposition efficiency of this method is low. In this article, CEEMDAN method is chosen to decompose photovoltaic sequences, which adds white noise with different amplitudes to decompose the optimal IMF component and solves the problems of modal aliasing and low decomposition efficiency. CEEMDAN decomposition steps are as follows.

1) Add the white noise sequence $n_i(t)$ to the original sequence $x(t)$, that is,

$$x_i(t) = x(t) + \varepsilon_i n_i(t), \tag{7}$$

where, ε_i is the control parameter; $x_i(t)$ is the data sequence after adding white Gaussian noise.

2) Perform empirical mode decomposition on data sequence $x_i(t)$, that is,

$$x_i(t) = \sum_{j=1}^{J} C_{i,j}(t) + r_i(t). \tag{8}$$

In this formula, $C_{i,j}(t)$ is the *jth* IMF component after the *ith* decomposition, and $r_i(t)$ is the residual term.

3) Average $C_{i,j}(t)$, cancel the influence of white noise on IMF component, and decompose to get the j IMF component $C_j(t)$:

$$C_j(t) = \frac{1}{N}\sum_{i=1}^{N} C_{i,j}(t). \tag{9}$$

4) The final decomposition result of CEEMDAN is

$$x(t) = \sum_{j=1}^{J} C_j(t) + r(t), \tag{10}$$

where $\sum_{j=1}^{J} C_j(t)$ is the modal component of different frequency segments of the data sequence, and $r(t)$ is the overall residual term.

3.3 Long-Term and Short-Term Memory Neural Network

3.3.1 Principle of Long-Term and Short-Term Memory Neural Network

By introducing a gating unit, the long-term memory neural network can selectively add or forget information, which keeps the feedback mechanism of the circulation neural network and solves the long-term dependence of the circulation neural network. A long-term memory neural network consists of input, output, and hidden layer containing a gated memory mechanism.

Data are memorized by controlling the forgetting gate, the input gate, and the output gate, and the calculation formulas are shown as follows:

$$\boldsymbol{f}_t = \sigma\left(\boldsymbol{W}_f \cdot [\boldsymbol{h}_{t-1}, \boldsymbol{x}_t] + \boldsymbol{b}_f\right), \tag{11}$$

$$\boldsymbol{i}_t = \sigma(\boldsymbol{W}_i \cdot [\boldsymbol{h}_{t-1}, \boldsymbol{x}_t] + \boldsymbol{b}_i), \tag{12}$$

$$\boldsymbol{o}_t = \sigma(\boldsymbol{W}_o \cdot [\boldsymbol{h}_{t-1}, \boldsymbol{x}_t] + \boldsymbol{b}_o), \tag{13}$$

where σ is sigmoid activation function; $\boldsymbol{h}_{t-1}$ is the state of the hidden layer at time t-1; $\boldsymbol{x}_t$ is a sequence input; $\boldsymbol{f}_t$, $\boldsymbol{W}_f$, and $\boldsymbol{b}_f$ are the result, weight matrix, and bias term of forgetting gate T; $\boldsymbol{i}_t$, $\boldsymbol{W}_i$ and $\boldsymbol{b}_i$ are the time result, weight matrix and bias term of the input gate T; $\boldsymbol{o}_t$, $\boldsymbol{W}_o$, $\boldsymbol{b}_o$ output gate t time result, weight matrix and bias term.

The calculation of the state $\boldsymbol{c}_t$ of the time memory cell of the time hidden layer $\boldsymbol{h}_t$ and t in t is as shown in the following equations:

$$\tilde{\boldsymbol{c}}_t = \tanh(\boldsymbol{W}_c \cdot [\boldsymbol{h}_{t-1}, \boldsymbol{x}_t] + \boldsymbol{b}_c), \tag{14}$$

$$\boldsymbol{c}_t = \boldsymbol{f}_t \circ \boldsymbol{c}_{t-1} + \boldsymbol{i}_t \circ \tilde{\boldsymbol{c}}_t, \tag{15}$$

$$\boldsymbol{h}_t = \boldsymbol{o}_t \circ \tanh(\boldsymbol{c}_t), \tag{16}$$

where $\tilde{\boldsymbol{c}}_t$ is the candidate state of the memory unit; $\boldsymbol{W}_c$ is the input unit state weight matrix.

3.3.2 Structure of Long-Term and Short-Term Memory Neural Network

The LSTM network model parameters are as follows: the dropout value is 0.2; the function is optimized to adam; the activation function takes tanh; the number of nodes is 50; training times are 1,000; batch size is 72, and the average absolute error function is selected as the loss function.

3.4 Construction of the VMD-EEMD-LSTM Model

The modeling steps of the VMD-CEEMAN-LSTM model built in this study are as follows:

1) The PV power sequence is decomposed by the VMD method, which is divided into the VMF component and the residual term
2) Normalize each VMF component and send it to LSTM network to obtain the VMF subcomponent prediction result
3) The remaining residual term is decomposed twice by CEEMAN, and the IMF component obtained by decomposition is sent to the LSTM network
4) Superposing the IMF subcomponent prediction results to obtain the residual prediction results
5) Superposing the VMF subcomponent prediction result and the residual prediction result to obtain the final photovoltaic power prediction result

The modeling process of the VMD-CEEMAN-LSTM model is shown in **Figure 1**.

3.5 Modeling Classification

Because the weather type has a great influence on the photovoltaic output, in order to improve the prediction accuracy, this article separately predicts the abrupt weather (sunny, cloudy, rainy, and snowy) and the non-abrupt weather (sunny to cloudy, sunny to cloudy, etc.). In order to test the accuracy of the VMD-CEEMDAN-LSTM model, ARIMA, SVM, LSTM, and VMD-LSTM models are established and compared with the proposed models. When evaluating the accuracy of the model, the average absolute percentage error e_{MAPE}, the root mean square error e_{RMSE}, and the Hill inequality coefficient e_{TIC} are selected, and the formula is as follows:

$$e\mathrm{MAPE} = \frac{1}{\mathrm{Z}}\sum_{i=1}^{\mathrm{Z}}\left|\frac{y'_i - y_i}{y_i}\right|, \tag{17}$$

$$e\mathrm{REMS} = \sqrt{\frac{\sum_{i=1}^{\mathrm{Z}}\left(y'_i - y_i\right)^2}{\mathrm{Z}}}, \tag{18}$$

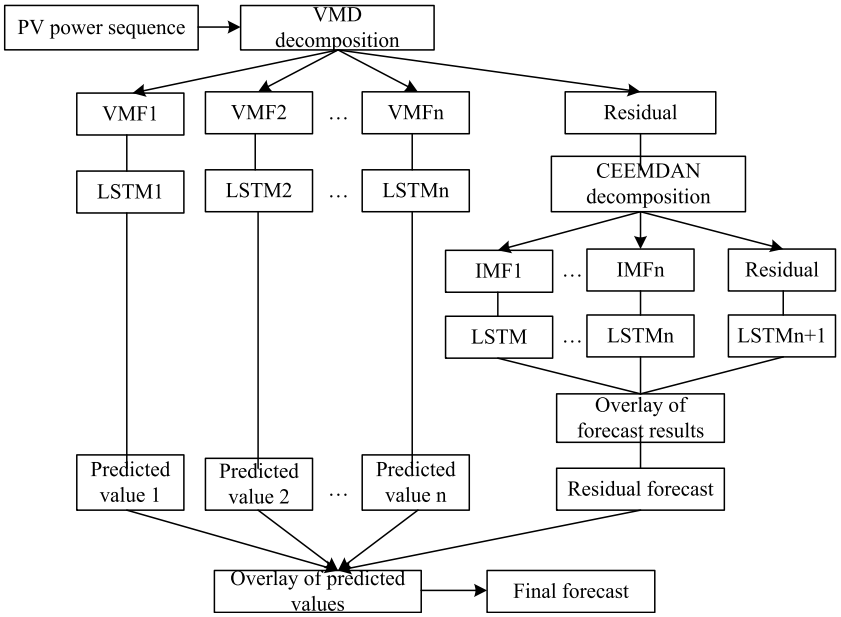

FIGURE 1 | VMD-CEEMDAN-LSTM model modeling process.

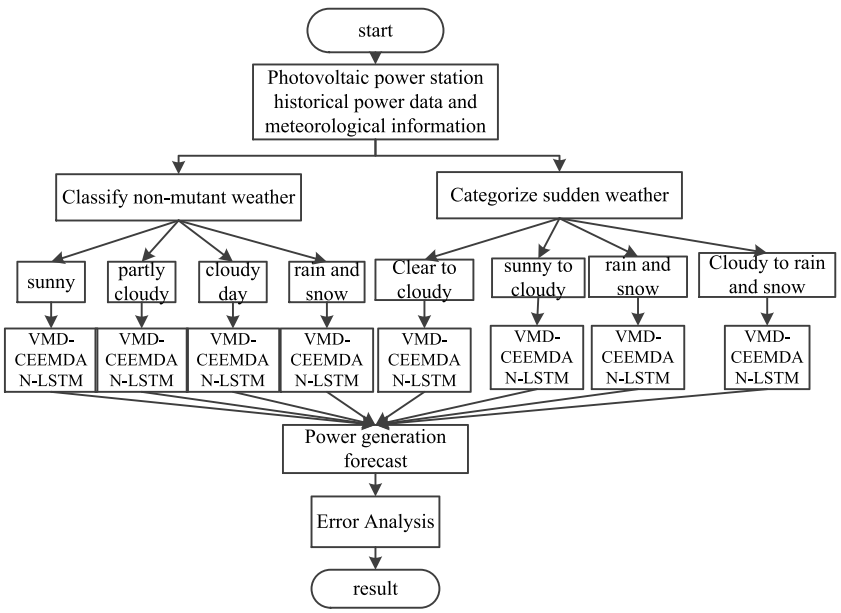

FIGURE 2 | Forecasting process.

$$e\mathrm{TIC} = \frac{\sqrt{\sum_{i=1}^{Z}\left(y'_i - y_i\right)^2}}{\sqrt{\sum_{i=1}^{Z}\left(y'_i\right)^2} + \sqrt{\sum_{i=1}^{Z}\left(y_i\right)^2}}, \tag{19}$$

where Y is the true value of power; Y′ is the predicted value of power; and Z is for sample purpose.

4.2 Non-Abrupt Weather Forecast Model

The photovoltaic power of different weather types is predicted separately, and the prediction process is shown in **Figure 2**. In non-abrupt weather, the output data of historical photovoltaic power plants in sunny, rainy, or cloudy weather are decomposed by VMD, and the residual term generated by VMD decomposition is decomposed by CEEMDAN secondary mode, and all subcomponents are added to meteorological

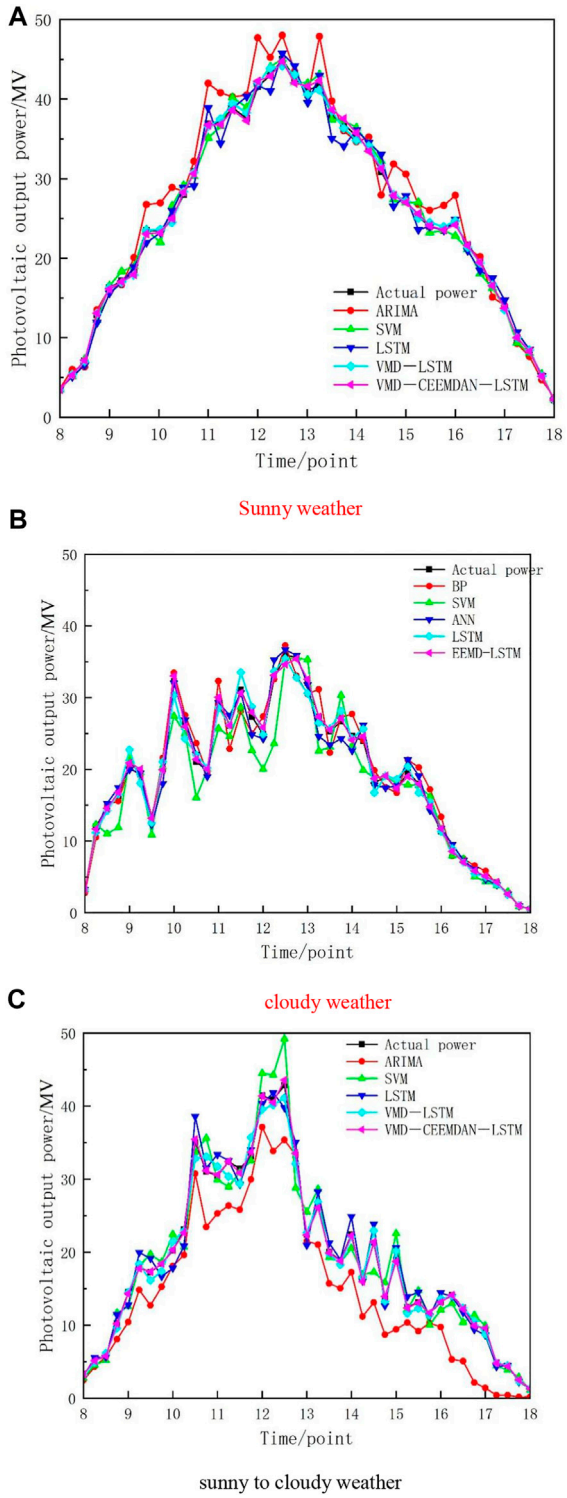

FIGURE 3 | Prediction results of different weather power. **(A)** sunny weather. **(B)** cloudy weather. **(C)** sunny-to-cloudy weather.

conditions and sent to the LSTM network for prediction. Photovoltaic output will fluctuate greatly in abrupt weather, so in abrupt weather forecast, the time of maximum output power in a day (2: 00 p.m.) is selected for decomposition, so that the original complex power sequence becomes a number of stable data sequences, and then meteorological factors are added and sent to LSTM network.

4 EXAMPLE ANALYSIS

4.1 Source of Examples

The historical power data from 2019 to 2020 of photovoltaic power stations with an installed capacity of 50 MW in the Inner Mongolia Autonomous Region are selected as samples to verify the validity of the VMD-CEEMDAN-LSTM model. The 71-day weather conditions are as follows: 265 days of sunny weather, 63 days of cloudy weather, 93 days of cloudy weather, 115 days of rain and snow, and 195 days of abrupt weather. Taking sunny, cloudy, and sunny-to-cloudy weather as examples, the days of training and testing samples are 221 and 44 days in sunny weather, 52 and 11 days in cloudy weather, and 21 and 4 days in sunny-to-cloudy weather.

4.2 Forecast Results

In sunny weather, the photovoltaic output prediction results are shown in **Figure 3A**, and the model evaluation results are shown in **Table 1**. In sunny weather, the fluctuation of photovoltaic output is small. In **Figure 3A**, it can be clearly observed that the prediction accuracy of the ARIMA model is insufficient, resulting in large errors, and the prediction effects of other models are better than those of the ARIMA model. Compared with ARIMA and SVM, the evaluation indexes of the three non-combination forecasting models show that the e_{MAPE} value of the LSTM model

TABLE 1 | Prediction error of different weather powers.

Type	Model	e_{MAPE}	e_{RMSE}	e_{TIC}
Sunny day	ARIMA	0.560	167.661	0.060
	SVM	0.477	135.637	0.053
	LSTM	0.375	102.516	0.040
	VMD-LSTM	0.304	82.444	0.028
	VMD-CEEMDAN-LSTM	0.203	62.884	0.019
Cloudy	ARIMA	0.554	222.537	0.257
	SVM	0.557	171.678	0.181
	LSTM	0.391	122.826	0.146
	VMD-LSTM	0.269	89.539	0.117
	VMD-CEEMDAN-LSTM	0.229	76.207	0.092
Clear and cloudy	ARIMA	0.684	258.058	0.322
	SVM	0.539	189.926	0.234
	LSTM	0.393	154.410	0.185
	VMD-LSTM	0.256	105.978	0.127
	VMD-CEEMDAN-LSTM	0.189	89.058	0.116

decreases by 0.185 and 0.102 respectively, the e_{RMSE} value decreases by 65.145 and 33.121, respectively, and the e_{TIC} value decreases by 0.02 and 0.013, respectively. The evaluation index can clearly show that the deep learning method can mine more features of photovoltaic data and is more suitable for the prediction of nonlinear and non-stationary data. According to the data in **Table 1**, e_{MAPE}, $e_{RMSE,}$ and e_{TIC} of the VMD-CEEMDAN-LSTM prediction model are the smallest, and at noon, when the photovoltaic power curve fluctuates, the VMD-CEEMDAN-LSTM power prediction curve still keeps a high degree of fit with the real power curve.

In cloudy weather, the forecast results are shown in **Figure 3B**. Compared with sunny weather, cloudy weather reduces photovoltaic power due to the blocking effect of clouds on the Sun's rays. Due to the change in cloud thickness, the photovoltaic power curve also fluctuates greatly. At this time, the predicted value of ARIMA model and SVM model has a big deviation from the real value, and the model accuracy decreases. On 4 May 2019 compared with ARIMA, SVM, and LSTM, the e_{MAPE} value of VMD-LSTM model decreased by 0.285, 0.288, and 0.122 respectively, and that of VMD-CEEMDAN-LSTM model decreased by 0.325, 0.328, and 0.162 respectively. The VMD-LSTM model and the VMD-CEEMDAN-LSTM model reduces the complexity of data series and the influence of data fluctuation through variational modal decomposition.

The forecast result of photovoltaic output in sunny weather is shown in **Figure 3C**. When the weather suddenly changes, because the complexity of photovoltaic power series increases, the predicted values of ARIMA, SVM, and LSTM have a high degree of dispersion with the real values, so the prediction accuracy is limited and the accuracy is difficult to guarantee. Comparing the error evaluation indexes, it can be seen that the VMD-CEEMDAN-LSTM model still maintains the highest prediction accuracy. On 13 August 2020, its e_{MAPE} value decreased by 0.204 and 0.067 compared with the LSTM and VMD-LSTM models.

In order to further highlight the accuracy of the proposed method, this article makes statistics on the test results of all test samples in the power station within 2 years. The errors of VMD-LSTM and VMD-CEEMD-LSTM were counted. Compared with the VMD-LSTM model, the e_{RMSE}, $e_{MAPE,}$ and e_{TIC} of the VMD-CEEMDAN-LSTM model decreased by 0.104, 16.596, and 0.038, respectively. The accuracy of the model is obviously improved after the second decomposition of the residual term obtained by VMD decomposition.

5 CONCLUSION

In order to further predict the accuracy of photovoltaic power, this article proposed a model combining modal decomposition with deep learning algorithm and built ARIMA, SVM, LSTM, and VMD-LSTM models to compare their errors with the proposed models. The main conclusions are as follows:

(1) In data processing, VMD decomposition and CEEMDAN secondary decomposition of residual terms greatly improve the prediction accuracy compared with the traditional non-combination prediction model
(2) The second CEEMDAN decomposition of the residual term obtained by VMD decomposition can fully improve the complex features of the residual term, which makes the e_{RMSE}, $e_{MAPE,}$ and e_{TIC} of the VMD-CEEMDAN-LSTM model lower than those of the VMD-LSTM model by 0.104, 16.596, and 0.038, respectively, and the prediction accuracy of the VMD-CEEMDAN-LSTM model is obviously higher than that of the VMD-LSTM model

DATA AVAILABILITY STATEMENT

The raw data supporting the conclusion of this article will be made available by the authors, without undue reservation.

AUTHOR CONTRIBUTIONS

SW and SL conceived the idea and designed the experiments. The experiments were led by XG, while SW contributed to data analysis and interpretation along with writing the manuscript. All authors read and approved the final manuscript.

REFERENCES

Abdel-Nasser, M., and Mahmoud, K. (2019). Accurate Photovoltaic Power Forecasting Models Using Deep LSTM-RNN[J]. *Neural Comput. Appl.* 31 (7), 2727–2740. doi:10.1007/s00521-017-3225-z

Alzahrani, A., Shamsi, P., Dagli, C., and Ferdowsi, M. (2017). Solar Irradiance Forecasting Using Deep Neural Networks. *Procedia Comput. Sci.* 114, 304–313. doi:10.1016/j.procs.2017.09.045

Chang, G. W., and Lu, H. J. (2018). Integrating Grey Data Preprocessor and Deep Belief Network for Day-Ahead PV Power Output Forecast[J]. *IEEE Trans. Sustain. Energy* 11 (1), 185–194. doi:10.1109/tste.2018.2888548

Changwei, L., Jinghua, L., Bo, C., et al. (2019). Summary of Research on Photovoltaic Power Generation Output Prediction Technology[J]. *J. Electrotech. Technol.*,34 (06), 1201–1217.

Chiang, C-H., and Young, C-H. (2022). An Engineering Project for a Flood Detention Pond Surface-type Floating Photovoltaic Power Generation System with an Installed Capacity of 32,600.88 kWp. *Energy Rep.* 8, 2219–2232. doi:10.1016/j.egyr.2022.01.156

Chiteka, K., and Enweremadu, C. C. (2016). Prediction of Global Horizontal Solar Irradiance in Zimbabwe Using Artificial Neural Networks. *J. Clean. Prod.* 135 (Complete), 701–711. doi:10.1016/j.jclepro.2016.06.128

Ding, Y. (2021). Research on Microgrid System Optimization Considering Wind and Light Prediction [D]. Dissertaion. Beijing, China: Beijing Jiaotong University.

Gao, M., Li, J., Hong, F., and Long, D. (2019). Short-Term Forecasting of Power Production in a Large-Scale Photovoltaic Plant Based on LSTM. *Appl. Sci.* 9 (15), 3192. doi:10.3390/app9153192

Ghimire, S., Deo, R. C., Downs, N. J., and Raj, N. (2019). Global Solar Radiation Prediction by ANN Integrated with European Centre for Medium Range Weather Forecast Fields in Solar Rich Cities of Queensland Australia[J]. *J. Clean. Prod.* 216, 288–310. doi:10.1016/j.jclepro.2019.01.158

Hassan, M. A., Bailek, N., Bouchouicha, K., and Nwokolo, S. C. (2021). Ultra-short-term Exogenous Forecasting of Photovoltaic Power Production Using

Genetically Optimized Non-linear Auto-Regressive Recurrent Neural Networks [J]. *Renew. Energy* 171, 191–209. doi:10.1016/j.renene.2021.02.103

Jang, H. S., Bae, K. Y., Park, H. S., and Sung, D. K. (2016). Solar Power Prediction Based on Satellite Images and Support Vector Machine[J]. *IEEE Trans. Sustain. Energy* 7 (3), 1255–1263. doi:10.1109/tste.2016.2535466

Le, S., Wu, Y., Guo, Y., and Vecchio, C. D. (2021). Game Theoretic Approach for a Service Function Chain Routing in NFV with Coupled Constraints. *IEEE Trans. Circuits Syst. II* 68, 3557–3561. Published online. doi:10.1109/TCSII.2021.3070025

Li, H., Deng, J., Feng, P., Pu, C., Arachchige, D. D. K., and Cheng, Q. (2021). Short-Term Nacelle Orientation Forecasting Using Bilinear Transformation and ICEEMDAN Framework. *Front. Energy Res.* 9, 780928. doi:10.3389/fenrg.2021.780928

Li, H., Deng, J., Yuan, S., Feng, P., and Arachchige, D. D. K. (2021). Monitoring and Identifying Wind Turbine Generator Bearing Faults Using Deep Belief Network and EWMA Control Charts. *Front. Energy Res.* 9, 799039. doi:10.3389/fenrg.2021.799039

Ma, T., Yang, H., and Lu, L. (2014). Solar Photovoltaic System Modeling and Performance Prediction. *Renew. Sustain. Energy Rev.* 36, 304–315. doi:10.1016/j.rser.2014.04.057

Mellit, A., Kalogirou, S. A., and Drif, M. (2010). Application of Neural Networks and Genetic Algorithms for Sizing of Photovoltaic Systems. *Renew. Energy* 35 (12), 2881–2893. doi:10.1016/j.renene.2010.04.017

Meng, A., Chen, J., Li, Z., et al. (2021). Short-Term Photovoltaic Power Prediction Based on Similar Day Theory and CSO-WGPR[J]. *High. Volt. Technol.* 47 (04), 1176–1184.

Mohammadi, K., Shamshirband, S., Tong, C. W., Arif, M., Petković, D., and Ch, S. (2015). A New Hybrid Support Vector Machine-Wavelet Transform Approach for Estimation of Horizontal Global Solar Radiation[J]. *Energy Convers. Manag.* 92 (Mar), 162–171. doi:10.1016/j.enconman.2014.12.050

Sohani, A., Shahverdian, M. H., Sayyaadi, H., Hoseinzadeh, S., and Memon, S. (2021). Enhancing the Renewable Energy Payback Period of a Photovoltaic Power Generation System by Water Flow Cooling. *Int. J. Sol. Therm. Vac. Eng.* 3 (1), 73–85. doi:10.37934/stve.3.1.7385

Toyoda, M., and Wu, Y. (2021). Mayer-type Optimal Control of Probabilistic Boolean Control Network with Uncertain Selection Probabilities. *IEEE Trans. Cybern.* 51, 3079–3092. (Regular Paper). doi:10.1109/tcyb.2019.2954849

Wang, H., Liu, Y., Zhou, B., Li, C., Cao, G., Voropai, N., et al. (2020). Taxonomy Research of Artificial Intelligence for Deterministic Solar Power Forecasting. *Energy Convers. Manag.* 214, 112909. doi:10.1016/j.enconman.2020.112909

Wang, X., Luo, D., Sun, Y., et al. (2020). Research on the Combination Forecasting Method of Daily Power Generation of Photovoltaic Microgrid Based on ABC-SVM and PSO-RF[J]. *J. Sol. Energy* 41 (03), 177–183.

Wu, Y., Guo, Y., and Toyoda, M. (2021). Policy Iteration Approach to the Infinite Horizon Average Optimal Control of Probabilistic Boolean Networks. *IEEE Trans. Neural Netw. Learn Syst.* 32 (6), 2910–2924. (Regular Paper). doi:10.1109/TNNLS.2020.3008960

Yang, L., Gao, X., Jiang, J., et al. (2020). Short-Term Power Prediction of Photovoltaic Power Station Based on Wavelet Transform and Neural Network[J]. *J. Sol. Energy* 41 (07), 152–157.

Yao, G. (2014). Design of Photovoltaic Grid-Connected Power Generation System and Research on MPPT Technology[D]. Dissertation. Hangzhou, China: Zhejiang University.

Ye, L., Ma, M., Jin, J., et al. (2021). Factor Analysis Considering the Correlation between Wind Power and Photovoltaic Power-Extreme Learning Machine Aggregation Method[J]. *Power Syst. Autom.* 45 (23), 31–40.

Yuan, Q., Zhao, B., Wang, L., et al. (2021). Photovoltaic Multi-Peak MPPT Control Based on TSA-P&O Hybrid Algorithm[J]. *Power Syst. Acta AutomaticaSinica)* 33 (12), 101–109.

Zang, H., Cheng, L., Ding, T., Cheung, K. W., Liang, Z., Wei, Z., et al. (2018). Hybrid Method for Short-Term Photovoltaic Power Forecasting Based on Deep Convolutional Neural Network[J].*IET Generation,Transmission,Distribution* 12 (20), 4557–4567. doi:10.1049/iet-gtd.2018.5847

Zhou, H., Zhang, Y., Yang, L., Liu, Q., Yan, K., and Du, Y. (2019). Short-Term Photovoltaic Power Forecasting Based on Long Short Term Memory Neural Network and Attention Mechanism. *IEEE Access* 7 (99), 78063–78074. doi:10.1109/access.2019.2923006

Conflict of Interest: The authors declare that the research was conducted in the absence of any commercial or financial relationships that could be construed as a potential conflict of interest.

Publisher's Note: All claims expressed in this article are solely those of the authors and do not necessarily represent those of their affiliated organizations, or those of the publisher, the editors, and the reviewers. Any product that may be evaluated in this article, or claim that may be made by its manufacturer, is not guaranteed or endorsed by the publisher.

frontiers | Frontiers in Energy Research

BRIEF RESEARCH REPORT
published: 15 July 2022
doi: 10.3389/fenrg.2022.944961

Research on the Rotor Fault Diagnosis Method Based on QPSO-VMD-PCA-SVM

Lu Wang[1,2,3], *Hui Liu*[3,4,5]*, *Jie Liang*[1,2,3], *Lijuan Zhang*[1,2,3], *Qingchang Ji*[1,2,3] and *Jianqiang Wang*[1,2,3]

[1]Hebei University of Water Resources and Electric Engineering, Cangzhou, China, [2]Water Resources Automation and Informatization Application Technology Research and Development Center of Hebei Colleges, Cangzhou, China, [3]Department of Mechanical Engineering, Hebei Institute of Water Conservancy and Electric Power, Cangzhou, China, [4]Hebei Industrial Manipulator Control and Reliability Technology Innovation Center, Cangzhou, China, [5]Cangzhou Industrial Manipulator Control and Reliability Technology Innovation Center, Cangzhou, China

The rotor system is a core part of rotating machinery equipment. Its safe and reliable operation directly affects the economic benefit of using the equipment and the personal safety of users. To fully explore the complex feature mapping relationship between rotor vibration signals and fault types, rotor vibration signals were studied under different working conditions from the perspective of feature parameter construction and feature information mining. First, a variational mode decomposition algorithm was used to decompose the vibration signals, and quantum behavior particle swarm optimization was used to minimize the mean envelope entropy of intrinsic mode function components to determine the optimal combination of modal number and penalty coefficient. Second, the principal component analysis was used to reduce the dimensionality of IMF components of vibration signals. Finally, a support vector machine was used to mine the feature mapping relationship between vibration data after dimensionality reduction and rotor operation state to accurately identify rotor fault types. The proposed method was used to analyze the measured vibration signals of the rotor system. The experimental results showed that the proposed method effectively extracted characteristic information of the rotor running state from the vibration data, and the accuracies of four types of fault diagnoses were 100%, 88.89%, 100%, and 100%, respectively. In addition, the accuracies of the four fault diagnoses in this study were better than those of the previously reported models.

Keywords: rotor fault diagnosis, support vector machine, VMD, QPSO, PCA

OPEN ACCESS

Edited by:
Tinghui Ouyang,
National Institute of Advanced Industrial Science and Technology (AIST), Japan

Reviewed by:
Gaurav Sachdeva,
DAV University, India
Gaurav Dhiman,
Government Bikram College of Commerce Patiala, India
Jaspreet Singh,
I. K. Gujral Punjab Technical University, India

***Correspondence:**
Hui Liu
jidianliuh@163.com

Specialty section:
This article was submitted to Smart Grids, a section of the journal Frontiers in Energy Research

Received: *16 May 2022*
Accepted: *06 June 2022*
Published: *15 July 2022*

Citation:
Wang L, Liu H, Liang J, Zhang L, Ji Q and Wang J (2022) Research on the Rotor Fault Diagnosis Method Based on QPSO-VMD-PCA-SVM. Front. Energy Res. 10:944961. doi: 10.3389/fenrg.2022.944961

INTRODUCTION

With the development of large mechanical equipment, motor-driven rotor systems have an important role in the fields of power and industrial control. Their safe and reliable operation state determines the safety and economic benefits of using mechanical equipment. Among all types of faults related to rotating machinery, the most obvious is the abnormal vibration of a rotor system (Liu and Tan, 2022; Miao et al., 2022; Song et al., 2022; Zhang et al., 2022). Therefore, it is important to improve the safe and efficient operation of mechanical equipment to fully explore the relationship between the rotor vibration signal and rotor system operation state. To date, there have been many

in-depth global studies in the field of rotor system fault diagnosis. Shi et al. (2021) analyzed rotor vibration signals from the perspective of time domain, frequency domain, and time-frequency domain, and used a local-global balanced orthogonal discriminant projection algorithm to reduce the high-dimensional features obtained. Luong and Wang (2020) proposed a fault detection method for induction motors based on current harmonic and vibration signals. Experimental results showed that the cooperative use of mechanical vibration and current harmonics effectively improved the accuracy of induction motor fault diagnosis. Hong et al. (2021) proposed a rotor system fault diagnosis model based on a residual neural network for multi-source heterogeneous data fusion. By fully mining the state relationship between multi-sensor heterogeneous monitoring data and the rotor system, the fault diagnosis accuracy was effectively improved.

The vibration signal of a rotor system is nonlinear and non-stationary. It is a key step to improving the accuracy of fault diagnosis by analyzing the characteristic information of signals in time-frequency domains and constructing characteristic parameters that fully represent the rotor operating conditions (Dhiman and Kumar, 2017; Dhiman and Kumar, 2018; Dhiman and Kaur, 2019). In recent years, the rapid development of signal processing technologies such as time domain and frequency domain analysis using the Hilbert transform technique, empirical mode decomposition (EMD), intrinsic time-scale decomposition (ITD), time-frequency analysis methods such as ITD and variational mode decomposition have become research hotspots in the field of fault diagnosis (Vekteris et al., 2020; Chen et al., 2021a; Chen et al., 2021b; Espinoza-Sepulveda and Sinha, 2021). Vekteris et al. (2020) combined EMD with the improved wavelet threshold decomposition method to fully explore the feature mapping relationship between the vibration signals of an aeroengine rotor and the operation status of mechanical equipment. Hu et al. (2021) proposed a fault diagnosis method for planetary gearboxes based on ITD and permutation entropy, and evaluated the fault degree by solving the PE of vibration signals. Dragomiretskiy and Zosso (2014) proposed the variational mode decomposition (VMD) analysis method to better solve the problems of modal aliasing and adaptive failure in time-frequency domain analysis methods such as EMD and wavelet analysis. Wang et al. (2015) proposed a VMD-based multi-friction vibration signal analysis method, which effectively improved the diagnostic accuracy of rotor and stator friction faults in rotating equipment. Experimental results showed that the VMD signal decomposition method better characterized the characteristic information of vibration signals compared with other time-frequency domain signal analysis methods. However, the above vibration signal analysis method ignored the influence of signal noise on fault characteristic information, and modal aliasing was common during signal decomposition, which led to a poor generalization performance of subsequent fault diagnosis models.

Therefore, to further improve the rotor fault diagnosis accuracy in rotating systems, rotor vibration signals were studied from the perspective of feature parameter construction and feature information mining and a rotor fault diagnosis model based on quantum behavior particle swarm optimization (QPSO)-VMD-PCA-support vector machine (SVM) was proposed. Considering that the rotor vibration signal was unstable and susceptible to noise, VMD was used to decompose the vibration signal, and the QPSO algorithm was used to optimize the number of modes and penalty coefficient of VMD to minimize the mean value of the intrinsic mode envelope entropy. Then, PCA was used to solve the variance contribution rate of the high-dimensional vibration signal features composed of each IMF-*i* component, and the feature compression of the vibration signal was realized based on this. Then, an SVM-based rotor fault diagnosis model was constructed based on the preprocessed vibration signal data set. Finally, the proposed rotor fault diagnosis method was compared with back propagation neural network (BPNN), extreme learning machine (ELM), and SVM under different frequency domain analysis methods and feature pretreatment methods to demonstrate its effectiveness.

MATHEMATICAL THEORY

Variational Mode Decomposition

Dragomiretskiy and Zosso (2014) proposed a completely non-recursive signal decomposition method, the VMD algorithm. Compared with signal time-frequency domain analysis methods such as EMD, ensemble empirical mode decomposition (EEMD), and wavelet decomposition, VMD breaks away from the common thinking pattern of progressive recursive decomposition and transforms it into solving constrained variational problems, which can better analyze unbalanced signals and solve modal aliasing and adaptive problems (Liu and Tan, 2022; Miao et al., 2022; Song et al., 2022; Zhang et al., 2022).

Suppose that the original signal a(t) is decomposed into $u_i(t)$, $i = 1, 2, \ldots, K$ by VMD, where $u_i(t)$ represents the ith IMF component. The algorithm implementation steps are as follows:

1) According to the Hilbert change formula, the unilateral spectrum of the Hilbert transformation of modal components is expressed as follows:

$$H_i = \left(\delta(t) + \frac{j}{\pi t}\right) * u_i(t) \tag{1}$$

In the formula, $\delta(t)$ represents the impulse function, H_i represents the Hilbert transformation expression of $u_i(t)$, j represents an imaginary unit, and "*" represents the convolution operation.

2) The frequency spectrum of each mode is moved to the corresponding base band:

$$H_{f_i,i} = \left[\left(\delta(t) + \frac{j}{\pi t}\right) * u_i(t)\right] e^{-j\omega_i t} = H_i e^{-j\omega_i t} \tag{2}$$

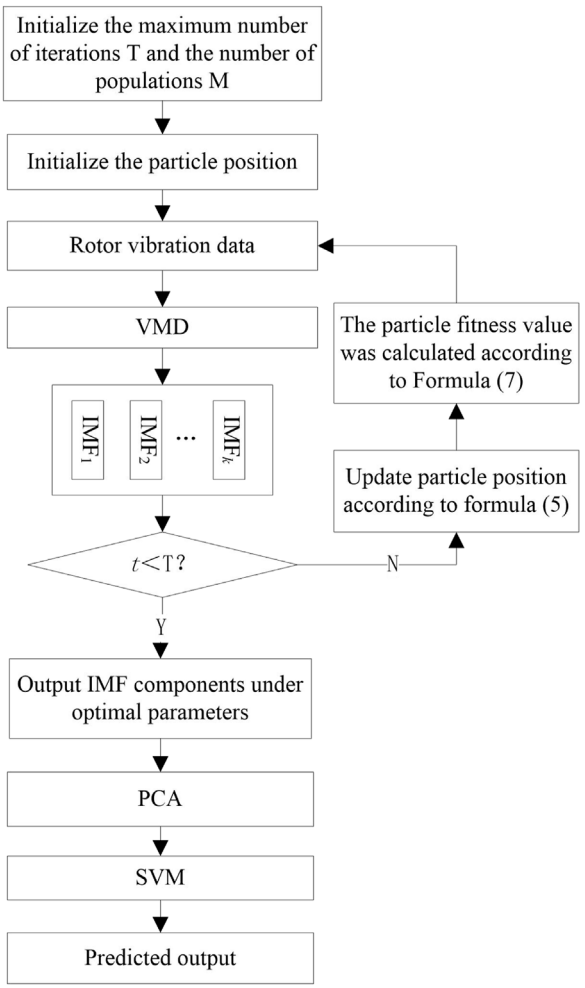

FIGURE 1 | Flow chart of the rotor fault diagnosis model based on the QPSO-VMD-PCA-SVM method.

In the formula, ω_i represents the center angular frequency of the ith mode, and $H_{f_i,i}$ represents the Hilbert transformation expression of shifting the center frequency of H_i to f_i.

3) Demodulation signal $H_{f_i,i}$ has Gaussian smoothness, so the square norm of the gradient can be used to solve the bandwidth of each modal component. The specific calculation method is as follows:

$$\begin{cases} \min\limits_{u_i(t),\omega_i} \sum\limits_{i=1}^{K} \left\| \partial_t \left[\left(\delta(t) + \dfrac{j}{\pi t} \right) * u_i(t) \right] e^{-j\omega_i t} \right\|_2^2 \\ s.t. \quad \sum\limits_{i=1}^{K} u_i(t) = a(t) \end{cases} \tag{3}$$

where ∂_t is the partial derivative with respect to t.

According to the convex optimization theory, to form the above highly nonlinear and non-convex variational problem, the augmented Lagrange function can be obtained:

TABLE 1 | Statistics of the sample number of rotor vibration data.

Fault type	Code	Training set	Test set
Normal	0	36	9
Unbalanced	1	36	9
Misaligned	2	36	9
Rubbing	3	36	9

$$L(\{u_i(t)\},\{\omega_i\},\lambda(t)) = \alpha \sum_{i=1}^{K} \left\| \partial_t \left[\left(\delta(t) + \frac{j}{\pi t} \right) * u_i(t) \right] e^{-j\omega_i t} \right\|_2^2 + \left\| a(t) - \sum_{i=1}^{K} u_i(t) \right\|^2 + < \lambda(t), a(t) - \sum_{i=1}^{K} u_i(t) > \tag{4}$$

where α is the penalty factor and $\lambda(t)$ is the Lagrange factor. The alternating direction method of multipliers was used to solve the variational constraint problem of **Eq. 4** to determine the optimal solution $\{u_i(t)\},\{\omega_i\},\lambda(t)$ of the Lagrange function.

Quantum Behavior Particle Swarm Optimization-Variational Mode Decomposition

Particle swarm optimization (PSO) is a classical meta-heuristic optimization algorithm. In recent years, many studies have shown that the performance of the algorithm is greatly affected by the particle update speed, and even falls into local optimization and fails to converge globally (Luo et al., 2021; Yu et al., 2021). Therefore, van den Bergh and Engelbrecht (2002) integrated the concept of quantum mechanics into the updating process of individual position and proposed a QPSO algorithm. Compared with the PSO algorithm, the QPSO algorithm eliminates the concept of speed and uses **Eq. 5** to update its position, which improves the global search ability and efficiency and accuracy of algorithm optimization to a certain extent.

$$\begin{cases} p_{ij}^t = \varphi_{ij}^t p_{ij}^t + \left(1 + \varphi_{ij}^t\right) G_j^t \\ x_{ij}^{t+1} = p_{ij}^t \pm \beta \left| x_{ij}^t - C_j^t \right| \ln\left(\dfrac{1}{Q}\right) \end{cases} \tag{5}$$

where p_{ij}^t and β are the individual historical optimum and control coefficient, respectively. Q∈ (0,1) represents a random number; C_j^t represents the mean value of individual optimal particles; x_{ij}^t and x_{ij}^{t+1} represent individual positions of particles before and after iteration, respectively; $\varphi_{ij}^t \in (0,1)$ represents a random number; and G_j^t represents the globally optimal individual position iterated to round t.

The decomposition effect of the VMD algorithm is significantly different from that of the number of modes K and the parameter configuration of the penalty coefficient α (Kaur et al., 2020; Dhiman et al., 2021a; Dhiman et al., 2021b). To obtain the best decomposition effect, this paper used the

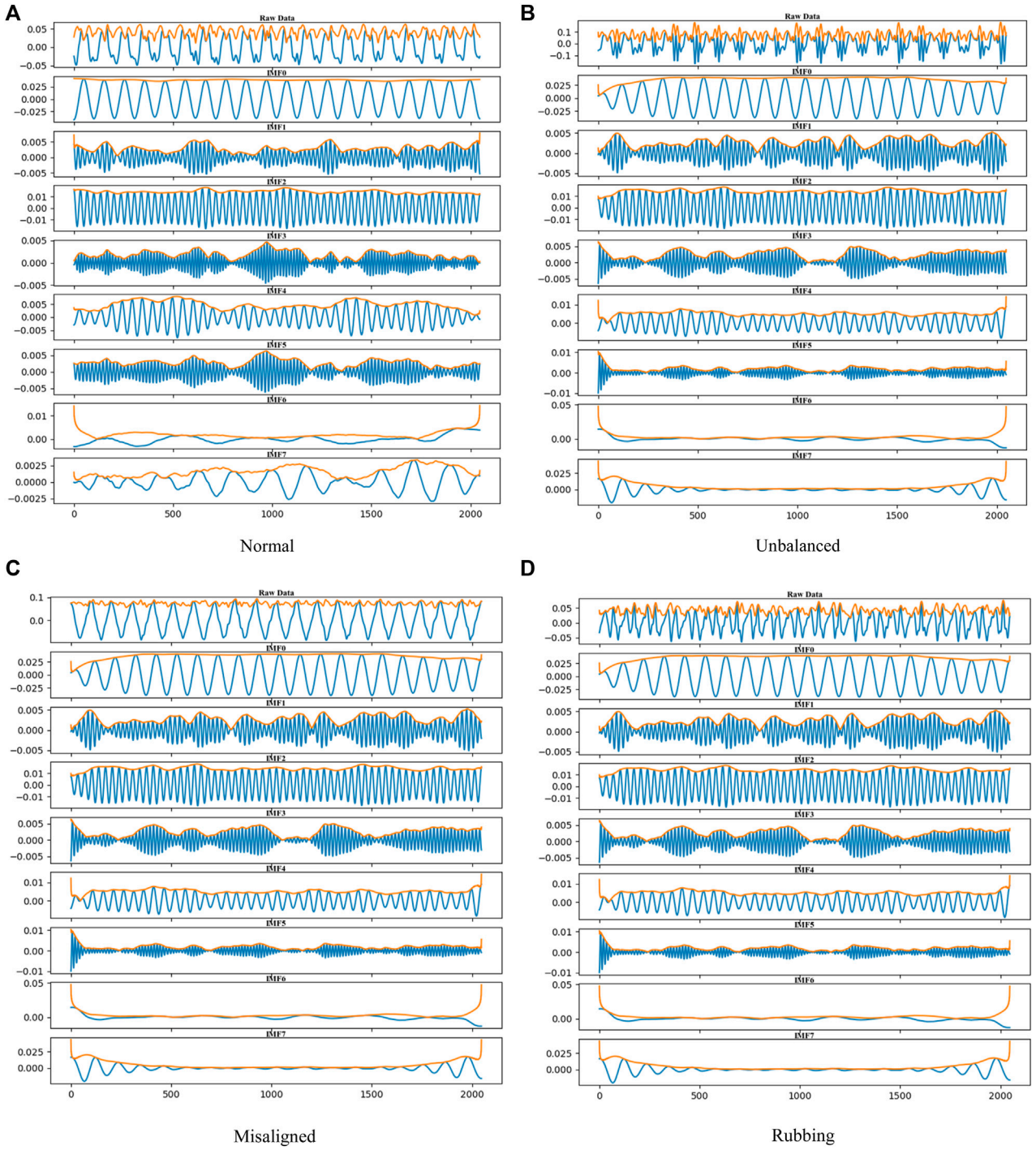

FIGURE 2 | VMD decomposition of various vibration signals. **(A)** Normal. **(B)** Unbalanced. **(C)** Misaligned. **(D)** Rubbing.

QPSO algorithm to optimize the VMD algorithm parameters. Entropy value is an effective method to measure the randomness and complexity of signals (Liu et al., 2020). The more obvious the periodic law of vibration signals, the lower the complexity, and the smaller the entropy value. Therefore, if the IMF component obtained by the VMD algorithm contains more periodic fault characteristic information, the envelope entropy value will be smaller, and the noise interference of the IMF component will be lower. At this point, the IMF component decomposed by the VMD algorithm better represents the characteristic information of the vibration signal, with better robustness.

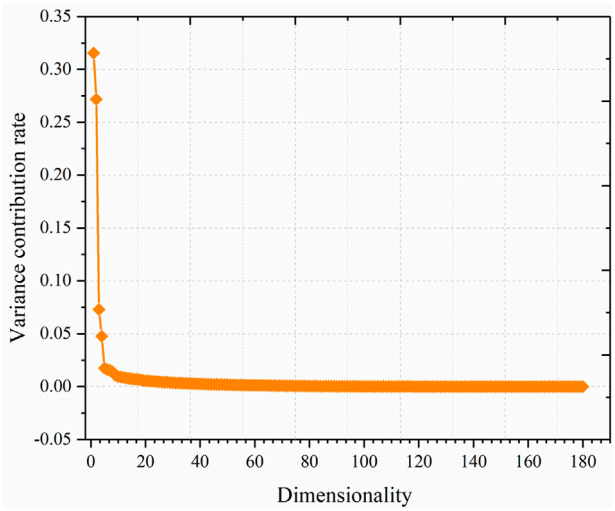

FIGURE 3 | Curve of the characteristic contribution rate.

$$\begin{cases} E_i = -\sum_{i=1}^{N} p_{i,j} \lg p_{i,j} \\ p_{i,j} = b_i(j) \Big/ \sum_{j=1}^{N} b_i(j) \end{cases} \tag{6}$$

Eq. 6 shows the formula used to solve the envelope entropy of the IMF component after Hilbert demodulation, where E_i represents the envelope entropy value; $b_i(j)$ represents the envelope function of IMF-*i*; and $p_{i,j}$ represents the normalized value of $b_i(j)$. As shown in **Eq. 7**, we used the mean of the *k* IMF component envelope entropy as the fitness function of the QPSO algorithm, and optimized the VMD algorithm parameters by minimizing the IMF component envelope entropy.

$$f = \frac{1}{k} \sum_{i=1}^{k} E_i \tag{7}$$

Support Vector Machines

SVM is a machine learning algorithm with strong classification performance in small sample learning. The essential idea is to use a kernel function to map problems that are not linearly separable to a high-dimensional space and establish a hyperplane in the high-dimensional space to classify the samples (Huang et al., 2020).

SVM can be used for binary classification problems, for example, the sample set $D = \{(x_i, y_i)\}$, $x_i \in \mathbb{R}^d$, $y_i \in \{-1, 1\}$, $i = 1, 2, \ldots n$, where y_i represents the label of the sample, D represents the dimension of the sample, and n represents the number of samples. The mathematical model expression of SVM is shown in **Eq. 8**:

$$\begin{aligned} &\min_{\omega,b} \frac{||\omega||^2}{2} + C\sum_{i=1}^{m} \varepsilon_i \\ &\text{s.t. } y_i\left(\omega^{\mathrm{T}} x_i + b\right) \geq 1 - \varepsilon_i,\ i = 1, 2, \ldots n. \\ &\varepsilon_i \geq 0,\ i = 1, 2, \cdots n. \end{aligned} \tag{8}$$

To improve the generalization performance of the SVM algorithm, **Eq. 8** was converted into a dual problem based on convex optimization theory and the kernel method was introduced to obtain **Eq. 9**:

$$\begin{aligned} &\max_{\alpha} \sum_{i=1}^{m} \alpha_i - \frac{1}{2}\sum_{i=1}^{m}\sum_{j=1}^{m} \alpha_i \alpha_j y_i y_j K\left(x_i, x_j\right) \\ &\text{s.t. } \sum_{i=1}^{m} \alpha_i y_i = 0, \\ &0 \leq \alpha_i \leq C,\ i = 1, 2, \cdots, m. \end{aligned} \tag{9}$$

where α_i is the Lagrange multiplier and $K(x_i, x_j)$ is the kernel function.

Principal Component Analysis

PCA is a common dimensionality reduction method for the pre-processing of high-dimension feature data. It achieves the compression of feature data by calculating a covariance matrix and correlation coefficient for orthogonal change and finally obtains mutually independent principal components (Fattoh and Safwat, 2022; Jamal et al., 2022). The characteristic compression mathematical expression of PCA for original data D is shown as follows:

$$Y_i = a_{i1}\mathbf{d}_1 + a_{i2}\mathbf{d}_2 + \ldots + a_{ip}\mathbf{d}_p = \mathbf{A}_i^T \mathbf{D} \tag{10}$$

where $\mathbf{A}_i = [a_{i1}, a_{i1}, \ldots, a_{ip}]^{\mathrm{T}}$ is the characteristic vector corresponding to the covariance matrix, and Y_i is the principal component after orthogonal change. Each principal component compressed by the PCA algorithm corresponds to

TABLE 2 | Accuracy statistics of different fault diagnosis methods.

	QPSO-VMD-PCA-SVM (K = 8, α = 5016.8)	QPSO-VMD (%) (K = 8, α = 5016.8)			EMD-PCA		
		ELM (%)	BPNN (%)	SVM (%)	ELM (%)	BPNN (%)	SVM (%)
0	100	88.89	88.89	77.78	88.89	77.78	100
1	88.89	88.89	88.89	100	77.78	88.89	88.89
2	100	100	88.89	100	100	100	88.89
3	100	100	100	100	100	100	100
Acc	97.22	94.44	91.67	94.44	91.67	91.67	94.44

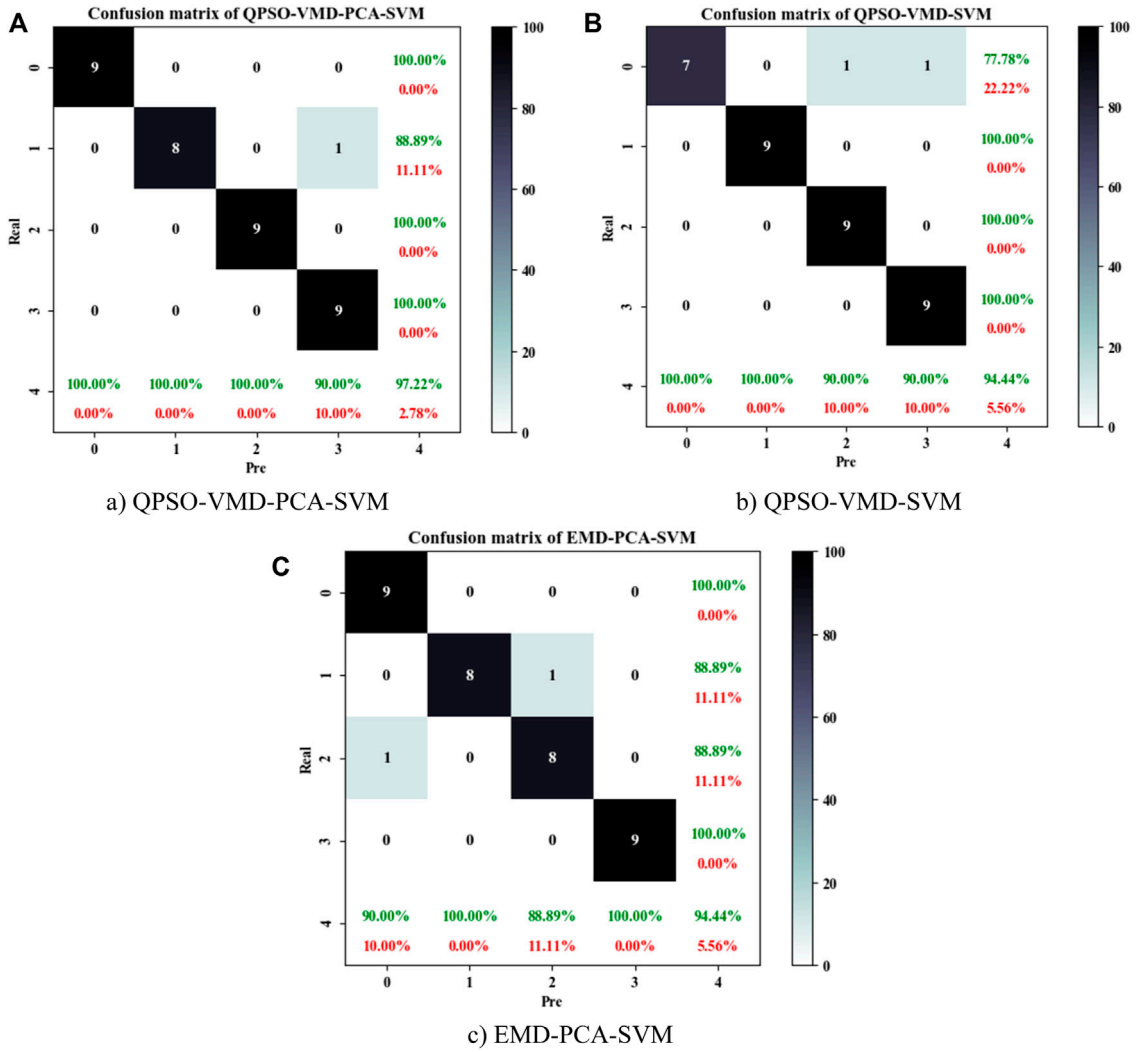

FIGURE 4 | Confusion matrix of the rotor fault diagnosis model under different signal processing methods. **(A)** QPSO-VMD-PCA-SVM. **(B)** QPSO-VMD-SVM. **(C)** EMD-PCA-SVM.

variance in the original data. The sum of the total variances is equal to the sum of the original variables. The ratio of variance to total variance represents the principal component contribution rate.

Rotor Fault Diagnosis Model Based on the Quantum Behavior Particle Swarm Optimization-Variational Mode Decomposition-Principal Component Analysis-Support Vector Machine Method

Considering the influence of the number of modes K and penalty coefficient α on the decomposition effect of the VMD algorithm, the QPSO algorithm was used to optimize the parameters of the VMD algorithm to minimize the envelope entropy. Then, the PCA algorithm was used to compress the IMF components obtained by VMD decomposition under optimal parameters. Finally, the vibration data preprocessed were input into the SVM model to predict the rotor system state. **Figure 1** shows the flow chart of the rotor fault diagnosis model based on the QPSO-VMD-PCA-SVM method in this study. The specific realization steps were as follows:

1) Initialize the maximum iteration time T and population number M of the QPSO algorithm. The maximum number of iterations T in this study was 50. The number of populations was set to 100;
2) Initialize the particle position: the search range of the modal number was (5, 20), and the corresponding dimension data adopted an integer type; the penalty weight search range was (5000, 10000);

3) Configure the VMD algorithm parameters according to individual positions and decompose the rotor vibration data;
4) If the number of iterations $t \leq T$, the particle position and particle fitness values were updated according to **Eq. 5** and **Eq. 7** successively; otherwise, the IMF component of the vibration signal under optimal parameter was output;
5) The PCA algorithm was used to perform feature compression for high-dimensional features with IMF components;
6) Trained the SVM model to predict the rotor fault type.

RESULTS AND DISCUSSION

Introduction of Experimental

The sample data used in this paper were from the open data set of rotor vibration from the state Key Laboratory of Hydraulic Machinery, Ministry of Education of China (Liu et al., 2019; Li et al., 2021a; Li et al., 2021b; Le et al., 2021; Toyoda and Wu, 2021). The sample size of the rotor vibration data set is shown in **Table 1**. There were 180 samples in four rotor system operating states. The original data set was divided into training and test sets at a ratio of 8:2. The experimental platform of the data set simulated the rotor unbalance, dislocation, and friction by controlling the mass block distribution at the edge of the rotor mass disc, the relative position of the two shafts on the coupling, and the contact between the friction screw shell and the rotating bearing. During signal collection, the rotor speed was set to 1200 r/min, the sampling frequency was set to 2048 Hz, and the sampling time length was 1 s.

Analysis of Simulation Results

According to the rotor system fault diagnosis flow chart shown in **Figure 1**, the rotor vibration signal was decomposed by VMD, and then the number of modes K and penalty coefficient α were optimized by the QPSO algorithm. After 50 iterations of the optimization algorithm, the optimal values of the modal number K and penalty coefficient α were 8 and 5016.8, respectively. The VMD algorithm was re-initialized according to the optimal value, and the original vibration signals were decomposed. **Figure 2** shows the original signals and curves of each modal component of the vibration signals of the rotor system under different working conditions. The yellow curve in **Figure 2** represents the envelope entropy curve of each IMF component after Hilbert demodulation. The curve in **Figure 2** shows that the optimized IMF components had a relatively obvious cyclical fluctuation trend in the time domain, and the corresponding envelope entropy curves of each component had good stationarity and uniformity. In addition, the IMF components of the vibration signals of the rotor system under different operating conditions were markedly different. Therefore, the QPSO-VMD algorithm proposed in this paper is feasible for the decomposition of the vibration signals of a rotating subsystem. The IMF component obtained could be used to extract the periodic rules of the vibration signals, and was markedly different under different working conditions, providing greater distinguishing feature information for the subsequent fault diagnosis model.

After the original vibration signal was decomposed by the VMD algorithm, the data dimension of the IMF component obtained was 8 times that of the original signal. To improve the robustness of the fault diagnosis model and reduce the sparsity of data in the high-dimensional space, the PCA algorithm was used to perform feature compression on the decomposed vibration signal. **Figure 3** shows the characteristic contribution rates of each dimension under different characteristic compression scales. The curve in **Figure 3** shows the feature contribution rate was mainly concentrated in feature dimensions 1 to 5, and when the feature dimension exceeded 5, the feature contribution rate tended to be 0. Therefore, this study used the PCA algorithm to compress high-dimensional vibration signals into 5-dimensional data.

To verify the effectiveness of the proposed method, we compared it with ELM, BPNN, and SVM based on different vibration signal decomposition methods, including the QPSO-VMD algorithm and EMD-PCA. **Table 2** shows the fault diagnosis accuracy rate of rotor systems under different fault diagnosis methods. In this study, the accuracy rate of each optimal type is marked in bold. Data in the table show that the proposed method had the highest fault diagnosis accuracy in the normal, dislocation, and friction classes, with accuracy reaching 100%. The overall accuracy of the proposed method was also optimal. Compared with other fault diagnosis methods, the overall accuracy was increased by 5.55%. Compared with various fault diagnosis methods based on the QPSO-VMD algorithm, the proposed method achieved the optimal fault diagnosis performance, which indicates that the proposed PCA algorithm effectively improved the robustness of the fault diagnosis model using high-dimensional IMF component compression. Compared with various fault diagnosis methods based on the EMD-PCA algorithm, the proposed method still achieved optimal results, which indicates that the QPSO-VMD decomposition method had a better performance for the analysis of vibration signals in a rotor system.

Vibration signal feature processing methods directly affect the accuracy of rotor fault diagnosis models, as shown in **Figure 4**, which is an SVM fault diagnosis confusion matrix based on different signal processing methods. By comparing the confusion matrices under different signal processing methods in **Figure 4**, we found that the fault diagnosis effect of the QPSO-VMD-PCA processing method was the best with an accuracy rate of 97.22%.

CONCLUSION

To improve the accuracy of rotor system fault diagnosis, relevant studies were performed from the perspective of characteristic parameter analysis and characteristic information mining of vibration signals. A rotor fault diagnosis method based on

QPSO-VMD-PCA-SVM was proposed, and the main conclusions were as follows:

1) The IMF components obtained by the vibration signal analysis method in this study contained more characteristic information about the periodic laws and showed marked differences in vibration signal components under different working conditions. Compared with the SVM fault diagnosis model based on the QPSO-VMD and EMD-PCA signal analysis methods, the proposed method achieved an optimal effect and its accuracy was improved by 2.78%.
2) The PCA algorithm *i*th was used in this study to compress the high-dimensional features of IMF components, which can reduce the sparsity of small-sample data in the high-dimensional feature space and improve the accuracy of the fault diagnosis model. Compared with the ELM, BPNN, and SVM models based on the QPSO-VMD method, the accuracy of the proposed method was improved by 2.78%, 5.55%, and 2.78%, respectively.

DATA AVAILABILITY STATEMENT

The original contributions presented in the study are included in the article/supplementary material, and further inquiries can be directed to the corresponding author.

AUTHOR CONTRIBUTIONS

LW was responsible for model design and program writing; HL was responsible for data analysis, paper writing and revision; JL and LZ were responsible for the proofreading of the mathematical formula. QJ and JW were responsible for English editing.

FUNDING

This research was supported by the Key Research and Development Program of the Cangzhou Science and Technology Plan (204204003, 213101007).

REFERENCES

Chen, J., Feng, Y., Lu, C., and Fei, C. (2021). Fusion Fault Diagnosis Approach to Rolling Bearing with Vibrational and Acoustic Emission Signals. *Cmes-Computer Model. Eng. Sci.* 129 (2), 1013–1027. doi:10.32604/cmes.2021.016980

Chen, W., Yu, M., and Fang, M. (2021). Research on Identification and Localization of Rotor-Stator Rubbing Faults Based on AF-VMD-KNN. *J. Vib. Eng. Technol.* 9 (8), 2213–2228. doi:10.1007/s42417-021-00357-z

Dhiman, G., Garg, M., Nagar, A., Kumar, V., and Dehghani, M. (2021). A Novel Algorithm for Global Optimization: Rat Swarm Optimizer. *J. Ambient. Intell. Hum. Comput.* 12 (8), 8457–8482. doi:10.1007/s12652-020-02580-0

Dhiman, G., and Kaur, A. (2019). STOA: A Bio-Inspired Based Optimization Algorithm for Industrial Engineering Problems. *Eng. Appl. Artif. Intell.* 82, 148–174. doi:10.1016/j.engappai.2019.03.021

Dhiman, G., and Kumar, V. (2018). Emperor Penguin Optimizer: A Bio-Inspired Algorithm for Engineering Problems. *Knowledge-Based Syst.* 159, 20–50. doi:10.1016/j.knosys.2018.06.001

Dhiman, G., and Kumar, V. (2017). Spotted Hyena Optimizer: A Novel Bio-Inspired Based Metaheuristic Technique for Engineering Applications. *Adv. Eng. Softw.* 114, 48–70. doi:10.1016/j.advengsoft.2017.05.014

Dhiman, G., Oliva, D., Kaur, A., Singh, K. K., Vimal, S., Sharma, A., et al. (2021). BEPO: A Novel Binary Emperor Penguin Optimizer for Automatic Feature Selection. *Knowledge-Based Syst.* 211, 106560. doi:10.1016/j.knosys.2020.106560

Dragomiretskiy, K., and Zosso, D. (2014). Variational Mode Decomposition. *IEEE Trans. Signal Process.* 62 (3), 531–544. doi:10.1109/TSP.2013.2288675

Espinoza-Sepulveda, N., and Sinha, J. (2021). Mathematical Validation of Experimentally Optimised Parameters Used in a Vibration-Based Machine-Learning Model for Fault Diagnosis in Rotating Machines. *Machines* 9 (8), 155. doi:10.3390/machines9080155

Fattoh, I. E., and Safwat, S. (2022). Prediction of Diabetic Obese Patients Using Fuzzy KNN Classifier Based on Expectation Maximization, PCA and SMOTE Algorithms. *Ijacsa* 13 (1), 233–238. doi:10.14569/IJACSA.2022.0130128

Hong, X., Duan, L., and Zhang, L. (2021). Multi-sensor Heterogeneous Data Fusion Method for Rotor System Diagnosis Based on Multi-Mode Residual Network and Discriminant Correlation Analysis. *Meas. Sci. Technol.* 32 (no. 10), 105114. doi:10.1088/1361-6501/ac05f6

Hu, A., Zhu, L., and Xiang, L. (2021). Fault Diagnosis Method of Planetary Gearbox Based on ITD and Permutation Entropy. *China Eng. J.* 19 (06), 542–548. doi:10.15999/j.carolcarrollnki311926.2021.06.010

Huang, X., Huang, X., Wang, B., and Xie, Z. (2020). Fault Diagnosis of Transformer Based on Modified Grey Wolf Optimization Algorithm and Support Vector Machine. *IEEJ Trans. Elec Electron Eng.* 15 (3), 409–417. doi:10.1002/tee.23069

Jamal, M. Z., Lee, D.-H., and Hyun, D. J. (2022). Making a Case for Application of the Unsupervised PCA Algorithm for Simultaneous and Proportional Myoelectric Intention Estimation of Individual Fingers. *IEEE Trans. Instrum. Meas.* 71, 1–12. doi:10.1109/TIM.2022.3152234

Kaur, S., Awasthi, L. K., Sangal, A. L., and Dhiman, G. (2020). Tunicate Swarm Algorithm: A New Bio-Inspired Based Metaheuristic Paradigm for Global Optimization. *Eng. Appl. Artif. Intell.* 90, 103541. doi:10.1016/j.engappai.2020.103541

Le, S., Wu, Y., Guo, Y., and Vecchio, C. D. (2021). Game Theoretic Approach for a Service Function Chain Routing in NFV with Coupled Constraints. *IEEE Trans. Circuits Syst. II* 68, 3557–3561. Published online. doi:10.1109/TCSII.2021.3070025

Li, H., Deng, J., Feng, P., Pu, C., Arachchige, D. D. K., and Cheng, Q. (2021). Short-Term Nacelle Orientation Forecasting Using Bilinear Transformation and ICEEMDAN Framework. *Front. Energy Res.* 9, 780928. doi:10.3389/fenrg.2021.780928

Li, H., Deng, J., Yuan, S., Feng, P., and Arachchige, D. D. K. (2021). Monitoring and Identifying Wind Turbine Generator Bearing Faults Using Deep Belief Network and EWMA Control Charts. *Front. Energy Res.* 9, 799039. doi:10.3389/fenrg.2021.799039

Liu, C., and Tan, J. (2022). An Enhanced Variational Mode Decomposition Based on Correntropy and a Periodicity-Assisted Log-Cycligram for Bearing Fault Diagnosis. *Meas. Sci. Technol.* 33 (6), 065108. doi:10.1088/1361-6501/ac50e5

Liu, D., Xiao, Z., Hu, X., Zhang, C., and Malik, O. P. (2019). Feature Extraction of Rotor Fault Based on EEMD and Curve Code. *Measurement* 135, 712–724. doi:10.1016/j.measurement.2018.12.009

Liu, Y., Chen, C., and Yang, R. (2020). Grounding Fault Location Method of DC System in Substation Based on Wavelet Relative Entropy. *High. Volt. Electr. Equip.* 56 (01), 169–174. doi:10.13296/j.1001-1609.hva.2020.01.025

Luo, J., Shao, Y., Liao, X., Liu, J., and Zhang, J. (2021). Complex Permittivity Estimation for Cloths Based on QPSO Method over (40 to 50) GHz. *IEEE Trans. Antennas Propagat.* 69 (1), 600–605. doi:10.1109/TAP.2020.3005032

Luong, P., and Wang, W. (2020). Smart Sensor-Based Synergistic Analysis for Rotor Bar Fault Detection of Induction Motors. *IEEE/ASME Trans. Mechatron.* 25 (2), 1067–1075. doi:10.1109/TMECH.2020.2970274

Miao, Q., Shu, Q., Wu, B., Sun, X., and Song, K. (2022). A Modified Complex Variational Mode Decomposition Method for Analyzing Nonstationary Signals with the Low-Frequency Trend. *Sensors* 22 (5), 1801. doi:10.3390/s22051801

Shi, M., Zhao, R., Wu, Y., and He, T. (2021). Fault Diagnosis of Rotor Based on Local-Global Balanced Orthogonal Discriminant Projection. *MEASUREMENT* 168, 108320. doi:10.1016/j.measurement.2020.108320

Song, Q., Jiang, X., Wang, S., Guo, J., Huang, W., and Zhu, Z. (2022). Self-Adaptive Multivariate Variational Mode Decomposition and its Application for Bearing Fault Diagnosis. *IEEE Trans. Instrum. Meas.* 71, 1–13. doi:10.1109/TIM.2021.3139660

Toyoda, M., and Wu, Y. (2021). Mayer-type Optimal Control of Probabilistic Boolean Control Network with Uncertain Selection Probabilities. *IEEE Trans. Cybern.* 51, 3079–3092. (Regular Paper). doi:10.1109/tcyb.2019.2954849

van den Bergh, F., and Engelbrecht, A. P. (2002). A New Locally Convergent Particle Swarm Optimiser. *IEEE Int. Conf. Syst. Man Cybern.* 3, 6. doi:10.1109/ICSMC.2002.1176018

Vekteris, V., Trumpa, A., Turla, V., Mokšin, V., Viselga, G., and Jurkonis, E. (2020). Diagnosing Faults in Rolling-Element Bearings of Rotor Systems Equipped with Vibration Dampers. *Adv. Mech. Eng.* 12 (no. 4), 168781402091541. doi:10.1177/1687814020915417

Wang, Y., Markert, R., Xiang, J., and Zheng, W. (2015). Research on Variational Mode Decomposition and its Application in Detecting Rub-Impact Fault of the Rotor System. *Mech. Syst. Signal Process.* 60-61, 243–251. doi:10.1016/j.ymssp.2015.02.020

Wu, Y., Guo, Y., and Toyoda, M. (2021). Policy Iteration Approach to the Infinite Horizon Average Optimal Control of Probabilistic Boolean Networks. *IEEE Trans. Neural Netw. Learn Syst.* 32 (6), 2910–2924. (Regular Paper). doi:10.1109/TNNLS.2020.3008960

Yu, S., Tan, W., Zhang, C., Fang, Y., Tang, C., and Hu, D. (2021). Research on Hybrid Feature Selection Method of Power Transformer Based on Fuzzy Information Entropy. *Adv. Eng. Inf.* 50, 101433. doi:10.1016/j.aei.2021.101433

Zhang, X., Li, D., Li, J., and Li, Y. (2022). Grey Wolf Optimization-Based Variational Mode Decomposition for Magnetotelluric Data Combined with Detrended Fluctuation Analysis. *Acta Geophys.* 70 (1), 111–120. doi:10.1007/s11600-021-00714-2

Conflict of Interest: The authors declare that the research was conducted in the absence of any commercial or financial relationships that could be construed as a potential conflict of interest.

Publisher's Note: All claims expressed in this article are solely those of the authors and do not necessarily represent those of their affiliated organizations, or those of the publisher, the editors, and the reviewers. Any product that may be evaluated in this article, or claim that may be made by its manufacturer, is not guaranteed or endorsed by the publisher.

frontiers | Frontiers in Energy Research

TYPE Review
PUBLISHED 19 July 2022
DOI 10.3389/fenrg.2022.966567

OPEN ACCESS

EDITED BY
Yusen He,
The University of Iowa, United States

REVIEWED BY
KEqiang Zhu,
Ningbo University, China
Xiang Zhu,
Huazhong University of Science and Technology, China

*CORRESPONDENCE
DaPeng Zhang,
1214265737@qq.com

SPECIALTY SECTION
This article was submitted to Smart Grids,
a section of the journal
Frontiers in Energy Research

RECEIVED 11 June 2022
ACCEPTED 30 June 2022
PUBLISHED 19 July 2022

CITATION
Yan J, Mei N, Zhang D, Zhong Y and Wang C (2022), Review of wave power system development and research on triboelectric nano power systems.
Front. Energy Res. 10:966567.
doi: 10.3389/fenrg.2022.966567

Review of wave power system development and research on triboelectric nano power systems

Jin Yan[1,2], Naerduo Mei[1], DaPeng Zhang[1]*, Yinghao Zhong[1] and Cheng Wang[1]

[1]Guangdong Ocean University, Zhanjiang, China, [2]Shenzhen Research Institute of Guangdong Ocean University, Shenzhen, China

With its huge energy storage and high energy density, ocean wave energy is one of the most promising marine renewable resources. Traditional wave energy generation technology, on the other hand, has a high maintenance cost, a bulky construction, and a low conversion efficiency, which limits its application. Due to its low cost, simple construction, and ease of fabrication, wave energy generating technology based on triboelectric nanogenerators has emerged as a potential new power generation technology in recent years. This paper elaborates on the power generation principle, working mode, and the latest research status of wave energy harvesting using different types of triboelectric nanogenerator structures, and finally summarises the current problems and challenges of this technology, and innovatively combines some current examples to propose future research trends, which can help relevant reseach. This will assist researchers in swiftly grasping the present state of wave energy harvesting research and promoting the field's progress.

KEYWORDS

wave energy generation, triboelectric nanogenerators, novel power generation technologies, research trends, power systems

1 Introduction

The development of green energy and the expansion of new energy supply has become a shared objective of the world (Shi and Liu, 2021) in order to alleviate the environmental pollution, global warming, and energy depletion concerns caused by the usage of traditional fossil energy. Wind and ocean power, the main renewable energy sources among them, have been extensively developed worldwide to complement and replace traditional fossil fuels (Li et al., 2021a; Li, 2022a). Because of its green, low-carbon, and clean properties, marine renewable energy has become a new development target. Making full use of marine renewable energy can help to solve not just environmental pollution and other issues, but also promote deep-sea development, national defense forces, and the creation of a strong marine state (Zhao and Zhou, 2013). Wave energy, among the various marine renewable energy sources, has become a focus of study and development because to its large reserves, high energy density, low environmental effect, high quality, and widespread distribution (Figure 1) (Zheng et al., 2014). Traditional wave energy

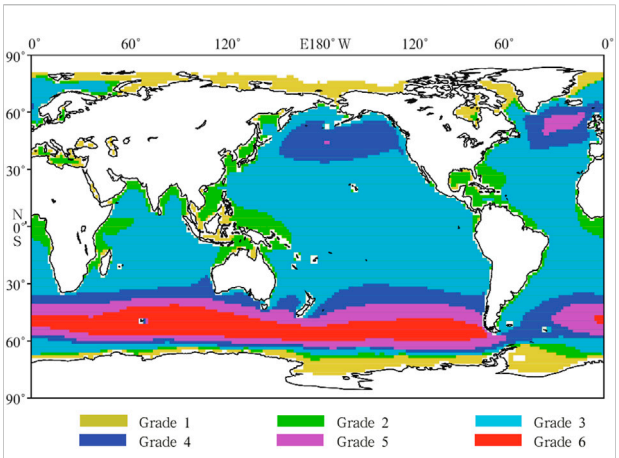

FIGURE 1
Map of the global ocean wave energy resources division (Zheng et al., 2014)

technologies have a restricted use due to high maintenance costs, low conversion efficiency, and inefficient conversion procedures (Xiao et al., 2014a; Ahamed et al., 2020). Due to its low cost, simple structure, and ease of fabrication, a novel wave energy generating technology based on Triboelectric Nanogenerator (TENG) has gotten a lot of interest. This study presents a focused evaluation of the new wave energy generation technology based on TENG by introducing the principle and application status of conventional wave energy generation technology. It then summarizes the technology's current problems and challenges, and suggests future research trends based on some current examples.

2 Status of research on conventional wave energy generation technology

2.1 Types and basic principles of wave energy generation

The Girard father and son in France were the first to be issued a patent for a wave energy conversion device in 1799 (Chen et al., 2020), and since then, patents on the conversion and utilisation of wave energy have increasingly increased. Different classification approaches can be used to categorise wave energy generation. They can be classified as coastal, nearshore (water depth <20 m), or offshore (water depth >40 m) depending on the installation location. They can be classified as oscillating water column, float, pendulum, duck, raft, clam, and contraction ramp, among others, based on the wave energy collection method (Chen R W et al., 2019). According to the power output system they can be divided into direct mechanical drives, hydraulic motor systems, hydro and air turbine delivery systems, direct electric drive systems, triboelectric nanogenerators, and composite systems (Ahamed et al., 2020), which often combine a direct electric drive system and a triboelectric nanogenerator, are the different types of power output systems.

A wave energy harvesting device and a power output system are the most common components of a wave energy producing system. The wave energy harvesting device collects the wave energy, which is then transmitted, stored, and converted by various power output systems till electricity is produced. Traditional wave energy generation technology, as shown in Figure 2, often requires three levels of energy conversion to convert wave energy into electricity, whereas new technologies, such as triboelectricnanogenerators and composite systems, can directly convert wave energy into electricity, which not only eliminates the complicated energy conversion process in between, but also greatly reduces maintenance costs. Because the economic viability, efficiency, and complexity of wave power systems are often determined by their power output systems, it is critical to understand the current state of application and development of various power output systems in the field of wave energy so that the study and deployment of power output systems can be better integrated.

2.2 Current status of conventional wave energy generation technology applications

2.2.1 Wave energy generation technology based on direct mechanical drive systems

A gearbox is often coupled to a generator to drive the generator (shown in Figure 3A), which is used to immediately transform the energy generated by the wave energy converter into electricity. Many investigations on wave energy generation based on direct mechanical drive systems have been conducted recently. For example, Resen Waves (Ahamed et al., 2020) created and developed the Smart Power Buoy, a lightweight and cost-effective wave energy conversion device (shown in Figure 3B). The device is not only easy to build, but it also delivers continuous power and autonomous real-time data connectivity for machines and devices in the water (shown in Figure 3C). Using a clutch and a speed-increasing gearbox, Elisabetta. T (Tedeschi et al., 2010) of the Norwegian University of Science and Technology et al. converted wave energy into electrical energy and investigated the function of irregular waves in the control and design of wave energy conversion devices. The advantage of using a direct drive mechanical system to generate wave energy is that it is more mature and only requires three energy conversions to attain excellent performance. However, the cost, efficiency, and maintenance of the gearbox system limit its application.

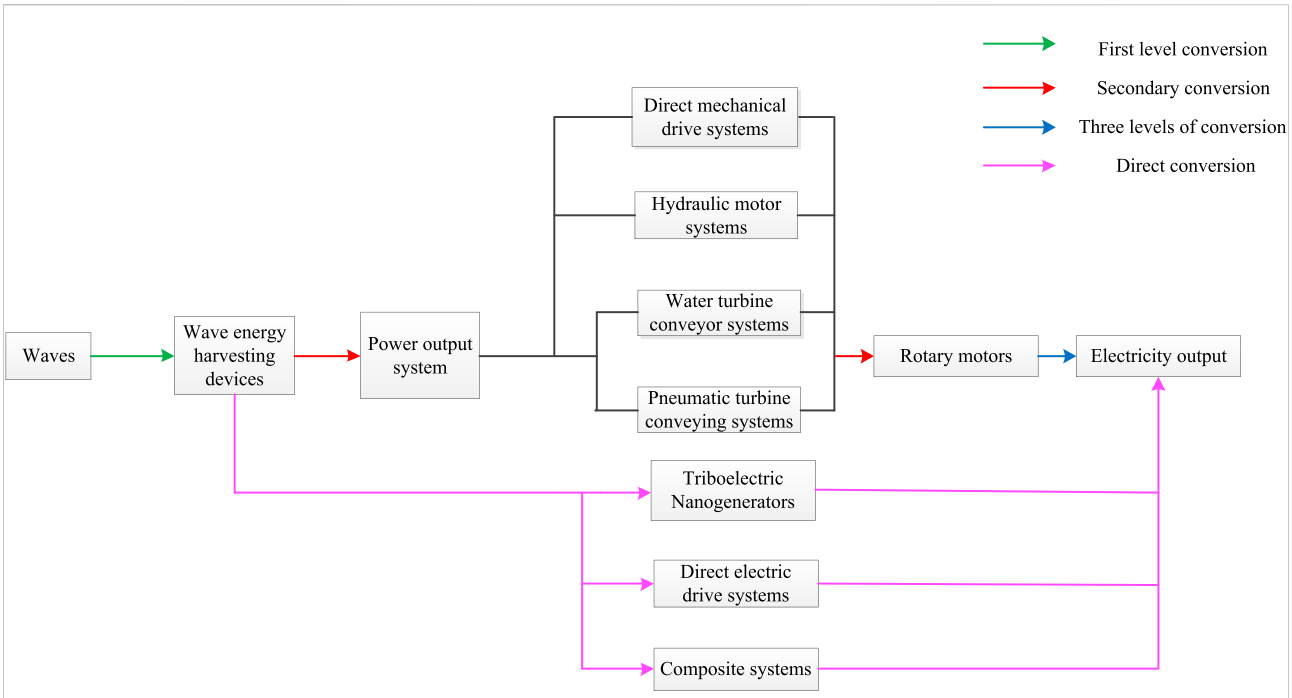

FIGURE 2
Schematic diagram of basic principle of wave energy power generation.

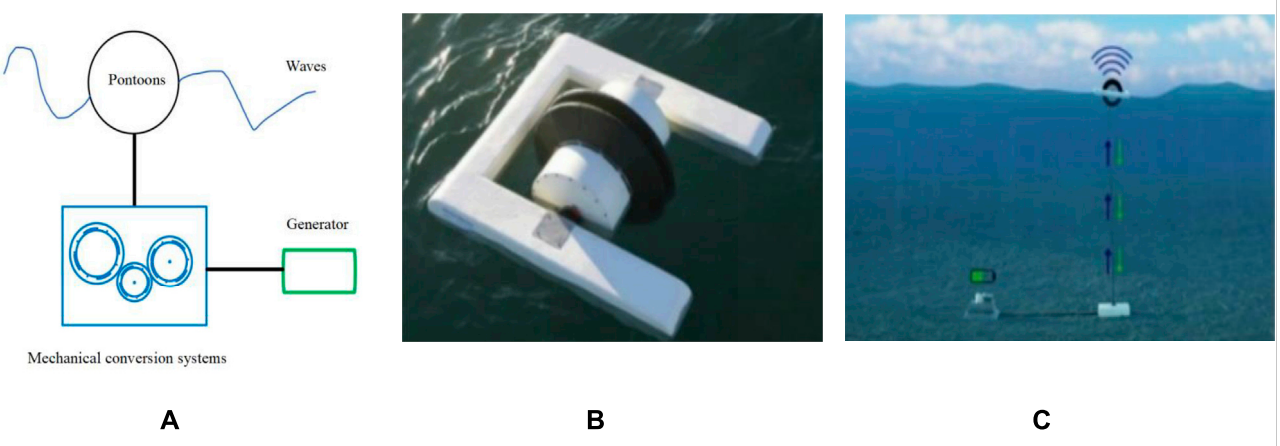

FIGURE 3
(A) Power output system based on direct mechanical drive. **(B)**Physical drawing of intelligent power buoy (Ahamed et al., 2020).**(C)** Schematic diagram of data transmission (Ahamed et al., 2020)

2.2.2 Wave energy generation technology based on hydraulic motor systems

A hydraulic cylinder, a hydraulic motor, an accumulator, and a generator are commonly found in a hydraulic motor-based power output system. The passage of a wave causes the hydraulic cylinder to expand, increasing the pressure of the hydraulic oil, which translates translational or rotational motion into hydraulic energy, which is used to power the hydraulic motor, and then the generator, which generates electricity. The hydraulic system is perfect for generating wave energy because it can apply huge forces at low speeds (Ricci et al., 2011). Wave energy conversion devices include rafts and pendulums, which are the most

FIGURE 4
Pelamis wave energy conversion device (Yemm et al., 2012)

prevalent. The Wave Power Deliver firm (Yemm et al., 2012) has devised a raft-type wave energy conversion device (shown in Figure 4) that should be built at sea in water depths greater than 40 m. Although the raft may be placed in the waves and has good wave resistance, it has not been used in a long time due to its big size, high cost, and easy wear and tear of the hinge parts.

Pendulum wave energy converters can be characterised as near-shore or seafloor (Xiao et al., 2014b) depending on their installation position, as shown in Figures 5A,B. When waves pass by, the pendulum is driven to oscillate by the waves, which causes a hydraulic turbine to work, which drives an electric motor to generate electricity. In 2007, the first prototype pendulum wave roller (shown in Figure 5C) was tested at sea (Lin et al., 2015). In normal sea conditions, the pendulum wave energy converter has the advantages of a wide frequency response, a simple structure, and a high energy conversion efficiency. However, it has drawbacks such as the mechanical element being prone to seawater contact, difficult maintenance, installation location restrictions, and low reliability (Flocard and Finnigan, 2010).

2.2.3 Wave energy generation technology based on air turbines and hydro transmission systems

Air turbine transmission systems are typically used for the oscillating water column type, as shown in Figure 6A. The forced vibration of the water column through the air chamber squeezes the air, converting it into compressive and kinetic energy, and the pressurised air flows through a turbine attached to the generator, driving the generator to generate electricity (Cai and Wang, 2012). The Japan Marine Science and Technology Centre's Yoshio Masuda (Falcão and Henriques, 2016) created a big barge called Kaimei (shown in Figure 6B), which was deployed off the west coast in 1978, and was the first large-scale wave energy conversion device to be deployed at sea.2019 Spain's LaudinoR (Rodríguez et al., 2019) researched a double turbine structure for power generation through enhanced design and discovered that radial turbines are especially ideal for turbine systems and have higher efficiency than axial turbines. 2021 By creating a new oscillating water column wave energy converter based on dielectric elastomers that leverages the deformation of dielectric elastomers to generate electrical energy, Du Xiaozhen et al. (Du et al., 2021) from Shandong University of Science and Technology enhanced the energy conversion efficiency.

Wave energy generating technology based on turbine transmission systems compresses water to drive a turbine, the turbine then drives the generator directly to generate electricity. In 2003, the Danish business Wave Dragon Aps (Kofoed et al., 2006) constructed and erected the world's first offshore wave energy converter, the "Wave Dragon" (shown in Figure 7). Zhang Bu'en (Zhang et al., 2019) from Hehai University created and constructed a new form of floating wave energy generation device in 2019, using hydro-turbine power generation technology, and

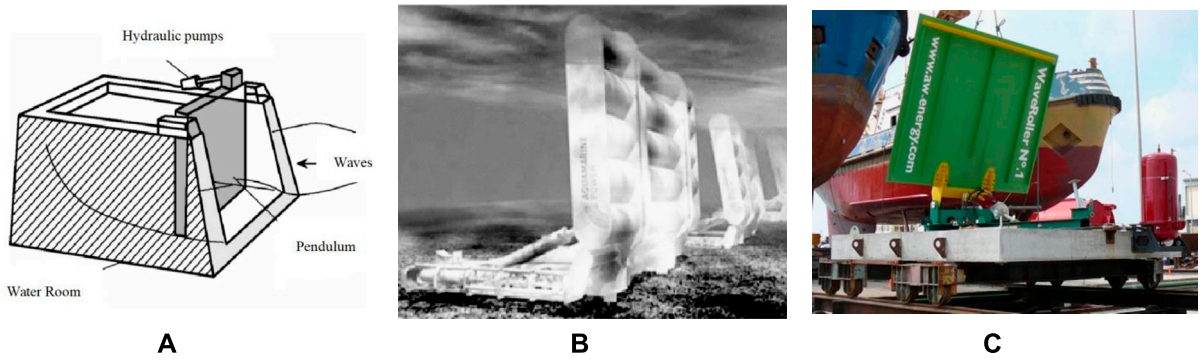

FIGURE 5
Pendulum wave energy conversion device**(A)**The offshore type.**(B)**The seabed type (Xiao et al., 2014b).**(C)**Wave Roller prototype (Lin et al., 2015)

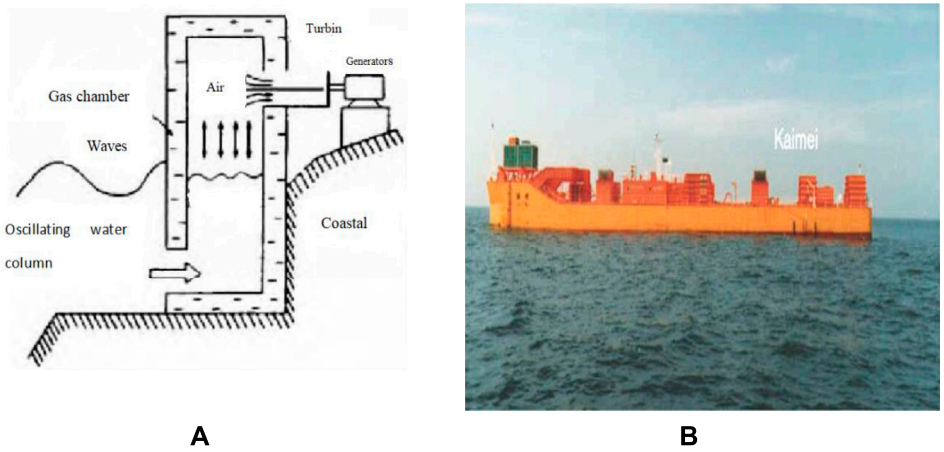

FIGURE 6
Wave energy conversion device with oscillating water column**(A)**Schematic diagram**(B)**Kaimei wave energy conversion device (Falcão and Henriques, 2016)

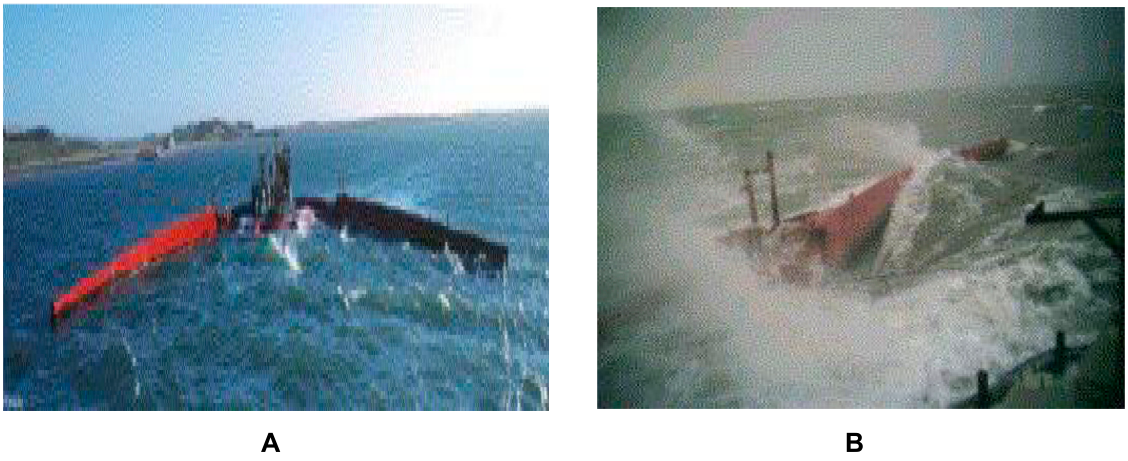

FIGURE 7
Sea dragon prototype**(A)**At the Nissum Bredning test site.**(B)**In big wave conditions (Kofoed et al., 2006).

the power generation efficiency was increased to 73.55 percent by modifying the shape of the float.

2.3 Wave energy generation technology based on direct electric drive systems

A wave energy generation device based on a direct electric drive system has been created and explored to minimize maintenance and reliability issues generated by complex hydraulic and turbine systems (Figure 8A). A linear motor, unlike traditional rotational motors, attaches a converter to a floating buoy, and as a wave passes, the converter, which is made up of permanent magnets, moves up and down with the buoy, generating a magnetic field in the stator coil windings, which provides electrical energy (Drew et al., 2009). There has been an increase in research into direct electric driven wave energy generators in the last 30 years, such as the Archimedes Wave Swing (AWS) (Polinder et al., 2004) in the United Kingdom, which completed its first successful test in Portugal in 2004 (Figure 8B). As the wave passes, the upper end cap moves up and down, squeezing the air between the upper and lower end caps and causing the generator coil connected to the upper end cap and the permanent magnet connected to the lower end cap to

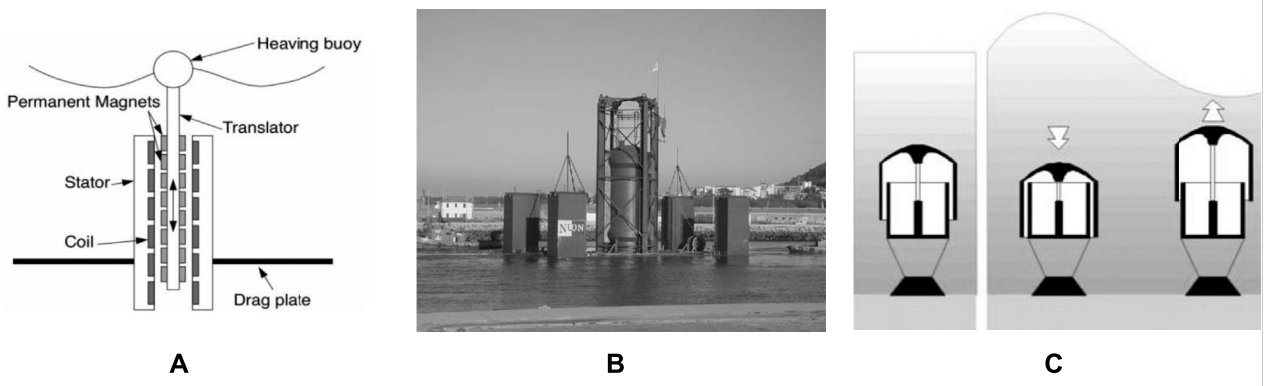

FIGURE 8
(A) Power take-off system based on direct electric drive.**(B)**AWS prototype.**(C)**Working principle diagram of AWS (Polinder et al., 2004).

move relative to each other, converting the wave energy into electrical energy (Figure 8C).

3 Triboelectric nanogenerator fundamentals

Professor Zhonglin Wang and colleagues at Georgia Tech proposed triboelectric nanogenerators (TENG) in 2012 to convert mechanical energy into electrical energy using a combination of triboelectric initiation and electrostatic induction (Wang, 2013; Wu et al., 2019). TENG is increasingly being used for energy harvesting and self-energy supply monitoring due to its many advantages, including low cost, easy manufacturing, high power density, a wide range of material possibilities, and the potential to operate as a self-energy supply sensor (Liu et al., 2015; Zhao et al., 2016; Liu et al., 2018; Wang et al., 2021). TENG has been proven to have substantial advantages over conventional power generation employing electromagnetic induction for harvesting low frequency energy (5 Hz) [31[]. As a result, TENG is a great option for harvesting low-frequency, irregular wave energy. The Maxwell displacement current (Wang et al., 2016) is the theoretical source of the fundamental TENG model, which is stated as:

$$\nabla \cdot D = P_f \tag{1}$$

$$\nabla \cdot B = 0 \tag{2}$$

$$\nabla \times E = -\frac{\partial B}{\partial t} \tag{3}$$

$$\nabla \times H = \boldsymbol{J}_f + \frac{\partial D}{\partial t} \tag{4}$$

where D represents the displacement field; B represents the magnetic field; E represents the electric field; H represents the magnetisation field; Pf represents the free charge density; and Jf represents the free current density.

$$D = \varepsilon_0 E + P \tag{5}$$

Where P represents the polarisation field density and ε_0 represents the vacuum dielectric constant. In Eq. (4), the second term is defined as the Maxwell displacement current.

$$J_D = \frac{\partial D}{\partial t} = \varepsilon_0 \frac{\partial D}{\partial t} + \frac{\partial P}{\partial t} \tag{6}$$

The first term in Eq. is the induced current resulting from the time-varying electric field, which is the theoretical basis for the existence of electromagnetic waves (Wang, 2013; Wang S et al., 2015; Wang et al., 2016); the second term is the current caused by the polarisation field generated by the electrostatic charge carried by the surface, which is the fundamental theoretical basis and source of the nanogenerator (Wang, 2017b).

4 The four modes of operation of TENG

The TENG (shown in Figure 9) has four modes of operation: vertical contact-separation mode, horizontal sliding mode, single electrode mode, and separate layer mode (Wang, 2015). Separating two dielectric films with metal electrodes coated on the back in vertical contact generates electricity in the vertical contact-separation mode. Because the two dielectric films are in distinct positions in the triboelectric electrical sequence and have varying electronegativity, when their surfaces come into touch, they will transport equal quantities of dissimilar charges through electron gain and loss. When the two dielectric films are separated, an induced potential difference is generated between them. If the metal electrodes on the back are connected by a load, the free moving electrons will circulate in the external circuit connected to the two electrodes in order to balance the potential difference. If the two dielectric films come into close contact again, the potential difference between the two

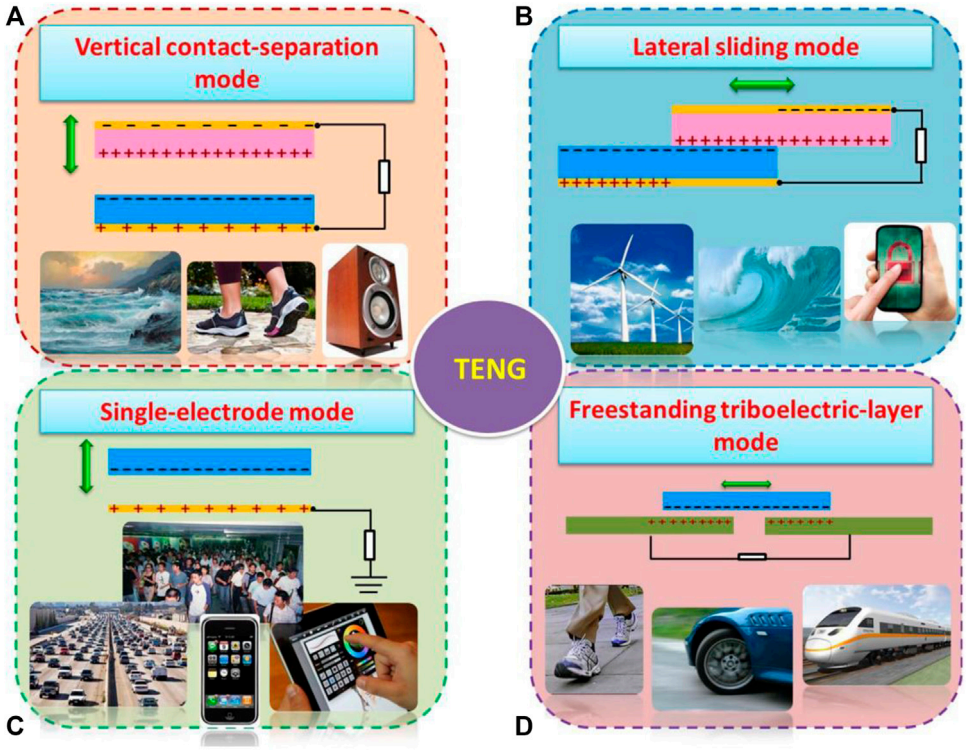

FIGURE 9
The four modes of operation of the TENG (Wang, 2015). **(A)** Vertical contact-separation mode, **(B)** lateral sliding mode, **(C)** single-electrode mode, **(D)** freestanding triboelectric-layer mode.

disappears and the electrons return to the original electrodes, and the Periodic contact separation leads to AC output from external circuits (Figure 9A). The horizontal sliding principle is similar to the vertical contact separation mode, with the exception that the dielectric film contact separation induced by vertical contact is substituted by relative sliding (Figure 9B). The load must only be attached to one electrode in the single-electrode mode, with the other end of the load acting as a potential reference electrode or being directly grounded. Although this mode is better for getting energy from freely moving objects (Figure 9C), the electrostatic shielding effect can reduce electron transfer efficiency in this mode. In addition, as shown in Figure 9D, the basic structure of the free-standing layer mode can be consisted of a freely movable dielectric film and two fixed electrodes at regular intervals. When an external excitation is applied to move the free dielectric film layer from contact with the left electrode to contact with the right electrode, an uneven charge is generated between the two electrodes resulting in a potential difference between them. In order to balance the potential difference, electrons will flow in an external circuit connecting the two electrodes, which will produce an alternating current output through the reciprocal movement of the dielectric film between the two electrodes. The separate layer mode is not limited to the two electrodes connected to the load being plated on the opposing moving device, which facilitates the design of the device and does not suffer from the shielding effect of the single electrode mode, so it has a high energy conversion efficiency and is very suitable for wave energy harvesting (Figure 9D).

5 Status of research on triboelectric nano-wave energy generation technology

By integrating distinct structural designs with their own mechanisms, TENG for wave energy generation not only supplies energy for offshore sensor networks, but also allows them to become self-energy supply sensors. As a result, TENG-based wave energy harvesting technology has become a popular topic. Wave energy harvesting with TENG can currently be classified as liquid-solid mode TENG (Lin et al., 2013; Li et al., 2018; Zhao et al., 2018; Liu et al., 2020; Gu et al., 2021), totally enclosed TENG (Wen et al., 2014; Wang X et al., 2015; Zhang et al., 2016; Xu et al., 2017; Xu et al., 2018; Zhang et al., 2018; Xu et al., 2019a; Cheng et al., 2019; Liu et al., 2019; Liang et al., 2021; Rodrigues et al., 2021), spinning disk TENG (Jiang et al., 2020), hybrid TENG (Yang H

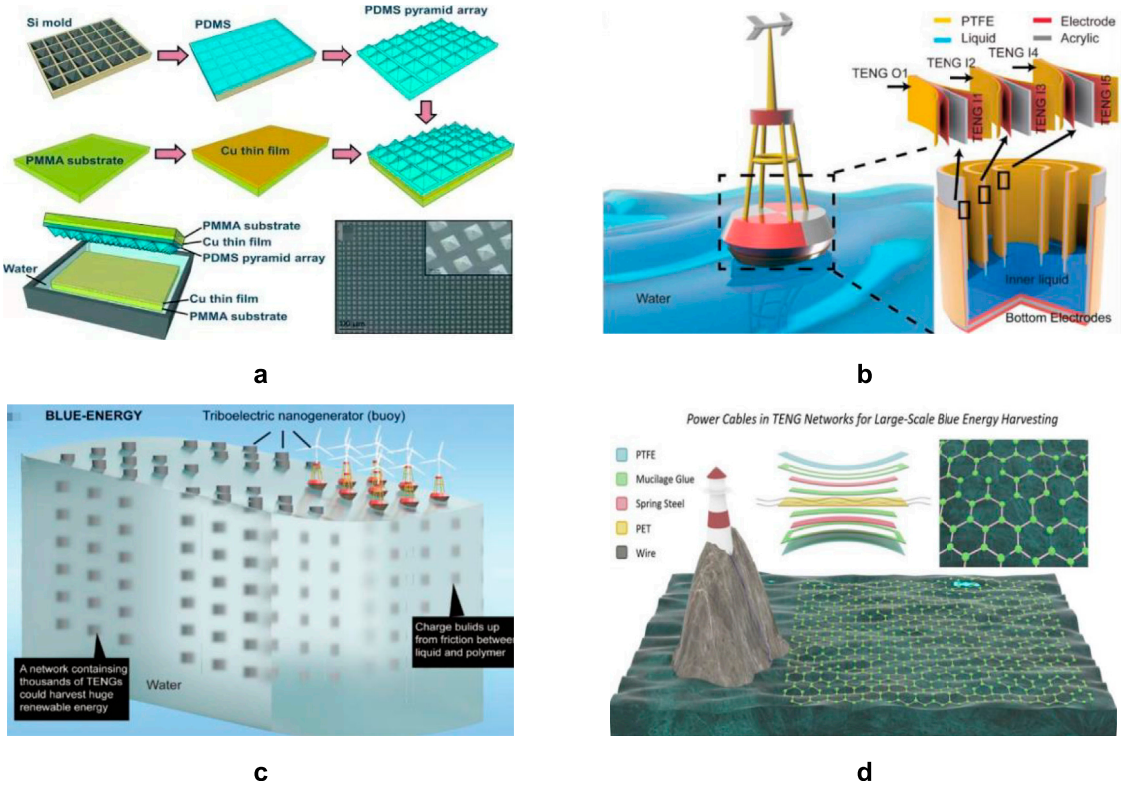

FIGURE 10
Liquid-solid contact TENG **(A)** First liquid-solid TENG structure (Lin et al., 2013). **(B)** Floating liquid-solid TENG power generation structure. **(C)** Application scenario of buoyed liquid-solid TENG (Li et al., 2018). **(D)** TENG network with a cellular topology connected by power cables (Liu et al., 2020).

et al., 2019; Chen X et al., 2019; Hao et al., 2019; Chandrasekhar et al., 2020; Jurado et al., 2020; Wu et al., 2020; Feng et al., 2021; Zheng et al., 2021), and so on.

5.1 Liquid-solid mode TENG

Lin et al. (Lin et al., 2013) proposed the first TENG based on liquid-solid mode in 2013 (shown in Figure 10A), in which contact separation of polydimethylsiloxane and water causes an electrical potential difference between the electrodes on the substrate, the two electrodes are connected by a load, and the potential difference drives the flow of electrons in the load pathway, thus generating electrical energy. Under periodic contact separation, the electrical energy produced by this liquid-solid TENG can charge a 33-F capacitor and successfully light up 60 light emitting diodes. In 2018, Li et al. (Li et al., 2018) created a buoy-like liquid-solid TENG (shown in Figures 10B,C) that can gather energy from various low frequency vibrations (up and down, rocking and rotational movements). By forming a network up to 290 μA, 16,725 nC, 300 V electrical output can drive an RF transmitter, illuminate hundreds of light emitting diodes and power the wireless SOS system to send out marine emergency signals. To avoid the problem of seawater erosion and entanglement of transmission lines in the TENG unit during large-scale wave energy harvesting, Liu et al. (Liu et al., 2020) in 2020 designed a TENG network of planar power cables consisting of spring steel strips and three layers of polymer film (shown in Figure 10D), with the steel strips inside the power cables acting not only as a structural skeleton but also as electrodes. Experimental analysis shows that a single cable achieves a maximum open circuit voltage of 34 V and a transferred charge of 25 nC in one cycle. Due to the novel working mechanism of the TENG, water itself can act as a triboelectric electrical material interacting with the insulating polymer film and therefore the liquid-solid mode can significantly reduce the effects of seawater corrosion and electrostatic interference on the TENG.

5.2 Fully enclosed TENG

Because the effect of ambient humidity on the output performance of the TENG must be considered when using solid-solid contact to harvest wave energy, fully enclosed structures are frequently employed to be able to operate in

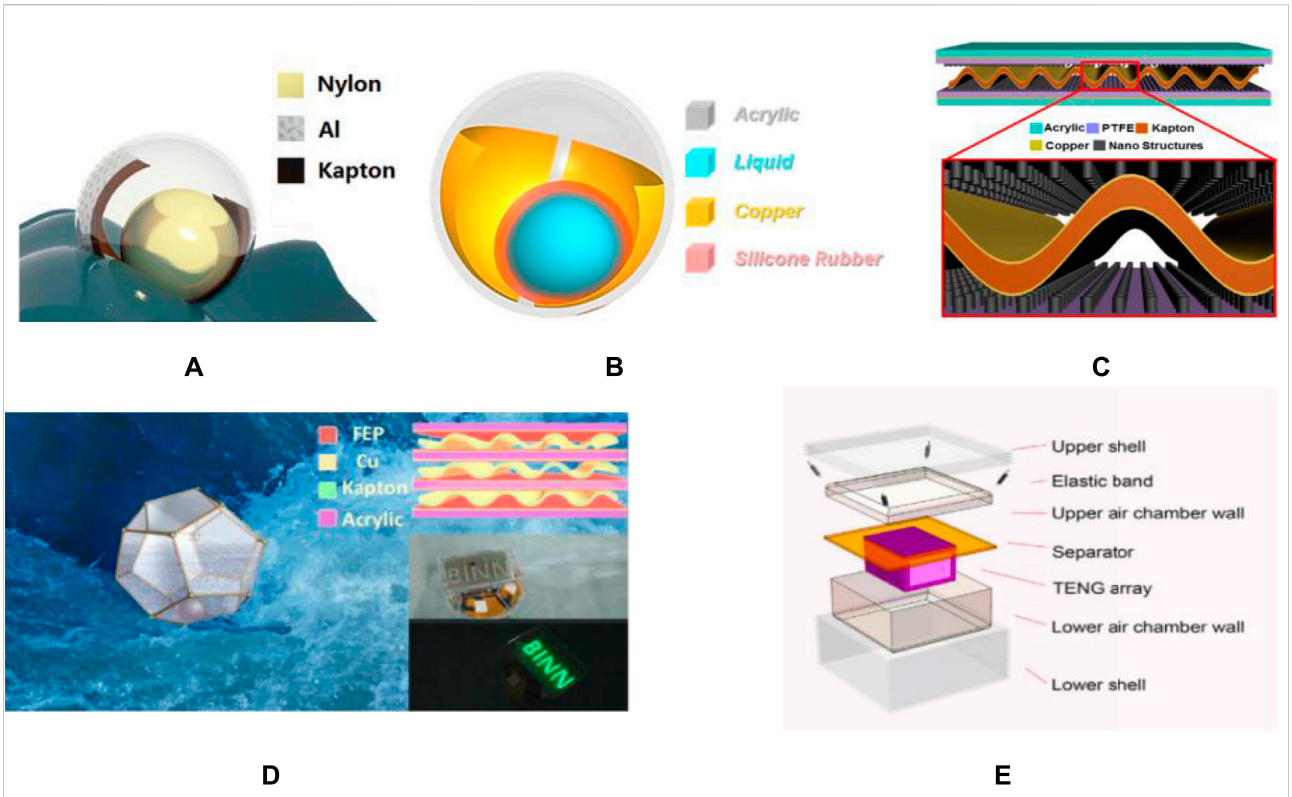

FIGURE 11
Fully enclosed TENG **(A)** Schematic diagram of the RF-TENG structure (Wang X et al., 2015). **(B)** Schematic diagram of SS-TENG structure (Cheng et al., 2019). **(C)** Schematic diagram of the wave-like TENG structure (Wen et al., 2014). **(D)** Schematic diagram of WS-TENGs (Zhang et al., 2016). **(E)** Schematic diagram of an integrated TENG array device based on an air-driven membrane structure (Xu et al., 2017).

harsh conditions. For wave energy harvesting, a variety of totally enclosed TENG structures have been reported, including rolling structures (Wang X et al., 2015; Xu et al., 2018; Zhang et al., 2018; Xu et al., 2019a; Cheng et al., 2019; Liu et al., 2019; Liang et al., 2021; Rodrigues et al., 2021), wave-shaped electrode structures (Wen et al., 2014; Zhang et al., 2016), air-driven membrane structures (Xu et al., 2017), and so on.

5.2.1 Rolling structures

In 2015, Wang et al. (Wang X et al., 2015) developed the RF-TENG, a freestanding and totally enclosed rolling TENG for wave energy harvesting that encompasses a rolling ball (nylon) inside a ball with an inner shell coated with a polyimide film (shown in Figure 11A). When driven by water waves, the 6 cm diameter RF-TENG may provide a short-circuit current of 1 μA and an instantaneous output power of up to 10 mW by optimising material and structural parameters. The performance of this TENG device is capable of directly driving more than 70 light emitting diodes and commercial thermometers at a duty cycle of 26.5 percent due to the excellent charge transfer efficiency of the freestanding TENG and the less frictional rolling construction. By optimising the material and structural design, Cheng et al. (Cheng et al., 2019) were able to convert a hard contact spherical TENG into a soft-contact spherical TENG (SS-TENG) (shown in Figure 11B), which raised the maximum output charge by a factor of ten over the standard TENG due to the increased contact area. Furthermore, in 2021, C. Rodrigues (Rodrigues et al., 2021) et al. created three TENG systems based on rolling spheres, as demonstrated by trials with large scale wave flumes in real sea conditions under a fixed navigation buoy: When the buoy is subjected to wave excitation, the electrical output is significantly reliant on pitch freedom, and the entire buoy dynamics, not just the TENG dynamics, must be considered.

5.2.2 Wave-like electrode structure

A wave-like structure-based TENG was invented by Wen (Wen et al., 2014) et al., in 2014 (shown in Figure 11C), which sandwiches a copper-polyimide-copper membrane between two flat nanostructured PTFE membranes to convert energy using the triboelectric initiation effect. The authors investigated different stirring methods to trigger a fully packed TENG and demonstrated the potential of this TENG for hydrological analysis by analysing the output signal and its corresponding Fourier transform spectrum, where the three stirring methods were distinguished from each other. Zhang et al. (Zhang et al.,

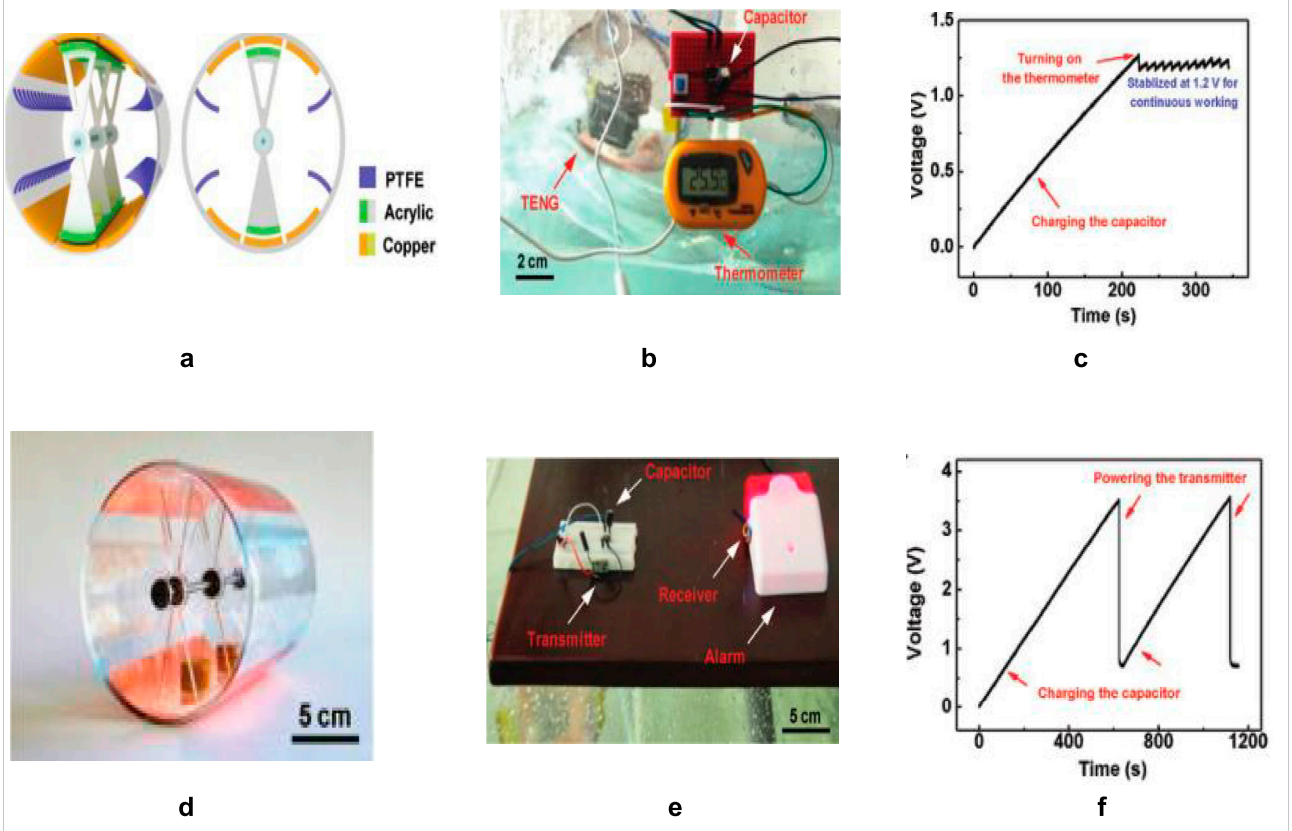

FIGURE 12
(A) Schematic diagram of the SS-TENG structure and cross-section. **(B)** Photograph of a digital thermometer powered by an SS-TENG driven by water waves. **(C)** Charge/discharge process of a 220 μF capacitor powering a thermometer at 10 cm amplitude and 1.2 Hz wave frequency. **(D)** Physical view of the SS-TENG. **(E)** Photograph of the wireless transmitter. **(F)** Charging and discharging process of a 220 μF capacitor powering a transmitter for two consecutive transmitting cycles (Jiang et al., 2020)

2016) fabricated an integrated 12-pack of multilayer wave-like structured orthododecahedral triboelectric nanogenerators (WS-TENGs) (Figure 11D shown). After rectification by wave driving, the device produced high output voltages and currents of 260 V and 220 μA, proving a viable way of energy harvesting that outperforms traditional water waves.

5.2.3 Air-driven membrane structures

In 2017, Xu et al. (Xu et al., 2017) designed a unique spring-suspended oscillator structure that employs air pressure to transfer and distribute the collected water wave energy, resulting in an integrated triboelectric nanogenerator array device based on an air-driven membrane structure (shown in Figure 11E). Experiments show that at low frequencies around 2.9 Hz, the device with 38 integrated TENG units can achieve a transferred charge per cycle of 15 μC, a short-circuit current of 187 μA, and an optimised peak power density of 13.23 W/m3, allowing 600 light emitting diodes to be lit simultaneously in real water waves, thanks to the innovative design of the spring-levitated oscillator structure and a mechanism that uses ai. Thanks to the revolutionary design of the spring-levitated oscillator structure, and a mechanism that employs air pressure to transport and disperse the collected water wave energy. The device can easily combine large scale high density TENG arrays in a single package, and greatly enhance output.

5.3 Disk rotation TENG

In 2020, Jiang et al. (Jiang et al., 2020) developed a swing structure triboelectric nanogenerator (SS-TENG) with a high energy conversion efficiency for ultra-low frequency water wave energy collecting (shown in Figure 12A). The air gap and flexible dielectric brushes are designed to reduce frictional resistance and maintain the frictional charge, boosting robustness and endurance. Experiments show a maximum peak power of 4.56 mW and an average power of 0.48 mW at motor parameters of 7 cm travel and acceleration of 7.5 m/s2. Importantly, the device can achieve a maximum oscillation time of 88 s with a single trigger and exhibits excellent

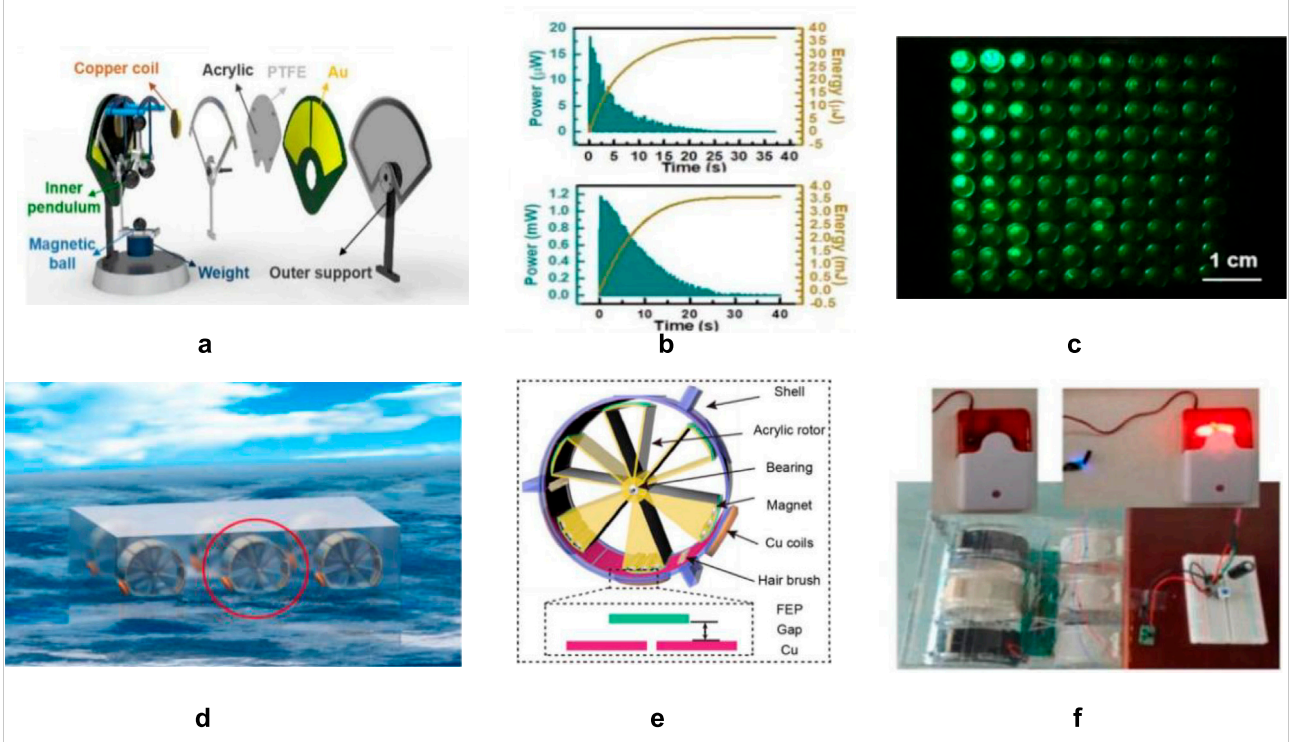

FIGURE 13
(A) Structure of the hybrid nanogenerator based on the disorder pendulum. **(B)** Output power and conversion energy of the TENG and EMG under water wave triggering with an impedance of 400 MΩ. **(C)** Lighting of 100 LEDs under water wave triggering (Chen X et al., 2019). **(D)** Schematic diagram of the hybrid nano-generator and its application in wave energy harvesting. **(E)** Diagram of the hybrid nanogenerator structure (enlarged view showing the gap between the FEP film and the copper electrode. **(f)** Powering a wireless transmitter by charging a 1,000 μF capacitor (Feng et al., 2021).

durability. Figure 12B,C show the successful driving of the digital thermometer after the wave is driven by the power generated by the SS-TENG and stored in the capacitor. The power created by the SS-TENG is held behind a capacitor to power a wireless transmitter, which successfully turns on the alarm by creating a signal to the receiver, as shown in Figure 12D,E. The investigations show that the SS-TENG could be used for self-powered temperature sensing and environmental monitoring using blue energy.

5.4 Hybrid TENG

Energy harvesting systems that can successfully gather wave energy at low frequencies are required for the advancement of marine technology. Integrating several energy harvesting systems for wave energy harvesting appears to be a very promising solution, according to several research. In 2019, Chen et al. (Chen X et al., 2019) suggested a self-powered wireless sensor node system using a disordered pendulum triboelectric (TENG) and electromagnetic (EMG) hybrid nanogenerator (shown in Figure 13A). The device's physical design takes advantage of the disordered pendulum's low operating frequency and high electromechanical conversion efficiency, allowing the nanogenerator's maximum output power to reach 15.21 W and the EMG's maximum output power to reach 1.23 mW under water wave excitation conditions (Figure 13B). Figure 13C shows how the hybrid nanogenerator can power up to 100 light emitting diodes. The hybrid nanogenerator can also power the wireless sensor node of the marine environmental monitoring system on the buoy, while the self-powered transmitter sends the data to the base station. The authors concluded that this research provides an innovative and effective method for harvesting blue energy and a new direction for aerospace and industry. Feng et al. (Feng et al., 2021) in 2021 designed a hybrid nanogenerator containing a soft-contact cylindrical triboelectric nanogenerator and an oscillating electromagnetic generator (Figure 13D). The stator-rotor pair was separated by introducing brushes made of flexible rabbit hair (Figure 13E), giving it the function of pumping charge to the dielectric surface, thereby reducing the operating resistance and improving the durability of the device. The

optimised hybrid nanogenerator exhibited the best output response to water wave stirring at 0.1 Hz, producing an instantaneous peak power of 4.8 mW, a peak power density of 10.16 W/m3 and an average power density of 0.23 W/m3. Finally, self-powered temperature mapping and wireless transmission was successfully demonstrated in ultra-low frequency water waves by the composed array (Figure 13F).

5.5 Comparison of the properties of TENG in different modes

Because of the liquid-solid mode TENG's revolutionary operating mechanism, water can operate as a frictional electrical substance interacting with the insulating polymer layer, considerably reducing the impacts of seawater corrosion and electrostatic interference on the TENG. The effect of ambient humidity on the output performance of the TENG must be taken into account when using solid-solid contact mode for wave energy harvesting, hence a fully enclosed structure is frequently employed to be able to work in difficult conditions. For wave energy harvesting, many different forms of fully enclosed TENG structures have been documented, such as rolling structures, undulating electrode structures, air-driven membrane structures, and so on. The disk-rotating TENG shows great potential in self-powered temperature sensing and blue energy environmental monitoring because it minimises frictional resistance through the design of the air gap and flexible dielectric brushes, and the frictional charge is sustainable, thus improving robustness and durability. Wave energy collecting by hybrid TENGs incorporating different energy harvesting methods appears to be a very viable approach, according to several research. Low operating frequency and excellent electromechanical conversion efficiency are two advantages of hybrid TENGs. A comparison of the characteristics of TENG in different modes is plotted in a table, as shown in Table 1.

6 Problems and research trends in triboelectric nano-wave energy generation technology

The expanding number of offshore operations and the growing integration with marine equipment has substantially raised the demand for energy in order to realize the smart ocean strategy. Traditional wave power technologies have high maintenance costs, bulky structures, and low conversion efficiency, and most of them can only be transmitted to large power grids, making direct power to marine equipment and platforms difficult, while battery power has high maintenance costs and poor endurance. TENG, in contrast to standard wave energy generating

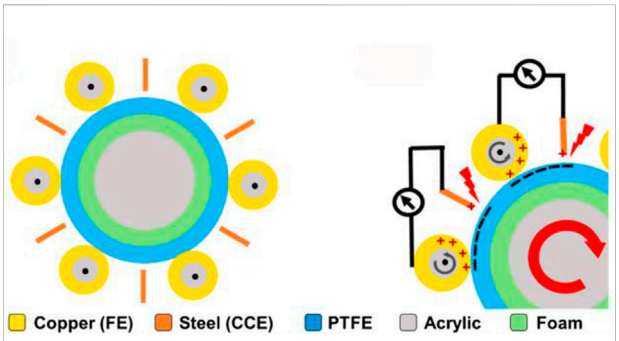

FIGURE 14
Rolling DC-TENG (Gao et al., 2021)

technologies that use electromagnetic power, can deliver high power output and continue to run efficiently at low frequencies and low amplitudes, considerably decreasing operation and maintenance costs (Wang, 2017a; Wang et al., 2017). TENG-based wave energy generating technology thus emerges as a very viable alternative solution in this context, not as a replacement for electromagnetic generators for large-scale power supply, but as a complement to them for the energy supply of offshore equipment and sensors. This is a novel sort of power generation technology, and it still has a lot of obstacles and challenges to overcome before it can mature and be used in practical applications. Future research trends in this discipline are primarily in the following areas in response to these issues:

6.1 Power circuit management optimisation

Because the majority of the electricity generated by TENGs is AC, while offshore equipment and sensors require only DC power, rectification bridges are frequently used to convert AC to DC. Multiple TENGs are frequently used to establish a network to feed power to widely spread offshore sensors, necessitating a high number of rectifier bridges, which surely increases the complexity of the power circuit transmission and the area occupied. As a result, for TENG-based wave energy generating technology, power circuit management optimization is critical. Gao et al. (Gao et al., 2021) constructed a DC TENG in rolling mode in 2021 (Figure 14), coupling frictional start and electrostatic breakdown effects for the first time to achieve constant current output in rolling mode. This strategy is unquestionably a fantastic way to optimize power circuit management when used to wave energy generation. Mechanical rectification, phase control, and dielectric breakdown are three general ways for generating DC from

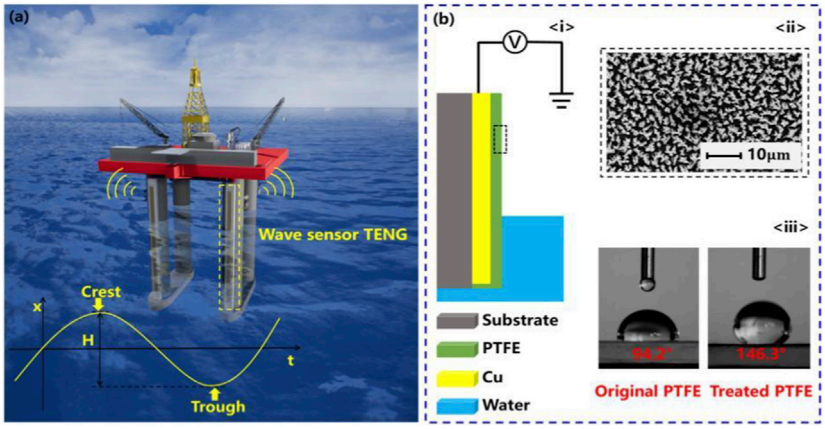

FIGURE 15
(A) Schematic diagram of WS-TENG used to monitor waves around a marine equipment.**(B)**Structural diagram of the WS-TENG (Xu et al., 2019b).

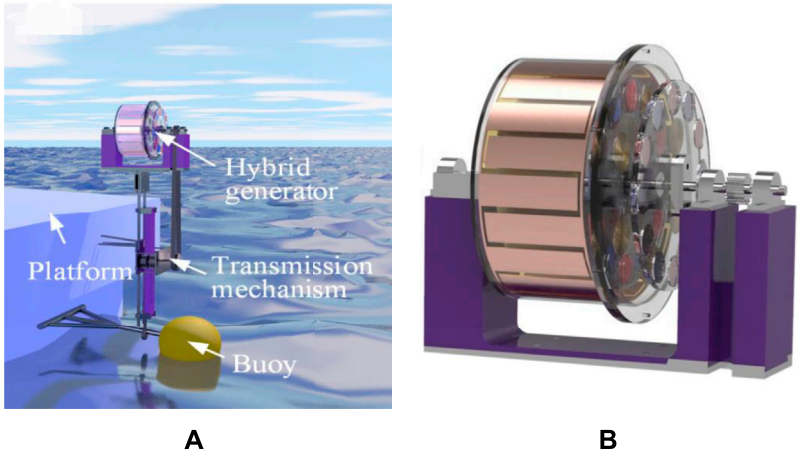

FIGURE 16
(A) Schematic illustration of the heaving point absorber-based wave energy converter and its application in ocean wave energy harvesting. **(B)** Overall structure of the hybrid generator (Zhao B et al., 2021)

TENG without sophisticated rectifier bridges. The application of the TENG DC generating method to wave power generation technology would be a breakthrough in power circuit management optimization.

6.2 Study of multi-energy utilisation of composite structures

Energy harvesting research is moving in the direction of integrated multi-energy utilization. The marine environment is complicated and varied, and marine platforms or buoys frequently incorporate a range of marine equipment with electronic systems such as sensors for marine weather monitoring, signal transmission, safety monitoring, and navigation, among other things. For battery storage, they are usually only fueled by solar power, which is expensive, inefficient, and easily impacted by light conditions. At sea, on the other hand, a wide range of environmental energy sources are available, including wave, raindrop, wind, and sun energy. Most researchers have so far focused solely on the structure and technology for collecting wave energy. When numerous energies can be collected and used at the

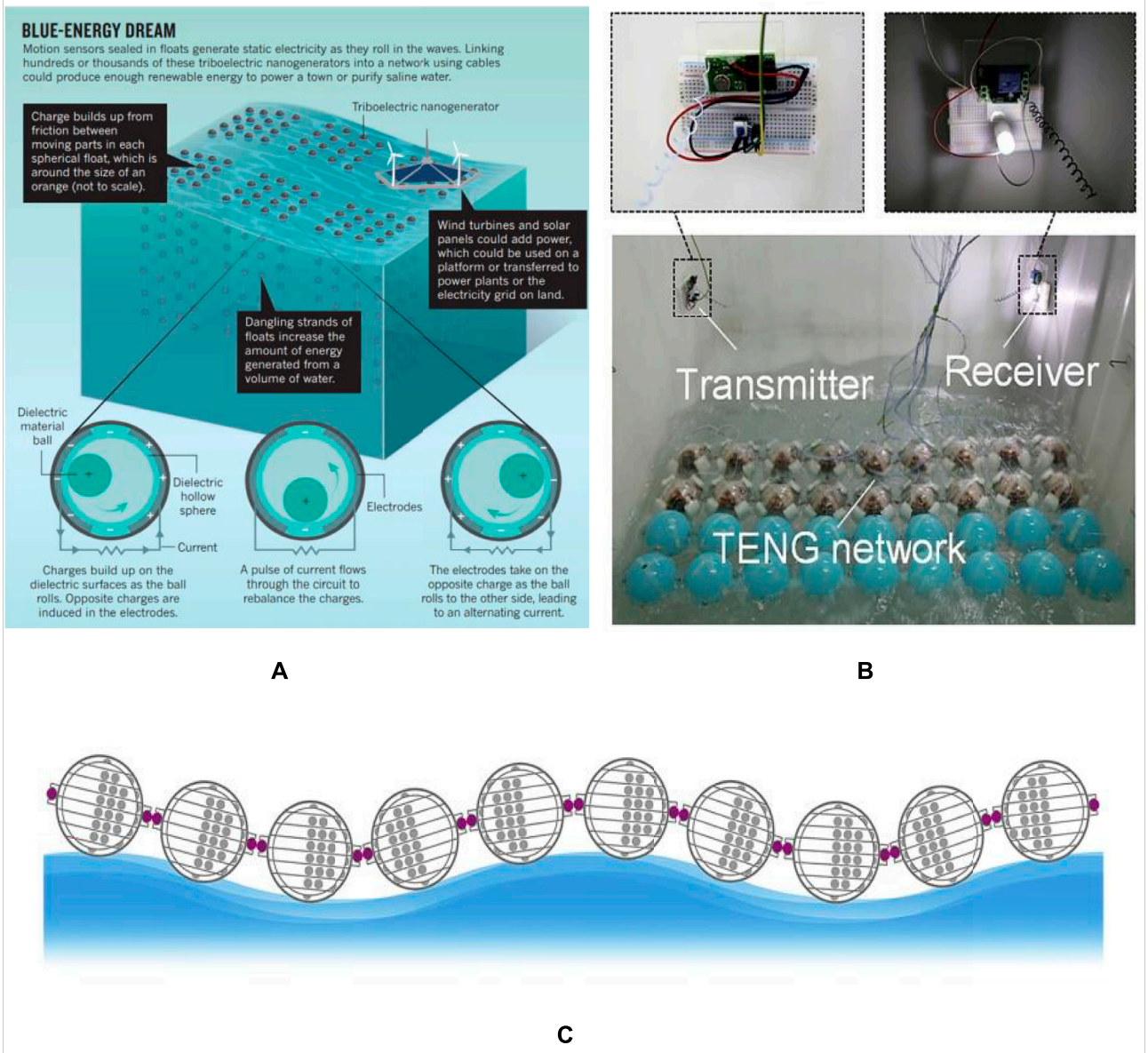

FIGURE 17
(A)TENG network (Zhao T et al., 2021). **(B)** Schematic illustration of the TENG networkagitated by water waves. **(C)** Photographs of the TENG network to power the wireless transmitter (Yang X et al., 2019)

same time using an integrated composite mechanism, it not only makes the power generating system more integrated, but it also enhances the energy conversion efficiency per unit area significantly. For example, Shao (Shao et al., 2017) et al. designed a multifunctional hybrid power device that can effectively harvest wave and solar energy and was experimentally demonstrated to be a practical power source for directly driving light-emitting diodes or charging energy storage devices using triboelectric nanogenerators and electromagnetic generators. Integrating a composite mechanism to collect multiple energies simultaneously is beneficial to produce higher output performance while also improving space utilization and achieving the goal of integrating energy harvesting structures with energy supply in order to adapt to environmental diversification.

6.3 Study of self-driven sensing

Wave sensors track parameters including wave height, period, and direction, and wave monitoring is essential for

TABLE 1 Comparison of the characteristics of TENG in different modes.

Type	Main structures	Advantages	Disadvantages
Liquid-solid mode TENG	vertical contact-separation mode	High output voltage, structure Simple	Large size of the device, not easy to seal assembly
	single electrode mode	Easy to make, simple construction	Low output power
	separate layer mode	Easy to package, easy to apply in practice	Output influenced by fluctuating frequency
Fully enclosed TENG	Rolling structures	High charge transfer efficiency and low friction	Complex production
	Wave-like electrode structure	High output efficiency	Large size of the device
	Air-driven membrane structure	Greatly increased output	Large size of the device
Disk rotation TENG	Swing structure	Low friction for increased durability	Complex production
Hybrid TENG	TENG + EMG	High output efficiency	Complex device structure, output influenced by fluctuating frequencies
	TENG + Solar Energy	High output efficiency	Influenced by light conditions

efficient use of marine resources, maritime safety, and marine disaster warning. Wave sensors today are frequently powered by batteries, resulting in insufficient range and expensive maintenance costs. Wave energy generation is used to power the sensors in the majority of current TENG wave energy harvesting studies. The relationship between the electrical signal generated and the waves can be derived by studying the relationship between the internal structure motion pattern and the waves, resulting in effective wave parameter monitoring and self-supply of energy if the characteristics of TENG generation can be used wisely, i.e. the electrical signal generated by it often has a certain relationship (e.g., linear relationship) with its own parameters or motion. For example, Xu et al. (Xu et al., 2019b) in 2018 proposed a highly sensitive wave sensor based on TENG at the liquid-solid interface (WS-TENG) (Figures 15A,B), which is made of a sensing copper electrode covered with a PTFE film on the surface, and the peak output voltage varies linearly with the wave height, which can sense wave heights in the millimetre range, and was successfully used for real-time monitoring around a simulated ocean platform through experiments in a wave tank. For intelligent marine equipment, this innovative self-driven wave sensor could be a viable alternative to wave monitoring. Triboelectric nanopower technology allows for self-energy monitoring of not just wave parameters but also other ocean factors. For miniaturised and extensively dispersed marine sensors, self-driven sensing must be realised, hence research into self-driven sensors will be a prominent topic in the future.

6.4 Stability and durability of the power generation unit

The longevity and stability of TENG-based wave energy harvesting devices has always been a concern, because the process of generating electricity from TENG is often based on repeated contact and separation of different frictional materials within the device, which inevitably leads to wear and tear on the materials over time and may change the output performance. Furthermore, the waves' kinetic and potential energy causes them to constantly contact the outside of the power generation unit during the process, as well as the unknown composition of the saltwater, which might cause corrosion of the power generation unit that cannot be ignored. As a result, solutions include how to increase the power plant's stability and durability through diverse material processing and structural design, as well as how to provide effective condition monitoring and early detection of fault symptoms in the power plant. The development of TENG-based wave power technology has become a serious concern (Li et al., 2021b; Li, 2022b). In 2021, Zhao (Zhao B et al., 2021) of China's Ocean University suggested a high-performance, long-lasting point-absorbing wave energy generation system based on triboelectric-electromagnetic composite generation technology (shown in Figures 16A,B). Through a multilayer soft bristle structure and a unidirectional driving mechanism, the device considerably increased the TENG's output performance and endurance, resulting in a continuous, high-performance output. High stability and durability are crucial criteria that researchers exploring TENG-based wave energy generating technologies must consider in order to realize large-scale application of TENG in wave energy harvesting.

6.5 Application of the TENG network

A single TENG wave energy generator can only power a single small sensor, but due to the simple and tiny TENG structure and the vast expanse of the sea, multiple TENGs can be combined to form a network on the surface, allowing a network of TENGs to power a widely distributed network of sensors and even provide useful power to a local power plant or grid on a small scale. Wave energy can be captured using the TENG network. The idea of employing TENG networks to absorb wave energy was first introduced in 2014 (Figure 17A shows) (Zhao T et al., 2021), and there are already a number of prototypes that demonstrate the principle's viability, but there are still numerous obstacles to overcome before it can be used on a big basis. The first is the unit's endurance, which is important because seawater and sunshine can degrade the material on the outside of the unit, and storms can cause fatigue damage to the TENG unit's connection structure. The second consideration is the network's location and size in order to minimize disruption to the public, marine life, and ships. Yang et al. (Yang X et al., 2019) proposed a self-assembling TENG network for wave energy harvesting based on encapsulated high performance units in 2019 (shown in Figures 17B,C). The device self-assembles through adaptive magnetic joints, working under the adaptive mechanism of magnetic poles and anisotropic degrees of freedom constraints, with the ability to self-heal ruptures and reconfigure quickly, greatly increasing the network's autonomy and mechanical robustness for large-scale fabrication and maintenance. There is significant value and promise in investigating the practical uses of large-scale TENG networks in the ocean to fulfill the growing energy demand and overcome the challenges and difficulties experienced by TENG networks.

7 Conclusion

The working principle, operating mode, and present research status of TENG-based wave energy generating technology are reviewed in this study, and it is discovered that wave energy harvesting employing various TENG structures has different output performance and application scope, then presenting some of the current problems with the technology. For example, due to the alternating current generated by TENGs, the complexity of the power circuit and the limited space utilisation, most TENG structures are only suitable for single energy harvesting, the lack of self-driven sensing research on ocean parameters, the poor stability and short lifespan of the power generation devices due to the fact that most TENGs generate electricity through frictional material contact separation, and there are still many challenges and difficulties in forming a TENG network, etc. Simultaneously, future research trends in this technology are proposed in the context of some current research cases, such as the application of DC TENG to wave energy generation for power circuit management optimization, the study of composite structures for multi-energy utilisation, the study of self-driven sensing of ocean parameters, the use of different structures and materials to enhance the device's stability and durability, and the exploration of large-scale applications. TENG-based wave energy generating technology is clearly a new power generation technology with enormous potential for development in the context of the current Internet of Things era and the trend of developing and utilizing new energy sources. With the maturation of this technology, it is thought that constructing a TENG network is a practical approach to realize the blue energy dream.

Author contributions

All authors listed have made a substantial, direct, and intellectual contribution to the work and approved it for publication.

Funding

The authors gratefully acknowledge the support provided for this research by Guangdong provincial special fund for promoting high quality economic development (Yuerong Office letter [(2020)161, GDNRC (2021)56] and Natural Science Foundation of Guangdong Province (2022A1515011562).

Conflict of interest

The authors declare that the research was conducted in the absence of any commercial or financial relationships that could be construed as a potential conflict of interest.

Publisher's note

References

Ahamed, R., McKee, K., and Howard, I. (2020). Advancements of wave energy converters based on power take off (PTO) systems: A review. *Ocean. Eng.* 204, 107248. doi:10.1016/j.oceaneng.2020.107248

Cai, N., and Wang, S. (2012). Development and prospects of wave energy utilization. *Land Nat. Resour. Res.* 6, 92–94. doi:10.16202/j.cnki.tnrs.2012.06.034

Chandrasekhar, A., Vivekananthan, V., and Kim, S. J. (2020). A fully packed spheroidal hybrid generator for water wave energy harvesting and self-powered position tracking. *Nano Energy* 69, 104439. doi:10.1016/j.nanoen.2019.104439

Chen, Q. M., Gao, G. Z., Yue, X. H., Geng, D. Z., and Xu, L. (2020). Hydropower and new energy opportunities and challenges: Advances in wave energy power technology research. *Hydropower New Energy* 34 (08), 1–6. doi:10.13622/j.cnki.cn42-1800/tv.1671-3354.2020.08.001

Chen, R. W., Liu, C., and Zhang, Y. X. (2019). Current status and perspectives of research on direct wave energy harvesting. *Data Acquis. Process.* 34 (02), 5–14. doi:10.16337/j.1004-9037.2019.02.001

Chen, X., Gao, L., Chen, J., Lu, S., Zhou, H., Wang, T., et al. (2019). A chaotic pendulum triboelectric-electromagnetic hybridized nanogenerator for wave energy scavenging and self-powered wireless sensing system. *Nano Energy* 69, 104440. doi:10.1016/j.nanoen.2019.104440

Cheng, P., Guo, H., Wen, Z., Zhang, C., Yin, X., Li, X., et al. (2019). Largely enhanced triboelectric nanogenerator for efficient harvesting of water wave energy by soft contacted structure. *Nano Energy* 57, 432–439. doi:10.1016/j.nanoen.2018.12.054

Drew, B., Plummer, A. R., and Sahinkaya, M. N. (2009). A review of wave energy converter technology. *Proc. Institution Mech. Eng. Part A J. Power Energy* 223 (8), 887–902. doi:10.1243/09576509jpe782

Du, Xiaozhen, Kong, Qingshuai, Guo, Yue, et al. (2021). Analysis of floating oscillating water column power generation based on dielectric elastomer. *J. Ocean Univ. China (Natural Sci. Ed.)* 51 (3), 110–116. doi:10.16441/j.cnki.hdxb.20180317

Falcão, A. F. O., and Henriques, J. C. C. (2016). Oscillating-water-column wave energy converters and air turbines: A review. *Renew. Energy* 85, 1391–1424. doi:10.1016/j.renene.2015.07.086

Feng, Y., Liang, X., An, J., Jiang, T., and Wang, Z. L. (2021). Soft-contact cylindrical triboelectric-electromagnetic hybrid nanogenerator based on swing structure for ultra-low frequency water wave energy harvesting. *Nano Energy* 81, 105625. doi:10.1016/j.nanoen.2020.105625

Flocard, F., and Finnigan, T. D. (2010). Laboratory experiments on the power capture of pitching vertical cylinders in waves. *Ocean. Eng.* 37 (11-12), 989–997. doi:10.1016/j.oceaneng.2010.03.011

Gao, Y., Liu, D., Zhou, L., Li, S., Zhao, Z., Yin, X., et al. (2021). A robust rolling-mode direct-current triboelectric nanogenerator arising from electrostatic breakdown effect. *Nano Energy* 85, 106014. doi:10.1016/j.nanoen.2021.106014

Gu, H., Zhang, N., Zhou, Z., Ye, S., Wang, W., Xu, W., et al. (2021). A bulk effect liquid-solid generator with 3D electrodes for wave energy harvesting. *Nano Energy* 87, 106218. doi:10.1016/j.nanoen.2021.106218

Hao, C., He, J., Zhai, C., Jia, W., Song, L., Cho, J., et al. (2019). Two-dimensional triboelectric-electromagnetic hybrid nanogenerator for wave energy harvesting. *Nano Energy* 58, 147–157. doi:10.1016/j.nanoen.2019.01.033

Jiang, T., Pang, H., An, J., Lu, P., Feng, Y., Liang, X., et al. (2020). Robust swing-structured triboelectric nanogenerator for efficient blue energy harvesting. *Adv. Energy Mat.* 10 (23), 2000064. doi:10.1002/aenm.202000064

Jurado, U. T., Pu, S. H., and White, N. M. (2020). Grid of hybrid nanogenerators for improving ocean wave impact energy harvesting self-powered applications. *Nano Energy* 72, 104701. doi:10.1016/j.nanoen.2020.104701

Kofoed, J. P., Frigaard, P., Friis-Madsen, E., and Sorensen, H. C. (2006). Prototype testing of the wave energy converter wave dragon. *Renew. energy* 31 (2), 181–189. doi:10.1016/j.renene.2005.09.005

Li, H., Deng, J., Feng, P., Pu, C., Arachchige, D., Cheng, Q., et al. (2021a). Short-term nacelle orientation forecasting using bilinear transformation and ICEEMDAN framework. *Front. Energy Res.* 9, 780928. doi:10.3389/fenrg.2021.780928

Li, H., Deng, J., Yuan, S., Feng, P., and Arachchige, D. (2021b). Monitoring and identifying wind turbine generator bearing faults using deep belief network and EWMA control charts. *Front. Energy Res.* 9, 799039. doi:10.3389/fenrg.2021.799039

Li, H. (2022). SCADA data based wind power interval prediction using LUBE-based deep residual networks. *Front. Energy Res.* 10, 920837. doi:10.3389/fenrg.2022.920837

Li, H. (2022). Short-term wind power prediction via spatial temporal analysis and deep residual networks. *Front. Energy Res.* 10, 920407. doi:10.3389/fenrg.2022.920407

Li, X., Tao, J., Wang, X., Zhu, J., Pan, C., and Wang, Z. L. (2018). Networks of high performance triboelectric nanogenerators based on liquid-solid interface contact electrification for harvesting low-frequency blue energy. *Adv. Energy Mat.* 8 (21), 1800705. doi:10.1002/aenm.201800705

Liang, X., Liu, Z., Feng, Y., Han, J., Li, L., An, J., et al. (2021). Spherical triboelectric nanogenerator based on spring-assisted swing structure for effective water wave energy harvesting. *Nano Energy* 83, 105836. doi:10.1016/j.nanoen.2021.105836

Lin, Y., Bao, J., Liu, H., Li, W., Tu, L., and Zhang, D. (2015). Review of hydraulic transmission technologies for wave power generation. *Renew. Sustain. Energy Rev.* 50, 194–203. doi:10.1016/j.rser.2015.04.141

Lin, Z. H., Cheng, G., Lin, L., Lee, S., and Wang, Z. L. (2013). Water-solid surface contact electrification and its use for harvesting liquid-wave energy. *Angew. Chem. Int. Ed.* 52 (48), 12545–12549. doi:10.1002/anie.201307249

Liu, G., Chen, J., Tang, Q., Feng, L., Yang, H., Li, J., et al. (2018). Wireless electric energy transmission through various isolated solid media based on triboelectric nanogenerator. *Adv. Energy Mat.* 8, 1703086. doi:10.1002/aenm.201703086

Liu, G., Leng, Q., Lian, J., Guo, H., Yi, X., and Hu, C. (2015). Notepad-like triboelectric generator for efficiently harvesting low-velocity motion energy by interconversion between kinetic energy and elastic potential energy. *ACS Appl. Mat. Interfaces* 7 (2), 1275–1283. doi:10.1021/am507477y

Liu, G., Xiao, L., Chen, C., Liu, W., Pu, X., Wu, Z., et al. (2020). Power cables for triboelectric nanogenerator networks for large-scale blue energy harvesting. *Nano Energy* 75, 104975. doi:10.1016/j.nanoen.2020.104975

Liu, W., Xu, L., Bu, T., Yang, H., Liu, G., Li, W., et al. (2019). Torus structured triboelectric nanogenerator array for water wave energy harvesting. *Nano Energy* 58, 499–507. doi:10.1016/j.nanoen.2019.01.088

Polinder, H., Damen, M. E. C., and Gardner, F. (2004). Linear PM generator system for wave energy conversion in the AWS. *IEEE Trans. Energy Convers.* 19 (3), 583–589. doi:10.1109/tec.2004.827717

Ricci, P., Lopez, J., Santos, M., Ruiz-Minguela, P., Villate, J., Salcedo, F., et al. (2011). Control strategies for a wave energy converter connected to a hydraulic power take-off. *IET Renew. Power Gener.* 5 (3), 234. doi:10.1049/iet-rpg.2009.0197

Rodrigues, C., Ramos, M., Esteves, R., Correia, J., Clemente, D., Goncalves, F., et al. (2021). Integrated study of triboelectric nanogenerator for ocean wave energy harvesting: Performance assessment in realistic sea conditions. *Nano Energy* 84, 105890. doi:10.1016/j.nanoen.2021.105890

Rodríguez, L., Pereiras, B., Fernández-Oro, J., and Castro, F. (2019). Optimization and experimental tests of a centrifugal turbine for an OWC device equipped with a twin turbines configuration. *Energy* 171, 710–720. doi:10.1016/j.energy.2019.01.029

Shao, H., Wen, Z., Cheng, P., Sun, N., Shen, Q., Zhou, C., et al. (2017). Multifunctional power unit by hybridizing contact-separate triboelectric nanogenerator, electromagnetic generator and solar cell for harvesting blue energy. *Nano Energy* 39, 608–615. doi:10.1016/j.nanoen.2017.07.045

Shi, H. D., and Liu, Z. (2021). Research progress and development trend of ocean wave energy. *Sci. Technol. Her.* 39 (6), 22–28.

Tedeschi, E., Molinas, M., Carraro, M., and Mattavelli, P. (2010). "Analysis of power extraction from irregular waves by all-electric power take off," in 2010 IEEE Energy Conversion Congress and Exposition, Atlanta, GA, USA, 12-16 September 2010 (IEEE), 2370–2377.

Wang, S., Lin, L., and Wang, Z. L. (2015). Triboelectric nanogenerators as self-powered active sensors. *Nano Energy* 11, 436–462. doi:10.1016/j.nanoen.2014.10.034

Wang, S., Wang, Y., Liu, D., Zhang, Z., Li, W., Liu, C., et al. (2021). A robust and self-powered tilt sensor based on annular liquid-solid interfacing triboelectric nanogenerator for ship attitude sensing. *Sensors Actuators A Phys.* 317, 112459. doi:10.1016/j.sna.2020.112459

Wang, X., Niu, S., Yin, Y., Yi, F., You, Z., and Wang, Z. L. (2015). Triboelectric nanogenerator based on fully enclosed rolling spherical structure for harvesting low-frequency water wave energy. *Adv. Energy Mat.* 5 (24), 1501467. doi:10.1002/aenm.201501467

Wang, Z. L. (2017). Catch wave power in floating nets. *Nature* 542 (7640), 159–160. doi:10.1038/542159a

Wang, Z. L., Jiang, T., and Xu, L. (2017). Toward the blue energy dream by triboelectric nanogenerator networks. *Nano Energy* 39, 9–23. doi:10.1016/j.nanoen.2017.06.035

Wang, Z. L., Lin, L., Chen, J., Niu, S. M., and Zi, Y. L. (2016). "Theoretical modeling of triboelectric nanogenerators," in *Triboelectric nanogenerators* (Cham: Springer), 155–183. doi:10.1007/978-3-319-40039-6_6

Wang, Z. L. (2017). On maxwell's displacement current for energy and sensors: the origin of nanogenerators. *Mater. Today* 20 (2), 74–82. doi:10.1016/j.mattod.2016.12.001

Wang, Z. L. (2015). Triboelectric nanogenerators as new energy technology and self-powered sensors – principles, problems and perspectives. *Faraday Discuss.* 176, 447–458. doi:10.1039/c4fd00159a

Wang, Z. L. (2013). Triboelectric nanogenerators as new energy technology for self-powered systems and as active mechanical and chemical sensors. *ACS Nano* 7 (11), 9533–9557. doi:10.1021/nn404614z

Wen, X., Yang, W., Jing, Q., and Wang, Z. L. (2014). Harvesting broadband kinetic impact energy from mechanical triggering/vibration and water waves. *Acs Nano* 8 (7), 7405–7412. doi:10.1021/nn502618f

Wu, C., Wang, A. C., Ding, W., Guo, H., and Wang, Z. L. (2019). Triboelectric nanogenerator: A foundation of the energy for the new era. *Adv. Energy Mat.* 9 (1), 1802906. doi:10.1002/aenm.201802906

Wu, Y., Zeng, Q., Tang, Q., Liu, W., Liu, G., Zhang, Y., et al. (2020). A teeterboard-like hybrid nanogenerator for efficient harvesting of low-frequency ocean wave energy. *Nano Energy* 67, 104205. doi:10.1016/j.nanoen.2019.104205

Xiao, X., Bai, N. Z., and Kang, Q. (2014a). etc.A review of wave power system development and research into direct-drive wave power systems. *J. Electr. Eng. Technol.* 29 (03), 1–11. doi:10.19595/j.cnki.1000-6753.tces.2014.03.001

Xiao, Xi, Nianzong, Pendulum, Kang, Qing, et al. (2014b). A review of wave power system development and research on direct-drive wave power systems. *J. Electrotechnol.* 29 (03), 1–11.

Xu, L., Jiang, T., Lin, P., Shao, J. J., He, C., Zhong, W., et al. (2018). Coupled triboelectric nanogenerator networks for efficient water wave energy harvesting. *ACS Nano* 12 (2), 1849–1858. doi:10.1021/acsnano.7b08674

Xu, L., Pang, Y., Zhang, C., Jiang, T., Chen, X., Luo, J., et al. (2017). Integrated triboelectric nanogenerator array based on air-driven membrane structures for water wave energy harvesting. *Nano Energy* 31, 351–358. doi:10.1016/j.nanoen.2016.11.037

Xu, M., Wang, S., Zhang, S. L., Ding, W., Kien, P. T., Wang, C., et al. (2019a). A highly-sensitive wave sensor based on liquid-solid interfacing triboelectric nanogenerator for smart marine equipment. *Nano Energy* 57, 574–580. doi:10.1016/j.nanoen.2018.12.041

Xu, M., Zhao, T., Wang, C., Zhang, S. L., Li, Z., Pan, X., et al. (2019b). High power density tower-like triboelectric nanogenerator for harvesting arbitrary directional water wave energy. *ACS Nano* 13 (2), 1932–1939. doi:10.1021/acsnano.8b08274

Yang, H. M., Wang, M. F., Deng, M. M., Guo, H. Y., Zhang, W., Yang, H. K., et al. (2018). A full-packaged rolling triboelectric-electromagnetic hybrid nanogenerator for energy harvesting and building up self-powered wireless systems. *Nano Energy* 56, 300–306. doi:10.1016/j.nanoen.2018.11.043

Yang, X., Xu, L., Lin, P., Zhong, W., Bai, Y., Luo, J., et al. (2019). Macroscopic self-assembly network of encapsulated high-performance triboelectric nanogenerators for water wave energy harvesting. *Nano Energy* 60, 404–412. doi:10.1016/j.nanoen.2019.03.054

Yemm, R., Pizer, D., Retzler, C., and Henderson, R. (2012). Pelamis: experience from concept to connection. *Phil. Trans. R. Soc. A* 1959 (370), 365–380. doi:10.1098/rsta.2011.0312

Zhang, B. E., Zheng, Y., Fu, S. F., Liu, H. W., Zhao, M. Z., and Li, C. (2019). Experimental study of a new wave energy generation conversion device. *Chin. J. Electr. Eng.* 39 (24), 7263–7271. doi:10.13334/j.0258-8013.pcsee.182298

Zhang, L. M., Han, C. B., Jiang, T., Zhou, T., Li, X. H., Zhang, C., et al. (2016). Multilayer wavy-structured robust triboelectric nanogenerator for harvesting water wave energy. *Nano Energy* 22, 87–94. doi:10.1016/j.nanoen.2016.01.009

Zhang, S. L., Xu, M., Zhang, C., Wang, Y. C., Zou, H., He, X., et al. (2018). Rationally designed sea snake structure based triboelectric nanogenerators for effectively and efficiently harvesting ocean wave energy with minimized water 1screening effect. *Nano Energy* 48, 421–429. doi:10.1016/j.nanoen.2018.03.062

Zhao, B., Li, Z., Liao, X., Qiao, L., Li, Y., Dong, S., et al. (2021). A heaving point absorber-based ocean wave energy convertor hybridizing a multilayered soft-brush cylindrical triboelectric generator and an electromagnetic generator. *Nano Energy* 89, 106381. doi:10.1016/j.nanoen.2021.106381

Zhao, C. J., and Zhou, Y. (2013). Overview of domestic research on marine buoy monitoring systems. *Mar. Dev. Manag.* 30 (11), 13–18.

Zhao, T., Xu, M., Xiao, X., Ma, Y., Li, Z., and Wang, Z. L. (2021). Recent progress in blue energy harvesting for powering distributed sensors in ocean. *Nano Energy* 88, 106199. doi:10.1016/j.nanoen.2021.106199

Zhao, X. J., Kuang, S. Y., Wang, Z. L., and Zhu, G. (2018). Highly adaptive solid–liquid interfacing triboelectric nanogenerator for harvesting diverse water wave energy. *ACS Nano* 12 (5), 4280–4285. doi:10.1021/acsnano.7b08716

Zhao, Z., Pu, X., Du, C., Li, L., Jiang, C., Hu, W., et al. (2016). Freestanding flag-type triboelectric nanogenerator for harvesting high-altitude wind energy from arbitrary directions. *ACS Nano* 10 (2), 1780–1787. doi:10.1021/acsnano.5b07157

Zheng, C., Shao, L., Shi, W., Su, Q., Lin, G., Li, X., et al. (2014). An assessment of global ocean wave energy resources over the last 45 a. *Acta Oceanol. Sin.* 33, 92–101. doi:10.1007/s13131-014-0418-5

Zheng, F., Sun, Y., Wei, X., Chen, J., Yuan, Z., Jin, X., et al. (2021). A hybridized water wave energy harvester with a swing magnetic structure toward intelligent fishing ground. *Nano Energy* 90, 106631. doi:10.1016/j.nanoen.2021.106631

frontiers | Frontiers in Energy Research

TYPE Brief Research Report
PUBLISHED 22 July 2022
DOI 10.3389/fenrg.2022.964516

OPEN ACCESS

EDITED BY
Yusen He,
The University of Iowa, United States

REVIEWED BY
Haoyun Shi,
Great Wall Motor, China
Mingxin Kang,
Northeastern University, China

*CORRESPONDENCE
Yibo Tang,
626323320@qq.com

SPECIALTY SECTION
This article was submitted to Smart Grids,
a section of the journal
Frontiers in Energy Research

RECEIVED 08 June 2022
ACCEPTED 27 June 2022
PUBLISHED 22 July 2022

CITATION
Jiang S, wu P, Peng X and Tang Y (2022), Research on generation scheduling mechanism of interconnected power system based on runoff forecast. *Front. Energy Res.* 10:964516. doi: 10.3389/fenrg.2022.964516

Research on generation scheduling mechanism of interconnected power system based on runoff forecast

Shiming Jiang, Ping wu, Xuhong Peng and Yibo Tang*

Provincial Key Laboratory of Informational Service for Rural Area of Southwestern Hunan, Shaoyang University, Shaoyang, China

In order to reduce power energy consumption and ensure the sustainable development of resources, a research on the generation scheduling mechanism of interconnected power systems based on runoff forecasting is proposed. First, by studying energy-saving power generation scheduling and using the average distribution method, there will be a lot of energy consumption and pollution emissions, so it is necessary to formulate a reasonable power generation scheduling plan; secondly, the medium and long-term runoff forecasting method is analyzed, and artificial neural networks are used to select appropriate hidden nodes Finally, the economic characteristics of the two-stage power generation of the hydropower station are explored, and the marginal benefit of the water level storage capacity and the total power generation is obtained by combining the current operating status and forecast information of the reservoir. Through experiments, it is proved that the method in this paper can better predict the power generation scheduling mechanism of hydropower stations, and the annual power generation of the optimized scheduling is 1.92% higher than that of conventional scheduling, which has significant advantages, ensuring the reasonable distribution of power resources and preventing unnecessary waste.

KEYWORDS

runoff forecast, power system, power generation scheduling mechanism, energy saving, sustainable development of resources

1 Introduction

The current power production scheduling method in the country is to share the power generation of each unit equally, and such a scheduling method will generate a lot of energy consumption and pollution (Le et al., 2021). Under the needs of energy conservation and environmental protection, the country has proposed the implementation of energy conservation and emission reduction plans, in order to achieve the purpose of energy conservation and emission reduction, promote the optimization of the energy structure (Zhang et al., 2022), and guide the energy structure to develop in the direction of high efficiency and low pollution (Li et al., 2021a). In today's energy shortage and increasingly prominent environmental pollution, developing clean energy, developing green power,

and promoting the transformation of energy strategies have become a new trend in global energy development (Li et al., 2021b), and it is also an important direction of energy strategy development. China has developed rapidly in the past 5 years, and will maintain rapid development in the next 10 years. While the country is developing clean energy on a large scale, how to conduct electricity market transactions in the new environment to ensure its efficient use and achieve optimal resource allocation is a practical problem that urgently needs to be studied and solved (Husin and Zaki, 2021), (Yang et al., 2021a).

In order to realize resource complementarity and improve power system operation security (Shang, 2007), it is necessary to interconnect small and medium power grids through tie lines to form a multi-domain interconnected power system. At present, all regions and provinces in China have gradually realized networking, and the networking form has changed from simple bilateral networking to complex networking. After the power systems are interconnected, each system can obtain power from other systems through tie lines, realize mutual support between interconnected subsystems, and obtain benefits such as mutual assistance, peak shifting and mutual backup, thereby improving the reliability level of the entire region. Reference (Fan et al., 2009) proposes an energy-saving power generation dispatching method that takes into account the government's macro-control and market mechanism, and implements optimal dispatching of various generator sets according to the energy consumption and pollutant emission levels to achieve the power generation dispatching target requirements. Reference (Zhang et al., 2009) proposes a regional power grid energy-saving power generation dispatching model that takes into account the bidding in the electricity market. First, it is sorted by province, and then the grid replacement algorithm is matched in the province, and finally the dispatching situation under various modes is calculated. Reference (Li and Tan, 2012) uses short-term marginal cost pricing as the premise to design a power generation scheduling model. According to the two-part on-grid electricity price mechanism, the transaction plan is clarified by ordering the electricity price of units approved by the government to form a suitable power generation scheduling mechanism. Reference (Yang et al., 2022a) uses the benefit compensation mechanism of the distribution model to formulate a dispatch model, and is compatible with coal consumption ranking and market bidding to implement the power generation dispatch mechanism of the transfer of power generation rights (Fan et al., 2009; Zhang et al., 2009; Li and Tan, 2012; Yang et al., 2022a).

The power generation scheduling situation is not perfect, there is a large planning deviation, lead to serious energy consumption, therefore, this paper puts forward the interconnected power system based on runoff forecast scheduling mechanism research, through the artificial neural network simulation runoff forecast method, analysis of energy-saving power generation scheduling, research of hydropower station optimization scheduling, make a reasonable plan. A power generation model of hydropower station is designed, combined with Markov correction of scheduling error, to improve the mechanism. Through this model, the annual power generation of optimized scheduling is 1.92% higher than that of conventional scheduling, and the optimization effect is obvious. The scheduling scheme formulated by the optimized BP neural network for prediction and runoff is closer to the actual scheduling operation process.

2 Energy-saving power generation scheduling analysis

The current power generation planning mode in the country is to distribute the power generation time of the units equally. For small thermal power units with high energy consumption and high pollution, the power generation time of the high-efficiency, environmental protection, and energy-saving units, no measures have been taken to encourage clean units to generate electricity. Due to the existence of a large number of clean and low-energy equipment in the country's power system, the use of an even distribution method has resulted in a large amount of energy consumption and pollution emissions. With the rapid development of the national economy, the electricity consumption of the whole society has increased rapidly, and the energy consumption, pollutants, and carbon dioxide emissions have also increased rapidly. The traditional power generation planning model can no longer meet the new needs.

However, the implementation of energy-saving power generation scheduling is a wide-ranging (Yang et al., 2022b) and complex system engineering, and it is also a major reform of the country's current power generation scheduling system. This reform will have a major impact on the security, continuous and reliable power supply of China's power grid, and will also cause major adjustments to the interests of power companies (power generation companies and power grid companies) and local interests (local government tax revenue). At the same time, in the actual scheduling process, a large number of technical support systems developed according to the original ideas need to be upgraded, and the operation process needs to be changed.

The power industry is also a producer and user of energy. China's power industry accounts for more than 80% of coal production and more than 50% of China's coal consumption. China's power industry is a real energy-consuming country. On the one hand, energy consumption and emissions can be reduced in the short term through the power-saving dispatch of power plants. On the other hand, in the process of investing in power generation, the introduction of energy-saving and emission-reduction technologies to maximize the elimination of backward production capacity (Wei et al., 2016) has a profound impact on the development of enterprises. The

implementation of the energy-saving power generation plan will greatly change the profit distribution of the country's power generation industry, and will also have a certain impact on power grid companies and users. Research on optimal dispatching of energy-saving power plants is helpful to formulate a reasonable power generation plan. At the same time, in the energy production plan, more technical support is needed, such as optimizing the dispatching scheme.

The economic essence of the current energy-saving power generation dispatching policy is to realize the "macro-control" of power generation (production) between units with different energy types and units with the same energy type and different energy consumption levels through the promulgation of administrative decrees.

1) The purpose of regulation is to overcome the limitation of simply using the market for resource allocation (Liu, 2021), which does not consider the externalities of electricity commodities that damage the environment and consume resources. Regulation is a supplement to market instruments.
2) The power generation of each unit before regulation is gradually determined according to the development and competition of power grids and power generation enterprises over the years. It can be regarded as similar to "market allocation" in economics, that is, each economic entity makes production and trade decisions according to its own economic interests, and the determined production capacity is also the result of market resource allocation. Under the premise that the market is fully competitive and all stakeholders have sufficient information, the result of this resource allocation can be regarded as an efficient, reasonable and optimal allocation for the present generation without considering the environmental impact on future generations.
3) The power generation of each unit after regulation is the result of the government's redistribution of the production of each enterprise on behalf of the interests of future generations and in accordance with the goal of sustainable development, so as to optimize the interests of present and future generations.

3 Medium- and long-term runoff forecasting methods

3.1 Multiple linear regression model

The multiple linear regression model is a commonly used model in medium and long-term runoff forecasting, and its form is as follows:

$$Y = \sum_{i=1}^{m} a_i X_i + b \qquad)$$

In the formula, Y describes the forecast object; m describes the number of predictors; $X_i\,(i = 1, \ldots, m)$ describes the predictor; a_i describes the contribution coefficient of the predictor; b describes the constant.

The multiple linear regression model treats the relationship between the forecast object and the forecast factor as a linear relationship. The principle is simple and the parameters are easy to set. It has always played an important role in hydrological forecasting. However, when the forecast object and the forecast factor have an obvious nonlinear relationship, the forecast accuracy of the multiple linear regression model will be significantly reduced.

3.2 Support vector machines

Support vector machine is a new type of machine learning method based on statistical learning theory and structural risk minimization principle (Pan et al., 2020). To this end, the support vector machine regression method equation for medium and long-term runoff forecasting is established as follows:

$$y = \sum_{i=1}^{n} (\beta_i - \beta_i^*) K(X, X_i) + B \qquad (2)$$

In the formula, y describes the forecast object, β_i and β_i^* describe the Lagrange multiplier, X describes the predictor vector, n describes the sample size, $X_i\,(i = 1, \ldots, n)$ describes the sample predictor vector, and $K(X, X_i)$ describes the sample predictor vector. Is the kernel function and B describes the bias (Ming et al., 2007). The corresponding runoff forecast model can be obtained through formula calculation, but it requires a long waiting time and occupies a large storage space.

In summary, Support vector machines use quadratic programming to solve support vectors. When the number of samples is large, quadratic programming involves high-order matrix calculations, which consume a lot of machine memory and calculation time. In addition, when using support vector machines to solve nonlinear problems, the kernel function should be selected carefully (Yang et al., 2021b).

3.3 Grey forecasting model

The grey theory was developed to solve the problem of lack of clarity and uncertainty of information, and gradually gained important attention internationally. There are a large number of location factors and uncertainties in medium and long-term runoff forecasting, so this theory can be used to construct a grey forecasting model. The formula is (Feng et al., 2010).

$$\ln x_{i+1} = (\ln x_1 - b/a)\left[e^{-ai} - e^{-a(i-1)}\right] \qquad (3)$$

In the formula, x_1 describes the first sample number in the runoff sequence; x_{i+1} describes the $i+1$-th sample number; a and b describe the gray model parameters, which can be determined by the least squares method.

The grey prediction model can effectively use the limited medium and long-term runoff data to forecast future runoff, but when the uncertainty of the runoff sequence is the main component, the prediction accuracy of the model will be seriously reduced.

3.4 Predictor identification and error correction of artificial neural networks

Artificial neural network is a nonlinear, self-adaptive information processing system that simulates the activity of biological neurons, and includes powerful nonlinear mapping capabilities. When the number of neurons in the hidden layer is not limited, the three-layer neural network can approximate any nonlinear function infinitely, and is widely used in hydrological forecasting.

According to Kolmogorov's principle, the empirical formula to clarify the number of nodes in the hidden layer of the neural network is as follows:

$$n_H = \sqrt{n_1 + n_O + 1} + l \tag{4}$$

In the formula, n_H describes the number of hidden layer nodes, n_1 describes the number of input nodes, n_O describes the number of output nodes, and l describes a constant between 1 and 10.

For nonlinear networks, it is difficult to select an appropriate neural network learning rate (Li et al., 2012). A learning rate that is too large will make learning unstable, and a learning rate that is too small will take a long time to learn. In addition, the number of nodes in the hidden layer of the network should also be limited to a certain area, otherwise there will be under-fitting or over-fitting. For this reason, the error is corrected by the Markov model, so that the forecast accuracy is higher and the power generation of the interconnected power system of the hydropower station is better dispatched.

Multivariate linear regression, artificial neural network and support vector machine for medium and long-term runoff forecasting models need to input predictor vectors. A set of predictors is constructed by correlation analysis, and on the premise of the significance level $\alpha = 0.05$, a stepwise regression analysis method is used to select important influencing factors from the set of predictors. Assuming that the number of important influencing factors does not exceed 3, then find the three predictors with the highest correlation with the forecast object as important influencing factors.

Under normal circumstances, there is still a corresponding deviation between the predicted value and the actual value of the medium and long-term runoff forecasting model. Using the Markov correction model to correct the error can better improve the forecasting accuracy of the model. In this paper, the positive error describes that the predicted value is greater than the actual value, and the negative error describes that the predicted value is smaller than the actual value. Usually, the error indicates that the difference between the predicted value and the actual value is small. Using the mean and standard deviation method, the errors are divided into 5 grades: extra large positive and negative errors, large positive and negative errors and general errors, and calculate the error mean and error state one-step transition probability matrix of all grades. If the error process satisfies Markov, the error correction expression is:

$$e_i^{cor} = \sum_{j=1}^{5} e_j^{avg} P_{kj}(i-1) \tag{5}$$

In the formula, e_i^{cor} describes the correction error of the $i\,(i = 2, \ldots, n)$-th predicted value, n describes the length of the error sequence, e_j^{avg} describes the j-th state average without correction error, and $P_{kg}(i-1)$ describes the uncertainty of the $i-1$-th predicted value. The one-step transition probability from the $k\,(k = 1, \ldots, 5)$ state where the correction error is located to the j state.

4 Analysis of benefit characteristics of hydropower stations

The power generation benefit function of a hydropower station is related to the water head and power generation flow, and is affected by the relationship between the water level storage capacity and the tail water level flow. Simplify the problem and treat the tail water level as a constant. In many cases, the dynamic effects of tailwater levels cannot be ignored. Therefore, under the premise of considering the dynamic influence of tail water level, this paper analyzes the economic characteristics of the two-stage power generation of the hydropower station, so as to provide a more effective decision-making basis for the real-time operation of the reservoir (Wang et al., 2012).

4.1 Mathematical description of two-stage power generation of hydropower station

Reservoir scheduling is a two-stage rolling decision problem. Among them, S_t, S_{t+1} is the initial and final storage capacity of period t, respectively; S_{t+2} is the final water storage capacity of $t+1$ in period t (Tan et al., 2012); I_t, I_{t+1} is the inflow of period t and $t+1$, respectively; r_t, r_{t+1} is the outflow of reservoir t + 1 in period t, respectively. During the dry season, the reservoir water level is low and the incoming water is small, so the reservoir

usually operates with guaranteed production. If the guaranteed output cannot be met, the reservoir operates at a reduced output. During the flood season, when the amount of water inflow is large, there is still wastewater in the installed power generation, and the reservoir generates power according to the installed capacity. Therefore, this paper only studies the case of $r_{t,\min} + r_{t+1,\min} < r_t + r_{t+1} < r_{t,\max} + r_{t+1,\max}$ ($r_{t,\min}$ is the minimum power generation water volume required by the hydropower station to meet the guaranteed output of the t phase, $r_{t,\max}$ is the maximum power generation water volume of the t phase of the hydropower station, and the installed capacity corresponds to the minimum power generation water volume and the turbine overcurrent capacity.

The two stages of power generation are:

$$\begin{cases} E_t = \eta \times \left[\frac{\mathrm{SSR}(S_t)+\mathrm{SSR}(S_{t+1})}{2} - \mathrm{SDR}(S_t + I_t - S_{t+1})\right] \times (S_t + I_t - S_{t+1}) \\ E_{t+1} = \eta \times \left[\frac{\mathrm{SSR}(S_{t+1})+\mathrm{SSR}(S_{t+2})}{2} - \mathrm{SDR}(S_{t+1} + I_{t+1} - S_{t+2})\right] \times (S_{t+1} + I_{t+1} - S_{t+2}) \\ E_{(t,t+1)} = E_t + E_{t+1} \end{cases} \quad (6)$$

In the formula: E_t, E_{t+1} is the first stage (face stage) and the second stage (remaining stage) (Sakthivel and Sathya, 2021); $E_{(t,t+1)}$ is the total power generation of the two stages; η is the power generation efficiency of the hydropower station; $\mathrm{SSR}(*)$ is the relationship between water level and storage capacity; $\mathrm{SDR}(*)$ is the relationship between the tail water level and flow rate.

In Eq. 6, it is assumed that the power generation efficiency η of the hydropower plant is known for a given reservoir. At time t, the initial reservoir capacity S_t is known, and the two-stage inflow of I_t, I_{t+1} can be obtained from the forecast information. The end storage capacity of Phase II S_{t+2} is the remaining storage capacity, and its size has an important impact on the later operation of the reservoir. According to the time of the two stages, combined with the current operation status and forecast information of the reservoir, it is determined according to the statistical law of historical operation. It can be seen that the two-stage power generation E_t, E_{t+1} and the total power generation $E_{(t,t+1)}$ are both functions of S_{t+1} facing the end of the stage.

4.2 Analysis on the benefit characteristics of power generation in two stages

The total power generation $E_{(t,t+1)}$ is not only related to the storage capacity S_{t+1} at the end of the facing phase (Ansarian et al., 2015), but also related to the state of the reservoir in the t phase, the engineering characteristics of the reservoir itself, and the characteristics of the downstream river. There are many influencing factors. How to decide to optimize the two-stage power generation $E_{(t,t+1)}$. Therefore, through mathematical analysis, this paper reveals the variation law of the two-level power generation E_t, E_{t+1} and the total power generation $E_{(t,t+1)}$ with the storage capacity S_{t+1} of the facing level (Ye et al., 2008), which provides a basis for making optimal decisions. This section mainly studies the variation law of power generation with the terminal storage capacity S_{t+1} in two stages.

The marginal contribution of the storage capacity A at the end of the facing period to the two-stage power generation (Zhan and Zuo, 2012) is:

$$\begin{cases} f_t = \frac{dE_t}{dS_{t+1}} = \eta\left[\left(\frac{\mathrm{SSR}'(S_{t+1})}{2} + SDR'(r_t)\right) \times r_t - \left[\frac{\mathrm{SSR}(S_t)+\mathrm{SSR}(S_{t+1})}{2} - \mathrm{SDR}(r_t)\right]\right] \\ f_{t+1} = \frac{dE_{t+1}}{dS_{t+1}} = \eta\left[\left(\frac{\mathrm{SSR}'(S_{t+1})}{2} + SDR'(r_t)\right) \times r_t - \left[\frac{\mathrm{SSR}(S_t)+\mathrm{SSR}(S_{t+1})}{2} - SDR(r_t)\right]\right] \end{cases} \quad (7)$$

In the formula, f_t, f_{t+1} is the marginal benefit of two-level power generation, that is, the change in power generation caused by the change of the terminal storage capacity S_{t+1}; $SSR'(S_{t+1})$ is the increase of the storage capacity of the unit S_{t+1} and the increase of the reservoir water level (Tan et al., 2014), and $SDR'(r_t)$ is when the reservoir flow is r_t., the increase in unit flow and downstream tail water level. In Formula 7, $(\frac{SSR'(S_{t+1})}{2} + SDR'(r_t))$ refers to the head increased by increasing the unit storage capacity (i.e., decreasing the flow rate by one unit) when the storage capacity at the end of the first stage is S_{t+1}. $\eta(\frac{SSR'(S_{t+1})}{2} + SDR'(r_t)) \times r_t$ refers to the increased power generation by increasing the water head $(\frac{SSR'(S_{t+1})}{2} + SDR'(r_t))$ when the power generation is r_t. $\eta(\frac{SSR'(S_{t+1})}{2} + SDR'(r_t))$ refers to the increased power generation by increasing the unit power generation when the water head is $[\frac{SSR(S_t)+SSR(S_{t+1})}{2} - SDR(r_t)]$. Therefore, the positive and negative marginal benefits of the first stage depend on who controls the water head and volume.

From Taylor's first-order expansion, we get:

$$\mathrm{SDR}(r_t) + \mathrm{SDR}(r_t) \times r_t \approx \mathrm{SDR}(2r_t) \quad (8)$$

$$\mathrm{SSR}(S_{t+1}) - \mathrm{SSR}'(S_{t+1}) \times r_t \approx \mathrm{SSR}(S_{t+1} - r_t) \quad (9)$$

Substitute $S_{t+1} = S_t + I_t - r_t$ into the above Formula 7, and combine Formulas 8, 9 to obtain:

$$f_t = \eta\left|\mathrm{SDR}(2r_t) - \frac{\mathrm{SSR}(S_t) + \mathrm{SSR}(S_t + I_t - 2r_t)}{2}\right| \quad (10)$$

Put $\frac{\mathrm{SSR}(S_t)+\mathrm{SSR}(S_t+I_t-2r_t)}{2} \approx \mathrm{SSR}(S_t + \frac{I_t}{2} - r_t)$ into Eq. 10, we can get:

$$f_t \approx \eta\left[\mathrm{SDR}(2r_t) - \mathrm{SSR}\left(S_t + \frac{I_t}{2} - r_t\right)\right] \quad (11)$$

In Formula 11, $\mathrm{SSR}(S_t + \frac{I_t}{2} - r_t)$ represents the power generation of the reservoir with the amount of water r_t when the inflow in the period t is $\frac{I_t}{2}$, and the water level value at the end of the period (Kumar et al., 2018). $SDR(2r_t)$ represents the downstream tail water level, and the amount of water corresponding to the power generation of the reservoir is $2r_t$. The results show that with the increase of r_t, $\mathrm{SDR}(2r_t)$ increases, $\mathrm{SSR}(S_t + \frac{I_t}{2} - r_t)$ decreases, and f_t also increases. Because $r_t \le r_{t,\max}$, so $f_t \approx \eta[\mathrm{SDR}(2r_{t\max}) - \mathrm{SSR}(S_t + \frac{I_t}{2} - r_t)$. In addition, during normal operation of the reservoir, $S_t \ge S_{\min}$ ($S_{\min}$ is usually the dead storage capacity), that is:

$$f_t \approx \eta\left[\mathrm{SDR}\left(2r_{t,\max}\right) - \mathrm{SSR}\left(S_{\min} - r_t\right)\right] \tag{12}$$

Since reservoirs with a large drop (Jinghua and Hua, 2011) usually satisfy $\mathrm{SDR}\left(2r_{t,\max}\right) - \mathrm{SSR}\left(S_{\min} - r_t\right) < 0$, that is, $f_t < 0$, this paper mainly studies the hydropower station satisfying $\mathrm{SDR}\left(2r_{t,\max}\right) - \mathrm{SSR}\left(S_{\min} - r_t\right) < 0$, and then brings $S_{t+2} = S_{t+1} + I_{t+1} - r_{t+1}$ into the above Eq. 7, and combines Eqs 8, 9 to obtain:

$$\begin{aligned} f_{t+1} &= \eta\left[\frac{\mathrm{SSR}\left(S_{t+1} + r_{t+1}\right) + \mathrm{SSR}\left(S_{t+1} + r_{t+1} + I_{t+1} - 2r_{t+1}\right)}{2} - \mathrm{SDR}\left(2r_{t+1}\right)\right] \\ &\approx \eta\left[\mathrm{SSR}\left(S_{t+1} + \frac{I_{t+1}}{2}\right) - \mathrm{SDR}\left(2r_{t+1}\right)\right] > \eta\left[\mathrm{SSR}\left(S_{\min} + \frac{I_{t+1}}{2}\right) - \mathrm{SDR}\left(2r_{t+1}, \max\right)\right] \end{aligned} \tag{13}$$

It can be seen that for the reservoir satisfying $\mathrm{SDR}\left(2r_{t,\max}\right) - \mathrm{SSR}\left(S_{\min} - r_t\right) < 0$, $f_{t+1} > 0$ is always established. To sum up, the marginal benefit of the first stage is less than 0, and the marginal benefit of the second stage is greater than 0, that is, when the water storage S_{t+1} increases at the end of the stage, the power generation in the facing stage decreases, and the power generation in the second stage increases, that is, two stages. There is a competitive relationship between power generation (Zhao et al., 2009). Next, we will further discuss the change law and economic characteristics of the two-stage total power generation with the decision to store water at the end of the stage.

4.2.1 Analysis of factors affecting total power generation

The marginal benefit of the total power generation $f_{(t,t+1)}$ is the sum of the marginal benefits of the two stages of power generation, which can be obtained by Formula 7:

$$\begin{aligned} f_{(t,t+1)} &= \frac{dE_{(t,t+1)}}{dS_{t+1}} = \frac{\eta}{2}\left[SSR'\left(S_{t+1}\right) \times \left(r_t + r_{t+1}\right) + \mathrm{SSR}\left(S_{t+2}\right) - \mathrm{SSR}\left(S_t\right)\right] \\ &-\eta\left[\mathrm{SDR}\left(r_{t+1}\right) + SDR'\left(r_{t+1}\right) \times r_{t+1} - \mathrm{SDR}\left(r_t\right) - SDR'\left(r_t\right) \times r_t\right] \end{aligned} \tag{14}$$

Using $G\left(S_{t+1}\right)$ and $D\left(r_t, r_{t+1}\right)$ to represent the first half and the second half of the marginal benefit of the total power generation respectively, the Formulas 15, 16 are obtained:

$$G\left(S_{t+1}\right) = \frac{\eta}{2}\left[\mathrm{SSR}'\left(S_{t+1}\right) \times \left(r_t + r_{t+1}\right) + \mathrm{SSR}\left(S_{t+2}\right) - \mathrm{SSR}\left(S_t\right)\right] \tag{15}$$

$$\begin{aligned} D\left(r_t, r_{t+1}\right) = \eta\Big[&\mathrm{SDR}\left(r_{t+1}\right) + \mathrm{SDR}'\left(r_{t+1}\right) \times r_{t+1} - \Big(\mathrm{SDR}\left(r_t\right) \\ &+ \mathrm{SDR}'\left(r_t\right) \times r_t\Big)\Big] \end{aligned} \tag{16}$$

It can be seen from Eq. 14 that the marginal benefit of the total power generation is affected by the current status of the reservoir and the engineering characteristics of the reservoir, namely the water level-capacity relationship of SSR (*) and the tailwater level-discharge relationship of SDR (*). Eq. 15 expresses the influence of the relationship between water level and storage capacity on the marginal benefit of total power generation, and Eq. 16 expresses the influence of the relationship between tail water level and flow on the marginal benefit of total power generation.

4.2.1.1 Influence of water level and storage capacity relationship

From the water balance [30] $r_t + r_{t+1} = S_t - S_{t+2} + I_t + I_{t+1}$, we can get:

$$\begin{aligned} \mathrm{SSR}'\left(S_{t+1}\right) \times \left(r_t + r_{t+1}\right) = &\ \mathrm{SSR}'\left(S_{t+1}\right) \times \left(S_t - S_{t+2}\right) \\ &+ \mathrm{SSR}'\left(S_{t+1}\right) \times \left(I_t + I_{t+1}\right) \end{aligned} \tag{17}$$

In addition, through the first-order Taylor expansion, it can be obtained:

$$\mathrm{SSR}\left(S_{t+2}\right) \approx \mathrm{SSR}\left(S_{t+1}\right) + \mathrm{SSR}'\left(S_{t+1}\right) \times \left(S_{t+2} - S_{t+1}\right) \tag{18}$$

$$\mathrm{SSR}\left(S_t\right) \approx \mathrm{SSR}\left(S_{t+1}\right) + \mathrm{SSR}'\left(S_{t+1}\right) \times \left(S_t - S_{t+1}\right) \tag{19}$$

From Eqs 15, 17, 18 we get:

$$G\left(S_{t+1}\right) \approx \frac{\eta}{2}\left[SSR'\left(S_{t+1}\right) \times \left(I_t + I_{t+1}\right)\right] > 0 \tag{20}$$

In the formula, $\mathrm{SSR}'\left(S_{t+1}\right) \times \left(I_t + I_{t+1}\right)$ is the increment of the reservoir water level when the reservoir capacity is S_{t+1} and the total water inflow in the two stages is stored in the reservoir. According to the characteristics of the relationship between water level and storage capacity, $SSR'(*) > 0, SSR''(*) < 0$ can be known. Therefore, it can be seen from Eq. 20 that when the two-stage inflow is known, $G\left(S_{t+1}\right)$ decreases with the increase of the storage capacity S_{t+1} at the end of the facing period, but is always positive, that is, the total inflow of the two-stage inflow is determined by the relationship between the water level and storage capacity Affects the marginal benefit of the total power generation, but promotes the increase of the total power generation, and $G\left(S_{t+1}\right)$ increases with the increase of the two-stage influent I_t, I_{t+1}. In addition, Formula 20 shows that for different reservoirs, when the two-stage water inflow is constant, the greater the slope $SSR'(*)$ of the water level storage capacity curve, the greater the reservoir slope, the greater the $G\left(S_{t+1}\right)$, that is, the difference between the water level storage capacity relationship and the marginal benefit of total power generation. The greater the impact, the smaller the vice versa.

4.2.1.2 The influence of tail water level and flow relationship

In Eq. 16, both the first half and the second half are functions of displacement. First analyze the change law of $SDR\left(r_t\right) + {}_tSDR'\left(r_t\right) \times r$, and then analyze the change characteristics of $D\left(r_t, r_{t+1}\right)$.

The derivative of $SDR\left(r_t\right) + {}_tSDR'\left(r_t\right) \times r$ is: $SDR''\left(r_t\right)r_t + 2 \times SDR'\left(r_t\right)$. According to the relationship between tail water level and flow characteristics, we can know:

TABLE 1 The running process of the conventional scheduling plan.

Month	Inbound traffic	Initial water level	End water level	Output flow	Water head	Contribute	Power generation	Abandoned water flow
1	1932	650	650	1932	225.16	370.13	24.74	0
2	1538	650	592.13	1987.51	221.23	374.35	26.04	0
3	1812	592.28	587.29	2051.49	231.92	374.35	26.87	0
4	1279	587.24	570.64	2324.18	196.87	409.04	29.12	0
5	2487	559.41	540	3186.28	172.33	469.18	34.78	0
6	3407	540	590	2708.93	174.06	399.18	27.89	0
7	9974	590	590	9974	174.98	1225.86	91.18	1680
8	8573	590	590	8573	175.16	1337.59	93.28	265
9	9308	590	650	7517.21	195.72	1263.41	91.37	0
10	5397	650	650	5397	217.99	1007.81	74.03	0
11	3624	650	650	3624	222.34	688.40	49.56	0
12	2207	650	650	2207	225.72	418.59	31.34	0

TABLE 2 The scheduling plan running process of the method in this paper.

Month	Inbound traffic	Initial water level	End water level	Output flow	Water head	Contribute	Power generation	Abandoned water flow
1	1930.81	650	650	1930.81	226.41	359.16	26.47	0
2	1526.1	650	594.21	1987.51	224.16	344.78	22.81	0
3	1823.23	594.21	593.15	1849.31	219.94	344.68	24.66	0
4	1298.16	593.15	586.10	1911.82	212.96	345.18	25.90	0
5	2485.05	586.10	594.24	1883.09	212.76	341.84	24.51	0
6	3409.18	594.24	552.05	5182.82	193.45	867.38	62.30	0
7	9974.03	552.05	540	9652.20	168.99	1194.58	88.50	1354.20
8	8537.63	540	540	8537.63	175.16	1237.59	93.63	264.37
9	9305.27	590	650	7419.26	195.72	1263.18	90.28	0
10	5394.35	650	650	5394.35	217.97	1007.78	74.09	0
11	3632.92	650	650	3632.92	223.42	685.84	48.13	0
12	2204.16	650	650	2204.16	224.72	419.76	32.12	0

$$\mathrm{SSR}'\left(^{*}\right) > 0, \mathrm{SSR}''\left(^{*}\right) < 0 \tag{21}$$

It can be assumed that the tail water level flow relationship curve conforms to the series of formulas:

$$\mathrm{SDR}\left(r_t\right) = a\left(r_t + b\right)^{c} + d \tag{22}$$

In the formula, $a > 0, b > 0, 0 < c < 1$, its first-order formula can be obtained:

$$SDR'\left(r_t\right) = ac\left(r_t + b\right)^{c-1} \tag{23}$$

Its second-order formula is

$$SDR''\left(r_t\right) = ac\left(c-1\right)\left(r_t + b\right)^{c-2} \tag{24}$$

From the above Formulas 23, 24, we can get:

$$\begin{aligned}&\mathrm{SDR}''\left(r_t\right) \times r_t + 2 \times SDR'\left(r_t\right) = ac\left(c-1\right)\left(r_t + b\right)^{c-2} \times r_t + 2ac\left(r_t + b\right)^{c-1} \\ &> ac\left(c-1\right)\left(r_t + b\right)^{c-2} \times \left(r_t + b\right) + 2ac\left(r_t + b\right)^{c-1} \\ &= ac\left(c+1\right)\left(r_t + b\right)^{c-1} > 0\end{aligned} \tag{25}$$

$SDR\left(r_t\right) + SDR'\left(r_t\right) \times r_t$ is an increasing function of r_t. When $r_{t+1} > r_t$, $D\left(r_t, r_{t+1}\right) > 0$, when $r_{t+1} < r_t$, $D\left(r_t, r_{t+1}\right) < 0$. As the water storage capacity of S_{t+1} increases, r_t reduces the power generation of the facing stage, r_{t+1} increases the power generation of the second stage, the first half of $D\left(r_t, r_{t+1}\right)$ increases, the second half decreases, and $D\left(r_t, r_{t+1}\right)$ increases as a whole. The negative impact of total power generation is gradually increasing.

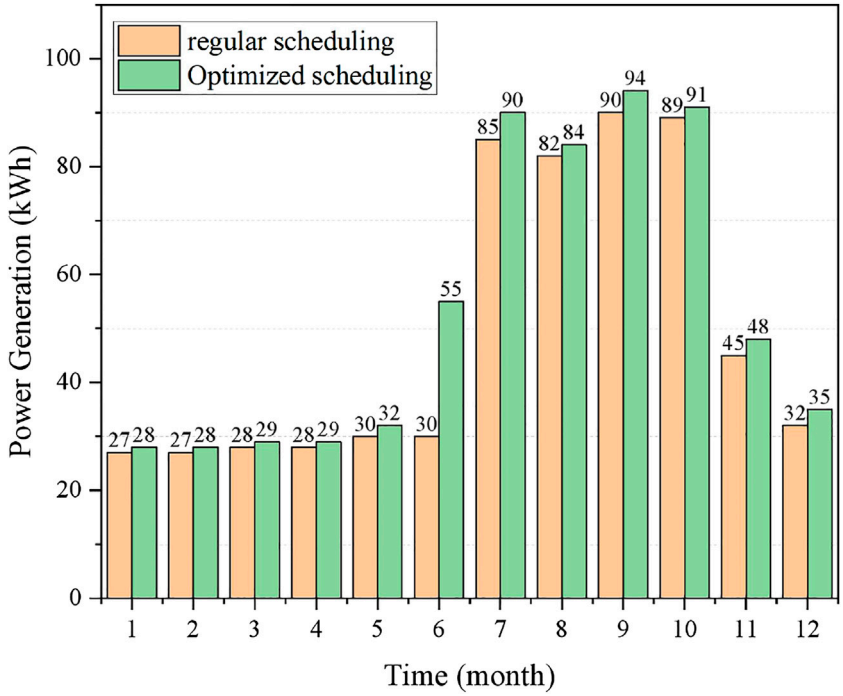

FIGURE 1
Comparison of monthly power generation.

In addition, it can be seen from Eq. 16 that the change of $D(r_t, r_{t+1})$ is also related to the relationship $\mathrm{SSR}(*)$ of tail water level and flow. When the relationship between the tail water level and flow rate is steeper, that is, the greater the slope, the narrower the lower part of the corresponding swim channel, the larger the relative variation range of $D(r_t, r_{t+1})$, and the greater the influence of the tail water level on the total power generation.

4.2.2 Concavity and convexity analysis of total power generation

The second derivative of the total power generation is:

$$f'_{(t,t+1)} = \frac{d^2 E_{(t,t+1)}}{dS_{t+1}^2} = \eta \frac{\mathrm{SSR}''(S_{t+1})}{2}(r_t + r_{t+1}) - \eta\left[SDR''(r_t) \times r_t + 2 \times SDR'(r_t) + \mathrm{SDR}''(r_{t+1}) \times r_{t+1} + 2 \times SDR'(r_{t+1})\right] \quad (26)$$

According to the characteristics of the water level storage capacity relationship curve, it can be known that $\mathrm{SSR}'(*) > 0, \mathrm{SSR}''(*) < 0$. In addition, combined with Formula 28, it can be seen that no matter what number r_t takes, $SDR''(r_t)r_t + 2 \times SDR'(r_t)$ is larger than 0, and because of $SSR''(*) < 0$, $f'_{(t,t+1)}$ is. When the total power generation of the two stages is a concave function of the storage capacity S_{t+1} at the end of the facing stage, it proves that with the increase of the storage capacity at the end of the facing stage, the marginal benefit of the total power generation decreases.

4.2.3 Monotonicity analysis of total power generation

It can be obtained by Formulas 8, 16:

$$D(r_t, r_{t+1}) \approx SDR(2r_{t+1}) - SDR(2r_t) \quad (27)$$

It can be obtained by Formulas 14, 20, 27:

$$f_{(t,t+1)} \approx \eta\left[\frac{1}{2}\mathrm{SSR}'(S_{t+1}) \times (I_t + I_{t+1}) - (\mathrm{SDR}(2r_{t+1}) - \mathrm{SDR}(2r_t))\right] \quad (28)$$

To sum up, it is assumed that $\mathrm{SSR}'(S_{t+1}) \times (I_t + I_{t+1})$ is always positive after the reservoir situation is clear; the water volume of the two-stage power generation changes with the change of the storage capacity S_{t+1} at the end of the facing stage, so that $\mathrm{SDR}(2r_{t+1}) - \mathrm{SDR}(2r_t)$ shows a positive and negative change.

It can be known from Formula 28 that if $S_{t+1} = S_{r_t=r_{t+1}}$ is $r_t = r_{t+1}, \mathrm{SDR}(2r_{t+1}) - \mathrm{SDR}(2r_t) = 0$, then $f_{(t,t+1)} > 0$. If $S_{t+1} < S_{r_t=r_{t+1}}$, $r_t > r_{t+1}$, $\mathrm{SDR}(2r_{t+1}) - SDR(2r_t) < 0$, then $f_{(t,t+1)} > 0$, then increase the water storage capacity S_{t+1} at the end of the stage, the total power generation $E_{(t+1)}$ will increase; assuming $S_{t+1} > S_{r_i=r_{t+1}}$, $r_t < r_{t+1}, SDR(2r_{t+1}) - \mathrm{SDR}(2r_t) > 0$,

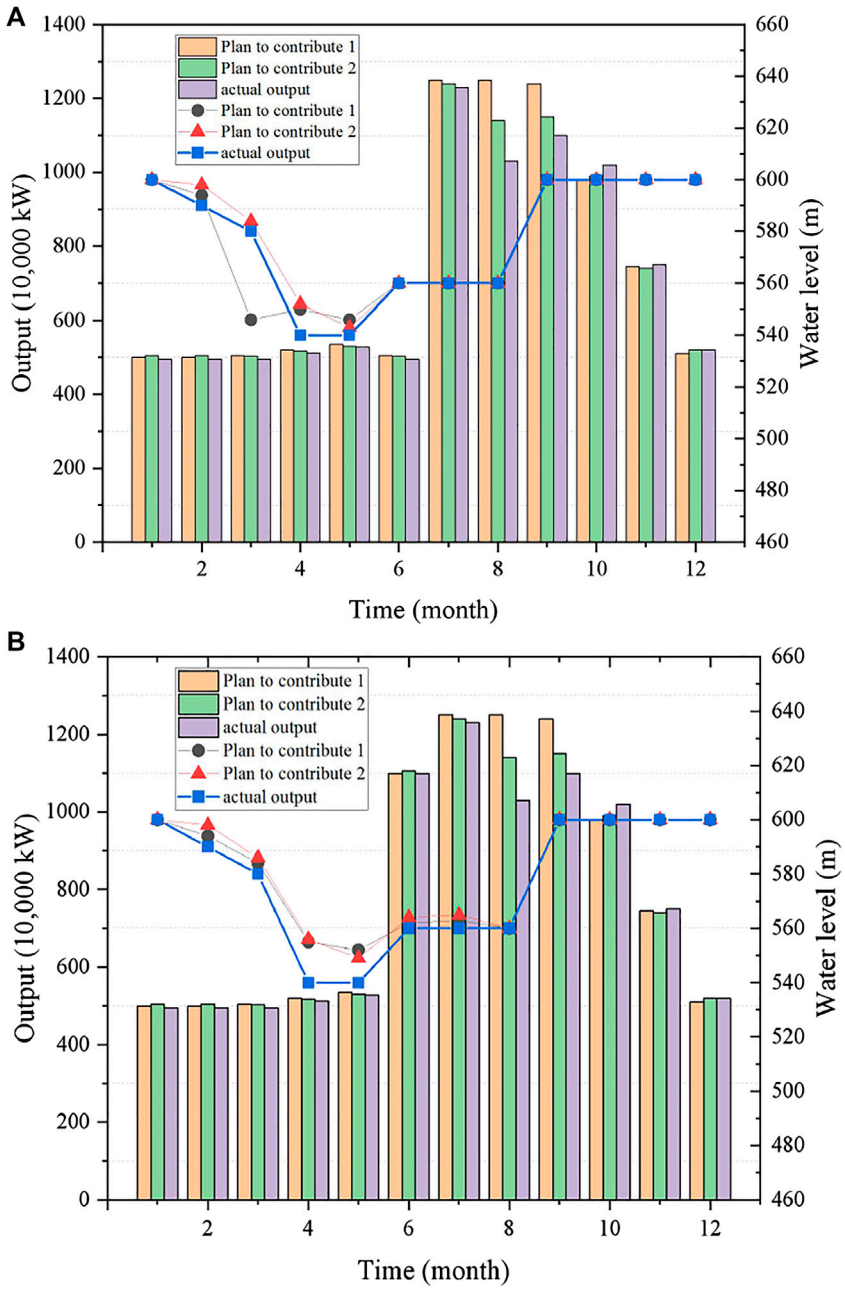

FIGURE 2
The actual operation process of the two scheduling methods and the operation process of different forecast runoff plans. **(A)** Comparison of the monthly average output process and the water level process in the actual process and planning process of traditional dispatching. **(B)** Comparison of the monthly average output process and the water level process in the actual process and planning process of optimal scheduling.

since the total power generation in the two stages is a concave function for the final storage capacity S_{t+1}, At this time, with the increase of the water storage amount S_{t+1} at the end of the stage, the marginal benefit gradually decreases. According to whether $f_{(t,t+1)}$ will be smaller than 0, it can be divided into two ways. 1) Assuming that there is a condition of $f_{(t,t+1)} < 0$, when S_{t+1} increases, the total power generation $E_{(t,t+1)}$ in the two stages increases first and then decreases, and the total power generation has an extreme value $E^{*}_{(t,t+1)}$, which is the maximum value; 2) Assuming that there is no condition $f_{(t,t+1)} < 0$, this When $E_{(t,t+1)}$ increases with the increase of S_{t+1}, the two-stage total power generation reaches the maximum value at the upper boundary.

5 Experiment and analysis of experimental results

This paper takes a hydropower station as the research object, and studies the medium and long-term power generation operation of the reservoir. The hydropower station is a comprehensive water conservancy project focusing on power generation and taking into account flood control. In addition, it also has comprehensive utilization benefits such as retaining sand, improving the navigation conditions of the reservoir area and the river section under the dam. The controlled area of the reservoir is 438,800 square kilometers, accounting for 95,200 square kilometers of the entire basin. The total storage capacity is 12.43 billion m^3, the normal water level is 650 m, and the dead water level is 590 m. The corresponding storage capacity is 11.02 billion m^3/s and 5.025 billion m^3/s respectively. Its annual regulatory performance is incomplete. The rated total installed capacity is 12 million kW, and the average annual power generation is 56.04 billion kW hours. Guaranteed output of 3.409 million kw h.

Combined with the artificial neural network model mentioned in 3.2, the runoff in 2018 is predicted month by month. According to the forecast runoff combined with different scheduling methods, the scheduling scheme is obtained, and the actual working conditions are obtained according to the actual water flow combined with different scheduling methods.

According to the neural network optimization scheduling model, using Java language programming, taking the hydropower station's maximum power generation as the optimal scheduling objective, a medium and long-term optimal scheduling model for hydropower stations is established. Input the runoff data representing the year, and the model parameters are set as follows: the penalty coefficient is 1, the penalty index is 2, the convergence accuracy is 5×10^{-5}, the maximum discrete step size is 0.4, and the maximum number of iterations is 100. Optimize the water level process for each month in 2018, and then perform scheduling calculations based on the optimized water level process. It was concluded that in 2018 the hydropower plant has a planned annual power generation capacity of 61.340 billion kWh. Tables 1, 2 are the scheduling of traditional and this method respectively.

It can be seen from Tables 1, 2 that in July, the amount of discarded water under conventional dispatch has reached 1680, while the amount of discarded water in this dispatch method is less than 1354.2. In August, the amount of water discarded by the conventional dispatch mechanism was 265, and the amount of water discarded by the dispatch mechanism in this paper was 264.37. This shows that the dispatching mechanism method in this paper has great advantages, reduces the waste of water resources, and can ensure the increase of the power generation of the hydropower station.

To better understand the scheduling situation, Figure 1 shows the comparison results between the traditional scheduling model and the scheduling model in this paper.

It can be seen from Figure 1 that the power generation of the hydropower station under the conventional dispatching method is not as much as the optimized power generation in this paper, especially in June, when the amount of rainwater is large, this paper can better allocate the water resources of the hydropower station, make better use of resources, and reduce waste, thereby producing more power energy.

The actual operation process of the two scheduling methods and the operation process of different forecast runoff plans are shown in Figure 2. Among them, plan one represents the running process of traditional BP neural network forecasting runoff plan, and plan two represents the running process of optimizing artificial neural network forecasting runoff plan.

The following conclusions can be drawn: the optimal dispatching effect after the whole year is better than the conventional dispatching effect, indicating that the optimal water level adjustment process is obviously helpful to increase the annual power generation. In the process of formulating the dispatch plan, the optimized BP neural network is reasonably used to provide the predicted runoff input for the dispatch model.

6 Conclusion

In this paper, a hydropower station is designed as the research object, and a systematic study on medium and long-term power generation dispatching of the reservoir is carried out according to a series of characteristics such as integrity and dynamicity of reservoir dispatching. It can be seen from the experiment that the annual power generation of optimal dispatch is 1.92% higher than that of conventional dispatch. Comparing the results of conventional dispatch and optimal dispatch, as well as the planned operation process and actual operation process of the two dispatch methods, the following conclusions can be drawn: It further verifies the rationality of BP neural network to provide forecast runoff input for scheduling planning; secondly, compared with conventional dispatching, optimal dispatching has an increase in total power generation; thirdly, according to the operating water level process, optimal dispatching The drop of the dispatched water level is smaller, and the water level process is more stable; fourth, because the water supply period does not fall to the dead water level at the end of the water supply period, the output value of the optimal dispatching in the first month of the water storage period is higher than that of the conventional dispatching, thereby increasing the power generation. To a certain extent, this paper reflects the flexibility of changes in the optimization of power generation scheduling in the medium and long term, and verifies the rationality of the BP neural network to provide runoff input for medium and long-term scheduling. Important guiding role.

Data availability statement

The original contributions presented in the study are included in the article/supplementary material,

further inquiries can be directed to the corresponding author.

Author contributions

SJ and YT conceived and designed the calculations and experiments; PW performed the simulation; XP contributed analysis tools; SJ and YT wrote the paper.

Funding

This work was supported by the Scientific Project of the science and technology Department of Hunan province (Grant No. 2020Gk4061, No. 2021Gk5055).

Conflict of interest

The authors declare that the research was conducted in the absence of any commercial or financial relationships that could be construed as a potential conflict of interest.

Publisher's note

All claims expressed in this article are solely those of the authors and do not necessarily represent those of their affiliated organizations, or those of the publisher, the editors and the reviewers. Any product that may be evaluated in this article, or claim that may be made by its manufacturer, is not guaranteed or endorsed by the publisher.

References

Ansarian, M., Sadeghzadeh, S. M., and Fotuhi-Firuzabad, M. (2015). Optimum generation dispatching of distributed resources in smart grids. *Int. Trans. Electr. Energy Syst.* 25 (7), 1297–1318. doi:10.1002/etep.1906

Fan, Y. H., Zhang, W., Han, W. C., and Tang, X. J. (2009). Research on energy-saving generation dispatching model in regional grid considering bidding mechanism. *Power Syst. Prot. Control* 37 (18), 83–88. doi:10.3969/j.issn.1674-3415.2009.18.018

Feng, P., Chen, Z., Wu, D., and Li, J. (2010). Research on implementation of energy-saving power generation dispatching mechanism in anhui province. *Energy Technol. Econ.* 22 (07), 25–29. doi:10.3969/j.issn.1674-8441.2010.07.005

Husin, H., and Zaki, M. (2021). A critical review of the integration of renewable energy sources with various technologies. *Prot. Control Mod. Power Syst.* 6 (1), 1–18. doi:10.1186/s41601-021-00181-3

Jinghua, L., and Hua, W. (2011). A multi-agent system to draw up energy-saving power generation dispatching schedule. *Power Syst. Technol.* 35 (5), 90–96. doi:10.1097/MCC.0b013e328344b397

Kumar, A., Bhadu, M., and Kumawat, H. (2018). "Unit commitment in thermal power generation dispatching with integration of PHEVs," in 2018 8th IEEE India International Conference on Power Electronics (IICPE).

Le, S., Wu, Y., Guo, Y., and Vecchio, C. D. (2021). Game theoretic approach for a service function chain routing in NFV with coupled constraints. *IEEE Trans. Circuits Syst. II* 68 (12), 3557–3561. doi:10.1109/tcsii.2021.3070025

Li, C., Lv, S., Cao, Y., He, L., Zhang, W., and Xia, Z. (2012). A new method for day-ahead unit commitment based on energy-saving generation dispatching. *Proc. CSEE* 16, 70–76.

Li, H., Deng, J., Feng, P., Pu, C., Arachchige, D., and Cheng, Q. (2021a). Short-term nacelle orientation forecasting using bilinear transformation and ICEEMDAN framework. *Front. Energy Res.* 697, 780–928. doi:10.3389/fenrg.2021.780928

Li, H., Deng, J., Yuan, S., Feng, P., and Arachchige, D. D. (2021b). Monitoring and identifying wind turbine generator bearing faults using deep belief network and EWMA control charts. *Front. Energy Res.*, 770. doi:10.3389/fenrg.2021.799039

Li, X. F., and Tan, L. J. (2012). Research on models and compensation mechanism of energy-saving generation dispatching. *Adv. Mater. Res.* 354, 1041–1046. doi:10.4028/www.scientific.net/AMR.354-355.1041

Liu, X. (2021). Multiple time-scale economic dispatching strategy for commercial building with virtual energy storage under demand response mechanism. *Int. J. Energy Res.* 45 (11), 16204–16227. doi:10.1002/er.6853

Ming, Z., Lianjun, S., and Jun, D. (2007). Study on issues related to Energy-Saving Dispatching of generation that conforms to the market mechanism. *Electr. Power Technol. Econ.* 1, 1–5. doi:10.3969/j.issn.1674-8441.2007.05.002

Pan, X., Liang, Y., Deng, X., Li, M., Cui, J., and Yang, J. (2020). Low-carbon economic dispatching model of electric-heating combined system considering multi-type energy storage. *IOP Conf. Ser. Earth Environ. Sci.* 546 (2), 022017. doi:10.1088/1755-1315/546/2/022017

Sakthivel, V. P., and Sathya, P. D. (2021). Single and multi-area multi-fuel economic dispatch using a fuzzified squirrel search algorithm. *Prot. Control Mod. Power Syst.* 6 (1), 1–13. doi:10.1186/s41601-021-00188-w

Shang, J. (2007). Research on energy-saving generation dispatching mode and operational mechanism considering market mechanism and government macro-Control. *Power Syst. Technol.* 31 (24), 55–62. doi:10.1016/S1005-8885(07)60138-1

Tan, Z. F., Song, Y., Li, X., Zhang, H., and An, J. (2014). Energy-saving generation dispatching optimization model based on time-of-use price mechanism. *Operations Res. Manag. Sci.* 23 (1), 101–107. doi:10.3969/j.issn.1007-3221.2014.01.015

Tan, Z., Liu, K., Song, Y., Rao, R., and Xu, J. (2012). Analysis model for the impact of energy-saving generation dispatching policy on energy and environment. *East China Electr. Power* 40 (9), 1464–1468.

Wang, D., Qiu, Y., Ping, A., and Liu, C. (2012). Problems and considerations on energy-saving generation dispatching in yunnan. *Power Syst. Clean Energy* 28 (12), 34–37. doi:10.3969/j.issn.1674-3814.2012.12.007

Wei, Q., Han, X., Guo, W., Yang, M., and Liu, G. (2016). Load following mechanism and power flow algorithm under generator rotor angle control mode. *IET Gener. Transm. & Distrib.* 10 (7), 1510–1518. doi:10.1049/iet-gtd.2015.0131

Yang, N., Dong, Z., Wu, L., Zhang, L., Shen, X., Chen, D., et al. (2021a). A comprehensive review of security-constrained unit commitment. *J. Mod. Power Syst. Clean Energy* 10 (3), 562–576. doi:10.35833/MPCE.2021.000255

Yang, N., Qin, T., Wu, L., Huang, Y., Huang, Y., Xing, C., et al. (2022b). A multi-agent game based joint planning approach for electricity-gas integrated energy systems considering wind power uncertainty. *Electr. Power Syst. Res.* 204, 107673. doi:10.1016/j.epsr.2021.107673

Yang, N., Yang, C., Wu, L., Shen, X., Jia, J., Li, Z., et al. (2021b). Intelligent data-driven decision-making method for dynamic multi-sequence: An E-Seq2Seq based SCUC expert system. *IEEE Trans. Industrial Inf.* 18 (5), 3126–3137. doi:10.1109/TII.2021.3107406

Yang, N., Yang, C., Xing, C., Ye, D., Jia, J., Chen, D., et al. (2022a). Deep learning-based SCUC decision-making: An intelligent data-driven approach with self-learning capabilities. *IET Generation Trans Dist* 16 (4), 629–640. doi:10.1049/gtd2.12315

Ye, Y., Zhang, W., and Zhang, Y. (2008). Research on benefit-compensation mechanism of energy saving power generation dispatching in compatible market mechanism. *Power Demand Side Manag.* 6, 7–10. doi:10.3969/j.issn.1009-1831.2008.06.003

Zhan, Y., and Zuo, Z. (2012). Energy-saving generation dispatching model about power dispatching under carbon emission trading mechanism. *Eng. J. Wuhan Univ.* 45 (5), 662–666.

Zhang, L., Guohui, X. I. E., and Ze, Z. H. U. (2009). Quasi marketization model of energy-saving generation dispatching. *Automation Electr. Power Syst.* 33 (8), 29–32.

Zhang, Y., Qian, T., and Tang, W. (2022). Buildings-to-distribution-network integration considering power transformer loading capability and distribution network reconfiguration. *Energy* 244, 123104. doi:10.1016/j.energy.2022.123104

Zhao, R., Kang, C. Q., Liu, M., Cheng, H., Huang, W., Chen, Z., et al. (2009). The platform of bus load forecasting for energy-conservation based generation dispatching. *Electr. Power* 42 (6), 32–36. doi:10.3969/j.issn.1004-9649.2009.06.007

frontiers | Frontiers in Energy Research

BRIEF RESEARCH REPORT
published: 22 July 2022
doi: 10.3389/fenrg.2022.950521

Optimal Configuration of Fire-Storage Capacity Considering Dynamic Charge-Discharge Efficiency of Hybrid Energy Storage

Hongbo Huang, Hui Wang, Yang Cai, Xiwei Chen and Tingting Li*

Powerchina Hubei Electric Engineering Co., Ltd, Wuhan, China

The combination of thermal power and hybrid energy storage is an effective way to improve the response ability of automatic generation control (AGC) command in thermal power plants. Notably, the configuration of hybrid energy storage capacity is directly related to improvement of the frequency modulation ability of thermal power plants and the coordination of economic benefits. However, the constant efficiency model adopted in capacity configuration will misjudge the actual operating status of each energy storage unit, resulting in unreasonable capacity allocation. In this context, a fire-storage capacity optimization configuration model considering the dynamic charge–discharge efficiency of hybrid energy storage is established. The model presents the functional relationship between charge and discharge power and the efficiency of different types of energy storage. Simulation proves that the proposed strategy can meet the tracking demand of area control error signal in thermal power plants and reduce the planning and operation cost of energy storage.

Keywords: energy storage-thermal power combination, AGC response, hybrid energy storage system, capacity configuration, dynamic efficiency

OPEN ACCESS

Edited by:
Xun Shen,
Tokyo Institute of Technology, Japan

Reviewed by:
Sandeep Kumar Duran,
Lovely Professional University, India
Gaurav Sachdeva,
DAV University, India

****Correspondence:***
Hongbo Huang
x997050035@163.com

Specialty section:
This article was submitted to Smart Grids, a section of the journal Frontiers in Energy Research

Received: *23 May 2022*
Accepted: *13 June 2022*
Published: *22 July 2022*

Citation:
Huang H, Wang H, Cai Y, Chen X and Li T (2022) Optimal Configuration of Fire-Storage Capacity Considering Dynamic Charge-Discharge Efficiency of Hybrid Energy Storage. Front. Energy Res. 10:950521. doi: 10.3389/fenrg.2022.950521

1 INTRODUCTION

In China, thermal power plants mainly undertake secondary frequency modulation auxiliary services (Jin et al., 2022): adjusting unit output in real time according to automatic generation control (AGC) instructions. In recent years, with the reform of China's energy structure, the complexity of system AGC instruction characteristics has increased (Sun et al., 2020; Yang et al., 2021; Yang et al., 2022). In this context, the problems of long inherent response delay and low climbing rate of traditional thermal power units (Zhang et al., 2018; Zhang et al., 2021) will increase the tracking error of AGC instructions and make it difficult to ensure the safety of power grid frequency. Energy storage, as a new type of frequency modulation resource, has the characteristics of fast response, accurate control, and two-way output (Meng et al., 2019), which can assist the thermal power plant in instantly tracking power instructions. Therefore, the configuration of a certain capacity energy storage system in a thermal power plant is an effective method to solve the AGC response problem of the whole plant.

There are various types of energy storage inside the hybrid energy storage, which can meet the energy density and power density requirements of frequency modulation instructions. Therefore, compared with single energy storage, hybrid energy storage can

greatly improve the AGC response capacity of thermal power plants (Ye et al., 2021; Saxena and Shankar, 2022) and effectively improve the stability and economy of energy storage combination plants. However, the capacity configuration cost of the hybrid energy storage system is contradictory to the improvement of AGC response capability of the whole plant: too much energy storage capacity configuration will lead to increase of energy storage operation planning cost, and too little configuration will lead to failure to compensate for the poor AGC response capability of thermal power units. Therefore, in order to improve the response capacity of AGC of thermal power plants and ensure the economy of energy storage system planning and operation, optimizing the configuration of hybrid energy storage capacity is an important link for energy storage to participate in the large-scale development of AGC response of thermal power plants.

The objectives of the capacity configuration of the AGC frequency modulation hybrid energy storage system for auxiliary thermal power units include the following: 1) improvement in AGC response performance of the whole plant; 2) reduction in the planning and operation cost of the hybrid energy storage system. In order to achieve this goal, it is necessary to allocate the power in the AGC frequency modulation responsibility signal of the energy storage system to different energy storage units so as to give full play to the technical advantages of different energy storage media in the hybrid energy storage system to meet the coordination of economy and regulation of the whole plant.

Yang (2016), Liu et al. (2021), and Meng et al. (2021) set the power distribution strategy of hybrid energy storage based on the decomposition of the Area Control Error (ACE) signal in the frequency domain and carried out capacity optimization on this basis. However, the control cycle of secondary frequency modulation is more than 1 min, and the response time of different types of energy storage devices is within 5 s, so the difference between different response characteristics can be ignored. Therefore, this method is not applicable to the power distribution of hybrid energy storage oriented to AGC of thermal power plants. Wang et al. (2018); Aghajan-Eshkevari et al. (2022) adopt the "priority" allocation method to carry out capacity configuration, such as preferential charging and discharging power allocation method for supercapacitors.

In this way, according to the analysis of the operation mechanism of some auxiliary service markets, the general rule of maximizing profits is obtained, and then the output priority level of each energy storage type is formulated according to the rule, which is more suitable for some specific scenarios. However, this method is subjective and poor in scalability. In the studies by Cheng et al. (2014) and Galatsopoulos et al. (2020), dynamic optimization of the ACE signal allocation ratio is considered in capacity configuration so as to give full play to the frequency modulation potential of different types of energy storage in various scenarios. In the abovementioned study, the charge and discharge efficiency of each type of energy storage is regarded as a constant. In fact, the efficiency of charge and discharge changes dynamically with the distribution of power. Ignoring the dynamic characteristics of charging and discharging efficiency will lead to unreasonable allocation of energy storage capacity and affect the frequency modulation performance and configuration cost of hybrid energy storage. In this regard, the charge–discharge power-efficiency model of the battery energy storage unit was established (Rancilio et al., 2019), but only the dynamic characteristics of the charge–discharge efficiency of a single type of energy storage were considered. Iclodean et al. (2017) discuss the dynamic characteristics of charge and discharge efficiency of compressed air energy storage and electrochemical energy storage, but it is only described by a simple model in the form of a segmented function, which is different from the dynamic model of actual power-charge and discharge efficiency. Furthermore, the previously mentioned pieces of literature did not consider the optimal allocation of capacity.

To sum up, this study adopts a hybrid energy storage system comprising batteries and supercapacitors to assist traditional thermal power plants in providing AGC auxiliary services. Aiming at the capacity configuration problem of the hybrid energy storage system, this study establishes a refinement dynamic model of charging and discharging power efficiency of each type of energy storage unit. Based on this, a fire-storage capacity configuration model considering the dynamic charge–discharge efficiency of hybrid energy storage is constructed to dynamically optimize the proportion of ACE signal allocation so as to obtain the rated energy storage capacity that meets the requirement of instruction tracking and minimizes the cost of energy storage planning and operation. Finally, the superiority and economy of the proposed strategy are verified by simulation.

2 THE DYNAMIC EFFICIENCY MODEL OF HYBRID ENERGY STORAGE CHARGE–DISCHARGE POWER

2.1 Dynamic Efficiency Model of Battery

When the battery participates in AGC frequency modulation in a thermal power plant, the incoming power can be changed by adjusting the charge and discharge current of the internal circuit so that it can meet the requirements of auxiliary frequency modulation power. With the dynamic change of charge and discharge current, the battery terminal voltage will also change, so the charge and discharge efficiency determined by the terminal voltage too will change. The mathematical model of dynamic charging and discharging efficiency of the previously mentioned batteries is as follows:

$$P_i^b = U_i^b I_i^b = \left(E_i^b - I_i^b R_i^b\right) I_i^b \tag{1}$$

$$\eta_{i,t}^b = \begin{cases} \dfrac{U_{i,t}^b}{E_i^b} = \dfrac{E_i^b - I_{i,t}^b R_{i,t}^b}{E_i^b}, I_{i,t}^b \geq 0 \\ \dfrac{E_i^b}{U_{i,t}^b} = \dfrac{E_i^b}{E_i^b + I_{i,t}^b R_{i,t}^b}, I_{i,t}^b < 0 \end{cases} \tag{2}$$

In the formula, R_i^b and E_i^b are equivalent internal resistance and open circuit potential of battery i respectively;$U_{i,t}^b$, $I_{i,t}^b$, $\eta_{i,t}^b$, and P_i^b are the terminal voltage, charge and discharge current, charge and discharge efficiency, and charge and discharge power

of battery i at time t (positive for discharge and negative for charge), respectively.

The SOC status of the battery is as follows:

$$S_{i,t}^{b}\eta_{i,t}^{b} = S_{i,t-1}^{b}\eta_{i,t-1}^{b} - \frac{P_{i,t}^{b}\Delta t}{C_i^{b}}. \tag{3}$$

In the formula, $S_{i,t}^{b}$ is the SOC state value of battery i at time t. During operation, $S_{i,t}^{b}$ should meet the constraints shown in the equation. C_i^{b} is the rated capacity of battery i.

$$S_i^{b,\min} \le S_{i,t}^{b} \le S_i^{b,\max} \tag{4}$$

In the formula, $S_i^{b,\max}$ and $S_i^{b,\min}$ are the maximum and minimum SOC values of battery I ,respectively.

2.2 Dynamic Efficiency Model of a Supercapacitor

In this study, the current loop of the supercapacitor adopts a constant power control mode, and the series structure of ideal capacitance and equivalent series internal resistance is used to simulate the internal circuit of the supercapacitor (Naseri et al., 2021). Unlike batteries, the charging and discharging efficiency of supercapacitors is related only to power.

$$\eta_{i,t}^{s} = \begin{cases} 1 + \dfrac{2R_i^{S}\ln d_i}{U_{s,i}^{\max}\left(1-d_i^{2}\right)}P_{i,t}^{s}, P_{i,t}^{s} \ge 0 \\ \dfrac{1}{1 - \dfrac{2R_i^{S}\ln d_i}{U_{s,i}^{\max}\left(1-d_i^{2}\right)}P_{i,t}^{s}}, P_{i,t}^{s} < 0 \end{cases} \tag{5}$$

In the formula, R_i^{S}, $U_{s,i}^{\max}$, and d_i are the equivalent resistance of supercapacitor I, the maximum voltage, and discharge factor of ideal capacitor i ,respectively; $P_{i,t}^{s}$ and $\eta_{i,t}^{s}$ are, respectively, the charge–discharge power and charge–discharge efficiency of supercapacitor i at time t (discharge is positive and charge is negative).

The SOC of the supercapacitor is as follows:

$$S_{i,t}^{s}\eta_{i,t}^{s} = S_{i,t-1}^{s}\eta_{i,t-1}^{s} - \frac{P_{i,t}^{s}\Delta t}{\eta_{i,t}^{s}C_i^{s}} \tag{6}$$

In the formula, $S_{i,t}^{s}$ is the SOC state value of supercapacitor i at time t. During operation, $S_{i,t}^{b}$ should meet the constraints shown in the formula. C_i^{s} is the rated capacity of supercapacitor i.

$$S_i^{s,\min} \le S_{i,t}^{s} \le S_i^{s,\max} \tag{7}$$

In the formula, $S_i^{s,\min}$ and $S_i^{s,\max}$ are the maximum and minimum SOC values of supercapacitor I, respectively.

2.3 Importance Analysis of the Dynamic Efficiency Model of the Energy Storage Unit

In order to analyze the importance of dynamic efficiency of the energy storage unit to capacity allocation, the electric quantity fluctuation range $\Delta E_{i,t}$ is introduced as follows:

$$\Delta E_{i,t}^{b} = C_i^{b}\left|S_{i,t}^{b} - S_{i,t-1}^{b}\right| = \begin{cases} \dfrac{P_{i,t}^{b}\Delta t}{\eta_{i,t}^{b}}, P_{i,t}^{b} \ge 0 \\ -\dfrac{P_{i,t}^{b}\Delta t}{\eta_{i,t}^{b}}, P_{i,t}^{b} < 0 \end{cases}. \tag{8}$$

$$\Delta E_{i,t}^{s} = C_i^{s}\left|S_{i,t}^{s} - S_{i,t-1}^{s}\right| = \begin{cases} \dfrac{P_{i,t}^{s}\Delta t}{\eta_{i,t}^{s}}, P_{i,t}^{s} \ge 0 \\ -\dfrac{P_{i,t}^{s}\Delta t}{\eta_{i,t}^{s}}, P_{i,t}^{s} < 0 \end{cases} \tag{9}$$

In the formula, $\Delta E_{i,t}^{b}/\Delta E_{i,t}^{s}$ represents the electric quantity fluctuation range of the battery/supercapacitor between $t-1$ and t. Under the same power curve and the smaller $\Delta E_{i,t}$ at each moment, the smaller the capacity requirement C_i to meet SOC constraints.

According to **Figure 1**, different from the constant state of charge and discharge efficiency in the configuration of energy storage capacity at that time, the actual charge and discharge power of the supercapacitor and battery changes dynamically with the power and is inversely proportional to the charge and discharge power. According to the numerical comparison between constant charge and discharge efficiency and dynamic charge and discharge efficiency, the charge and discharge power of each energy storage unit is segmented according to **Table 1**.

3 HYBRID ENERGY STORAGE CAPACITY ALLOCATION POLICY

After the hybrid energy storage system is configured in the thermal power plant, the AGC-responsive hybrid energy storage capacity configuration strategy is shown in **Figure 2**. In **Figure 2**, P^{ref} depicts the ACE signal transmitted by the AGC dispatching center to a thermal power plant, P^{m} is the real-time output of the conventional units in the thermal power plant jointly responding to the ACE signal, and the ACE signal tracking error P_{ref}^{s-b} caused by the inherent AGC response weakness of the traditional units is fully compensated by the hybrid energy storage system.

The key to the hybrid energy storage capacity configuration strategy is to propose a hybrid energy storage capacity configuration model to reduce the AGC response cost of hybrid energy storage on the premise of ensuring P_{ref}^{s-b} is fully compensated. At the same time, aiming at the nonlinear constraint and nonlinear objective function of the model, the linearization process is carried out by the BIG-M method and product type decomposition method so as to realize the optimal distribution of P_{ref}^{s-b} within the energy storage cluster and obtain the economic allocation of the capacity of each energy storage unit.

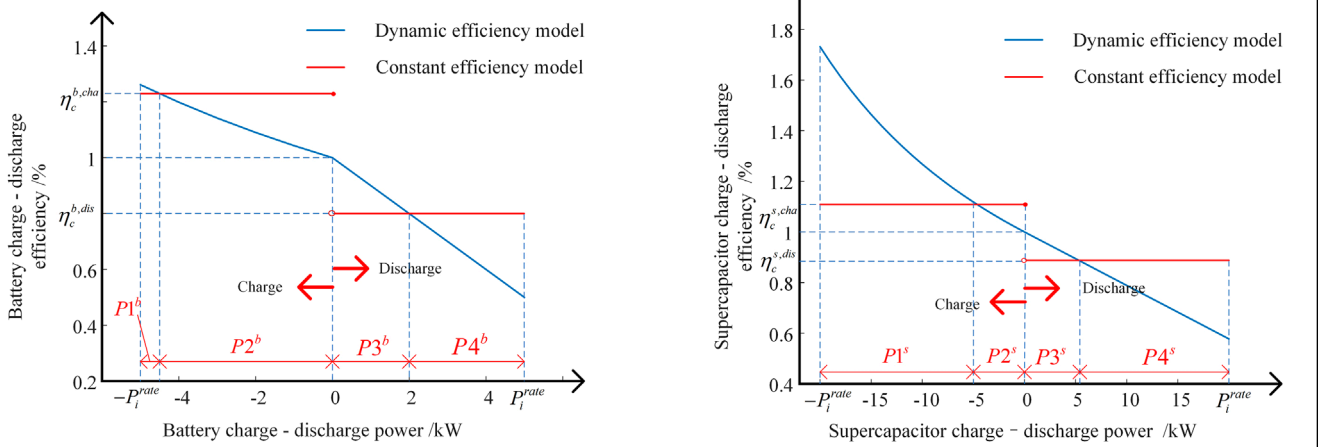

FIGURE 1 | Dynamic/constant efficiency curve of the energy storage unit with power.

3.1 Construction of the Hybrid Energy Storage Capacity Configuration Model

3.1.1 The Optimization Objective

The objective of the hybrid energy storage capacity configuration model is to minimize the total planning and operation cost F of the hybrid energy storage. F includes the fixed investment C^e of the capacity of each energy storage unit, the maintenance cost C^w of the machine, and the cost C^p of running electricity loss.

$$C^e = \sum_{i=1}^{E1} k_i^{e,b} C_i^b + \sum_{j=1}^{E2} k_j^{e,s} C_j^s \tag{10}$$

$$k_i^{e,b} = \frac{c_i^{e,b}\left(1+r_i^b\right)^{N_i^b}}{365\left[r_i^b\left(1+r_i^b\right)^{N_i^b}-1\right]} \tag{11}$$

$$k_j^{e,s} = \frac{c_j^{e,s}\left(1+r_j^s\right)^{N_j^s}}{365\left[r_j^s\left(1+r_j^s\right)^{N_j^s}-1\right]} \tag{12}$$

$$C^w = \sum_{i=1}^{E1} \frac{c_i^{w,b} C_i^b}{365} + \sum_{j=1}^{E2} \frac{c_j^{w,s} C_j^s}{365}. \tag{13}$$

TABLE 1 | Charge and discharge power segmentation basis.

Power of charge and discharge segments	Judgement method
$P1^s$, $P1^b$	Dynamic charging efficiency ≥ Constant charging efficiency
$P2^s$, $P2^b$	Dynamic charging efficiency < Constant charging efficiency
$P3^s$, $P3^b$	Dynamic discharge efficiency ≥ Constant discharge efficiency
$P4^s$, $P4^b$	Dynamic discharge efficiency < Constant discharge efficiency

$$C^p = \sum_{t=1}^{17280}\left[\sum_{i=1}^{E1} c_i^{p,b}\cdot P_{i,t}^b\left(\frac{1}{\eta_{i,t}^b}-1\right) + \sum_{j=1}^{E2} c_j^{p,s}\cdot P_{j,t}^s\left(\frac{1}{\eta_{j,t}^s}-1\right)\right] \tag{14}$$

In the formula, $c_i^{e,b}$ and $c_j^{e,s}$ are the investment cost coefficients of battery I and supercapacitor j per unit capacity, respectively; $c_i^{w,b}$ and $c_j^{p,s}$ are maintenance cost coefficients of battery i and supercapacitor j per unit electric quantity, respectively; $c_i^{p,b}$ and $c_j^{p,s}$ are the cost coefficients of battery i and supercapacitor j (unit price of online connection), respectively. r_i^b and r_j^s are the discount rates of battery i and supercapacitor j; N_i^b and N_j^s are the floating charge life of battery i and supercapacitor j.

Since the capacity unit price of the power energy storage unit is much higher than that of the capacity energy storage unit as well as the maintenance cost and Internet access unit price of each unit, the fixed investment of the capacity of the power energy storage unit becomes the main cost of the hybrid energy storage system. Therefore, reducing the capacity configuration of the power energy storage unit can effectively improve the economy of the hybrid energy storage system.

3.1.2 Constraint Conditions

In addition to **Eqs 1–7**, the constraint conditions of the fire-storage capacity configuration model also includes power balance constraint 15, charge–discharge power constraint 16–17, climbing constraint 18–19, current constraint 20, and charge–discharge efficiency constraint 21–22.

$$P_{ref,t}^{s-b} = \sum_{i=1}^{E1} P_{i,t}^b + \sum_{j=1}^{E2} P_{j,t}^s. \tag{15}$$

$$-P_i^{b,rate} \le P_{i,t}^b \le P_i^{b,rate}. \tag{16}$$

$$-P_i^{s,rate} \le P_{i,t}^s \le P_i^{s,rate}. \tag{17}$$

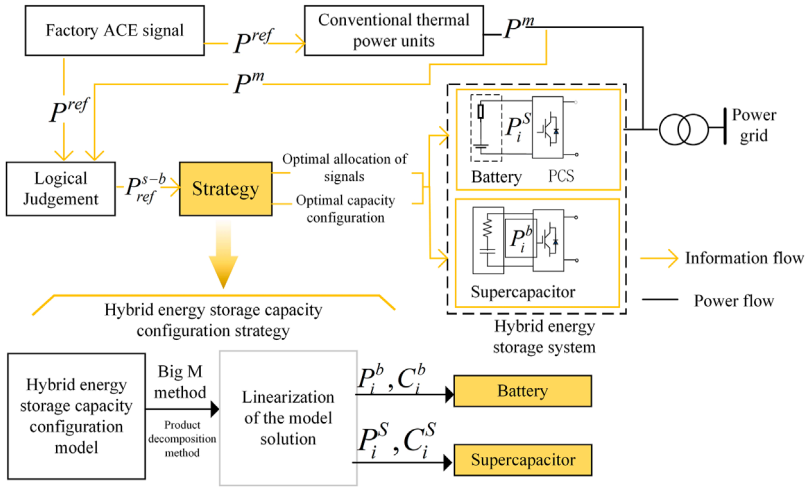

FIGURE 2 | Hybrid energy storage capacity configuration strategy.

TABLE 2 | Classification of non-convex terms for the model.

Category	Characteristics	Correspondence	Log-linear
1	$z = \frac{x}{y}$	(14)	*Continuousiterativealgorithm* (Song et al., 2018)
2	$z = xy$	(1)	*Continuousiterativealgorithm* (Song et al., 2018)
3	$z = \frac{1}{1+k1*x}$	(2) (5)	*Continuousiterativealgorithm*
4	$z = \begin{cases} x, if\, y \geq 0 \\ p, if\, y \leq 0 \end{cases}$	(2) (5)	*BigMmethod* (Anderson-Cook and Robinson, 2009)
5	$z = \lvert x \rvert$		*BigMmethod* (Anderson-Cook and Robinson, 2009)

In this Table, x, y, z, p are variables.

$$-R_i^{b,dn} \leq P_{i,t}^b - P_{i,t-1}^b \leq R_i^{b,up}. \quad (18)$$

$$-R_i^{s,dn} \leq P_{i,t}^s - P_{i,t-1}^s \leq R_i^{s,up}. \quad (19)$$

$$-I_i^{b,rate} \leq I_{i,t}^b \leq I_i^{b,rate} \quad (20)$$

$$\eta_i^{b,\min} \leq \eta_{i,t}^b \leq \eta_i^{b,\max}. \quad (21)$$

$$\eta_i^{s,\min} \leq \eta_{i,t}^s \leq \eta_i^{s,\max}. \quad (22)$$

In the formula stated above, $P_{i,t}^{ref}$ is the incoming power of energy storage unit i at time t; the number of units of $E1$ and $E2$ battery cluster and supercapacitor cluster is the number of units of the hybrid energy storage system. $P_i^{b,rate}$ and $P_i^{s,rate}$ are the rated power of battery i and supercapacitor i, respectively; $R_i^{s,up}$ and $R_i^{b,dn}$ demonstrate the ascending and descending climbing rates of supercapacitor i respectively. $I_i^{b,rate}$ is the rated current of battery i; $\eta_i^{b,\max}$ and $\eta_i^{b,\min}$ are the maximum and minimum charge and discharge efficiency of battery i, respectively. $\eta_i^{s,\max}$ and $\eta_i^{s,\min}$ are the maximum and minimum charge and discharge efficiency of supercapacitor i, respectively.

3.2 Model Processing and Solution

3.2.1 Model Linearization

The configuration model of hybrid energy storage capacity has five types of non-convex terms as shown in **Table 2**, resulting in increased difficulty in optimization. In this regard, this study adopts different linearization methods for these five types of non-convex terms, as shown in **Table 2** below:

3.2.2 Model Solving

According to the abovementioned linearization method, the solution process of the hybrid energy storage capacity configuration model considering the dynamic charging–discharge efficiency model is shown in **Figure 3**.

4 EXAMPLE ANALYSIS

This study takes a thermal power plant with a hybrid energy storage system consisting of batteries and supercapacitors as a simulation example. The total output and ACE signal of the whole plant without energy storage on a certain day are selected, and the parameters of the hybrid energy storage system are shown in **Table 3**. Considering the actual operating conditions of the project-SOC differences among energy storage units, each energy

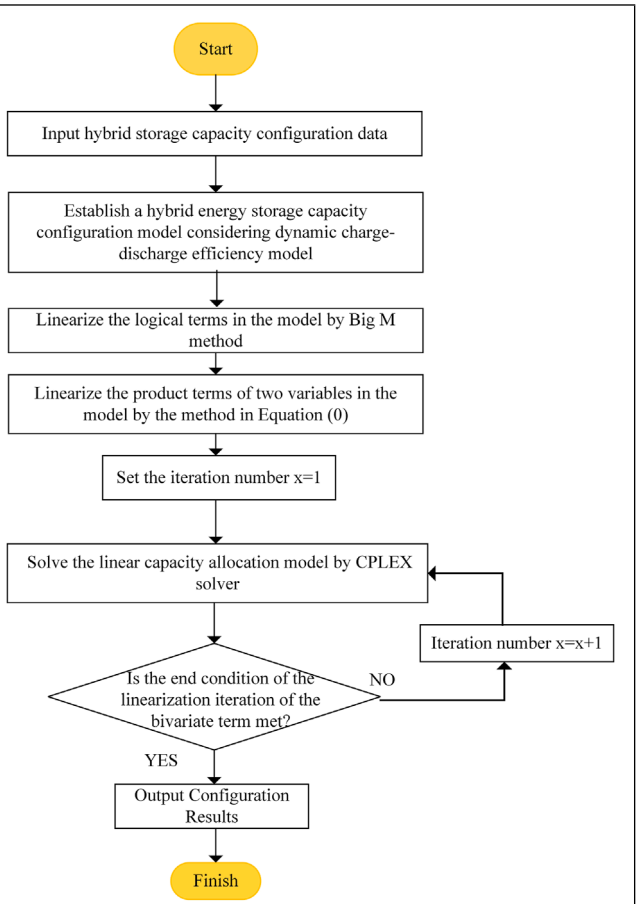

FIGURE 3 | Solution process.

TABLE 3 | Unit parameters.

Index	Battery	Supercapacitor
R^b/Ω	7.8	–
$E^b/V\Omega$	60	–
U_E^{max}/V	–	70
U_E^{max}/V	–	70
R^S/Ω	–	2.8
P^{rate}/kW	10	20
$c^l/(\$/kW.h)$	2,000	1,500
$c^e/(\$/kW.h)$	2,000	1,500
$c^e/(\$/kW.h)$	640	27,000
$c^w/(\$/kW.h)$	0.05	0.05
$c^p/(\$/kW.h)$	1	1
r	0.08	0.08
N/a	4	20
η_{PCS}^{inv}	0.85	0.85
η_{PCS}^{conv}	0.85	0.85
S_{max}	0.8	0.9
S_{min}	0.2	0.1
$R^{up}/(kW/s)$	20	2,000
$R^{dn}/(kW/s)$	20	2,000

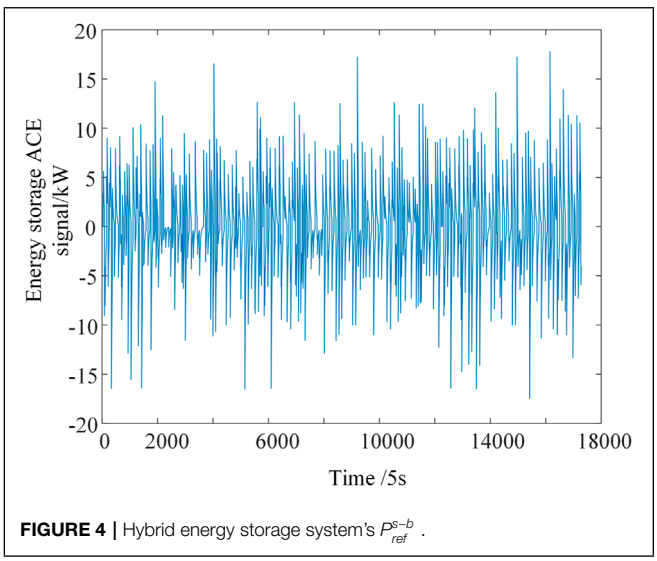

FIGURE 4 | Hybrid energy storage system's P_{ref}^{s-b} .

storage unit is set to have SOC differences, and the initial SOC of the battery and supercapacitor is 0.4 and 0.5, respectively. The model was built and solved on MATLAB 2018b platform using YALMIP toolbox and GUROBI9.1.2 solver on a computer configured with Win10 system, AMD R7-5800H processor, and 16G RAM.

The common full compensation strategy in power plant energy storage engineering introduced by the energy storage demonstration project of Shijingshan Power Plant, which has been practiced online, is adopted: energy storage complete compensation for the difference between real-time monitoring AGC command and unit output data, namely, $P_{ref}^{s-b} = P^{ref} - P^{m}$. P_{ref}^{s-b} curve is shown in **Figure 4**, and the sampling period of the original data is $\Delta t = 5s$.

To verify the effectiveness and superiority of the strategies proposed in this study,the comparison strategies shown in **Table 4** is set.

4.1 Capacity Optimization Results

The purpose of capacity configuration is to ensure the frequency modulation effect of AGC and reduce the operation cost of energy storage planning. The capacity optimization results of different strategies are shown in **Table 5**. In energy storage output to P_{ref}^{s-b} command signal tracking error $\zeta_t(\zeta_t = \left|\sum_{i=1}^{M} P_{i,t} - P_{ref,t}^{s-b}\right|)$ to represent the AGC frequency modulation effect, the effect of different strategies of AGC response is shown in **Figure 5**. The actual operation of the energy storage system includes dynamic charge–discharge efficiency model and corresponding dynamic SOC constraints. The capacity of energy storage unit optimized by strategy 3 is put into the actual operation model of energy storage to obtain the actual value of strategy 3. The ideal value of strategy 3 is the result of direct optimization of the corresponding model of strategy 3.

According to the analysis of **Table 5** and **Figure 5**, the results are as follows:

TABLE 4 | Capacity optimization strategy comparison settings.

Capacity configuration strategy	Implication
Strategy 1	The strategy of this study: the hybrid energy Storage and dynamic charge–discharge Efficiency model
Strategy 2	Single energy storage and dynamic Charge–discharge efficiency model
Strategy 3	Hybrid energy storage and constant Charge–discharge efficiency model

TABLE 5 | Configuration results for different capacity optimization strategies.

Index	Strategy 1	Strategy 2	Strategy 3 – ideal value	Strategy 3 – actual value
$C^b/(kW.h)$	4,326.4	—	687.7	687.7
$C^S/(kW.h)$	1,762.4	5,007.1	839.9	839.9
$\sum_{i=1}^{M} F_i/(\$)$	13,548	32,293	5,766.7	5,765.8
Daily Average ζ_t	0	1	0	0.5

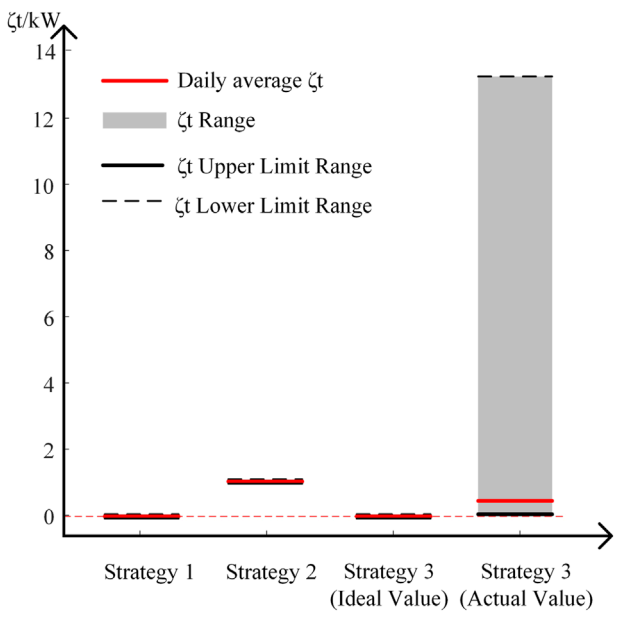

FIGURE 5 | AGC response effects for different strategies.

1) The operation planning cost of strategy 1 is lower than that of strategy 2. Furthermore, the daily average ζ_t (0 kW) and ζ_t lower limit (0 kW) of strategy 1 are less than the daily average ζ_t (1 kW) and ζ_t lower limit (1 kW) of Strategy 2. Therefore, compared with single energy storage, hybrid energy storage can reduce energy storage operation planning costs and tracking error ζ_t;

2) The operation planning cost calculated by the scheduling model of different strategies is the expected cost value. Among them, the expected cost of strategy 3 is \$5766.7, less than the planned operating cost of strategy 1 which is \$13,548. Taking the capacity optimization result of the dynamic charge–discharge model as the actual value, it can be seen that the capacity optimization strategy using the constant charge–discharge model is easy to cause investors to expect too low investment costs.

3) Under the actual dynamic charge–discharge model and SOC constraints, the actual output and charge–discharge efficiency of strategy 3 are all different from those of the optimized model. In strategy 3, the actual daily average ζ_t (0.5 kw) is higher than the minimum value (0 kw), and there exists the ζ_t margin. However, in strategy 3, without considering the actual dynamic charge–discharge efficiency, the actual daily average ζ_t judged by the optimization model of strategy 3 is the lowest value, and there is no ζ_t margin. Therefore, the capacity optimization strategy of the constant charging–discharge model will lead to low prediction of tracking error of P_{ref}^{s-b} instruction signal by the operator.

(4) The daily average ζ_t of strategy 1 is the minimum, and there is no ζ_t margin. Therefore, the capacity optimization strategy of the dynamic charge–discharge model can improve the utilization rate of the energy storage system, fully compensate the P_{ref}^{s-b} command signal, and guarantee the AGC frequency modulation effect of the whole plant.

4.2 Analysis of Capacity Optimization Results

The output comparison of each energy storage unit under strategy 1 and Strategy 3 (ideal) is shown in **Figure 6**. It can be seen that the output results of the unit under the capacity optimization strategy of the constant charge–discharge efficiency model and the capacity optimization strategy of the dynamic charge–discharge efficiency model are similar. At this point, under the same output situation, the capacity configuration of the dynamic charge–discharge efficiency model and the constant charge–discharge efficiency model

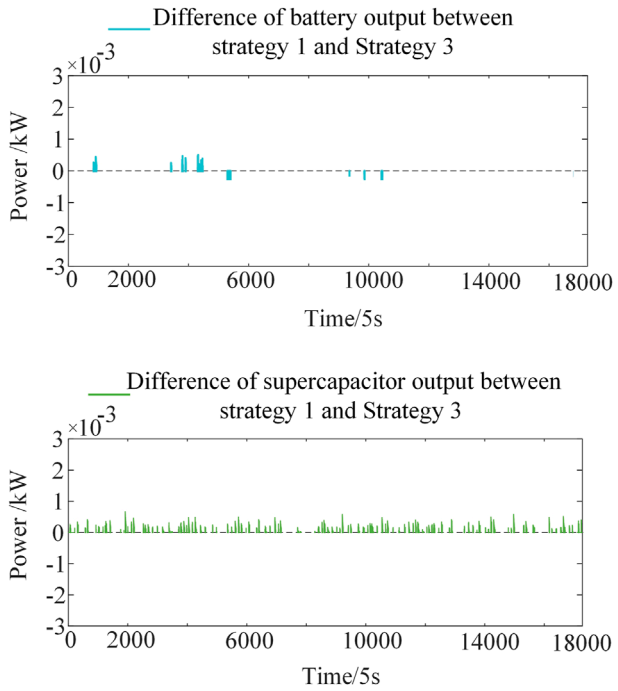

FIGURE 6 | Comparison of energy storage output between strategy 1 and strategy 3.

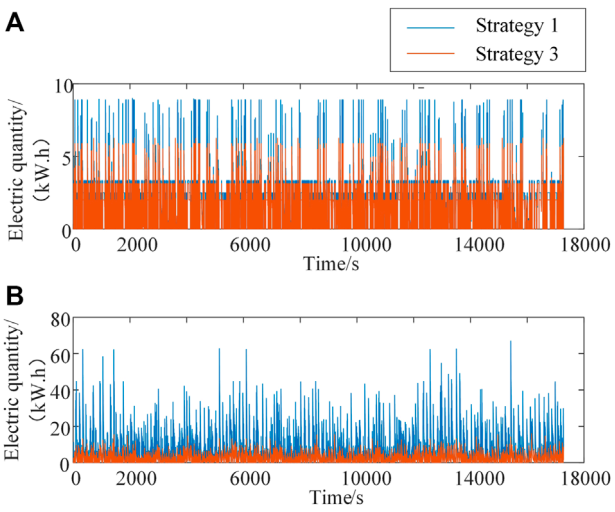

FIGURE 7 | Strategy 1/3's ΔE **(A)** Variation range of battery electric quantity per unit time.**(B)**Variation range of supercapacitor electric quantity per unit time.

is mainly influenced by the comparison of the amount of electric quantity $\Delta E^{s}_{i,t-1\to t}$ increased (or lost) per unit time, which depends on the charge–discharge efficiency of the two models.

Figure 7 shows the ΔE curves of Strategy 1 and Strategy 3 (ideal). As the charge–discharge efficiency of strategy 1 is lower than that of strategy 3 (ideal) in most time periods (as shown in **Figure 7**), ΔE of strategy 1 is higher than ΔE of Strategy 3 (ideal). In order to meet the SOC constraints of energy storage units, the capacity configuration of strategy 1 is higher than that of strategy 3 (as shown in **Table 5**).

As shown in **Figure 8**, considering the dynamic charge–discharge efficiency model, under the capacity configuration and power allocation of strategy 1 and Strategy 3 (ideal), the SOC curve of strategy 1 or strategy 3 is shown in **Figure 9**. It can be seen that the capacity configuration under the constant charge–discharge efficiency model makes the energy storage system over-charge and over-discharge, and the energy storage system will exit the AGC response in some period of time, resulting in the tracking error of P^{s-b}_{ref} command signal and reducing the AGC response performance of the energy storage.

However, the dynamic charge–discharge efficiency model, due to the appropriately expanded capacity configuration, makes the SOC state of each energy storage unit within the constraint range, meets the continuity requirements of P^{s-b}_{ref} command signal tracking, and improves the AGC response performance of energy storage.

To sum up, the strategy in this study takes into account the dynamic charge–discharge efficiency model and combines

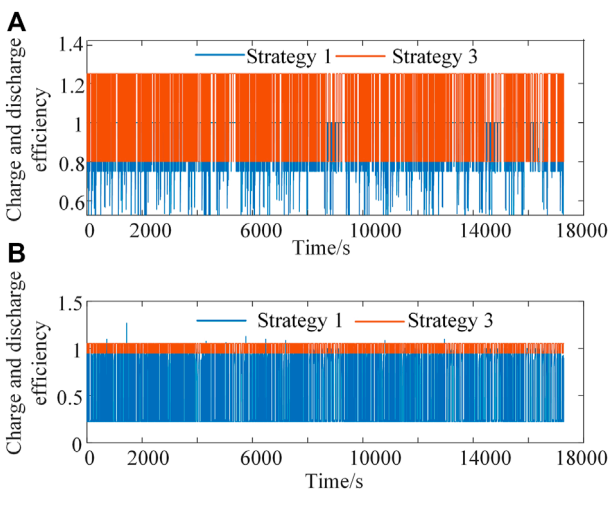

FIGURE 8 | Charge–discharge efficiency of strategy 1 and strategy 3. **(A)** Charge and discharge efficiency of battery. **(B)** Charge and discharge efficiency of supercapacitor.

the characteristics of each energy storage unit to economically distribute P^{s-b}_{ref} instruction signals. At the same time, compared with the constant charge–discharge efficiency model, the strategy in this study can sense the charge–discharge efficiency conforming to the actual situation, rationally allocate the energy storage capacity, meet the continuity requirements of P^{s-b}_{ref} command signal tracking under the condition of considering SOC constraints, and improve the AGC response performance of the energy storage.

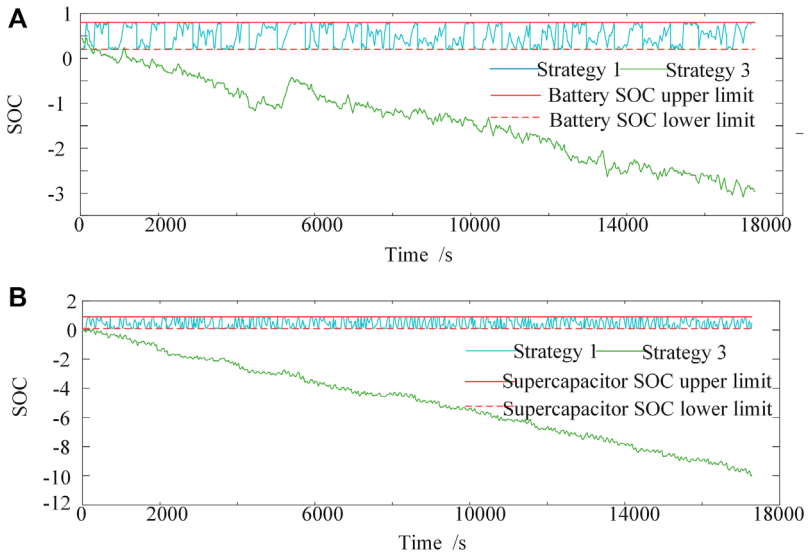

FIGURE 9 | SOC for strategy 1 and strategy 3 **(A)** Battery SOC. **(B)** Supercapacitor SOC.

5 CONCLUSION

The combined AGC response of hybrid energy storage and thermal power unit is an effective way to improve the AGC command tracking demand of thermal power plants. In this study, a fine dynamic model of charging and discharging power-efficiency of storage battery and supercapacitor is established. On this basis, the fire-storage capacity configuration model is established, which is used to realize the corresponding capacity configuration to meet the requirements of ACE signal tracking in thermal power plants and the minimum planning and operation cost of the energy storage system. The results of examples state that

1) The dynamic charge–discharge efficiency model can avoid over-charge and over-discharge of units, improve the energy storage availability, completely compensate for the ACE signal tracking error caused by the inherent AGC response disadvantage of conventional units, and improve the AGC response performance of thermal power plants;

2) The use of the constant charge–discharge efficiency model will lead to low investment cost expectations of investors, while the dynamic charge–discharge efficiency model can more accurately evaluate the operation planning cost of hybrid energy storage.

DATA AVAILABILITY STATEMENT

The raw data supporting the conclusions of this article will be made available by the authors, without undue reservation.

AUTHOR CONTRIBUTIONS

HH determined the direction and main points of the research, HH and HW proposed the technical route of the research, HH and YC completed the writing of the research content, YC, and XC completed the simulation verification of the numerical example, and TL revised the grammar and sentence structure of the study.

FUNDING

This manuscript was supported in part by the Science and Technology Project of Hubei Electric Power Survey and Design Institute K2020-2-06.

REFERENCES

Aghajan-Eshkevari, S., Azad, S., Nazari-Heris, M., Ameli, M. T., and Asadi, S. (2022). Charging and Discharging of Electric Vehicles in Power Systems: An Updated and Detailed Review of Methods, Control Structures, Objectives, and Optimization Methodologies. *Sustainability* 14 (4), 2137. doi:10.3390/su14042137

Anderson-Cook, C. M., and Robinson, T. J. (2009). A Designed Screening Study with Prespecified Combinations of Factor Settings. *Qual. Eng.* 21 (4), 392. doi:10.1080/08982110903179069

Cheng, Y., Tabrizi, M., Sahni, M., Povedano, A., and Nichols, D. (2014). Dynamic Available Agc Based Approach for Enhancing Utility Scale Energy Storage Performance. *IEEE Trans. Smart Grid* 5 (2), 1070–1078. doi:10.1109/tsg.2013.2289380

Galatsopoulos, C., Papadopoulou, S., Ziogou, C., Trigkas, D., and Voutetakis, S. (2020). Optimal Operation of a Residential Battery Energy Storage System in a Time-Of-Use Pricing Environment. *Appl. Sci.* 10 (17), 5997. doi:10.3390/app10175997

Iclodean, C., Varga, B., Burnete, N., Cimerdean, D., and Jurchiş, B. (2017). Comparison of Different Battery Types for Electric Vehicles. *IOP Conf. Ser. Mat. Sci. Eng.* 252, 012058. doi:10.1088/1757-899x/252/1/012058

Jin, L., He, L., and Lv, R. (2022). Single-time Power Frequency Modulation and Peak -modulation Market Combined Clearing Method Considering New Energy Absorption Capacity. *IOP Conf. Ser. Earth Environ. Sci.* 1011, 012011. doi:10.1088/1755-1315/1011/1/012011

Liu, D., Jin, Z., Chen, H., Cao, H., Yuan, Y., Fan, Y., et al. (2021). Peak Shaving and Frequency Regulation Coordinated Output Optimization Based on Improving Economy of Energy Storage. *Electronics* 11 (1), 29. doi:10.3390/electronics11010029

Meng, G., Lu, Y., Liu, H., Ye, Y., Sun, Y., and Tan, W. (2021). Adaptive Droop Coefficient and Soc Equalization-Based Primary Frequency Modulation Control Strategy of Energy Storage. *Electronics* 10 (21), 2645. doi:10.3390/electronics10212645

Meng, L., Zafar, J., Shafiuzzaman, K., Collinson, A., Murchie, K. C., Coffele, F., et al. (2019). Fast Frequency Response from Energy Storage Systems—A Review of Grid Standards, Projects and Technical Issues. *IEEE Trans. smart grid* 11 (2), 1566. doi:10.1109/TSG.2019.2940173

Naseri, F., Karimi, S., Farjah, E., and Schaltz, E. (2021). *Supercapacitor Management System: A Comprehensive Review of Modeling, Estimation, Balancing, and Protection Techniques*. Renewable and Sustainable Energy Reviews, 2021.

Rancilio, G., Lucas, A., Kotsakis, E., Fulli, G., Merlo, M., Delfanti, M., et al. (2019). Modeling a Large-Scale Battery Energy Storage System for Power Grid Application Analysis. *Energies* 12 (17), 3312. doi:10.3390/en12173312

Saxena, A., and Shankar, R. (2022). Improved Load Frequency Control Considering Dynamic Demand Regulated Power System Integrating Renewable Sources and Hybrid Energy Storage System. *Sustain. Energy Technol. Assessments* 52, 102245. doi:10.1016/j.seta.2022.102245

Song, C., Feng, J., Yang, D., Zhou, B. W., and Qi, G. (2018). Collaborative Optimization of Integrated Energy Considering System Coupling. *Automation Electr. Power Syst.* 42 (10), 38. doi:10.7500/AEPS20170914008

Sun, B., He, X., Zhang, W., Li, Y., Gong, M., Yang, Y., et al. (2020). Control Strategies and Economic Analysis of an Lto Battery Energy Storage System for Agc Ancillary Service. *Energies* 13 (2), 505. doi:10.3390/en13020505

Wang, H., Wang, T., Xie, X., Ling, Z., Gao, G., and Dong, X. (2018). Optimal Capacity Configuration of a Hybrid Energy Storage System for an Isolated Microgrid Using Quantum-Behaved Particle Swarm Optimization. *Energies* 11 (2), 454. doi:10.3390/en11020454

Yang, N., Dong, Z., Wu, L., Zhang, L., Shen, X., Chen, D., et al. (2021). A Comprehensive Review of Security-Constrained Unit Commitment. *J. Mod. Power Syst. Clean Energy* 10 (3), 562–576. doi:10.35833/MPCE.2021.000255

Yang, N., Yang, C., Xing, C., Ye, D., Jia, J., Chen, D., et al. (2022). Deep Learning-based SCUC Decision-making: An Intelligent Data-driven Approach with Self-learning Capabilities. *IET Generation Trans Dist* 16 (4), 629–640. doi:10.1049/gtd2.12315

Yang, R. (2016). *Design And Optimization of Hybrid Energy Storage for Photovoltaic Power Fluctuation Smoothing Based on Frequency Analysis*. PhD Thesis. The University of Wisconsin-Milwaukee.

Ye, J., Zhao, D., Zhang, L., Li, Z., and Zhang, T. (2021). Research on Combined Electricity and Heating System Scheduling Method Considering Multi-Source Ring Heating Network. *Front. Energy Res.* 826, 906. doi:10.3389/fenrg.2021.800906

Zhang, F., Yang, Z., Wang, G., and Meng, K. (2018). "Control Strategy of Hybrid Energy Storage System to Improve Agc Performance of Thermal Generator," in *2018 IEEE Innovative Smart Grid Technologies-Asia (ISGT Asia)* (IEEE), 1299–1304. doi:10.1109/isgt-asia.2018.8467771

Zhang, L., Xie, Y., Ye, J., Xue, T., Cheng, J., Li, Z., et al. (2021). Intelligent Frequency Control Strategy Based on Reinforcement Learning of Multi-Objective Collaborative Reward Function. *Front. Energy Res.* 587, 760525. doi:10.3389/fenrg.2021.760525

Conflict of Interest: HH, HW, YC, XC, and TL were employed by Powerchina Hubei Electric Engineering Co., Ltd.

Publisher's Note: All claims expressed in this article are solely those of the authors and do not necessarily represent those of their affiliated organizations, or those of the publisher, the editors and the reviewers. Any product that may be evaluated in this article, or claim that may be made by its manufacturer, is not guaranteed or endorsed by the publisher.

frontiers | Frontiers in Energy Research

BRIEF RESEARCH REPORT
published: 26 July 2022
doi: 10.3389/fenrg.2022.952354

A Cost Effective Solution to Dynamic Economic Load Dispatch Problem Using Improved Chimp Optimizer

Jianming Xu[1], *Anfeng Liu*[2], *Yang Qin*[1], *Guangrong Xu*[1] *and Yibo Tang*[1,3]*

[1]*Provincial Key Laboratory of Informational Service for Rural Area of Southwestern Hunan, Shaoyang University, Shaoyang, China,* [2]*School of Computer Science and Engineer, Central South University, Changsha, China,* [3]*College of Physics and Electronics, Central South University, Changsha, China*

The electricity sector has encountered several economic challenges in recent years. Increasing the expense of fossil fuels and environmental legislation such as the Kyoto Protocol and the Low Carbon Transition Plan have compelled governments to use renewable energy sources (RESs) more widely. In the proposed research, the dynamic economic load dispatch problem has been solved using improved chimp optimizer algorithm. The test systems consisting of 6, 7 and 10-unit generators has been taken into consideration along with significant contribution of renewable energy sources for effective research studies. The test systems has been evaluated for different cases considering renewable energy sources and electric vehicles using proposed algorithms. Experimentally, it has been observed that proposed optimizer yields better results as compared to other recently proposed optimizers.

Keywords: dynamic economic load dispatch, chimp optimizer, meta-heuristics search algorithms, renewable energy sources, green house gase

OPEN ACCESS

Edited by:
Xun Shen,
Tokyo Institute of Technology, Japan

Reviewed by:
Vikram Kamboj,
Lovely Professional University, India
Haoyun Shi,
Great Wall Motor, China

****Correspondence:***
Yibo Tang
626323320@qq.com

Specialty section:
This article was submitted to Smart Grids, a section of the journal Frontiers in Energy Research

Received: *25 May 2022*
Accepted: *24 June 2022*
Published: *26 July 2022*

Citation:
Xu J, Liu A, Qin Y, Xu G and Tang Y (2022) A Cost Effective Solution to Dynamic Economic Load Dispatch Problem Using Improved Chimp Optimizer. Front. Energy Res. 10:952354. doi: 10.3389/fenrg.2022.952354

1 INTRODUCTION

In recent years, the electrical power sector has faced a slew of economic issues which evoked a thought in Governments to encourage in adopting nonconventional energy sources noticing that the cost of fossil fuels has risen, the amount of fossil fuels has decreased, and the amount of Green House Gases (GHGs) emissions has increased. The Plug-in Electric Vehicles (PEVs) are a hybrid of Plug-in Hybrid Electric Vehicles (PHEVs) and Electric Vehicles (EVs) with a Vehicle to Grid (V2G) facility that looks to be a viable solution to the problem of GHG emissions. In (Kintner-Meyer et al., 2010) the impact of PEVs on the electrical system's overall economics and emissions is explained in depth. The benefits of PEVs have been discussed in (Kempton and Tomić, 2005a), (Kempton and Tomić, 2005b). The available energy from PEVs has been wisely planned in (Hutson et al., 2008). The effect of integrating PEVs in the power system for charging (G2V) and auxiliary backing (V2G) to the grid was detailed in (Gholami et al., 2014). RESs and PEVs are discussed in depth in (IEEE Std, 2011). The impact of PEVs/PHEVs on a power system, as well as the integration of RESs into that system, is explored in (Aghaei et al., 2016). The use of RESs by GVs to reduce the price and emissions in a power system was explored in (Saber and Venayagamoorthy, 2010).

Safari (2018) described a clear distinction between the mainstream of BEVs and a hypothetical group of BEVs that are technically on a par with internal combustion vehicles (ICVs). Chen et al. (2015) presented an improved particle swarm optimization for engine/motor hybrid electric vehicles to develop an online suboptimal energy management system. Richardson (2013) described to considerably reduce carbon emissions from both power generation and transportation sectors by

offering the potential of electric vehicles and renewable energy sources. Manzetti and Mariasiu (2015) presented an assessment of green chemistries as novel green energy sources for the electric vehicle and microelectronics portable energy landscape which provides a cradle-to-grave analysis of the emerging technologies in the transport sector. Hu et al. (2016) examined the role of renewable energy and power train optimization in minimizing daily carbon emissions of plug-in hybrid vehicles. Li et al. (2017) presented India's ability to finance its ambitious renewable energy targets hinges on three significant factors. The first is based on how its regulatory framework can make the market attractive to finance providers. Second is in the context of effective implementation of RE policies. (Lopez-Behar et al., 2018, 2019) described the challenges and decision-making processes involved in the installation of EV charging infrastructure in Multi-Unit Residential Buildings in BC, from the perspective of different stakeholders. Yong et al. (2015) provided in-depth analyses on the current state, effects, and potential of EV deployment, as well as the most recent advancements in EV technology. Implementation of an incentive-based strategy to reduce the cost of EV purchases, the development of charging infrastructure, and improved public knowledge of environmental issues are all facilitators for expanded EV adoption (Li et al., 2021a), (Li et al., 2021b). Xu et al. (2015) presented a report on the multi-objective optimization problem of power train parameters for a predefined driving cycle regarding fuel economy and system durability. Yang et al. (2017) developed a revolutionary energy management technique for plug-in hybrid electric buses that optimizes the equivalent factor of each driving cycle segment. Liu et al. (2015) described the penetration of EVs is reshaping the transportation system. Clement-Nyns et al. (2011) presented PHEVs as they can provide storage to take care of the excess of produced energy and use it for driving or release into the grid at a later time would be a good combination. Tan et al. (2016) presented the optimization techniques to achieve different vehicle to grid objectives while satisfying multiple constraints and reviews the framework, benefits and challenges of vehicle to grid technology. Mwasilu et al. (2014) presented a review of the recent research and forecasting of electric vehicles (EVs) interaction with smart grid portraying the future electric power system model. The concept goal of the smart grid along with the future deployment of the EVs puts forward various challenges in terms of electric grid infrastructure, communication and control. Krishna et al. (2021a), (Krishna et al., 2021b) has developed two recent variants of pattern search algorithm to improve the local search capability of the existing Harris hawks optimizer and slime mould algorithm and had suggested to solve the economic load dispatch as future prospective. Arora et al. (2020) presented optimization methodologies for testing the Load Frequency Control for Interconnected multi area power system in smart grids. Nandi and Kamboj (2020) presented the a new solution approach for Profit Based Unit Commitment Problem Considering PEVs/BEVs and Renewable Energy Sources. Following an intensive review on advanced smart metering and communication infrastructures, the strategy for integrating the EVs into the electric grid is presented.

2 PROBLEM FORMULATION

The basic purpose of single-area economic and dynamic load dispatch is to lower total fuel costs of power generating units while satisfying different constraints. The entire objective function for economic dispatch, taking into account PEVs, BEVs, and renewable energy sources, is as follows:

$$F\left(P^G\right) = \sum_{n=1}^{NG}\left[a_n\left(P_n^G\right)^2 + \left(b_n P_n^G + c_n\right)\right] \tag{1a}$$

The dispatch of power generating units for 'H' Hours may be represented as:

$$F\left(P^G\right) = \sum_{h=1}^{H}\left(\sum_{n=1}^{NG}\left[a_n\left(P_n^G\right)^2 + \left(b_n P_n^G + c_n\right)\right]\right) \tag{1b}$$

The actual mathematical formulation for *Dynamic Dispatch* was expressed by this **Eq. (1b)**. For time-varying load demand, the hour "h" can be changed from 1 to H hours.

2.1 Power Balance Constraint

The entire generation from all generators must meet the overall power demand and real power loss of the system.

$$\sum_{n=1}^{NG} P_n^G = P^{Demand} + P^{Loss} \tag{2}$$

where, P^{Demand} is the demand of power.

In **Eq. (2)** renewable energy source is integrated with generating units.

$$\sum_{n=1}^{NG} P_n^G + P^{\text{Renewable}} = P^{Demand} + P^{Loss} \tag{3}$$

where, $P^{Renewable}$ is the penetrated renewable energy source and P^{Loss} is loss in power.

Case-1: During Charging

The following **Eq. (4)** can be used to calculate the power balance constraints for PEVs, BEVs, and RES during the charging phase.

$$\sum_{n=1}^{NG} P_n^G + P^{\text{Renewable}} = P^{Demand} + P^{Loss} + \sum_{n=1}^{NPEVs} P^{PEVs} + \sum_{n=1}^{NBEVs} P^{BEVs} \tag{4}$$

Case-2: During Discharging

The power balancing constraints for PEVs, BEVs, and RES during the discharging phase may be mathematically stated using the following eqns:

$$\sum_{n=1}^{NG} P_n^G + P^{\text{Renewable}} = P^{Demand} + P^{Loss} - \sum_{n=1}^{NPEVs} P^{PEVs} - \sum_{n=1}^{NBEVs} P^{BEVs} \tag{5}$$

Where, P^{Loss} is loss in power.

$$P^{Loss} = \sum_{n=1}^{NG}\sum_{m=1}^{NG} P_n^G B_{nm} P_m^G \tag{6}$$

if B_{i0} and B_{00} matrices for loss coefficients are given, then the above equation can be modified as:

$$P^{Loss} = P_n^G B_{nm} P_m^G + \sum_{n=1}^{NG} P_n^G \times B_{i0} + B_{00} \tag{7}$$

The expanded version of the above equation may be represented as:

$$P^{Loss} = \begin{bmatrix} P_1 & P_2 & \ldots & p^{Loss} = [\, P_1 & P_2 & \cdots & P_{NG} \,] \end{bmatrix}$$

$$\begin{bmatrix} B_{11} & B_{12} & \cdots & B_{1n} \\ B_{21} & B_{22} & \cdots & B_{2n} \\ \vdots & \vdots & \vdots & \vdots \\ B_{n1} & B_{n2} & \cdots & B_{nn} \end{bmatrix} \begin{bmatrix} P_1 \\ P_2 \\ \vdots \\ P_{NG} \end{bmatrix} + [\, P_1 \quad P_2 \quad \cdots \quad P_{NG} \,] \begin{bmatrix} B_{01} \\ B_{02} \\ \vdots \\ B_{0NG} \end{bmatrix} + B_{00} \tag{8}$$

2.2 Generator Limit Constraint

Each generator's actual power output must be kept within its respective upper and lower operating limitations.

$$P_{n(\min)}^G \le P_n^G \le P_{n(\max)}^G \quad n = 1, 2, 3, \ldots, NG \tag{9}$$

where, $P_{n(\min)}^G$ represents the lowest real power allotted at unit n and $P_{n(\max)}^G$ presents the highest real power allotted at unit n.

2.3 Ramp Rate Limits

The output power of the generating unit is boosted between the lower and upper limits of active power generation.

1) As a result of an increase in generated power,

$$P_n^G - P_0^{G_o} \le UR_n \quad n = 1, 2, 3, \ldots, NG \tag{10}$$

2) By reducing the amount of generated power,

$$P_n^{G_o} - P_n^G \le DR_n \quad n = 1, 2, 3, \ldots, NG \tag{11}$$

As a result, the generator ramp rate is represented in the equation below.

$$\max\left[P_{n(\max)}^G, \left(UR_n - P_n^G\right)\right] \le P_n^G \le \min\left[P_{n(\max)}^G, \left(P_n^{G_o} - DR_n\right)\right] n = 1, 2, 3, \ldots, NG \tag{12}$$

where, P_n^G is the earlier outcome of nth generation unit's active power DR_n, UR_n are the lower and upper range for a nth generation unit ramp rate limits.

3 TEST SYSTEMS

The single area dynamic load dispatch problem has been described, considering plug-in electric vehicles, battery electric vehicles and renewable energy sources along with the system and physical limits of thermal generating units. The dynamic load dispatch problem has been solved and tested for 6-unit, 7-unit, and 10-unit systems. To validate the proposed algorithms, standard power systems consisting 6, 7, and 10 generating units have been considered.

4 RESULTS AND DISCUSSION

Proposed algorithms such as chimp optimizer, slime mould, improved chimp optimizer and improved slime mould algorithms fruitfully handle the electric power system's single area dynamic load dispatch problem. This section looks at how to solve the single area dynamic load dispatch problem using plug-in electric vehicles, renewable energy sources and combined plug-in electric vehicles and renewable energy sources for 6, 7 and 10 generating units, respectively. On an Intel corei3 processor laptop with a 7th generation CPU and 8GB RAM, the proposed approaches were evaluated using the MATLAB R2016a programme. For comparison reasons, the efficacy of the proposed algorithms is compared to that of other well-known evolutionary, heuristics, and meta-heuristics search techniques.

4.1 Dynamic Load Dispatch Using Chimp Optimizer Algorithm

In order to verify the chimp optimizer algorithm, the algorithm is accepted by search agents 50, 500 iterations and 30 maximum runs. The effectiveness of the proposed algorithm is tested on a variety of test systems, including plug-in electric vehicles, renewable energy sources, and combined plug-in electric vehicles and renewable energy sources as detailed in this section. This approach has been tested on a 6-unit, 7-unit and 10-unit test system.

4.1.1 Six Generator Test System (SADLD With EVs)

Chimp optimizer algorithm is suggested to get optimized outcomes for dynamic load dispatch with the effect of EVs as V2G and G2V. A six-generator test system is studied, with no valve point loading impact and a loss coefficient matrix of zero (Debnath et al., 2015). **Table 1** displays that the fuel price is **397294.1087** \$/day using the chimp optimizer algorithm.

4.1.2 Six Generator Test System (SADLD With RES)

Chimp optimizer algorithm is suggested to get optimized outcomes for dynamic load dispatch with the effect of RES. A six generator test system without valve point loading effect, with loss coefficient matrix as zero is considered (Debnath et al., 2015). The renewable energy sources wind and solar are incorporated. **Table 2** displays that the fuel price is **316498.35** \$/day using the chimp optimizer algorithm.

4.1.3 Six Generator Test System (SADLD With EVs and RES)

Chimp optimizer algorithm is suggested to get optimized outcomes for dynamic load dispatch with the combined effect

TABLE 1 | 6-unit generator Dynamic Load Dispatch with EVs (without valve point loading effect without losses) using Chimp optimizer Algorithm.

Time (hr)	PD (MW)	G1 (MW)	G2 (MW)	G3 (MW)	G4 (MW)	G5 (MW)	G6 (MW)	Electric Vehicles (MW)	Fuel Cost ($)/hr
1	700	352.72	99.50	190.13	50	89.41	50	−131.76	9834.43
2	750	352.94	103.28	190.89	50	87.89	50	−85	9873.09
3	850	367.15	112.59	202.17	61.72	98.87	50	−42.5	10564.56
4	950	379.67	125.64	210.36	72.99	111.34	50	0	11267.25
5	1000	392.20	129.99	220.79	82.53	124.48	50	0	11887.03
6	1100	410.35	146.03	241.79	102.77	147.31	51.75	0	13152.39
7	1150	429.15	156.35	243.49	109.17	150.81	61.02	0	13796.10
8	1200	442.53	162.73	252.15	112.86	156.85	72.87	0	14447.13
9	1300	458.22	175.35	266.64	127.04	178.34	94.51	0.102	15770.06
10	1400	471.82	189.10	282.36	148.41	200	110.45	2.142	17147.01
11	1450	493.87	200.00	300.00	150	200	120	13.872	17994.97
12	1500	500.00	200.00	360.00	150	200	120	34.782	82862.50
13	1400	481.45	194.92	290.51	150	200	117.90	34.782	17593.33
14	1300	459.73	179.90	273.89	137.39	176.69	86.28	13.872	15954.50
15	1200	435.49	165.65	254.57	116.05	157.44	72.94	2.142	14474.65
16	1050	404.57	141.65	229.31	97.25	127.46	50	0.2359	12519.09
17	1000	394.07	133.14	221.89	81.52	127.20	50	−7.8157	11984.77
18	1100	420.10	146.04	236.48	104.81	149.68	61.10	18.207	13386.30
19	1200	439.09	169.25	264.32	120.43	174.31	78.24	45.6514	15046.90
20	1400	485.09	198.46	293.46	150	200	118.64	45.6514	17742.83
21	1300	453.77	179.75	274.54	135.34	181.10	93.70	18.207	16011.99
22	1100	412.30	147.43	239.59	103.30	147.36	52.83	2.8114	13188.22
23	900	366.69	114.45	205.11	65.21	104.77	50	−6.2411	10731.43
24	800	354.79	103.67	193.05	50	90.99	50	−42.5	9962.79
								Fuel Cost ($) per day	**397294.1087**

Bold represents better fuel cost as compared to others methods.

TABLE 2 | 6-unit generator Dynamic Load Dispatch with RES (without valve point loading effect without losses) using Chimp optimizer algorithm.

Time (hr)	PD (MW)	G1 (MW)	G2 (MW)	G3 (MW)	G4 (MW)	G5 (MW)	G6 (MW)	Wind (MW)	Solar (MW)	Fuel Cost ($)/hr
1	700	309.00	69.42	157.92	50	53.13	50	10.54	0	8179.70
2	750	320.37	78.89	166.32	50	62.15	50	22.27	0	8616.48
3	850	350.83	99.31	187.58	50	86.78	50	25.5	0	9747.97
4	950	377.02	117.10	205.77	67.94	106.68	50	25.5	0	10954.23
5	1000	385.10	127.32	217.71	75.00	119.37	50	25.5	0	11569.88
6	1100	409.18	144.40	230.65	99.02	140.64	50.61	25.5	0	12826.62
7	1150	421.25	150.65	241.41	107.80	151.42	51.87	25.5	0.09	13465.98
8	1200	423.39	157.55	246.61	107.19	156.87	65.44	25.5	17.46	13887.15
9	1300	449.19	162.95	259.82	122.80	166.97	81.32	25.5	31.45	15012.68
10	1400	466.73	184.46	268.37	133.98	182.57	102.38	25.5	36.01	16285.31
11	1450	467.03	189.68	260.91	150	194.41	104.40	25.5	38.06	16933.40
12	1500	481.88	199.54	290.33	150	200	116.82	25.5	35.93	17645.39
13	1400	458.76	184.28	282.49	133.35	179.83	99.01	25.5	36.78	16274.79
14	1300	443.73	167.61	263.77	116.13	175.20	77.14	24.82	31.59	15019.99
15	1200	421.90	158.40	253.73	113.22	155.60	66.71	20.74	9.7	14049.95
16	1050	398.47	135.26	228.68	84.67	125.39	50	14.62	12.92	12168.47
17	1000	382.01	127.84	212.25	78.99	123.41	50	25.5	0	11570.27
18	1100	411.24	144.79	236.41	97.02	136.50	54.99	19.04	0	12908.99
19	1200	432.81	157.70	254.21	107.49	156.84	65.45	25.5	0	14114.10
20	1400	464.17	187.80	282.86	143.34	200	103.82	18.02	0	16873.02
21	1300	446.59	173.49	259.03	128.95	178.31	88.13	25.5	0	15429.22
22	1100	406.31	147.27	233.23	96.61	141.69	53.47	21.42	0	12878.69
23	900	368.74	114.97	199.24	64.31	102.74	50	0	0	10655.64
24	800	342.42	94.59	181.44	50	79.01	50	2.55	0	9427.80
									Fuel Cost ($) per day	**316498.35**

TABLE 3 | 6-unit generator Dynamic Load Dispatch with EVs and RES (without valve point loading effect without losses) using Chimp optimizer algorithm.

Time (hr)	PD (MW)	G1 (MW)	G2 (MW)	G3 (MW)	G4 (MW)	G5 (MW)	G6 (MW)	EV (MW)	Wind (MW)	Solar (MW)	Fuel Cost ($)/hr
1	700	350.24	97.80	186.27	50	86.91	50	−131.76	10.54	0	9709.02
2	750	344.96	97.62	184.78	50.16	85.21	50	−85	22.27	0	9608.30
3	850	359.51	106.26	194.76	57.73	99.74	50	−42.5	25.5	0	10256.61
4	950	372.78	120.23	205.71	67.58	108.20	50	0	25.5	0	10954.22
5	1000	383.01	127.24	218.11	79.68	116.46	50	0	25.5	0	11569.94
6	1100	409.02	143.86	236.27	93.19	142.17	50	0	25.5	0	12826.49
7	1150	417.06	148.15	244.83	101.58	151.96	60.83	0	25.5	0.09	13465.81
8	1200	428.13	152.75	249.06	109.70	157.18	60.22	0	25.5	17.46	13887.30
9	1300	440.61	164.96	257.23	123.89	173.75	82.71	0.102	25.5	31.45	15013.97
10	1400	457.48	182.88	278.01	131.23	188.01	103.02	2.142	25.5	36.01	16313.87
11	1450	473.02	191.47	286.18	150	194.31	105.33	13.872	25.5	38.06	17121.97
12	1500	500	200	300	150	200	120	34.782	25.5	35.93	21432.50
13	1400	468.45	186.09	280.11	150	185.29	102.57	34.782	25.5	36.78	16744.58
14	1300	448.76	165.92	266.40	122.57	173.09	80.72	13.872	24.82	31.59	15203.01
15	1200	427.99	160.56	252.19	105.90	157.80	65.27	2.142	20.74	9.7	14077.55
16	1050	398.94	136.71	224.02	87.38	125.65	50	0.2359	14.62	12.92	12171.36
17	1000	388.61	128.71	215.44	76.95	122.6	50	−7.8157	25.5	0	11666.95
18	1100	415.78	146.47	242.20	95.85	148.87	50	18.207	19.04	0	13141.91
19	1200	440.44	161.39	258.05	124.73	161.67	73.87	45.6514	25.5	0	14711.13
20	1400	477.54	194.43	291.21	150	200	114.45	45.6514	18.02	0	17495.19
21	1300	446.15	173.83	271.08	128.58	181.13	91.95	18.207	25.5	0	15671.44
22	1100	413.93	144.92	239.56	95.98	137.00	50	2.8114	21.42	0	12914.46
23	900	367.76	113.85	204.95	67.53	102.15	50	−6.2411	0	0	10731.49
24	800	355.82	102.10	191.71	50	90.32	50	−42.5	2.55	0	9932.21
										Fuel Cost ($) per day	**326625.6**

Bold represents better fuel cost as compared to others methods.

TABLE 4 | 7-unit generator Dynamic Load Dispatch with EVs (without valve point loading effect without losses) using Chimp Optimizer Algorithm.

Time (hr)	PD (MW)	G1 (MW)	G2 (MW)	G3 (MW)	G4 (MW)	G5 (MW)	G6 (MW)	G7 (MW)	EV (MW)	Fuel Cost ($)/hr
1	800	311.40	71.56	140	50	100	50	100	−22.96	10018.49
2	780	297.66	61.43	140	50	100	50	100	−19.09	9749.63
3	750	280.68	50	134.98	50	100	50	100	−15.66	9380.535
4	750	283.69	51.09	137.38	50	100	50	100	−22.16	9451.726
5	720	269.15	50	126.00	50	100	50	100	−25.15	9158.026
6	700	253.61	50	112.92	50	100	50	100	−17.52	8863.511
7	700	251.67	50	112.41	50	100	50	100	−14.08	8827.264
8	700	259.68	50	118.64	50	100	50	100	28.32	8977.915
9	800	314.05	74.15	140	50	100	50	102.87	31.07	10110.78
10	900	347.29	98.74	140	50	100	50	137.74	23.77	11189.39
11	1000	378.52	100	140	73.24	111.24	50	167.56	20.56	12360.18
12	1200	443.99	100	140	100	169.76	82.77	236.59	73.1	15583.27
13	1400	487.25	100	140	100	207.41	100	280.37	15.03	17499.22
14	1500	522.49	100	140	100	237.98	100	316.29	16.76	18929.83
15	1750	575.00	100	140	100	340.08	100	410	15.08	22644.93
16	1800	574.99	100	140	100	396.44	100	410	−21.43	23568.64
17	1500	529.56	100	140	100	243.45	100	324.32	−37.33	19225.17
18	900	345.06	96.20	140	50	100	50	135.01	−16.27	11100.5
19	850	327.92	84.17	140	50	100	50	117.25	19.34	10550.8
20	800	321.44	79.37	140	50	100	50	109.92	50.73	10335.9
21	780	301.05	63.93	140	50	100	50	100	24.98	9815.545
22	750	280.64	50	134.95	50	100	50	100	−15.59	9379.77
23	700	263.56	50	126.66	50	100	50	100	−35.22	9051.488
24	800	323.50	80.63	140	50	100	50	112.15	−56.28	10399.8
									Fuel Cost ($) per day	**296174.3**

of EVs and RES. A six generator test system without valve point loading effect, with loss coefficient matrix as zero is considered (Debnath et al., 2015). The Electric vehicles and renewable energy sources wind and solar are incorporated. **Table 3** displays that the fuel price is **326625.6** $/day using the chimp optimizer algorithm.

4.1.4 Seven Generator Test System (SADLD With EVs)

Chimp optimizer algorithm is suggested to get optimized outcomes for dynamic load dispatch with the effect of EVs as V2G and G2V. A seven generator test system without valve point loading effect, with loss coefficient matrix as zero is considered (Tariq et al., 2020), (Gholami et al., 2014). **Table 4** displays that the fuel price is **296174.3087** $/day using the chimp optimizer algorithm.

5 CONCLUSION

In the proposed research, dynamic load dispatch problem has been solved using chimp optimizer algorithm. The test systems consisting of 6, 7 and 10-unit generators when incorporated with only electric vehicles, only renewable energy sources, and combined electric vehicles and renewable energy sources have been successfully tested using proposed algorithms. The results of the test systems with EVs and RES have been compared without EVs and RES results. The simulation results show that the suggested methods found satisfactory load dispatch at a reasonable cost. These dominating algorithms may also be used to solve the problem of multi-area dynamic load dispatch in electrical power networks.

DATA AVAILABILITY STATEMENT

The original contributions presented in the study are included in the article/Supplementary Material, further inquiries can be directed to the corresponding author.

AUTHOR CONTRIBUTIONS

JX put forward the main research points; AL, YQ, GX, and YT completed manuscript writing and revision; AL, YQ, and GX completed simulation research; YQ, GX, and YT collected relevant background information; AL, GX, and YT revised grammar and expression. All authors contributed to manuscript revision, read, and approved the submitted version.

REFERENCES

Aghaei, J., Nezhad, A. E., Rabiee, A., and Rahimi, E. (2016). Contribution of Plug-In Hybrid Electric Vehicles in Power System Uncertainty Management. *Renew. Sustain. Energy Rev.* 59 (99), 450–458. doi:10.1016/j.rser.2015.12.207

Arora, K., Kumar, A., Kamboj, V. K., Prashar, D., Jha, S., Shrestha, B., et al. (2020). Optimization Methodologies and Testing on Standard Benchmark Functions of Load Frequency Control for Interconnected Multi Area Power System in Smart Grids. *Mathematics* 8 (6), 980. doi:10.3390/math8060980

Chen, S.-Y., Hung, Y.-H., Wu, C.-H., and Huang, S.-T. (2015). Optimal Energy Management of a Hybrid Electric Powertrain System Using Improved Particle Swarm Optimization. *Appl. Energy* 160, 132–145. doi:10.1016/j.apenergy.2015.09.047

Clement-Nyns, K., Haesen, E., and Driesen, J. (2011). The Impact of Vehicle-To-Grid on the Distribution Grid. *Electr. Power Syst. Res.* 81 (1), 185–192. doi:10.1016/j.epsr.2010.08.007

Debnath, U. K., Ahmad, I., Habibi, D., and Saber, A. Y. (2015). Energy Storage Model with Gridable Vehicles for Economic Load Dispatch in the Smart Grid. *Int. J. Electr. Power & Energy Syst.* 64, 1017–1024. doi:10.1016/j.ijepes.2014.09.004

Gholami, A., Ansari, J., Jamei, M., and Kazemi, A. (2014). Environmental/economic Dispatch Incorporating Renewable Energy Sources and Plug-in Vehicles. *IET Generation, Transm. Distribution* 8 (12), 2183–2198. doi:10.1049/iet-gtd.2014.0235

Hu, X., Zou, Y., and Yang, Y. (2016). Greener Plug-In Hybrid Electric Vehicles Incorporating Renewable Energy and Rapid System Optimization. *Energy* 111, 971–980. doi:10.1016/j.energy.2016.06.037

Hutson, C., Venayagamoorthy, G. K., and Corzine, K. A. (2008). "Intelligent Scheduling of Hybrid and Electric Vehicle Storage Capacity in a Parking Lot for Profit Maximization in Grid Power Transactions," in 2008 IEEE Energy 2030 Conf. ENERGY 2008, Atlanta, GA, USA, 17-18 Nov. 2008, 1–8. doi:10.1109/energy.2008.47810512008

IEEE Std (2011). .2030-2011, *IEEE Guide For Smart Grid Interoperability Of Energy Technology And Information Technology Operation With the Electric Power System (EPS), End-Use Appl. Loads*, September

Kempton, W., and Tomić, J. (2005). Vehicle-to-grid Power Fundamentals: Calculating Capacity and Net Revenue. *J. Power Sources* 144 (1), 268–279. doi:10.1016/j.jpowsour.2004.12.025

Kempton, W., and Tomić, J. (2005). Vehicle-to-grid Power Implementation: From Stabilizing the Grid to Supporting Large-Scale Renewable Energy. *J. Power Sources* 144 (1), 280–294. doi:10.1016/j.jpowsour.2004.12.022

Kintner-Meyer, M., Nguyen, T. B., Jin, C., Balducci, P., and Secrest, T. (2010). "Impact Assessment of Plug-In Hybrid Vehicles on the U.S. Power Grid," in The 25th World Battery, Hybrid and Fuel Cell Electric Vehicle Symposium & Exhibition, Shenzhen, China, November 5–9, 2010 Vol. EVS25, 1–6.

Krishna, A. B., Saxena, S., and Kamboj, V. K. (2021). A Novel Statistical Approach to Numerical and Multidisciplinary Design Optimization Problems Using Pattern Search Inspired Harris Hawks Optimizer. *Neural Comput. Applic* 33, 7031–7072. doi:10.1007/s00521-020-05475-5

Krishna, A. B., Saxena, S., and Kamboj, V. K. (2021). A Novel Statistical Approach to Numerical and Multidisciplinary Design Optimization Problems Using Pattern Search Inspired Harris Hawks Optimizer. *Neural Comput. Applic* 33 (12), 7031–7072. doi:10.1007/s00521-020-05475-5

Li, H., Deng, J., Feng, P., Pu, C., Arachchige, D. D. K., and Cheng, Q. (2021). Short-Term Nacelle Orientation Forecasting Using Bilinear Transformation and ICEEMDAN Framework. *Front. Energy Res.* 9, 780928. doi:10.3389/fenrg.2021.780928

Li, H., Deng, J., Yuan, S., Feng, P., and Arachchige, D. D. K. (2021). Monitoring and Identifying Wind Turbine Generator Bearing Faults Using Deep Belief Network and EWMA Control Charts. *Front. Energy Res.* 9, 799039. doi:10.3389/fenrg.2021.799039

Li, L., Zhou, L., Yang, C., Xiong, R., You, S., and Han, Z. (2017). A Novel Combinatorial Optimization Algorithm for Energy Management Strategy of Plug-In Hybrid Electric Vehicle. *J. Frankl. Inst.* 354 (15), 6588–6609. doi:10.1016/j.jfranklin.2017.08.020

Liu, L., Kong, F., Liu, X., Peng, Y., and Wang, Q. (2015). A Review on Electric Vehicles Interacting with Renewable Energy in Smart Grid. *Renew. Sustain. Energy Rev.* 51, 648–661. doi:10.1016/j.rser.2015.06.036

Lopez-Behar, D., Tran, M., Froese, T., Mayaud, J. R., Herrera, O. E., and Merida, W. (20182019). Charging Infrastructure for Electric Vehicles in Multi-Unit Residential Buildings: Mapping Feedbacks and Policy Recommendations. *Energy Policy* 126, 444–451. doi:10.1016/j.enpol.2018.10.030

Manzetti, S., and Mariasiu, F. (2015). Electric Vehicle Battery Technologies: From Present State to Future Systems. *Renew. Sustain. Energy Rev.* 51, 1004–1012. doi:10.1016/j.rser.2015.07.010

Mwasilu, F., Justo, J. J., Kim, E.-K., Do, T. D., and Jung, J.-W. (2014). Electric Vehicles and Smart Grid Interaction: A Review on Vehicle to Grid and Renewable Energy Sources Integration. *Renew. Sustain. Energy Rev.* 34, 501–516. doi:10.1016/j.rser.2014.03.031

Nandi, A., and Kamboj, V. K. (2020). A New Solution to Profit Based Unit Commitment Problem Considering PEVs/BEVs and Renewable Energy Sources. *E3S Web Conf.* 184, 01070. doi:10.1051/e3sconf/202018401070

Richardson, D. B. (2013). Electric Vehicles and the Electric Grid: A Review of Modeling Approaches, Impacts, and Renewable Energy Integration. *Renew. Sustain. Energy Rev.* 19, 247–254. doi:10.1016/j.rser.2012.11.042

Saber, A. Y., and Venayagamoorthy, G. K. (2010). Efficient Utilization of Renewable Energy Sources by Gridable Vehicles in Cyber-Physical Energy Systems. *IEEE Syst. J.* 4 (3), 285–294. doi:10.1109/jsyst.2010.2059212

Safari, M. (2018). Battery Electric Vehicles: Looking behind to Move Forward. *Energy Policy* 115 (December 2017), 54–65. doi:10.1016/j.enpol.2017.12.053

Tan, K. M., Ramachandaramurthy, V. K., and Yong, J. Y. (2016). Integration of Electric Vehicles in Smart Grid: A Review on Vehicle to Grid Technologies and Optimization Techniques. *Renew. Sustain. Energy Rev.* 53, 720–732. doi:10.1016/j.rser.2015.09.012

Tariq, F., Alelyani, S., Abbas, G., Qahmash, A., and Hussain, M. R. (2020). Solving Renewables-Integrated Economic Load Dispatch Problem by Variant of Metaheuristic Bat-Inspired Algorithm. *Energies* 13 (23), 6225. doi:10.3390/en13236225

Xu, L., Mueller, C. D., Li, J., Ouyang, M., and Hu, Z. (2015). Multi-objective Component Sizing Based on Optimal Energy Management Strategy of Fuel Cell Electric Vehicles. *Appl. Energy* 157, 664–674. doi:10.1016/j.apenergy.2015.02.017

Yang, C., Du, S., Li, L., You, S., Yang, Y., and Zhao, Y. (2017). Adaptive Real-Time Optimal Energy Management Strategy Based on Equivalent Factors Optimization for Plug-In Hybrid Electric Vehicle. *Appl. Energy* 203, 883–896. doi:10.1016/j.apenergy.2017.06.106

Yong, J. Y., Ramachandaramurthy, V. K., Tan, K. M., and Mithulananthan, N. (2015). A Review on the State-Of-The-Art Technologies of Electric Vehicle, its Impacts and Prospects. *Renew. Sustain. Energy Rev.* 49, 365–385. doi:10.1016/j.rser.2015.04.130

Conflict of Interest: The authors declare that the research was conducted in the absence of any commercial or financial relationships that could be construed as a potential conflict of interest.

frontiers | Frontiers in Energy Research

TYPE Brief Research Report
PUBLISHED 16 August 2022
DOI 10.3389/fenrg.2022.972570

OPEN ACCESS

EDITED BY
Tinghui Ouyang,
National Institute of Advanced Industrial Science and Technology (AIST), Japan

REVIEWED BY
Yang Tian,
Yanshan University, China
Wenting Chen,
Yanshan University, China

*CORRESPONDENCE
Ying Liang,
yluniversity1030@163.com

SPECIALTY SECTION
This article was submitted to Smart Grids,
a section of the journal
Frontiers in Energy Research

RECEIVED 18 June 2022
ACCEPTED 18 July 2022
PUBLISHED 16 August 2022

CITATION
Liang Y and Wang J (2022), Research on multi-phase flow test and flow simulation test in energy enterprise automation.
Front. Energy Res. 10:972570.
doi: 10.3389/fenrg.2022.972570

Research on multi-phase flow test and flow simulation test in energy enterprise automation

Ying Liang[1,2,3]* and Jinxi Wang[1,3]

[1]School of Chemistry & Chemical Engineering, Yulin University, Yulin, China, [2]School of Chemical Engineering, Northwest University, Xi'an, China, [3]Shaanxi Key Laboratory of Low Metamorphic Coal Clean Utilization, School of Chemistry and Chemical Engineering, Yulin University, Yulin, China

Abstract:In the process of oil extraction and transportation, due to the interaction between oil, gas and water, hydrates are easily generated and pipelines are blocked. Based on this, from the perspective of energy enterprise automation technology, testing and research on oil and gas multiphase flow models and flow models are carried out. The hydrate formation area is analyzed by using the hydrate formation phase equilibrium theory, and the formation rate, deposition characteristics and blockage formation mechanism are analyzed. The influence of phase flow and heat transfer; after the boundary interface coefficient between oil, gas and water is clarified, a multiphase flow model of oil, gas and water is established. In the experimental test, the differential pressure signal is used to carry out the research on the oil and gas multiphase flow model and flow model, and it is concluded that the minimum critical superficial liquid velocity among the three flow patterns of oil, water and gas is 0.113 m/s, It can clearly characterize the characteristics of the flow pattern transition, which has certain practical significance for the sustainable development of energy enterprises.

KEYWORDS

energy, multiphase flow test, hydrate, continuity equation, multiphase flow model

Introduction

Oil has played a very important role in the development of the country, so the mixed transportation of oil and gas has been more widely used. In order to make the oil and gas mixing technology (Wu et al., 2021) more suitable for the actual needs of the project, experts in related fields have carried out in-depth research on it, and multiphase flow testing (Li et al., 2021a) and flow model testing (Mitsuru and Yuhu, 2019) have gradually become hot topics in the industry. In the multiphase flow test model, the parameters have a certain random variability, and the use of energy enterprise automation technology to identify the flow pattern of the changing parameter signals can greatly improve the oil and gas transmission efficiency in my country (Mouketou and Kolesnikov, 2018). However, at present, the development of automation in energy enterprises is still in its infancy, and relevant theoretical knowledge and practical applications are constrained by various conditions, such as lack of scientific research funds and lack of advanced technical support, and have not played its real role. Moreover, considering the incorporation of

liquid phase in the oil transmission process, the oil pipeline will be blocked to a certain extent, thereby reducing the oil transmission efficiency. In order to take the oil and gas mixed transportation technology to a new level, corresponding measures must be taken to accurately predict the location and area where the oil pipeline may be blocked, analyze the relationship between the various phases, and lead and guide the automation technology of energy enterprises (Le et al., 2021)] development of. However, how to accurately predict the blockage position of oil pipelines is still an important factor affecting the efficiency of oil production due to the lack of corresponding theoretical guidance and experimental data.

In view of the above problems, the literature (Yan et al., 2017) combined the optical fiber distributed acoustic wave sensing system with the optical fiber temperature pressure gauge and the optical fiber distributed temperature monitoring system by analyzing the main performance parameters and technical indicators of the multiphase flow hydrate environment. At the same time, various information of oil and gas wells are obtained, and experimental values of multiphase flow hydrate suitable for large-diameter, long-distance and high-pressure oil pipelines are proposed.

This method has the advantages of long life, long transmission distance, long monitoring distance and high temperature resistance. It can eliminate the electromagnetic influence during downhole operation, but when the oil pipeline is blocked, the blockage position cannot be predicted in time. Reference (Li and Dong, 2019) focuses on oil and natural gas. Equal pipeline transportation, in order to ensure the ideal accuracy of the multiphase flow test results, on the basis of ensuring the reliability of transportation management, the V-cone flowmeter structure is built, and the multiphase flow measurement correction model is introduced to ensure the high accuracy of the multiphase flow experiment. Precision. This method does not reach the environment where water and oil are mixed downhole, and there is a certain error between the accuracy of multiphase flow and the actual results. Reference (Han et al., 2019) established a multiphase flow test system based on the principle of optical fiber distributed acoustic wave sensing. Carry out monitoring and research on oil wells. Although the system obtains accurate downhole acoustic signals and realizes real-time monitoring of downhole production and susceptibility, it also does not consider the downhole hydrate formation area, which makes the research results unsatisfactory.

The above methods have achieved certain results in multiphase flow test accuracy and acoustic signal acquisition, but they do not consider the current development trend of the oil industry, and use advanced automation technology to seek more accurate pipeline blockage location prediction methods to help energy companies improve oil production. Quantity. Based on this, this paper conducts in-depth research on oil and gas multiphase flow testing and flow simulation testing from the perspective of energy enterprise automation. First, measure the hydrate in the oil pipeline. The measurement is mainly carried out from the hydrate formation area, decomposition rate (Li et al., 2021b), deposition characteristics and blockage formation mechanism, and the hydrate deposition rate at each location in the oil pipeline is determined, so that corresponding measures can be taken to ensure the normal exploitation and transportation of oil; A hydrate-containing multiphase flow model was established to analyze the thermal resistance effect of hydrate blockage on oil pipelines. Based on the continuity equation (Zhang et al., 2022), momentum equation and energy equation (Aglave et al., 2015), the relationship between the three phases of water is established; the multiphase flow model of oil, gas and water is established, and the boundary interface coefficient value of each phase is clarified (Wu et al., 2018). In the experimental test, the minimum critical superficial liquid velocity between laminar flow, wavy flow and slug flow is obtained as 0.113 m/s. Using the method in this paper, the transformation characteristics between the three flow patterns can be well described, as It has played a major role in promoting the development of the oil industry.

Measurement method of gas hydrate

In actual oil mining mines, there will inevitably be a certain degree of hydrate, forming the phenomenon of water-oil mixture. In the long run, hydrate formation will have a serious impact on normal oil exploitation and transportation. In order to get accurate test results of multiphase flow, the areas where hydrate usually forms, decomposition rate (Bahrami et al., 2016), sedimentary characteristics and blocking formation mechanism are analyzed, so as to have an in-depth understanding of hydrate deposition law in petroleum mine system, providing scientific reference for accurate prediction of hydrate area and prevention and control of oil exploitation.

Hydrate formation zone

Firstly, the possible regions of hydrate formation are analyzed, and the equilibrium theory of hydrate formation phase is used in this paper. The hydrate formation phase equilibrium theory refers to the fact that under different environmental factors, different temperatures and pressures of natural gas hydrates correspond to different phase systems in which hydrates exist. When the temperature in the mine is lower than the phase equilibrium temperature, the mine pressure value is larger than the phase equilibrium pressure value at the current temperature, and hydrate will be formed.

In this paper, the temperature and pressure required for hydrate formation are calculated by using hydrate phase equilibrium equation:

$$\frac{\Delta\mu_0}{RT_0} - \int_{T_0}^{T_{eq}} \frac{\Delta H_0 + \Delta C_k\left(T_{eq} - T_0\right)}{RT_{eq}^2} dT_{eq} + \int_{p_0}^{p_{eq}} \frac{\Delta V}{RT_{eq}} dp_{eq} = In\left(\frac{f_w}{f_{wr}}\right) - \sum_{i=1}^{l} M_i In\left(1 - \sum_{i=1}^{l} \theta_{ij}\right) \quad (1)$$

$$\ln\left(f_w / f_{wr}\right) = \ln x_w \quad (2)$$

In the formula, $\Delta\mu_0$ represents the chemical potential difference between the hydrate lattice and pure water in a standard environment, and the unit is J/mol; R represents the universal gas constant, the unit is J/(mol.k); T_0 represents the temperature value in a petroleum mine under standard environment, in unit of K; T_{eq} represents the temperature value of hydrate phase equilibrium, in unit of K; ΔH_0 represents the specific enthalpy difference between the hydrate lattice and pure water, expressed in J/kg; ΔC_k represents the specific heat tolerance difference between the hydrate lattice and pure water, in unit of Pa; p_{eq} represents the pressure value of hydrate phase equilibrium, and the unit is Pa; p_0 represents the pressure value of oil mine in standard state, and the unit is Pa; ΔV represents the specific tolerance difference between the hydrate lattice and pure water, in m3/kg; f_w is the fugacity of water in standard environment, and the unit is Pa; f_{wr} is the fugacity of water under the reference condition, in unit of Pa; l represents the number of types of hydrate in the mine; L represents the number of components required for hydrate formation; M_i is the dimensionless ratio of the number of type i holes to the number of water molecules in hydrate phase; θ_{ij} represents the proportion of type i holes occupied by type j gas molecules in hydrate crystal, dimensionless; x_w is molar concentration of water, dimensionless; $i = 1, 2 \ldots l$; $j = 1, 2 \ldots L$.

Rate of hydrate formation and decomposition

In the hydrate formation zone, gas and water molecules constantly interact to form new hydrates. The speed of hydrate formation is related to many conditions, which can be roughly divided into three categories: intrinsic kinetic factors, heat transfer process and mass transfer process. At present, there are many calculation methods for hydrate formation rate. By comprehensive comparison, Formula 3 is used in this paper to complete the calculation of hydrate formation rate. In the ring fog flow system, part of the water will evaporate with the air flow through the way of small droplets, drift mine environment; Some of the water will flow along the pipe, forming a liquid film of a certain thickness on the pipe wall. Both droplet and liquid film contain hydrates, but the gas-phase contact relationship between them and hydrates is very different. Hydrate formation rate is calculated under the ring fog flow theory, and the formula is shown in Eq. 3:

$$R_{hf} = \frac{A_s k_1 M_h}{M_g} \exp\left(-\frac{k_2}{T_f}\right)(\Delta T_{sub}) \quad (3)$$

In the formula, R_{hf} represents the formation rate of hydrate in a petroleum mine within unit length, and the unit is kg/(m s); A_s represents the gas-liquid contact area in A petroleum mine within unit length, and the unit is m2/m; M_h represents the molar mass of hydrate, in kg/mol; M_g represents the molar mass of hydrate and oil mixture, in kg/mol; T_f represents the liquid temperature in the test oil pipeline, in unit of K; ΔT_{sub} represents the degree of supercooling (Jiang and Yang, 2018), in unit K; $k_1 = 2.608 \times 10^{16} kgm^{-2}K^{-1}s^{-1}$, $k_2 = 13600K$.

The hydrate formation rate under other conditions can be calculated by Vsniausk as& Bishnoi model (Martins et al., 2021).

When the gas hydrate is generated in the oil mine, it will move upward along with the upward transportation of oil. As it moves, the hydrates decompose under pressure (Li, 2022a). The calculation formula of hydrate decomposition rate is shown in Eq. 4:

$$R_d = k_d A_s M_h\left(f_{eq} - f_g\right) \quad (4)$$

$$k_d = 1.24 \times 10^{11} \times \exp\left(-\frac{\Delta E}{RT}\right) \quad (5)$$

In the formula, R_d is the decomposition rate of hydrate, in kg/(m.s); k_d represents the hydrate decomposition constant, in mol/(m2. pa.s); f_{eq} represents the fugacity of a gas at three-phase equilibrium, in Pa; f_{eq} represents the fugacity (Li, 2022b) value of gas in an oil mine, in unit of Pa; ΔE represents the activation energy in J per mole.

Characteristics of hydrate deposition and mechanism of blockage formation

Under the circumstance of annular mist flow, part of the hydrate in the oil mine will sublime with the gas, and the other part will be deposited on the wall of the pipeline to form a hydrate layer of a certain thickness. In severe cases, it can lead to blockage of the pipeline. Under the action of the liquid film of the oil pipeline, the super-strong adhesive force makes the hydrate tightly adsorb on the pipeline wall, which can easily cause the blockage of the oil pipeline. Then it can be obtained that the hydrate deposition rate (Aziz et al., 2015) under the condition of annular fog flow is:

$$R_{hd} = \frac{2\pi r_f k_1 M_h}{M_g} \exp\left(-\frac{k_2}{T_f}\right)(\Delta T_{sib}) \quad (6)$$

In the formula, R_{hd} is the deposition rate of hydrate in the inner wall of oil pipeline within unit length, in kg/(m s); r_f represents the inner diameter of the oil pipeline, in unit of m.

After a long time of deposition, the hydrate on the inner wall of the oil pipeline will gradually thicken and form the hydrate

layer (Emmanuel and Dimitrios, 2019), whose specific thickness can be calculated by Eq. 7:

$$\delta_h = r_{ti} - r_f = \int_0^t \frac{k_1 M_h \Delta T_{sub}}{\rho_h M_g} e^{-k_2/T_f} \mathrm{d}t \tag{7}$$

Then, the dimensionless hydrate layer thickness δ_D is introduced into Eq. 7 to obtain:

$$\delta_D = \frac{\delta_h}{r_{ti}} \tag{8}$$

In the formula, δ_h represents the specific thickness of the hydrate layer of the oil pipeline, in unit of m; r_{ti} represents the inner diameter of oil pipeline before hydrate bonding, in unit of m; t stands for time in s; ρ_h represents the density value of hydrate adsorbed on the wall of oil pipeline, in kg/m3; δ_D represents the thickness value of dimensionless hydrate (Khayat et al., 2017).

It should be noted here that the data error between the hydrate thickness calculation method used in this paper and the standard ring fog flow condition is controlled within ±10%.

Hydrate formation takes time to accumulate, which is not a slow process, and some of it is carried away by sublimation, not all of it adsorbed to the wall of the pipeline. Therefore, even if the current environment meets all the conditions for hydrate formation, it will not cause hydrate blockage immediately. In practical application, the formation and blockage of hydrate in each position can be understood by calculating the thickness value of hydrate in different positions, so as to take corresponding measures to minimize the probability of hydrate blockage and ensure the normal operation of oil pipeline (Podryga et al., 2021).

Gas hydrate multiphase flow model

In hydrate formation conditions, two essential factors are water and gas, which interact with each other to form a new solid phase and change with the change of heat during hydrate formation and decomposition. At the same time, with more and more hydrate adsorbed on the inner wall of the oil pipeline, the oil flow area will continue to decrease and hydrate layer with thermal resistance effect will be formed gradually (Song et al., 2020). With the passage of time, the thermal resistance effect gradually increases. After considering the influence of hydrate generation and deposition on multi-phase flow and heat transfer in oil mines (Frank et al., 2019), a multi-phase flow model of oil and gas containing hydrate was established. Phase transformation exists between gas phase and hydrate phase, but cannot be completed between gas phase and liquid phase due to lack of mass transfer. There is a stable radial heat transfer between the oil mine and the bottom layer, and the fluid in the mine is always in a state of thermodynamic equilibrium. In the multiphase flow model, the interface between each phase can be regarded as a discontinuity plane, and the fluid in each phase satisfies the basic laws of conservation of mass, momentum and energy. These laws describe the relevant laws that should be followed in the process of oil exploitation from three aspects of continuity equation momentum equation and energy equation respectively.

Continuity equation

Based on the mass conservation law (Li et al., 2018), the continuity equation between each phase is calculated as follows:

The gas phase:

$$\frac{\partial}{\partial t}\left(A\rho_g E_g\right) + \frac{\partial}{\partial s}\left(A\rho_g v_g E_g\right) = q_g - x_g R_{hf} \tag{9}$$

The liquid phase:

$$\frac{\partial}{\partial t}\left(A\rho_m E_m\right) + \frac{\partial}{\partial s}\left(A\rho_m v_m E_m\right) = -\left(1 - x_g\right) R_{hf} \tag{10}$$

The cutting phase:

$$\frac{\partial}{\partial t}\left(A\rho_c E_c\right) + \frac{\partial}{\partial s}\left(A\rho_c v_c E_c\right) = q_c \tag{11}$$

Hydrate phase:

$$\frac{\partial}{\partial t}\left(A\rho_h E_h\right) + \frac{\partial}{\partial s}\left(A\rho_h v_h E_h\right) = R_{hf} - R_{hd} \tag{12}$$

In the formula, A is annular cross-sectional area, unit: m2; ρ_g、ρ_m、ρ_c、ρ_h represent the density values of natural gas, drilling fluid (Al-Qutami et al., 2017), cuttings and hydrate in the annulus, in kg/m3; E_g、E_m、E_c、E_h respectively represent the volume fractions of natural gas, drilling fluid, cuttings and hydrate in annulus respectively, without dimensionality; v_g、v_m、v_c、v_h respectively represent the up-return velocities of natural gas, drilling fluid, cuttings and hydrate in the annulus, expressed in m/s; q_g represents the gas flow rate of oil pipeline within unit length, in kg/(m/s); x_g represents the mass fraction of natural gas in gas hydrate (Sun, 2016), dimensionless; q_c represents the cuttings generation rate of the oil pipeline per unit length, in kg (m/s).

Momentum equation

According to the momentum conservation theorem, momentum equations of multiphase flow of gas, liquid and solid phases can be calculated, as shown in Eq. 13:

$$\frac{\partial}{\partial t}\left(AE_g\rho_g v_g + AE_m\rho_m v_m + AE_c\rho_c v_c + AE_h\rho_h v_h\right) + \frac{\partial}{\partial s}\left(AE_g\rho_g v_g^2 + AE_m\rho_m v_m^2 + AE_c\rho_c v_c^2 + AE_h\rho_h v_h^2\right) \tag{13}$$

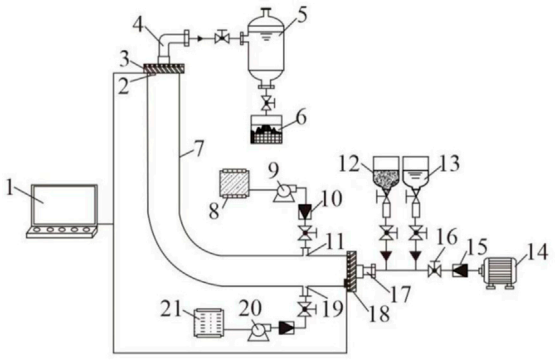

FIGURE 1
Device diagram of oil-gas-water multiphase flow model.

In the formula, g represents the acceleration of gravity, in m/s2; θ is the depth of oil mine, in unit m; p represents the pressure value in the annulus, in Pa; F_r represents the frictional force in the annulus in Pa.

Energy equation

1) Temperature field equation

In the oil mine, the heat transfer process of gas is not a stable one. Under multiple constraints of temperature and pressure, gas and hydrate will undergo phase transformation and absorb or release some heat. Due to the influence of hydrate's own characteristics, it is endothermic during decomposition and exothermic during formation. Therefore, the effect of hydrate phase transition must be taken into account when establishing the energy equation.

The temperature field equation of unsteady flow of gas-liquid mixture in annular air can be expressed as:

$$\frac{\partial}{\partial t}\left[\left(\rho_g E_g C_{pg} T_a A\right)+\left(\rho_l E_l C_l T_a A\right)\right]+\frac{R_{hf}\cdot\Delta H_h}{M_h}-\left[\frac{\partial\left(w_g C_{pg} T_a\right)}{\partial s}+\frac{\partial\left(w_l C_l T_a\right)}{\partial s}\right]=2\left[\frac{1}{A'}\left(T_{ei}-T_a\right)-\frac{1}{B'}\left(T_a-T_t\right)\right] \tag{14}$$

The temperature field equation in the drill string can be expressed as:

$$\frac{\partial}{\partial t}\left(\rho_l C_l T_t\right)A_t+\frac{\partial\left(w_l C_l T_t\right)}{\partial s}=\frac{2}{B'}\left(T_a-T_t\right) \tag{15}$$

In the formula, C_{pg} and C_1 respectively represent the specific heat of the gas phase and liquid phase, and the unit is J/(kg); T_a 、 T_{ei} and T_t represent the temperature values in annulus, formation and drill string respectively, in unit K; ρ_l represents the density value of the liquid phase, in kg/m3; E_l represents the volume fraction of the liquid phase, dimensionless; ΔH_h represents the enthalpy of hydrate, expressed in J/mol; w_g and w_l respectively represent the mass flow rate of gas phase and liquid phase, in kg/s; A' , B' both represent intermediate parameters; A_t represents the cross section of the drill string in m2.

2) Energy equation

The energy balance equation (Peng et al., 2017) between oil pipeline and drill string can be expressed as:

$$\frac{\partial}{\partial t}\left[\left(\rho_g E_g\left(h+\frac{1}{2}v_g^2-gs\cos\theta\right)\right)+\left(\rho_l E_l\left(h+\frac{1}{2}v_l^2-gs\cos\theta\right)\right)\right]A+\frac{R_{hf}\cdot\Delta H_h}{M_h}-\left[\frac{\partial\left(w_g\left(h+\frac{1}{2}v_g^2-gs\cos\theta\right)\right)}{\partial s}+\frac{\partial\left(w_l\left(h+\frac{1}{2}v_l^2-gs\cos\theta\right)\right)}{\partial s}\right]=2\left[\frac{1}{A'}\left(T_{ei}-T_a\right)-\frac{1}{B'}\left(T_a-T_t\right)\right] \tag{16}$$

$$\frac{\partial}{\partial t}\left(\rho_l E_l\left(h+\frac{1}{2}v_l^2-gs\cos\theta\right)\right)A_t+\frac{\partial\left(w_l\left(h+\frac{1}{2}v_l^2-gs\cos\theta\right)\right)}{\partial s}=\frac{2}{B'}\left(T_a-T_t\right) \tag{17}$$

In the formula, h stands for enthalpy and the unit is J.

Oil-gas-water multiphase flow model

The oil-gas-water multiphase flow model established in this paper is shown in Figure 1. Among them, one for the computer monitoring system, two for pressure sensor, three for the open joint, four for the mixture export, five for liquid storage tanks, six for the cuttings collection barrels, seven for transparent pipe, eight for gas storage tank, A nine for air compressor, 10 for A gas flowmeter, 11 for the gas phase entrance, 12 for the cuttings funnel, 13 for water funnel, 14 for electromagnetic air pump, 15 is gas flowmeter B, 16 is ball valve, 17 is mixture inlet, 18 is temperature sensor, 19 is solid phase inlet, 20 is air compressor B, 21 is ozone storage tank.

For oil flow calculation, turbine flowmeter is adopted in this paper (Cheng et al., 2018). Because gas has certain compressibility, it is greatly affected by temperature and pressure in oil pipeline. Therefore, real-time compensation and correction technology of temperature and pressure is introduced here (Fatemi, 2015). After accurate calculation of gas flowmeter, turbine flowmeter and vortex flowmeter, the control of gas phase flow is realized under the action of ball valve.

TABLE 1 Basic experimental data of oil pipeline end.

The depth of an oil min		4000 m	The depth of the water	1500 m
Casing size		10–3/42,000–3000 m 9–5/83,000–5000 m	drill string	50–4000 m
Throttle line size		3	inside diameter of riser	472 mm
Drilling fluid	Density	1.1g/cm3	plastic viscosity	3 mPa s
	yield value	1.5Pa	displacement	30L/s
Bit size		8–1/2	rate of penetration	6 m/h
Reservoir	Pressure	45.6 MPa	bursting pressure	49.8 MPa
	gas phase permeability	550md	sand thickness	15 m
Bottom-water temperature		2°C	geothermal gradient	2.7°C/100 m

By calculating the continuity equation for the volume ratio of a single phase, the interface between multiple phases can be obtained. Assuming that phase exists, its boundary interface can be calculated by:

$$\frac{\partial \alpha_m}{\partial q} + \vec{v} \cdot \nabla \alpha_m = \frac{S_{\alpha_m}}{\rho_m} \tag{18}$$

In the formula, $\vec{v}$ represents the multiphase interface coefficient value, ρ_m represents the volume ratio of the m phase (Bs et al., 2019), q represents the number of phases, S_{α_m} represents the density value of the m phase, and α represents the volume ratio, satisfying the conditions of Eq. 19:

$$\sum_{m=1}^{n} \alpha_m = 1 \tag{19}$$

The properties of produced oil are determined by the phase fractions of all the controlled volumes in the annulus. The formula for calculating the average density of the volume ratio is:

$$\rho = \sum_{m=1}^{n} \alpha_m \rho_m \tag{20}$$

Through the momentum equation solved above, the velocity field of each phase is calculated, as shown in Eq. 21:

$$\frac{\partial}{\partial t}\left(\rho_v^r\right) + \nabla \cdot \left(\rho_{vv}^{rr}\right) = -\nabla p + \nabla \cdot \left[\mu\left(\nabla_v^r + \nabla_v^{rT}\right)\right] + \rho \overset{r}{g} + \overset{r}{F} \tag{21}$$

In the formula, r represents the phase constraint function; $\overset{r}{g}$ represents the density value of the gas phase, and $\overset{r}{F}$ represents the velocity field sharing coefficient.

Then, the formula for calculating the pressure drop between each phase interface is:

$$\Delta p = p_2 - p_1 = \sigma\left(\frac{1}{R_1} + \frac{1}{R_2}\right) \tag{22}$$

In the formula, p_1 and p_2 respectively represent the pressure values on both sides of the phase interface; σ represents the surface tension coefficient; R_1 and R_2 respectively represents the radius of the oil pipeline before and after pressure.

The normal vector of the unit surface around the inner wall of the oil pipeline is calculated as:

$$\hat{n} = \hat{n}_w \cos\theta_w + \hat{t}_w \sin\theta_w \tag{23}$$

In the formula, θ_w represents the surface tension coefficient; $\hat{n}_w$ and $\hat{t}_w$ respectively represents the radius of the oil pipeline before and after pressure.

The equation of the average variable of the calculated vector is:

$$\frac{\partial}{\partial t}(\rho E) + \nabla \cdot \left[\vec{v}(\rho E + p)\right] = \nabla \cdot \left(k_{eff} \nabla T\right) + S_k \tag{24}$$

In the formula, T is the temperature in the variable; E is the energy in the variable. The two expressions are as follows:

$$E = \frac{\sum_{m=1}^{n} \alpha_m \rho_m E_m}{\sum_{m=1}^{n} \alpha_m \rho_m} \tag{25}$$

$$T = \frac{\sum_{m=1}^{n} \alpha_m \rho_m T_m}{\sum_{m=1}^{n} \alpha_m \rho_m} \tag{26}$$

Assuming that the normal line of the surface n is the gradient value of the volume share α_m of the m phase, then:

$$n = \nabla \alpha_m \tag{27}$$

The calculation formula of surface curvature κ is:

$$\kappa = \nabla \cdot \hat{n} \tag{28}$$

In the formula, the value of the normal vector coefficient $\widehat{n}$ is expressed as:

$$\widehat{n} = \frac{n}{|n|} \tag{29}$$

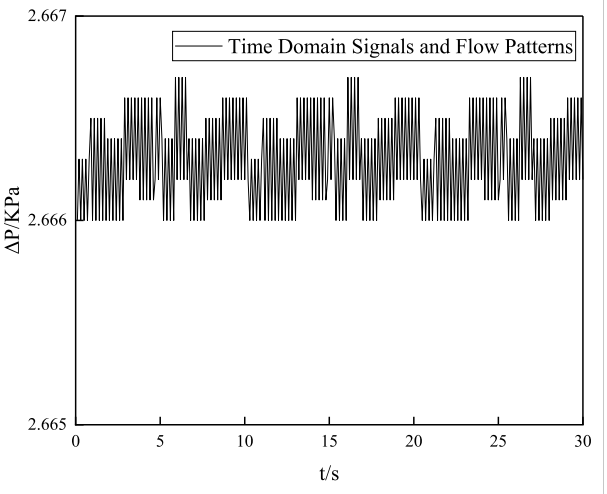

FIGURE 2
Stratified flow differential pressure time domain signal and flow pattern diagram.

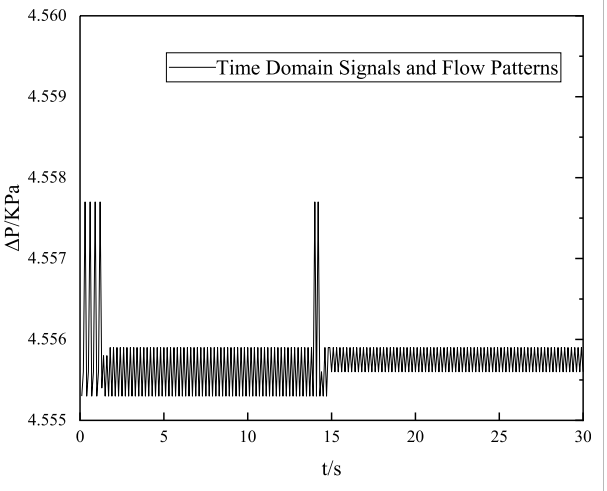

FIGURE 3
Time-domain signal and flow pattern of undulating flow differential pressure.

According to the divergence theorem, surface tension can be converted into volume force and substituted into the left and right source terms in the equation of average variables:

$$F_{vol} = \sum_{paisij,i<j} \sigma_{ij} \frac{\alpha_i \rho_i \kappa_j \nabla \alpha_j + \alpha_j \rho_j \kappa_i \nabla \alpha_i}{\frac{1}{2}\left(\rho_i + \rho_j\right)} \tag{30}$$

Assuming that only two phases can exist in a unit, then $\kappa_i = \kappa_j$, $\nabla \alpha_i = \nabla \alpha_j$, Eq. 30 can be transformed into Eq. 31:

$$F_{vol} = \sigma_{ij} \frac{\rho K_i \nabla \alpha_i}{\frac{1}{2}\left(\rho_i + \rho_j\right)} \tag{31}$$

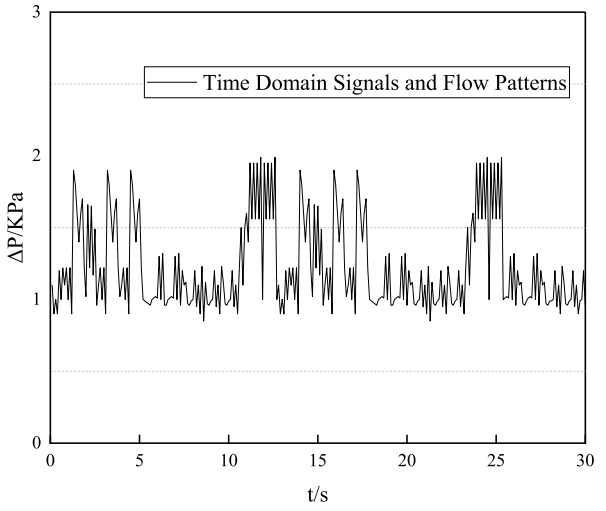

FIGURE 4
Slug flow differential pressure signal and flow pattern diagram.

Experimental verification

Using differential pressure signal to study flow characteristics is a very common way in multiphase flow test. On the basis of differential pressure signal, the multi-phase flow model and flow model of oil and gas are tested. Differential pressure signal was obtained through experimental simulation in this paper. The diameter of oil pipeline 8 times was taken as the pressure sampling interval, i.e. 1000mm, and the sampling frequency was set as 100 Hz (Wang et al., 2018). The experimental platform uses Windows2018 operating system, with CPU of 8 GB and operating memory size of 4 GB. The multi-phase flow experimental system of oil, gas and water has been established. The oil phase is no. 40 oil. In addition to the casing at the mine end, the plexiglass pipe with an inner diameter of 40 mm and a total length of 20 m was used in the experiment (Hulsurkar et al., 2018), which was placed 15 m away from the entrance of the oil mine. Two groups of pressure transmitters are placed on the plexiglass tube with a distance of 200 mm between them. Each group consists of transmitters placed on the upper and lower sides of the plexiglass tube. In addition, the fluctuation of differential pressure signal in the experiment was obtained by the capacitive differential pressure transmitter. The total length of differential pressure measurement was 200m, which could meet the experimental needs. Other basic data about oil pipeline ends are shown in Table 1.

When the apparent velocity of both the gas and liquid phases in the pipeline is low, lamellar flow will be formed in the pipeline (Zhang and Tao, 2016). Stratified flow is one of the most common flow patterns in oil pipelines. A very smooth interface forms between the gas phase and the liquid phase, separating them, with the gas phase on top and the liquid phase on the bottom. When layered flow occurs, the time domain signal and flow pattern are shown in Figure 2.

As can be seen from Figure 2, when the apparent velocity of gas and liquid phase is small, the differential pressure time-domain signal and flow pattern present a layered flow, which is in a relatively stable state with only a small range of fluctuation (Gharaibah et al., 2015). At this time, the oil pipeline is normal, there is no blockage and other circumstances. At the same time, it can be considered that the time-domain signal has a stable value of 4.56 KPa and does not change with time.

With the increase of the apparent velocity, the boundary between gas and liquid phase begins to appear disturbance waves moving along the flow direction. Under the influence of such disturbed waves, a certain degree of fluctuation appeared on the interface, so the layered flow was transformed into a wave-like flow. At this time, the fluctuation of differential pressure signal gradually increased, as shown in Figure 3.

It can be clearly seen from Figure 3 that compared with stratified flow, undulating flow fluctuates more clearly, but the overall fluctuation range is not very large and always fluctuates around 2.666Kpa (Khayat et al., 2017). In addition, it can be seen from Figure 3 that the time-domain signal curve is less affected by time and does not change greatly with time.

In the oil pipeline, when the apparent velocity of the fluid rises to a certain extent, the wavy flow gradually begins to transform into slug flow, and the time-domain curve of the differential pressure signal will fluctuate greatly with obvious peaks and troughs. At this point, the liquid phase will rapidly fill the pipeline and form a long liquid plug. Behind the liquid plug is a very long air mass, and there will be liquid phase under the air mass, as shown in Figure 4.

By observing Figure 4, it can be concluded that when slug flow occurs in oil pipeline, the fluctuation of time domain signal curve is very large. Within 30 s of the experiment, there were eight obvious peaks. However, it can also be seen that the time-domain signal curve of slug flow has no obvious rule with the change of time, so it can also be considered that the time-domain signal curve of slug flow is not affected by time.

In conclusion, by analyzing the changes of time domain signal curves of middle-layer flow, wavy flow and slug flow in Figure 2 to Figure 4, it can be concluded that: The multiphase flow model and flow model in this paper can well extract the time-domain curve of differential pressure signal, and on the basis of the trend of the three curves, the transition characteristics between oil, water and gas multiphase flow patterns can be analyzed. By analyzing the transition characteristics of each phase, it can be found that the minimum critical apparent liquid velocity for the transition from layered flow to slug flow is $V_{SL} = 0.113m/s$, and the gas phase apparent velocity for the transition from layered flow to slug flow begins to decline with the continuous increase of liquid phase apparent velocity, which is specifically shown as the fluctuation of curves in Figure 2 to Figure 4. Therefore, the multi-phase flow model and flow model established by the proposed method, combined with differential pressure signals, can well obtain the characteristics of flow pattern transformation, which verifies the effectiveness and feasibility of the proposed method.

Conclusion

In this paper, from the perspective of energy enterprise automation, the multiphase flow model and flow model of oil and gas pipelines are tested, and three flow patterns of laminar flow, wavy flow and slug flow are obtained, and the conversion between the three flow patterns is obtained. Interface.

First, under the action of the liquid film on the oil pipeline wall, hydrate deposits form a hydrate layer, which is very prone to blockage of the oil pipeline. In this paper, after analyzing the hydrate formation area, decomposition rate, deposition characteristics and blockage formation mechanism, a multiphase flow model including hydrate is constructed. A multiphase flow model of oil and gas is established to obtain the volume ratio, velocity field and pressure drop of each phase. In the channel, while the apparent velocity of liquid phase increases, the apparent velocity of the transition between laminar flow and slug flow shows a downward trend. Therefore, it can be concluded that the method in this paper can describe and characterize the flow pattern transition clearly and unambiguously. This of great significance to the exploration, development and transportation of oil. We will further study the influence mechanism of various factors to provide more scientific and favorable guidance for oil exploitation and transportation.

Data availability statement

The raw data supporting the conclusion of this article will be made available by the authors, without undue reservation.

Author contributions

YL conceived the idea and designed experiments, JW performed data analysis and drawn conclusions, finally, YL and JW wrote the manuscript.

Funding

This paper is supported by Bureau of Science and Technology in Yulin “Design and application of a new type sampler for multiphase flow in wellhead,” (2019-84-1).

Conflict of interest

The authors declare that the research was conducted in the absence of any commercial or financial relationships that could be construed as a potential conflict of interest.

Publisher's note

References

Aglave, R., Baran, O., Tandon, M. P., and Karnik, S. L. (2015). "Numerical simulation of dense Gaslogolid fluidized beds: Comparison between eulerian multiphase and discrete element methods," in AICHE Annual Conference, Salt lake city, UT, November 8-13, 2015.

Al-Qutami, T. A., Ibrahim, R., and Ismail, I. (2017). "Radial basis function network to predict gas flow rate in multiphase flow," in International Conference on Machine Learning & Computing, 24 February 2017 (ACM).

Aziz, I. A., Brandt, I., Gunasekera, D., and Håtveit, B. (2015). Multiphase flow simulation-optimizing field productivity[J]. *Oilfield Rev.* 27 (1), 26–37.

Bahrami, N., Pena, D., and Lusted, I. (2016). Well test, rate transient analysis and reservoir simulation for characterizing multi-fractured unconventional oil and gas reservoirs. *J. Pet. Explor. Prod. Technol.* 6 (4), 675–689. doi:10.1007/s13202-015-0219-1

Bs, A., Wf, A., and Ning, W. B. (2019). Multiphase flow modeling of gas intrusion in oil-based drilling mud[J]. *J. Petroleum Sci. Eng.* 174, 1142–1151. doi:10.1016/j.petrol.2018.12.018

Cheng, L., Gao, Z. K., and Jin, N. D., Springerbriefs in applied sciences and technology multiphase flow series editors nonlinear analysis of gas-water/oil-water two-phase flow in complex networks 123. 2018.

Emmanuel, I. E., and Dimitrios, I. G. (2019). Drill cuttings transport and deposition in complex annular geometries of deviated oil and gas wells: A multiphase flow analysis of positional variability ScienceDirect. *Chem. Eng. Res. Des. Trans. Institution Chem. Eng.* 151, 214–230. doi:10.1016/j.cherd.2019.09.013

Fatemi, M. S. (2015). Multiphase flow and hysteresis phenomena in oil recovery by water alternating gas (WAG) injection. *Engineering*.

Frank, M., Kamenicky, R., Drikakis, D., Thomas, L., Ledin, H., and Wood, T. (2019). Multiphase flow effects in a horizontal oil and gas separator. *Energies* 12 (11), 2116. doi:10.3390/en12112116

Gharaibah, E., Read, A., and Scheuerer, G. (2015). "Overview of CFD multiphase flow simulation tools for subsea oil and gas system design, optimization and operation," in OTC Brasil, Rio de Janeiro, Brazil, October 27–29, 2015.

Han, S., Wang, T., and Zhu, S. (2019). Research on factors influencing the detection accuracy of multiphase flow based on CFD simulation. *Sci. public Sci. Technol. innovation* (11), 2.

Hulsurkar, P., Awoleke, O. O., and Ahmadi, M. (2018). Experimental study of the multiphase flow of sand, viscous oil, and gas in a horizontal pipe. *SPE Prod. operations* 33 (4), 837–856. doi:10.2118/187212-pa

Jiang, Z., and Yang, Y. (2018). Design and numerical simulation of double-grade gas-liquid separator. *Petroleum Tubul. Goods Instrum*.

Khayat, O., Afarideh, H., and Mohammadi, A. H. . Computational fluid dynamics (CFD) analysis and modeling of mass flow rates of gas, oil and water in multiphase flow through venturi meter using LSSVM method. 2017

Le, S., Wu, Y., Guo, Y., and Del Vecchio, C. (2021). Game Theoretic Approach for a service function chain routing in NFV with coupled constraints. *IEEE Trans. Circuits Syst. II Express Briefs* 68, 3557–3561. doi:10.1109/TCSII.2021.3070025

Li, H. (2022). SCADA data based wind power interval prediction using LUBE-based deep residual networks. *Front. Energy Res.* 10, 920837. doi:10.3389/fenrg.2022.920837

Li, H. (2022). Short-term wind power prediction via spatial temporal analysis and deep residual networks. *Front. Energy Res.* 10, 920407. doi:10.3389/fenrg.2022.920407

Li, H., Deng, J., Yuan, S., Feng, P., and Arachchige, D. (2021). Monitoring and identifying wind turbine generator bearing faults using deep belief network and EWMA control charts. *Front. Energy Res.* 9, 770. doi:10.3389/fenrg.2021.799039

Li, H., Deng, J., Feng, P., Pu, C., Arachchige, D., and Cheng, Q. (2021). Short-term nacelle orientation forecasting using bilinear transformation and ICEEMDAN framework. *Front. Energy Res.* 9, 780928. doi:10.3389/fenrg.2021.780928

Li, W., and Dong, J. (2019). Experimental apparatus and testing technology for multiphase flow hydrate in large submarine mixed transportation pipeline. *Chem. Eng. Equip.* 10, 3.

Li, Y., Chen, J., and Kong, W. (2018). Design and optimization of the fiber-optic probe array for measuring gas holdup in oil-gas-water multiphase flow. *J. Ambient Intell. Humaniz. Comput* (1). doi:10.1007/s12652-017-0674-2

Martins, O., Nduka, N. B., and Abam, F. (2021). Diagnostic and prognostic development of a mechanistic model for multiphase flow in oil-gas pipelines. *J. King Saud University-Science* (1). doi:10.1016/j.jksues.2020.12.010

Mitsuru, T, and Yuhu, W (2019). MayerType optimal control of probabilistic boolean control network with uncertain selection probabilities. *IEEE Trans. Cybern.* 51, 3079–3092. doi:10.1109/TCYB.2019.2954849

Mouketou, F. N., and Kolesnikov, A. (2018). Modelling and simulation of multiphase flow applicable to processes in oil and gas industry. *Chem. Prod. Process Model.* 14. doi:10.1515/cppm-2017-0066

Peng, W. F., Yao, Z. Y., and Sui, G. (2017). *Detection of the radiation of multiphase flow meter on the oil and gas production platform in a sea area in 2015*. Occupation and Health.

Podryga, V. O., Polyakov, S. V., and Tarasov, N. I. (2021). Developing of multiscale Approach to HPC-simulation of multiphase fluid flows. *Lobachevskii J. Math.* 42 (11), 2626–2636. doi:10.1134/s1995080221110160

Song, G., Li, Y., and Sum, A. K. (2020). Characterization of the coupling between gas hydrate formation and multiphase flow conditions. *J. Nat. Gas Sci. Eng.* 83, 103567. doi:10.1016/j.jngse.2020.103567

Sun, B. (2016). *Multiphase flow in oil and gas well drilling (Sun/Multiphase flow in oil and gas well drilling)*. Weiley. doi:10.1002/9781118720288:1-24

Wang, H., Gala, D. P., and Sharma, M. M. (2018). Effect of fluid type and multiphase flow on sand production in oil and gas wells. *SPE J.* 24, 733–743. doi:10.2118/187117-PA

Wu, S., Dong, J., Wang, B., Fan, T., and Li, H. (2018). "A general purpose model for multiphase compositional flow simulation," in SPE Asia Pacific Oil and Gas Conference and Exhibition, Brisbane, Australia, October 23–25, 2018. doi:10.2118/191996-ms

Wu, Y., Guo, Y., and Toyoda, M. (2021). Policy iteration approach to the infinite horizon average optimal control of probabilistic boolean networks. *IEEE Trans. Neural Netw. Learn. Syst.* 32, 2910–2924. doi:10.1109/TNNLS.2020.3008960

Yan, Z., Luo, D., and Tang, S. (2017). Research on downhole multiphase flow measurement based on optical fiber distributed acoustic sensor. *Oil gas well Test.* 26 (2), 4.

Zhang, Y., Qian, T., and Tang, W. (2022). Buildings-to-distribution-network integration considering power transformer loading capability and distribution network reconfiguration. *Energy* 244, 123104. doi:10.1016/j.energy.2022.123104

Zhang, Z., and Tao, L. (2016). "Multiphase transient slugging flow in subsea oil and gas production," in Asme International Conference on Ocean, Busan, South Korea, June 19–24, 2016.

frontiers | Frontiers in Energy Research

BRIEF RESEARCH REPORT
published: 16 August 2022
doi: 10.3389/fenrg.2022.958384

Research on Power System Joint Optimal Generation Scheduling Based on Improved Balance Optimizer

Jianming Xu[1], *Anfeng Liu*[2], *Yang Qin*[1], *Guangrong Xu*[1] *and Yibo Tang*[1,3]*

[1]*Provincial Key Laboratory of Informational Service for Rural Area of Southwestern Hunan, Shaoyang University, Shaoyang, China,* [2]*School of Computer Science and Engineer, Central South University, Changsha, China,* [3]*College of Physics and Electronics, Central South University, Changsha, China*

This article presents a power system joint optimization generation regulation method based on the improved balance optimizer, which takes the five factors of power system network loss, voltage offset, generation cost, fuel cost, and comprehensive pollution emission as the objective function and takes the internal power balance of the system, each generator set, generation capacity, generation flow, and up and down climbing as the constraints. Fully considering the current energy-saving development objectives and the impact of economic dispatching, taking stable and safe operation as the core, the power generation dispatching model is established by improving the balance optimizer. The model realizes the maximum power generation with the lowest energy consumption parameters and transitions from the original power generation energy consumption of the power system to the best energy-saving power generation energy consumption so that the power value of the system reaches the target balance and completes efficient dispatching. Simulation experiments show that the proposed method can ensure the most reasonable power load in both summer and winter. The average load in summer and winter is reduced from 254.78/mw to 205.36/mw, down about 19.39%, which can ensure the power generation stability of the power system. The average power generation cost after dispatching is 129,920 $/h, which is significantly improved by comparing with 131,225 $/h before dispatching and can realize certain environmental benefits.

Keywords: balance optimizer, power system, objective function, energy consumption parameters, power generation cost

OPEN ACCESS

Edited by:
Yusen He,
The University of Iowa, United States

Reviewed by:
Heming Huang,
Wuhan University, China
Yan Zhang,
Tokyo University of Agriculture and Technology, Japan

***Correspondence:**
Yibo Tang
626323320@qq.com

Specialty section:
This article was submitted to Smart Grids, a section of the journal Frontiers in Energy Research

Received: *31 May 2022*
Accepted: *13 June 2022*
Published: *16 August 2022*

Citation:
Xu J, Liu A, Qin Y, Xu G and Tang Y (2022) Research on Power System Joint Optimal Generation Scheduling Based on Improved Balance Optimizer. Front. Energy Res. 10:958384. doi: 10.3389/fenrg.2022.958384

INTRODUCTION

At this stage, with the continuous development of the power era, the development of power technology is an important task that cannot be ignored by all countries at this stage. People's life, entertainment, and social production are inseparable from the support of power. However, with the increasing power consumption of users and the large-scale high load (Le et al., 2021) power consumption of various large enterprises, in order to speed up the pace of production, system failures occur frequently and the internal power distribution is uneven. The long-term uneven distribution will not only lead to short circuit (Toyoda and Wu, 2019), power climbing, and insufficient or excessive power generation but will also lead to unstable operation of the power system, increased cost, and poor power generation efficiency (Wu et al., 2020). Based on this, it is necessary to make reasonable arrangement and dispatching planning. Effective generation dispatching can not only

make the operation of the power system more stable without fault impact but also recover the highest benefit return with the lowest generation cost.

This literature (Zhang et al., 2022) mainly aims at the mixed phenomenon of AC and DC in the power system. The power generation problem of the system is quasi-transformed into the optimal power flow calculation problem. Taking four groups of phenomena such as network loss, power generation cost, pollutant emission, and voltage offset as the objective function, the differential evolution method is used to solve the generation scheduling parameters of the four groups of objective functions. The literature (Li et al., 2021a) proposed a genetic algorithm based on the neural network. Compared with the traditional methods, the genetic algorithm can capture the key information affecting power generation faster so as to converge to higher quality reactive power optimization scheme better and faster. The document (Li et al., 2021b) proposes the generation scheduling optimization strategy of swarm intelligence algorithm, which divides the optimal generation scheduling into two stages: search and utilization. The search process generally introduces disturbance variables so that the whole optimization process can find the target value faster and achieve global and large-scale optimization. Hu et al., (2020) propose an optimal generation scheduling algorithm with key parameter constraints. By setting different scheduling parameters for different generation values, it makes detailed optimization in the process of continuous updating among them. Shan et al., (2020) adopt a cross-platform generation scheduling algorithm, set models that can describe different nodes in the power system, and establish a joint scheduling threshold for scheduling. Yan et al., (2016) calculates the power value with linear change in the power system, sets the standard threshold, finds the power points that do not conform to the linear change, and implements generation dispatching.

On this basis, considering the abovementioned shortcomings and adverse effects, this study proposes a power system joint optimal generation scheduling method based on the improved balance optimizer. Balance optimizer is a new intelligent algorithm. It adopts the power generation optimization strategy inspired by the balance physical phenomenon based on the control volume mass and has strong data optimization ability, fast calculation speed, and fast convergence speed. First, the objective function is established, and then the condition constraints are carried out. An improved balance optimizer method is used to build a joint optimal generation scheduling model. On the basis of the original balance optimizer, the power variation objective function considering the actual maximization of the power system is added, and the objective constraint function is used to further approximate the optimal dispatching value. The optimization strategy can better adapt to the actual power generation situation of the power system and shows relatively best optimization performance. After the completion of dispatching, the system generates electricity smoothly, reduces the cost and power consumption, and greatly improves the operation efficiency.

OBJECTIVE FUNCTION ESTABLISHMENT

The improved balance optimizer follows the principle of mass balance equation in physics and describes the whole process of mass entering, leaving, and generating in a control volume. When applied to the joint optimal generation scheduling of the power system, the power target can be regarded as a mass point, the process of this mass point can be described, and finally the most balanced power value can be output. The objective function described, based on the improved balance optimizer, is

1) Power system network loss, expressed as

$$\min f_1 = \sum_{i,j\in N} G_{ij}\left(U_i^2 + U_j^2 - 2U_iU_j\cos\theta_{ij}\right) \tag{1}$$

In the formula, N represents the number of all nodes in the power system; G_{ij} represents node i and node j line conductance; U_i、 U_j represents the maximum voltage value of node i and j at the position of the node, respectively; θ_{ij} represents the maximum electrical damage that node i and node j can withstand.

2) Voltage offset

$$\min f_2 = \sum_{i\in N_B} \left|U_B^i - 1.0\right| \tag{2}$$

In the formula, U_B^i represents the voltage value of the power load node i; N_B indicates the number of nodes.

3) Power generation cost, the average cost consumption of power generation fuel can be expressed as

$$\min f_3 = \sum_{i=1}^{N_G}\left[a_i + b_iP_G^i + c_i\left(P_G^i\right)^2\right]. \tag{3}$$

In the formula, a_i represents the lowest cost coefficient of the power system; b_i represents the highest cost factor; N_G indicates the number of generator nodes; and P_G^i indicates the active power value of the second generator set. The penalty function (Li et al., 2016) is established to restrict the state variables of uneven output in the i power system, and the objective function to be optimized is expressed as

$$\min J = f_k + \eta_U\sum_{i\in N_B}\Delta U_i + \eta_Q\sum_{j\in N_G}\Delta Q_j, \tag{4}$$

of which

$$\Delta U_i = \begin{cases} U_i - U_i^{\max}, U_i > U_i^{\max} \\ 0, U_i^{\min} < U_i < U_i^{\max} \\ U_i^{\min} - U_i, U_i < U_i^{\min} \end{cases}. \tag{5}$$

$$\Delta Q_j = \begin{cases} Q_{G.j} - Q_{G.j}^{\max}, Q_{G.j} > Q_{G,j}^{\max} \\ 0, Q_{G.j}^{\min} < Q_{G.j} < Q_{G,j}^{\max} \\ Q_{G,j}^{\min} - Q_{G,j}, Q_{G.j} < Q_{G,j}^{\min} \end{cases}. \tag{6}$$

In the formula, f_k represents the solution objective; η_U represents the penalty coefficient indicating reactive power output of the load node; η_Q indicates the penalty coefficient of generator reactive power output; ΔU_i represents the penalty variable representing load node; ΔQ_j represents the penalty variable of the generator.

4) Fuel costs. The power generation fuel characteristics of the power system can be expressed by the quadratic function (Long et al., 2018), and the system fuel cost is

$$\min F = \sum_{i=1}^{N_G} F_i(P_i). \tag{7}$$

In the formula, N_G indicates the number of generator sets in the system; P_i indicates the active output value of the generator; and $F_i(P_i)$ represents the energy consumption characteristics. Considering that the normal valve point effect will appear when the generator set is affected by other factors (Martinez Caama et al., 2017), the energy consumption characteristics of the generator are expressed as

$$F_i(P_i) = a_i + b_i P_i + c_i P_i^2 + \left| e_i \sin\left(f_i (P_{i\min} - P_i) \right) \right|.$$

In the formula, a_i, b_i, and c_i all represent the rated cost coefficient of the power system generator; e_i, f_i indicates the valve point effect parameter; and$P_{i\min}$ indicates the output limit of generator active power.

5) Comprehensive emission of pollution (Souza et al., 2018a). The emission calculation formula is

$$E = \sum_{i=1}^{N_G} \left[10^{-2} \left(\alpha_i + \beta_i P_i + \gamma_i P_i^2 \right) + \zeta_i \exp(\lambda_i P_i) \right]. \tag{8}$$

In the formula, α_i, β_i, γ_i, ζ_i, and λ_i all represent the pollution emission coefficient generated by power generation; E represents total emissions.

CONSTRAINT FUNCTION

The objective function and constraint conditions belong to a complementary variable relationship. In the whole power generation dispatching system, the objective function is not only the reference of the dispatching model but also the independent variable, and the constraint conditions are appropriate linear programming based on the objective function, which is also the dependent variable. The constraint model of the power system is given as follows.

Internal power balance constraints (Souza et al., 2018b) refer to the balance between power supply and load in the power system. The generation capacity of the power system is determined according to the predicted power system load, which is a part of power planning. Restricting it can help the power system to achieve smooth operation:

$$\sum_{i=1}^{N_t} P_{gi,t} + \sum_{j=1}^{N_h} P_{hj,t} = P_{D,t} + P_{L,t}. \tag{9}$$

In the formula, N_h indicates the number of generator sets in the power system; $P_{hj,t}$ represents the generation output constraint value of the t generator set in the time period; $P_{D,t}$ indicates the system load; and $P_{L,t}$ indicates the system network loss.

Output (Abdin et al., 2022) constraint of the fuel generator set. As an important part of the power system, the fuel generator set can help achieve accurate dispatching in the next step by adopting the targeted constraint strategies:

TABLE 1 | Load required in 24 h.

Period	1	2	3	4	5	6
Load/MW	1288	1623	1300	1389	1520	1679
Period	7	8	9	10	11	12
Load/MW	789	1450	1300	925	1600	1450
Period	13	14	15	16	17	18
Load/MW	1620	1300	1450	1360	1700	985
Period	19	20	21	22	23	24
Load/MW	1350	1254	1311	1786	1426	1654

$$P_{gi}^{\min} \le P_{gi,t} \le P_{gi}^{\max}. \tag{10}$$

In the formula, $P_{gi}^{\max}$ indicates the upper limit of the output of the fuel generator set.

Output constraint of the kerosene generator set:

$$P_{hj}^{\min} \le P_{hj,t} \le P_{hj}^{\max}. \tag{11}$$

In the formula, $P_{hj}^{\max}$ indicates the upper limit of the active output of the kerosene generator set and $P_{hj}^{\min}$ indicates the lower limit of the active output of kerosene generator set.

Generation capacity limitations. Including normal operation capacity, emergency reserve capacity, and maintenance reserve capacity and taking the maximum capacity that the power system can bear as the objective, the constraint function is established:

$$V_j^{\min} \le V_{j,t} \le V_j^{\max}. \tag{12}$$

In the formula, $V_{j,t}$ represents the rated generating capacity of the j generator set in the time period (Silva et al., 2021); $V_j^{\max}$ represents the maximum generating capacity; and $V_j^{\min}$ represents the minimum generating capacity.

The power generation flow is about (Ebramsyah et al., 2017) bundles. Generation flow is an important index to evaluate the superiority of power dispatching, and the constraint function is established according to the national flow standard:

$$Q_j^{\min} \le Q_{j,t} \le Q_j^{\max}. \tag{13}$$

In the formula, $Q_{j,t}$ represents the generation flow value of the j generator set in the time period; $Q_j^{\max}$ represents the maximum value of power generation flow; and $Q_j^{\min}$ represents the minimum value of power generation flow.

Generation Load Balancing Constraints

Table 1 shows the load required for power generation load balance, and the average value used as the load reference standard.

$$V_{j,t} = V_{j,t-1} + I_{j,t} - Q_{j,t} - S_{j,t} + \sum_{k=1}^{N} \left(Q_{h,t-\tau_{ij}} + S_{h,t-\tau_{ij}} \right). \tag{14}$$

In the formula, $I_{j,t}$ indicates the system charge and inflow power of the j generator set in the time period; $S_{j,t}$ represents the system charge and outflow of the j generator set in the time period; N_u indicates the inflow time; and τ_{ij} indicates the outflow time.

Generation constraints at the beginning and end of the power system. The power period is segmented to restrict the power generation at the beginning and end of the period:

$$\begin{cases} V_{j,0} = V_{j,bepin} \\ V_{j,T} = V_{j,ead} \end{cases}. \tag{15}$$

In the formula, $V_{j,bepin}$ indicates the initial electric capacity and $V_{j,ead}$ indicates the final capacitance.

The reactive power constraint of the generator set. It means that in an AC circuit with reactance, the electric field or magnetic field absorbs energy from the power supply in one part of a cycle and releases energy in the other part of the cycle. The average power in the whole cycle is zero. It is related to the problem of repeated energy exchange between the power system and power supply:

$$\begin{cases} P_{gi,t} - P_{gi,t-1} \le R_{U,i} \\ P_{gi,t-1} - P_{gi,t} \le R_{D,i} \end{cases}. \tag{16}$$

In the formula, $R_{U,i}$ represents the upper limit value of reactive power output of the generator set and $R_{D,i}$ indicates the lower limit of reactive power output of the generator set.

Climbing Event Constraints on Power Load

Due to the influence of external factors or human factors, the power system is prone to power load climbing events. Power load climbing (Meyendorf et al., 2017) refers to the phenomenon of large-scale increase or decrease of system power in a short time, which is easy to cause an imbalance of system active power, destroy the frequency stability, and even cause large-scale die-cutting load, which seriously threatens the safety and stability of power grid and economic operation. In this article, this kind of event is regarded as an accidental event for optimal generation scheduling for scheduling regulation, and the changes of power system voltage, fluctuation rate (Dong et al., 2020), and other parameters during power load climbing are solved. The prediction algorithm is used to predict the linear change of power in the next step, and reasonable scheduling is carried out according to the change value.

There is T_{s1} increasing trend at the second time point, so the load shedding strategy is adopted. When the downhill climbing event occurs in the power system, it will disrupt the original power generation plan and lead to insufficient reserve capacity, which will affect the effective implementation of the system dispatching plan. Therefore, by increasing the power load climbing power constraint, the standby capacity of the conventional units in the power system is always higher than the maximum amplitude of power fluctuation, and the climbing rate is always lower than the maximum rate of power fluctuation by using the same principle. In this way, the power value and climbing value are in a stable suppression state for a long time:

$$\sum_{i=i}^{N} U_{i,t} \ge \Delta P_d + \Delta P_{Lu}. \tag{17}$$

$$\sum_{i=i}^{N} D_{i,t} \ge \Delta P_u + \Delta P_{Ld}. \tag{18}$$

$$\sum_{i=i}^{N} U'_{i,t} \ge \Delta P_d + \Delta P_{Lu}. \tag{19}$$

$$U'_{i,t} = r_{i,u} \times t. \tag{20}$$

In the formula, ΔP_{Ld} represents the rise of the power system per unit step during the whole climbing process; ΔP_{Lu} indicates the amount of decline; ΔP_d represents the maximum rise amplitude per unit step; and ΔP_u indicates the maximum drop amplitude.

Climbing Event Constraint Under Power Load

The downward climbing and upward climbing performance of the power load are basically the same, both in a phased downward (Calzarossa et al., 2019) trend, and there is a downward trend at the second time point. The maximum climbing amplitude is set in the unit of rated step size of the power system (Prada, 2017) as ΔP. The starting time of power load climbing is T_{end} and end time is T_s. According to the abovementioned **Formula 18**, it is determined whether the rated power generation value meets the minimum demand when the system ascends. If so, the abovementioned process is used to restrict; if not, specific constraints shall be imposed according to the following conditions:

1) When the system goes downhill, a reasonable load shedding method shall be adopted before starting time T_s to shorten the power climbing time and increase the power correction time of the system.
2) When the system goes downhill, after the starting time T_s, according to the dispatching strategy proposed (Tian et al., 2016) previously, the output value of other units in the system can be increased by properly adjusting the output value so as to achieve operation balance and improve the overall adaptability of the system.

GENERATION SCHEDULING MODEL OF POWER SYSTEM

Based on the peak valley TOU price on the demand side, the energy-saving power generation dispatching on the generation side (Chao et al., 2016) is globally optimized. Through the analysis of the time price response of the user end, it can be seen that the market means will change the original system load distribution pattern. Through peak load regulation (Faghihi et al., 2016) and valley filling, the system load fluctuation level is reduced, the unit peak load regulation pressure is reduced, the utilization rate of the high-energy units is improved, and the coal consumption of the corresponding units is reduced. In view of this, an energy-saving generation scheduling optimization model based on the global (Kelley et al., 2018) energy consumption optimization is constructed with the adjustment range of peak valley TOU price on the demand side, unit output on the generation side, and unit startup and shutdown status as the central policy variables. **Figure 1** 1) shows the daily power consumption and operation cost scheduling analysis of the power system.

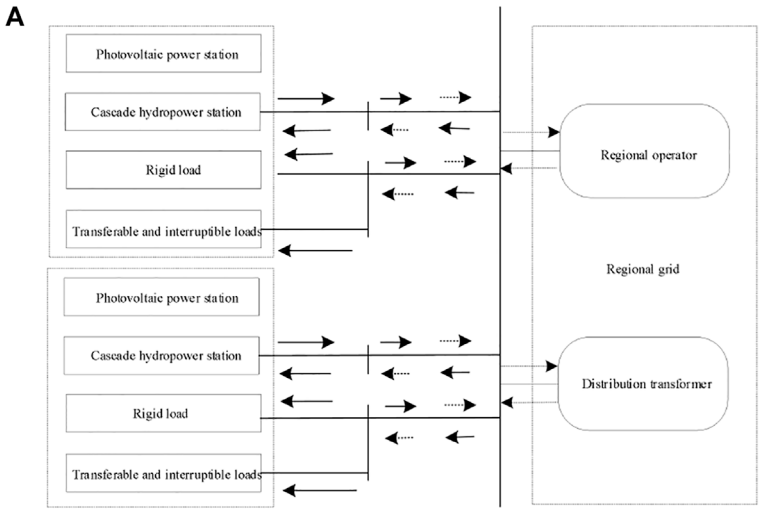

Schematic diagram of power system power generation cycle operation

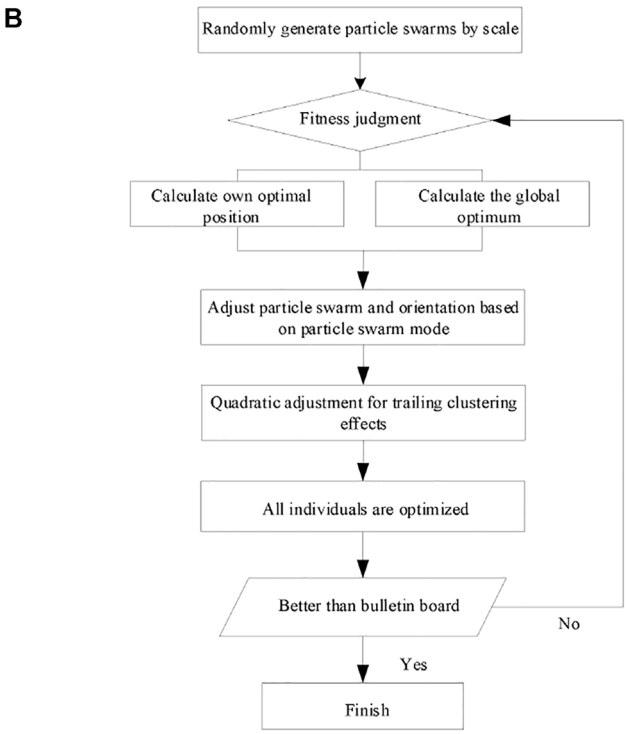

Schematic diagram of power system joint optimization generation dispatching process

FIGURE 1 | Schematic diagram of power system operation and dispatch. **(A)** Schematic diagram of power system power generation cycle operation. **(B)** Schematic diagram of power system joint optimization generation dispatching process.

The power system joint optimization energy-saving generation scheduling model is constructed as follows:

$$\min z_1 = \sum_{t=1}^{r}\sum_{j=1}^{J}\left[u_j f_j\left(g_{ji}\right) + u_{jt}\left(1-u_{j,t-1}\right)SC_{jt} + u_{j,t-1}\left(1-u_{jt}\right)SD_{jt}\right]. \quad (21)$$

$$s.t.\sum_{j=1}^{J} u_{jt} g_{jt}\left(1-\theta_j\right) = G_i^{(0)}. \quad (22)$$

$$\sum_{j=1}^{J} g_j^{\max}\left(1-\theta_j\right) \geq G_t^{(0)} + R_t^{(0)}. \quad (23)$$

$$f_j\left(g_{jt}\right) = a_j g_{jt}^2 + b_j g_{jt}. \tag{24}$$

$$u_{jt} g_j^{\min} \le g_{jt} \le u_{jt} g_j^{\max}. \tag{25}$$

$$\Delta g_j^- \le g_{jt} - g_{j,t-1} \le \Delta g_j^+. \tag{26}$$

$$\left(T_{j,t-1}^{on} - MT_j^{on}\right)\left(u_{j,t-1} - u_{jt}\right) \ge 0. \tag{27}$$

$$\left(T_{j,t-1}^{off} - MT_j^{off}\right)\left(u_{jt} - u_{j,t-1}\right) \ge 0. \tag{28}$$

In the formula, u_{jt} indicates the state variable value of the generator t set at the second time t. The initial startup state is set as 1 and the initial shutdown state as 0; g_{jt} represents the maximum output value of the generator set at the second time t; $f_j(g_{jt})$ represents the total coal consumption of the unit at time (Wang et al., 2016) t; a_j and b_j represents the corresponding start-up parameters; SC_{jt} indicates the shutdown parameters; and SD_{jt} represents coal consumption. **Formula 20** makes the system t generation power value reach the target balance. At this time, it is expressed as the average power consumption rate of the second generator set (Calzarossa et al., 2018); θ_j**Formula 21** is used to dispatch the standby power of the system, $g_j^{\max}$ represents the maximum power output t of the generator set; Δg_j^- represents the power requirements required for system power generation at the second t time before dispatching; Δg_j^+**Formula 22** is used to dispatch the power output of the system t, indicating the minimum output of the generator set; $T_{j,t-1}^{on}$**Formula 23** the unit carries out climbing scheduling for the system, indicating the maximum rising and falling power limits of the generator unit; MT_j^{on} **Eqs 24**, **25** carry out the shortest start-up scheduling for the system, indicating that the operation t $t-1$ time of the generator unit at the time and the shortest operation time that can be borne; $T_{j,t-1}^{off}$ **Eqs 26–28** schedule the minimum shutdown time $t-1$ of the system, MT_j^{off} which represents the shutdown time $t-1$ of the generator unit at time, and u_{jt} the minimum shutdown time that the unit can bear.

In order to further ensure the scheduling quality, a secondary constraint of the decision variable (Kadota et al., 2018) on the scheduling model (Bhattacharya et al., 2019) g_{it} is established, and the expression formula is

$$\Delta z = z_1 - z_2. \tag{29}$$

$$\beta_{coal}^{(0)} = z_1 \Big/ \sum_{i=1}^{I}\sum_{k=1}^{K}\sum_{t=1}^{T} D_{ikt}^{(0)}. \tag{30}$$

SIMULATION EXPERIMENT

In order to verify the effectiveness of the proposed scheduling model and method, two different power system generation environments are set, summer and winter, respectively. The power system consists of one with four hydropower stations and three thermal power generating units. The typical test system is used for calculation and analysis. The total installed capacity of the system is 297.5 mw. The average power consumption rate of the power generation side of the hydropower station and thermal power plant is 80%. The maximum power load is 300 MW, and the minimum power load is 150 MW. The population size of the two algorithms is 40, and the maximum number of iterations is 1,000.

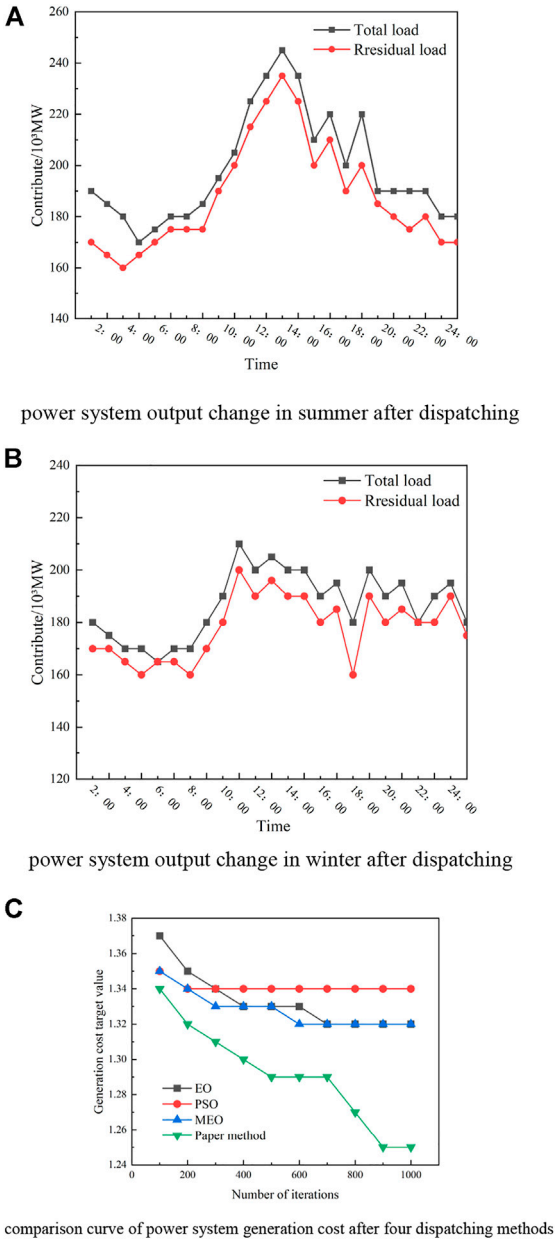

FIGURE 2 | Post-dispatch changes in the power system. **(A)** Power system output change in summer after dispatching. **(B)** Power system output change in winter after dispatching. **(C)** Comparison curve of power system generation cost after the four dispatching methods.

It can be seen from **Figures 2A,B**, the generation scheduling model proposed in this article can make full use of the internal adjustability of power system generator units, effectively reduce the peak valley difference of load, and make the residual load more stable. After power generation dispatching, the mean square deviation of the load is greatly reduced, and the peak valley difference is significantly reduced. In summer, the original power generation load variance is 256.813/mw. After effective dispatching, the residual power generation load variance is reduced to 197.265/mw, and the power generation load drop difference is 26.31%.

TABLE 2 | Target value of power system generation cost obtained by the four methods.

Algorithm	Average value	Minimum	Maximum value	Standard deviation
EO	130000	129959	130500	82
PSO	137000	139059	132500	154
MEO	125000	122459	131540	45
Paper method	129920	129908	130059	15

From **Figure 2**, the power generation cost of this method is the lowest among them, and the computational robustness is better than that of the particle swarm optimization algorithm. When the number of scheduling iterations is 600, the cost target value in this study is about 1.290, while the target values of the other three methods are 1.332, 1.338, and 1.348, respectively, which are higher than those in this study. The overall cost value of the EO method shows a flat trend, indicating that the cost has not been improved after iteration. Among all methods, the declining trend of this method is the most obvious. After power generation dispatching, the cost improvement phenomenon is the best.

The dispatching results of the four comparison algorithms on the target value of power generation cost of the power system are shown in **Table 2**.

Through the comparison of the maximum values in **Table 2**, it can be seen that this study is 130,059, and the other three methods are 130,500, 132,500, and 131,540. This study is the lowest among them, and the scheduling performance is the best. Compared with the lowest value, this study is 129,908, and the other three methods are 129,959, 139,059, and 122,459. This study is still the lowest value. Through comprehensive comparison, this study performs the best.

CONCLUSION

In this article, a power system joint optimal generation scheduling method based on the improved balance optimizer is proposed, and the following conclusions are drawn:

1) Through the establishment of conditional constraint function including the concept of objective, the effective constraint on the power load climbing event is realized, which greatly reduces the subsequent calculation error caused by misjudgment and improves the quality of dispatching.
2) Based on the current comprehensive power saving policy and the premise of safety core, this study also establishes the power system joint optimization generation scheduling model, which fundamentally solves the problems of high power generation cost and high power generation energy consumption.
3) After adopting this method, the cost is reduced from the initial USD 131225/h to USD 129920/h, and the power load is also reduced from 254.78/mw to 205.36/mw. This method has high practical value.

DATA AVAILABILITY STATEMENT

The original contributions presented in the study are included in the article/Supplementary Material. Further inquiries can be directed to the corresponding author.

AUTHOR CONTRIBUTIONS

JX and YT conceived and designed the calculations and experiments; YQ and AL performed the simulation; GX contributed analysis tools; JX and YT wrote the manuscript.

REFERENCES

Abdin, A. F., Caunhye, A., Zio, E., and Cardin, M.-A. (2022). Optimizing Generation Expansion Planning with Operational Uncertainty: A Multistage Adaptive Robust Approach. *Appl. Energy* 306, 118032. doi:10.1016/j.apenergy.2021.118032

Bhattacharya, B., Chakraborty, N., and Mandal, K. K. (2019). A Cost-optimized Power Management Strategy for Combined Wind Thermal–Pumped Hydro Generation Considering Wind Power Uncertainty[J]. *Int. Trans. Electr. Energy Syst.* 29 (7). e12104. doi:10.1002/2050-7038.12104

Calzarossa, M. C., Vedova, M. D., and Tessera, D. (2018). A Methodological Framework for Cloud Resource Provisioning and Scheduling of Data Parallel Applications under Uncertainty[J]. *Future Gener. Comput. Syst.* 93. 212–223. doi:10.1016/j.future.2018.10.037

Calzarossa, M. C., Della Vedova, M. L., and Tessera, D. (2019). A Methodological Framework for Cloud Resource Provisioning and Scheduling of Data Parallel Applications under Uncertainty. *Future gener. Comput. Syst.* 93 (APR), 212–223. doi:10.1016/j.future.2018.10.037

Chao, Z., Li, H., Tian, M., and Zhou, J. (2016). "Analysis on the Influence of Rotational Inertia Level of Sending System on Transmission Capability[C]," in 2015 5th International Conference on Electric Utility Deregulation and Restructuring and Power Technologies (DRPT) (IEEE).

Dong, H., Li, S., Dong, H., Tian, Z., and Hillmansen, S. (2020). Coordinated Scheduling Strategy for Distributed Generation Considering Uncertainties in Smart Grids[J]. *IEEE Access* 8, 86171–86179. doi:10.1109/ACCESS.2020.2992342

Ebramsyah, A., Joy, A., Miller, C., Stevens, J., and Patil, P. (2017). *Optimizing Student Workforce Scheduling at PSU Office of Information Technology (OIT).*

Faghihi, V., Reinschmidt, K. F., and Kang, J. H. (2016). Objective-driven and Pareto Front Analysis: Optimizing Time, Cost, and Job-Site Movements. *Automation Constr.* 69, 79–88. doi:10.1016/j.autcon.2016.06.003

Hu, J., Chen, H., Heidari, A. A., Wang, M., and Pan, Z. (2020). Orthogonal Learning Covariance Matrix for Defect of Grey Wolf Optimizer: Insights, Balance, Diversity, and Feature Selection. *Knowledge-Based Syst.* 213. doi:10.1016/j.knosys.2020.106684

Kadota, I., Sinha, A., and Modiano, E. H. (2018). "Optimizing Age of Information in Wireless Networks with Throughput Constraints," in IEEE INFOCOM 2018 - IEEE Conference on Computer Communications.

Kelley, M. T., Pattison, R. C., Baldick, R., and Baldea, M. (2018). An MILP Framework for Optimizing Demand Response Operation of Air Separation Units[J]. *Inst. Electron. Inf. Commun. Eng.* 222, 951–966. doi:10.1016/j.apenergy.2017.12.127

Le, S., Wu, Y., Guo, Y., and Vecchio, C. D. (2021). Game Theoretic Approach for a Service Function Chain Routing in NFV with Coupled Constraints[J]. *Circuits Syst. II Express Briefs, IEEE Trans.* 99, 1.

Li, H., Deng, J., Feng, P., Pu, C., Arachchige, D. D. K., and Cheng, Q. (2021a). Short-Term Nacelle Orientation Forecasting Using Bilinear Transformation and ICEEMDAN Framework. *Front. Energy Res.* 9, 780928. doi:10.3389/fenrg.2021.780928

Li, H., Deng, J., Yuan, S., Feng, P., and Arachchige, D. D. K. (2021b). Monitoring and Identifying Wind Turbine Generator Bearing Faults Using Deep Belief Network and EWMA Control Charts. *Front. Energy Res.* 9, 799039. doi:10.3389/fenrg.2021.799039

Li, Y. Z., Zheng, X. W., and Lu, D. J. (2016). "Virtual Network Embedding Based on Multi-Objective Group Search Optimizer," in International Conference on Broadband & Wireless Computing.

Long, W., Jiao, J., Liang, X., and Tang, M. (2018). An Exploration-Enhanced Grey Wolf Optimizer to Solve High-Dimensional Numerical Optimization. *Eng. Appl. Artif. Intell.* 68, 63–80. doi:10.1016/j.engappai.2017.10.024

Martinez Caama, O. J. M., Selva, M., Clauss, P., et al. (2017). Full Runtime Polyhedral Optimizing Loop Transformations with the Generation, Instantiation, and Scheduling of code-Bones[J]. *Concurrency Comput. Pract. Exp.* 29 (15), e4192. doi:10.1002/cpe.4192

Meyendorf, N. G., Nithin, A. H., and Omenzetter, P. (2017). *Scheduling Structural Health Monitoring Activities for Optimizing Life-Cycle Costs and Reliability of Wind Turbinesat*.

Prada, J. F . (2017). *Ensuring the Reliable Operation of the Power Grid: State-Based and Distributed Approaches to Scheduling Energy and Contingency Reserves*. United States: Carnegie Mellon University.

Shan, W., Qiao, Z., Heidari, A. A., Chen, H., and Teng, Y. (2020). Double Adaptive Weights for Stabilization of Moth Flame Optimizer: Balance Analysis, Engineering Cases, and Medical Diagnosis. *Knowledge-Based Syst.* 214. doi:10.1016/j.knosys.2020.106728

Silva, F., Torresknoop, A., Coopmans, T., Maier, D., and Wehner, S. (2021). Optimizing Entanglement Generation and Distribution Using Genetic Algorithms. *Quantum Sci. Technol.* 035007, 26. doi:10.1088/2058-9565/abfc93

Souza, G., Deus, D., Tadaiesky, V., et al. (2018a). Optimizing Tasks Generation for Children in the Early Stages of Literacy Teaching: a Study Using Bio-Inspired Metaheuristics. *Soft Comput. A fusion Found. Methodol. Appl.* 22, 6811–6824. doi:10.1007/s00500-018-3409-1

Souza, G., Deus, D., Tadaiesky, V., et al. (2018b). Optimizing Tasks Generation for Children in the Early Stages of Literacy Teaching: a Study Using Bio-Inspired Metaheuristics[J]. *Soft Comput.* 22 (3). 6811–6824. doi:10.1007/s00500-018-3409-1

Tian, X. Q., Xu, T., Wang, X. L., et al. (2016). "The Synergic Scheduling Optimization and Effectiveness Evaluation Model for Multi-Types Generation Resources Considering Emission Constraints," in International Conference on Material Engineering & Application.

Toyoda, M., and Wu, Y. (2019). Mayer-type Optimal Control of Probabilistic Boolean Control Network with Uncertain Selection Probabilities. *IEEE Trans. Cybern.* 51, 3079–3092. doi:10.1109/TCYB.2019.2954849

Wang, Y.-R., Huang, K.-C., and Wang, F.-J. (2016). Scheduling Online Mixed-Parallel Workflows of Rigid Tasks in Heterogeneous Multi-Cluster Environments. *Future Gener. Comput. Syst.* 60 (jul), 35–47. doi:10.1016/j.future.2016.01.013

Wu, Y., Guo, Y., and Toyoda, M. (2020). Policy Iteration Approach to the Infinite Horizon Average Optimal Control of Probabilistic Boolean Networks[J]. *IEEE Trans. Neural Netw. Learn. Syst.* 32, 2910–2924. doi:10.1109/TNNLS.2020.3008960

Yan, J., Ruan, S., Cai, Q., et al. (2016). "A Novel Bi-objective Model with Particle Swarm Optimizer for Structural Balance Analytics in Social Networks," in 2016 IEEE Congress on Evolutionary Computation (CEC), Vancouver, BC, Canada, 24-29 July 2016. doi:10.1109/cec.2016.7743864

Zhang, Y., Qian, T., and Tang, W. (2022). Buildings-to-distribution-network Integration Considering Power Transformer Loading Capability and Distribution Network Reconfiguration[J]. *Energy* 244. doi:10.1016/j.energy.2022.123104

Conflict of Interest: The authors declare that the research was conducted in the absence of any commercial or financial relationships that could be construed as a potential conflict of interest.

Publisher's Note: All claims expressed in this article are solely those of the authors and do not necessarily represent those of their affiliated organizations, or those of the publisher, the editors, and the reviewers. Any product that may be evaluated in this article, or claim that may be made by its manufacturer, is not guaranteed or endorsed by the publisher.

frontiers | Frontiers in Energy Research

TYPE Brief Research Report
PUBLISHED 17 August 2022
DOI 10.3389/fenrg.2022.972437

OPEN ACCESS

EDITED BY
Tinghui Ouyang,
National Institute of Advanced Industrial Science and Technology (AIST), Japan

REVIEWED BY
Sandeep Kumar Duran,
Lovely Professional University, India
Tao Wang,
Chang'an University, China

*CORRESPONDENCE
Dakuan Yu,
ydk202206@163.com
Xueguang Qiao,
xgqiao@nwu.edu.cn
Xiangyu Wang,
wxy@xsyu.edu.cn

SPECIALTY SECTION
This article was submitted to Smart Grids, a section of the journal Frontiers in Energy Research

RECEIVED 18 June 2022
ACCEPTED 22 July 2022
PUBLISHED 17 August 2022

CITATION
Yu D, Qiao X and Wang X (2022), Light intensity optimization of optical fiber stress sensor based on SSA-LSTM model.
Front. Energy Res. 10:972437.
doi: 10.3389/fenrg.2022.972437

Light intensity optimization of optical fiber stress sensor based on SSA-LSTM model

Dakuan Yu[1]*, Xueguang Qiao[2]* and Xiangyu Wang[1]*

[1]School of Physical Science and Technology, Northwestern Polytechnical University, Xi'an, China, [2]School of Physics, Northwest University, Xi'an, China

In order to further improve the measurement range and accuracy of optical fiber stress sensor based on the interference between rising vortex beam and plane wave beam, a new stress demodulation model is designed. This model proposes a method to optimize the long-term and short-term memory network (LSTM) model by using sparrow search algorithm (SSA), extract the main characteristics of the influence of various variables on optical fiber stress sensor, and fit the relationship between sensor stress and beam phase difference. This method is an attempt of the deep learning model LSTM in the study of stress mediation model. There are very few related studies, and it is very necessary to fill this gap. In the experiment, the SSA-LSTM neural network is trained by using the data of stress and phase difference measured by the optical fiber stress sensor. The test results show that the mean error of SSA-LSTM neural network is less than that of LSTM neural network, which shows that the combination of SSA-LSTM model and optical fiber stress sensor can make its measurement accuracy higher, The algorithm can more effectively reduce the influence of the surrounding environment and the influence of the light source fluctuation on the measurement range and accuracy of the optical fiber sensor, and has good practical application value. It is proved that the deep learning LSTM neural network has good application value in the light intensity optimization of optical fiber stress sensor.

KEYWORDS

sparrow search algorithm, long and short term memory network, optical fiber stress sensor, light intensity optimization, SSA-LSTM

Introduction

Force sensor is one of the most important components in the robot control system, especially at the robot joint. When installed on the robot's foot and wrist, it can realize the functions of robot center of gravity tendency perception and balance state monitoring, and plays an irreplaceable role in the force analysis and stability of the robot. Traditional mechanical sensors mainly include resistive sensors, capacitive sensors, *etc.* (Zhou et al., 2014; Yue et al., 2022), which have the characteristics of high precision and high sensitivity, and are widely used in various mechanical sensing fields. However, traditional resistive sensors and capacitive sensors are vulnerable to

electromagnetic interference, corrosion, high temperature and high voltage, and can not be used normally in harsh environment (Zm et al., 2020).

Optical fiber sensor has the advantages of light weight, small volume, high sensitivity and easy reuse to form distributed measurement. It is widely used to measure physical quantities such as stress and strain in engineering projects such as bridge construction, pipeline leakage and deepwater riser (Zhao et al., 2021). Researchers have proposed various types of optical fiber stress sensors (Asriani et al., 2020; Cai et al., 2020; Guo et al., 2020; Tan et al., 2020; Zheng et al., 2020; Tang et al., 2021; Xiang, 2021), which are based on single-mode multi-mode single-mode tapered fiber Bragg grating sensors. The measurement range of the sensor is 0–960 με; A Fabry Perot based strain sensor (He et al., 2020). The cavity is formed by splicing a new advanced silicon tube between two standard single-mode fibers. The maximum strain range measured by the sensor is 2500 με。 However, these sensors usually use ordinary Gaussian light source, and due to the limitation of the structure itself, they can not measure large strain, or the measurement results have errors.

In recent years, with the continuous development of vortex rotation, some scholars have proposed an optical fiber sensor based on vortex rotation. According to the spiral and fork characteristics of the interference pattern between vortex and Gaussian light, researchers have proposed several different types of interference optical fiber sensors. A new strain sensing method based on the interference of vortex light and Gaussian spherical wave (Ning et al., 2020). The rotation angle of spiral image caused by strain is recognized by digital image processing technology. In theory, high-resolution strain measurement can be realized, but no experimental research has been carried out. An optical fiber stress sensor based on the interference between vortex beam and plane wave beam extracts two main features of interference pattern set by principal component analysis (PCA) (Lv et al., 2018), and realizes the demodulation process according to the variation law of interference pattern correlation coefficient group corresponding to different phase difference, but the demodulation process is complex and the stress measurement range is small.

In this paper, the optical power output of optical fiber stress sensor depends on many environmental factors, such as ambient light change, vibration noise and light source fluctuation. The measurement of optical fiber stress sensor depends on the stress phase difference relationship of light and the change value of power. The output optical power value will be affected by the fluctuation of light source and the coupling between light source and optical fiber, resulting in measurement error. In view of the nonlinear impact of the above problems, the hardware and software can be optimized, and the hardware can be replaced with a new structure. Although the above problems can be solved to a certain extent, it will lead to the increase of cost and circuit complexity, and the electronic devices themselves will also produce new interference, which will affect the range and accuracy of the whole optical fiber stress sensor measurement system.

Therefore, it is necessary to introduce the algorithm to optimize the experimental data in order to improve the measurement accuracy of the optical fiber stress sensor system. Based on the short-term and long-term memory network method optimized by sparrow search algorithm, SSA-LSTM neural network is proposed to improve the measurement accuracy. Because the LSTM network is a nonlinear optimization, the weights and thresholds are generated randomly, which will cause the structure to be accidental and locally optimal (Jiang et al., 2021). The search of SSA (sparrow search algorithm) algorithm is based on the optimal location and the historical optimal location of all discoverers in the population, which can quickly achieve the goal of global optimization. This feature can be used to optimize the weight and threshold of LSTM neural network and avoid falling into the situation of partial optimization in solvable space (Yao et al., 2022). This paper introduces the composition of optical fiber stress sensor measurement system, the principle and method of experiment and the principle of sparrow search algorithm optimizing LSTM neural network, and compares the experimental data after light intensity optimization of SSA-LSTM neural network with the experimental data of LSTM neural network without optimized weight threshold, which provides a certain reference value for improving the measurement range and precision optimization of optical fiber stress sensor.

Methodology

Fiber optic stress sensing system structure

The design of stress sensing system based on the interference between vortex beam and plane wave beam is shown in Figure 1. The light source is a 632.8 nm He Ne laser. After passing through a 1:1 beam splitter, the collimated laser is divided into a reference light path and a sensing light path: the reference light path is coupled into a 3 m long single-mode fiber through a lens with a focal length of 240 mm, emitted through a fiber collimator (74UV-FC), and then the first-order vortex light is obtained through a polarizer, a quarter wave plate and a vortex wave plate (VR1-633); The sensing optical path is coupled into a 3 m long single-mode optical fiber through a lens with a focal length of 240 mm. The single-mode optical fiber is fixed on the tensile test bench. After being emitted by the optical fiber collimator (74UV-FC), the plane wave beam is obtained through the polarizer. Finally, the reference light interferes with the sensing light beam

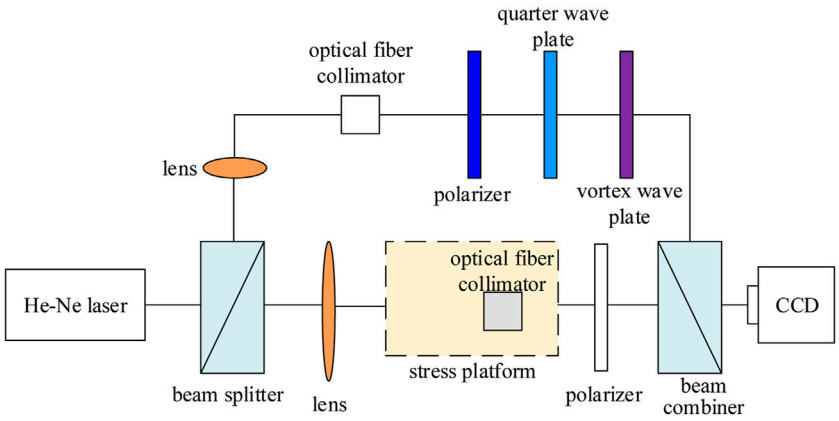

FIGURE 1
Fiber optic stress sensing system structure.

mirror, and the charge coupled element (CCD) collects the interference pattern.

Principle of light interference in sensing system

Vortex light is a special light field with helical phase wavefront. The phase distribution contains $\exp(il\theta)$ term, θ is the rotation azimuth and l is the topological charge. When the vortex light propagates along the positive direction of the Z axis, the complex amplitude E_1 of the electric field on the observation surface (Ying et al., 2021) with $Z = 0$ can be expressed as:

$$E_1(X,Y) = E_0 \exp(il\theta + i\varphi) \tag{1}$$

Where E_0 is the beam amplitude and φ is the additional phase difference.

When the plane wave with inclined wavefront propagates along the Z axis direction, the complex amplitude E_2 of the electric field on the observation surface with $Z = 0$ can be expressed as:

$$E_2(X,Y) = E_0 \exp(ikX \sin\alpha) \tag{2}$$

Where X is the component of rectangular coordinate system, k is the wave number, and α is the included angle between k and the positive direction of Z axis.

If two beams of light interfere on the plane of $Z = 0$, according to $E = E_1 + E_2$, the expression of electric field E after interference is:

$$E = E_0 \exp(il\theta + i\varphi) + E_0 \exp(ikX \sin\alpha) \tag{3}$$

According to $I = EE^*$, the light intensity distribution I after interference is:

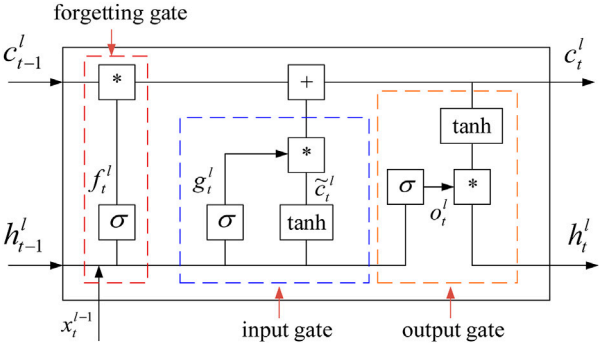

FIGURE 2
Cell structure of LSTM.

$$I = 2 + 2\cos(l\theta + \varphi - kX \sin\alpha) \tag{4}$$

System optimization by SSA-LSTM

The SSA-LSTM model is used to extract the main characteristics of the interference wave, and the relationship between the phase difference between the two beams and the correlation coefficient of the corresponding main characteristics of the interference is fitted. According to the stress phase difference relationship, the relationship between the stress and the correlation coefficient is obtained.

LSTM neural network

LSTM makes information selectively affect the state of each time in the model by adding gate structure (Vpn et al., 2021;

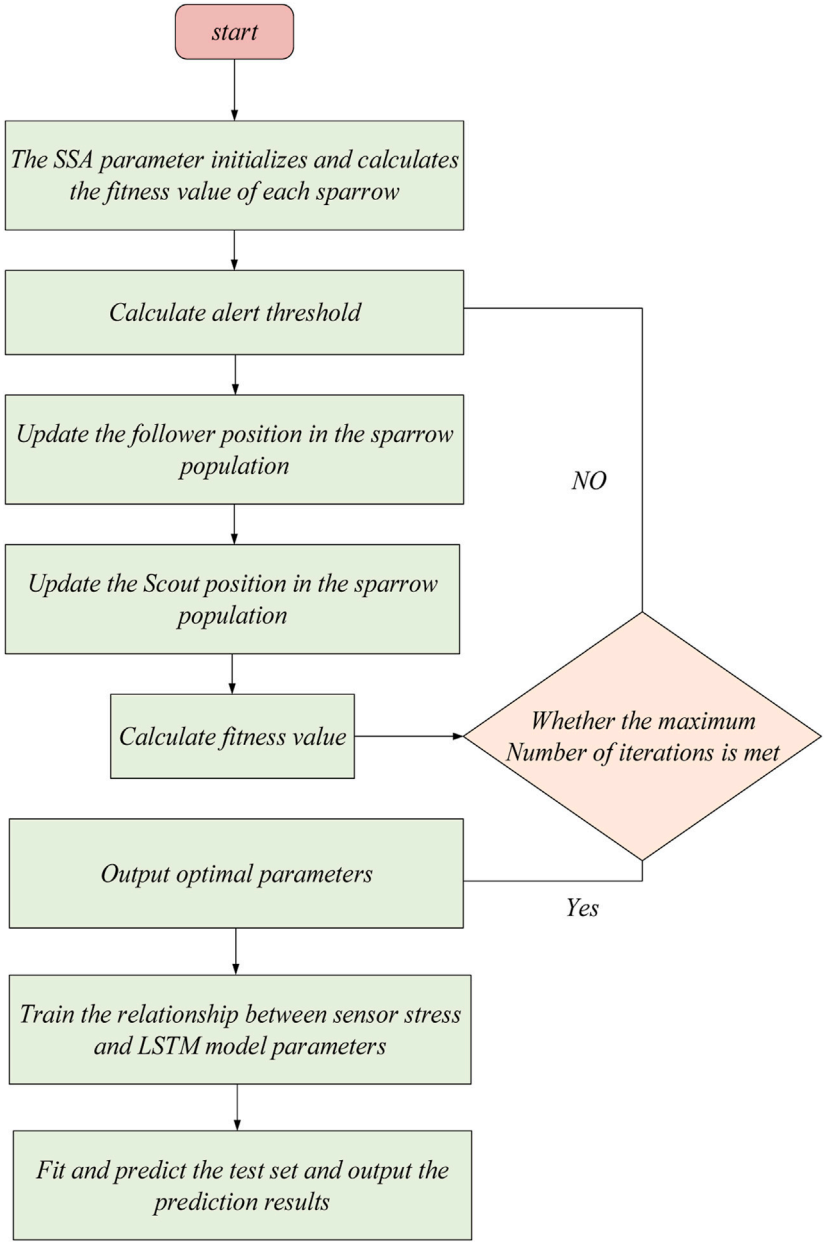

FIGURE 3
Flow chart of LSTM optimized based on SSA.

Delgado et al., 2020), which is mainly composed of input gate, output gate and forgetting gate. The specific formula is shown in (5–10), and the specific structure of LSTM unit is shown in Figure 2.

If the input is $[x_1, x_2, ..., x_t]$ and the state of the hidden layer is $[h_1, h_2, ..., h_t]$, the following operations are performed at time t:

(1) Forgetting gate operation: determine whether to forget the hidden cell state h_t^{l-1} transmitted by the upper layer with a certain probability in LSTM, and control the output range between [0,1] through sigmoid function. *See* formula (5) for details.

$$f_t^l = \sigma\left(w_f^l \cdot \left[h_{t-1}^l, x_t^{l-1}\right] + b_f^l\right) \tag{5}$$

In Eq. 5, $\sigma()$ is the activation function, $\bullet$ is the vector inner product, t is the time, l is the number of layers of LSTM neural network, f is the forgetting gate, w is the weight, b is the bias, and h is the cell output.

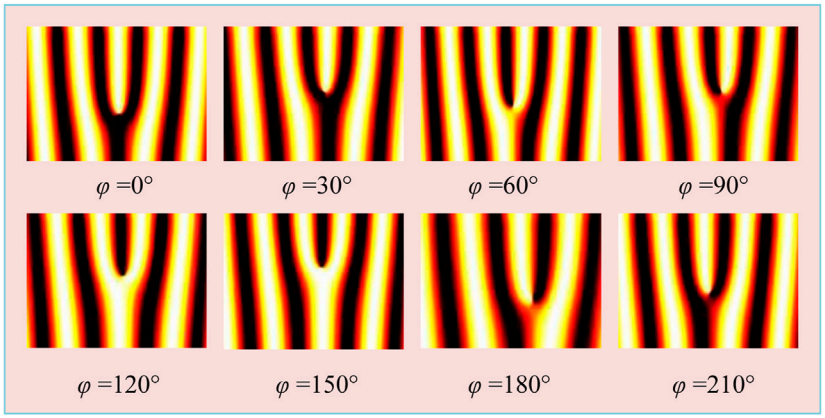

FIGURE 4
Interference patterns corresponding to different phase differences.

(2) Input gate operation: the input gate consists of two parts. Sigmoid and tanh activation functions are used to control the range of output value respectively, and the product of the two parts is used to participate in the update of cell state. *See* formulas (6) and (7) for details.

$$g_t^l = \sigma\left(w_g^l \cdot \left[h_{t-1}^l, x_t^{l-1}\right] + b_g^l\right) \tag{6}$$

$$\tilde{c}_t^l = \tanh\left(w_c^l \cdot \left[h_{t-1}^l, x_t^{l-1}\right] + b_c^l\right) \tag{7}$$

In Eqs 6, 7, tanh ( ) is the activation function, g represents the input gate, c represents the cell state, and $\tilde{c}$ represents the current input unit state.

(3) Cell state update: the cell state is updated by calculating the product of the cell state at the previous time and the output of the forgetting gate and the product of the results of the two parts of the input gate, and adding the products of the two parts. See formula (8) for details.

$$c_t^l = f_t^l * c_{t-1}^l + g_t^l * \tilde{c}_t^l \tag{8}$$

Equation 8, * represents the multiplication of the elements of the corresponding dimensions of two vectors.

(4) Output gate operation: the output gate consists of two parts. The first part is also the hidden state at the previous time and the input variable at this time as the input, and the output range is controlled by sigmoid function. The second part controls the output range by tanh activation function, and then multiplies the output result of the first part to update the hidden layer state. The specific formulas are as follows (9) and (10).

$$o_t^l = \sigma\left(w_o^l \cdot \left[h_{t-1}^l, x_t^{l-1}\right] + b_o^l\right) \tag{9}$$

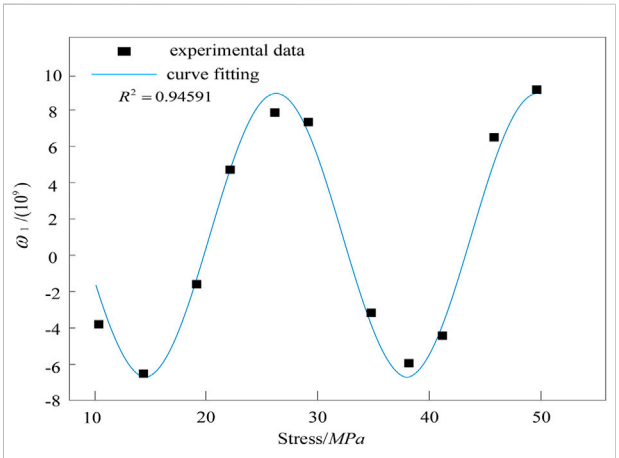

FIGURE 5
Relationship between characteristic correlation coefficient ω_1 and stress.

$$h_t^l = o_t^l \cdot \tanh\left(c_t^l\right) \tag{10}$$

o in Eqs 9, 10 represents the output gate.

SSA optimization algorithm

Sparrow search algorithm (SSA) (Jia et al., 2022; Qi et al., 2021; Wc et al., 2021) is a new intelligent optimization algorithm based on sparrows' foraging behavior and anti predation behavior. The algorithm can optimize several super parameters of LSTM at the same time, and has strong optimization ability and convergence speed. The basic theory of SSA optimization algorithm is as follows:

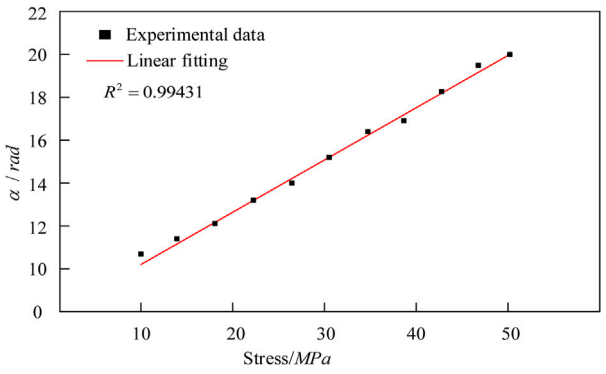

FIGURE 6
Relationship between α and different stresses.

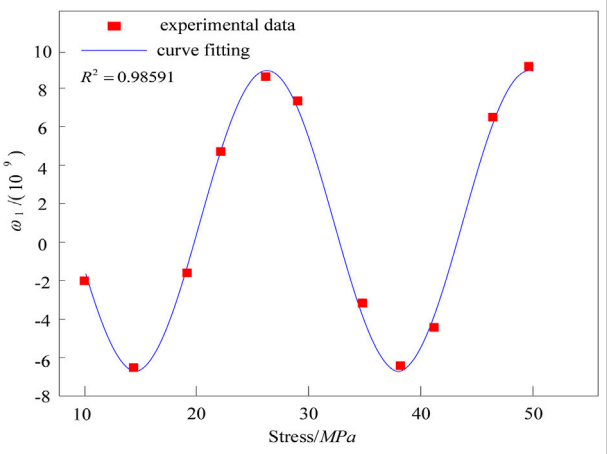

FIGURE 7
Relationship between characteristic correlation coefficient ω_1 and stress.

When using SSA algorithm to optimize the super parameters of LSTM model, n sparrows form a population to search for food. The population is expressed as follows:

$$X = \begin{bmatrix} x_{1,1} & x_{1,2} & \cdots & x_{1,d} \\ x_{2,1} & x_{2,2} & \cdots & x_{2,d} \\ \cdots & \cdots & \cdots & \cdots \\ x_{n,1} & x_{n,2} & \cdots & x_{n,d} \end{bmatrix} \tag{11}$$

Where, d represents the dimension of the problem to be optimized. Therefore, the sparrow fitness value is expressed as follows:

$$F_X = \begin{bmatrix} f([x_{1,1} & x_{1,2} & \cdots & x_{1,d}]) \\ f([x_{2,1} & x_{2,2} & \cdots & x_{2,d}]) \\ & \cdots & & \\ f([x_{n,1} & x_{n,2} & \cdots & x_{n,d}]) \end{bmatrix} \tag{12}$$

Where f is the fitness value.

Since the discoverer provides foraging directions for all participants, once the existence of predators is found, the individual starts to sound an alarm. If the alarm value is greater than the safe value, the discoverer will shift the location and bring the participants into a new area for foraging. During the iteration, the location of the discoverer is updated as follows:

$$X_{i,j}^{t+1} = \begin{cases} X_{i,j}^{t} \cdot \exp\left(-\dfrac{i}{\alpha \cdot T}\right) & if \quad R_2 < ST \\ X_{i,j}^{t} + Q \cdot L & if \quad R_2 \geq ST \end{cases} \tag{13}$$

Where t represents the current number of iterations, T is the maximum number of iterations, $j = 1, 2, \ldots, d$. $X_{i,j}$ represents the position information of the ith sparrow in the j dimension. R_2 and St are the early warning value and safety value respectively. The ranges are [0,1], [0.5,1] and α is a random number within [0,1]. L is the matrix of $1 \times d$ whose internal elements are all 1. Among them, when the early warning value is less than the safety value, the sparrow can perform the search operation. When the early warning value is greater than the safety value, it indicates that predators have appeared within the search range, and all sparrows need to be transferred to a safe place to look for food immediately.

For those who join in the process of sparrow foraging, if the energy is too low, they need to fly to other places for foraging to obtain more energy. Some participants will compete for food in order to increase their energy and even monitor the discoverer. If the participants win, they will get new food. The location update is shown in the formula:

$$X_{i,j}^{t+1} = \begin{cases} Q \cdot \exp\left(\dfrac{X_{worst} - X_{i,j}^{t}}{i^2}\right) & if \quad i > n/2 \\ X_{p}^{t+1} + \left|X_{i,j}^{t} - X_{p}^{t+1}\right| \cdot A^{T}\left(AA^{T}\right)^{-1} \cdot L & if \quad otherwise \end{cases} \tag{14}$$

Where A is a $1 \times d$ matrix, each element is 1 or - 1, X_{worst} is the global worst position, and X_p is the best position occupied by the current discoverer.

During the experiment, we assume that the number of sparrows aware of danger accounts for 10%–20%. The location of these sparrows is shown in formula (8):

$$X_{i,j}^{t+1} = \begin{cases} X_{best}^{t} + \beta \cdot \left|X_{i,j}^{t} - X_{best}^{t}\right| & if \quad f_i > f_g \\ X_{i,j}^{t} + K \cdot \left(\left|\dfrac{X_{i,j}^{t} - X_{worst}^{t}}{(f_i - f_w) + \varepsilon}\right|\right) & if \quad f_i = f_g \end{cases} \tag{15}$$

X_{best} and β are the globally optimal position and step control parameters respectively, which obey the standard normal distribution. f_i, f_g and f_w are the fitness values of individual sparrow, global optimal position and worst position respectively, $K \in [-1, 1]$, ε is a very small constant, in order to avoid the occurrence of zero denominator.

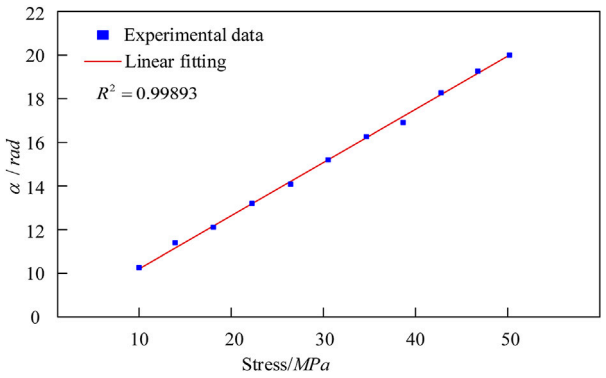

FIGURE 8
Relationship between α and different stresses.

In formula (8), when $f_i = f_g$, it indicates that the sparrows in the population have realized the danger and need to quickly move to other positions to avoid being preyed on, where K is the moving step.

The algorithm calculates the fitness of sparrows in the population and sorts them to select the optimal value and the worst value; Then, update the location of the discoverer, entrant and aware of the dangerous sparrow. Finally, obtain the current best location. If the current location is better than the result of the previous iteration, stop the iteration. Otherwise, continue the iteration until the termination conditions are met. The process is shown in Figure 3.

Experimental comparison and analysis

In this paper, the sensing system (Figure 1) is built to study the response characteristics of stress sensing. The optical fiber in the sensing optical path is fixed on the tension platform, and the stress is applied from 10.18 MPa to 50.88 mpa in steps of 4.07 MPa, that is, the maximum value of strain measurement is 3492 με, CCD collects interferograms corresponding to different stresses (Li et al., 2021a; Li et al., 2021b; Li 2022a; Li 2022b).

General collection and mediation methods

According to the analysis process in Section 2.1 and Figure 4 is the collected picture, this paper processes the bifurcation interferogram collected in the experiment, regards the collected interferogram as a pattern set, calculates the main features of the pattern set, obtains the correlation coefficient ω_1 of each interferogram for the main features, and obtains the relationship between the correlation coefficient ω_1 of the bifurcation interferogram and the stress, as shown in Figure 5. It can be seen that there is a periodic trigonometric function distribution between stress and correlation coefficient ω_1. Through trigonometric function curve fitting, the fitting degree R^2 is 0.94591. In order to obtain high-quality images and improve the fitting effect, higher precision CCD equipment can be used to collect interference patterns. The mathematical expression of the demodulation model obtained by fitting is:

$$y = y_0 + A\sin\left(\pi\frac{x - x_c}{\omega}\right) \tag{16}$$

Where, y is the correlation coefficient of the main features of the fitted fork image, x is the stress, and y_0, A, ω and x_c are the known constants, $y_0 \approx 0.39813$, $A \approx 7.03067$, ω and x_c. This document defines:

$$(y - y_0)/A = \beta \tag{17}$$

$$\sin\left(\pi\frac{x - x_c}{\omega}\right) = \sin\alpha \tag{18}$$

It can be obtained according to Eqs 17, 18

$$\beta = \sin\alpha \tag{19}$$

According to the properties of trigonometric function, given the value of β and the shape of $\beta - \alpha$ curve, the value of a can be expressed as:

$$\begin{cases} \alpha = 2k\pi + \arcsin\beta, -\frac{\pi}{2} + 2k\pi \le \alpha \le \frac{\pi}{2} + 2k\pi \,(\text{Increasing interval}) \\ \alpha = (2k+1)\pi - \arcsin\beta, \frac{\pi}{2} + 2k\pi < \alpha < \frac{3}{2}\pi + 2k\pi \,(\text{Decreasing interval}) \end{cases} \tag{20}$$

Where k is an integer, that is, the number of cycles from $\alpha = 0$.

Judge the period and monotonic interval of α at any position according to Figure 4, and substitute Eq. 20 to calculate the α value of each point. It is concluded that there is a linear relationship between α and stress, as shown in Figure 6. The fitting curve can be expressed as:

$$\alpha = 7.21344 + 0.25694x \tag{21}$$

The fitting results show that the phase adjustment method can achieve the sensitivity of stress measurement of 0.257 rad/MPa.

Fitting method based on SSA-LSTM

The method based on SSA-LSTM takes the relationship between ω_1, α and stress as training data, and fits a more suitable corresponding relationship through the training of neural network. Because the LSTM model is suitable for fitting the relationship between nonlinear quantities, this

method is different from the method in Section 3.1. SSA-LSTM does not need to fit any relevant equations or mathematical expressions. Instead, it tests the values between the stress of multiple groups of data and relevant variables, and takes these values as the training data of the model. Through training, the corresponding values can be obtained through SSA-LSTM by inputting the measured data without mathematical calculation.

For example, taking the data in Section 3.1 as the test, the fitting curve of the relationship between the characteristic correlation coefficient ω_1 and stress is finally obtained, as shown in Figure 7. It can be seen that there is a periodic trigonometric function distribution between stress and correlation coefficient ω_1. Through trigonometric function curve fitting, the fitting degree R^2 is 0.98591, which is higher than the fitting degree 0.94591 of the formula calculation method used in 3.1. Similarly, for the relationship between α and stress, the fitting degree is 0.99893, which is more accurate than the method without LSTM neural network. As shown in Figure 8, the fitting curve is expressed as:

$$\alpha = 7.31361 + 0.28634x \tag{22}$$

The fitting results show that using SSA-LSTM method, the sensitivity of stress measurement can be 0.286 rad/MPa, which is greater than the original 0.257, so the performance is better.

Conclusion

In this paper, an optical fiber stress sensing system is designed, and a new stress demodulation model is proposed. The feasibility of realizing large range monitoring by the sensor is verified by simulation and experiment. In the experiment, an interferometric sensing system based on vortex rotation light is built, and the fork interferograms corresponding to different stresses are collected. The main features of the fork interferogram are extracted by SSA-LSTM method. Through model regression analysis, the periodic triangular function distribution of the correlation coefficient between the stress and the image is obtained; Through further training and fitting of LSTM model, the linear relationship related to stress is obtained. The experimental results show that the sensitivity of the sensing system is 0.286 rad/MPa and the maximum measurement range is 3492 με. In this study, the performance of deep learning model has been greatly improved by applying it to the related research of fiber optic stress sensor. In the future, deep learning will be combined with more studies and be more fully applied.

Data availability statement

The raw data supporting the conclusions of this article will be made available by the authors, without undue reservation.

Author contributions

DY and XQ conceived the idea and designed the experiments. XW and XQ led the experiments and contributed to data analysis and interpretation. DY and XW wrote the paper. All authors read and approved the final manuscript.

Funding

1 The National Natural Science Foundation of China (Nos.61735041, 61927812).

2 Scientific Research Program Funded by Shaanxi Provincial Education Department of China (No.08JS093).

Conflict of interest

The authors declare that the research was conducted in the absence of any commercial or financial relationships that could be construed as a potential conflict of interest.

Publisher's note

All claims expressed in this article are solely those of the authors and do not necessarily represent those of their affiliated organizations, or those of the publisher, the editors and the reviewers. Any product that may be evaluated in this article, or claim that may be made by its manufacturer, is not guaranteed or endorsed by the publisher.

References

Asriani, F., Winasisand Pamudji, G. (2020). Sensitivity of optical fiber sensors to deflection of reinforced concrete beam. *IOP Conf. Ser. Mat. Sci. Eng.* 982, 012025. doi:10.1088/1757-899x/982/1/012025

Cai, Y., Li, M., Wang, M., Li, J., Zhang, Y., and Zhao, Y. (2020). Optical fiber sensors for metal ions detection based on novel fluorescent materials. *Front. Phys.* 8, 598209. doi:10.3389/fphy.2020.598209

Delgado, I., and Fahim, M. (2020). Wind turbine data analysis and LSTM-based prediction in SCADA system. *Energies* 14, 125. doi:10.3390/EN14010125

Guo, J., Geng, T., Yan, H., Du, L., Zhang, Z., and Sun, C. (2020). Implementation of a load sensitizing bridge spherical bearing based on low-coherent fiber-optic sensors combined with neural network algorithms. *Sensors* 21 (1), 37. doi:10.3390/s21010037

He, X., Ran, Z., Xiao, Y., Xu, T., Shen, F., Ding, Z., et al. (2020). Three-dimensional force sensors based on all-fiber Fabry-Perot strain sensors. *Opt. Commun.* 490, 126694. doi:10.1016/j.optcom.2020.126694

Jia, J., Yuan, S., Shi, Y., Wen, J., Pang, X., and Zeng, J. (2022). Improved sparrow search algorithm optimization deep extreme learning machine for lithium-ion battery state-of-health prediction. *iScience* 25 (4), 103988. doi:10.1016/j.isci.2022.103988

Jiang, Z., Hu, W., and Qin, H. (2021). WSN node localization based on improved sparrow search algorithm optimization. *Int. Conf. Sensors Instrum.* 2021, 11887. doi:10.1117/12.2602966

Li, H. (2022b). SCADA data based wind power interval prediction using LUBE-based deep residual networks. *Front. Energy Res.* 10, 920837. doi:10.3389/fenrg.2022.920837

Li, H. (2022a). Short-term wind power prediction via spatial temporal analysis and deep residual networks. *Front. Energy Res.* 10, 920407. doi:10.3389/fenrg.2022.920407

Li, H., Deng, J., Feng, P., Pu, C., Arachchige, D. D., and Cheng, Q. (2021b). Short-term nacelle orientation forecasting using bilinear transformation and ICEEMDAN framework. *Front. Energy Res.* 697, 780928. doi:10.3389/fenrg.2021.780928

Li, H., Deng, J., Yuan, S., Feng, P., and Arachchige, D. D. (2021a). Monitoring and identifying wind turbine generator bearing faults using deep belief network and EWMA control charts. *Front. Energy Res.* 9, 770. doi:10.3389/fenrg.2021.799039

Lv, R., Qiu, L., Hu, H., Meng, L., and Zhang, Y. (2018). The phase interrogation method for optical fiber sensor by analyzing the fork interference pattern. *Appl. Phys. B* 124 (2), 32. doi:10.1007/s00340-018-6901-5

Ning, X., Duan, P., and Zhang, S. (2020). Real-time 3D face alignment using an encoder-decoder network with an efficient deconvolution layer. *IEEE Signal Process. Lett.* 27, 1944–1948. doi:10.1109/LSP.2020.3032277

Qi, S., Ning, X., Yang, G., Zhang, L., Li, W., Cai, W., et al. (2021). Review of multi-view 3D object recognition methods based on deep learning. *Displays* 69 (1), 102053. doi:10.1016/j.displa.2021.102053

Tan, X., and Bao, Y. (2020). Measuring crack width using a distributed fiber optic sensor based on optical frequency domain reflectometry. *Measurement* 172, 108945. doi:10.1016/j.measurement.2020.108945

Tang, F., Zhou, G., Li, H., and Verstrynge, E. (2021). A review on fiber optic sensors for rebar corrosion monitoring in RC structures. *Constr. Build. Mater.* 313, 125578. doi:10.1016/j.conbuildmat.2021.125578

Vpn, A., Hao, L., At, A., Chao, H., and Atzc, D. (2021). Ensembles of probabilistic LSTM predictors and correctors for bearing prognostics using industrial standards. *Neurocomputing* 491, 575–596. doi:10.1016/j.neucom.2021.12.035

Wc, A., Dong, L., Xin, N., Chen, W., and Gx, D. (2021). Voxel-based three-view hybrid parallel network for 3d object classification. *Displays* 69, 102076. doi:10.1016/j.displa.2021.102076

Xiang, P., and Wang, H. P. (2021). Optical fiber sensors for monitoring railway infrastructures: A review towards smart concept. *Symmetry* 13, 2251. doi:10.3390/sym13122251

Yao, Ji., Wu, W., and Li, S. (2022). Anomaly detection model of mooring system based on LSTM PCA method. *Ocean. Eng.* 254, 111350. doi:10.1016/j.oceaneng.2022.111350

Ying, L., Nan, Z., Ping, W., Kiang, C., Pang, L., Chang, Z., et al. (2021). Adaptive weights learning in cnn feature fusion for crime scene investigation image classification. *Connect. Sci.* 33 (3), 719–734. doi:10.1080/09540091.2021.1875987

Yue, Q., Xiao, S., Li, Z., Yang, J., Chen, B., Feng, J., et al. (2022). Ultra-sensitive pressure sensors based on large alveolar deep tooth electrode structures with greatly stretchable oriented fiber membrane. *Chem. Eng. J.* 443, 136370. doi:10.1016/j.cej.2022.136370

Zhao, M., Zhou, X., and Chen, Y. (2021). A highly sensitive and miniature optical fiber sensor for electromagnetic pulse fields. *Sensors* 21 (23), 8137. doi:10.3390/s21238137

Zheng, H., Lv, R., Zhao, Y., Tong, R., Lin, Z., Wang, X., et al. (2020). Multifunctional optical fiber sensor for simultaneous measurement of temperature and salinity. *Opt. Lett.* 45 (24), 6631–6634. doi:10.1364/OL.409233

Zhou, J., Wang, Y., Liao, C., Yin, G., Li, Z., Yang, K., et al. (2014). Intensity-modulated strain sensor based on fiber in-line mach-zehnder interferometer. *IEEE Photonics Technol. Lett.* 26 (5), 508–511. doi:10.1109/LPT.2013.2295826

Zm, A., Kib, C., Gz, B., Yw, A., Ml, A., and Lei, W. (2020). Foot type classification using sensor-enabled footwear and 1D-CNN. *Measurement* 165, 108184. doi:10.1016/j.measurement.2020.108184

frontiers | Frontiers in Energy Research

BRIEF RESEARCH REPORT
published: 17 August 2022
doi: 10.3389/fenrg.2022.942408

Influence for Ambient Relative Humidity and Pollution on Infrared Detection of Zero Resistance Insulators

Ling Chen, Feng Lin, Minjiang Chen, Xiongtao Huang, Ruomei He and Yaqing Zheng*

EVH Branch Company of State Grid Fujian Electric Power Co. LTD., Fuzhou, China

Porcelain insulators play a vital role for the safety and stability operations of electric systems. In a strong electric field, these insulators easily break down and become zero resistance insulators, which impacts the safety and stability operations of an electric system. As a result, a three-dimensional zero resistance insulator model is set up based on COMSOL. To proceed, first, we studied the voltage and current density law of insulator string when ambient relative humidity, pollution degree, and pollution salt composition are different. Then, the insulator infrared detection test is carried out in an artificial fog chamber. Results showed that the zero resistance insulator has the greatest influence on voltage when it is at a high voltage terminal, and it has the least influence on voltage when it is in the middle position. As the relative range between non-adjacent insulators and zero resistance insulators increases, the implications for a zero resistance insulator on adjacent position insulators will decrease continuously. Farther is the range between different positions on the insulators and the center axis of rotation and lower is the current density and temperature rise. The overall temperature rise of the insulator string gradually increases due to the increase in the relative humidity and pollution degree of the environment. Finally, the results indicate that the temperature difference between zero resistance insulators and other insulators gradually increases and can provide support for the infrared detection of zero resistance insulators.

Keywords: zero resistance insulator, ambient relative humidity, dirty degree, dirty salt content, infrared detection

OPEN ACCESS

Edited by:
Tinghui Ouyang,
National Institute of Advanced Industrial Science and Technology (AIST), Japan

Reviewed by:
Dr. Sandeep Kumar Duran,
Lovely Professional University, India
Vikram Kamboj,
Lovely Professional University, India

****Correspondence:***
Ling Chen
471225957@qq.com

Specialty section:
This article was submitted to Smart Grids, a section of the journal Frontiers in Energy Research

Received: *12 May 2022*
Accepted: *16 June 2022*
Published: *17 August 2022*

Citation:
Chen L, Lin F, Chen M, Huang X, He R and Zheng Y (2022) Influence for Ambient Relative Humidity and Pollution on Infrared Detection of Zero Resistance Insulators. Front. Energy Res. 10:942408. doi: 10.3389/fenrg.2022.942408

1 INTRODUCTION

Insulation and mechanical properties of porcelain insulators decline and deteriorate due to long-term operations in the outdoor environment, which contains mechanical and electrical loads, air pollution, cold and heat changes, and other effects. Under the action of a strong electric field, insulators are easily broken down and then transform into zero resistance insulators, which will lead to disconnection accidents and impact the safety and stability operation of the electric system (Liu et al., 2018; Yuan et al., 2018).

Zhang et al. (2018) studied the implications of humidity on the deterioration string with zero resistance through experiments. It shows that the voltage of the contaminated insulator string is greatly influenced by humidity. Humidity raise will reduce the asymmetry of the insulator string's voltage which is beneficial for the detection of zero resistance insulators. However, it is not conducive to detection while the humidity is overly high, which will easily lead to misjudgment. Xu et al. (2011) proposed a modeling simplification and calculation optimization scheme based on the electric field type, unit, area, and other factors by calculating

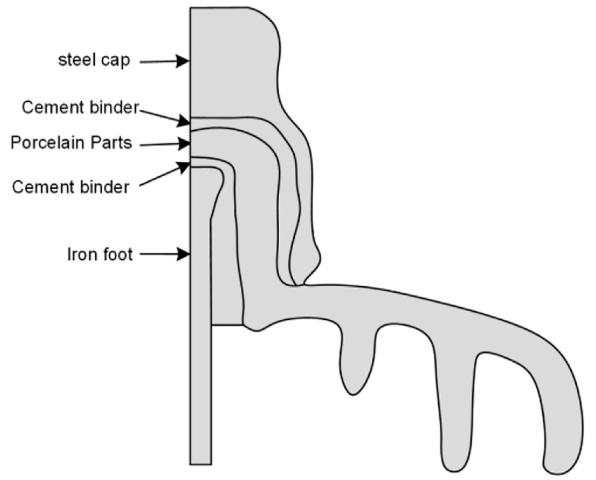

FIGURE 1 | Two-dimensional axisymmetric section of insulators.

the electric field distribution of 110 kV porcelain pillar insulators under different surface states, such as pollution and ice coating. Ilha et al. (2015) and Ilha et al. (2012) used graphite powder and epoxy resin to simulate the potential distribution of insulator strings with different pollution conductivities. By combining the experimental data with the numerical results, it is found that a small contamination conductivity would change the potential and electric field of an insulator string.

Chen et al. (2015) carried out the infrared temperature measurement test. Based on this fact, the zero resistance insulator is located in different positions of the insulator string, and a comparison between the filthy insulator string and the clean condition is established. The experimental results show that the thermal image has obvious changes while the insulator string is polluted and then results in zero resistance insulators. Therefore, a high-precision infrared thermal imager can be used to identify zero resistance insulators and polluted insulators in string. The test (Reddy & Nagabhushana 2003) of damp contaminated porcelain insulator string shows that the heating condition of porcelain surface, steel cap, and iron foot is different. Three cases of the iron foot, porcelain surface, and steel cap will cause a high-to-low temperature rise. According to the electromagnetic field and heat transfer theory, Vitelli et al. (2000) using Maxwell and heat transfer equation solved the surface heat distribution of porcelain insulators.

The previous research studies lack comprehensive consideration of the implications for ambient relative humidity, fouling degree, and

TABLE 1 | Various material properties.

Dielectric material	Porcelain	Cement agent	Iron steel cap	Air
Relative dielectric constant	4.7	8	$1e^{10}$	1
Specific conductance $\mu s \cdot cm^{-1}$	$2e^{-11}$	$1.7e^{-9}$	$1.2e^{11}$	$1e^{-8}$

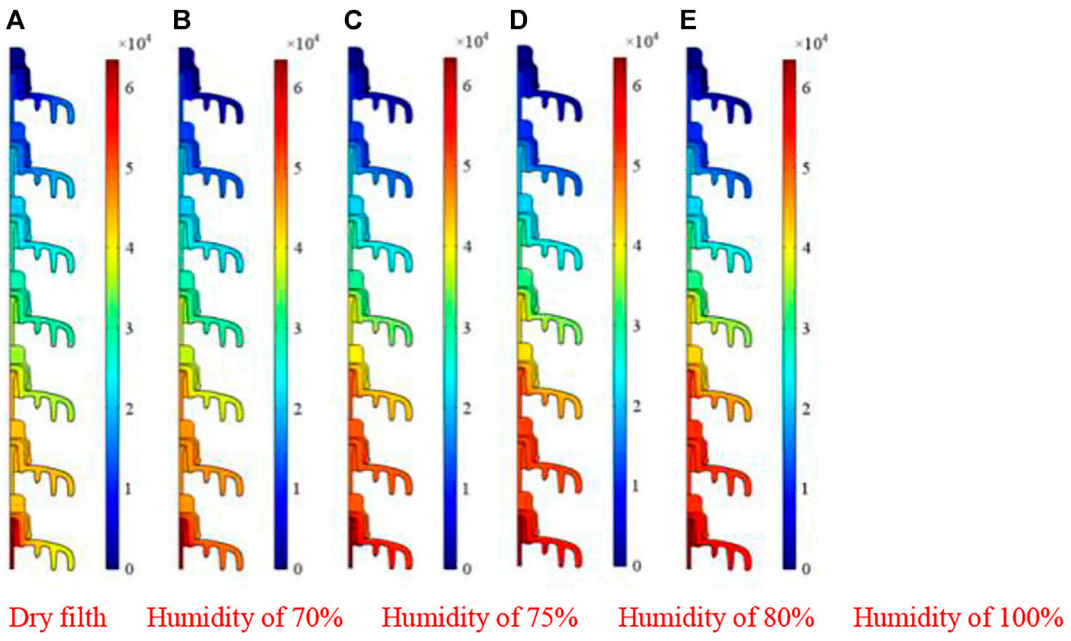

FIGURE 2 | Voltage of 2-th zero resistance insulator string as humidity raises (V). **(A)** Dry filth, **(B)** humidity of 70%, **(C)** humidity of 75%, **(D)** humidity of 80%, and **(E)** humidity of 100%.

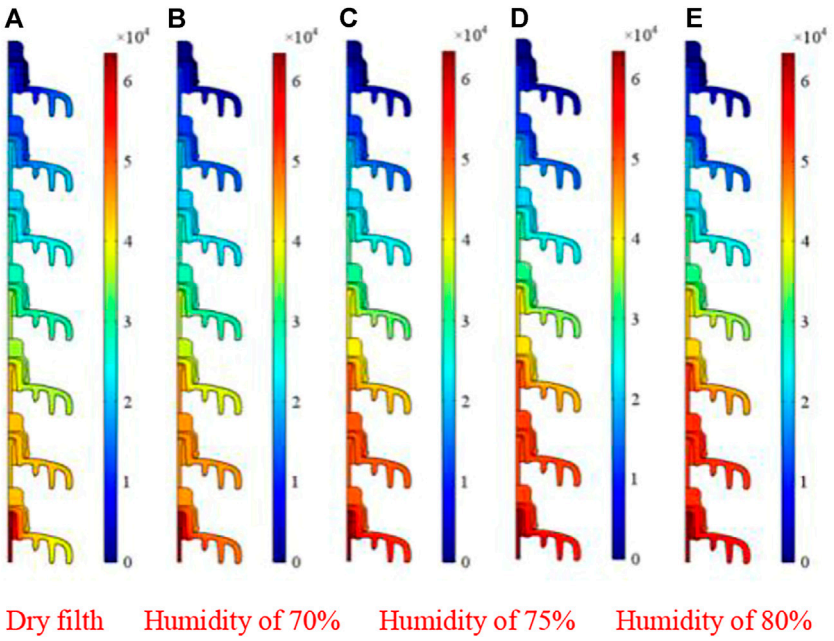

FIGURE 3 | Current density of 2-th zero resistance insulator string as humidity increases (A/m^2). **(A)** Dry filth, **(B)** humidity of 70%, **(C)** humidity of 75%, **(D)** humidity of 80%, and **(E)** humidity of 100%.

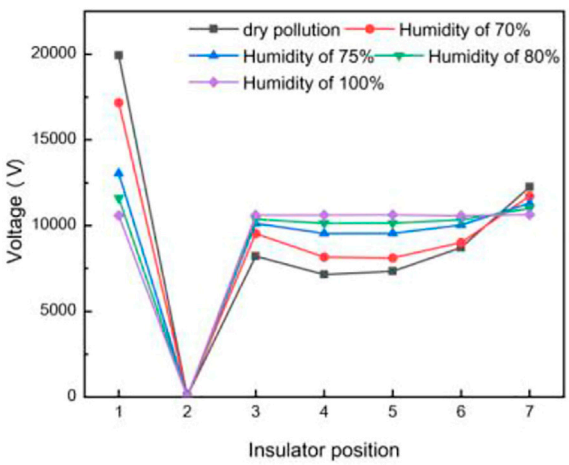

FIGURE 4 | Implications for the environmental relative humidity on voltage.

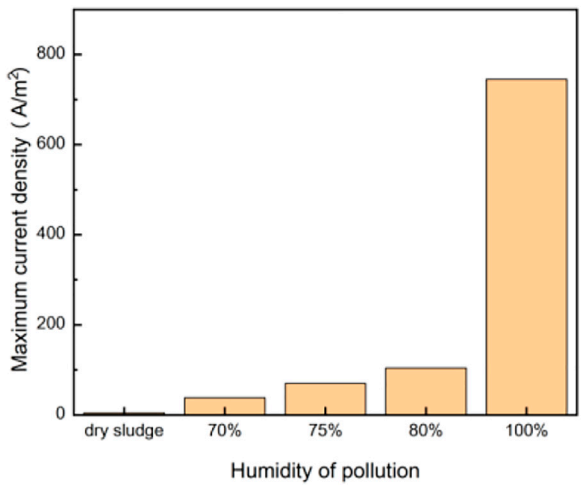

FIGURE 5 | Implications for the environmental relative humidity on the maximum current density.

fouling salt composition on the infrared detection of zero resistance insulators. Therefore, the zero resistance insulator model is set up for a more complex infrared detection environment. The effects of relative humidity and pollution on voltage and potential distribution of insulators were studied. At the same time, the infrared imaging method was used to study the heat characteristics of an insulator surface in an artificial fog chamber. The conclusion can provide further support for the research of the zero resistance insulator detection technology.

2 EMULATION MODEL OF PORCELAIN INSULATORS

The standard porcelain suspension insulators used for 110 kV line are taken as emulation objects to conduct full-scale modeling, and a simplified two-dimensional axisymmetric model of porcelain insulators is established, as shown in **Figure 1**.

Table 1 shows the material properties of the relative permittivity and conductivity of density of each insulator's

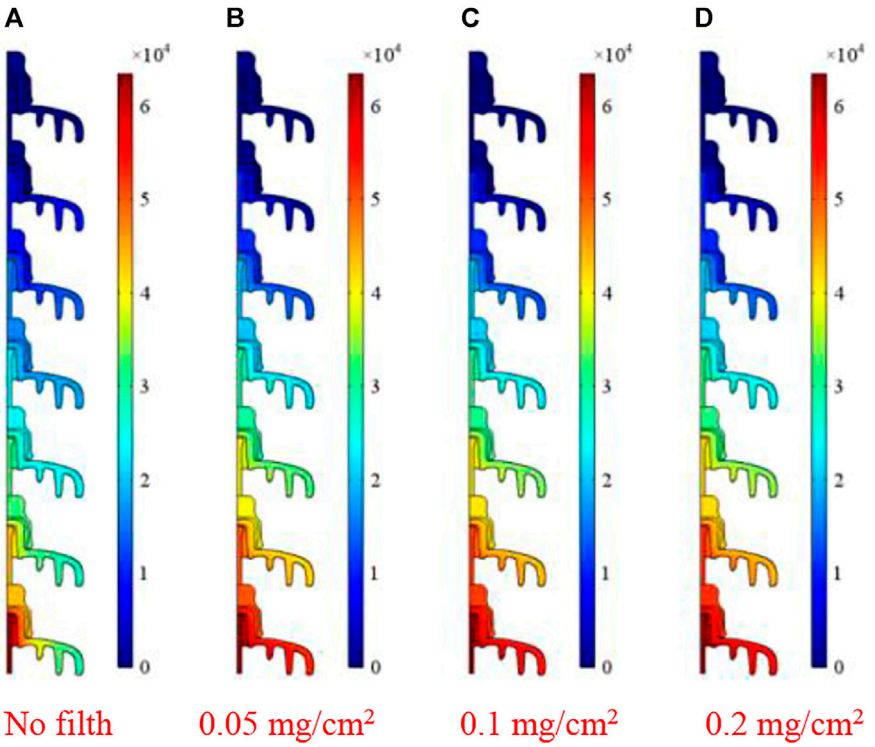

FIGURE 6 | Voltage under different pollution degrees (case of NaCl). **(A)** No filth, **(B)** 0.05 mg/cm^2, **(C)** 0.1 mg/cm^2, and **(D)** 0.2 mg/cm^2.

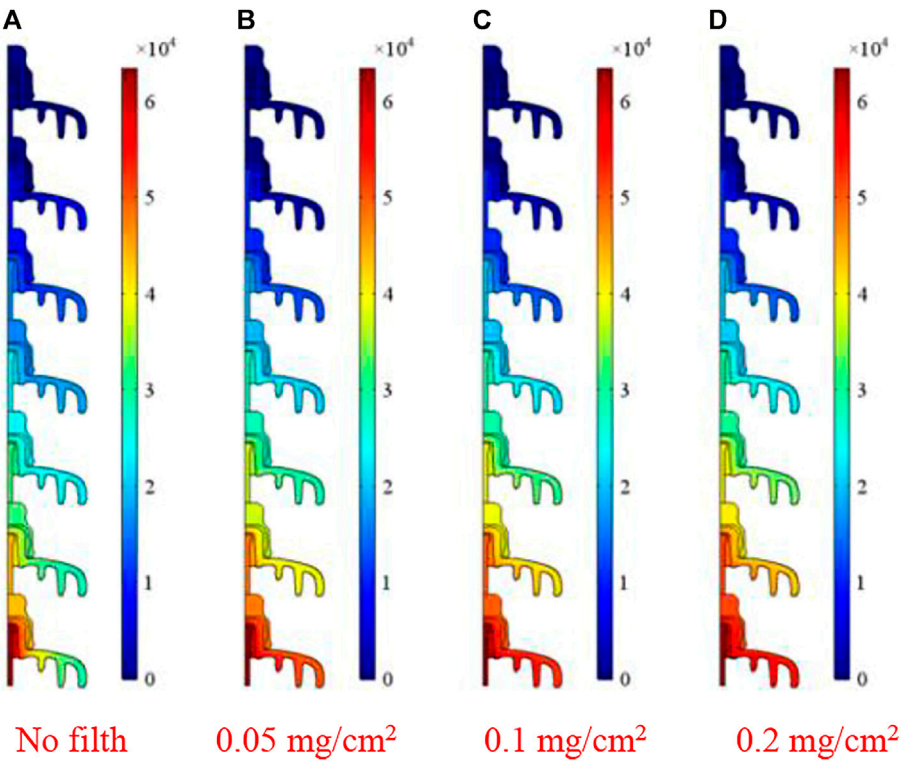

FIGURE 7 | Voltage under different pollution degrees (case of salt-mixture). **(A)** No filth, **(B)** 0.05 mg/cm^2, **(C)** 0.1 mg/cm^2, and **(D)** 0.2 mg/cm^2.

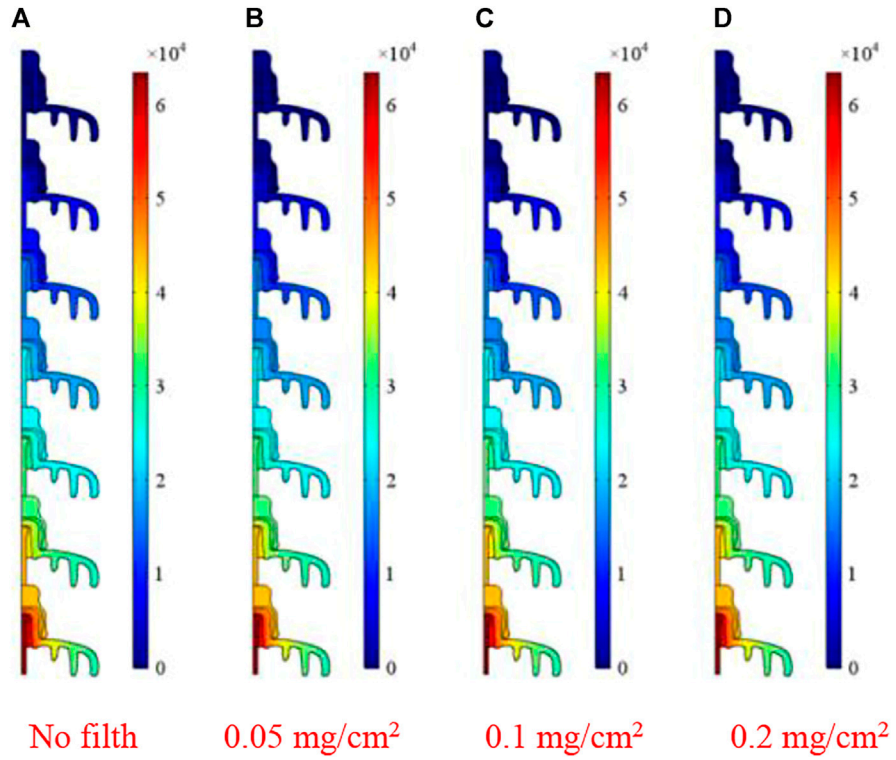

FIGURE 8 | Voltage under different pollution degrees (case of $CaSO_4$). **(A)** No filth, **(B)** 0.05 mg/cm^2, **(C)** 0.1 mg/cm^2, and **(D)** 0.2 mg/cm^2.

part. In the emulation calculation, the applied voltage of the high end of the insulator string is 63.5 kV, the applied voltage of the low end is 0 kV, and the frequency domain is 50 Hz.

The calculation formula used to convert the equivalent relation between the conductivity value of the dirty layer on the insulator surface at saturation and wetting and the salt density and gray density on the surface cover is defined by Yuan (2008). The conductivity of the dirty layer can be obtained through the conversion relationship between the experimental results obtained in Mei et al. (2014) and the conditions of different salt types and relative humidity[12–17].

3 ELECTRIC FIELD EMULATION RESULTS AND ANALYSIS

The insulators are numbered by positions 1–7 from the high voltage terminal to the grounding end, while the 2-nd, 4-th, and 7-th are selected as zero resistance insulators in the emulation calculation.

3.1 Implications for Ambient Relative Humidity on the Electric Field of Polluted Insulator String Containing Zero Resistance

The 2-th insulators are selected as zero resistance insulators with the pollution of NaCl(0.1 mg/cm^2). **Figure 2** and **Figure 3** show the emulation calculation results of voltage and current density of polluted insulator string, while the ambient relative humidity gradually rises, respectively. As the environment's relative humidity raises from 0% to 100%, the voltage of each other insulators tends to be equal, while the pollution condition of the zero resistance insulator string is constant. Meanwhile, the current density also changes with the change in ambient humidity. As the relative humidity value raises gradually, the current density value of each position in the insulator string also raises gradually.

Figure 4 shows the voltage of the insulator string that presents an obvious uniform distribution as the pollution changes from dry to 100% ambient relative humidity, which indicates that the dirty layer conductivity gradually becomes the dominant factor of the dirty insulator string voltage. Ilha et al. (2015) and Ilha et al. (2012) found that the surface voltage would not change, while the conductivity of the polluted layer is greater than the critical value 5 μs cm^{-1}. The dirty layer's conductivity is 0.22 μs cm^{-1}, while the relative humidity is 70%. The voltage is unevenly distributed. The conductivity of the polluted layer is 23 μs cm^{-1}, while the relative humidity reaches 100%. **Figure 5** shows that the maximum current density raises significantly while the pollution changes from dry to the ambient relative humidity reaching 100%. Under the same pollution degree conditions, the conductivity of the surface pollution layer will increase exponentially with the rise in relative humidity, which will cause the current density at each position in the insulator string to raise nonlinearly with the raise of ambient relative humidity.

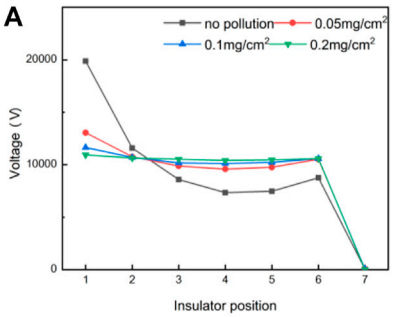

The voltage changes with fouling degree under fouling of NaCl

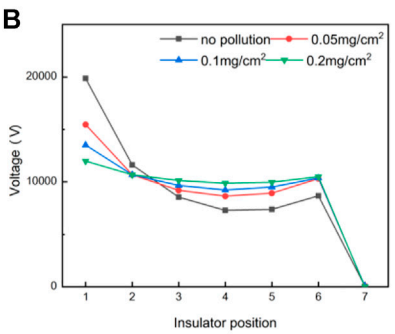

The voltage varies with fouling degree under fouling of salt-mixture(40%NaCl and 60% $CaSO_4$)

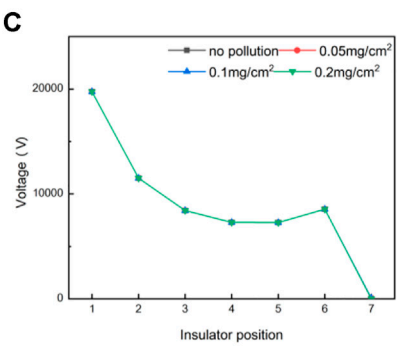

Voltage changes with fouling degree under fouling of $CaSO_4$

FIGURE 9 | Voltage of insulator surface containing different pollution salts under different degrees and types of pollution. **(A)** Voltage changes with the fouling degree under the fouling of NaCl. **(B)** Voltage varies with the fouling degree under the fouling of salt mixture (40%NaCl and 60% $CaSO_4$). **(C)** Voltage changes with the fouling degree under the fouling of $CaSO_4$.

3.2 Implications for the Pollution Degree and Pollution Salt Type on Electric Field of Pollution Containing Zero Resistance Insulator String

The 7-th insulators are selected as zero resistance insulators. The pollution-containing salt types include only NaCl, mixed salt (40% NaCl and 60% $CaSO_4$) and only $CaSO_4$ under the case of an 80% environment relative humidity. **Figure 6**, **Figure 7**, and **Figure 8** show the emulation calculation results of the voltage of insulator string under a pollution degree of 0 mg/cm^2, 0.05 mg/cm^2, 0.1 mg/cm^2, and 0.2 mg/cm^2. The voltage tends to be uniform with the raise of the pollution degree, while the pollution types are NaCl and mixed salt (NaCl and $CaSO_4$) while the voltage will not change where the pollution layer is only $CaSO_4$.

Figure 9 shows the insulator string's voltage. The insulator surface pollution is NaCl, mixed salt (40%NaCl and 60% $CaSO_4$),

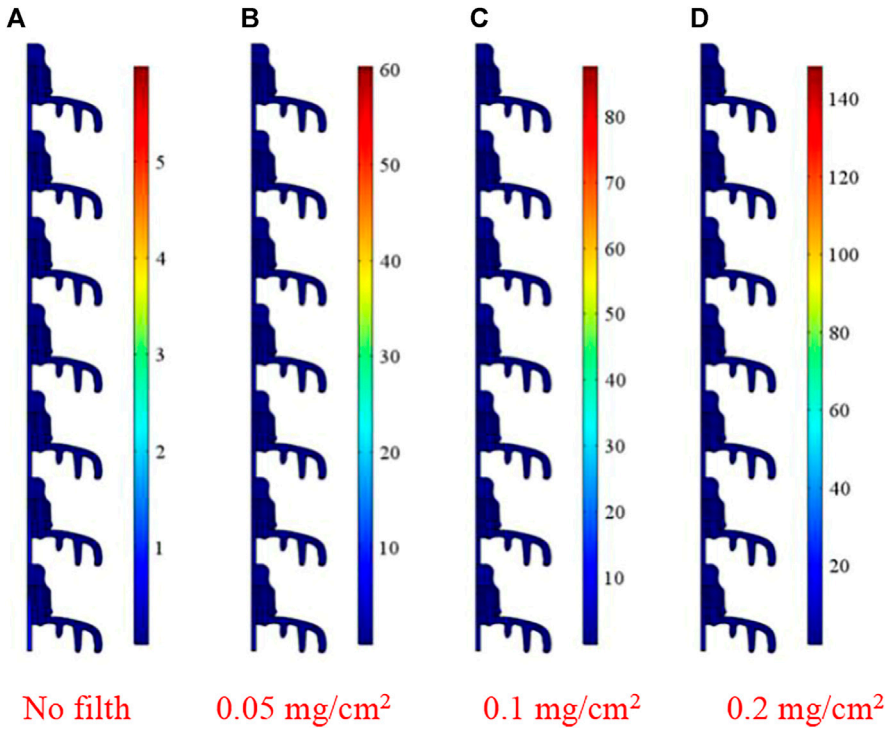

FIGURE 10 | Current density under different pollution degrees (NaCl). **(A)** No filth, **(B)** 0.05 mg/cm^2, **(C)** 0.1 mg/cm^2, and **(D)** 0.2 mg/cm^2.

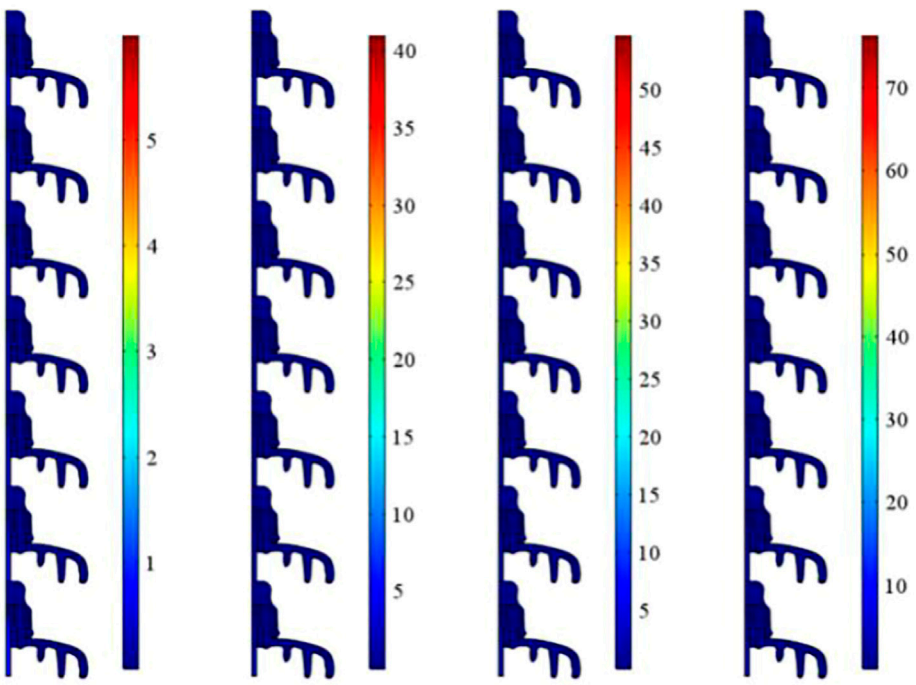

FIGURE 11 | Current density at different pollution degrees (salt mixture).

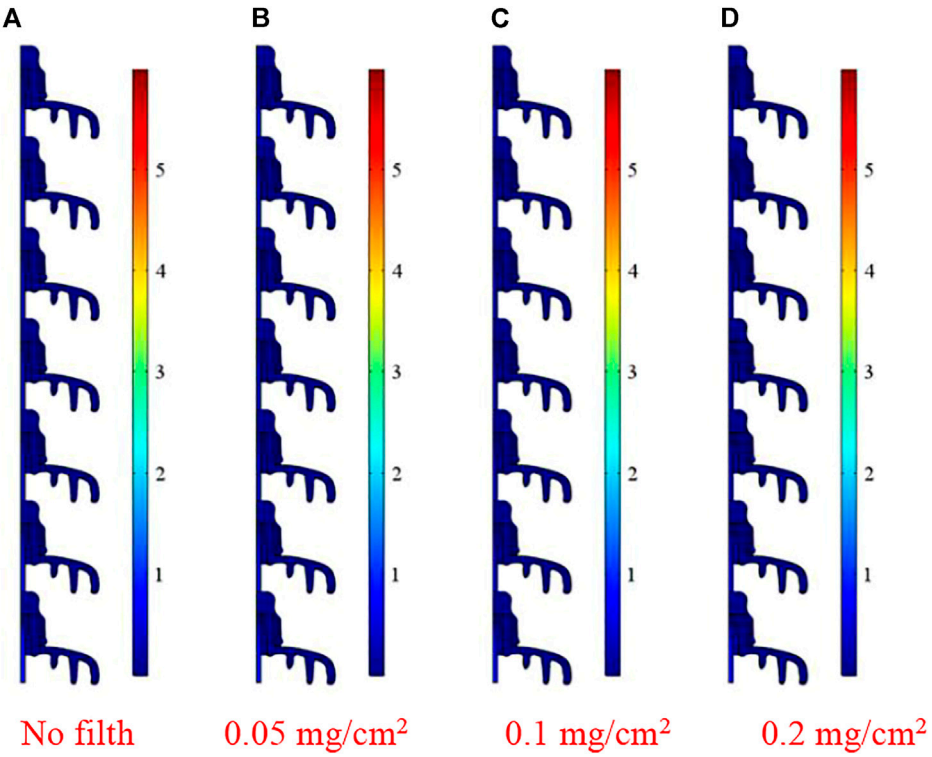

FIGURE 12 | Current density under different pollution degrees ($CaSO_4$). **(A)** No filth, **(B)** 0.05 mg/cm^2, **(C)** 0.1 mg/cm^2, and **(D)** 0.2 mg/cm^2.

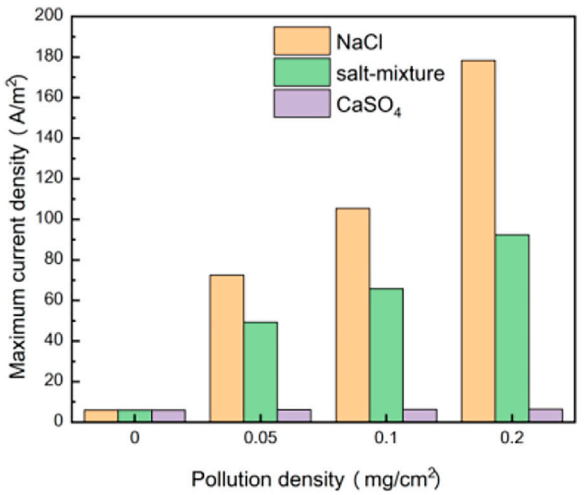

FIGURE 13 | Maximum current density of insulator surface contaminated with different types of salts.

and $CaSO_4$. The surface pollution of insulators is 0.05 mg/cm^2, 0.1 mg/cm^2, and 0.2 mg/cm^2, respectively. The voltage in the insulator string except the set zero resistance insulator tends to be uniform with the raise of the pollution degree under cases of the pollution of NaCl and mixed salt. **Figure 9A** shows that the partial voltage of non-zero resistance insulators is about 10580 V, while the pollution degree is 0.2 mg/cm^2, which is similar to the result shown in **Figure 9B**. The voltage is even in this condition. The reason is that the pollution layer's conductivity on the insulator surface is slightly greater than the critical value (5 μs cm^{-1}), while the pollution degree is 0.2 mg/cm^2; this results in the pollution layer's conductivity can no longer impact the voltage of the insulator string. **Figure 9C** shows that the voltage is not uniform and will not change with the change of the surface pollution degree under cases of the pollution of $CaSO_4$.

Figure 10, **Figure 11**, and **Figure 12** show that the current density at all insulator string increases gradually with the raise of insulator surface pollution degree, while the pollution layer is NaCl or mixed salt. The current density in the insulator string does not change with the rise in the pollution degree under the case of the pollution of only CaSO4.

Figure 13 shows the maximum current density of different pollution degrees and salt types under the ambient relative humidity of 80%. The pollution type contains only NaCl, the mixed salt of NaCl, and only $CaSO_4$ with the pollution degree of $0mg/cm^2$, $0.05mg/cm^2$, $0.1mg/cm^2$, and $0.2mg/cm^2$. An increase in the pollution degree of salts with high solubilities, such as NaCl, covering the insulator surface will highly increase the maximum current density. This is the reason that the salt content with a high solubility per unit area is defined as pollution. Under the same voltage, the maximum

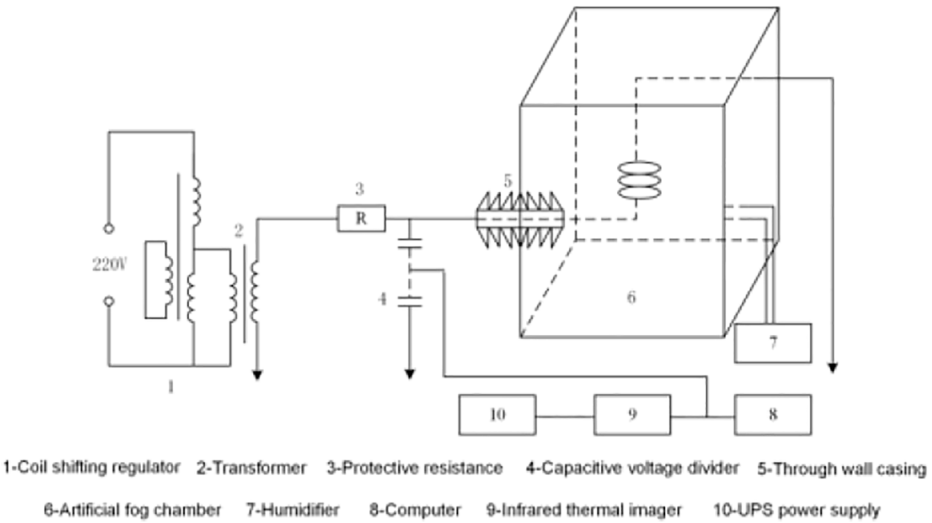

FIGURE 14 | Schematic diagram of the test.

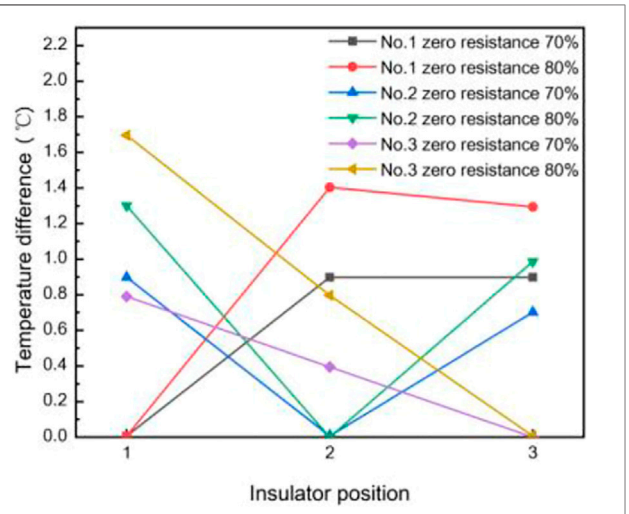

FIGURE 15 | Temperature difference between zero resistance insulators and the others under a relative humidity of polluted string of 70% and 80%.

current density raises with the raise of the conductivity of the polluted layer. However, due to the low solubility of some salts like $CaSO_4$ when the salt content in the dirty layer has exceeded the amount of salt that can be dissolved after the dirty hygroscopicity, the maximum current density of the insulator string will not be changed by the ascent of pollution density. At this time, the conductivity of the insulator pollution layer will not rise with the rise of pollution degree but is mainly affected by the environmental relative humidity.

4 RESEARCH ON THE INFRARED DETECTION TEST OF ZERO RESISTANCE INSULATOR

4.1 Testing Apparatus

The test is carried out on the basis of GB/T4585-2004/IEC60507:1991—artificial pollution test for high voltage insulators used in AC systems" standard. **Figure 14** shows the test principle. A voltage regulator is a moving coil voltage regulator with a rated input voltage of 220 V, an output voltage of 0–250 V, and a rated capacity of 15 kV A. The protection resistance value is 10kΩ. The power supply is provided by a 10 kV A/100 kV power frequency test AC transformer. The high pressure side leads to the artificial fog chamber through the epoxy sleeve. During pressurization, voltage shall be rapidly boosted to the test voltage by uniform boosting, and the temperature distribution diagram of the insulator string shall be shot by an FLIR T440 infrared thermal imager. Three U70BP standard porcelain suspension insulators are tested.

4.2 Test Results and Analysis

4.2.1 Heat Characteristics of Insulator String With Zero Resistance Under Different Ambient Relative Humidities

Figure 15 shows the temperature difference between zero resistance insulators and others, while the relative humidity of pollution is 70% and 80%. The temperature rise of zero resistance insulators is relatively low, which results in the temperature difference between them and other insulators to be large. With the gradual raise of relative humidity, the temperature difference also gradually becomes larger. Based

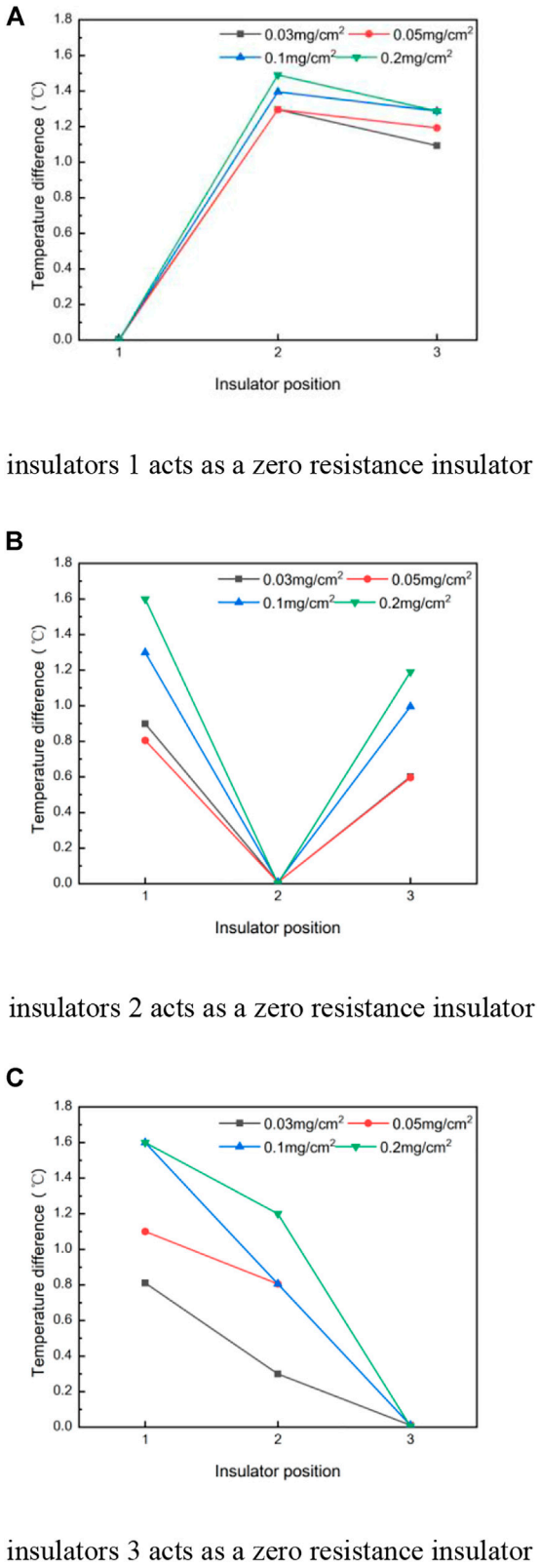

FIGURE 16 | Temperature difference between the zero resistance and other insulators in the connection position between the iron foot and the lower surface under different pollution degrees. **(A)** Insulator 1 acts as a zero resistance insulator. **(B)** Insulator 2 acts as a zero resistance insulator. **(C)** Insulator 3 acts as a zero resistance insulator.

on different humidities or different positions of zero resistance insulators in the string, the temperature difference of insulators on the high-voltage side is greater than or equal to that of insulators on the low-voltage side.

4.2.2 Heat Characteristics of Insulator String With Zero Resistance Under Different Pollution Degrees

Figure 16 shows the temperature difference between zero resistance insulators and the others in the string with different pollution degrees at the connection position between the iron foot and the lower surface. The temperature difference between zero resistance insulator and the others will raise gradually with the raise of pollution degree (raising from 0.03 mg/cm^2 to 0.2 mg/cm^2). The insulator 1 is selected as a zero resistance insulator in the real test. The temperature rise difference of insulator 2 is 1.3°C and that of insulator 3 is 1.1°C, while the pollution degree is 0.03 mg/cm^2; The temperature rise difference of insulator 2 is 1.3°C and that of insulator 3 is 1.2°C, while the pollution degree is 0.05 mg/cm^2. The temperature rise difference of insulator 2 is 1.4°C and that of insulator three is 1.3°C, while the pollution degree is 0.1 mg/cm^2; the temperature rise difference of insulator 2 is 1.5°C and that of insulator 3 is 1.3°C, while the pollution degree is 0.2 mg/cm^2. The temperature difference between other insulators and zero resistance insulators raises with the raise of pollution degree. Although some data of temperature difference do not increase significantly, the overall raise trend is the same as the emulation results.

5 CONCLUSION

Through the three-dimensional zero-value insulator model simulation and insulator infrared detection test, the following three conclusions are drawn. The research results can provide support for the infrared detection of zero-value insulators:

(1) Zero resistance insulators have a great influence on adjacent position insulators, while the influence on other non-adjacent position insulators has a distance correlation. In other words, with the increase in the relative distance between the non-adjacent insulators and the zero resistance insulator, the influence will decrease continuously.
(2) The temperature rise at different positions on the insulators is related to the distance from its own center axis. Farther the distance from the rotation center axis is, the smaller the temperature will rise. The test shows that the maximum temperature rise occurs at the connection between the iron foot and the lower surface.

(3) With the raise of relative humidity and pollution degree, the overall temperature rise of the insulator string gradually raises. The temperature difference between zero resistance insulator and other insulators also raises gradually, but the temperature difference between adjacent non-zero resistance insulators is still small.

DATA AVAILABILITY STATEMENT

The raw data supporting the conclusion of this article will be made available by the authors, without undue reservation.

AUTHOR CONTRIBUTIONS

LC, FL, and MC conceived the idea and designed the experiments. XH, RH, and YZ led the experiments. All authors read and approved the final manuscript.

FUNDING

This study was supported by the State Grid FujianElectric Power Co., Ltd. technology project (Grant No.52130A2000F). The funder was not involved in the study design, collection, analysis, interpretation of data, the writing of this article or the decision to submit it for publication.

REFERENCES

Chen, Y., Gou, J. f., and Wu, X. J. (2015). Experimental Study of Zero Resistance and Pollution Insulators Rapid Detection Based on Infrared Temperature Measurement. *High. Volt. Appar.* 51 (06), 191–194+199. doi:10.13296/j.1001-1609.hva.2015.06.033

Ilha, S., Ozdemir, A., Jayaram, S. H., and Cherney, E. A. (2012). Emulations of Pollution and Their Effects on the Electrical Performance of Glass Suspension Insulators. 2012 Annual Report Conference on Electrical Insulation and Dielectric Phenomena, 14-17 October 2012, Montreal, QC, Canada, 803–806. doi:10.1109/CEIDP.2012.6378902

Ilha, S., Ozdemir., A., Jayaram., S. H., and Cherney, E. A. (2015). Numerical and Experimental Investigation of the Effects of Pollution on Glass Suspension-type Insulators. *IEEE Trans. Dielect. Electr. Insul.* 22 (5), 2987–2994. doi:10.1109/TDEI.2015.004863

Liu, Y. P., Zhang, K. Y., and Fu, W. P., (2018). Thermal Characteristics of Low Value Porcelain Insulators under Different Humidity. *High. Volt. Technol.* 44 (06), 1741–1749. doi:10.13336/j.1003-6520.hve.20180529003

Mei, H. W., Zhao, C. L., Dai, H. Q., and Wang, L. (2014). Study on Wetting Characteristics of Contaminated Porcelain and Glass Insulators. *Proc. csee* 34 (09), 1471–1480. doi:10.13334/j.0258-8013.pcsee

Reddy, B. S., and Nagabhushana, G. R. (2003). Study of Temperature Distribution along an Artificially Polluted Insulator String. *Plasma Sci. Tech.* 5 (2), 1715–1720. doi:10.1088/1009-0630/5/2/006

Vitelli, M., Tucci, V., and Petrarca, C. (2000). Temperature Distribution along an Outdoor Insulator Subjected to Different Pollution Levels. *IEEE Trans. Dielect. Electr. Insul.* 7 (3), 416–423. doi:10.1109/94.848929

Xu, Z. N., Lu, F. C., Li, H. M., and Liu, Y. (2011). Influence Factors and Optimization of Electric Field Finite Element Analysis of Insulators. *High. Volt. Technol.* 37 (04), 944–951. doi:10.13336/j.1003-6520.hve.2011.04.021

Yuan, L., Zhao, R., and Tan, X. Y., (2018). Zero Resistance Insulator Detection Based on Infrared Imaging Technology. *High. Volt. Appar.* 54 (02), 97–102. doi:10.13296/j.1001-1609.hva.2018.02.016

YuanJ, H. (2008). *Study on Ac Pollution Flashover Characteristics and Discharge Process of Insulators (String) in Transmission Line*. Chongqing: Chongqing University.

Zhang, Y., Peng, Z. J., and Fu, Q., (2018). Implications for Ambient Humidity on Voltage and Infrared Thermal Image Detection of Ceramic Insulators String. *Power Grid Technol.* 42 (04), 1342–1349. doi:10.13335/j.1000-3673.pst.2017.1369

Conflict of Interest: LC, FL, MC, XH, RH, and YZ were employed by the EVH Branch Company of State Grid Fujian Electric Power Co. LTD.

Publisher's Note: All claims expressed in this article are solely those of the authors and do not necessarily represent those of their affiliated organizations, or those of the publisher, the editors, and the reviewers. Any product that may be evaluated in this article, or claim that may be made by its manufacturer, is not guaranteed or endorsed by the publisher.

frontiers | Frontiers in Energy Research

TYPE Brief Research Report
PUBLISHED 23 August 2022
DOI 10.3389/fenrg.2022.975462

OPEN ACCESS

EDITED BY
Tinghui Ouyang,
National Institute of Advanced Industrial Science and Technology (AIST), Japan

REVIEWED BY
Zhang Zhao,
Yanshan University, China
Cheng Wang,
Yanshan University, China

*CORRESPONDENCE
QiongYao Xie,
4565919@qq.com

SPECIALTY SECTION
This article was submitted to Smart Grids,
a section of the journal
Frontiers in Energy Research

RECEIVED 22 June 2022
ACCEPTED 20 July 2022
PUBLISHED 23 August 2022

CITATION
Liu Z, Xie Q, Dai L, Wang H, Deng L, Wang C, Zhang Y, Zhou X, Yang C, Xiang C and Qin S (2022), Research on comprehensive evaluation method of distribution network based on AHP-entropy weighting method.
Front. Energy Res. 10:975462.
doi: 10.3389/fenrg.2022.975462

Research on comprehensive evaluation method of distribution network based on AHP-entropy weighting method

ZiWei Liu, QiongYao Xie*, Lu Dai, HaiLiang Wang, Ling Deng, Chun Wang, Yu Zhang, XiaoXia Zhou, ChuYuan Yang, Chuan Xiang and SiYu Qin

State Grid Yichang Power Supply Company, Yichang, China

In the context of smart grid planning and construction, how to tackle the future distribution network, a comprehensive evaluation of smart distribution network planning has become an urgent problem to be solved. To address this issue, this research provides a method for comprehensive evaluation that combines subjective and objective weighing approaches. Firstly, a set of evaluation index system is constructed and quantified based on the characteristics of the future distribution network; after that a comprehensive evaluation model is established and a subjective and objective weighting method combining AHP-entropy weighting method is used to weight the indicators; Finally, the actual data from the distribution network is evaluated and scored. Based on the scoring verification results, the correctness and effectiveness of the method proposed in this paper are verified.

KEYWORDS

future distribution, smart grid planning and construction, overview, a method combining subjective and objective weighting methods, AHP-entropy weight method

Introduction

Smart grid offers unrivaled capabilities, making it an unavoidable trend in the evolution of modern electricity grids. The smart distribution network is especially important in a smart power grid (Zhang et al., 2014; Liu et al., 2015; Wang et al., 2015). The comprehensive evaluation of smart distribution networks is critical in the context of smart power grid design and development (Zeng et al., 2018; Yang et al., 2021a). The current comprehensive examination has yielded many benefits, but it is insufficient for the future distribution network's quick growth. Therefore, it is of far-reaching practical significance to establish a set of distribution network evaluation index system and evaluation method in line with China's national conditions (Yang et al., 2021b; Yang et al., 2021c; Yang et al., 2022a).

Nowadays, there are many literatures on comprehensive evaluation. Comprehensive evaluation includes two aspects: analysis and evaluation index system and evaluation method based on existing index system. Practical experience is frequently used in the

examination and evaluation of the index system. Subjective considerations have far too much influence, despite the fact that it is practical and intuitive. The other kind of evaluation approach examines a specific metric, such as economy, reliability, environmental protection, etc. (Zhang et al., 2015; Dong et al., 2016; Boutaba et al., 2018; Chen et al., 2018; He et al., 2018; Wei et al., 2018; Huang et al., 2019; Yang et al., 2021b; Yang et al., 2021c; Yang et al., 2022a; Yang et al., 2022b).

Literature (Wei et al., 2018) establishes an evaluation index system from five aspects: power supply capability, power supply reliability, power quality, economy and abundance, and then uses analytic hierarchy approach to create an evaluation model. Based on the evaluation method of analytic hierarchy Process, literature (Huang et al., 2019) analyses the technical, economic, and environmental aspects of distribution networks. Literature (He et al., 2018) is based on the construction of the evaluation system of the target grid, and quantitative evaluation of the distribution network is carried out with the comprehensive evaluation method of fuzzy mathematics. Chen B et al. used network analysis method with anti-entropy method to determine index weight and scoring function, and tackled the problem of cross and mutual influence among indicators caused by inaccurate weight (Chen et al., 2018). In the evaluation of distribution network, literature (Zhang et al., 2015; Dong et al., 2016) builds a comprehensive evaluation index system including economy, sociality and environment. Different from the previous literature that only studied a single user group, the traditional variable weight calculation method in literature (Yang et al., 2022b) is characterized by difficult selection of state variable weight vector and weak operability. As a result, this research provides a shape similarity-based variable weight computation method. In order to reduce disparities caused by artificial subjective selection and improve the credibility of evaluation results, literature (Boutaba et al., 2018) proposed the combinatorial fuzzy comprehensive evaluation method. Literature (Zhang and Lv, 2018) determined the weight assignment of each indicator based on analytic hierarchy process and enhanced entropy weight method, and established VIKOR multi-criteria evaluation system. Literature (Tian et al., 2019) provided a discrete energy flow calculation approach and an energy efficiency evaluation method based on a weighted directed graph equivalent model of the system. Literature (Yu et al., 2016) makes an overall review of distribution network evaluation. On the whole, the evaluation system cannot be studied solely from the subjective or objective standpoint. As a result, it is vital to investigate an evaluation precess that incorporates both subjective and objective components in order to conduct a full evaluation that is more comprehensive and complete, as well as more accurate and compelling evaluation outcomes.

To sum up, this research presents a comprehensive weight assignment mechanism based on AHP-entropy weighting method for future distribution network system (Xiong et al., 2022). The combination of subjective and objective weights makes the evaluation method more scientific, which makes up for the problems of too subjective and unstable weights in traditional AHP method. Firstly, a system of evaluation indexes is created, with the first level indexes being economy, dependability, environmental protection, and interactivity. Then, the comprehensive weighting method is used to assign weights to the indexes. Finally, the distribution network of Yichang city is selected to substitute the actual data to score and calculate the indexes. The results of an example verify the effectiveness of the proposed method, and the relevant research can provide an auxiliary decision-making basis for the construction and transformation of distribution network.

Comprehensive evaluation system construction

Comprehensive evaluation index

The establishment of a comprehensive evaluation index system is the basis of regional smart grid evaluation. It is necessary to cover all aspects of smart grid based on the development situation and objectives of China's smart grid and reflect the planning benefits and technical characteristics of regional smart grid (Ma et al., 2022). It mainly includes the following four indicators, Figure 1 shows the evaluation index system:

(1) Economic index

Economic index can reflect the interdependence of various technological and economic phenomena and processes. Also, it reflects the technical level, management level and economic results of production and management activities.

1) Investment Cost: It can be broken down into three categories: initial investment, operation and maintenance, and failure costs. The initial investment cost includes design and planning cost, equipment purchase cost and building installation cost. The design and planning cost and equipment purchase cost will vary substantially between regions, reflecting regional differentiation according to different coefficients. Operation and maintenance costs are made up of three components: operation, maintenance, and other charges, all of which are influenced by the line loss rate. Failure cost mainly includes outage loss cost and failure loss cost.

$$C_a = C_i + C_{OM} + C_F \tag{1}$$

In the equation: C_a is the investment cost, C_i is the initial investment cost, C_{OM} is the operation and maintenance cost, and C_F is the failure cost.

2) Comprehensive line loss rate: represents the percentage of the power lost on the line to the power output of the first section of the line.

$$\Delta P = \frac{Q_s - Q_p}{Q_s} \tag{2}$$

In the equation, ΔP is the comprehensive line loss rate, Q_s is the electricity supply, and Q_p is the electricity consumption.

3) Increased load of unit investment: refers to the ratio of increased load to investment cost.

$$Q_l = \frac{Q_{\ln} - Q_{ll}}{Q_{al}} \tag{3}$$

In the equation: Q_l is the increased load of investment, $Q_{\ln}$ is the current year's load, Q_{ll} is the last year's load, and Q_{al} is the last year's grid investment cost.

(2) Reliability index

Power system reliability is measured by quantitative reliability indexes, which can be the probability, frequency and duration of unfavorable impacts caused by faults on power users, as well as the expected power loss and expected power energy loss caused by faults.

1) Total pass rate: refers to the ratio of the number of lines satisfying N-1 to the total number of lines.

$$K_{pr} = \frac{N_N}{N_{al}} \tag{4}$$

In the equation, K_{pr} is the total pass rate, N_N is the number of lines satisfying N-1, and N_{al} is the total number of lines.

2) Total main transformer overload rate: refers to the proportion of the number of overload main transformer stations in the total number of main transformer stations. Overload main transformer refers to a transformer that has a maximum load ratio of more than 80% and a single duration of more than 2 hours.

$$K_{ol} = \frac{N_{ol}}{N_{mt}} \tag{5}$$

In the equation, K_{ol} is the overall overload rate, N_{ol} is the number of overload main transformer stations, and N_{mt} is the total number of main transformer stations.

3) Average user outage time: refers to the ratio of the total user outage duration to total number of users in a unit of time.

$$T_{ap} = \frac{T_i}{N_i} \tag{6}$$

In the equation: T_{ap} is the average outage time of users, T_i is the total outage time of users, and N_i is the total number of users.

(3) environmental protection index

Under the influence of global warming and energy crisis, various governments n the world are vigorously advocating a low-carbon economy and building green power grid. The so-called development of green power grid refers to the construction of resource-saving and environment-friendly power grid based on the principles of "security, economy, green and harmony" (Guo and Xiang, 2022).

1) Distributed power permeability: refers to the ratio of distributed power installed capacity to 110 kV public substation capacity.

$$K_p = \frac{Q_{dg}}{Q_r} \tag{7}$$

In the equation, K_p is the permeability of distributed power; Q_{dg} is the installed capacity of distributed power; Q_r is 110 kV public substation capacity.

2) Percentage of installed renewable energy: refers to the percentage of installed renewable energy power generation capacity in the total installed regional power generation capacity.

$$K_r = \frac{Q_{re}}{Q_{al}} \tag{8}$$

In the equation: K_r is the proportion of installed renewable energy, Q_{re} is the installed capacity of renewable energy power generation, and Q_{al} is the total installed capacity.

3) Proportion of renewable energy generation in electricity generation: refers to the proportion of renewable energy generation in electricity generation.

$$K_p = \frac{Q_{rp}}{Q_{al}} \tag{9}$$

In the equation: K_p is the proportion of renewable energy in electricity generation, Q_{rp} is the amount of renewable energy, and Q_{al} is the total installed capacity.

(4) interactive index

Interaction is another crucial feature of intelligent distribution network (Li et al., 2021a). The interaction of distribution networks not only alters the traditional distribution network's single direction of source-load and enables power distribution to be connected to the grid, but also alters the traditional distribution network's monogeneity of power flow, and increases the network frame's flexibility.

1) Power distribution information collection rate: refers to the ratio of the number of distribution transformers that collect information to the total number of distribution transformers.

$$K_{as} = \frac{N_{as}}{N_{um}} \tag{10}$$

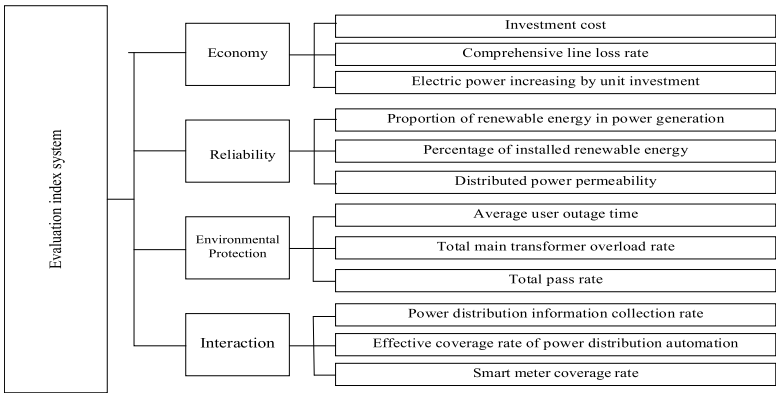

FIGURE 1
Evaluation index system diagram.

TABLE 1 Evaluation criteria of comprehensive evaluation indexes.

First-level Index	Second-level Index	Criteria					
		0	20	40	60	80	100
Economy	Investment cost (100 Million Yuan)	30	26	22	18	14	10
	Comprehensive line loss rate (%)	4.2	4.0	3.8	3.6	3.4	3.2
	Electric power increasing by unit investment (kWh/10 Thousand-yuan)	0	4,000	8,000	12000	16000	20000
Reliability	Total pass rate (%)	0	20	40	60	80	100
	Total main transformer overload rate (%)	10	8	6	4	2	0
	Average user outage time(h)	20	16	12	8	4	0
Environmental Protection	Distributed power permeability (%)	0	2	4	6	8	10
	Percentage of installed renewable energy (%)	0	20	40	60	80	100
	Proportion of renewable energy in power generation (%)	0	20	40	60	80	100
Interaction	Power distribution information collection rate (%)	95	96	97	98	99	100
	Effective coverage rate of power distribution automation (%)	0	20	40	60	80	100
	Smart meter coverage rate (%)	0	20	40	60	80	100

TABLE 2 Distribution network comprehensive score of Yichang in 2021.

Year	Category	Total Score	First-level Index Score			
			Economy	reliability	Environmental protection	Interaction
2021	Full Mark	100	29.65	36.4	18.45	15.5
	Actual Point	59.085	15.72	20.56	11.02	11.785
	Loss Point	40.915	13.93	15.84	7.43	3.715
2025	Full Mark	100	29.65	36.4	18.45	15.5
	Actual Point	79.86	23.72	29.02	11.62	15.5
	Loss Point	20.14	5.93	7.38	6.83	0

In the equation, K_{as} is the distribution information collection rate, N_{as} is the number of distribution stations for information collection, and N_{nm} is the total number of distribution stations.

2) Effective coverage rate of distribution automation: refers to the ratio of the number of 10 kV lines effectively covered by distribution automation in a region to the total number of 10 kV lines in a region.

$$K_c = \frac{N_{dc}}{N_{10a}} \tag{11}$$

In the equation, K_c is the effective coverage rate of power distribution, N_{dc} is the number of 10 kV lines effectively covered by power distribution automation, and N_{10a} is the total number of 10 kV lines.

3) Smart meter coverage rate: refers to the proportion of smart meters installed in the total number of installed meters.

$$K_{sm} = \frac{N_{sm}}{N_{un}} \tag{12}$$

In the equation: K_{sm} is the coverage rate of smart meter; N_{sm} is the number of smart meter users; N_{um} is the total number of power users.

Comprehensive evaluation method

The first step in a complete evaluation of a system is to weight the index, and then use the weight analysis method to obtain the final result of the evaluation. The selection of weight method and weight evaluation method is particularly important in the process (Li et al., 2021b). Typical systematic evaluation methods are mainly weighted by subjective analysis or objective data. When either of them is used alone, the evaluation results will be overly subjective or too objective. Therefore, the complete weighting approach, which combines subjective and objective weighting methods, can be applied.

The analytic hierarchy process is commonly used in the subjective weighting method. The weighting of each tier in the analytic hierarchy process will eventually effect the result, either directly or indirectly, and the degree of influence of each component in each layer on the result is quantifiable and extremely evident. This method can be used especially for the system evaluation of unstructured characteristics and the system evaluation of multi - objective, multi - criteria and multi—period (Li, 2022a). The analytic hierarchy process is focused mainly on the evaluator's understanding of the essence and elements of the evaluation problem, and focuses on qualitative analysis and judgment more than general quantitative methods.

The entropy weight technique is commonly used in objective weighting method, which can profoundly reflect the ability to distinguish indicators, determine better weight, weighting is more objective, has theoretical basis, and has higher credibility.

As a result, the index weight adopts the method of combining subjective and objective weights. The analytic hierarchy process is used to calculate the subjective weight, and the entropy weight method is used to evaluate the objective weight. In this way, the subjective error can be minimized as much as possible, resulting in more scientific and fair outcomes (Li, 2022b).

(1) Basic steps of analytic hierarchy process

1) Build a hierarchy model. A clear hierarchy structure is established for the evaluation target. Then, an evaluation index system is formed.

2) Construct the judgment matrix and form the comparative judgment matrix of every two indexes layer by layer.

Construct the judgment matrix X, and its expression is denoted as:

$$X = \begin{bmatrix} x_{11} & x_{12} & \cdots & x_{1p} \\ x_{21} & x_{22} & \cdots & x_{2p} \\ \cdots & \cdots & \cdots & \cdots \\ x_{n1} & x_{n2} & \cdots & x_{np} \end{bmatrix} \tag{13}$$

In the equation, x_{ij} represents the importance of x_i relative to x_j.

3) Take consistency test, the calculation equation of consistency index CR is as follows:

$$CR = \frac{CI}{RI} \tag{14}$$

In the equation, when CR is less than 0.1, the judgment matrix satisfies the consistency requirements, CI stands for the consistency index, RI is the average random consistency index, and the consistency index CI is calculated as follows:

$$CI = \frac{\lambda_{\max} - n}{n - 1} \tag{15}$$

4) After passing the consistency test, the vector of the maximum characteristic root of $\lambda_{\max}$ is solved, which is the weight of the index through normalization.

(2) Basic steps of entropy weight method

1) The original data matrix is selected and the calculation equation is as follows:

$$R = \begin{bmatrix} r_{11} & r_{12} & r_{13} & \cdots & r_{1n} \\ r_{21} & r_{22} & r_{23} & \cdots & r_{2n} \\ \vdots & \vdots & \vdots & \vdots & \vdots \\ r_{m1} & r_{m2} & r_{m3} & \cdots & r_{mn} \end{bmatrix} \tag{16}$$

In the equation, $r_{ij(m*n)}$ represents the jth evaluation value of i evaluation objects.

2) Calculate the characteristic proportion of the evaluation object i under jth index, and the calculation equation is as follows:

$$p_{ij} = r_{ij} \Big/ \sum_{i=1}^{n} r_{ij} \tag{17}$$

3) Calculate the entropy value of *j*th index, and the calculation equation is as follows:

$$e_j = -k \sum_{n=1}^{n} p_{ij} Inp_{ij} \tag{18}$$

4) To calculate the difference coefficient of *j*th index, the equation is as follows:

$$g_j = 1 - e_j \tag{19}$$

5) Determine the weight coefficient of *j*th index, and the calculation equation is as follows:

$$w_j = e_j \Big/ \sum_{j=1}^{m} e_j \tag{20}$$

(3) Comprehensive weighting method

According to their own experience and subjective assessment of the scenario, experts determine the subjective weighting technique. The weight of indicators is directly given by experts, and the rationality of the weight is affected by their subjective understanding. Combination weighting method is the combination of subjective weighting method and objective weighting method, which can ensure not only the important index judgment of experts, but also the value of data information, resulting in a more appropriate weight obtained by combination weighting.

If the subjective weight obtained by analytic hierarchy process is:

$$z = [\, z_1 \quad z_2 \quad \cdots \quad z_n \,] \tag{21}$$

If the objective weight obtained by the entropy weight method is:

$$w = [\, w_1 \quad w_2 \quad \cdots \quad w_n \,] \tag{22}$$

Then, the calculation equation of combination weighting is:

$$u = \beta z + (1 - \beta) w \tag{23}$$

In Eq 23, β is the resolution coefficient, usually defined as 0.5.

(4) Comprehensive evaluation model

In order to obtain the final comprehensive evaluation results, a comprehensive evaluation model is established, as shown below:

$$P = \sum S_{ij} F_{ij} \tag{24}$$

In the equation, S_{ij} represents the weight of *j*th index at the *i*th index level, and F_{ij} represents the score value of *j*th index at the *i*th index level.

According to the comprehensive evaluation index system of smart distribution network established above, a two-layer index system of economy, reliability, environmental protection and interaction is established. The comprehensive evaluation model of smart distribution network planning is shown as follows:

$$P = S_1 \times F_1 + S_2 \times F_2 + S_3 \times F_3 + S_4 \times F_4 \tag{25}$$

In the equation, S_1, S_2, S_3 and S_4 represent the weights of first-level indicators of economy, reliability, environmental protection and interaction respectively. Moreover, $S_1 + S_2 + S_3 + S_4 = 1$. F_1, F_2, F_3 and F_4 represent the score values of first-level indicators of economy, reliability, environmental protection and interaction respectively, and their calculation equations are as follows:

$$P = \sum S_{ij} f_{ij} \quad (\mathrm{i} = 1, 2, 3, 4, 5) \tag{26}$$

In the equation, s_{ij} represents the weight of second-level indicators under first-level indicators, and f_{ij} represents the score value of second-level indicators under first-level indicators.

Index weight determination and criterion selection

According to Eqs 13–15, the weight of economy, reliability, environmental protection and interaction of the first-level index can be obtained: $z = [\, 0.33 \quad 0.47 \quad 0.13 \quad 0.07 \,]$

In the same way, the weight of investment cost, comprehensive line loss rate and power supply increment per unit investment for second-level index under economy of first-level index is: $z = [\, 0.54 \quad 0.30 \quad 0.16 \,]$

Under the reliability of the first-level index, the weights of the second-level index, such as total pass rate, total main transformer overload rate and average user outage time, are as follows: $z = [\, 0.24 \quad 0.14 \quad 0.62 \,]$

The weight of distributed power permeability, installed proportion of renewable energy, and proportion of renewable energy power in electricity generation under environmental protection are as follows: $z = [\, 0.5 \quad 0.25 \quad 0.25 \,]$

Through analytic hierarchy process, the initial weight of the 12 indexes are 0.1782.0.099.0.0528.0.1128.0.0658.0.2914.0.065. 0.0325.0.0325.0.065.0.0325.0.0325.

According to Eq 18, the index entropy value e_j can be obtained as follows: 0.48.0.622.0.441.0.514.0.5.0.562.0.434.0.631. 0.617.0.631.0.419.0.631.

According to the entropy value e_j and Eq 19, the index difference coefficient g_j are 0.52.0.378.0.559.0.486.0.5.0.438. 0.566.0.369.0.383.0.369.0.581.0.369.

According to Equation 20, the weight coefficient w_j of the 12 indicators can be obtained as 0.094.0.068.0.101.0.088.0.091. 0.079.0.103.0.067.0.069.0.067.0.105.0.068.

According to Eq 23, the initial weight obtained by analytic hierarchy process is modified by weight coefficient, and the combined weight of 12 indexs is finally calculated as follows: 0.1361.0.0835.0.0769.0.1004.0.0784.0.1852.0.084.0.04975, 0.05075,0.051.0.06125,0.04275.

Because the index value is in a certain range, the distribution network can ensure proper operation. In combination with the values specified in some indicators in technical Guidelines for Distribution Network Planning and Design of State Grid, and the experience of several experts in existing studies, the evaluation criteria of indicators are finally determined. The Table 1 shows the specific standard setting.

Example analysis

This paper takes the actual data of urban distribution network planning in Yichang, Hubei Province in 2021 as an example and compares it with the planning data in 2025. The data comes from the city power company. The comprehensive evaluation index system and comprehensive evaluation model method established in this research are used to analyze the urban distribution network of the city and validate the rationality and practicality of this study.

From the four aspects of distribution network economy, reliability, environmental protection and interaction, the actual situation of distribution network operation in Yichang city is described. According to the indexes established above, the situation of power grid in Yichang region in 2021 is completely assessed, and the specific work is as follows. The Table 2 shows the Distribution network comprehensive score of Yichang in 2021.

(1) Economic analysis

1) Investment cost: The investment cost of Yichang Power grid in 2021 is 1996.004 million yuan, and the score calculated according to the weight is 6.83 points (full mark 13.61 points);

2) Comprehensive line loss rate: the comprehensive line loss rate of Yichang power grid is 3.6% in 2021, and the score calculated according to the weight is 5.01 points (full mark 8.35 points);

3) Electric power increasing by unit investment: electric power increasing by unit investment of Yichang Power grid is 10100 (kWh/ten thousand yuan) in 2021, and the score calculated according to the weight is 3.88 points (full mark 7.69 points).

(2) Reliability analysis

1) Total pass rate: In 2021, the total pass rate of Yichang Power grid is 59.8%, and the score calculated based on weight is 6.00 points (full mark 10.04 points);

2) Total main transformer overload rate: In 2021, the total main transformer overload rate of Yichang power grid is 4.4%, the score calculated according to the weight is 4.39 points (full mark 7.84 points);

3) Average user outage time: In 2021, the average power outage time of Yichang power grid users is 9.02 h, and the score calculated according to the weight is 10.17 points (full mark 18.52 points).

(3) Environmental protection analysis

1) Distributed power permeability: the distributed power permeability of Yichang power grid in 2021 is 3.55%, with a score of 2.98 points (full mark 8.4 points) calculated based on weights;

2) Percentage of installed renewable energy: the percentage of installed renewable energy in Yichang power grid in 2021 will be 80%, with a score of 3.98 points (full mark 4.975 points) calculated based on weights;

3) Proportion of renewable energy in power generation: the proportion of renewable energy in power generation of Yichang power grid in 2021 will be 80%, with a score of 4.06 points (full mark 5.075 points) calculated according to the weight.

(4) Interactive analysis

1) Power distribution information collection rate: the power distribution information collection rate of Yichang power grid in 2021 is 100%, with a score of 5.1 points (full mark 5.1 points) calculated based on weights;

2) Effective coverage rate of power distribution automation: the effective coverage rate of power distribution automation of Yichang power grid in 2011 is 39.35%, and the score calculated based on weight is 2.41 points (full amrk 6.125 points);

3) Smart meter coverage rate: The coverage rate of smart meters in Yichang power grid will be 100% in 2021. The score calculated based on weights is 4.275 points (full mark 4.275 point).

Similarly, from four aspects of distribution network economy, reliability, environmental protection and interaction, the planning data of Yichang power distribution network in 2025 are comprehensively scored, and the specific work is as follows.

(1) Economic analysis

1) Investment cost: The investment cost of Yichang Power grid in 2025 is 1,400 million yuan, and the score calculated according to the weight is 10.89 points (full mark 13.61 points);

2) Comprehensive line loss rate: the comprehensive line loss rate of Yichang power grid is 3.4% in 2025, and the score

calculated according to the weight is 6.68 points (full mark 8.35 points);

3) Electric power increasing by unit investment: electric power increasing by unit investment of Yichang Power grid is 16000 (kWh/ten thousand yuan) in 2025, and the score calculated according to the weight is 6.15 points (full mark 7.69 points).

(2) Reliability analysis

1) Total pass rate: In 2025, the total pass rate of Yichang Power grid is 75%, and the score calculated based on weight is 7.53 points (full mark 10.04 points);

2) Total main transformer overload rate: In 2025, the total main transformer overload rate of Yichang power grid is 0%, the score calculated according to the weight is 7.84 points (full mark 7.84 points);

3) Average user outage time: In 2021, the average power outage time of Yichang power grid users is 5.26 h, and the score calculated according to the weight is 13.65 points (full mark 18.52 points).

(3) Environmental protection analysis

1) Distributed power permeability: the distributed power permeability of Yichang power grid in 2025 is 7%, with a score of 3.48 points (full mark 8.4 points) calculated based on weights;

2)Percentage of installed renewable energy: the percentage of installed renewable energy in Yichang power grid in 2025 will be 80%, with a score of 3.98 points (full mark 4.975 points) calculated based on weights;

3)Proportion of renewable energy in power generation: the proportion of renewable energy in power generation of Yichang power grid in 2025 will be 82%, with a score of 4.16 points (full mark 5.075 points) calculated according to the weight.

(4) Interactive analysis

1) Power distribution information collection rate: the power distribution information collection rate of Yichang power grid in 2025 is 100%, with a score of 5.1 points (full mark 5.1 points) calculated based on weights;

2) Effective coverage rate of power distribution automation: the effective coverage rate of power distribution automation of Yichang power grid in 2011 is 100%, and the score calculated based on weight is 6.125 points (full amrk 6.125 points);

3) Smart meter coverage rate: The coverage rate of smart meters in Yichang power grid will be 100% in 2025. The score calculated based on weights is 4.275 points (full mark 4.275 point).

Conclusion

In this paper, a comprehensive weight assignment method based on AHP-entropy weight method is proposed for future distribution network system. According to the simulation example, after comparing the actual data in 2021 with the planned data in 2025, the conclusions are as follows:

Following the implementation of the evaluation system in Yichang, the comprehensive evaluation results can clearly reflect the overall development level of the future distribution network in Yichang, and are essentially consistent with Yichang's economic and social positioning, which verifies the feasibility and rationality of the comprehensive evaluation system and evaluation method proposed in this paper.

1) In terms of economy, the power grid investment in 2021 is excessive, resulting in a low value of increased power per unit investment, and a high comprehensive line loss rate due to the influence of the management system, resulting in a negative economic score.
2) In terms of reliability in 2021, the line with heavy load is not properly distributed and the load rate of the line is not balanced. A low total pass rate is caused by an invalid connection and a high line load rate. Meanwhile, the average power outage time of users is long, resulting in a low final reliability score.
3) In 2021, The poor score of distributed power permeability owing to the little amount of distributed power is the key element impacting the environmental protection score.
4) In 2021, The main element effecting the score of interactive index is that at least two "three-remote" switches are configured on the main line, as well as a low number of 10 kV lines with at least three sections, resulting in a low effective coverage rate of distribution automation.

In this paper, only a few representative indicators are selected in the selection of indicators, and more indicators can be selected for subsequent calculation to make the evaluation system more complete and scientific. In the present and the future integrated energy system is the development trend of future energy field, with the emergence of integrated energy system, various forms of energy can replace, mutual transformation and ensure the operation of power system great changes have taken place, its running state will be more complex, not only at this time to study distribution network from the distribution network more extended to evaluate the whole integrated energy system.

Data availability statement

The original contributions presented in the study are included in the article/supplementary material further inquiries can be directed to the corresponding author.

Author contributions

ZL: Conceptualization, Software, Investigation, Formal Analysis, Writing—Original Draft; QX: Data Curation, Methodology, Writing—Original Draft; LuD: Visualization; HW: Visualization; LiD: Investigation; CW: Investigation; YZ: Supervision; XZ: Supervision; CY: Visualization; CX: Writing—Review and Editing; SQ: Writing—Review and; Editing.

Conflict of interest

The authors declare that the research was conducted in the absence of any commercial or financial relationships that could be construed as a potential conflict of interest.

Publisher's note

All claims expressed in this article are solely those of the authors and do not necessarily represent those of their affiliated organizations, or those of the publisher, the editors and the reviewers. Any product that may be evaluated in this article, or claim that may be made by its manufacturer, is not guaranteed or endorsed by the publisher.

References

Boutaba, R., Salahuddin, M. A., Limam, N., Ayoubi, S., Shahriar, N., Estrada-Solano, F., et al. (2018). A comprehensive survey on machine learning for networking: Evolution, applications and research opportunities. *J. Internet Serv. Appl.* 9 (1), 16–99. doi:10.1186/s13174-018-0087-2

Chen, B., Liao, Q., Liu, D., and Wang, W. (2018). Comprehensive evaluation indices and methods for regional integrated energy system. *Automation Electr. Power* 42 (4), 174–182. doi:10.7500/AEPS20170605005

Dong, F., Zhang, Y., and Shang, M. (2016). Research on multi-index comprehensive evaluation of distributed energy system [J]. *Proc. CSEE* 36 (12), 3214–3223. doi:10.13334/j.0258-8013.pcsee.152536

Guo, Y., and Xiang, Y. (2022). Low-carbon strategic planning of integrated energy systems. *Front. Energy Res.* 10, 858119. doi:10.3389/fenrg.2022.858119

He, Y., Chen, Y., Yang, Z., He, H., and Liu, L. (2018). A review on the influence of intelligent power consumption technologies on the utilization rate of distribution network equipment. *Prot. Control Mod. Power Syst.* 3, 18. doi:10.1186/s41601-018-0092-2

Huang, W., Zhang, N., Kang, C., Li, M., and Huo, M. (2019). From demand response to integrated demand response: Review and prospect of research and application. *Prot. Control Mod. Power Syst.* 4, 12. doi:10.1186/s41601-019-0126-4

Li, H., Deng, J., Yuan, S., Feng, P., and Arachchige, D. D. (2021a). Monitoring and identifying wind turbine generator bearing faults using deep belief network and EWMA control charts. *Front. Energy Res.* 9, 770. doi:10.3389/fenrg.2021.799039

Li, H., Deng, J., Feng, P., Pu, C., Arachchige, D. D., and Cheng, Q. (2021b). Short-term nacelle orientation forecasting using bilinear transformation and ICEEMDAN framework. *Front. Energy Res.* 697. doi:10.3389/fenrg.2021.780928

Li, H. (2022a). Short-term wind power prediction via spatial temporal analysis and deep residual networks. *Front. Energy Res.* 10, 920407. doi:10.3389/fenrg.2022.920407

Li, H. (2022b). SCADA data based wind power interval prediction using LUBE-based deep residual networks. *Front. Energy Res.* 10, 920837. doi:10.3389/fenrg.2022.920837

Liu, K., Sheng, W., Zhang, D., Jia, D., Hu, L., and He, K. (2015). Research on application requirements and scenario analysis of big data in smart distribution network. *Proc. CSEE* 35 (02), 287–293. doi:10.13334/j.0258-8013.pcsee.2015.02.004

Ma, W., Deng, W., Pei, W., Yang, H., Wang, Y., Wang, L., et al. (2022). Operation optimization of electric power - hot water - steam integrated energy system. *Energy Rep.* 8 (S5), 475–482. doi:10.1016/j.egyr.2022.02.218

Tian, L., Cheng, L., Li, R., Sun, S., Shi, C., and Gao, W. (2019). A multi-scenario energy efficiency evaluation method for the integrated energy system in the park based on a weighted directed graph. *Proc. CSEE* 39 (22), 6471–6483. doi:10.13334/j.0258-8013.pcsee.181552

Wang, J., Ji, Z., Shi, M., Huang, F., Zhu, C., and Zhang, D. (2015). Research on demand analysis and application of big data for intelligent power distribution. *Proc. CSEE* 35 (08), 1829–1836. doi:10.13334/j.0258-8013.pcsee.2015.08.001

Wei, X., Yu, K., Chen, X., Yan, Y., Zhang, S., Jing, W., et al. (2018). Analysis of power large user segmentation based on Affinity propagation and K-means algorithm. *Power Demand Side Manag.* 20 (01), 15–19. doi:10.3969/j.issn.1009-1831.2018.01.005

Xiong, J., Sun, Y., Wang, J., Li, Z., Xu, Z., and Zhai, S. (2022). Multi-stage equipment optimal configuration of park-level integrated energy system considering flexible loads. *Int. J. Electr. Power Energy Syst.* 140, 108050. doi:10.1016/j.ijepes.2022.108050

Yang, N., Qin, T., Wu, L., Huang, Y., Huang, Y., Xing, C., et al. (2021a). A multi-agent game based joint planning approach for electricity-gas integrated energy systems considering wind power uncertainty. *Electr. Power Syst. Res.* 204, 107673. doi:10.1016/j.epsr.2021.107673

Yang, N., Dong, Z., Wu, L., et al. (2021b). A comprehensive review of security-constrained unit commitment. *J. Mod. Power Syst. Clean Energy* 10 (3), 562–576. doi:10.35833/MPCE.2021.000255

Yang, N., Yang, C., Xing, C., Ye, D., Jia, J., Chen, Y. W., et al. (2021c). Deep learning based SCUC decision-making: An intelligent data-driven approach with selflearning capabilities. *IET Generation Trans. Dist.* 16, 629–640. doi:10.1049/gtd2.12315

Yang, N., Yang, C., Wu, L., Shen, X., Jia, J., Li, Z., et al. (2022a). Intelligent data-driven decision-making method for dynamic multi-sequence: An E-Seq2Seq based SCUC expert system. *IEEE Trans. Ind. Inf.* 18, 3126–3137. doi:10.1109/TII.2021.3107406

Yang, N., He, Y., Dong, B., Qin, T., Ding, L., Yang, X., et al. (2022b). A multi-agent game-based incremental distribution network source–load–storage collaborative planning method considering uncertainties. *Front. Energy Res.* 10, 803716. doi:10.3389/fenrg.2022.803716

Yu, X., Xu, X., Chen, S., and Wu, J. (2016). A brief review to integrated energy system and energy internet. *Trans. China Electrotech. Soc.* 31 (01), 1–13. doi:10.19595/j.cnki.1000-6753.tces.2016.01.002

Zeng, M., Liu, Y., Zhou, P., et al. (2018). Review and prospects of integrated energy system modeling and benefit evaluation. *Power Syst. Technol.* 42 (6), 1697–1708. doi:10.13335/j.1000-3673.pst.2018.0150

Zhang, S., and Lv, S. (2018). Comprehensive energy system evaluation method for park microgrid. *Power Syst. Technol.* 42 (08), 2431–2439. doi:10.13335/j.1000-3673.pst.2018.0693

Zhang, T., Zhu, T., Gao, N., and Wu, Z. (2015). Research on optimal design and multi-index comprehensive evaluation method of distributed cooling, heating and power energy system [J]. *Proc. CSEE* 35 (14), 3706–3713. doi:10.13334/j.0258-8013.pcsee.2015.14.027

Zhang, X., Ge, S., Liu, H., Huang, X., and Huang, H. (2014). Comprehensive evaluation system and method of intelligent distribution network. *Power Syst. Technol.* 38 (01), 40–46. doi:10.13335/j.1000-3673.pst.2014.01.007

frontiers | Frontiers in Energy Research

TYPE Brief Research Report
PUBLISHED 23 August 2022
DOI 10.3389/fenrg.2022.954250

OPEN ACCESS

EDITED BY
Tinghui Ouyang,
National Institute of Advanced Industrial Science and Technology (AIST), Japan

REVIEWED BY
Gaurav Sachdeva,
DAV University, India
Sandeep Kumar Duran,
Lovely Professional University, India

*CORRESPONDENCE
Jun Wei Yao,
yao-721210@163.com

SPECIALTY SECTION
This article was submitted to Smart Grids,
a section of the journal
Frontiers in Energy Research

RECEIVED 27 May 2022
ACCEPTED 01 July 2022
PUBLISHED 23 August 2022

CITATION
Zhu XF, Yao JW, Xie QY, Dai L, Yang CY, Wang HL, He Q, Deng L, Shen R and Zhou XX (2022), Research on the user comprehensive energy consumption decision-making method based on the evolutionary game.
Front. Energy Res. 10:954250.
doi: 10.3389/fenrg.2022.954250

Research on the user comprehensive energy consumption decision-making method based on the evolutionary game

Xian Feng Zhu, Jun Wei Yao*, Qiong Yao Xie, Lu Dai, Chu Yuan Yang, Hai Liang Wang, Qi He, Ling Deng, Ran Shen and Xiao Xia Zhou

State Grid Yichang Power Supply Company, Yichang, China

With the increasing diversification of human energy consumption forms in the integrated energy market, analyzing the comprehensive energy consumption behavior of user groups according to their changing energy demand characteristics is an important issue to be urgently addressed. To solve this problem, an analysis method of user's comprehensive energy consumption behavior based on the evolutionary game is proposed in this article. First, three types of users including residents, large industries, and commercial users are considered for this purpose. Then, a utility model which takes into account the energy consumption characteristics of these users and their comfort factors is constructed based on the subjective and objective combination weighting method. Thereafter, an evolutionary game theory is used to analyze the dynamic selection process for users by selecting energy suppliers and then using the selection results when the evolutionary equilibrium is reached. Finally, the model is solved by using a distributed iterative method. The correctness and validity of the proposed method are verified by the simulation results.

KEYWORDS

integrated energy market, evolutionary game, user's comprehensive energy consumption behavior, subjective and objective combination weighting method, user utility model, evolutionary equilibrium

1 Introduction

With the deepening of the energy crisis, the integrated energy system, which can break the heterogeneous energy barrier and improve comprehensive energy consumption efficiency (Yu et al., 2016; Ai and Hao, 2018; Chen et al., 2020) has developed rapidly in the recent years. With the gradual advancement of the comprehensive energy marketization process, people have more and more diversified energy forms available to them in the process of energy consumption, such as natural gas, electric energy, coal, etc (Cui et al., 2019). On a longer time scale, people's energy consumption load may shift

between different forms of energy (Boutaba et al., 2018; Huang et al., 2019). Therefore, for an integrated energy system, different forms of heterogeneous energy will form new coupling nodes (Zeng et al., 2018) on the user side by linking people's energy consumption behavior (Yang et al., 2022a). In the aforementioned context, it is of great theoretical and practical significance (Yang and Wang, 2016; Liu et al., 2019) to study users' choice behavior of different forms of energy for the planning and operation of the future integrated energy system (Yang et al., 2021a; Yang et al., 2021b; Yang et al., 2022b).

Thus, this study proposes a comprehensive user energy consumption behavior analysis method based on the evolutionary game. First, a utility model is constructed according to the subjective and the objective combination weighting method taking into account the residential, large industrial, and the commercial users as the main users. This model is based upon their energy consumption characteristics and comfort level factors (Guan and Pu, 2010). On this basis, a game model is proposed to describe the dynamic process of user energy consumption choice based on the evolutionary game method. Finally, Jorgen (2015) the distributed iterative method is used to solve the model, and then the evolutionary equilibrium result is obtained (Samadi et al., 2012). Compared with the traditional method, the proposed method is more accurate and effective as it fully considers the dynamic evolutionary game process when users choose to consume different forms of energy. The results verify the effectiveness of the proposed method. Therefore, the research can provide a reference for energy suppliers to formulate a reasonable pricing strategy.

2 User utility index construction

This study comprehensively considers the reaction mechanism of users towards energy prices and incentive policies in the integrated energy market. It constructs the user utility evaluation index system from the angle of energy consumption characteristics and the user psychology, which mainly consists of the following four indicators: comprehensive energy consumption cost (*B1*), energy supply occupancy (*B2*), energy supply reliability rate (*B3*), and user comfort level (*B4*).

2.1 Comprehensive energy consumption cost

The energy price of different energy types will directly affect the energy consumption cost of users which will further affect users' energy consumption choices. Furthermore, the transformation cost of the user in the process of changing the energy type will also affect their energy choice decision. Therefore, this research studies the comprehensive energy consumption cost from the perspective of different types of user groups, including energy consumption cost and transformation cost. First, the research period is set as T, and in the research period, if m type users choose energy type n, then the comprehensive energy consumption cost of m type users choosing energy type n is illustrated as follows:

$$B_1 = \left(C_n^m + T_n^m\right) \Big/ \sum_{t=1}^{24} L_n^m(t). \tag{1}$$

In the aforementioned formula: C_{n}^m is the total energy consumption cost of an m-type user selecting energy type n, T_{n}^m is the total transformation cost of an m-type user selecting energy type n, and $L_n^m(t)$ is the actual energy consumption load of an m-type user selecting energy type n in period t.The calculation formula of energy consumption cost for each period when m type users select energy type n is as follows:

$$C_n^m = \sum_{t=1}^{24} \mathrm{p}_n(t) L_n^m(t). \tag{2}$$

In the aforementioned formula: $\mathrm{p}_{\mathrm{n}}(t)$ is the selling price of energy type n in time period t.

T_{n}^m in Eq. 1 contains the equipment installation cost of the user selecting a certain energy type for the first time and the equipment transformation cost after selecting a new energy type.

Taking into account the equipment differences caused by the conversion of electricity to natural gas, then the natural gas to heat and other energy sources as well as the user's equipment removal and installation costs, the specific formula is as shown as follows:

$$T_n^m = \sum_{t=1}^{24} \left(\Phi_n^m + \}Y_n^m\right) = \sum_{t=1}^{24} \left[\phi_{0,\mathrm{n}} \cdot \mathrm{x}_{0n}^m + \gamma_{c,n}^m \cdot \Delta \mathrm{x}_n^m(t)\right], \mathrm{t} = 2, \cdots, T, \tag{3}$$

$$\Delta \mathrm{x}_n^m(t) = \mathrm{x}_n^m(t) - \mathrm{x}_n^m(t-1), \Delta \mathrm{x}_n^m(t) > 0. \tag{4}$$

In the formula stated previously: Φ_n^m stands for the direct installation cost of the equipment generated by the user's first choice of an energy type; $\phi_{0,\mathrm{n}}$ is the direct cost of new installation of the equipment of energy type n; $\}Y_n^m$ represents the user-side equipment transformation cost generated by energy using the equipment transformed by other forms of energy (i.e., dismantling of original equipment and installation of new equipment); $\gamma_{c,n}^m$ stands for the cost of dismantling old equipment and installing new equipment after the energy type changes from c to n; $\mathrm{x}_n^m(\mathrm{t})$ is the energy supply occupancy rate of energy type n selected by m type users at time t (t = 2, 3. . .n); x_{0n}^m is the energy supply occupancy rate corresponding to the user's first selection; $\Delta \mathrm{x}_n^m(t)$ takes the positive value from the variation of the before and after energy supply occupancy rates, so $\Delta \mathrm{x}_n^m(t) > 0$.

2.2 Energy supply occupancy

The energy supply occupancy in the integrated energy market reflects the image of energy suppliers in the market, which indirectly affects the decision-making of user energy consumption. In general, the energy supply occupancy is closely related to the user's choice of energy consumption. Thus, this study is divided based on user type and load usage, and the specific formula is as follows:

$$B_2 = \left(\sum_{m=1}^{M} x_n^m D^m\right) / \sum_{m=1}^{M} D^m. \tag{5}$$

In the formula: D^m is a total load of *m-type* users in the research period.

2.3 Energy supply reliability rate

The reliability rate of the energy supply directly reflects the energy supply level of the supplier. Longer the effective energy supply times of the supplier, the better the reliability of the energy supply, and correspondingly, the higher the probability of users choosing this type of energy. This study uses the ratio of the user's valid time of energy supply to the research period as an indicator of reliability of energy supply, and the formula is as follows:

$$B_3 = 1 - \frac{\chi_n}{H_n} \times 100\%. \tag{6}$$

In the formula: χ_n is the average energy failure time of energy type n (unit: hour/user type). H_n depicts the energy supply time of energy type n (unit: hour).

2.4 User comfort level

In the user's decision-making process to choose different types of energy, their energy consumption experience, and their comfort level changes with the influence of external factors. The reference (De Greve et al., 2017) describes user comfort level in the form of quadratic function, exponential function, and logarithmic function. In this study, an exponential function considering the influence of environmental factors is used to characterize the user comfort level, and the formula is illustrated as follows:

$$B_4 = \zeta\left(\beta e^{-x_n^m} / t + \delta\right). \tag{7}$$

\In the formula: ζ is the profit coefficient of user comfort level, β is the user's energy consumption experience coefficient, x_n^m is the energy supply occupancy rate of energy type n selected by m-type users, and δ is the random quantity related to external factors, $\delta \in (0,1)$.

3 User energy consumption behavior decision based on the evolutionary game

The construction of the user utility function needs to consider multiple indexes. Each index has a different influence on the user utility index system. Therefore, it is necessary to determine the influence of each index in the decision-making process of different types of user groups by applying the weight coefficient (Jalali and Kazemi, 2015). At present, the subjective weighting method and the objective weighting method are usually used to determine weight. However, in this study, the method of combination weighting is used to calculate the weight index (Guo et al., 2017). The analytic hierarchy process and the coefficient of variation are respectively used to calculate the subjective and objective weight values of the user utility index.

The evolutionary game is used to analyze users' comprehensive energy consumption behavior. Electricity, natural gas, and heat suppliers first release the energy supply information to the users, then calculate their utility of energy type selection and update their game strategy based on this. The energy supplier will update the energy supply occupancy rate according to the current user 'group's selection status and then release it to the users. Both sides achieve the final evolutionary equilibrium in the process of the evolutionary game (Cheng and Yu, 2018). Figure 1 shows the relation of the evolutionary game.

Setting $x_n^m(t)$ as the proportion of m type users choosing energy type n at time t, $x_n^m(t)$ satisfies that $0 \le x_n^m(t) \le 1$ and $\sum_{n=1}^{N} x_n^m(t) = 1$. The group's state of *m-type* users can be expressed as $X^m = [x_1^m, .., x_n^m, ..., x_N^m]$. The user group state in the region can be expressed by matrix X:

$$X = \begin{bmatrix} x_1^1 & \cdots & x_n^1 & \cdots & x_N^1 \\ \vdots & \ddots & & \iddots & \vdots \\ x_1^m & & x_n^m & & x_N^m \\ \vdots & \iddots & & \ddots & \vdots \\ x_1^M & \cdots & x_n^M & \cdots & x_N^M \end{bmatrix}. \tag{8}$$

In the process of energy type selection, users will constantly update the utility function and optimize their own strategies according to the utility function (Xiao, 2010). Therefore, this article introduces the correction factor $\rho_{q,n}^m[U^m(X)]$ in order to represent the proportion of *m-type* users transferring from strategy q to strategy n. At any random point in time, each user can transfer proportionally from strategy q to strategy n by the factor $\rho_{q,n}^m[U^m(X)]$. It has been assumed that all users modify their own strategies. The dynamic change process of user group state X shown previously can be described by a differential equation. The specific formula is as follows:

$$\frac{\partial x_n^m}{\partial t} = \sum_{q=1}^{N} x_q^m \rho_{q,n}^m[U^m(X)] - x_n^m \sum_{q=1}^{N} \rho_{n,q}^m[U^m(X)]. \tag{9}$$

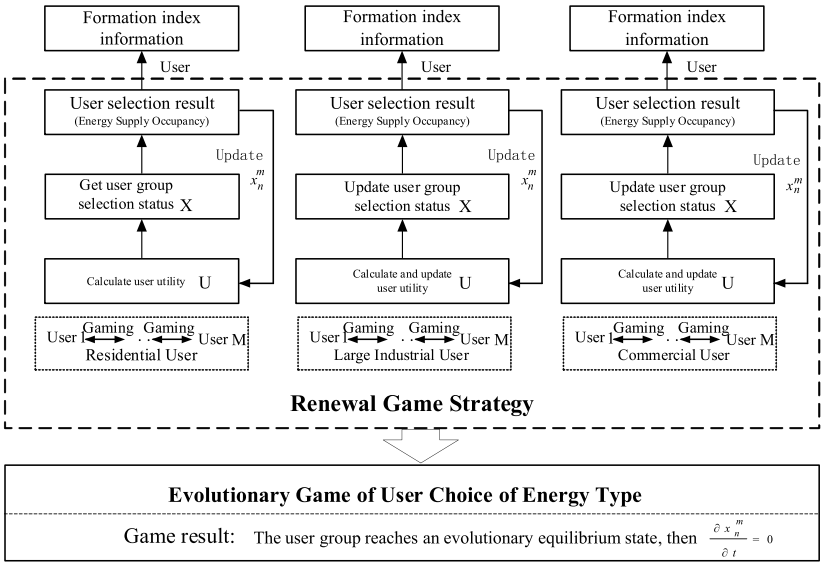

FIGURE 1
Evolutionary game relation of users' choices for energy types.

In the Eq. 9, the first and the second item on the right side of the equation represents the proportion of *m-type* users who transfer from other strategies to strategy n and those who change from strategy n to other strategies. Where, $\rho_{q,n}^{m}[\mathrm{U}^{m}(\mathrm{X})]$ is related to the current user utility function and user group state. In order to construct the mathematical relationship between the user selection ratio and the optional strategy, the Logit discrete choice model [28] is used to solve the problem, and the formula is as follows:

$$\rho_{\mathrm{q,n}}^{m}[\mathrm{U}^{\mathrm{m}}(\mathrm{X})] = \frac{exp[U_n^m(X)]}{\sum_{n=1}^{N} exp[U_n^m(X)]} - \mathrm{x}_n^m. \tag{10}$$

By substituting the aforementioned equation into Eq. 9, the final dynamic change formula of the user group is as follows:

$$\frac{\partial \mathrm{x}_{\mathrm{n}}^{m}}{\partial \mathrm{t}} = \frac{exp[U_n^m(X)]}{\sum_{\mathrm{n=1}}^{N} exp[U_n^m(X)]} - x_n^m = \rho_{\mathrm{q,n}}^{m}[U^m(X)] - x_n^m. \tag{11}$$

Since the heat consumption of large industrial users and the natural gas and heat consumption ratio of commercial users are limited by actual production, the load absorption capacity is limited. The aforementioned load constraint conditions are as follows:

$$\begin{cases} x_{\mathrm{HeatSupply}}^{\mathrm{LargeIndustrial}} \varepsilon [0, 0.3], \\ x_{\mathrm{HeatSupply}}^{\mathrm{Commercial}} \varepsilon [0, 0.3], \\ x_{\mathrm{Gas\ Supply}}^{\mathrm{Commercial\ Nutural}} \varepsilon [0, 0.3]. \end{cases} \tag{12}$$

4 Example analysis

4.1 Example explanation

In this study, the dynamic selection behavior between residential, large industrial, and commercial user groups (M = 3) and electricity, natural gas, and heat suppliers (n = 3) is simulated. The simulation program used MATLAB R2016a to calculate the evolutionary game model of chapter 3. The research period is 1 day, and Δt = 1 h which is divided into 24 periods. At the same time, the distributed iterative algorithm is used to calculate the evolutionary equilibrium.

For the convenience of calculation due to the difference in energy load units of different forms of energy,, this study unified the energy load units of electricity, natural gas, and heat according to the conversion standard between different energy sources and standard coal (Feng, 2011). Specific energy load data $L_n^m(t)$ (typical daily energy load data) was quoted from reference [29]. Table 1 shows the parameters $\phi_{0,\mathrm{n}}$ and $\gamma_{c,q}^{m}$ in indicator B_1. The average failure time of the parameter χ_n/h in indicator B_3 is

TABLE 1 Weight of index and parameter value of different types of users.

Weight user type	$\omega^m_{T,1}$			$\omega^m_{T,2}$			$\omega^m_{T,3}$			$\omega^m_{T,4}$		
	$\omega^m_{1T,1}$	$\omega^m_{2T,1}$	$\omega^m_{T,1}$	$\omega^m_{1T,2}$	$\omega^m_{2T,2}$	$\omega^m_{T,2}$	$\omega^m_{1T,3}$	$\omega^m_{2T,3}$	$\omega^m_{T,3}$	$\omega^m_{1T,4}$	$\omega^m_{2T,4}$	$\omega^m_{T,4}$
Resident	0.380	0.353	0.369	0.120	0.150	0.132	0.250	0.223	0.239	0.250	0.274	0.260
Large industry	0.083	0.096	0.088	0.350	0.342	0.347	0.350	0.346	0.348	0.217	0.216	0.217
Commerce	0.281	0.243	0.228	0.033	0.065	0.046	0.468	0.463	0.466	0.218	0.229	0.260

Parameter value in indicator *B*1

Weight user type	$\phi_{0,n}$/yuan			$\gamma^m_{c,q}$/yuan		
	Electricity supply	Heat supply	Natural gas supply	Electricity supply	Heat supply	Natural gas supply
Resident	1900	1750	1,600	2,300	2,100	2000
Large industry	2000	1,500	1,400	2,600	1900	1700
Commerce	1800	1,600	1900	2,350	2000	2,700

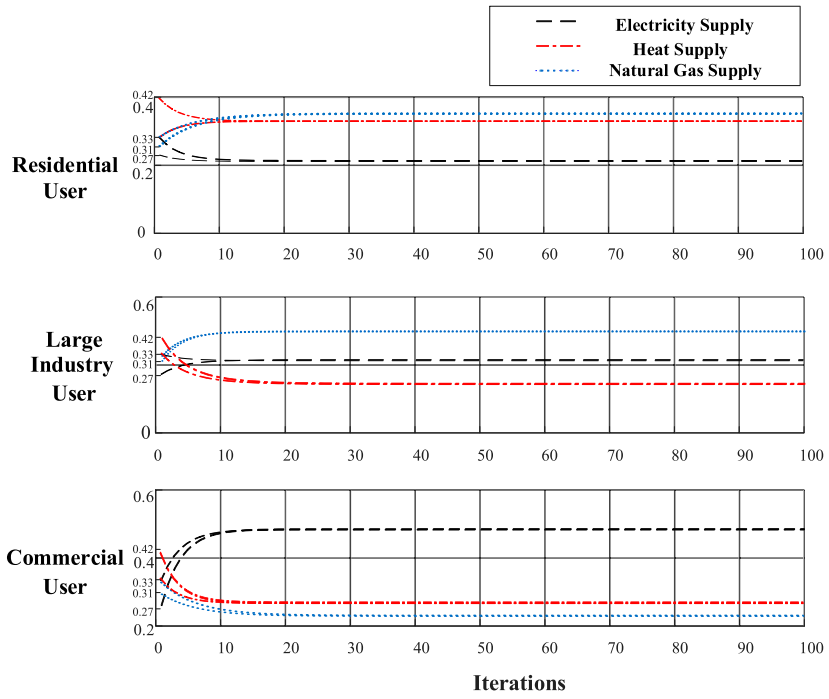

FIGURE 2
Selection results of three types of users.

0.5 for the electricity supplier, 0.86 for the heat supplier, and 1.05 for the natural gas supplier.

In order to avoid the influence of large fluctuation of energy load on the evaluation results, α in this study is 0.6, which can be adjusted according to the actual situation. Table 1 shows the subjective and objective weight values$\omega^m_{1T,h}$, $\omega^m_{2T,h}$ and combined weight values $\omega^m_{T,h}$ of each utility index based on the combination weighting method.

TABLE 2 Users' utility results of two methods.

Utility U_n^m	Static cluster analysis method			Utility U_n^m	Proposed method		
User type	Electricity supply	Heat supply	Natural gas supply	User type	Electricity supply	Heat supply	Natural gas supply
Resident	0.548	0.546	0.487	Resident	0.645	0.587	0.512
Large industry	1.501	1.152	1.127	Large industry	1.576	1.163	1.178
Commerce	1.982	0.718	0.502	Commerce	2.029	0.789	0.537

4.2 Simulation results and analysis

The evolutionary game method is used to calculate the model of the user's energy choice. The energy supply occupancy rates of electric, heat, and natural gas energy types in the initial state are set as (0.27, 0.42, 0.31) and (0.33, 0.33, 0.33) respectively. The comprehensive energy selection results of the three types of user groups are calculated respectively, as shown in Figure 2.

According to Figure 2, the selection process of residential, large industrial, and commercial user groups all converge iteratively. Furthermore, the evolutionary equilibrium results obtained by the aforementioned three types of user groups are the same under the initial state of two different energy supply occupancy rates. It indicates that the user group's selection of different energy types is unrelated to the initial state of energy supply occupancy.

Also according to Figure 2, among the total energy consumption load of the residential user group, the proportions of the final electricity load, heat load, and natural gas load are 0.229, 0.382, and 0.389 respectively. In the final evolution result of residential user energy load, heat and natural gas load account for a relatively higher proportion. The main reason is residential users are more sensitive to price and energy cost, which has the highest weight of energy consumption cost (0.369). Compared with the electricity load, the unit price of natural gas and heat after conversion is 0.23 yuan and 0.19 yuan less respectively. Therefore, residential users are more inclined toward increasing the proportion of natural gas and heat load as much as possible under the premise of ensuring the reliability and comfort of users' energy supply.

In the total energy consumption load of the large industrial user group, the proportion of final electricity load, heat load, and natural gas load are 0.309, 0.231, and 0.460 respectively. The main reason is similar to residential users. Large industrial users engaged in production are also very sensitive to the price of energy consumption. Therefore, they tend to choose primary energy for energy supply, which leads to natural gas accounting for a relatively high proportion of their comprehensive energy consumption. However, compared with residential users, large industrial users have higher requirements for energy supply reliability, and their weight of energy supply reliability is 0.109 higher than that of residential users. The electricity supply reliability of electric load is 0.015 higher than that of heat load. Moreover, according to the actual production limitation, the heat load absorption capacity of large industrial users is very low. As a result, although from the point of view of cost, electricity cost is 2,539.4 yuan higher than the heating cost, in the final energy consumption result the electric load accounts for a higher proportion.

In the total energy consumption load of the commercial user group, the proportion of final electricity load, heat load, and natural gas load are 0.510, 0.278, and 0.212 respectively. The main reason is that commercial users care more about user comfort and energy supply reliability, which is different from residential users and large industrial users. The weights of these two indicators i.e. user comfort and energy supply reliability are 0.260 and 0.466 respectively, which are the highest among the three types of users. Overall, the user comfort and energy supply reliability of electric load is the best. Moreover, for industry reasons, commercial users have a high cost of retrofitting electricity to other forms of energy and a limited capacity to absorb heat and natural gas loads (Yang et al., 2013). Therefore, in the energy consumption results of commercial users, their electrical load accounts for the highest proportion.

4.3 Comparison and analysis

In order to verify the correctness and effectiveness of the proposed method, the static clustering analysis method and the proposed method were used for the simulation, and the calculation results were compared. The two methods are as follows:

1) Static cluster analysis. The clustering decision is made directly according to the energy consumption characteristics of the three types of users without considering the dynamic change of load proportion of different types in the decision-making process.
2) The proposed method. According to the energy attributes of three types of users, the dynamic changes of different load proportions in the decision-making process are described by using evolutionary game theory.

The user utility results of the two methods are shown in Table 2.

According to Table 2, in comparison with the static clustering analysis method, the user utility value calculated by the proposed method in this article is higher. Specifically, for residential users, the utility of electricity supply, heat supply, and natural gas supply calculated by the proposed method is 9.7, 4.1, and 2.5% higher, respectively. For large industrial users, the utility of electricity supply, heat supply, and natural gas supply calculated by the proposed method is 7.5, 1.1, and 5.1% higher, respectively. For commercial users, the utility of electricity supply, heat supply, and natural gas supply calculated by the proposed method is 4.7, 7.1, and 3.5% higher, respectively.

The analysis shows that the proposed method in this study is better in assisting users to make decisions on energy selection. The reason is that the perspective of the static clustering analysis method is to evaluate the energy consumption selection of user utility statically. However, the dynamic game between users and energy types in the process of choosing their own comprehensive energy consumption ratio is not considered, which makes it difficult for users and energy suppliers to optimize their own utility through interaction in the process of energy consumption selection and decision making. Contrary to the static clustering analysis method, the proposed method of this study aims to build an evolutionary game model of user energy choice decisions. The main objective of this model is to ensure that users and energy suppliers can dynamically adjust their decisions according to the situation of the evolutionary game so as to achieve utility maximization and increase the effectiveness and accuracy of decision results.

5 Conclusion

In this study, the idea of a dynamic game is applied to the decision-making process of users' comprehensive energy consumption. Moreover, an analysis method of user comprehensive energy consumption behavior based on an evolutionary game is proposed. According to the simulation examples, the conclusions are as follows:

1) The user group's choice of different energy types is unrelated to the initial state of energy supply occupancy and is only related to the energy consumption selection bias and the utility index of different types of energy.
2) When the evolutionary equilibrium is reached, if the specificity of user behavior is higher, the proportion of users choosing this kind of energy would be greater. Therefore, in the process of comprehensive energy market competition, the cultivation of user specificity is conducive to improving the market share of energy suppliers.
3) The proposed method in this study can ensure that users and energy suppliers adjust their decisions dynamically according to the situation of the evolutionary game, which assists them to realize the optimization of utility. As a result, the effectiveness and accuracy of decision results are higher.

Data availability statement

The raw data supporting the conclusion of this article will be made available by the authors, without undue reservation.

Author contributions

XFZ: methodology, software, investigation, formal analysis, and writing—original draft; JY: data curation, writing—original draft, and funding acquisition; QX: investigation; LuD: investigation; CY: resources; HW: resources; QH: supervision; LiD: validation; RS: writing—review and editing; XXZ: writing—review and editing.

Conflict of interest

XFZ, JY, QX, LuD, CY, HW, QH, LiD, RS, and XXZ were employed by the State Grid Yichang Power Supply Company.

The authors declare that the research was conducted in the absence of any commercial or financial relationships that could be construed as a potential conflict of interest.

Publisher's note

All claims expressed in this article are solely those of the authors and do not necessarily represent those of their affiliated organizations, or those of the publisher, the editors, and the reviewers. Any product that may be evaluated in this article, or claim that may be made by its manufacturer, is not guaranteed or endorsed by the publisher.

References

Ai, Q., and Hao, R. (2018). Key technologies and challenges for multi-energy complementarity and optimization of inte grated energy system[J]. *Automation Electr. Power Syst.* 42 (4), 2–10. (in Chinese). doi:10.7500/AEPS20170927008

Boutaba, R., Salahuddin, M. A., Limam, N., Ayoubi, S., Shahriar, N., Estrada-Solano, F., et al. (2018). A comprehensive survey on machine learning for networking: Evolution, applications and research opportunities. *J. Internet Serv. Appl.* 9 (1), 1–99. doi:10.1186/s13174-018-0087-2

Chen, B., Sun, H., Chen, Y., Guo, Q., Wu, W., and Qiao, Z. (2020). Energy circuit theory of integrated energy system Analysis (I): Gaseous circuit[J]. *Proc. CSEE* 40 (02), 436–444. (in Chinese). doi:10.13334/j.0258-8013.pcsee.200028

Cheng, L., and Yu, T. (2018). Typical scenario analysis of equilibrium stability of multi-group asymmetric evolutionary games in the open and ever-growing electricity market[J]. *Proc. CSEE* 38 (19), 5687–5703. (in Chinese). doi:10.13334/j.0258-8013.pcsee.172219

Cui, Q., Bai, X., Dong, W., and Huang, B. (2019). Joint optimization of planning and operation in user-side multi-energy systems. *Proc. CSEE* 39 (17), 4967–4981. (in Chinese). doi:10.13334/j.0258-8013.pcsee.181874

De Greve, Z., Lecron, F., Vallee, F., Mor, G., Perez, D., Danov, S., et al. (2017). Comparing time-series clustering approaches for individual electrical load patterns. *CIRED - Open Access Proc. J.* 2017 (1), 2165–2168. doi:10.1049/oap-cired.2017.1222

Feng, X. (2011). *Research on power user classification Technology based on actual load curve [D]*. North China: Electric Power University.

Guan, H., and Pu, L. (2010). A drivers' choice behavior model based on evolutionary game theory[J]. *J. Beijing Univ. Technol.* 36 (08), 1077–1083. (in Chinese). doi:10.11936/bjutxb2010081077

Guo, H., Cheng, H., Ma, Z., and Ge, L. (2017). Comprehensive evaluation of power quality based on probability theory and combination weighting method[J]. *Smart Grid* 5 (06), 524–528. (in Chinese). doi:10.14171/j.2095-5944.sg.2017.06.002

Huang, W., Zhang, N., Kang, C., Li, M., and Huo, M. (2019). From demand response to integrated demand response: Review and prospect of research and application. *Prot. Control Mod. Power Syst.* 4 (1), 1–13. doi:10.1186/s41601-019-0126-4

Jalali, M. M., and Kazemi, A. (2015). Demand side management in a smart grid with multiple electricity suppliers. *Energy* 81 (1), 766–776. doi:10.1016/j.energy.2015.01.027

Jorgen, W. (2015). *Weibull. Evolutionary game theory [M]*. Shanghai: Shanghai People's Publishing House, 26–32.

Liu, N., Wang, J., and Wang, L. (2019). Hybrid energy sharing for multiple microgrids in an integrated heat–electricity energy system. *IEEE Trans. Sustain. Energy* 10 (3), 1139–1151. doi:10.1109/tste.2018.2861986

Samadi, P., Mohsenian-Rad, H., Schober, R., and Wong, V. W. S. (2012). Advanced demand side management for the future smart grid using mechanism design. *IEEE Trans. Smart Grid* 3 (3), 1170–1180. doi:10.1109/tsg.2012.2203341

Xiao, H. (2010). *Research on several game problems in traffic planning [D]*. China: Wuhan University.

Yang, N., Dong, Z., Wu, L., Zhang, L., Shen, X., Chen, D., et al. (2022b). A comprehensive review of security-constrained unit commitment. *J. Mod. Power Syst. Clean Energy* 10 (3), 562–576. doi:10.35833/MPCE.2021.000255

Yang, N., Qin, T., Wu, L., Huang, Y., Huang, Y., Xing, C., et al. (2021b). A multi-agent game based joint planning approach for electricity-gas integrated energy systems considering wind power uncertainty. *Electr. Power Syst. Res.* 204, 107673. ISSN 0378-7796. doi:10.1016/j.epsr.2021.107673

Yang, N., Yang, C., Wu, L., Shen, X., Jia, J., Li, Z., et al. (2022a). Intelligent data-driven decision-making method for dynamic multi-sequence: An E-Seq2Seq based SCUC expert system. *IEEE Trans. Ind. Inf.* 18, 3126–3137. doi:10.1109/TII.2021.3107406

Yang, N., Yang, C., Xing, C., Ye, D., Jia, J., Chen, D., et al. (2021a). Deep learning-based SCUC decision-making: An intelligent data-driven approach with self-learning capabilities. *IET Generation Trans. Dist.* 16, 629–640. doi:10.1049/gtd2.12315

Yang, P., Tang, G., and Nehorai, A. (2013). A game-theoretic approach for optimal time-of-use electricity pricing. *IEEE Trans. Power Syst.* 28 (2), 884–892. doi:10.1109/tpwrs.2012.2207134

Yang, Z., and Wang, L. (2016). *Demand response management for multiple utility companies and multi-type users in smart grid[C]//Chinese Control Conference*. China: IEEE, 10051–10055.

Yu, X., Xu, X., Chen, S., Wu, J., and Jia, H. (2016). A brief review to integrated energy system and energy internet [J]. *Trans. China Electrotech. Soc.* 31 (01), 1–13. (in Chinese). doi:10.19595/j.cnki.1000-6753.tces.2016.01.002

Zeng, M., Liu, Y., Zhou, P., Wang, Y., and Hou, M. (2018). Review and prospects of integrated energy system modeling and benefit evaluation[J]. *Power Syst. Technol.* 42 (6), 1697–1708. (in Chinese). doi:10.13335/j.1000-3673.pst.2018.0150

frontiers | Frontiers in Energy Research

TYPE Brief Research Report
PUBLISHED 26 August 2022
DOI 10.3389/fenrg.2022.984107

OPEN ACCESS

EDITED BY
Yusen He,
The University of Iowa, United States

REVIEWED BY
Ting Zhang,
Yanshan University, China
Wang Yaxuan,
Nanjing Agricultural University, China

*CORRESPONDENCE
Guimin Xu,
xuguimin2022@163.com

SPECIALTY SECTION
This article was submitted to Smart Grids,
a section of the journal
Frontiers in Energy Research

RECEIVED 01 July 2022
ACCEPTED 22 July 2022
PUBLISHED 26 August 2022

CITATION
Xu G (2022), State-of-charge estimation method for lithium-ion batteries based on competitive SIR model.
Front. Energy Res. 10:984107.
doi: 10.3389/fenrg.2022.984107

State-of-charge estimation method for lithium-ion batteries based on competitive SIR model

Guimin Xu*

School of Physics and Mechanical & Electrical Engineering, Hubei University of Education, Wuhan, China

In order to meet the needs of life and production and ensure the battery is stable when using the battery, a scheme for reckoning the state of charge of lithium-ion batteries derived from the competitive SIR model is proposed. During the charging process of the battery, the electrolyte and the diaphragm reach the negative electrode of the battery, and the electrolyte escapes from the graphite of the negative electrode to the positive electrode in the case of discharge. The analysis shows that the SIR model belongs to the internal information evolution process, which can infect the surrounding data and evaluate the state of charge better. Through experiments, it is substantiated that the scheme is able to better estimate the state of lithium-ion batteries, the error value is 0.0189, the accuracy is good, and the battery usage can be predicted in time.

KEYWORDS

li-ion battery, SIR model, state of charge, energy crisis, battery

1 Introduction

With the continuous growth of the population, the human society and the world economy have also developed rapidly (Xiong et al., 2021). However, energy crisis and environmental pollution have become increasingly serious problems faced by people. Therefore, both the government and scientists have paid attention to it (Zhang et al., 2015a).

In order to solve the above problems, electric vehicles with clean energy as the power source came into being. With the emergence of energy crisis and environmental problems, the new energy automobile university gradually occupies an important position in the global automobile industry (Yang et al., 2022).

In recent years, the development of hybrid electric vehicles has boosted the research and development of batteries. At the same time, more lithium batteries are required to meet the quality of life (Dey et al., 2015). In terms of principle and characteristics, different types of batteries have their own characteristics, such as chemical composition, performance (Li et al., 2021a), cost and safety. Later, dry batteries and nickel-cadmium batteries appeared. Later, for environmental protection, the research focus turned to batteries.

The battery state of charge (SOC) is an important parameter of the battery management system (Li et al., 2021b). However, the SOC peak cannot be directly

measured, and it is affected by factors such as application environment, declining degree, self-discharge, current amplification. Therefore, SOC reckoning, especially online reckoning, is a hot and difficult issue in lithium battery research. Based on this, a proportional-integral (PI) observer was proposed in (Xu, 2014) to estimate the SOC of Li-ion batteries in EDVs (End-diastolic volume). In literature (Ya-Xiong and Zhang, 2016), in order to reckon SOC of lithium batteries, the primary battery model is improved to develop the accuracy of the model and enable the battery model to reflect the actual internal state of the battery. The corresponding battery test experiments are carried out. Reference (Jiang et al., 2022) uses the EDVs Extended Rauch-Tung-Striebel Smoother (ERTSS) to estimate SOC. Using a Genetic Algorithm (GA) to search for the smoothing time interval for the optimal ERTSS, various dynamic unit tests were performed. Reference (Hu et al., 2022) extracts higher-level spatial features between multi variables into the current SOC and historical input, to achieve state assessment. However, the above-mentioned methods have low accuracy and large errors, so they cannot be accurately evaluated. Therefore, in this paper, the competitive SIR model is used to reckon the state of charge, and its advantages are clarified by analyzing the condition of lithium-ion batteries, and the SIR model is used to reckon SOC of the battery, providing a better method for battery condition assessment.

2 Lithium-ion batteries working principle and performance

2.1 Analysis of the advantages of lithium batteries

Lithium-ion batteries have superior properties that drive their rapid development. Its advantages are as follows:

1) High energy density (Zou et al., 2014). There are many kinds of materials that make up lithium-ion batteries, and different materials have different electrical conductivity. The power density of lithium-ion batteries is superior to other batteries in terms of mass and volume.
2) The open circuit voltage is too high. The materials that make up a lithium-ion battery determine its high open-circuit voltage, about three times that of the same nickel-chromium and nickel-metal hydride batteries.
3) The output power is large. This is also determined by the materials that make up the lithium-ion battery.
4) No memory effect (Yang et al., 2021). This feature allows the battery to function when it is not fully charged, avoiding the need to fully charge and discharge the battery every time, which is simpler to use and maintain than normal batteries.
5) The self-discharge rate of the battery is low. Self-discharge is not obvious and the efficiency is low. Even if it does not work for a long time, the average monthly excretion is only 5–10%.
6) Wide operating temperature range. It can work in a wide temperature range and can work normally at −20°C~+50°C.
7) The charging speed is fast. Lithium-ion batteries have high charging efficiency. They can be charged with 1C or more and can reach full state in a short period of time.
8) Long cycle life. Its cycle life is significantly better than other batteries. The cycle life of ordinary lithium batteries can reach 500 times or even more than 1,000 times. However, the theoretical charge-discharge cycles of batteries can reach more than 2000 times.
9) Safe and pollution-free. This is an environmentally friendly battery that can provide energy without producing heavy metals (Zhang et al., 2015b), harmful gases and other pollutants.

The superior performance of lithium-ion batteries is suitable for electric vehicles, which has prompted more research on them.

2.2 Lithium-ion batteries working principle

This paper mainly introduces the internal structure of lithium iron phosphate battery. Its cathode (Vo et al., 2015) material is composed of lithium iron phosphate. On the left is $LiFePo_4$, and the positive electrode of the battery is composed of olivine-structured bubbles. Aluminum foil connects it to the battery positive. On the right is the battery negative. Its material is graphite (Xie et al., 2018). Copper foil connects it to the battery negative. The middle part is the polymer membrane (Hu et al., 2018). It separates the positive and negative electrodes, allowing Li + to pass but preventing e- from passing through. The battery electrolyte is usually an organic electrolyte, which is located at the upper and lower ends of the battery. The working process of the battery is shown in Eq. 1 and Eq. 2:

In charge state:

$$LiFePo_4 - xLi^+ - xe^- \rightarrow xFePo_4 + (1-x)LiFePo_4 \quad (1)$$

In discharge state:

$$FePo_4 + xLi^+ + xe^- \rightarrow xLiFePo_4 + (1-x)FePo_4 \quad (2)$$

During the charging situation, the Li + escaped from the anode reaches the negative electrode of the battery through the electrolyte and the diaphragm through the action of the electric field, and the current flows reversely from the cathode to the anode. During the discharging situationf, Li + escapes from the graphite of the cathode to the anode through the electrolyte, and the current flows from the anode to the cathode.

3 State of charge estimation research status

3.1 State of charge definition

State-of-charge batteries are usually expressed as a percentage, with values ranging from 0 to 1. Remaining power is an important parameter reflecting battery performance. In many cases, SOC is often used to indicate the remaining power of the battery. Strictly speaking, however, the two definitions are different and the units adopted are inconsistent.

At present, the definition of SOC is not unified (Sakile and Sinha, 2021). Only a few simple definitions are introduced below, and the following definitions are given from different perspectives.

Definition 1. The most classic expression in the definition of SOC is as follows:

$$SOC = \frac{Q_{remain}}{Q_{rated}} \times 100\% \tag{3}$$

where Q_{remain} is the remaining charge scope (Le et al., 2021). Q_{rated} is the rated charge capacity. If we think that Q_{rated} is a fixed value (Gholizadeh and Salmasi, 2013), the definition (3) of SOC can be rewritten as Eq. 4:

$$SOC = \frac{Q_{remain}}{Q_{ramain} + Q_d} \times 100\% \tag{4}$$

Among them, compared with the Eq. 3, the extra denominator Q_d in the Eq. 4 represents the amount that has been released in the electric charge after the latest charging point.

Definition 2. Definition from the perspective of electricity: the battery is discharged at a certain rate, the current remaining battery capacity of the battery is used as the numerator (Zhang et al., 2022), and the total available capacity is used as the denominator. The corresponding mathematical expression is shown in Eq. 5.

$$SOC = \frac{Q_t}{Q_0} \times 100\% \tag{5}$$

In Eq. 5, Q_t represents the remaining power of the battery during calculation, that is, the battery is fully discharged to the discharge cut-off (Mitsuru and Yuhu, 2019) voltage under the conditions of a certain discharge rate and temperature specified in the actual experiment; Q_0 indicates the total capacity of the battery.

There is also a definition of SOC as shown in the following Eq. 6:

$$SOC = \frac{Q(t) - Q_0}{Q_E - Q_0} \times 100\% \tag{6}$$

Among them, $Q(t)$ is the remaining scope, Q_E represents the maximum scope, and Q_0 represents the total capacity of the battery.

Definition 3. , according to the definition of SOC:

$$SOC = SOC_0 - \frac{1}{C_N}\int_0^t \eta i d\tau \tag{7}$$

In the above formula: C_N is the rated scope; i is the battery current; η represents the efficiency during charge-discharge situation, and SOC_0 is the initial state under working conditions.

Definition 4, defined in terms of energy:

$$SOC = \frac{\text{remaining available energy}}{\text{total available energy}} \times 100\% = 1 - \frac{W_h}{W_{hE}} \tag{8}$$

In Eq. 8, W_h represents the used energy, and W_{hE} represents the total usable energy.

3.2 Reckoning scheme

Battery SOC evaluation plays a primary role in battery systems. The state of charge can only be estimated indirectly (Zheng et al., 2016), which needs to be estimated with the help of information such as voltage, current, internal resistance, and temperature. This is a physical quantity that cannot be directly measured (Hu et al., 2018). Many scholars and experts have done a series of related researches and discussions on the online reckoning scheme. In line with the different algorithm modeling methods, SOC estimation methods can be divided into simple calculation methods, fitting methods and nonlinear filtering methods (Tian et al., 2022). The specific classification is as follows.

3.2.1 Simple calculation method

The so-called calculation methods (such as the open circuit voltage method, the internal resistance method (Wu et al., 2021), the ampere-hour integration method, the discharge experiment method and the ultrasonic detection method) calculate the SOC of the battery through the definition formula of SOC. The simple parameter used in the formula is the charge and discharge current collected by the “black box”, without using any intelligent model or equivalent model (Chen et al., 2022), and not caring about the internal structure of the battery, but treating the battery as a whole as a “black box”, which is a relatively basic estimation method. The direct calculation method is a method that realizes SOC estimation only by defining the formula calculation. The direct calculation method referred to in this article is the ampere-hour integration method.

According to the ampere-hour integration method, SOC is defined as follows:

$$SOC(t) = SOC(t_0) - \frac{\eta \int_{t_0}^{t} Idt}{Q_N} \quad (9)$$

η is the Coulomb efficiency coefficient, Q_N is the nominal capacity of the battery, I is the discharge current, and $SOC(t_0)$ is the state of charge at t_0.

The nonlinear relationship between OCV and SOC is first fitted, and then the relationship is used to reckon SOC indirectly, the so-called open circuit voltage method. In general, the open circuit voltage method has a clear relationship with SOC in the early and late stages of charging, and it is best to estimate SOC within this range. The ampere-hour integration method has become the most widely used method in practice due to its simplicity and ease of implementation. Combining the advantages and disadvantages of the two methods, it is found that the two methods are obviously complementary. Therefore, many scholars have proposed new ideas to combine these two methods. The use of high-performance current sensors to measure current solves the problem of current inaccuracy, but also increases the cost. The advantage is that the principle is simple, and the calculation of the internal resistance value is simple. However, due to the influence of other factors, it is difficult to determine the relationship with SOC. Ultrasonic testing is a relatively new method. According to the advantage that ultrasound is very sensitive to porosity changes, it can detect the SOC state of the battery with high sensitivity.

3.2.2 Fitting method

The fitting estimation method fits the internal relationship between the external characteristics and SOC (such as load voltage method and the linear model method) according to the experimental data of the battery under various operating conditions, or uses various intelligent learning algorithms (such as neural network, network method, fuzzy inference method, support vector machine, etc.) offline training of the relationship model between battery performance parameters and state of charge, and then based on the relationship model, using experimental data to reckon SOC, which is called the fitting scheme. With the development of modern sensor technology and data storage and processing technology, data-driven system health prediction methods (neural network method, fuzzy inference method, support vector machine, correlation vector machine, etc.) have been widely used and popularized. The SOC reckoning scheme can be enforced to various lithium-ion batteries, the estimation accuracy is improved.

Fuzzy inference methods can estimate the time-varying parameters of circuit models well, but lack the ability of self-learning and self-adaptation. The SVM method uses a limited number of samples. The algorithm is simple and stable, but requires much data for computation. Support vector regression has the ability to learn from small samples, but the algorithm is not adaptive when battery performance parameters change (Liu et al., 2021).

3.2.3 Nonlinear filtering method

The nonlinear filtering method treats the battery as a dynamic system. The state variables of the system include SOC, which is updated by observing the variable value (usually selecting the battery terminal voltage as the observation variable), and finally the standard error of the state variable is minimized, sliding mode observer method, H filter method, etc, are used in nonlinear stochastic systems, and this kind of SOC estimation method is more suitable in terms of estimation accuracy.

To sum up, among the existing SOC estimation methods, the simple calculation scheme is straightforward to implement, and is widely used in occasions with low precision requirements. In occasions with high accuracy requirements, this method is usually used as an auxiliary tool for other SOC estimation methods; the fitting method is straightforward to perform and has high accuracy, but requires much data for computation, training data and method will directly affect the estimation accuracy; The nonlinear filtering method can track the changes of battery voltage and current in real time, update the SOC estimation value, and realize online SOC estimation, but the implementation process of this method is relatively complicated and the amount of calculation is large.

3.2.4 SI model

Assuming that the total population of an area is a constant, then in the process of spreading infectious diseases, it is divided into susceptible groups (Susceptible) and infected persons (Infective). Susceptible populations are those who are not yet infected but are at risk of infection. $S(t)$ represents the number of people who are vulnerable at t , and $I(t)$ represents to the number of people who are infected at t. Obviously:

$$S(t) + I(t) = N \quad (10)$$

Assuming that the infection rate is β , the number of people who are newly infected is:

$$\frac{dI(t)}{dt} = \beta I(t) S(t) \quad (11)$$

The change of susceptible population per unit time is:

$$\frac{dS(t)}{dt} = -\beta I(t) S(t) \quad (12)$$

Assuming the initial infection number $I_0 = I(0)$, the simultaneous Eqs 10–12 can be obtained:

$$I(t) = \frac{N}{1 + \left(\frac{N}{I_0} - 1\right) e^{-\beta N t}} \quad (13)$$

As time t approaches infinity, the number of infected people will approach N . Based on this feature, this paper uses the SI model to represent the dissemination model of rumor-refuting information in competitive information, that is, after the rumor-

TABLE 1 Lithium-ion battery parameters.

Parameter	Numerical value
Rated Capacity/mAh	2000
Discharge initial voltage/V	4.1
Discharge cut-off voltage/V	2.5
Ambient temperature/°C	25
Discharge current/A	2

refuting information begins to spread, the number of users who finally receive the information approaches N .

3.2.5 SIR model

Similar to the SI model, the SIR model has an additional removal population. Removal populations are those who received treatment after infection and then migrated from the infected population. For example, such a population would not become infected after developing antibodies to infectious diseases. $R(t)$ represents the number of people who are removed at time t , γ and represents the probability of an infected person being removed per unit time. Based on the advantages of the SIR model over the SI model, this paper adopts the SIR model as the propagation model.

Since the SIR model is similar to the SI model, the change equation can be rewritten as:

$$\frac{dI(t)}{dt} = \beta I(t)S(t) - \gamma I(t) \tag{14}$$

$$\frac{dS(t)}{dt} = -\beta I(t)S(t) \tag{15}$$

$$\frac{dR(t)}{dt} = \gamma I(t) \tag{16}$$

$$S(t) + I(t) + R(t) = N \tag{17}$$

Under normal circumstances, since the initial infected population is not 0, so $I_0 = I(0) > 0$, $S_0 = S(0) > 0$.

Based on this, this paper proposes a SOC reckoning for Li-ion batteries under a competitive SIR model. The SIR model was first used to study the spread and evolution of infectious diseases (Du et al., 2021). Since the 18th century, many research results have been formed, most of which focus on the improvement of the model and the application of the model in different fields. SIR is an infectious disease model developed from the SI model, which uses mathematical methods to analyze changes in the number of infections, predict peak periods, and identify regulatory and preventive mechanisms (Chen et al., 2020).

In the traditional SIR model, all participants in the system are divided into three parties: S is the susceptible group, I is the infected, i.e. the disseminator of opinions, and R is the immune, i.e. the person who is immune to the current information and no longer transmits it information. The mutual transformation of the three groups reflects the evolution of public opinion or information within the group.

4 Results and analysis

In this paper, a competitive SIR model is used to estimate the SOC during steady-state discharge of lithium-ion batteries. Experimental data was gathered during discharge situation of a set of lithium-ion batteries. The specification of the lithium-ion battery used in the experiment is shown in Table 1.

The SOC recorded during the entire discharge process is calculated by Eq. 18:

$$SOC = SOC_0 + \frac{1}{C_R}\int_{t_0}^{t} I_{cm}d\tau,\ C_R = \int_0^{t_{EDV}} I_{cm}d\tau \tag{18}$$

In Eq. 18, SOC_0 represents the original SOC, C_R is the rated scope, I_{cm} is the discharge current, and t_{EDV} represents the discharge time.

The root-mean-square error (RMSE) was used to evaluate the accuracy of the SIR model estimation. RMSE is defined as follows:

$$\delta_{RMSE} = \sqrt{\frac{1}{n}\sum_{i=1}^{n}\left|f(x_i) - y_i\right|^2} \tag{19}$$

In Eq. 19, $f(x_i)$ represents the estimated value based on the model, y_i represents the true value of the equation SOC, n is the number of reckoned points.

Design experiments to complete the state of the battery, and continuously charge and discharge the battery under specific set conditions.

The capacity is obtained by the corresponding standard measurement, and the specific steps are as follows:

1) Charging experiment, keep the lithium-ion battery charged at a constant current of 0.2°C at an ambient temperature of 36°C, and switch to constant voltage charging when the voltage reaches 4.2 V. When the charging current reaches 0.12 A, stop charging. It was left to stand for 15 min, cycling this process until the charge cut off current.
2) The discharge experiment is also carried out at the same ambient temperature. When the battery terminal voltage drops to 2.75 V, the discharge is stopped.

It was left to stand for 30 min; this process was applied to two batteries, called No. 4 and No. 5, respectively, to discharge the No. 4 battery at a constant current of 1.0°C, and the No. 5 battery to discharge at a constant current of 2.0°C.

Based on this step, the accelerated aging test of the battery under the corresponding conditions was carried out.

Data such as degree, number of charge and discharge cycles and time are saved and recorded. The experiment was carried out for a

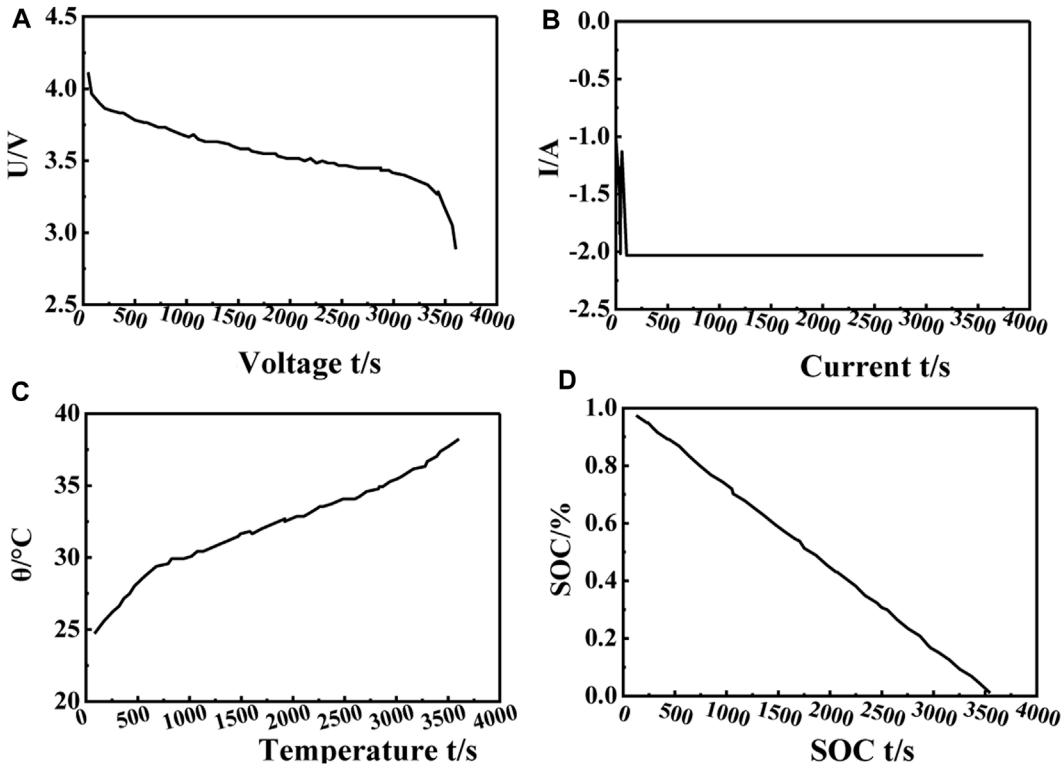

FIGURE 1
Discharge data. When the current is constant, the voltage drops slowly with time, and at 3500s, the voltage reaches 2.8 V. The temperature gradually increased with time, and the highest value could reach 3.7°C. The SOC value increases with time, from the initial 0.92 to 0 at 3500s

month, and the 4th and 5th batteries were respectively charged and discharged cyclically. However, due to the failure of the experimental platform, the 4th battery was overcharged, resulting in damage to the internal mechanism of the battery, and it could not continue to charge. A total of 200 times were charged. Discharge, only 200 sets of data. It took nearly a year for the AA battery to complete 789 charge and discharge experiments. So far, the capacity of the battery has dropped to the failure value. The aging experiment of the battery has been completed, and a total of 789 sets of data have been obtained.

During stable discharge experiment, the data used is the lithium-ion battery data provided by the database prediction center (Kim et al., 2021). The data of the No. 5 lithium-ion battery during discharge situation is used as the basis for the experimental data. In data set No. 5, the first to fourth groups of discharge data are used as the training set of the model, the seventh group of discharge data is used for the accuracy estimation of the model, and the seventh group of discharge process data are as follows Figure 1.

The battery voltage, current, and temperature are the characteristic input of the model, and the SOC value is the model output. The number of random forest trees is set to 500 (the test results show that the model is guaranteed to converge), and the randomly selected features are set to 2. In order to verify the evaluation performance of the random forest regression algorithm in the SOC reckoning scheme of lithium-ion batteries, the BP neural network and the T-S fuzzy neural network use the same parameters as the benchmark for comparison. The obtained sixth group of experimental prediction results and experimental errors are shown in Figure 2.

Figure 2 shows that the SIR model, BP neural network and T-S fuzzy neural network all have high estimation accuracy. Compared with the BP neural network and the T-S fuzzy neural network, the SOC prediction of the SIR model is almost close to the true value. The reckoning lapse of BP neural network and T-S fuzzy neural network is in a large range with the change of input vector, and the SIR model can assure that the lapse is within a certain range. Figure 2D shows that the maximum reckoning lapse of the SIR model, BP neural network and T-S fuzzy neural network are 0.0189, 0.021 and 0.026, respectively. Through the simulation results of the MATLAB platform, it is concluded that the root mean square error (RMSE) of the SIR model, BP neural network and T-S fuzzy neural network are 0.003203, 0.044561, and 0.018213, respectively.

The calculation error of the nuclear state of the lithium-ion battery calculated by the SIR model is shown in Figure 3. It can be seen from Figure 3 that with the increase of the number of iterations, the calculation error gradually becomes in a stable state, that is, to say,

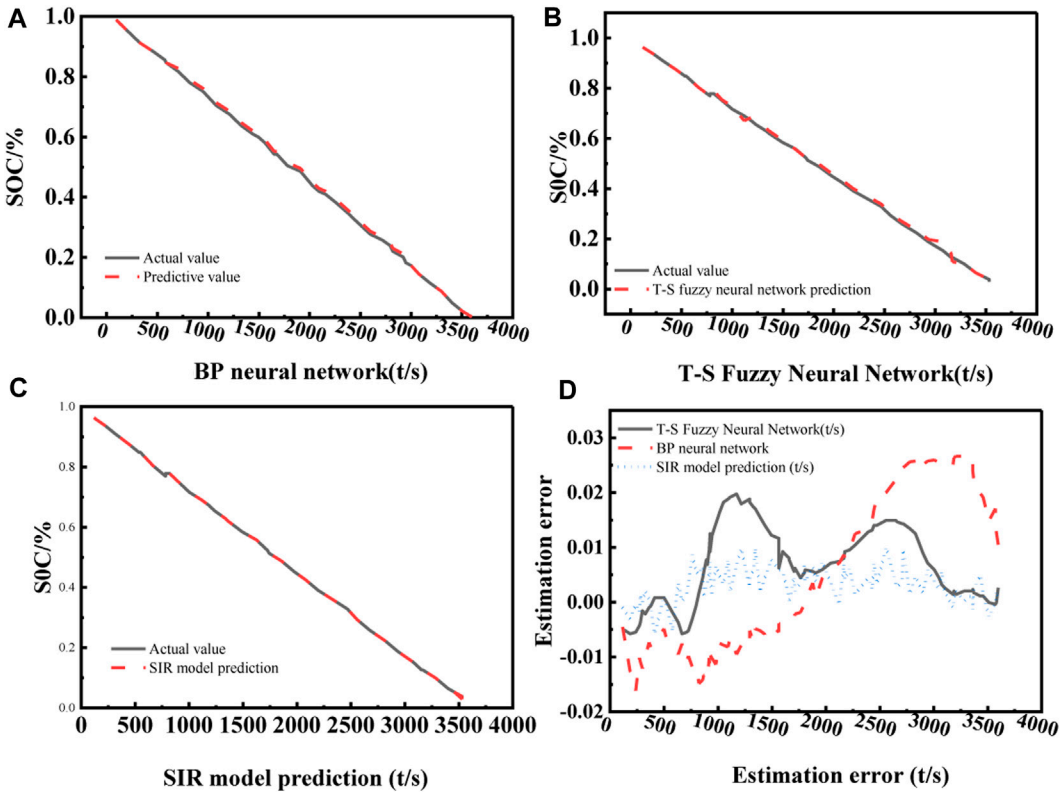

FIGURE 2
Prediction results of the sixth group of experiments. **(A)** the BP neural network has an error between the SOC prediction and the real value, but the value is small. Observing **(B)**, it can be seen that the T-S fuzzy neural network has obvious errors at 3000s, indicating that there is a small gap with the real value. **(C)** shows the SIR model. The SOC prediction of the SIR model is almost close to the real value, and is basically in a coincident state. The SIR model can ensure that the error is within a certain range. It can be seen from **(D)** that the maximum estimation errors of the SIR model, BP neural network and T-S fuzzy neural network are 0.0189, 0.021, and 0.026, respectively. Through the simulation results of the MATLAB platform, it is concluded that the root mean square error (RMSE) of the SIR model, BP neural network and T-S fuzzy neural network are 0.003203, 0.044561, and 0.018213, respectively.

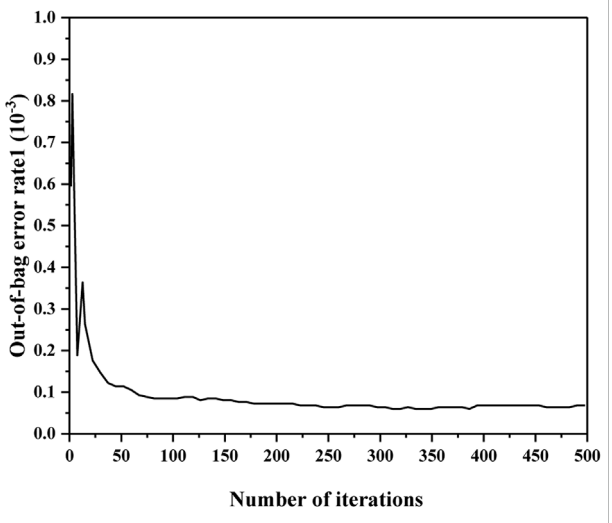

FIGURE 3
Iterations and errors.

when the number of iterations reaches a certain number, the estimated error result will not be greatly improved.

5 Discussion

The scheme for reckoning SOC of lithium-ion batteries should be studied in depth, because the parameters will change when the capacity fades and temperature changes, which allows the circuit parameters in the model to be adjusted as the conditions change, so that the static circuit model can be adjusted. Converting into a dynamic model, inevitably, this will increase the difficulty of the processor's operation, and at the same time, more experiments are required as a basis, which also means that more manpower, material resources and time are required. In estimating SOC, there are many parameters that need to be measured, such as current and voltage. However, due to noise, electromagnetic

interference and other factors, the accuracy of the measured value may be distorted, which will affect the estimated result. Improve the measurement accuracy as much as possible, and try to eliminate the influence of noise and other factors on it is the direction of future efforts.

6 Conclusion

This paper proposes a scheme for reckoning SOC of lithium-ion battery using the competitive SIR model, and compares the error value between the method proposed in this paper and the BP neural network and T-S fuzzy neural network method through experiments. The experimental results of the designed research show that:

1) We have compared the SIR model, BP neural network and T-S fuzzy neural network to reckon SOC of lithium-ion batteries, and concluded that the estimation error of the SIR model is the smallest compared to 0.0189. Through the simulation results of the MATLAB platform, it is concluded that the root mean square error of the SIR model is 0.003203.
2) Compared with BP neural network and T-S fuzzy neural network, the competitive SIR model has higher accuracy in estimating the battery charge; in the case of a limited number of estimated samples, the SIR model can effectively avoid the problem of overfitting.
3) The variable importance analysis of the SIR model can analyze the importance of the features, which can improve the accuracy of the parameters by improving the accuracy of the parameters when measuring the parameters, thereby improving the estimation accuracy of the results.

The method in this paper has higher accuracy and can avoid the probability of fitting problems. The competitive SIR model in this paper can be adopted to estimate SOC of lithium-ion batteries, which provides a reference for the model building of future lithium-ion battery charge reckoning systems.

Data availability statement

The raw data supporting the conclusions of this article will be made available by the authors, without undue reservation.

Author contributions

GX conceived the idea, completed the experiments and wrote the final manuscript.

Conflict of Interest

The author declares that the research was conducted in the absence of any commercial or financial relationships that could be construed as a potential conflict of interest.

Publisher's note

All claims expressed in this article are solely those of the authors and do not necessarily represent those of their affiliated organizations, or those of the publisher, the editors and the reviewers. Any product that may be evaluated in this article, or claim that may be made by its manufacturer, is not guaranteed or endorsed by the publisher.

References

Chen, L., Wu, X., Lopes, A. M., Yin, L., and Li, P. (2022). Adaptive state-of-charge estimation of lithium-ion batteries based on square-root unscented Kalman filter. *Energy* 252, 123972. doi:10.1016/j.energy.2022.123972

Chen, Z., Zhou, J., Zhou, F., and Xu, S. (2020). State-of-charge estimation of lithium-ion batteries based on improved H infinity filter algorithm and its novel equalization method. *J. Clean. Prod.* 290, 125180. doi:10.1016/j.jclepro.2020.125180

Dey, S., Ayalew, B., and Pisu, P. (2015). Nonlinear robust observers for state-of-charge estimation of lithium-ion cells based on a reduced electrochemical model. Control systems technology. *IEEE Trans.*23, 1935–1942. doi:10.1109/TCST.2014.2382635

Du, B., Yu, Z., Yi, S., He, Y., and Luo, Y. (2021). State-of-charge estimation for second-life lithium-ion batteries based on cell difference model and adaptive fading unscented Kalman filter algorithm. *Int. J. Low-Carbon Technol.* 16, 927–939. doi:10.1093/ijlct/ctab019

Gholizadeh, M., and Salmasi, F. R. (2013). Estimation of state of charge, unknown nonlinearities, and state of health of a lithium-ion battery based on a comprehensive unobservable model. *IEEE Trans. Ind. Electron.* 61 (3), 1335–1344. doi:10.1109/tie.2013.2259779

Hu, C., Cheng, F., Ma, L., and Li, B. (2022). State of charge estimation for lithium-ion batteries based on TCN-LSTM neural networks. *J. Electrochem. Soc.* 169, 030544. doi:10.1149/1945-7111/ac5cf2

Hu, X., Yuan, H., Zou, C., Li, Z., and Zhang, L. (2018). Co-estimation of state of charge and state of health for lithium-ion batteries based on fractional-order calculus. *IEEE Trans. Veh. Technol.* 67, 10319–10329. doi:10.1109/tvt.2018.2865664

Jiang, Y., Song, W., Zhu, H., Zhu, Y., Du, Y., and Yin, H. (2022). Extended rauch–tung–striebel smoother for the state of charge estimation of lithium-ion batteries based on an enhanced circuit model. *Energies* 15, 963. doi:10.3390/en15030963

Kim, W. Y., Lee, P. Y., Kim, J., and Kim, K. S. (2021). A robust state of charge estimation approach based on nonlinear battery cell model for lithium-ion batteries in electric vehicles. *IEEE Trans. Veh. Technol.* 70, 5638–5647. doi:10.1109/tvt.2021.3079934

Le, S., Wu, Y., Guo, Y., and Del Vecchio, C. (2021). Game Theoretic Approach for a service function chain routing in NFV with coupled constraints. Circuits and Systems II: Express Briefs. *IEEE Trans.*68, 3557–3561. doi:10.1109/TCSII.2021.3070025

Li, H., Deng, J., Feng, P., Pu, C., Arachchige, D., and Cheng, Q. (2021). Short-term nacelle orientation forecasting using bilinear transformation and ICEEMDAN framework. *Front. Energy Res.* 9, 780928. doi:10.3389/fenrg.2021.780928

Li, H., Deng, J., Yuan, S., Feng, P., and Arachchige, D. (2021). Monitoring and identifying wind turbine generator bearing faults using deep belief network and EWMA control charts. *Front. Energy Res.* 9, 799039. doi:10.3389/fenrg.2021.799039

Liu, Y., Li, J., Zhang, G., Hua, B., and Xiong, N. (2021). State of charge estimation of lithium-ion batteries based on temporal convolutional network and transfer learning. *IEEE Access* 9, 34177–34187. doi:10.1109/access.2021.3057371

Mitsuru, T, and Yuhu, W (2019). Mayer-type optimal control of probabilistic boolean control network with uncertain selection probabilities. *IEEE Trans. Cybern.* 51, 3079–3092. doi:10.1109/tcyb.2019.2954849

Sakile, R., and Sinha, U. K. (2021). Estimation of state of charge and state of health of lithium-ion batteries based on a new adaptive nonlinear observer. *Adv. Theory Simul.* 4 (11), 2100258. doi:10.1002/adts.202100258

Tian, Y., Huang, Z., Tian, J., and Li, X. (2022). State of charge estimation of lithium-ion batteries based on cubature Kalman filters with different matrix decomposition strategies. *Energy* 238, 121917. doi:10.1016/j.energy.2021.121917

Vo, T. T., Chen, X., Shen, W., and Kapoor, A. (2015). New charging strategy for lithium-ion batteries based on the integration of Taguchi method and state of charge estimation. *J. Power Sources* 273, 413–422. doi:10.1016/j.jpowsour.2014.09.108

Wu, Y., Guo, Y., and Toyoda, M. (2021). Policy iteration approach to the infinite horizon average optimal control of probabilistic boolean networks. *IEEE Trans. Neural Netw. Learn. Syst.* 32, 2910–2924. doi:10.1109/tnnls.2020.3008960

Xie, J., Ma, J., and Bai, K. (2018). Enhanced Coulomb counting method for state-of-charge estimation of lithium-ion batteries based on peukert's law and coulombic efficiency. *J. POWER Electron.* 18 (3), 910–922. doi:10.6113/JPE.2018.18.3.910

Xiong, R., Wang, J., Shen, W., Tian, J., and Mu, H. (2021). Co-estimation of state of charge and capacity for lithium-ion batteries with multi-stage model fusion method. *Engineering* 7, 1469–1482. doi:10.1016/j.eng.2020.10.022

Xu, J., Mi, C. C., Cao, B., Deng, J., Chen, Z., and Li, S. (2014). The state of charge estimation of lithium-ion batteries based on a proportional-integral observer. *IEEE Trans. Veh. Technol.* 63, 1614–1621. doi:10.1109/tvt.2013.2287375

Ya-Xiong, G. U., and Zhang, Y. J. (2016). Estimation of state of charge of lithium-ion battery based on dual extend Kalman filter. *Chin. J. Power Sources*.

Yang, B., Wang, Y., and Gao, H. (2021). State-of-charge estimation of lithium-ion batteries based on PSO-BP neural network. *Sci. Publ. Group* 10 (6), 115–120. doi:10.11648/j.ijepe.20211006.13

Yang, K., Tang, Y., Zhang, S., and Zhang, Z. (2022). A deep learning approach to state of charge estimation of lithium-ion batteries based on dual-stage attention mechanism. *Energy* 244, 123233. doi:10.1016/j.energy.2022.123233

Zhang, C., Li, K., Pei, L., and Zhu, C. (2015). An integrated approach for real-time model-based state-of-charge estimation of lithium-ion batteries. *J. Power Sources* 283 (1), 24–36. doi:10.1016/j.jpowsour.2015.02.099

Zhang, C., Wang, L. Y., Li, X., Chen, W., Yin, G. G., and Jiang, J. (2015). Robust and adaptive estimation of state of charge for lithium-ion batteries. *IEEE Trans. Ind. Electron.* 62 (8), 4948–4957. doi:10.1109/tie.2015.2403796

Zhang, Y., Qian, T., and Tang, W. (2022). Buildings-to-distribution-network integration considering power transformer loading capability and distribution network reconfiguration. *Energy* 244, 123104. doi:10.1016/j.energy.2022.123104

Zheng, L., Zhang, L., Zhu, J., Wang, G., and Jiang, J. (2016). Co-estimation of state-of-charge, capacity and resistance for lithium-ion batteries based on a high-fidelity electrochemical model. *Appl. Energy* 180 (15), 424–434. doi:10.1016/j.apenergy.2016.08.016

Zou, Z., Xu, J., Mi, C., Cao, B., and Chen, Z. (2014). Evaluation of model based state of charge estimation methods for lithium-ion batteries. *Energies* 7 (8), 5065–5082. doi:10.3390/en7085065

frontiers | Frontiers in Energy Research

TYPE Original Research
PUBLISHED 13 September 2022
DOI 10.3389/fenrg.2022.1009840

OPEN ACCESS

EDITED BY
Yusen He,
The University of Iowa, United States

REVIEWED BY
Tangshao Duan,
Mie University, Japan
Sheng Hu,
Xi'an Polytechnic, China

*CORRESPONDENCE
Qian Fan,
qianfann@outlook.com

SPECIALTY SECTION
This article was submitted to Smart Grids,
a section of the journal
Frontiers in Energy Research

RECEIVED 02 August 2022
ACCEPTED 19 August 2022
PUBLISHED 13 September 2022

CITATION
Yao L, Fan Q, Zhao L, Li Y and Mei Q (2022), Establishing the energy consumption prediction model of aluminum electrolysis process by genetically optimizing wavelet neural network.
Front. Energy Res. 10:1009840.
doi: 10.3389/fenrg.2022.1009840

Establishing the energy consumption prediction model of aluminum electrolysis process by genetically optimizing wavelet neural network

Lizhong Yao[1], Qian Fan[2]*, Lei Zhao[1], Yanyan Li[2] and Qingping Mei[3]

[1]College of Physics and Electronic Engineering, Chongqing Normal University, Chongqing, China, [2]School of Mechanical Engineering, Sichuan University, Chengdu, China, [3]School of Big Data and Information Industry, Chongqing City Management College, Chongqing, China

Nowadays, it is very popular to employ genetic algorithm (GA) and its improved strategies to optimize neural networks (i.e., WNN) to solve the modeling problems of aluminum electrolysis manufacturing system (AEMS). However, the traditional GA only focuses on restraining the infinite growth of the optimal species without reducing the similarity among the remaining excellent individuals when using the exclusion operator. Additionally, when performing arithmetic crossover or Cauchy mutation, a functional operator that conforms to the law of evolution is not constructed to generate proportional coefficients, which seriously restricted the exploitation of the hidden potential in genetic algorithms. To solve the above problems, this paper adopts three new methods to explore the performance enhancement of genetic algorithms (EGA). First, the mean Hamming distance (H-Mean) metric is designed to measure the spatial dispersion of individuals to alleviate selection pressure. Second, arithmetic crossover with transformation of the sigmoid-based function is developed to dynamically adjust the exchange proportion of offspring. Third, an adaptive scale coefficient is introduced into the Gauss-Cauchy mutation, which can regulate the mutation step size in real time and search accuracy for individuals in the population. Finally, the EGA solver is employed to deeply mine the optimal initial parameters of wavelet neural network (EGAWNN). Moreover, the paper provides the algorithm performance test, convergence analysis and significance test. The experimental results reveal that the EGAWNN model outperforms other relevant wavelet-based forecasting models, where the RMSE in test sets based on EGAWNN is 305.72 smaller than other seven algorithms.

Abbreviations: AEMS, Aluminum electrolysis manufacturing system; ANS, Adaptive neighborhood search; BRK-GA, Biased random key genetic algorithm; EC, Enhanced crossover; EGA, Enhanced genetic algorithm; EM, Enhanced mutation; ES, Enhanced selection; GA, Genetic algorithm; IGA, Improved genetic algorithm; MSP, Multi Supper parent; POX, Preserving order-based crossover; RG, Reference group; RMSE, Root mean square error; SD, Standard deviation; SGA, Standard genetic algorithm; SSP, Single supper parent; WNN, Wavelet neural network.

KEYWORDS

aluminium electrolysis, enhanced genetic algorithm, wavelet neural network, energy consumption prediction, intelligent modeling

1 Introduction

The aluminum electrolysis industry consumes enormous energy, and its energy utilization rate is less than 50% (Gui et al., 2018). An effective way to achieve efficiency enhancement and consumption reduction is to determine the optimal operating parameters for maintaining the best condition of the electrolytic cell. However, it is necessary to establish a high-precision and stable prediction model for process energy consumption (Yang et al., 2019). And so far, the methods for predicting the energy consumption of aluminum electrolysis have been roughly divided into two categories (Wu et al., 2019). The first contains physical methods, which tracks the process of aluminum electrolysis based on the exact mathematical mechanism. Because there are many complex physical and chemical reactions inside aluminum electrolysis and unpredictable external interference, it is very difficult to obtain a precise system model through the process mechanism (Slowik and Kwasnicka, 2020). The other category includes data-driven methods, which can acquire the complex corresponding relationships between decision variables and performance indicators (Li et al., 2021a; Li, 2022a). This type of method does not need to know the complex mechanism of a manufacturing system, it performs learning and training only on a series of process data samples (Yao et al., 2019; Li, 2022b). Therefore, such a method is of noticeable value with broad practical applications in modeling algorithms for process manufacturing systems (Yi et al., 2018; Li et al., 2021b).

A wavelet neural network (WNN), as a universal function approximation model that is widely accepted in data-driven methods (Pauline and Zarita, 2019; Khelil et al., 2021), learns the same task with higher accuracy, a simpler structure and faster convergence speed compared with traditional neural networks (Guan et al., 2013). Song et al. (2016) proposed a wavelet-based scheme to generate the individual forecaster. Jha and Senroy (2018) used the wavelet ridge method to analyze the dynamic characteristics of the power system. Sabouri et al. (2017) adopted the orthogonal discrete wavelet transform (ODWT) to research the plasma electrolytic oxidation (PEO) of aluminum at various periods during the electrolysis process. A WNN has the potential to handle the issue of the AEMS modeling.

Nevertheless, the stochastic generation of the initial parameters in a WNN gives rise to the nonconvergence of the whole learning process and even major prediction errors, which hardly satisfy the modeling requirements of high accuracy and stability in an AEMS. There is a consistent trend in current research regarding the integration genetic algorithms into WNNs to adjust their weights and factors (Majeed et al., 2017; Peng and Xiang, 2020; Tian et al., 2020; Khelil et al., 2021). Furthermore, the combination of a GA and a WNN has diversified applications, such as calculating the greenhouse effects of aircraft cruises (Tian et al., 2020), adjusting the parameters used in a hybrid fuzzy wavelet neural network (Huang et al., 2018), and establishing the thermal error prediction models for machine tools (Li and Zhang, 2019). Compared with the traditional WNN, the model established by a GAWNN can overcome its weakness in obtaining relatively stable initial parameters.

There are two ways to further promote the accuracy of the prediction model. One is to seek breakthroughs from the structure of the WNN, the other is to overcome the premature deficiencies of GA (Tinos et al., 2018) that our studies looked at. Plus, almost all the modified measures revolve around three genetic operators (Song et al., 2019), which are the cores of evolution and determine the performance of the algorithm. Unfortunately, there are still three areas of anxiety that are worthy of our attention and resolution. First, most of the existing studies on the use of crowding selection to eliminate similar individuals are based on the Hamming distance between each individual in the population and the optimal individual (Li and Kou, 2002; Osuna and Sudholt, 2020). Li and Kou (2002) utilized the fitness-sharing method, by which individuals are measured with the Euclidean or Hamming distance (Prugel-Bennett and Tayarani-Najaran, 2012), to maintain population diversity. Although the above methods alleviate overcrowding, they simply curb the uncontrolled growth of certain particular species, and they cannot guarantee sufficient discreteness among advanced individuals. Second, the adaptive crossover principle (Shojaedini et al., 2019; Mishra and Bajpai, 2021; Sun et al., 2021), which can adjust its crossover rate in different fields based on the population fitness of every iteration, has been extensively reported. Although adaptive crossover reduces the adverse effect caused by an improper definition of the rate, its essence is still that of stochastic crossover. Its randomness of intersection inevitably increases the possibility of damaging good genes. Third, the Gauss-Cauchy mixture mutation, a type of the real-coded mutation, has been an investigative hotspot due to its local and global search abilities (Li et al., 2017a; Li et al., 2017b; Wu and Law, 2011). There are some mutation formulas combining the Gauss-Cauchy function that have been recommended in (Li et al., 2017b; Lha et al., 2018). However, the current studies mostly adopt the standard Cauchy function for mixing throughout the mutation process. That results in a relatively single range of variation generated by the mixed formula.

Based on the issues stated in above analyses, the measures utilized by this paper and innovations contained therein are mainly summarized as follows:

(1) To increase the dispersion of subpopulations and effectively avoid precocity, the presented scheme adopts the mean Hamming distance (H-Mean), which performs secondary selection from the perspective of superior offspring populations, to design the selection operator rather than a single Hamming distance.
(2) Considering that arithmetic crossover is essentially a linear combination of alleles, the proposed scheme uses it to mitigate the above negative effect. Moreover, by rotating the sigmoid function vertically with $y = 0.5$ as the axis of symmetry, and taking the part of the curve where x is greater than or equal to 0, a new type of α-function that slowly approaches from 0.5 to 0 is designed, to regularly set the cross proportion of parents involved in the evolution. This scheme does not casually destroy the good genes, and ensures that the algorithm can converge to the global optimum.
(3) In order to improve the accuracy of local search by making the ranges of variation change dynamically with the iteration process, this paper introduces an adaptive scale coefficient γ into the Cauchy function to randomly set the change rate of the fitness of the iterative population. Therefore, the mutation steps can be updated in a timely manner, which will improve the time-variance and convergence rate of the algorithm.

Through the deep integration of the above three strategies, this paper further explores the hidden potential of genetic algorithms. The proposed EGA solver is employed to optimize the weights and factors of a WNN, which helps to establish an energy consumption model for an AEMS. The EGAWNN model overcomes the weaknesses of early convergence and poor search speed in the middle and late stages when the GA is applied to the wavelet network. Finally, the accuracy and improvement of the prediction model are verified through industrial experiments.

The remaining content of this paper is as follows. Section 2 presents the specific implementations of three enhanced strategies. Section 3 provides some standard numerical experiments as well as their results contained tables and figures. Section 4 overviews the design flow and convergence analysis of EGAWNN. An experiment based on a real-world industrial application of aluminum electrolysis is conducted and discussed through certain performance indices in Section 5. Section 6 gives a summary of the paper.

2 Enhanced genetic algorithms

A GA is an adaptive probability optimization technology based on biological genetics and evolution mechanisms. When a GA is used to solve optimization problems, premature convergence and evolutionary obstruction inevitably occur during the solving process. This paper tries to solve the above problems from the following three aspects.

First, taking the dispersion and diversity of the initial population into account, the offspring are selected based on the H-Mean criterion so that the newly generated individuals can crowd out similar parents. Second, a dynamic nonlinear arithmetic crossover based on the α-function is designed to ensure that the population has sufficient diversity in the early stages without destroying the excellent individuals in the later stages. Finally, an adaptive proportional coefficient is introduced into the Cauchy function to adjust the variation step size, which helps individuals move quickly towards the direction of the global optimum.

2.1 Crowding strategy based on the H-Mean metric

The proportional selection method in the standard genetic algorithm (SGA) may increase the number of individuals whose fitness values are close to those of others in the later period. The above phenomenon can result in the stagnation of the evolution of the population, or individuals with higher fitness values misleading the evolution direction of the population, which will cause the population to lose diversity and result in premature convergence problems (Amini and Hu, 2021).

Although the standard crowding method can keep a population diversified and relieve the congestion between the best individual and other excellent populations to some degree, spatial dispersion within an excellent population is difficult to be guaranteed. To address the problem, this study provides a crowding strategy through the ranking of the H-Mean values, for the selection of outstanding individuals with high fitness values and large population differences. This strategy maintains the dispersion of good subpopulations and restrains the endless growth of some superior species.

Figure 1 simulates the spatial dispersion of excellent subpopulations before and after employing the proposed crowding strategy. The two coordinate axes represent the two requirements of high fitness and high H-Mean values. There are good individuals with high fitness values in the large dotted circle above the black curve; the blue star represents the best individual with the highest fitness value in the current evolution; the yellow balls are overcrowded in the small red dotted circle, as seen in Figure 1A. The green balls are made up of two parts: One part contains the individuals with good dispersion in the excellent population; the other part is derived from changes in the remaining individuals by deleting the yellow balls with low H-Mean value, which are plotted in Figure 1B. It is easy to see that a higher H-Mean criterion-based crowding strategy can alleviate the congestion among outstanding individuals and thus increase population diversity.

Definition of the Hamming distance (denoted by (i, j)): Suppose that there are two equal-length strings S_1 and S_2, where $H(i, j)$ is the minimum number of character substitutions that change one string into the other; i and j represent different individuals in the population.

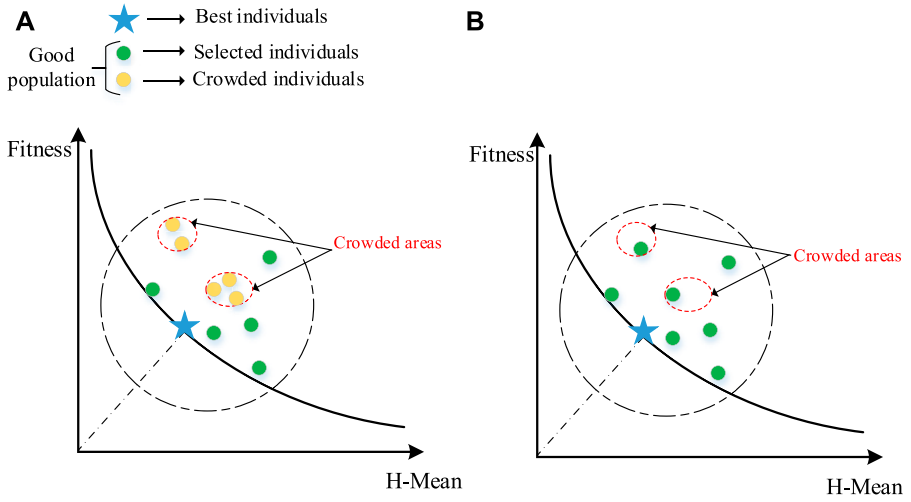

FIGURE 1
The simulative spatial dispersion of good subpopulations: **(A)** Before employing the crowding strategy based on H-Mean, **(B)** After employing the crowding strategy based on H-Mean.

The basic calculation process is as follows: 1) The population is sorted into superior and inferior population according to the ranking of fitness; 2) In the superior population, the number on each gene site of individuals are kept four significant digits, and then their $H(i, j)$ are calculated; 3)The superior population selecte offspring through the elitist strategy and the sorting-elimination rule based on H-Mean (marked as $H_{mean}(i, j)$). The inferior population directly eliminates the individuals in proportion whose fitness values are low; 4) New individuals are randomly generated to replace the eliminated ones. The pseudocode of the specific process is shown in Table 1.

2.2 α-Function-based arithmetic crossover

A crossover operation is the main feature that distinguishes a GA from other evolutionary algorithms, and it is an important method for generating new individuals. The crossover operation of the SGA selects two individuals as objects, and then generates an intersection to exchange gene codes for producing subindividuals (Dang et al., 2016). The widely used adaptive crossover dynamically adjusts its crossing rate in accordance with the fitness values of the population involved in the evolution process. However, the position of a single-point or multipoint crossover is stochastic (Xu et al., 2018). The uncertainty of intersections raises the risk of destroying excellent genes, which may cause the algorithm to swing around the optimal solution at the end of a search, resulting in a state of convergence stagnation. In addition, it essentially serves the binary encoding genes, which causes part of the genetic information to lose when dealing with unrelated and multi-parameter real encoding. This paper adopts a nonlinear combination crossover to solve the above problem, as shown in Eq. 1.

$$\begin{cases} X_A^{t+1} = \alpha X_B^t + (1-\alpha) X_A^t \\ X_B^{t+1} = \alpha X_A^t + (1-\alpha) X_B^t \end{cases} \tag{1}$$

where, X_A^t and X_B^t represent the two selected parents, and X_A^{t+1} and X_B^{t+1} represent the offspring after crossover.

Because α must be in the range of (0, 0.5), we try to design $S(\alpha)$ through a transformation of the sigmoid curve feature; the curve of $S(\alpha)$ is shown in Figure 2.

$$S(\alpha) = \frac{e^{-\alpha}}{1+e^{-\alpha}} \tag{2}$$

$\alpha = t/\beta$ and $\beta = T/5$, where t is the current number of iterations, and T is the maximum number of iterations. The new crossover strategy is obtained as given in Eq. 3.

$$\begin{cases} X_A^{t+1} = \dfrac{e^{-\frac{t}{\beta}}}{1+e^{-\frac{t}{\beta}}} X_B^t + \dfrac{1}{e^{-\frac{t}{\beta}}} X_A^t \\ X_B^{t+1} = \dfrac{e^{-\frac{t}{\beta}}}{1+e^{-\frac{t}{\beta}}} X_A^t + \dfrac{1}{e^{-\frac{t}{\beta}}} X_B^t \end{cases} \tag{3}$$

Figure 3 indicates the differing principles of adaptive crossover and a-function arithmetic crossover, where we use different colors, i.e., orange, green, pink and blue, to distinguish the genes of different parents. We can see that Figure 3A has a

TABLE 1 Pseudocode of utilizing the H-Mean metric for selection.

Algorithm 1: H-Mean-based crowding algorithm

Input: The initial individual k (k = 1,2,...,n) with a fitness value f_k below

InitChrom = [K, F_K]

Output: The selected individual with its fitness value f_k listed below

SelChrom = [K_Sel, F_{K_Sel}]

Steps

1. Initialization

Set the parameters: Number_of_F, Number_of_Scale (1), Number_of_Scale (2)

GoodChrom [], BadChrom []

2. Sort the individuals in InitChrom [] in descending order by fitness value

3. If f_k > Number_of_F then

i. Individual k enters GoodChrom [], and its number is recorded as n_1

else

i. Individual k enters BadChrom []

end if

4. Calculate the $H(i, j)$ s in GoodChrom [] between individual i and all the remaining individuals

5. Calculate the sum of the $H(i, j)$ s between the ith individual and all the others, namely

$\sum_{j=1}^{n_1-1} H(i, j),\ (j = 1, 2...n_1, j \neq i)$

6.Calculate the $H_{mean}(i, j)$ of individual i and arrange them in descending order, namely

$H_{mean}(i, j) = \frac{\sum_{j=1}^{n_1-1} H(i,j)}{n_1-1}$

7. If f_k = Max(f) then

i. Individual k enters GoodChrom []; record it as k_best

else

i. Compare the $H_{mean}(i, j)$ s of all individuals except k_best

ii. In GoodChrom [], eliminate the individuals with the smallest $H_{mean}(i, j)$ s according to the ratio of Number_of_Scale (1)

end if

8. In BadChrom [], eliminate individuals with the smallest f_k values according to the ratio of Number_of_Scale (2)

9. Randomly generate new individuals to replace the eliminated individuals

10. Put all individuals from GoodChrom [] and BadChrom [], as well as the newly generated individuals, into SelChrom []

End the H-Mean-GA procedure

different number of parents involved in each crossover from that in Figure 3B, which realizes the requirement of self-control because its crossover rate changes each iteration according to the population fitness. However, the intersection is stochastic, thus making the gens unordered. α-function arithmetic crossover is applicable to floating operations, and its working principle is shown in Figure 3B. Its essence is only a linear combination of the alleles of parental individuals, so no crossover points are required. It is worth mentioning that this paper improves the proportionality coefficient α in arithmetic crossover into a S(α) function related to t (the number of iterations). From Figure 2 and Eq. 3, at the beginning of the iterative process, t is small, resulting in S(α) converging to 0.5, and each offspring inherits half the genes from each parent, such as the orange and green genes in Figure 3B. Therefore, obtaining more diverse offspring from the above crossover increases the possibility of obtaining high-performing individuals. As the number of iterations increases, t becomes larger, which causes S(α) to be approximately 0, and the paternal genes remain largely unchanged, such as the pink and blue genes in Figure 3B. Small exchanges of parent alleles can increase the local optimization power of the algorithm. In this way, not only can the diversity of the population be maintained but the population also moves towards the direction of global convergence during later iterations without destroying the optimal individuals.

2.3 Gaussian and adaptive Cauchy mutation (Gauss-γ.Cauchy)

The mutation operator replaces the original gene with a new one to improve the local search ability of the GA (Das and Pratihar, 2021), as well as that of an auxiliary method for

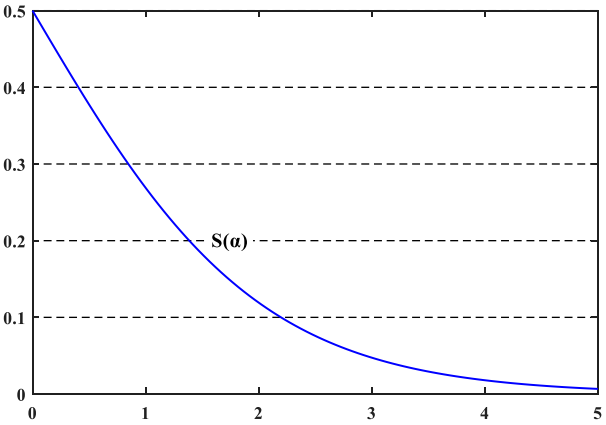

FIGURE 2
$S(\alpha)$ function curve.

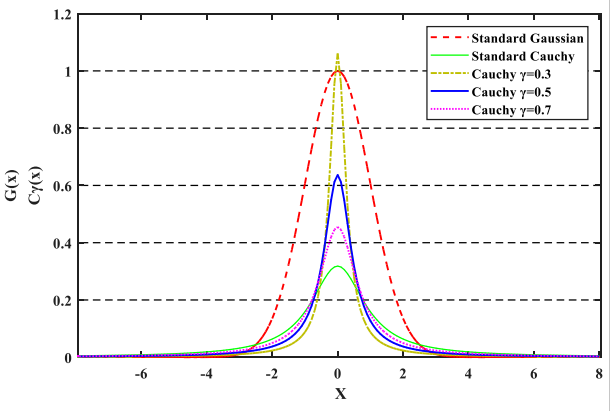

FIGURE 4
Comparison between the Gaussian and Cauchy distribution curves.

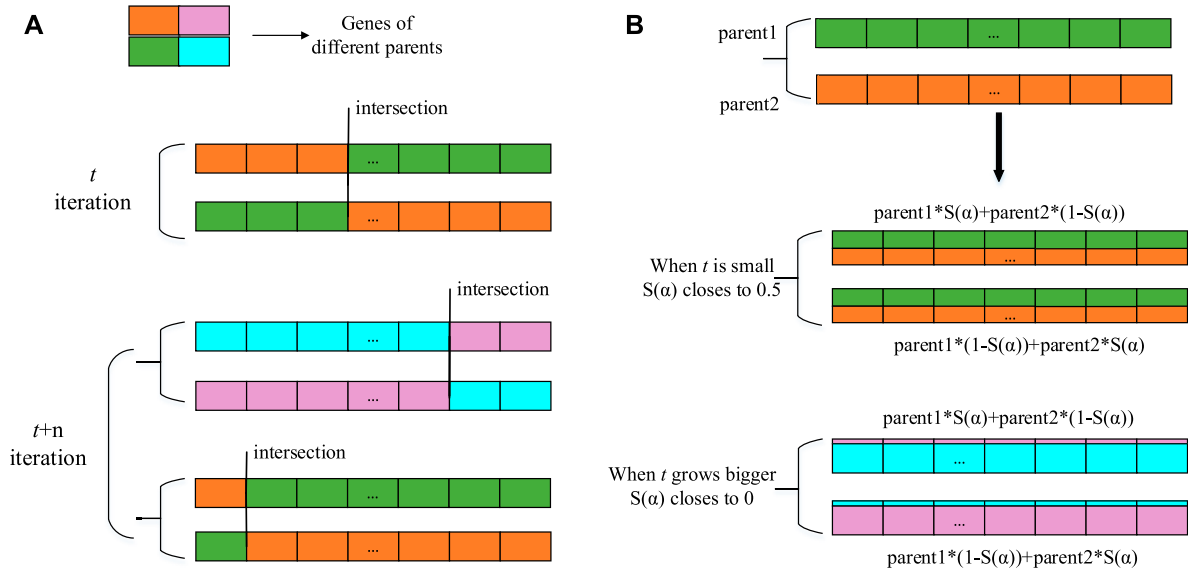

FIGURE 3
A contrast between different strategies under single-point crossover: **(A)** Adaptive crossover, **(B)** α-function arithmetic crossover.

generating new individuals to increase population diversity. The real coding number in this paper is up to 108 bits, so it cannot achieve the expected effect if only single-point variation is used. If multipoint variation is employed, the randomness of the mutation value will produce a large uncorrelated disturbance, consequently damaging the original good genes. To solve the above problems, this paper introduces an adaptive proportional coefficient γ to design a hybrid mutation equation on the basis of the Gauss-Cauchy mutation. The designed equation produces related perturbations to change the original genes and overcome uncertainty. The range of the disturbance produced by the Cauchy function is instantly adjusted by changing the γ, thereby generating a new mutation step that makes the hybrid equation time-varying.

The Gaussian distribution function is given as $G(x) = \frac{1}{2\pi}\exp(-\frac{x^2}{2})$, $x \in (-\infty, \infty)$, and the Cauchy function is $C_\gamma(x) = \frac{\gamma}{\pi} \cdot \frac{1}{\gamma^2+x^2}$, $x \in (-\infty, \infty)$, where γ is the scale coefficient. Their density distribution curves are shown in Figure 4.

Figure 4 shows that the standard Gaussian function has a larger peak value at its origin and a shorter distribution on both

sides than the other function. Gaussian mutation can produce disturbances close to the origin, and hence, it has a strong local development ability. Conversely, the Cauchy function has a smaller peak value at its origin and a longer distribution on both sides. Notably, the γ affects the features of the curvilinear distribution. Cauchy mutation can generate a disturbance with a wider range near the current mutated individual, making it easier to leap out of local optima. Combing the distribution features of the two functions, the hybrid mutation equation is introduced as follows (Wu and Law, 2011; Li et al., 2017a):

$$\begin{cases} \eta_{ij}^{'}(t) = \eta_{ij}\exp\left(\tau C(\gamma) + \tau_1 C_j(\gamma)\right) \\ x_{ij}^{'}(t) = x_{ij}(t) + \eta_{ij}^{'}(t)\cdot G_j(0,1) \end{cases},\ j = 1,2,...,n \tag{4}$$

$$\tau = \left(\sqrt{2\sqrt{n}}\right)^{-1},\ \tau_1 = \left(\sqrt{2n}\right)^{-1} \tag{5}$$

where $x_{ij}^{'}$and $\eta_{ij}^{'}$are the target and decision variables of the *jth* individual; τ and τ_1 are used to define the step size of the whole population and single individual respectively. $C(\gamma)$ represents the Cauchy random numbers of the whole population generated at this time, and it is updated only once per iteration. $C_j(\gamma)$ denotes the Cauchy random number of the single individual. Everyone participating in the current mutation generates one random number and needs to be updated once. $G_j(0,1)$ indicates a random number from the standard Gaussian distribution. As with $C_j(\gamma)$, each mutation requires a new Gaussian random number.

Since the γ of the Cauchy function affects the curve peak and the distribution features on both sides, the value can be regulated to randomly change the disturbance range. The selection of γ is based on the distance between offspring. First, this paper introduces the range rate of offspring, as given in Eq. 6:

$$P_{dis}(t) = \frac{\max(objv(t)) - \min(objv(t))}{\max(objv(t-1)) - \min(objv(t-1))} \tag{6}$$

where t is the current iteration number and $objv(t)$ is the fitness value of the *tth* generation. Let $d(t) = P_{dis}(t)/P_{dis}(t-1)$. If $d(t)$ stays stationary on both sides of one or moves slowly to its right during three successive generations, we should reset the mutation size by changing γ.

It can be seen from Figure 4, $\gamma = 0.3$, $\gamma = 0.5$, $\gamma = 0.7$, and $\gamma = 1.0$ are the critical points with large differences, so the proposed scheme sets two intervals. A brief explanation of the mutation process is plotted in Figure 5. Figure 5A uses orange genes to represent the range limit of the mutation at $\gamma = 1$. To visually show the change rule, the interval is artificially set to (0.010 and 0.100). Figure 5B uses green gene to represent the mutation range limit at $\gamma \in [0.7, 1]$. At this time, $d(t)$ fluctuates greatly, so we implement a global search and still assume the interval to be (0.010 and 0.100). The γ in this interval can produce a larger disturbance, so the updated mutation step size can force the process to leap out of the local optimum and ensure the global convergence of EGA. Figure 5B uses a blue gene to show the mutation range limit at $\gamma \in [0.3, 0.5]$. Currently, $d(t)$ is stable at approximately one for three successive generations, indicating that the evolution has reached the late stage. Therefore, we implement a local search and still assume the interval to be (0.005 and 0.050). In this interval, the distribution is short on both sides of the function curve, and the disturbance is small, which results in diminishing mutation step size.

The specific adjustment process is as below:

When $d(t-i) \sim 1$, $t > 3$, $(i = 0, 1, 2)$, let $\gamma \in [0.3, 0.5]$; if not, $\gamma \in [0.7, 1]$, and then put the updated γ into Eq. 6.

3 Numerical experiments and results

The above three methods in Section 2 are implemented in MATLAB R2020a with an Intel Core i5 2.00 GHz CPU. To highlight the performance differences of various methods, we adopt the Enhanced selection (ES), Enhanced crossover (EC), Enhanced mutation (EM) methods and Enhanced genetic algorithm (EGA) combining the above three strategies to compare with the Reference group (RG). Meanwhile, for evaluating the superiority and timeliness of the new algorithm, this paper also performs the following four comparison experiments, which were new strategies proposed by researchers on genetic algorithms in the past 2 years. The above four methods are as follows. 1) Priority based genetic algorithms (PGA) (Mishra and Bajpai, 2021) contained single supper parent algorithm (SSP); 2) PGA contained multi supper parents algorithm (MSP); 3) Biased random key genetic algorithm (BRK-GA) (Cicek and Ozturk, 2021): ELITE and NONELITE selection; BRK crossover; 4) Improved genetic algorithm (IGA) (Zhang et al., 2020): precedence preserving order-based crossover (POX) and adaptive neighborhood search mutation (ANS). All the genetic operators used in the above evolution processes of the functions are shown in Table 2. Bold operators in Table 2 emphasize the innovative part of the corresponding methods.

We used the above nine groups of comparative experiments to optimize the 6 standard single-objective test functions separately, i.e., function1, function2, function3, function4, function5, and function6, as shown in Eqs 7–12. The performance of the nine methods is measured by the objective function value (regarded as the fitness value of the optimal solution). Since the six test functions only have one actual value and one predicted value after each independent run, only the change of fitness is observed while analyzing the global indices and convergence traits. The population size is set to 200, and the maximum number of iterations is set to 500.

Function1. Global minimum $f(x) = 0;\ x(i) = 0,\ \mathrm{i} = 1\text{: n}.$

$$f_1(x) = \sum_{i=1}^{n} x_i^2, -5.12 \le x_i \le 5.12 \tag{7}$$

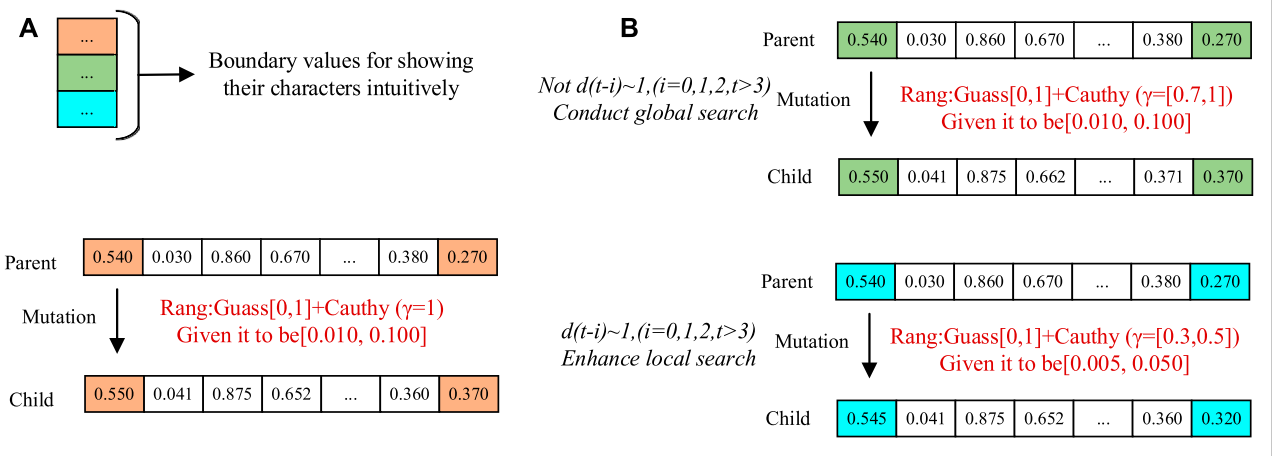

FIGURE 5
The mutation processes of different methods under real number coding: **(A)** Standard Guass-Cauchy mutation, **(B)** Gauss-γ Cauchy mutation.

TABLE 2 The genetic operators contained in the nine designed experiments.

No	Methods	Selection operator	Crossover operator	Mutation operator
1	RG	Standard crowding	Single-point adaptive	Standard Gauss-Cauchy
2	ES	**H-Mean crowding**	Single-point adaptive	Standard Gauss-Cauchy
3	EC	Standard crowding	**S(α) arithmetic**	Standard Gauss-Cauchy
4	EM	Standard crowding	Single-point adaptive	**Gauss-γ .Cauchy**
5	**EGA**	**H-Mean crowding**	**S(α) arithmetic**	**Gauss-γ .Cauchy**
6	SSP	**Single Supper parent**	Multi-point adaptive	Adaptive mutation
7	MSP	**Multi Supper parents**	Multi-point adaptive	Adaptive mutation
8	BRK-GA	**ELIT/NON-ELITE**	**BRK**	MultiNonUnifMutation
9	IGA	Sus selection	**POX**	**ANS mutation**

Function2. Global minimum $f(x) = 0;\ x(i) = 1,\ \mathrm{i} = 1\text{: n}.$

$$f_2(x) = \sum_{i=1}^{n-1} 100 \cdot \left(x_{i+1} - x_i^2\right)^2 + (1 - x_i)^2, -2.048 \le x_i \le 2.048 \tag{8}$$

Function3. Global minimum $f(x) = 0;\ x(i) = 1,\ \mathrm{i} = 1\text{: n}.$

$$f_3(x) = 10 \cdot n + \sum_{i=1}^{n} \left(x_i^2 - 10 \cdot \cos(2\pi \cdot x_i)\right), -5,12 \le x_i \le 5.12 \tag{9}$$

Function4. Global minimum $f(x) = 0;\ x(i) = 0,\ \mathrm{i} = 1\text{: n}.$

$$f_4(x) = \sum_{i=1}^{n} \frac{x_i^2}{4000} - \prod_{i=1}^{n} \cos\left(\frac{x_i}{\sqrt{i}}\right) + 1, -600 \le x_i \le 600 \tag{10}$$

Function5. Global minimum $f(x) = 0;\ x(i) = 0,\ \mathrm{i} = 1\text{: n}.$

$$f_5(x) = \sum_{i=1}^{n} |x_i|^{(i+1)}, -1 \le x_i \le 1 \tag{11}$$

Function6. Global minimum $f(x) = 0;\ x(i) = 0,\ \mathrm{i} = 1\text{: n}.$

$$f_6(x) = -a \cdot e^{-b\sqrt{\frac{\sum_{i=1}^{n} x_i^2}{n}}} - e^{\frac{\sum_{i=1}^{n} \cos(c \cdot x_i)}{n}} + a + e^1, -1 \le x_i \le 1 \tag{12}$$

In Tables 3, 4, the global indices based on the best, mean, worst, standard deviation (SD), root mean square error (RMSE) and the *p*-value (from Wilcoxon matched-pairs rank sum test) of the fitness values for 100 runs are tabulated. The bold parts in the Tables 3, 4 indicate the performance index of the proposed method. The significance test is calculated with results of the EGA as the reference group and the single bound value a is set to 0.05. Those values approach perfect modeling results for all enhanced

10.3389/fenrg.2022.1009840

TABLE 3 Results of global indices for each evolutionary process of design experiments (1).

Test function	Combination forms	Fitness					
		Best	Mean	Worst	SD	RMSE	*p*-value
Function1	RG	6.38e-09	5.97e-08	4.05e-07	5.64e-08	8.19e-08	5.82e-35
	ES	8.47e-11	1.55e-09	6.88e-09	1.32e-09	2.03e-09	1.95e-08
	EC	7.93e-09	4.67e-08	1.49e-07	2.62e-08	5.35e-08	2.56e-34
	EM	5.34e-10	6.71e-09	3.32e-08	6.13e-09	9.07e-09	1.07e-28
	EGA	**3.34e-11**	**7.70e-10**	**9.20e-09**	**1.02e-09**	**1.27e-09**	—
	SSP	5.17e-12	1.40e-07	1.70e-06	2.78e-07	3.09e-07	1.16e-27
	MSP	3.39e-10	5.19e-10	1.05e-09	1.45e-10	5.39e-10	6.11e-02
	BRK-GA	2.63e-05	7.49e-05	1.99e-04	3.18e-05	8.13e-05	2.56e-34
	IGA	1.14e-14	7.95e-08	6.42e-07	1.51e-07	1.70e-07	1.12e-18
Function2	RG	1.17e-10	1.30e-03	4.60e-02	5.20e-03	5.40e-03	1.56e-10
	ES	1.71e-12	3.00e-04	5.60e-03	8.70e-04	9.22e-04	6.25e-02
	EC	0.00	3.28e-04	1.55e-02	1.80e-03	1.80e-03	1.59e-09
	EM	1.89e-12	4.30e-04	9.00e-03	1.30e-04	1.30e-04	6.53e-09
	EGA	**0.00**	**2.00e-04**	**5.70e-03**	**7.35e-04**	**7.64e-04**	—
	SSP	1.04e-10	2.30e-03	3.70e-02	5.90e-03	6.30e-03	3.00e-10
	MSP	1.73e-08	1.40e-03	7.40e-03	1.90e-03	3.23e-03	2.78e-19
	BRK-GA	3.48e-09	5.41e-06	5.18e-05	8.57e-06	1.01e-05	1.16e-04
	IGA	—	—	—	—	—	—
Function3	RG	7.64e-10	6.53e-02	5.02e-01	6.93e-02	9.49e-02	2.88e-34
	ES	3.05e-11	1.78e-02	1.18e-01	2.61e-02	3.15e-02	7.10e-24
	EC	5.31e-07	7.71e-05	7.40e-03	7.39e-04	7.39e-04	0.22
	EM	2.60e-09	4.41e-02	3.89e-01	4.92e-02	6.59e-02	4.36e-11
	EGA	**1.61e-11**	**2.04e-10**	**1.62e-09**	**2.34e-10**	**3.10e-10**	—
	SSP	1.49e-10	8.72e-03	1.73e-01	1.92e-02	2.10e-02	0.17
	MSP	3.38e-11	5.72e-03	2.86e-02	9.43e-03	1.01e-02	3.70e-10
	BRK-GA	1.36e-05	1.63e-05	1.87e-05	1.09e-06	1.64e-05	0.13
	IGA	1.43e-12	7.84e-09	8.80e-08	1.44e-08	1.63e-08	2.3e-03

measures. Considering the adaptive Neighborhood Search in IGA requires variation points greater than five in hierarchical optimization, while the standard coding length of function2 is 2, so IGA is not used to solve the function2. A comparison of the results based on the performance measures in Tables 3, 4 is also plotted in Figures 6, 7. To obtain the convergence data based on the number of runs, Table 5 details the statistical results that fall into different fitness intervals during the 100 independent runs, in which EGA has been shown in bold. Though for relatively severe standards, 100 runs are not enough, the experienced number of runs is still to attain reasonable level of accuracy, which shows the optimization potential of the method proposed in this paper to improve the optimal solution of objective functions.

Further analysis demonstrates that the three enhanced genetic operators and the EGA balance the distribution and convergence of the algorithm with the number of iterations. Taking function1 as an example in Table 3, the best values, mean values and worst values for designed experiments 1–5 (from EG to EGA) lie in the ranges of 10^{-09} to 10^{-11}, 10^{-08} to 10^{-10}, and 10^{-07} to 10^{-09}, respectively. Only when using above methods to optimize function4, is the performance of EGA slightly worse than that of the Reference group.

Compared with other strategies proposed in the latest research, the EGA shows certain advantages in different aspects. Specifically, taking function1 as an example, the SD and RMSE of the EGA in Table 3 are smaller than those of SSP, which proves that EGA's stability is higher. Taking function2 and 3 as examples, the performance of the EGA is better than the MSP algorithm in all aspects. In function4,

TABLE 4 Results of global indices for each evolutionary process of design experiments (2).

Test function	Combination forms	Fitness					
		Best	Mean	Worst	SD	RMSE	*p*-value
Function4	RG	4.30e-06	5.34e-02	2.91e-01	6.27e-02	8.21e-02	0.10
	ES	5.18e-07	4.82e-02	2.65e-01	5.70e-02	7.44e-02	0.50
	EC	6.66e-08	4.63e-02	3.07e-01	5.54e-02	7.20e-02	0.18
	EM	1.91e-06	5.21e-02	6.00e-01	8.03e-02	9.54e-02	0.06
	EGA	**2.64e-05**	**4.44e-02**	**2.60e-01**	**4.92e-02**	**6.60e-02**	—
	SSP	1.81e-06	1.72e-02	8.83e-02	1.81e-02	2.49e-02	4.19e-05
	MSP	3.80e-07	8.90e-03	6.38e-02	1.03e-02	1.36e-02	3.03e-11
	BRK-GA	3.12e-04	1.10e-03	2.60e-03	4.01e-04	1.20e-03	1.97e-05
	IGA	4.85e-13	1.39e-08	1.53e-07	2.68e-08	3.01e-08	2.56e-34
Function5	RG	6.81e-13	3.80e-10	2.80e-09	5.82e-10	6.93e-10	7.14e-30
	ES	4.68e-14	8.59e-11	2.55e-09	2.94e-10	3.05e-10	1.23e-10
	EC	1.84e-14	3.61e-11	4.22e-10	6.97e-11	7.82e-11	9.67e-31
	EM	2.18e-14	4.62e-11	1.13e-09	1.47e-10	1.54e-10	3.73e-05
	EGA	**1.25e-14**	**9.20e-12**	**4.32e-10**	**4.42e-11**	**4.49e-11**	—
	SSP	3.37e-13	7.58e-13	9.08e-13	1.34e-13	7.70e-13	6.80e-03
	MSP	1.31e-13	6.93e-13	9.07e-13	1.66e-13	7.12e-13	2.30e-03
	BRK-GA	6.59e-15	9.83e-10	7.01e-09	1.45e-09	1.74e-09	2.71e-29
	IGA	3.17e-13	3.45e-09	3.02e-08	5.48e-09	6.46e-09	6.32e-31
Function6	RG	6.42e-09	5.31e-01	2.31e+01	7.77e-01	9.30e-01	5.87e-36
	ES	1.73e-10	5.90e-01	2.01e+01	7.03e-01	9.21e-02	4.79e-34
	EC	1.44e-06	3.28e-06	7.32e-06	1.10e-06	3.45e-06	2.56e-34
	EM	1.36e-09	3.90e-01	2.01e+01	6.57e-01	7.61e-01	1.47e-34
	EGA	**6.73e-12**	**1.83e-10**	**9.22e-10**	**1.91e-10**	**2.64e-10**	—
	SSP	1.51e-05	1.76e-05	1.90e-05	8.20e-07	1.77e-05	2.56e-31
	MSP	1.36e-05	1.63e-05	1.87e-05	1.09e-06	1.64e-05	3.16e-34
	BRK-GA	1.06e-03	3.04e-03	7.10e-03	8.73e-04	3.17e-03	5.27e-31
	IGA	1.18e-06	7.96e-05	4.65e-04	7.70e-05	1.10e-04	3.56e-34

for example, the best value in 100 runs is smaller than BRK-GA as shown in Figure 7. Compared with IGA, although the performance enhancement of EGA in function4 is average, the optimization effect of function5 and six are better as shown in Figure 7.

As long as *p*-value is less than α (0.05), the two results can be considered to be significantly different. According to the simulation results of rank sum test, except for the Enhanced crossover, SSP and BRK-GA in function3, which are greater than α, all the other results are far less than α. It can be said that the EGA proposed in this paper shows superiority over the latest algorithms.

These results show the effectiveness and superiority of the proposed EGA scheme in terms of accuracy and convergence.

4 Design and analysis of enhancement of genetic algorithms wavelet neural network

4.1 Wavelet neural network)

The WNN (Tinos et al., 2018) has always been deemed a wavelet-based functional linkage network or an extension of radial basis function (RBF) network containing its unique virtue, i.e., potent self-adaptability, and brief network structure. From the perspective of its structural form, the transfer neuron of a single hidden layer in the WNN is the Morlet wavelet windowing function, where the built-in function includes scaling and shifting arguments. Each neuron connects to its adjacent neuron *via* connection weights (Peng and Xiang, 2020). The basic topology of the WNN is shown in Figure 8.

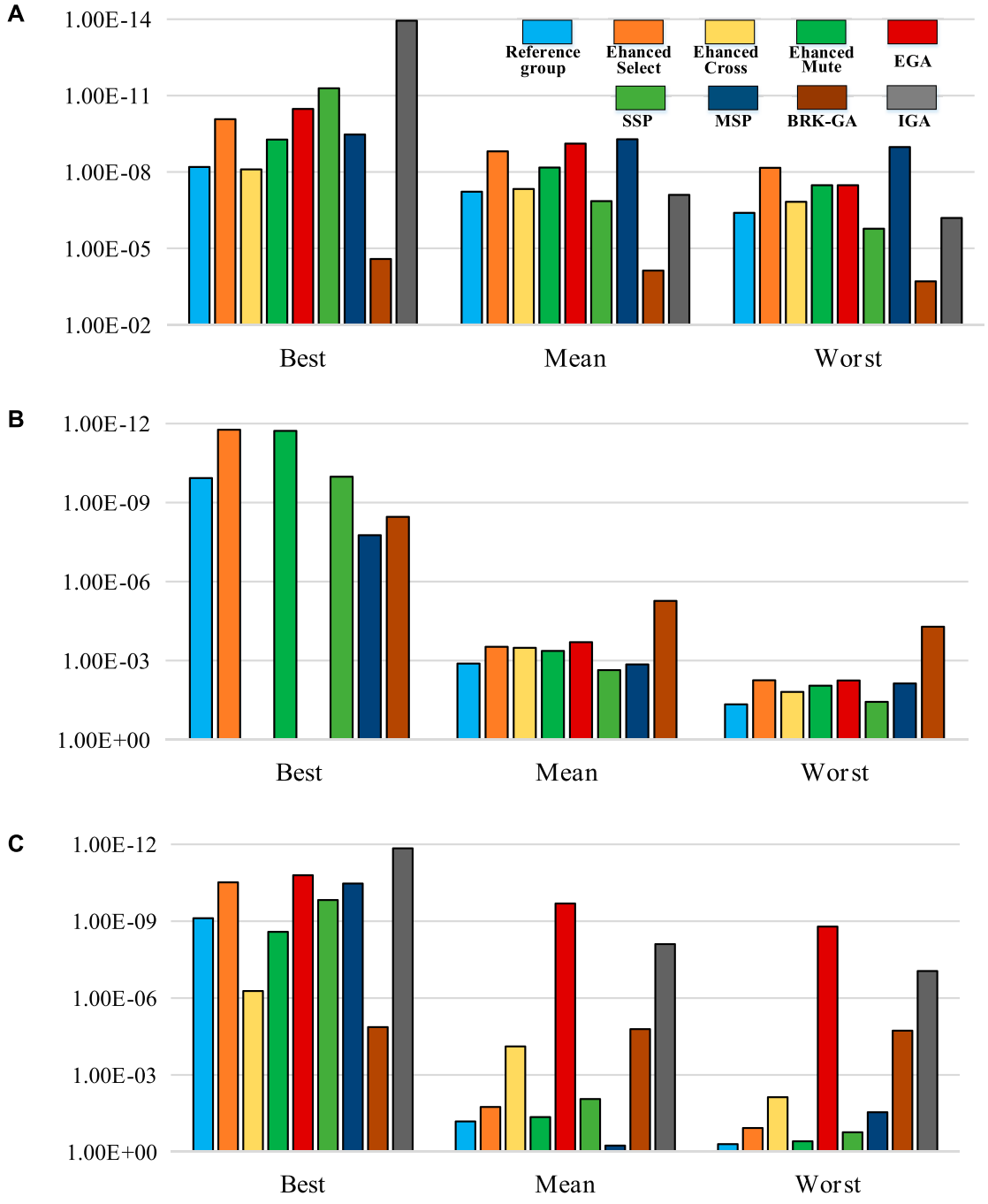

FIGURE 6
Comparison of the nine designed experiments on the basis of their best, mean, and worst fitness values for the six test functions (1): **(A)** funtion1, **(B)** funtion2 and **(C)** function3.

In Figure 8, $X_1, X_2, \cdots, X_k$ are the input signals of the WNN, and $Y_1, Y_2, \cdots, Y_m$ denote the output signals of the WNN. ω_{ij} and ω_{jk} are the connection weights from the input layers to the hidden layers and from the hidden layers to the output layer, respectively.

In this paper, the Morlet function is employed as φ (wavelet basis function), and it is given as follows:

$$\psi_{a,b}(x) = \cos(1.75x)\exp(-x^2/2) \tag{13}$$

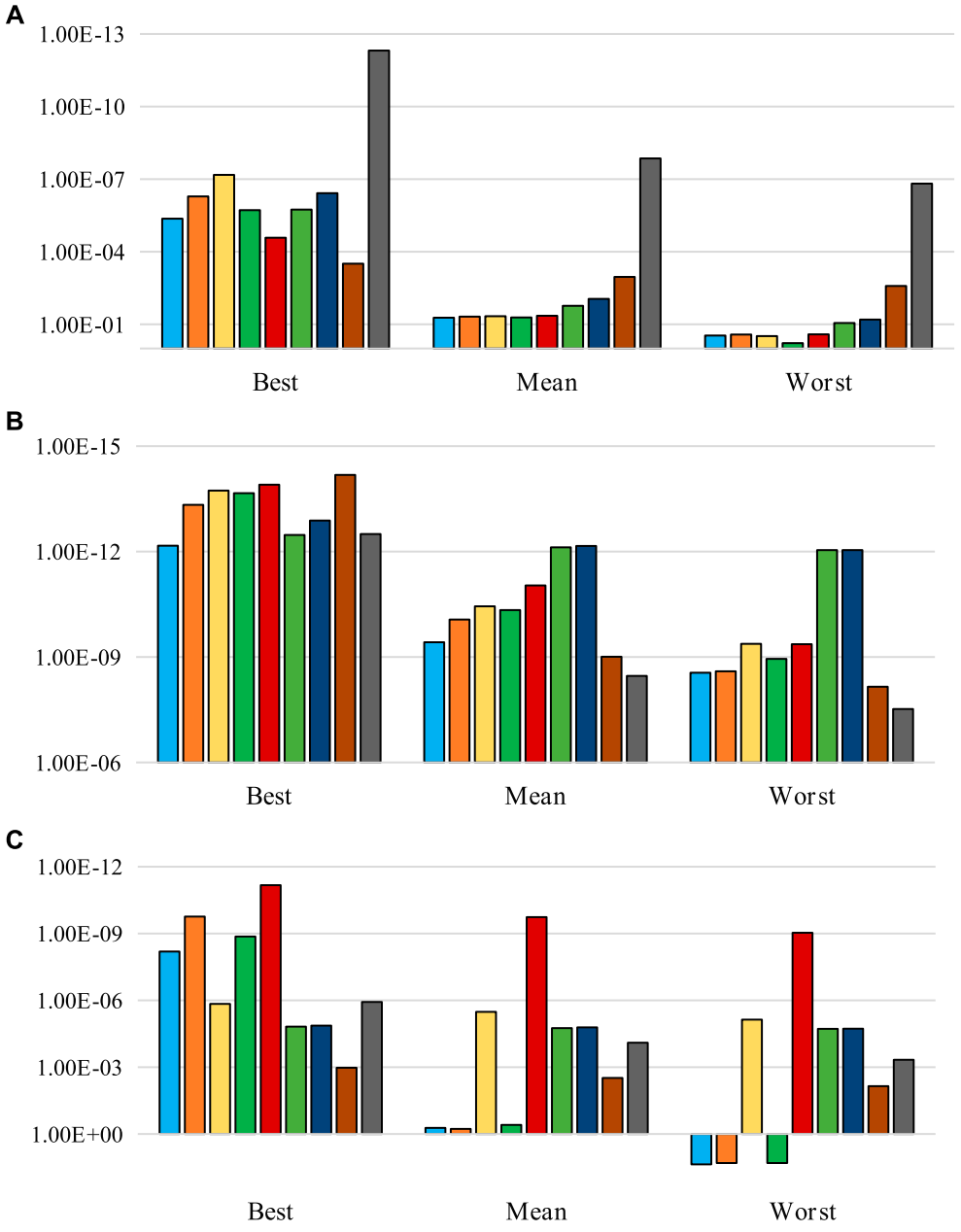

FIGURE 7
Comparison of the nine designed experiments on the basis of their best, mean, and worst fitness values for the six test functions (2): **(A)** funtion4, **(B)** funtion5 and **(C)** function6.

4.2 The design flow of enhancement of genetic algorithms wavelet neural network

Considering that the EGA has a strong global search ability and high search precision, optimizing the initial weights, as well as the scaling and shift factors of the WNN, with the EGA is expected to make improve the prediction performance of the network model. The enhanced algorithmic flow is shown in Figure 9.

The specific implementation steps are as follows:

(1) The topology of the WNN (as described by Figure 8), where the wavelet basis function is the Morlet function, is used by the EGA algorithm to find $\omega_{ij}, \omega_{jk}, a_j, b_j$.
(2) Population initialization: determining the population size and the maximum number of iterations. Individuals are coded with real numbers, and each individual is composed of weights ω_{ij} and ω_{jk}, a scaling factor a_j, and

TABLE 5 Convergence analysis for each evolutionary process of design experiments.

Test function	Combination forms	Fitness≤			Test function	Combination forms	Fitness≤		
		10^{-06}	10^{-08}	10^{-10}			10^{-03}	10^{-05}	10^{-07}
Function1	RG	100	86	0	Function2	RG	94	60	22
	ES	100	100	47		ES	100	73	25
	EC	100	94	0		EC	99	88	64
	EM	100	100	7		EM	100	67	30
	EGA	**100**	**100**	**75**		**EGA**	**100**	**82**	**65**
	SSP	96	26	1		SSP	73	39	0
	MSP	100	100	0		MSP	63	13	2
	BRK-GA	0	0	0		BRK-GA	100	82	6
	IGA	100	45	9		IGA	\	\	\
Test function	**Combination forms**	**Fitness≤**			**Test function**	**Combination forms**	**Fitness≤**		
		10^{-04}	10^{-06}	10^{-10}			10^{-02}	10^{-05}	10^{-07}
Function3	RG	16	16	1	Function4	RG	81	38	35
	ES	55	55	2		ES	86	40	40
	EC	98	5	0		EC	87	39	35
	EM	30	19	0		EM	84	40	40
	EGA	**100**	**100**	**13**		**EGA**	**88**	**35**	**32**
	SSP	50	50	0		SSP	46	23	23
	MSP	62	62	57		MSP	64	40	40
	BRK-GA	100	0	0		BRK-GA	100	47	47
	IGA	100	100	14		IGA	100	100	100
Test function	**Combination forms**	**Fitness≤**			**Test function**	**Combination forms**	**Fitness≤**		
		10^{-09}	10^{-11}	10^{-13}			10^{-04}	10^{-07}	10^{-09}
Function5	RG	100	42	1	Function6	RG	65	35	0
	ES	100	88	20		ES	66	49	13
	EC	100	91	17		EC	100	0	0
	EM	100	89	25		EM	78	62	0
	EGA	**100**	**99**	**42**		**EGA**	**100**	**100**	**100**
	SSP	100	100	0		SSP	100	0	0
	MSP	100	100	0		MSP	100	0	0
	BRK-GA	70	6	1		BRK-GA	0	0	0
	IGA	89	18	1		IGA	69	0	0

a shift factor b_j from the WNN. ω^1 signifies the weight from the input layers to the hidden layers, and ω^2 signifies the weight from the hidden layers to the output layer. The encoding form is as follows (Cicek and Ozturk, 2021):

$$\omega_{11}^1..\omega_{19}^1\omega_{21}^1..\omega_{29}^1..\omega_{91}^1..\omega_{99}^1\omega_{11}^2..\omega_{91}^2..a_1..a_9..b_1..b_9$$

(3) Fitness selection and individual calculation: the individual fitness value is obtained according to the training results produced by the WNN. If the fitness meets the accuracy requirements, the loop is terminated; otherwise, it proceeds to the next step. To avoid the absolute error being too small, the fitness function is given as follows:

$$f = {}^{1}/_{(1+E)} \tag{14}$$

$$E = \frac{1}{2P}\sum_{n=1}^{N}\sum_{n=1}^{N}\left(d_n^p - y_n^p\right) \tag{15}$$

where d_n^p is the desired output of the nth node in the output layers; y_n^p is the actual output of the network; and P (p = 1,2, . . . ,P) is the group number of the input and output samples.

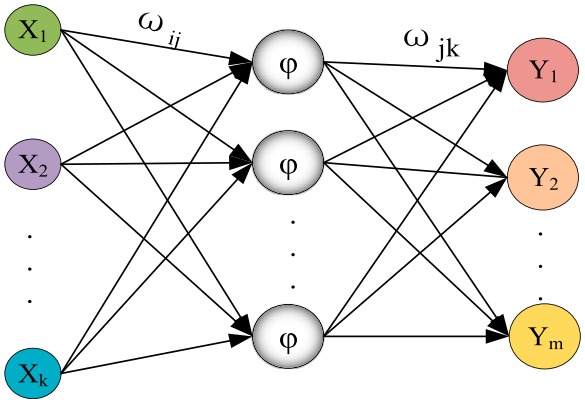

FIGURE 8
Fundamental topology of the WNN.

(4) Genetic operations: i. Selection: The H-mean crowding strategy is carried out according to the pseudocode in Table 1 ii. Crossover: New individuals are generated by performing nonuniform arithmetical crossover on the selected parents, as shown in Eq. 3. iii. Mutation: The Gauss-r. Cauchy function is performed on the participating individuals, as shown in Eqs 4, 5.
(5) The loop is stopped, the current optimal solution is obtained, and the decoded weights ω_{ij} and ω_{jk}, scaling factor a_j and shift factor b_j are used as the initial input parameters of the WNN.
(6) The WNN is used for training; it is judged whether the network training process is finished according to the preset error and number of iterations. Finally, ω_{ij_best}, ω_{jk_best}, a_{j_best}, and b_{j_best} are obtained by the above steps, and then the parameters are applied to the WNN model.
(7) The trained model is used to test the samples, and the resulting performance indicators are analyzed.

4.3 The convergence analysis of enhancement of genetic algorithms wavelet neural network

The essence of EGAWNN is to optimize the initial parameters of the WNN through the EGA solver so that they are independent of the operation process. We only need to prove the convergence of the EGA and WNN. Regarding the convergence of the WNN, references (Jafarmadar, 2020), (Li et al., 1997; Liu et al., 2021) have given relevant proofs, so there is no need to repeat these steps. The convergence analysis of the EGA is given below.

Reference (Wang et al., 1996) deduced sufficient conditions for the convergence of the GA. The intensity function f of this paper is Eqs 14, 15, the problem space N is the code of the solution, and each point has a corresponding solution.

The class S existing in N satisfies the following derivation:

$\exists r \in V, (\forall i \in N, i \in S \Rightarrow f(i) \geq r) \cap (f(i) \geq r \Rightarrow i \in S)$; then, S is a superior class. According to theorem one in (Wang et al., 1996), class S is a conformance class.

Because the crowding strategy in this paper divides a population into GoodChrom and BadChrom, the following derivation conforms to the above properties:

$$\exists r \in BadChrom\_V, (\forall i \in S, GoodChrom \in S \Rightarrow f(i) \geq r) \cap (f(i) \geq r \Rightarrow i \in S)$$

In summary, the EGA proposed by this article contains a conformance class S.

For each class $S^r \in N$, the following theorem two from (Liu et al., 2021) holds:

If $f(S^r, N) \geq f(S, N)$, $\exists S^r \cap N \subseteq S$ or $f(S \cap S^r, N) > f(S^r, N)$, class S has stability. $f(Pop, N), Pop \in N$ is the average fitness of Pop.

Because the elitist strategy is used in the selection process of this article, $f_{t+1}(best) \geq f_t(best), best \in S$ must hold, so $\exists best \in S^r, S^r \in S \Rightarrow S^r \cap N \subseteq S, st. f(S^r, N) \geq f(S, N)$.

The above derivation proves that regardless of the number of iterations, S^r does not replace S in the next generation; instead, they grow together, which ensures that the conformance class is not replaced by other classes.

If the conformance class is stable, the GA can converge to the optimal solution (Wang et al., 1996). Additionally, Pan (Pan, 1998) proved that adopting the elitist model can enhance the stability of the algorithm, and this model makes the SGA easily converge to the global optimum with a probability of one in the end. All of the above factors certify that the EGA is convergent.

5 An industrial experiment regarding aluminum electrolysis

5.1 Experimental objects and model parameters

A new-type aluminum cell, combined with a perforated anode and a heteromorphic cathode, is used to test the reliability of the EGAWNN solver, as shown in Figure 10, where W represents the DC energy consumption per ton of aluminum, the perforated anode has multiple holes built into it to allow air bubbles to escape and the heteromorphic cathode can reduce molten aluminum fluctuations by optimizing cathode structure.

Modern aluminum electrolysis devices are complex process equipment with multiphase and multifield

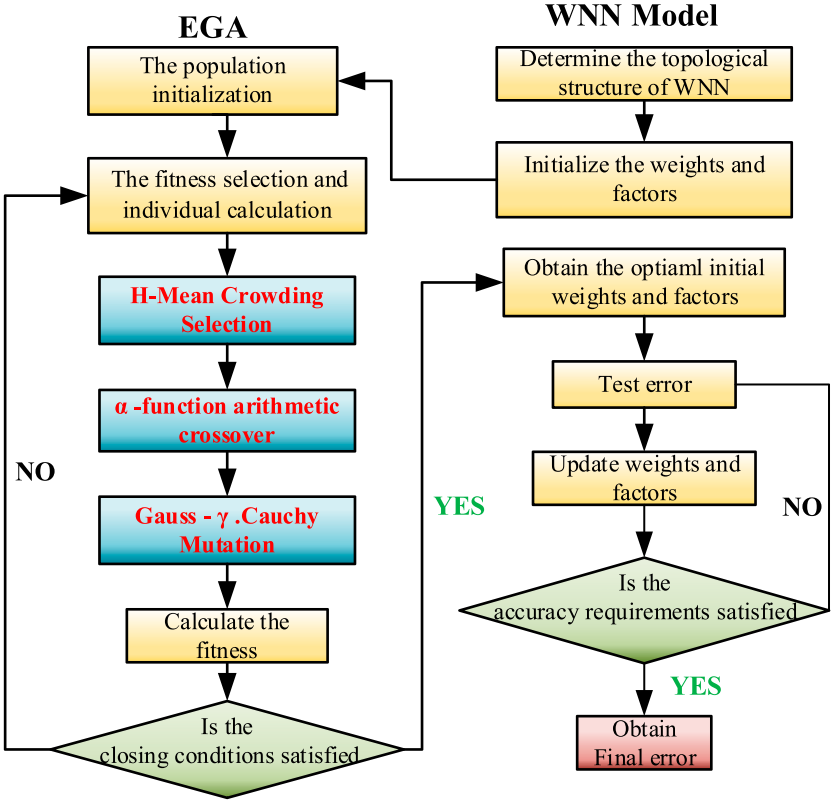

FIGURE 9
The flow chart of EGAWNN.

interactions (Gui et al., 2018). There are diversified physical and chemical changes inside these devices, as well as frequent exchanges of raw materials, energy and labor information with the external environment. When modeling the energy consumption of aluminum electrolysis using the traditional WNN, the structure is unstable due to the stochastic determination of the initial parameters, which may lead to a large forecasting error. The proposed EGAWNN solver can mine the best initial weights and factors and thereby increase the accuracy and authenticity of the prediction results.

Considering the experiences of expert and the impact of the real process on the DC energy consumption of an aluminum electrolyzer, we select the following nine effective decision parameters: the series current (A), molecular ratio (1), aluminum level (cm), electrolyte level (cm), cell temperature (°C), aluminum output (kg), daily consumption of fluoride salt (kg), NB times (s), and cell voltage (mV) (Tai-Fu et al., 2014). Based on the computer measurement and control system of Chongqing Tiantai Aluminum Co., Ltd. In Southwest China, the daily reported data of the electrolytic cell are collected, and 773 groups of data samples are obtained, as shown in Table 6.

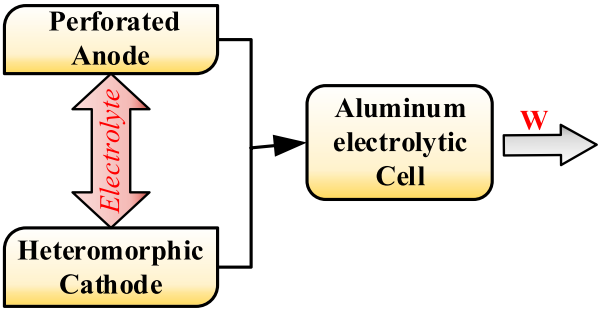

FIGURE 10
The core structure of the new aluminium electrolysis equipment.

5.2 The analysis of the experimental results based on enhancement of genetic algorithms wavelet neural network

The 773 groups of aluminum electrolysis data samples in Table 6 are assigned to the training group (n = 700) and test group (n = 73). The inputs are the nine selected decision

TABLE 6 Data samples of aluminium electrolytic cell.

Parameters	Samples				
	1	2	3	—	773
Series current (A)	1,679	1,679	1,685	—	1,682
Molecular ratio	2.32	2.43	2.41	—	2.54
Aluminium level (cm)	22.1	18	21	—	23
Electrolyte level (cm)	17	15	16.2	—	17
Cell temperature (°C)	948	951	942	—	947
Aluminium output (kg)	1,240	1,280	1,310	—	1,300
Daily consumption of fluoride salt (kg)	19.8	29	22.4	—	21
NB times (1)	952	947	948	—	961
Cell voltage (mV)	3,712	3,679	3,808	—	3,721
DC power consumption (kW.h/t-Al)	11,842	11,839	11,359	—	11,863

parameters, and the output is the unit DC power consumption. When the number of hidden layers is too small, the error rate of the predicted output may be too large. When the number of hidden layers is 9, the errors are reduced to a small amount. Therefore, the wavelet network structure is 9-9-1. Thus, it can be concluded that the dimensions of the state variable in EGAWNN are $9 \times 9 + 1 \times 12 + 1 \times 12 + 1 \times 12 = 118$. In this algorithm, the selection rate η_s is 0.87; the number of parents for crossover η_c is three; the number of mutation η_m individuals is two; the population size N is 40; the maximum number of iterations (MAXGEN) is 100; the learning rate of the WNN lr1 is 0.01, and lr2 is 0.001; the adjustment rate is 1.04; and the wavelet basis function is the Morlet function.

To prove the validity of the presented algorithm, under the same experimental samples and simulation platform, MATLAB R2020a (CPU: RTMi5-1038NG7; RAM: 15.8 GB; CPU: 2.00 GHz), the WNN, GAWNN, particle swarm optimized wavelet neural network (SOWNN), the four new algorithms mentioned in Section 3 optimized the WNN(SSPWNN, MSPWNN, BRK-GAWNN, and IGAWNN) and EGAWNN are separately used to model the energy consumption of the aluminum electrolytic tank, helping obtain contrastive experimental results.

Figure 11 visually shows the fitting effect of the real process energy consumption based on the above-mentioned eight modeling techniques. The performance ranking of process energy modeling effect from excellent to poor is as follows: EGAWNN, IGAWNN/BRK-GAWNN, MSPWNN, SSPWNN, GAWNN, PSOWNN, and WNN, where the fitting effect of IGAWNN and BRK-GAWNN is close. Overall, the prediction performance of EGAWNN is better than other models, which proves that this approach is feasible to further develop the modeling capabilities of the GAWNN.

The EGAWNN uses three enhanced operators, i.e., the H-Mean selection strategy, a new crossover function and an adaptive proportional coefficient γ into the Cauchy mutation, to mine the optimal parameter combination inside the model, which greatly enhances the convergence and the prediction accuracy of the built model. Based on the above analysis and Figure 12, EGAWNN has a lower relative error rate and better predictive performance than the other seven models, especially on some of the data with large fluctuations. The above analysis also shows that EGAWNN has good stability.

Table 7 compares the indicative data of each energy consumption model, for which 6 regression evaluation indicators, significance tests and algorithmic complexity metrics are listed, including the Maximum, Minimum, Mean, error sum of squares (SSE), mean square error (MSE), and RMSE. In addition, we carry out an analysis of algorithmic complexity and perform hypothesis testing based on the Wilcoxon matched-pairs signed-ranks test, where the significance test is calculated with the prediction results of EGAWNN as the reference group, and the single bound value α is set to 0.1, as shown in Table 7. The bold part in the table highlights the performance of the proposed method.

According to the numerical results in Table 7, it can be seen that the absolute error indicators of EGAWNN are obviously lower than those of WNN, GAWNN and PSOWNN, and slightly better than those of SSPWNN, MSPWNN, BRK-GAWNN, and IGAWNN. From the perspective of algorithmic complexity, compared with GAWNN control groups, the time complexity of EGAWNN increases due to secondary sorting in the selection operation of the EGA. However, this small difference does not affect the feasibility of the algorithm. The above results prove that the method proposed in this paper has certain modeling advantages over other methods.

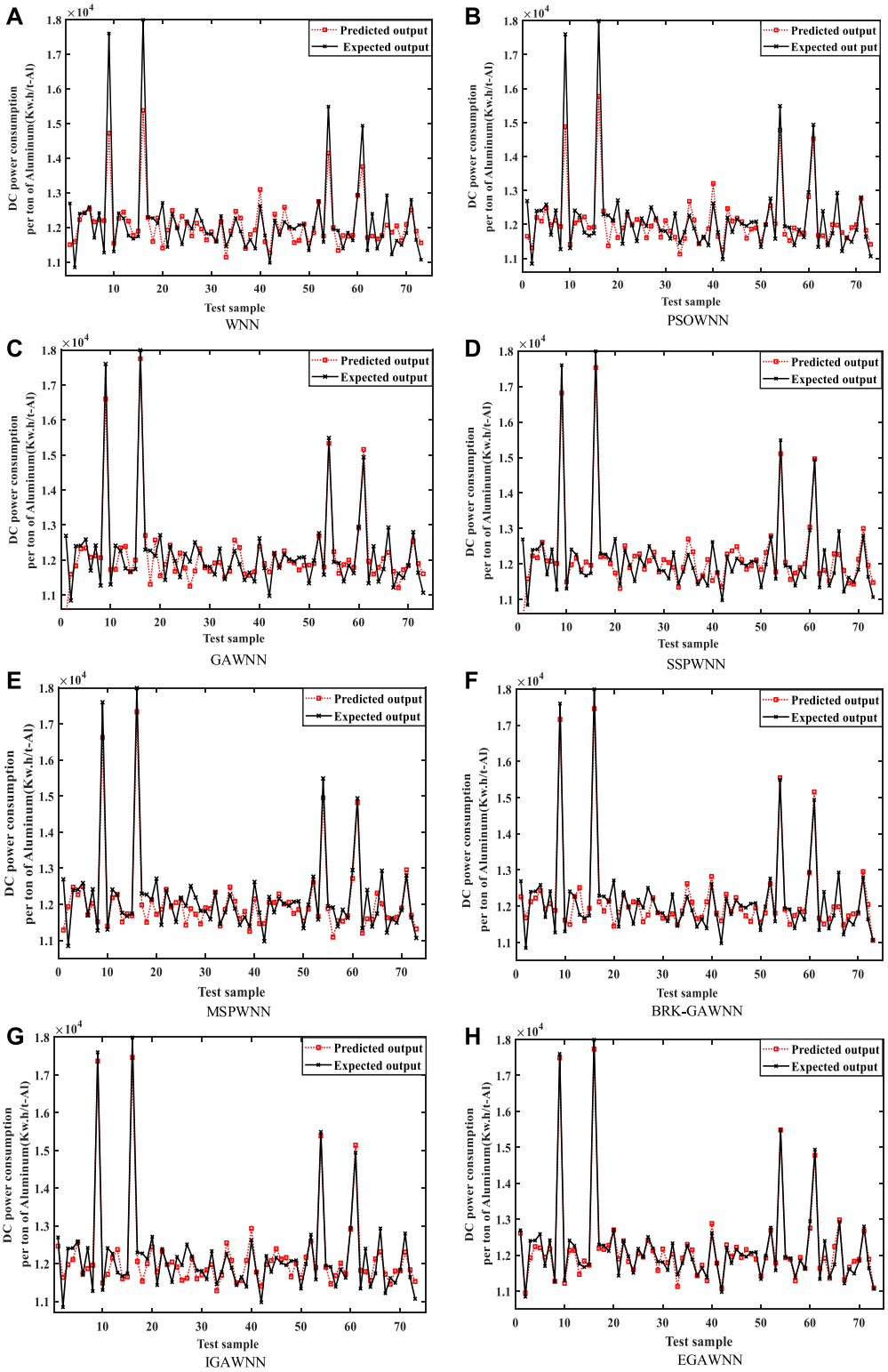

FIGURE 11
The prediction outputs in terms of DC power consumption based on: **(A)** WNN, **(B)** PSOWNN, **(C)** GAWNN, **(D)** SSPWNN, **(E)** MSPWNN, **(F)** BRK-GAWNN, **(G)** IGAWNN, and **(H)** EGAWNN.

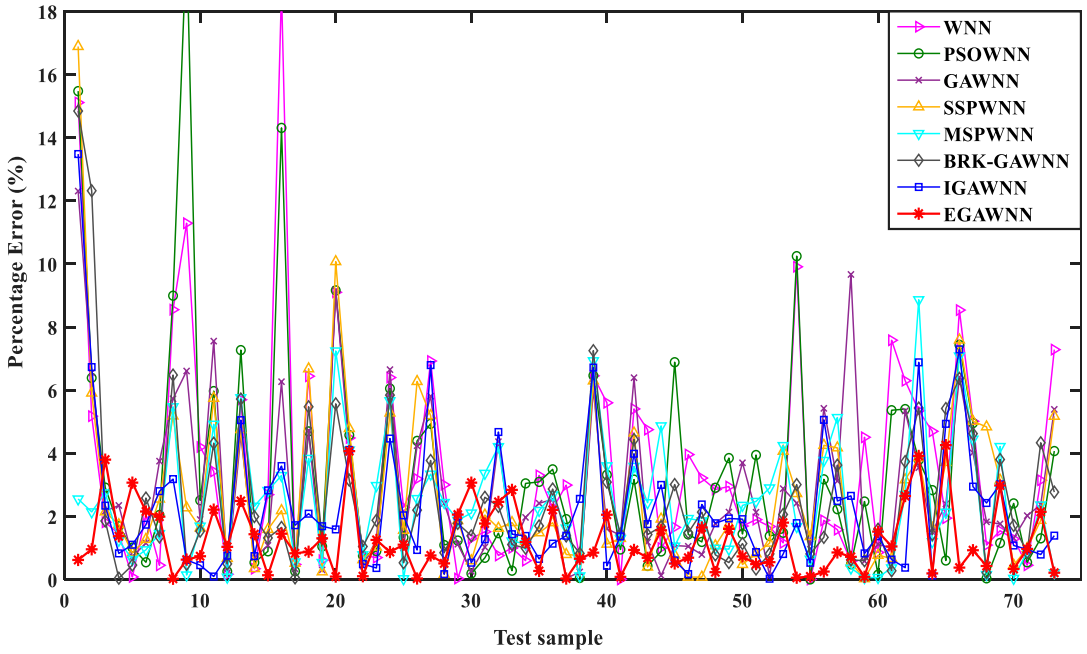

FIGURE 12
A comparison of the relative error percentages yielded by different models.

TABLE 7 Relevant performance indices yielded by different models.

Model	Comparison of absolute error indicators in test sets						Statistical test	Complexity	
	Max	Min	Mean	SSE	MSE	RMSE	*p*–value	Time	Space
WNN	18.6	2.6e+03	3.5	2.97e+07	4.08e+05	638.72	0.04	O (n^2)	O (n^2)
PSOWNN	20.2	5.9e+03	3.3	3.26e+06	2.38e+05	571.45	0.06	O (n^2)	O (n^2)
GAWNN	12.3	3.7e+02	2.9	1.89e+07	2.59e+05	508.90	0.09	O (n^2)	O (n^2)
EGAWNN	**6.3**	**2.5e+02**	**1.2**	**1.62e+05**	**2.21e+03**	**305.72**	—	O (n^3)	O (n^2)
SSPWNN	16.1	2.7e+02	2.6	1.57e+07	2.15e+05	464.60	0.10	O (n^3)	O (n^2)
MSPWNN	8.7	2.6e+02	2.4	1.07e+07	1.46e+05	382.17	0.13	O (n^3)	O (n^2)
BRKWNN	14.0	4.2e+02	2.6	1.39e+07	1.91e+05	437.55	0.20	O (n^3)	O (n^2)
IGANWNN	11.4	2.7e+02	2.2	1.11e+07	1.52e+05	389.91	0.32	O (n^3)	O (n^2)

To avoid the accidental influence of the original randomized parameters on the model evaluation, this algorithm conducts 20 independent repeated experiments on each model. Then, the relevant performance indicators are calculated based on the experimental results, including the mean absolute error (MAE), the mean relative error (MRE), the correlation (R) (Li W. et al., 2017) and the best population fitness value. Figure 13 shows the favorable stability of the energy consumption model based on EGAWNN in the form of boxplots. Simultaneously, compared with the SGA, although the SSP, MSP, BRK-GA IGA, and EGA all improves the best fitness value of the population, EGA's effect is more obvious. These results verify the advantage and validity of the EGA, which can deeply mine the predictive potential of the model by finding the optimal initial parameter combination of the energy consumption model. Meanwhile, the limitation of the proposed method in this paper for industrial production is that the input parameters of the model need to be collected continuously.

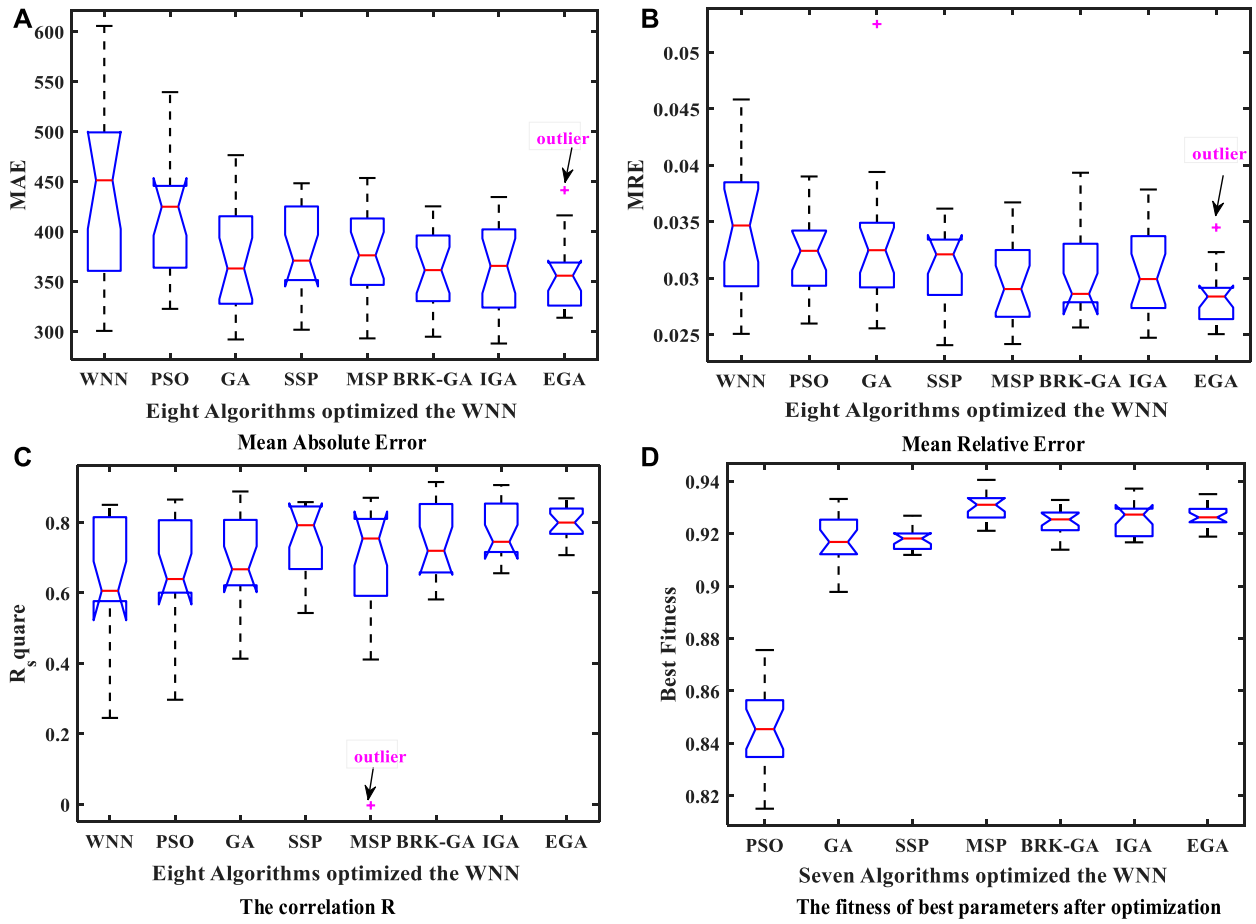

FIGURE 13
Boxplots of related performance indicators for 20 repeated tests: **(A)** Mean absolute error, **(B)** Mean relative error, **(C)** The correlation R and **(D)** The fitness of best parameters after optimization.

6 Conclusion

To obtain a high-precision energy consumption model for an AEMS, this study presents a novel framework based on a WNN and the EGA. In the EGAWNN algorithm, there are three main improvements, as follows:

(1) The H-Mean metric is developed to maintain the discreteness of the crowding strategy and is effectively applied to prevent premature convergence.
(2) A new sigmoid-based function S(α) is designed to update the nonuniform arithmetic crossover operation by setting intersections regularly.
(3) An adaptive proportional coefficient γ is introduced into the Gauss-Cauchy mutation to flexibly adjust the mutation step size.

A series of numerical experiments are performed, and these prove the efficacy of the proposed scheme. The algorithm has good potential to be exploited as an alternate, accurate and robust computing framework for building prediction models in various complex systems. However, it is worth highlighting here that the EGA is restricted to obtaining only the initial weights and factors of the WNN. In the future, we will explore the integration of the EGA into the internal topology structure of the WNN during every training process.

Data availability statement

The original contributions presented in the study are included in the article/supplementary material, further inquiries can be directed to the corresponding author.

Author contributions

Conceptualization, LY and QF; methodology, LY and QF.; software, QF and YL; validation, LY; formal analysis, LZ, LY, and QF; data curation, LZ and QM; writing—original draft preparation, LY and QF; writing—review and editing, YL and QM; visualization, LY and QF All authors have read and agreed to the published version of the manuscript.

Funding

This work is supported by the Foundation Program of Chongqing Normal University (No. 22XLB014), the Science and Technology Research Program of Chongqing Municipal Education Commission (Nos KJQN202200531 and KJQN202103306).

Conflict of interest

The authors declare that the research was conducted in the absence of any commercial or financial relationships that could be construed as a potential conflict of interest.

Publisher's note

All claims expressed in this article are solely those of the authors and do not necessarily represent those of their affiliated organizations, or those of the publisher, the editors and the reviewers. Any product that may be evaluated in this article, or claim that may be made by its manufacturer, is not guaranteed or endorsed by the publisher.

References

Amini, F., and Hu, G. (2021). A two-layer feature selection method using genetic algorithm and elastic net. *Expert Syst. Appl.* 166, 114072. doi:10.1016/j.eswa.2020.114072

Cicek, Z, and Ozturk, Z. K. (2021). Optimizing the artificial neural network parameters using a biased random key genetic algorithm for time series forecasting. *Appl. Soft Comput.* 102 (6), 107091. doi:10.1016/j.asoc.2021.107091

Dang, D. C., Friedrich, T., Ktzing, T, Krejca, M. S., Sutton, A. M., Oliveto, P. S., et al. (2016). Escaping local optima using crossover with emergent diversity. *IEEE Trans. Evol. Comput.* 22 (3), 484–497. doi:10.1109/tevc.2017.2724201

Das, A. K., and Pratihar, D. K. (2021). Solving engineering optimization problems using an improved real-coded genetic algorithm (irga) with directional mutation and crossover. *Soft Comput.* 25, 5455–5481. doi:10.1007/s00500-020-05545-9

Guan, C., Luh, P. B., Michel, L. D., Wang, Y., and Friedland, P. B. (2013). Very short-term load forecasting: Wavelet neural networks with data pre-filtering. *IEEE Trans. Power Syst.* 28 (1), 30–41. doi:10.1109/tpwrs.2012.2197639

Gui, W. H., Yue, W. C., Xie, Y. F., Zhang, H. L., and Yang, C. H. (2018). A review of intelligent optimal manufacturing for aluminum reduction production. *Acta Autom. Sin.* 44 (11), 1957.

Huang, W., Oh, S. K., and Pedrycz, W. (2018). Hybrid fuzzy wavelet neural networks architecture based on polynomial neural networks and fuzzy set/relation inference-based wavelet neurons. *IEEE Trans. Neural Netw. Learn. Syst.* 29 (8), 3452–3462. doi:10.1109/TNNLS.2017.2729589

Jafarmadar, S. (2020). Numerical investigation and prediction of effects of applying anatase tio2 nanoparticle on performance and emissions of ci engine by using wnn-ga. *J. Clean. Prod.* 267 (10), 122130. doi:10.1016/j.jclepro.2020.122130

Jha, R., and Senroy, N. (2018). Wavelet ridge technique based analysis of power system dynamics using measurement data. *IEEE Trans. Power Syst.* 33 (4), 4348–4359. doi:10.1109/tpwrs.2017.2783347

Khelil, K., Berrezzek, F., and Bouadjila, T. (2021). Ga-based design of optimal discrete wavelet filters for efficient wind speed forecasting. *Neural comput. Appl.* 32 (16), 4373–4386. doi:10.1007/s00521-020-05251-5

Lha, C., Jhd, B., Jrw, B., and Ez, A. (2018). A hyper-heuristic approach to automated generation of mutation operators for evolutionary programming - sciencedirect. *Appl. Soft Comput.* 62, 162–175.

Li, M. Q., and Kou, J. (2002). Coordinate multi-population genetic algorithms for multi-modal function optimization. *Acta Autom. Sin.* 28 (8), 497–504.

Li, L. W. B., and Zhang, Y. (2019). Modeling for cnc machine tool thermal error based on genetic algorithm optimization wavelet neural networks. *J. Mech. Eng.* 55 (21), 215–220.

Li, Y., Zhang, B., and Cao, C. (1997). Wavelet neural network and its structural design method. *Pattern Recognit. Artif. Intell.* 10 (3), 197–205.

Li, C., Zhang, N., Lai, X., Zhou, J., and Xu, Y. (2017). Design of a fractional-order pid controller for a pumped storage unit using a gravitational search algorithm based on the cauchy and Gaussian mutation. *Inf. Sci.* 396, 162–181. doi:10.1016/j.ins.2017.02.026

Li, C., Mao, Y., Zhou, J., Zhang, N., and An, X. (2017). Design of a fuzzy-pid controller for a nonlinear hydraulic turbine governing system by using a novel gravitational search algorithm based on cauchy mutation and mass weighting. *Appl. Soft Comput.* 52, 290–305. doi:10.1016/j.asoc.2016.10.035

Li, H., Deng, J., Yuan, S., Feng, P., and Arachchige, D. (2021). Monitoring and identifying wind turbine generator bearing faults using deep belief network and EWMA control charts. *Front. Energy Res.* 9, 799039. doi:10.3389/fenrg.2021.799039

Li, H., Deng, J., Feng, P., Pu, C., Arachchige, D., and Cheng, Q. (2021). Short-Term nacelle orientation forecasting using bilinear transformation and ICEEMDAN framework. *Front. Energy Res.* 9, 780928. doi:10.3389/fenrg.2021.780928

Li, W., Kong, D., and Wu, J. (2017). A novel hybrid model based on extreme learning machine, k-nearest neighbor regression and wavelet denoising applied to short-term electric load forecasting. *Energies* 10 (5), 694–710. doi:10.3390/en10050694

Li, H. (2022). Short-Term wind power prediction via spatial temporal analysis and deep residual networks. *Front. Energy Res.* 10, 920407. doi:10.3389/fenrg.2022.920407

Li, H. (2022). SCADA data based wind power interval prediction using LUBE-based deep residual networks. *Front. Energy Res.* 10, 920837. doi:10.3389/fenrg.2022.920837

Liu, J. W., Zuo, F. L., Guo, Y. X., Li, T. Y., and Chen, J. M. (2021). Research on improved wavelet convolutional wavelet neural networks. *Appl. Intell. (Dordr).* 51, 4106–4126. doi:10.1007/s10489-020-02015-5

Majeed, K., Masood, Z., Samar, R., and Raja., M. (2017). A genetic algorithm optimized Morlet wavelet artificial neural network to study the dynamics of nonlinear Troesch's system. *Appl. Soft Comput.* 56, 420–435. doi:10.1016/j.asoc.2017.03.028

Mishra, R., and Bajpai, M. K. (2021). A priority based genetic algorithm for limited view tomography. *Appl. Intell. (Dordr).* 51 (2), 6968–6982. doi:10.1007/s10489-021-02192-x

Osuna, E. C., and Sudholt, D. (2020). Runtime analysis of crowding mechanisms for multimodal optimization. *IEEE Trans. Evol. Comput.* 24 (3), 581–592. doi:10.1109/tevc.2019.2914606

Pan, Z. (1998). Evolutionary computing. *Inf. Process. Lett.* 82 (1), 1–6.

Pauline, Z., and Zarita, O. (2019). Optimizing wavelet neural networks using modified cuckoo search for multi-step ahead chaotic time series prediction. *Appl. Soft Comput.* 80, 374–386. doi:10.1016/j.asoc.2019.04.016

Peng, Y., and Xiang, W. (2020). Short-term traffic volume prediction using ga-bp based on wavelet denoising and phase space reconstruction. *Phys. A Stat. Mech. its Appl.* 549, 123913. doi:10.1016/j.physa.2019.123913

Prugel-Bennett, A., and Tayarani-Najaran, M.-H. (2012). Maximum satisfiability: Anatomy of the fitness landscape for a hard combinatorial optimization problem. *IEEE Trans. Evol. Comput.* 16 (3), 319–338. doi:10.1109/tevc.2011.2163638

Sabouri, M., Khoei, S., and Neshati, J. (2017). Plasma current analysis using discrete wavelet transform during plasma electrolytic oxidation on aluminum. *J. Electroanal. Chem.*, 79–87. doi:10.1016/j.jelechem.2017.03.035

Shojaedini, R. S. E., Majd, M, and Safabakhsh, R. (2019). Novel adaptive genetic algorithm sample consensus. *Appl. Soft Comput.* 77, 635–642. doi:10.1016/j.asoc.2019.01.052

Slowik, A., and Kwasnicka, H. (2020). Evolutionary algorithms and their applications to engineering problems. *Neural comput. Appl.* 32 (16), 12363–12379. doi:10.1007/s00521-020-04832-8

Song, L., Peng, W., and Goel, L. (2016). A novel wavelet-based ensemble method for short-term load forecasting with hybrid neural networks and feature selection. *IEEE Trans. Power Syst.* 31 (3), 1788–1798. doi:10.1109/tpwrs.2015.2438322

Song, Y. Y., Wang, F. L., and Chen, X. X. (2019). An improved genetic algorithm for numerical function optimization. *Appl. Intell. (Dordr).* 49, 1880–1902. doi:10.1007/s10489-018-1370-4

Sun, J., Liu, X., Bck, T., and Xu, Z. (2021). Learning adaptive differential evolution algorithm from optimization experiences by policy gradient. *IEEE Trans. Evol. Comput.* 25 (4), 666–680. doi:10.1109/tevc.2021.3060811

Tai-Fu, L. I., Yao, L. Z., Jun, Y. I., Wen-Jin, H. U., Ying-Ying, S. U., and Jia, W. (2014). Improved ukfnn based on square root filter and strong tracking filter for dynamic evolutionary modeling of aluminium reduction cell. *Acta Autom. Sin.* 40 (3), 522–530.

Tian, Y., Ma, L., Yang, S., and Wang, Q. (2020). A methodology for calculating greenhouse effect of aircraft cruise using genetic algorithm-optimized wavelet neural network. *Complexity*, 7141320. doi:10.1155/2020/7141320

Tinos, R., Liang, Z., Chicano, F., and Whitley, D. (2018). Nk hybrid genetic algorithm for clustering. *IEEE Trans. Evol. Comput.* 22 (5), 748–761. doi:10.1109/tevc.2018.2828643

Wang, L., Yong, H., and Hong, J. (1996). Research on the convergence of the genetic algorithm. *Chin. J. Comput. Chin. J. Comput.* 19 (10), 794–797.

Wu, Q, and Law, R. (2011). Cauchy mutation based on objective variable of Gaussian particle swarm optimization for parameters selection of svm. *Expert Syst. Appl.* 38 (6), 6405–6411. doi:10.1016/j.eswa.2010.08.069

Wu, Y., Li, W., Wang, Y., and Zhang, K. (2019). Remaining useful life prediction of lithium-ion batteries using neural network and bat-based particle filter. *IEEE Access* 7, 54843–54854. doi:10.1109/access.2019.2913163

Xu, J., Pei, L., and Zhu, R. z. (2018). Application of a genetic algorithm with random crossover and dynamic mutation on the travelling salesman problem. *Procedia Comput. Sci.* 131, 937–945. doi:10.1016/j.procs.2018.04.230

Yang, C., Zhou, L., Huang, K., Ji, H., Long, C., Chen, X., et al. (2019). Multimode process monitoring based on robust dictionary learning with application to aluminium electrolysis process. *Neurocomputing* 332 (7), 305–319. doi:10.1016/j.neucom.2018.12.024

Yao, L., Li, T., Li, Y., Wei, L., and Yi, J. (2019). An improved feed-forward neural network based on ukf and strong tracking filtering to establish energy consumption model for aluminum electrolysis process. *Neural comput. Appl.* 31 (8), 4271–4285. doi:10.1007/s00521-018-3357-9

Yi, J., Bai, J., Zhou, W., He, H., and Yao, L. (2018). Operating parameters optimization for the aluminum electrolysis process using an improved quantum-behaved particle swarm algorithm. *IEEE Trans. Ind. Inf.* 4 (8), 3405–3415. doi:10.1109/tii.2017.2780884

Zhang, G., Hu, Y., Sun, J., and Zhang, W. (2020). An improved genetic algorithm for the flexible job shop scheduling problem with multiple time constraints. *Swarm Evol. Comput.* 54 (4), 100664. doi:10.1016/j.swevo.2020.100664

frontiers | Frontiers in Energy Research

TYPE Original Research
PUBLISHED 16 September 2022
DOI 10.3389/fenrg.2022.1008927

OPEN ACCESS

EDITED BY
Yusen He,
The University of Iowa, United States

REVIEWED BY
Jiahao Deng,
DePaul University, United States
Sun Mingrui,
Nanyang Technological University, Singapore
Bo Jiang,
Beihang University, China
Chenghang Zheng,
Zhejiang University, China

*CORRESPONDENCE
Shengqiang Shen,
zzbshen@dlut.edu.cn
Kun Zhang,
zhk@dlou.edu.cn

SPECIALTY SECTION
This article was submitted to Smart Grids, a section of the journal Frontiers in Energy Research

RECEIVED 01 August 2022
ACCEPTED 29 August 2022
PUBLISHED 16 September 2022

CITATION
Ren X, Guo Y, Shen S and Zhang K (2022), Large eddy simulation of flow field in thermal vapor compressor. *Front. Energy Res.* 10:1008927. doi: 10.3389/fenrg.2022.1008927

Large eddy simulation of flow field in thermal vapor compressor

Xiaotong Ren[1,2], Yali Guo[1,2], Shengqiang Shen[1,2]* and Kun Zhang[3]*

[1]National Joint Engineering Research Center for Thermal Energy Integration, Dalian, China, [2]School of Energy and Power Engineering, Dalian University of Technology, Dalian, China, [3]School of Ocean and Civil Engineering, Dalian Ocean University, Dalian, China

In the low-temperature multi-effect evaporation (LT-MEE) desalination plant, improving the performance of thermal vapor compressor (TVC) could reduce the energy loss, and increase the gained output ratio (GOR) and consequently improve the system economy efficiency. Implementing large eddy simulation (LES) as the numerical method, a 3-D computational fluid dynamics model of TVC is established to simulate the flow field under various conditions. The effects of motive steam pressure on the flow field, vortex core, turbulent viscosity and vortex iso-surface of the TVC are discussed, and the corresponding interior flow field distribution is obtained as well. Q criterion and normalized Q criterion are applied to visualize the vortex cores and vortex iso-surfaces. The distributions of vortexes in different scales are displayed, large-scale vortexes are mainly distributed in the exit area of the nozzle, the constant section of the mixing chamber and the diffuser. Additionally, the large-scale vortexes are primarily located along the axis in different morphology while the small-scale ones are randomly distributed near the wall.

KEYWORDS

thermal vapor compressor, steam ejector, large eddy simulation, Q criteria, flow field, vortex analysis

1 Introduction

Desalination seems to be one of the most promising solutions to meet the freshwater demand and address water shortage because of the abundant seawater storage. Among various desalination technologies, low-temperature multi-effect evaporation (LT-MEE) desalination with a thermal vapor compressor (TVC) may be a good solution. In an LT-MEE system, there are a range of multi-effect evaporators. LT-MEE system with TVC is capable of achieving high thermal efficiency with lower energy consumption, which could realize more efficient utilization of the low-grade energy. As illustrated in Figure 1, the MEE-TVC system mainly consists of multi-evaporators, a condenser, pumps, a seawater supply unit and the TVC (Liu et al., 2012). TVC could recover the low-pressure steam from the certain effect, increase gained output ratio (GOR) and reduce the consumption of new steam. Run by the motive steam extracted from several kinds of devices (e.g., turbine, boiler), TVC could compress the suction steam to reach the desired pressure

(Mazini et al., 2014). The discharged steam at the outlet of the TVC leaves and condenses in the first effect, it simultaneously provides the energy that the seawater needs to evaporate. The steam from the outlet of TVC is usually superheated, it could pass through the desuperheater and leave as saturated steam by mixing with the saturated water (Shen et al., 2011). According to the working principle of a TVC, the entrainment process could greatly decrease the external steam demand and the input resource consumption by reuse of the vapor. Therefore, as a considerably important device of MEE-TVC system, it could definitely improve energy efficiency and competitiveness of the system, and thus reduce the steam consumption.

In recent years, various studies have been conducted to investigate the flow phenomena and the interior flow field on the steam ejector by means of Reynolds Averaged Navier-Stokes (RANS). Li. (2004) simulated the complex flow field of a steam ejector with the k-ε turbulent model, a shock diamond pattern is observed at exit area of the nozzle and another oblique shock occurs in the diffuser in the velocity profile. Sriveerakul et al. (2007) selected the "*realizable k-ε model*" to investigate the turbulence characteristic and mixing process of a steam ejector, hence the flow behaviors were obtained. The flow structures were established, and the phenomena in the flow passage were discussed. Allouche et al. (2014) presented a numerical study of a steam ejector on the flow structure by the "*realizable k-ε model*" to better understand the mixing phenomenon and the shock wave location. Under a variety of operating conditions, the flow structure and the mixing process were performed in the ejector. It was found that two distinct shock waves occurred in the diffuser section with a relatively low condenser pressure (< 2.5 kPa). In TVC, since the flow is turbulent with an extremely high Reynolds number, a superior turbulence model is necessary to obtain more accurate results. In the past few years, most of the studies were carried out through the RANS technique in the numerical simulations of TVC. However, much more turbulent properties and relevant vortex characteristics could be obtained by LES turbulence model. Sharifi. (2020) studied the effects of variations of the suction flow inside the ejector by RANS. By comparing with the ideal gas model, the contours of shock waves by non-equilibrium supersaturated steam model presented a more extended supersonic region. The results revealed the presence of strong normal-shock waves in the non-equilibrium supersaturated steam model, while the weak oblique-shock waves existing in the ideal gas model.

Wu et al. (2018) analyzed the effect of nozzle outlet diameter, throat distance, mixing chamber throat and diffuser chamber diameter on the ejector performance. The results indicated that the nozzle outlet diameter is the most sensitively influencing factor, and the optimized ejector has better performance. Sun et al. (2021) investigated the effects of the wall roughness and temperature on the ejector performance. The simulation results indicated that the increase of the roughness height would significantly reduce the ejector performance and attenuate the non-equilibrium condensation phenomenon. Liu et al. (2017) studied the influence of the area ratio on the ejector efficiencies, and the results show that the mixing efficiency plays a more important role in ejector performance than other efficiencies. Besagni and Inzoli. (2017) presented a numerical study of the turbulent compressible fluid in a supersonic ejector, and seven turbulence closures were compared. According to their work, the k-ω SST model shows better performance in global and local flow phenomena predictions. Liu et al. (2018) analyzed the performance of the ejector under both critical and subcritical mode. The influence of component efficiencies on the ejector performance for different working fluids is presented. Reis et al. (Reis and Gioria, 2021) investigated the optimization of the entire geometry of LJL ejectors with multiple parameters to maximize energy efficiency. The effect is mainly governed by the nozzle diameter, the nozzle position and mixing chamber length. It was found that the flow profiles in the optimized geometry tend to be more homogenous, hence less dissipative, and it was also confirmed by local energy dissipation rate. Sun et al. (2022) characterized the influence on pressure drop and heat transfer coefficient, they investigated Kelvin cells with different throat areas and structures. The results revealed that the elliptical Kelvin

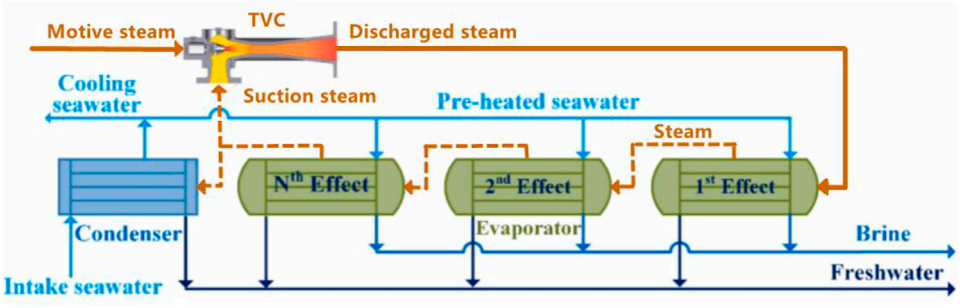

FIGURE 1
Schematic diagram of a MEE-TVC desalination plant.

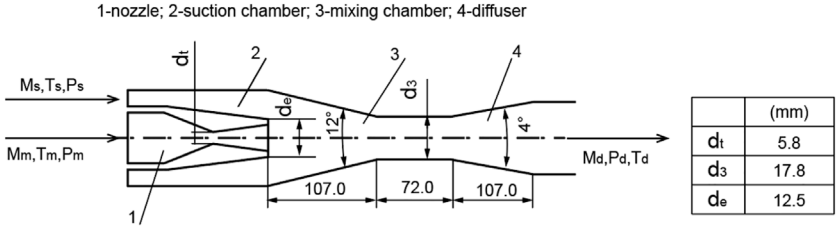

FIGURE 2
Schematic diagram of a thermal vapor compressor.

cell (EKC) structures reduced the pressure drop with minimal heat transfer performance of heat transfer devices.

Besides, some scholars have gradually carried out studies on jet pump by LES. He et al. (2003) studied the flow of a jet pump by two-dimensional LES method, the distributions of axial pressure and velocity were obtained. It was proved that LES could simulate the flow field and provide a reliable basis for the research of jet pump. Wen et al. (2007) carried out a series of numerical simulation calculations for a jet pump under various operating conditions, especially simulating the backflow vortex near the nozzle outlet. The reliability of LES for jet pump is proved through the results of flow field. Zhou and Yuan. (2013) simulated a three-dimensional jet pump with RANS and LES, and made a comparison under different models. The vortex structures were captured by LES, and the results obtained by LES are more consistent with that of experiments.

A lot of theories on the extraction of vortex structures have been established and applied in the relevant studies on turbulent flow. In the literatures, the vortex-related issues have been addressed by a lot of scholars with several vortex identification methods (e.g., Q criteria and λ_2 criteria). Cai. (2011) calculated the viscoelastic fluid by LES and visualized the vortex with Q-criteria to investigate the structural characteristics of vortexes in different scales. The results showed that the existence of viscoelasticity in the fluid inhibits the vortex structures, especially for small-scale vortex structures. Luo et al. (2008) conducted a study on the vortex structures of the three-dimensional planar transition jet flow by vorticity iso-surfaces. Masud (Zaheer and Masud, 2017) adopted the embedded LES method to capture the vortex stretching phenomenon in a liquid ejector pump. The method combined the benefits of both RANS and LES model, and provided the flow instabilities information which cannot be obtained by the usage of RANS approach. Gao et al. (2019) identified six core issues of vortex and proposed a Liutex-based definition of vortex core center. It was found that the proposed method could successfully identify the rotation axis of vortexes without any user-specified threshold, so this method is straightforward, robust and high-efficiency. Dubief and Delcayre (2000) investigated the identification issue of coherent vortices on the basis of LES of turbulent flows, the results showed that decent coherent vortices were displayed by Q-isosurfaces. The contribution of near-wall vortex structures to the fluctuations of velocity and vorticity is obviously isolated. Pinakichakraborty et al. (Chakraborty et al., 2005) analyzed the currently popular vortex identification criteria and explored the inter-relationships between the different criteria. It was observed that in the strong swirling region, the vortex structures educed using several thresholds were identical for the kinematic and dynamic explanation. Fraňa et al. (2005) obtained the vortex identification results by the λ_2 criterion and Q criterion, and there is no essential difference between these two criteria if a proper threshold is chosen. Besides, the vortex cores could be verified by the visualization in fluctuating velocity of two-dimensional vortices.

Although two-dimensional model and RANS method of TVC have been widely applied, LES method is rarely used in the study of TVC. Therefore, it is necessary to focus on our research object, and it is of significance on practical application. Besides, the discussions on the vortex structure are seldom involved (Li et al., 2021a). In this study, the three-dimensional numerical simulations of TVC are performed with LES turbulence model, then the results are visualized by Q-criterion and normalized Q-criterion technique (Li et al., 2021b). The objective of the paper is to give several new insights into the effects of motive steam pressure on the interior flow field and to explore the relationships between the results.

2 Numerical method

2.1 Thermal vapor compressor geometry and working process

As illustrated in Figure 2, a typical TVC mainly consists of the nozzle, the suction chamber, the mixing chamber and the diffuser section. The inlet diameter and outlet diameter of the nozzle is 22.4 mm and 12.5 mm respectively, and the throat diameter is 5.8 mm. The straight section diameter of the mixing chamber is 17.8 mm, and the corresponding length is

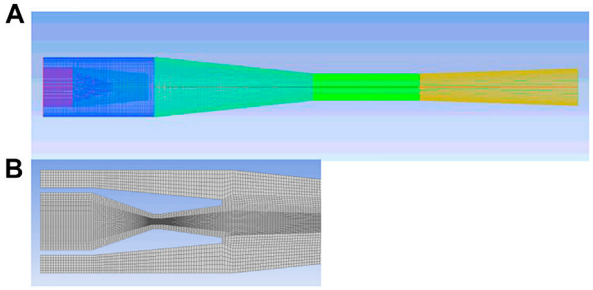

FIGURE 3
Computational grids of TVC **(A)** Grid distribution **(B)** Grid details at nozzle and mixing chamber.

72 mm. In addition, the inlet diameter of the suction steam is 40.2 mm, and the outlet diameter of the diffuser is 25.2 mm. High-pressure motive steam enters the nozzle, and adiabatically expands through the nozzle and converts the mechanical energy into kinetic energy. During the process, the motive steam pressure P_m is rapidly reduced and the motive steam velocity V_m is accelerated to supersonic in the Laval nozzle, consequently the suction steam is drawn into the suction chamber by the pressure difference. With the action of viscous force, the two streams of steam mix and exchange energy to reach the same velocity and pressure in the mixing chamber simultaneously. Finally, there is a pressure rise of the mixed steam in the diffuser so that the discharged steam pressure P_d is higher than the suction steam pressure P_s. The mixed steam is decelerated in the diffuser and the kinetic energy is converted to the potential energy.

All motions of fluid are based on the following governing equations, and the corresponding governing equations for fluid flow are the mathematical statements of three fundamental physical principles (Li, 2022a). The continuity equation, the momentum equation and the energy equation (Li, 2022b) are shown in Eqs. 1–6.

- Mass is conserved—the continuity equation.

$$\frac{\partial \rho}{\partial t} + \frac{\partial}{\partial x}(\rho v_x) + \frac{\partial}{\partial y}(\rho v_y) + \frac{\partial}{\partial z}(\rho v_z) = 0 \tag{1}$$

- Newton's second law—the momentum equation:

$$\frac{\partial(\rho v_x)}{\partial t} + \frac{\partial(\rho v_x v_x)}{\partial x} + \frac{\partial(\rho v_y v_x)}{\partial y} + \frac{\partial(\rho v_z v_x)}{\partial z} = \rho f_x - \frac{\partial p}{\partial x} + \frac{\partial}{\partial x}\left(2\mu \frac{\partial v_x}{\partial x} + \bar{\lambda}\nabla \cdot V\right) + \frac{\partial}{\partial y}\left[\mu\left(\frac{\partial v_y}{\partial x} + \frac{\partial v_x}{\partial y}\right)\right] + \frac{\partial}{\partial z}\left[\mu\left(\frac{\partial v_z}{\partial x} + \frac{\partial v_x}{\partial z}\right)\right] \tag{2}$$

$$\frac{\partial(\rho v_y)}{\partial t} + \frac{\partial(\rho v_x v_y)}{\partial x} + \frac{\partial(\rho v_y v_y)}{\partial y} + \frac{\partial(\rho v_z v_y)}{\partial z} = \rho f_y - \frac{\partial p}{\partial y} + \frac{\partial}{\partial x}\left[\mu\left(\frac{\partial v_x}{\partial y} + \frac{\partial v_y}{\partial x}\right)\right] + \frac{\partial}{\partial y}\left(2\mu \frac{\partial v_y}{\partial y} + \bar{\lambda}\nabla \cdot V\right) + \frac{\partial}{\partial z}\left[\mu\left(\frac{\partial v_z}{\partial y} + \frac{\partial v_y}{\partial z}\right)\right] \tag{3}$$

$$\frac{\partial(\rho v_z)}{\partial t} + \frac{\partial(\rho v_x v_z)}{\partial x} + \frac{\partial(\rho v_y v_z)}{\partial y} + \frac{\partial(\rho v_z v_z)}{\partial z} = \rho f_z - \frac{\partial p}{\partial z} + \frac{\partial}{\partial x}\left[\mu\left(\frac{\partial v_x}{\partial z} + \frac{\partial v_z}{\partial x}\right)\right] + \frac{\partial}{\partial y}\left[\mu\left(\frac{\partial v_y}{\partial z} + \frac{\partial v_z}{\partial y}\right)\right] + \frac{\partial}{\partial z}\left(2\mu \frac{\partial v_z}{\partial z} + \bar{\lambda}\nabla \cdot V\right) \tag{4}$$

$$\nabla \cdot V = \frac{\partial v_x}{\partial x} + \frac{\partial v_y}{\partial y} + \frac{\partial v_z}{\partial z} \tag{5}$$

- Energy is conserved—the energy equation.

$$\frac{\partial(\rho h)}{\partial t} + \frac{\partial(\rho v_x h)}{\partial x} + \frac{\partial(\rho v_y h)}{\partial y} + \frac{\partial(\rho v_z h)}{\partial z} = -pdivV + \frac{\partial}{\partial x}\left(\lambda \frac{\partial T}{\partial x}\right) + \frac{\partial}{\partial y}\left(\lambda \frac{\partial T}{\partial y}\right) + \frac{\partial}{\partial z}\left(\lambda \frac{\partial T}{\partial z}\right) + \Phi \tag{6}$$

2.2 Computational grid

In order to study the interior 3D flow field of TVC, ICEM CFD is adopted to establish a 3D grid and create mesh work. Due to the wide range of velocity variation at the throat, high-quality mesh refinement is applied at this position. Besides, because of the high gradient of the velocity, the grids are also refined near the wall, at the nozzle outlet and in the mixing chamber to improve the accuracy. O-type grids are adopted to solve the mesh distortion at the arcs of inlet and outlet, and it is convenient to generate a boundary layer grid. Additionally, by implementing the grid independence verification in comparison with the grid number of 787,729 and 2543184 respectively, the optimum grid number is determined to be 1114384. The grid distribution of TVC is shown in Figure 3, and the grid of nozzle is also displayed in detail. In this study, simulations are carried out under various conditions without altering the grid to reduce errors caused by the grid.

2.3 Turbulence model selection

Generally, there are three kinds of turbulence numerical simulation methods: Direct Numerical Simulation (DNS), Large Eddy Simulation (LES) and Reynolds-averaged Navier-

TABLE 1 Motive steam mass flow rate correction.

Pm (Pa)	Mm1 (kg/s)	Mm2 (kg/s)	Mm3 (kg/s)	Mm4 (kg/s)	Mean Mm (kg/s)
6,000	0.00028168	0.00028168	0.00028167	0.00028161	0.00028166
8,000	0.00037698	0.00037711	0.00037711	0.00037704	0.00037706
10,000	0.00047252	0.00047248	0.00047264	0.00047256	0.00047255
12,000	0.00056789	0.00047248	0.00047264	0.00047256	0.00047255
14,000	0.00066342	0.00066324	0.00066424	0.00066305	0.00066349
16,000	0.00075878	0.00075852	0.00075894	0.00075852	0.00075869
18,000	0.00085402	0.00085397	0.00085385	0.00085369	0.00085388
20,000	0.00094969	0.00094954	0.00094936	0.00094955	0.00094954
22,000	0.00106965	0.00104446	0.00104460	0.00104479	0.00105088
24,000	0.00113978	0.00113967	0.00114033	0.00114033	0.00114003

TABLE 2 Suction steam mass flow rate correction.

Ps (Pa)	Ms1 (kg/s)	Ms2 (kg/s)	Ms3 (kg/s)	Ms4 (kg/s)	Mean Ms (kg/s)
6,000	0.00018708	0.00018126	0.00018319	0.000177366	0.00018222
8,000	0.00031565	0.00029259	0.00035454	0.00032241	0.00032130
10,000	0.00033071	0.00034231	0.00032393	0.00033238	0.00033233
12,000	0.00019531	0.00028391	0.00030664	0.00026263	0.00026212
14,000	0.00034911	0.00036280	0.00035669	0.00036167	0.00035757
16,000	0.00025840	0.00024038	0.00024413	0.00026225	0.00025129
18,000	0.00018600	0.00025048	0.00031119	0.00022070	0.00024209
20,000	0.00023561	0.00023571	0.00023598	0.00023605	0.00023584
22,000	0.00027583	0.00026688	0.00026433	0.00026290	0.00026749
24,000	0.00027778	0.00027468	0.00027696	0.00027021	0.00027491

Stokes equations (RANS). As a turbulence model in computational fluid dynamics (CFD), the aim of LES is to reduce the computational cost by ignoring the smallest length scales. By means of low-pass filtering of the Navier-Stokes equations, the most computationally expensive issues would be resolved (Smagorinsky, 1963). In this paper, LES is selected among all turbulence models. As a Subgird-Scale model, Smagorinsky-Lilly model is chosen during the simulation process.

In LES, the governing equations are spatially filtered, and the influence of the unresolved scales is modeled using an SGS model. In essence, the large or resolved scale field is a local average of the complete field. For one-dimensional flow, the filtered velocity is defined by

$$\bar{\Phi}(x) = \int \Phi(x')G(x,x')dx' \tag{7}$$

where G (x,x') is the filter kernel. Filter kernel, mainly include Gaussian, box and Cutoff, is a function which determines the scale of the unresolved vortex in the simulation (Cai, 2011). In Eq. 7, x and x' are the coordinates of the flow region and the filtered space respectively.

When finite volume method is adopted, the formula is transformed to:

$$\bar{\Phi}(x) = \frac{1}{V}\int \Phi(x')dx', x' \subset V \tag{8}$$

where V is the control volume. According to the LES turbulence model (Jiang and Lai, 2009), the filtered N-S equation is given as:

$$\frac{\partial \bar{u}_i}{\partial x_i} = 0 \tag{9}$$

$$\frac{\partial \bar{u}_i}{\partial t} + \frac{\partial \bar{u}_i \bar{u}_j}{\partial x_j} = \frac{\partial}{\partial x_j}\left(\mu \frac{\partial \rho \bar{u}_i}{\partial x_j}\right) - \frac{1}{\rho}\frac{\partial \bar{P}}{\partial x_i} - \frac{\partial \tau_{i,j}}{\partial x_j} \tag{10}$$

where $\tau_{i,j}$ is called the subgrid scale (SGS) Reynolds stress, it is given in Eq. 11.

$$\tau_{i,j} = u_i u_{j-} \bar{u}_i \bar{u}_j \tag{11}$$

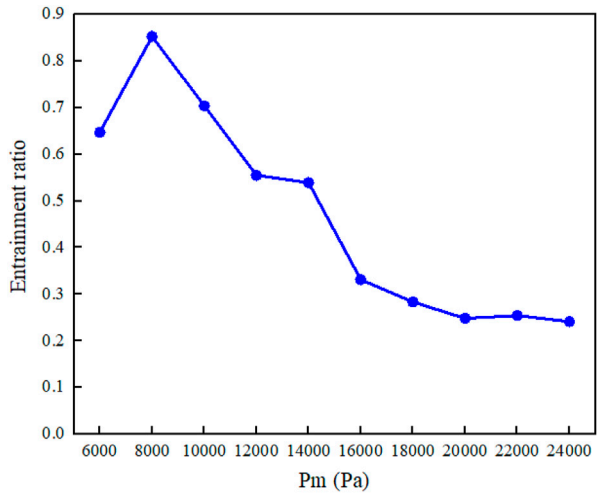

FIGURE 4
Variation of entrainment ratio with motive steam pressure.

TABLE 3 Entrainment ratio.

Ps (Pa)	6,000	8,000	10,000	12,000	14,000
Entrainment ratio	0.64695	0.85212	0.70327	0.55469	0.53892
Ps (Pa)	16,000	18,000	20,000	22,000	24,000
Entrainment ratio	0.33121	0.28352	0.24,837	0.25454	0.24114

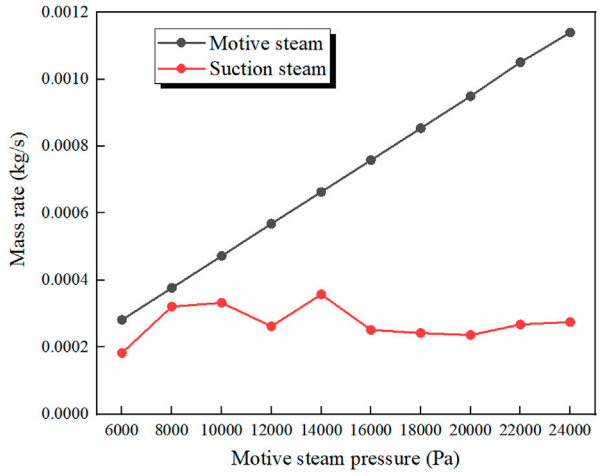

FIGURE 5
Variation of mass flow rates with motive steam pressure.

As a combination of the filtered field and subgrid scale field, the complete velocity field would be obtained. The subgrid scale Reynolds stress (SGSRS) can be decomposed into three sets of terms:

$$\tau_{ij} = \left(\overline{\bar{u}_i\bar{u}_j} - \bar{u}_i\bar{u}_j\right) + \left(\overline{\bar{u}_i u_j'} - \overline{\bar{u}_j u_i'}\right) + \overline{u_i' u_j'} \tag{12}$$

Until now, the most widely used subgrid scale model is proposed by Smagorinsky (1963). It is an eddy viscosity model which marks the beginning of LES, and it is given as:

$$\tau_{i,j} - \frac{1}{3}\tau_{kk}\delta_{ij} = -2\mu_t\bar{S}_{ij} \tag{13}$$

$$\bar{S}_{ij} = \frac{1}{2}\left(\frac{\partial\bar{u}_i}{\partial x_j} + \frac{\partial\bar{u}_j}{\partial x_i}\right) \tag{14}$$

where μ_t is the eddy viscosity, δ_{ij} is the Kronecker delta, and $\bar{S}_{ij}$ is the resolved strain rate tensor. The well-known Smagorinsky-Lily model is directly equivalent to the Prandtl's mixing length model, which is used in the statistical turbulence modeling. The corresponding mixing length is described as the following expression:

$$\mu_t = \rho L_s^2|\bar{S}| \tag{15}$$

$$L_s = min\left(kd, C_s V^{\frac{1}{3}}\right) \tag{16}$$

In Eq. 15, $|\bar{S}| = \sqrt{2\bar{S}_{ij}\bar{S}_{ij}}$ is a measure of the velocity gradient. C_s represents the Smagorinsky constant, and C_s = 0.18 is the most commonly used value.

2.4 Boundary conditions and assumption

In this paper, ANSYS Fluent is utilized for the simulation. The boundary conditions are pressure inlets and pressure outlet, and steam is used as the working fluid for the simulation, assuming an ideal gas. The corresponding specific heat is 2014 J/kg·k, thermal conductivity is 0.0261 w/m·k, viscosity is 1.34 kg/m·s × 10^5 kg/m·s and molecular weight is 18.01534 kg/kmol. The flow behavior near the wall is assumed to be logarithmic, and the density-based solver is adopted with the implicit formulation. Moreover, the wall is assumed as adiabatic and the shear condition of the wall is set as no-slip. The temperature of motive steam and suction steam are both set at saturation, the appropriate turbulence boundary conditions and other relevant numerical disposal are applied. According to the convergence rule of LES method, the solution is considered to be converged when the scaled residual is less than 10^{-5} and the relative error of net mass flow rate is less than 0.5%.

3 Results and discussion

In all numerical calculations of the following sections, the pressure of "discharged steam" is a fixed value (P_d = 1.9 kPa), and P_d is kept constant (P_s = 1.8 kPa). However, P_m is varied from 8 kPa to 24 kPa (i.e., 6 kPa, 8 kPa, 10 kPa, 12 kPa, 14 kPa, 16 kPa, 18 kPa, 20 kPa, 22 kPa, and 24 kPa). The simulation results are

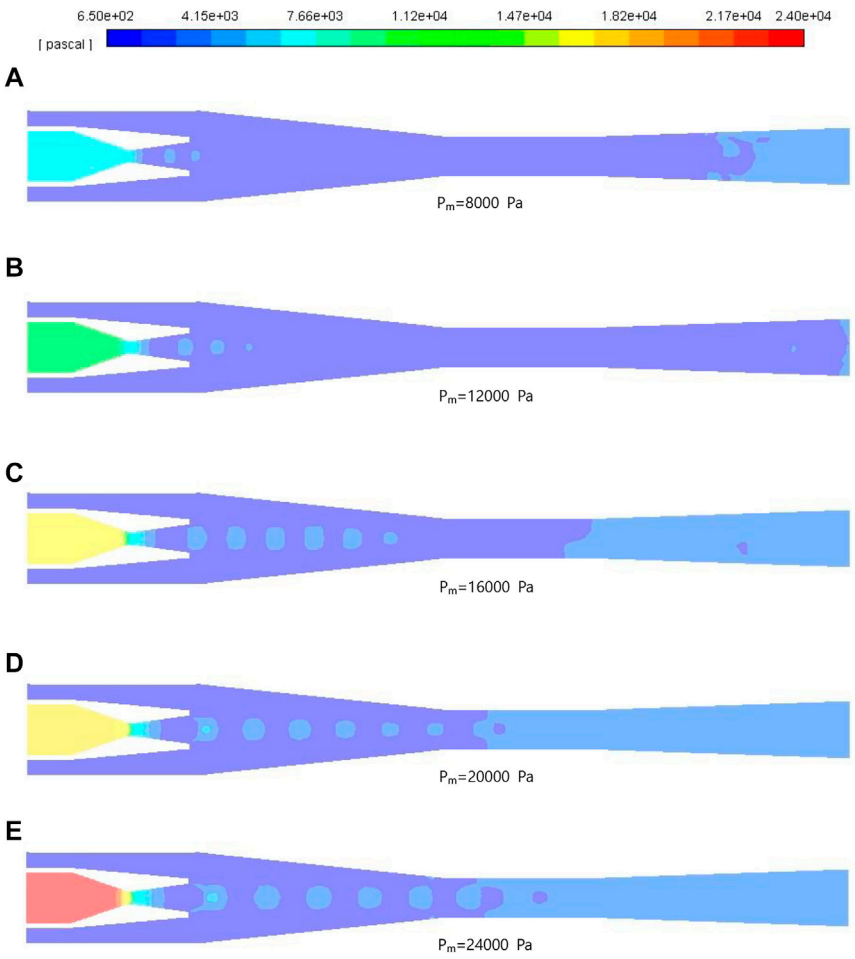

FIGURE 6
Contours of pressure with motive steam pressure. **(A–E)** show the contours of pressure with motive pressure P_m = 8000 Pa, 12000 Pa, 16000 Pa, 20000 Pa, and 24000 Pa respectively.

discussed and analyzed after collecting data under ten sets of conditions, and the effect of P_m on the interior flow field of TVC is obtained as follows.

3.1 Entrainment ratio

The performance of LT-MEE system could be represented by GOR (gained output ratio), which is defined as the ratio of gross fresh water production to the motive steam supplied externally, like Eq. 17.

$$GOR = \frac{M_d}{M_m + M_{NCG}} \tag{17}$$

where M_d represents the mass flow rate of the discharged steam, M_m is the mass flow rate of motive steam, M_{NCG} is the mass flow rate of the steam extracting the non-condensable gas, and n is the number of effects of LT-MEE plant. The entrainment ratio ε is a key indicator in evaluation of the performance of TVC, and it is defined as,

$$\varepsilon = \frac{M_s}{M_m} \tag{18}$$

where M_s is the mass flow rate of the suction steam. Therefore, as the ratio of M_s to M_m, ε has a relationship with GOR. P_s and P_d are set to be constant, while P_m is set to be variable ranging from 6 kPa to 24 kPa.

Table 1 gives the correction of motive steam mass flow rate, and Table 2 shows the correction of suction steam mass flow rate. The entrainment ratios are shown in Table 3, and they were obtained by mean M_m and M_s. As shown in Figure 4, as P_m increases, the entrainment ratio rises dramatically in the early stage, from 0.647 at 6 kPa to the peak of 0.852 with P_m of 8 kPa. Then the entrainment ratio shows a downward trend when P_m continues to go up till 12 kPa, where the ratio plummets to 0.555. Though the ratio vibrates to 0.539 at 14 kPa, it drops to 0.331 at

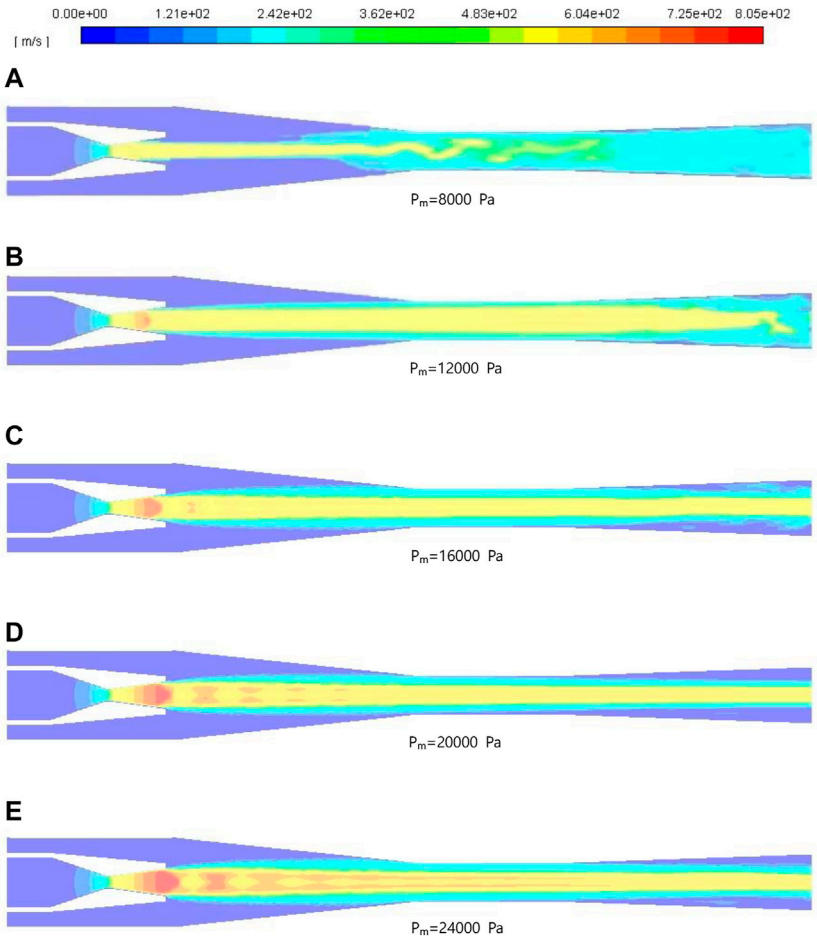

FIGURE 7
Contours of velocity with motive steam pressure. **(A–E)** show the contours of velocity with motive pressure P_m = 8000 Pa, 12000 Pa, 16000 Pa, 20000 Pa, and 24000 Pa respectively.

16 kPa and starts to fluctuate between 0.284 and 0.241 within the range of 16 kPa and 24 kPa.

As illustrated in Figure 5, M_m almost grows linearly from 0.000282 kg/s to 0.00114 kg/s with the increase of P_m. In addition, when P_m increases to 8 kPa, M_s shows an upward trend from 0.000182 kg/s to 0.000332 kg/s. Then, as P_m continues to grow, M_s starts to decline to 0.000262 kg/s and then fluctuates between 0.000236 kg/s and 0.000267 kg/s. When P_m is 8 kPa, it's worth noting that the ratio of M_s–M_m reaches to maximum due to the minimum difference between them so that the entrainment ratio nearly reaches the peak under this condition.

3.2 Pressure profile

Effect of motive steam pressure on the pressure profile is discussed in this section, the pressure contours are displayed from Figures 6A–E. Several simulations are carried out by increasing motive steam pressure from 8 kPa to 24 kPa while the other boundary conditions are kept constants.

As can be seen from Figure 6, static pressure instantaneously drops at the throat of the nozzle, and shock waves are formed by the interaction between the expansion wave and the compression wave near the exit of nozzle. The presence of shock waves indicates the phenomenon of stratification between motive steam and suction steam at outlet of the nozzle, and the two streams do not mix at the moment. With the development of shock waves, there are periodic plunge in pressure and surge in velocity of motive steam, and the near-wall static pressure of suction steam is increasing simultaneously. Moreover, the mixability and viscosity of mixed steam could definitely lead to the weakening in strength of the shock waves. In the diffuser, there is a slight rise in pressure at the exit due to the disturbance of mixed steam.

For the case with P_m of 8 kPa, the shock waves are generated both in the nozzle and the mixing chamber. As P_m increases, the

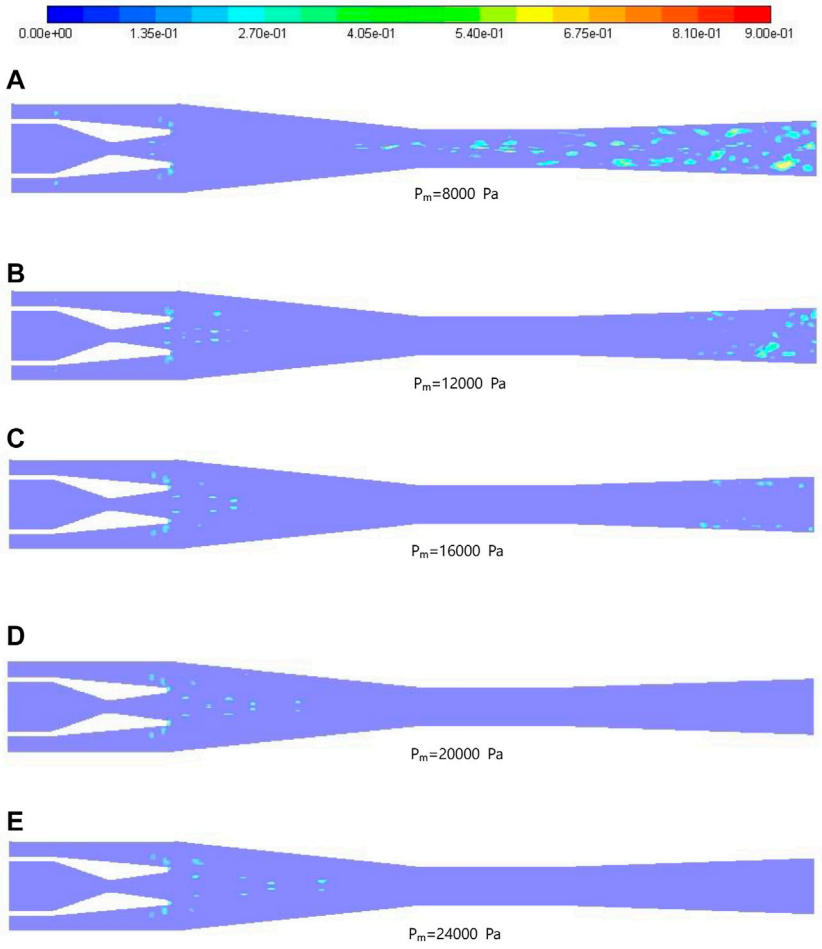

FIGURE 8
Contours of vortex core with motive steam pressure. **(A–E)** show the contours of vortex core with motive pressure P_m = 8000 Pa, 12000 Pa, 16000 Pa, 20000 Pa, and 24000 Pa respectively.

number of shock waves continues to grow and the length of shock chain along the ceterline also increases, and the original location where shock wave starts to generate moves downstream. Besides, the position of the pressure-rise moves upstream from the diffuser to the straight part of the mixing chamber, it demonstrates that the pressure rise has been achieved in a smaller area.

3.3 Velocity profile

From the velocity contours in Figure 7, motive steam is accelerated to supersonic speed in the nozzle, and internal energy is transferred into kinetic energy during the process. Suction steam is entrained into the suction chamber from the other inlet, then the mixed steam undergoes multiple velocity oscillation process through shock waves in the mixing chamber and finally jet out. In the mixing chamber, the occurrence of elliptical structures is often referred to the "diamond waves", which can be observed. This phenomenon could be explained by the imperfect expansion of the jet at the nozzle exit section. In addition, the formation of the shock waves is due to the sharp increase in velocity at an extremely short distance. The complex momentum exchanges between the two streams of steam, resulting in the formation of "diamond waves". The phenomenon is reflected by a chain of oscillations of the Mach number and pressure along the centerline in the mixing chamber. As P_m increases, the number of "diamond waves" significantly increases and the distribution region expands as well. Especially, in Figure 7A, when P_m is 8 kPa, the initial formation of the "diamond waves" could be clearly seen. This phenomenon will definitely promote the energy transfer between the high-velocity motive steam and the suction steam. However, with the increase of "diamond waves" chain length, the excessive length and quantity of shock waves aggravate the energy dissipation. Additionally, it is worth noting that the location where the pressure surges and the velocity sharply declines is approximately the same. Besides, it is also the location where the "diamond waves" begin to generate.

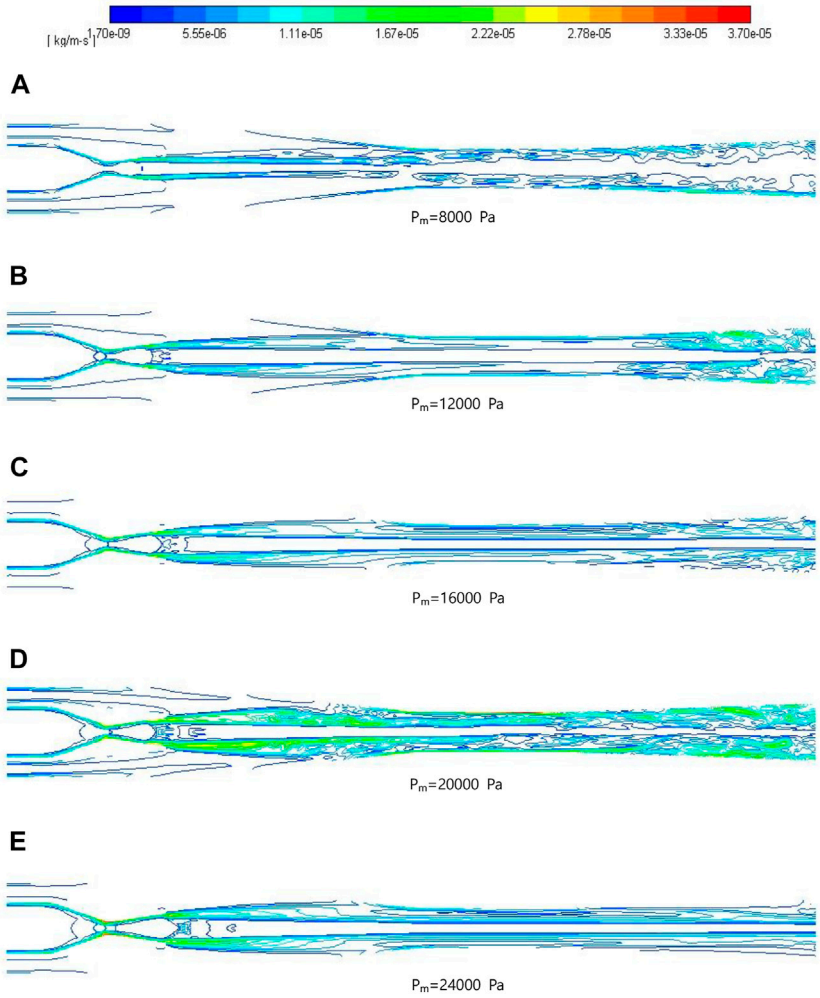

FIGURE 9
Contours of turbulent viscosity with motive steam pressure. **(A–E)** show the contours of turbulent viscosity with motive pressure P_m = 8000 Pa, 12000 Pa, 16000 Pa, 20000 Pa, and 24000 Pa respectively.

3.4 Vortex core distribution

In order to identify and visualize the features of the vortex, normalized Q criterion is applied to the simulation on the basis of that the minimum pressure appears in the vortex core. Fluid deformation can be described by the velocity gradient tensor, which is separated into vortex tensor and strain rate tensor (Bai et al., 2019). Q criterion is defined in Eq. 19.

$$Q = \frac{1}{2}\left(\Omega^2 - S^2\right), s^{-2} \tag{19}$$

Since vortex tensor dominates where vortex exists, normalized Q criterion is

$$Q_n = \frac{Q}{\frac{1}{2}\Omega^2} \tag{20}$$

In Eqs. 19, 20, Ω represents the vortex tensor, and S indicates the strain rate tensor. According to the equation, the value of normalized Q is between -1 and 1, and an optimal value in this range is selected to identify the vortex core in the flow field.

Figure 8 shows the distribution of vortex core in the TVC. As can be seen in Figure 8 (a), vortex cores are mainly generated in the area near the nozzle exit, in the constant area section of the mixing chamber and in the diffuser. The regular-shaped vortex cores are generated in pairs near the exit of nozzle, and the distribution of vortex core in the mixing chamber is relatively close to the center axis. It is worth noting that the distribution is in good symmetry in the mixing chamber due to the low mixed degree between motive steam and suction steam. As the flow proceeds, the interaction between two waves of steam is enhanced, the steam is fully mixed and the energy is dissipated, consequently the shapes of the vortex cores

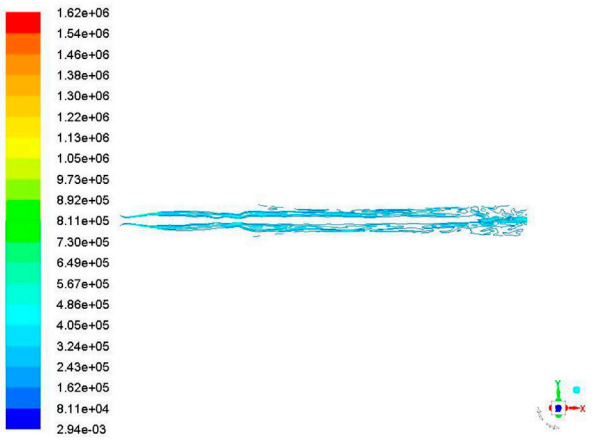

FIGURE 10
2D vorticity iso-surface.

become irregular in the diffuser. Moreover, the vortex cores are asymmetrically located in the area relatively closer to the wall in the diffuser than those in the mixing chamber, and the fusion phenomenon of multiple vortexes occurs at the moment.

Considering the effect of P_m, as can be noticed from Figure 8, when P_m increases, the location where vortex cores generated moves downstream gradually. Besides, the region that the vortex cores existing is more likely to get larger in the contraction section of the mixing chamber. The cores grow layer by layer, and the effect of interaction diminishes with the increase of distance between vortex cores. However, when P_m is greater than 0.02 MPa, no more original vortex cores will be generated in the diffuser.

3.5 Subgrid turbulent viscosity

Turbulent viscosity stands for the intense eddy diffusion caused by random fluctuations when the fluid is turbulent. In other words, it is actually referring to the high momentum transfer rate resulted from the random motion of fluid particles driven by the vortex. In fact, the generation of vortexes and the intense mixing between vortexes are the main ways of mass transfer, which is much greater than the effect of molecular motion.

In purpose of evaluation of energy dissipation, subgrid turbulent viscosity is obtained under various operating pressure conditions. In Figure 9, the energy dissipation caused by vortex diffusion mainly occurs near the wall in the entire TVC, and the maximum turbulent viscosity appears inside the nozzle, near the nozzle outlet and in the diffuser. Particular attention is paid to Figure 9 (b), by comparing with the results of vortex cores distribution, it is found that the maximum turbulent viscosity position is consistent with the region where vortex cores are generated.

Since the attenuation of turbulent motion is caused by the viscosity, the hindrance to the flow is strengthened and the kinetic energy is converted into heat with the increase of viscosity. The large-scale vortex absorbs energy from the time-averaged flow and transmits it to the small-scale vortex step by step, and the turbulent kinetic energy is converted into thermal energy simultaneously. Although the energy of small-scale vortexes is fairly low, most of the energy will be dissipated by them, particularly those near the wall.

Figure 9 depicts the effect of P_m on the turbulent viscosity. It can be clearly seen that the high-viscosity region is enlarged with the rise of pressure, which are proportional to the zone of vortex cores formation. As P_m rises, the energy dissipation increases as well. Besides, when P_m is greater than 0.016 MPa, the reduction of turbulent viscosity in the diffuser is related to the absence of vortex cores at this time, as given in Figures 9C–E.

3.6 Vortex iso-surface

With regard to the visualization of the vortexes, as shown in Figures 10, 11, the 2D iso-surface and 3D iso-surface will be identified by Q criterion, respectively. In general, the vortexes generated in the contraction section of the mixing chamber seem to be more symmetrical, and then they break up into

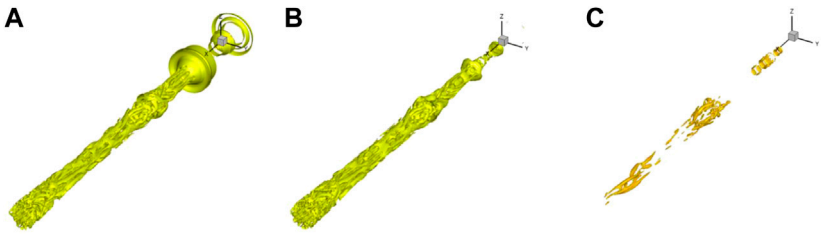

FIGURE 11
3D iso-surfaces identified by Q criterion.

smaller ones, move downstream and transfer energy between each other. In the turbulent fluid, the kinetic energy is gradually passed from the large energy eddies to the small dissipative eddies, and the process is also termed as energy cascade. Most obviously, due to the fluctuations in velocity and a wide distribution of length scales, the mixing within the turbulent flow is much stronger than that in the laminar flow. During the mixing process, a large amount of energy, mass and heat exchange occurs between them, resulting in a relatively unstable flow field. Additionally, the turbulence is composed of vortexes in different scales, and the large-scale vortex obtains energy from the mainstream and transmits energy to the small-scale ones through the transformation between vortexes. Eventually, the small-scale vortex gradually disappears with the dissipation of energy, and a complex vorticity field is finally formed downstream due to the suction of the ejected steam.

As illustrated in Figure 10, it is found that clumps of fluid particles, also can be called eddies, they generate, interact, break up, and reform in the turbulence. The length scale of these eddies varies from the overall scale of the flow to the microscale, which is much larger than the mean free-path of molecules. Thus, the continuum hypothesis could be applied where viscosity plays a dominant role and turbulent kinetic energy is dissipated into heat. Most of the turbulent kinetic energy is contained in the integral length scales, which are the largest scales in an energy spectrum. In other words, the distribution of turbulent kinetic energy is according to the length scale.

In order to improve and detail the visualization of the spatial vortex, as can be noticed from Figure 11, the "Q criterion" vortex identification technique is introduced to identify the vortex structure based on the 3D vortex iso-surface. The "Q criterion" is given by the expression in Eq. 13. Since "Q" parameter is entirely computed within the whole domain, it is composed of both negative and positive values. When the strain rates are larger than the vorticity rates, Q shows negative values and vice versa. By taking positive values of Q, it represents that more vorticity occurs than the strain in this flow region. Additionally, it is the characteristic of turbulent coherent structures.

In Figure 11A, a large number of vortexes in different scales are distributed within the TVC when "Q" is relatively small. With the increase of Q value, the small-scale vortex with low intensity is eliminated and the large-scale vortex with high intensity is screened out gradually. Therefore, as illustrated in Figure 11C, the large-scale vortexes are mainly distributed in the exit area of the nozzle, the constant area section of mixing chamber and diffuser. By comparison with Figure 11A, the large-scale vortexes are randomly located along the axis in different morphology while the small-scale ones are distributed near the wall.

Furthermore, it's worth noting that the typical structure "Ring Vortices" are generated in the area near the nozzle exit due to the annular shear layer formed between the motive steam and the suction steam. According to the cross-directional Kelvin–Helmholtz instability, the shear layer immediately rolls up downstream. In the iso-surface of Q criterion figures, these vortex rings undergo pairing or merging procedure downstream before breaking up into smaller ones.

4 Conclusion

An investigation on pressure parameter of TVC is carried out to discuss and analyze its interior flow field employing LES method, which could provide more turbulent properties than previous RANS approach, and the following conclusions can be summarized.

- The initial formation of "diamond waves" in the nozzle is the primary reason for promoting the heat transfer between the two waves of steam. However, excessive shock waves could significantly lead to the entrainment ratio decline of TVC.
- The regular-shaped vortex cores generated in the area near the nozzle exit are almost in pairs close to the center axis while those in the diffuser are asymmetrically located near the wall. As P_m increases over 20 kPa, there are no more vortex cores in the constant-area mixing section and diffuser. When P_m rises 50% from 8 kPa to 20 kPa, the number of vortex inside the diffuser drops to a half.
- The energy dissipation caused by vortex diffusion mainly occurs near the wall in the entire TVC, and the maximum turbulent viscosity appears inside the nozzle, near the nozzle outlet and in the diffuser. Moreover, the maximum turbulent viscosity location is consistent with the region where vortex cores are generated.
- The simulation of TVC by LES could provide more turbulent properties which cannot be obtained from RANS approach. The large-scale vortexes are primarily located along the axis in different morphology while the small-scale ones are randomly distributed near the wall. 3D iso-surfaces identified by Q criterion helps to capture and visualize more small-scale vortexes, superiority to 2D vorticity.

Data availability statement

The original contributions presented in the study are included in the article/Supplementary Material, further inquiries can be directed to the corresponding authors.

Author contributions

XR carried out the numerical simulation and analyzed the results. SS contributed significantly to the analysis and preparation of the manuscript. KZ contributed to the preparation for the simulation. YG helped to develop the methodology and analyze the existing simulating results. All authors have read and agreed to the published version of the manuscript.

Funding

The research is supported by Key Programme of the National Natural Science Foundation of China (Grant No.51936002).

Conflict of interest

The authors declare that the research was conducted in the absence of any commercial or financial relationships that could be construed as a potential conflict of interest.

Publisher's note

All claims expressed in this article are solely those of the authors and do not necessarily represent those of their affiliated organizations, or those of the publisher, the editors and the reviewers. Any product that may be evaluated in this article, or claim that may be made by its manufacturer, is not guaranteed or endorsed by the publisher.

References

Allouche, Y., Bouden, C., and Varga, S. (2014). A CFD analysis of the flow structure inside a steam ejector to identify the suitable experimental operating conditions for a solar-driven refrigeration system. *Int. J. Refrig.* 39, 186–195. doi:10.1016/j.ijrefrig.2013.07.027

Bai, X. D. A. X., Zhang, W., Fang, Q. h., Wang, Y., Zheng, J. h., Guo, A. X., et al. (2019). The visualization of turbulent coherent structure in open channel flow. *J. Hydrodyn.* 31, 266–273. doi:10.1007/s42241-019-0026-0

Besagni, G., and Inzoli, F. (2017). Computational fluid-dynamics modeling of supersonic ejectors: Screening of turbulence modeling approaches. *Appl. Therm. Eng.* 117, 122–144. doi:10.1016/j.applthermaleng.2017.02.011

Cai, W. H. (2011). *Study on the characteristics of isotropic turbulence in viscoelastic fluid*. Heilongjiang China: D. Harbin institute of technology.

Chakraborty, P., Balachandar, S., and Adrian, R. J. (2005). On the relationships between local vortex identification schemes. *J. Fluid Mech.* 535, 189–214. doi:10.1017/s0022112005004726

Dubief, Y., and Delcayre, F. (2000). On coherent-vortex identification in turbulence. *J. Turbul.* 01, N11. doi:10.1088/1468-5248/1/1/011

Fraňa, K., Stiller, J., and Grundmann, R. (2005). Taylor-Görtler vortices in the flow driven by a rotating magnetic field in a cylindrical container. *J. Vis. (Tokyo).* 8, 323–330. doi:10.1007/bf03181551

Gao, Y. S., Liu, J. M., Yu, Y. F., and Liu, C. Q. (2019). A Liutex based definition and identification of vortex core center lines. *J. Hydrodyn.* 31, 445–454. doi:10.1007/s42241-019-0048-7

He, P. J., Lu, H. Q., and Long, X. P. (2003). Two-dimensional large eddy simulation of internal flow in jet pump. *J. Fluid Mach.* 08, 10–13. doi:10.3969/j.issn.1005-0329.2003.08.004

Jiang, X., and Lai, C. H. (2009). *LES numerical techniques for Direct and large-eddy simulations*. Boca Raton Florida: CRC Press, 19

Li, H. (2022). SCADA data based wind power interval prediction using LUBE-based deep residual networks. *Front. Energy Res.* 10, 920837. doi:10.3389/fenrg.2022.920837

Li, H. (2022). Short-term wind power prediction via spatial temporal analysis and deep residual networks. *Front. Energy Res.* 10, 920407. doi:10.3389/fenrg.2022.920407

Li, H., Deng, J., Feng, P., Pu, C., Arachchige, D. D., and Cheng, Q. (2021). Short-term nacelle orientation forecasting using bilinear transformation and ICEEMDAN framework. *Front. Energy Res.* 697, 780928. doi:10.3389/fenrg.2021.780928

Li, H., Deng, J., Yuan, S., Feng, P., and Arachchige, D. D. (2021). Monitoring and identifying wind turbine generator bearing faults using deep belief network and EWMA control charts. *Front. Energy Res.* 9, 770. doi:10.3389/fenrg.2021.799039

Li, H. J. (2004). *Study of the performance, configuration and particular flow phenomena of an ejector*. Liaoning China: D. Dalian University of Technology.

Liu, J. P., Wang, L., Jia, L., and Wang, X. L. (2017). The influence of the area ratio on ejector efficiencies in the MED-TVC desalination system. *Desalination* 413, 168–175. doi:10.1016/j.desal.2017.03.017

Liu, J. P., Wang, L., Jia, L., and Wang, X. L. (2018). Thermodynamic model for all modes performance analysis of supersonic ejector considering non-uniform distribution of flow field. *Int. J. Refrig.* 96, 17–24. doi:10.1016/j.ijrefrig.2018.08.023

Liu, X. H., Liu, D. W., Shen, S. Q., Yang, Y., and Gao, F. (2012). Performance analysis of mixed feed LT-MED desalination system with thermal vapor compressor. *J. Desalination Water Treat.* 42, 248–255. doi:10.5004/dwt.2012.2930

Luo, K., Yan, J., and Fan, J. (2008). Coherent structure of jet-flow-transition on three dimensional plane. *J. Sci. Sin. Techo.* 38, 736–745. doi:10.3321/j.issn:1006-9275.2008.05.008

Mazini, M. T., Yazdizadeh, A., and Ramezani, M. H. (2014). Dynamic modeling of multi-effect desalination with thermal vapor compressor plant. *Desalination* 353, 98–108. doi:10.1016/j.desal.2014.09.014

Reis, L. B., and Gioria, R. S. (2021). Optimization of liquid jet ejector geometry and its impact on flow fields. *Appl. Therm. Eng.* 10, 117132. doi:10.1016/j.applthermaleng.2021.117132

Sharifi, N. (2020). Numerical study of non-equilibrium condensing supersonic steam flow in a jet-pump based on supersaturation theory. *J. Int. J. Mech. Sci.* 165, 105221. doi:10.1016/j.ijmecsci.2019.105221

Shen, S. Q., Zhou, S. H., Yang, Y., Yang, L. P., and Liu, X. H. (2011). Study of steam parameters on the performance of a TVC-MED desalination plant. *Plant. J. Desalination Water Treat.* 33, 300–308. doi:10.5004/dwt.2011.2653

Smagorinsky, J. (1963). General circulation experiments with the primitive equations. *Mon. Weather Rev.* 91, 99–164. doi:10.1175/1520-0493(1963)091<0099:gcewtp>2.3.co;2

Sriveerakul, T., Aphornratana, S., and Chunnanond, K. (2007). Performance prediction of steam ejector using computational fluid dynamics: Part 2. Flow structure of a steam ejector influenced by operating pressures and geometries. *Int. J. Therm. Sci.* 46, 823–833. doi:10.1016/j.ijthermalsci.2006.10.012

Sun, M. R., Zhang, L. X., Hu, C. Z., Zhao, J. F., Tang, D. W., and Song, Y. C. (2022). Forced convective heat transfer in optimized kelvin cells to enhance overall performance. *Energy* 10, 122995. doi:10.1016/j.energy.2021.122995

Sun, W. X., Ma, X. J., Ma, S. L., Zhang, H. L., Zhang, L. P., Xue, H. Y., et al. (2021). Effects of surface roughness and temperature on non-equilibrium condensation and entrainment performance in a desalination-oriented steam ejector. *Appl. Therm. Eng.* 10, 117264. doi:10.1016/j.applthermaleng.2021.117264

Wen, J. Y., Yu, B., Lu, H. Q., Cui, T., and Zhu, Z. (2007). Large eddy simulation for jet pump flow. *J. Eng. J. Wuhan Univ.* 02, 110–114. doi:10.3969/j.issn.1671-8844.2007.02.024

Wu, Y. F., Zhao, H. X., Zhang, C. Q., Wang, L., and Han, J. T. (2018). Optimization analysis of structure parameters of steam ejector based on CFD and orthogonal test. *Energy* 151, 79–93. doi:10.1016/j.energy.2018.03.041

Zaheer, Q., and Masud, J. (2017). Visualization of flow field of a liquid ejector pump using embedded LES methodology. *J. Vis. (Tokyo).* 20, 777–788. doi:10.1007/s12650-017-0429-3

Zhou, L. J., and Yuan, L. L. (2013). Comparison of internal flows in jet pump predicted by various turbulence models. *J. J. Drainage Irrigation Mach. Eng.* 01, 25–30. doi:10.3969/j.issn.1674-8530.2013.01.006

Nomenclature

Abbreviations

d_t Throat diameter of the nozzle [mm]

d_e Diameter of nozzle exit [mm]

d_3 Diameter of constant section [mm]

T Temperature [K]

G Filter kernel

V Control volume

$\tau_{i,j}$ Subgrid scale Reynolds stress [Pa]

μ_t Eddy viscosity [Pa.s]

δ_{ij} Kronecker delta

$\bar{S}_{ij}$ Resolved strain rate tensor [N]

λ Superficial isentropic velocity [m/s]

P_m Motive steam pressure [Pa]

P_s Suction steam pressure [Pa]

P_d Discharged steam pressure [Pa]

V_m Motive steam velocity [m/s]

V_s Suction steam velocity [m/s]

V_d Discharged steam velocity [m/s] **Ω** Vortex tensor [N]

S Strain rate tensor [N]

Subscripts

t Nozzle

e Nozzle exit

3 Constant section

in Inlet

out Outlet

m Motive steam

s Suction steam

d Discharged steam

LT-MEE Low-temperature multi-effect evaporation

TVC Thermal vapor compressor

GOR Gained output ratio

LES Large eddy simulation

RANS Reynolds Averaged Navier-Stokes

DNS Direct Numerical Simulation

frontiers | Frontiers in Energy Research

TYPE Original Research
PUBLISHED 21 September 2022
DOI 10.3389/fenrg.2022.988772

OPEN ACCESS

EDITED BY
Tinghui Ouyang,
National Institute of Advanced Industrial Science and Technology (AIST), Japan

REVIEWED BY
Xupeng Wen,
Central South University, China
Lisen Wei,
Lanzhou University of Technology, China

*CORRESPONDENCE
Lining Xing,
xinglining@gmail.com

SPECIALTY SECTION
This article was submitted to Smart Grids, a section of the journal Frontiers in Energy Research

RECEIVED 07 July 2022
ACCEPTED 10 August 2022
PUBLISHED 21 September 2022

CITATION
Li J, Zou K and Xing L (2022), Coarse-to-fine evolutionary search for large-scale multi-objective optimization: An application to ratio error estimation of voltage transformers.
Front. Energy Res. 10:988772.
doi: 10.3389/fenrg.2022.988772

Coarse-to-fine evolutionary search for large-scale multi-objective optimization: An application to ratio error estimation of voltage transformers

Jun Li[1], Kai Zou[1] and Lining Xing[2]*

[1]School of Public Administration, Xiangtan University, Xiangtan, China, [2]School of Mathematics and Big Data, Foshan University, Foshan, China

Multi-objective optimization problems (MOPs) are commonly confronted in various fields, such as condition monitoring for renewable energy systems, and ratio error estimation of voltage transformers. With the increase in decision variables of MOPs, their exponentially growing search spaces are challenging for existing evolutionary algorithms. To handle this challenge, this paper suggests a coarse-to-fine large-scale evolutionary multi-objective search, called CF-LEMO. In the coarse search phase, CF-LEMO performs evolutionary search on both the original and transformed large-scale MOPs alternately, accelerating the population to approach the Pareto-optimal fronts. In addition, to alleviate the issue of diversity loss, we design a diversity preservation mechanism to preserve a well-distributed archive to support subsequent fine search. In the fine search stage, CF-LEMO conducts local search on the current population to mine high-quality solutions, which are used to update the population and archive. Then, based on the archive, the multi-objective optimization based on decomposition is employed to evolve all decision variables, so as to obtain a population with good convergence and diversity near the Pareto-optimal fronts. To assess the effectiveness of the proposed CF-LEMO, we compare its performance against four representative baseline algorithms on a benchmarks suite LSMOP1-LSMOP9 with 2 and 3 objectives. The empirical results confirm its super performance by significanlty outperforming all the four competitors on 12 out of 18 benchmarks. Moreover, the experiments demonstrate the superior performance of CF-LEMO in sovling multi-objective ratio error estimation problems with up to 6,000 decision variables.

KEYWORDS

voltage transformers, ratio error estimation, multi-objective optimization, evolutionary optimization, large scale

1 Introduction

Multi-objective optimization problems (MOPs) are common in diverse fields (Abdel-Basset et al., 2021; Li T. et al., 2021; Jiang et al., 2021; Wang et al., 2021; Liao and Li, 2022; Zong et al., 2022). For instance, ratio error (RE) estimation of voltage transformers involves three conflicting objectives, e.g., the total time-varying REs, the sum of the RE variation, and the variance of the phase angle RE variations (Fadaee and Radzi, 2012; He et al., 2020). Scheduling workflows for cloud platforms need to balance makespan and monetary cost (Chen et al., 2021; Belgacem and Beghdad-Bey, 2022). They are mathematically constructed as:

$$P1: \begin{cases} \text{Minimize} & \vec{f}(\vec{x}) = \left[f_1(\vec{x}), f_2(\vec{x}), \ldots, f_m(\vec{x})\right], \\ \text{S.t.} & \vec{x} \in \Omega, \end{cases} \tag{1}$$

where $\vec{x} = (x_1, x_2, \ldots, x_n)$ denotes a decision vector, m and n respectively indicate the count of objectives and decision variables, $\Omega \subseteq \mathbb{R}^n$ represents MOP's feasible area. The objective function $\vec{f}(\vec{x})$ is to map each n-dimensional feasiable decision vector to an m-dimensional objective vector.

Real-world MOPs often involve hundreds or thoudsands of decision variables, which are generally termed large-scale MOPs (LSMOPs). With the increase in decision variables of an LSMOP, its search space grows exponentially and fitness landscape becomes more complex. During the past 3 decades, the studies on large-scale multi-objective optimization have attracted increasing enthusiasms, and evolutionary algorithms have been extensively accepted as one practical technique to resolve LSMOPs (Yi et al., 2020; Hong et al., 2021; Omidvar et al., 2021; Tian et al., 2021). So far, scholars have suggested a large number of evolutionary optimization approaches to solve LSMOPs, and these existing approaches can be roughly partitioned into three categories (Tian et al., 2021): powerful search mechanism, decision variable decomposition, and problem transformation.

The first category is to develop powerful search mechanisms to reproduce superior quality offspring populations by evolving all the decision variables. For instance, to tackle thousands of decision variables, Hong *et al.* used a probabilistic prediction model to enhance population convergence while employing importance sampling to maintain the population diversity (Hong et al., 2022). Ghorbanpour *et al.* proposed an integer programming-based initialization, crossover, and mutation operators to resolve multi-objective energy disaggregation problems (Ghorbanpour et al., 2021). Yang *et al.* suggested a fuzzy evolution strategy to blur LSMOPs' decision vectors to compress the search space, such accelerating the convergence of populations (Yang et al., 2021). Huang *et al.* suggested an ensemble of multiple offspring reproduction and environmental selection operators to handle the massive volume of search space in the voltage transformer ratio error estimation problems (Huang et al., 2021). Rizk *et al.* suggested a multi-orthogonal opposition scehme to diversify offspring solutions (Rizk-Allah et al., 2020). Li *et al.* formulated the power flow optimization with uncertain wind and solar energy into multi-objective problems, and introduced constraint handle technique to resolve it (Li et al., 2022). Kropp *et al.* proposed a sparse population sampling approach to initialized population for large-scale sparse multi-objective algorithms (Kropp et al., 2022). Liu *et al.* employed a feedforward neural network to learn a gradient-descent-like direction to reproduce offspring solutions for efficiently tackling LSMOPs (Liu et al., 2022).

The second category is based on decision variable decomposition. The approaches belonging to this category often divide the decision variables into multiple groups, and then evolve the decision variables in different groups alternately. For instance, Antonio *et al.* suggested to randomly divide decision variables into multiple groups, and employed the cooperative coevolutionary framework to evolve each group of decision variables (Antonio and Coello, 2013). *Sander et al.* employed differential grouping techniques Omidvar et al. (2017) to detect the interactions among decision variables, and assigned the ones interating with each other into the same group (Sander et al., 2018). There also exist some works (Ma et al., 2016; Zhang et al., 2018; Chen et al., 2020) performing variable analysis to decompose decision variables. Yang *et al.* suggested a coarse-to-fine decomposition to divide the reservoir flood control problem into a sequence of sub-problems being solved simultaneously (Yang et al., 2022). Although random grouping approaches are simple and easy, they ignore the interactions among decision variables, which likely push the populations to local optimal regions. Besides, the differential grouping technique and variable analysis consume considerable function evaluations to group decision variables, which is inefficient to solve real-world LSMOPs.

The third category is to reformulate the original LSMOPs into simplified ones, and perform evolutionary search on both the original and transformed problems. For instance, Zille *et al.* suggested a weighted optimization framework (WOF) to transform orginal LSMOPs into small-scale multi-objective weight optimization problems by assigning a weight to the decision variables in the same group (Zille et al., 2018). Liu *et al.* improved WOF using a random dynamic grouping approach to adjust group size and a multiple search strategies assisted particle swarm optimization (Liu et al., 2020). Li *et al.* integrated the problem reformulation technique with decomposition-based MOEAs to handle the growing complex relationships among decision variables (Li L. et al., 2021). He *et al.* used the decision vectors of obtained solutions to reformulate the original LSMOPs into small-scale single-objective problem (He et al., 2019). Qin *et al.* suggested to perform directed sampling on solutions nearer to ideal point for assisting reproducing an offspring population (Qin et al., 2021).

Compared with the other two categories of approaches, problem reformulatation-based approaches are more prevalent in solving real-world LSMOPs (Feng et al., 2021). On the one hand, the search spaces of LSMOPs can be drastically compressed by suitable reformulatation functions to improve algorithms' search efficiency. On the other hand, problem reformulatation approaches are handy for inseparable LSMOPs without deliberate handling interactions among decision variables. However, these approaches accelerate the population to only a tiny fraction of the Pareto-optimal front. Besides, local search shows competitive capability in solving large-scale single-objective optimization problems and small-scale MOPs (Tseng and Chen, 2009; Chen et al., 2015), but is rarely used to solve large-scale MOPs. Furthermore, recent study (Pang et al., 2022) pointed out a counterintuitive observation that traditional EMO algorithms performs better than state-of-the-art LEMO algorithms on some LSMOPs.

Inspired by the above existing works, we develop a coarse-to-fine evolutionary search to handle exponentially growing search spaces of LSMOPs. The proposed CF-LEMO first carries out coarse search in the simplified search spaces to quickly approximate a tiny fraction of the Pareto-optimal front. Meanwhile, to alleviate the issue of diversity loss during coarse search process, a diversity preservation mechanism is designed to maintain the archive based on fitness between solutions and subproblems, such preserving a well-distributed archive for the subsequent fine search. Then, CF-LEMO leverages traditional MOEAs, such as local search and decomposition based MOEAs, to perform fine search on the results of coarse search, so as to obtain a population with well diversity and convergence.

We organize this paper as follows. **Section 2** elaborates the proposed CF-LEMO, including problem transformation, pseudo-codes, and descriptions. Then, **Section 3** provides comparison experiments on benchmark functions and ratio error estimation of voltage transformers to verify CF-LEMO's effectiveness. At last, this paper is concluded in **Section 4**.

2 Algorithm design

This section introduces the transformation method to reformulate the LSMOPs, and details the proposed CF-LEMO.

2.1 Problem transformation

We divide the large-scale decision variabels into g groups, denoted as $(G_1, G_2, \ldots, G_g)$, and assign a weight w_k to the decision variables in the kth group G_k. Referring to works (Yang et al., 2008; Zille et al., 2018), given a fixed decision vector $\vec{x}$, we employ a transformation function $\psi(\vec{w}, \vec{x})$ to reformulate the original LSMOP in **(1)** as a small-scale multi-objective weight optimization problem as follows.

$$P2: \begin{cases} \text{Minimize} & \vec{f}_{\vec{x}}(\vec{w}) = \left[f_{1,\vec{x}}(\vec{w}), f_{2,\vec{x}}(\vec{w})), \ldots, f_{m,\vec{x}}(\vec{w})\right], \\ \text{S.t.} & \vec{w} \in \Phi \subseteq \mathbb{R}^n, \\ & f_{j,\vec{x}}(\vec{w}) = f_j(\psi(\vec{w}, \vec{x})), j \in \{1, 2, \ldots, m\}, \\ & \psi(\vec{w}, \vec{x}) \coloneqq \left(w_1 \cdot G_1, w_2 \cdot G_2, \cdots, w_g \cdot G_g\right), \end{cases} \tag{2}$$

Figure 1 provides an intuitive example to the illustrate the transformation function. Suppose an MOP has ten decision variables $\vec{x} = \{x_1, x_2, \ldots, x_{10}\}$, which are divided into three groups, denoted as $G_1 = \{x_5, x_2, x_1, x_7\}$, $G_2 = \{x_3, x_8, x_9, x_6\}$, and $G_3 = \{x_{10}, x_4\}$. For a given decision vector $\vec{x}$, after assigning a weight to all the variables in one group, the 10-dimensional problem is transformed into a 3-dimensional problem.

Using the above transformation method, an n-dimensional LSMOP is reduced into one with g decision variables. If it satisfies $g \ll n$, the dimensionality of the original LSMOP is reduced substantially.

2.2 Description of CF-LEMO

The main process of the proposed CF-LEMO are summarized in **Algorithm 1**. CF-LEMO's main inputs include the original problem, transformed problem, population size, and termination condition. After CF-LEMO finishes the optimization process, it output a population for decision makers.

As illustrated in **Algorithm 1**, CF-LEMO starts with initializing a set of weight vectors, a random population, and an empty archive. Notice that the ith element A_i of the archive stores the solution reserved by the ith weight vector.

In the coarse search phase (Lines 5–21), CF-LEMO consumes α ($0 < \alpha < 1$) of the total function evaluations to search original space and transformed space in turn. When searching the original space, CF-LEMO performs variantion operator on

$$\psi(\vec{w}, \vec{x}) = (\underbrace{w_1 \cdot x_5, w_1 \cdot x_2, w_1 \cdot x_1, w_1 \cdot x_7}_{w_1 \cdot G_1}, \underbrace{w_2 \cdot x_3, w_2 \cdot x_8, w_2 \cdot x_9, w_2 \cdot x_6}_{w_2 \cdot G_2}, \underbrace{w_3 \cdot x_{10}, w_3 \cdot x_4}_{w_3 \cdot G_3})$$

FIGURE 1
An example of the transformation function.

Input: The original MOP $P1$; transformed MOP $P2$; population size N; termination condition
Output: A population P;
1 $V \leftarrow$ Initialize a set of weight vectors;
2 $P \leftarrow$ Initialize a population;
3 $A_{1\times N} \leftarrow \emptyset$;
4 $A \leftarrow$ *UpdateArchive*(P, A, V);
5 **while** $FE < \alpha \cdot FE_m$ **do**
6 **for** $i = 1 \rightarrow t_1$ **do**
7 $Q \leftarrow$ Reproduce an offspring population via evolving decision variables of $P1$;
8 $P \leftarrow$ *EnvironmentalSelection*($P \bigcup Q$, N);
9 $A \leftarrow$ *UpdateArchive*(P, A, V);
10 $P' \leftarrow$ Select $m+1$ solutions from P;
11 **for** $p \in P'$ **do**
12 $W \leftarrow$ Initialize a population for $P2$;
13 **for** $i = 1 \rightarrow t_2$ **do**
14 $W' \leftarrow$ Reproduce an offspring population via evolving weight variables of $P2$;
15 $W \leftarrow$ *EnvironmentalSelection*($W \bigcup W'$, N');
16 $Q \leftarrow \emptyset$;
17 **for** $j = 1 \rightarrow |W|$ **do**
18 $q \leftarrow$ Apply W_j on solution p;
19 $Q \leftarrow Q \bigcup \{q\}$;
20 $P \leftarrow$ *EnvironmentalSelection*($P \bigcup Q$, N);
21 $A \leftarrow$ *UpdateArchive*(P, A, V);
22 **while** $FE < \beta \cdot FE_m$ **do**
23 $Q \leftarrow$ Reproduce an offspring population via conducting local search on P;
24 $P \leftarrow$ *EnvironmentalSelection*($P \bigcup Q$, N);
25 $A \leftarrow$ *UpdateArchive*(P, A, V);
26 **for** $i = 1 \rightarrow N$ **do**
27 **if** $f^{tch}(P_i, V_i) > f^{tch}(A_i, V_i)$ **then**
28 $P_i \leftarrow A_i$;
29 **while** $FE < FE_m$ **do**
30 **for** $i = 1 \rightarrow N$ **do**
31 $p \leftarrow$ Reproduce an offspring solution;
32 $P \leftarrow$ Use p to update the i-th subproblem and its neighbourhood;

Algorithm 1. The main process of CF-LEMO.

all decision variables to obtain an offspring population and environmental selection operator to update the population (Lines 6–8). It also updates the archive using the current population (Line 9), and selects $m+1$ well-diversified solutions (Line 10) to support the search of transformed space. The selected $m+1$ solutions include m extreme solutions and one solution with the maximum acute angle to these extreme solutions. Then, CF-LEMO searches the transformed space as follows. For each selected solution, it evolves the weight vector of the transformed LSMOPs to reproduce a weight population (Line 14), and applies each weight vector to the selected solution to obtain the corresponding solution in the original space (Line 18). Also, the new generated solutions by evolving the weight vector will update the archive (Line 21).

In the fine search phase (Lines 22–32), CF-LEMO consumes $\beta - \alpha$ $(\alpha < \beta < 1)$ of the total function evaluations to perform local search (Lines 23–25). During this sub-phase, CF-LEMO reproduces an offspring population by perturbing the decision variables one by one (Line 23), and update the population and archive (Lines 24–25). After the local search, the algorithm merges the population P and the archive A. If the ith solution A_i in the archive is better than the ith solution P_i in the population, A_i will replace the P_i. After that, CF-LEMO employs the decomposition based MOEA to further search well-diversified and well-distributed solutions using the remaining function evaluations.

The pseudo-code of the function UpdateArchive() is briefly shown in **Algorithm 2**. Its main inputs are the current population, the archive, and the set of weight vectors. After this function runs, a new archive will be returned.

Input: A population P; the archive A; weight vectors V;
Output: An updated archive A;
1 **for** $i = 1 \rightarrow |P|$ **do**
2 $j^* \leftarrow \arg\min_{j\in\{1,2,\cdots,|V|\}} f^{tch}(P_i, V_j)$;
3 $A_{j^*} \leftarrow A_{j^*} \bigcup \{P_i\}$;
4 **for** $i = 1 \rightarrow |A|$ **do**
5 $p^* \leftarrow \arg\min_{p\in A_i} f^{tch}(p, V_i)$;
6 $A_i \leftarrow \{p\}$;

Algorithm 2. Function UpdateArchive().

As illustrated in **Algorithm 2**, function *UpdateArchive*() first assigns each solution in the population P to the weight vector with the best fitness (Line 2). Note that A_j stores all the solutions assigned to the jth weight vector. Then, this function traverses the solution set assigned to each weight vector, and retains a solution with the best fitness value for each weight vector (Lines 4–6).

3 Experiment studies

In this section, we verify the performance of CF-LEMO by comparing it with four baselines in the context of a complicated benchmark functions and 5 test cases on ratio error estimation of voltage transformers.

3.1 Experimental setup

Comparison algorithms: We choose four relevant baseline MOEAs for performance comparison: WOF (Zille et al., 2018), NSLS (Chen et al., 2015), CCGDE3 (Antonio and Coello, 2013), and NSGA-III (Deb and Jain, 2014). WOF suggests a weighted optimization framework to transform large-scale decision variables into small-scale weight variables, and employs existing MOEAs to successively optimize the original and transformed problems during each iteration. NSLS employs a local search mechanism to reproduce offspring population, and is a representative MOEAs based on local search. CCGDE3 embeds a cooperative coevolution mechanism into existing MOEAs to handle large-scale decision variables. NSGA-III is the recent version of the popular multi-objective optimization algorithm NSGA-II, and NSGA-III employs a reference-vector-based selection mechanism to balance the convergence and diversity for the solutions in the last accepted front.

Significance test: Similar to existing works (Chen et al., 2019; Wang et al., 2019; Ishibuchi et al., 2022; Lin et al., 2022), we adopt the Wilcoxon's ranksum test with a confidence level of 0.05 to distinguish the statistical significance between the CF-LEMO and the corresponding competitors. The signs +, −, and ≈ respectively represent that the corresponding MOEA performs

significantly better, worse, and similar to the CF-LEMO on a test case.

Benchmark functions: LSMOP1-LSMOP9 (Cheng et al., 2017) are tailored for meansure the performance of MOEAs in solving large-scale MOPs. They reflect challenges in real-world applications, such as complex relationships among decision variables and inhomogeneous correlations from decision variables to objectives.

Population size: The population sizes of 2- and 3-objective benchmark functions are set to 100 and 190, respectively.

Stop Condition: Similar to works (Deb and Jain, 2014; Chen et al., 2015; Zille et al., 2018), the maximum number of fitness evaluations is set to $n \times 10^4$, where n is the number of decision variables.

Metrics: The inverted generational distance (IGD) (Zitzler et al., 2003) and hypervolume (HV) (While et al., 2006) are employed for performance measurement. Both the IGD and HV metrics are capable of simultaneously measuring the convergence and diversity of the populations obtained by MOEAs. When caculating the IGD metric, about 10,000 uniformly distributed Pareto optimal points on the PF are sampled for each benchmark function. Besides, the HV metric refers to the volume of objective space construted by a reference vector and the objective vectors of the obtained solutions. The reference vector is set as 1.5 times the upper bounds of each benchmark function's PF.

All the experiments are run on a workstation with 64-bit operating system, 256 GB memory, two Intel(R) Xeon(R) Gold 6226R CPU @ 2.90GHz.

3.2 Comparison on benchmarks

In terms of IGD metrics, the average values and standard deviations (in brackets) of the algorithms CF-LEMO, WOF, NSLS, CCGDE3, and NSGA-III are summarized in **Table 1**.

As illustrated in **Table 1**, the proposed CF-LEMO poses better overall performance than all the four comparison MOEAs. Specifically, CF-LEMO obtains 14 out of 18 lowest IGD values, while comparison algorithms WOF, NSLS, CCGDE3, and NSGA-III respectively only obtain 1, 3, 0, and 0 best results. These numerical results demonstrate the competitive performance of the CF-LEMO in solving complex LSMOPs.

The main difference between CF-LEMO and WOF is that the proposed CF-LEMO employs an archive to store a set of well-diversified solutions to support fine search, and a multi-objective local search to improve the results of coarse search. The comparison results in **Table 1** show that CF-LEMO significantly outperforms WOF except for the tri-objective LSMOP3. The comparison results demonstrate that the proposed components in CF-LEMO, i.e., diversity maintaince and local search mechanism, is effective.

NSLS is a multi-objective optimization algorithm based on local search. In each generation, it perturbs the decision variables one by one to obtain an offspring population. It poses the best performance among the four comparison algorithms, but it is far inferior to CF-LEMO proposed in this paper. This can be explained as that even if local search has strong exploitative ability, simple local search based MOEA is difficult to cope with the exponential growth of search space.

For baseline CCGDE3 employing cooperative coevolutionary framework to deal with the large-scale decision variables, it performs the worst among the five algorithms. This can be explained as that the relationships among decision variables of LSMOPs and the landscapes are complex. The random grouping mechanism in CCGDE3 divides the interacting decision variables into the same group with very low probability, which seriously weakens the performance of the cooperative coevolutionary framework. The comparison between CF-LEMO and CCGDE3 shows that the problem transformation-based mechanism is more effective than the cooperative coevolutionary framework in dealing with complex LSMOPs to a certain extent.

NSGA-III is a representative multi-objective optimization algorithm, which has been widely used for experimental comparison. Recent study (Pang et al., 2022) shows that in the benchmark suite LSMOP1-LSMOP9 (Cheng et al., 2017), the NSGA-III performs better than many recent large-scale multi-objective optimization algorithms. As shown in **Table 1**, CF-LEMO is much better by significantly outperming NSGA-III on 17 out of the 18 benchmark functions. These comparison results demonstrate the superior performance of CF-LEMO over the traditional multi-objective optimization algorithms.

Figure 2 depicts the populations with the lowest IGD values obtained by the five algorithms on LSMOP1, LSMOP2, LSMOP6, and LSMOP8 with 200 decision variables.

As can be seen in **Figure 2**, on the four benchmark functions, the populations obtained by CCGDE3 are far away from their PFs, indicating poor convergence of the CCGDE3. These are consistent with the extremely high IGD values of CCGDE3 in the **Table 2**. Compared with the CCGDE3, the other four MOEAs, i.e., CF-LEMO, WOF, NSLS, and NSGA-III, can converge to near PFs.

More specifically, the proposed CF-LEMO performs better than all the comparison MOEAs in terms of both convergence and diversity. For example, on bi-objective LSMOP1 with a linear PF, the diversity of CF-LEMO is similar to that of WOF, while CF-LEMO obviously has better convergence. For NSGA-III, its output population only converges to two extreme points. For NSLS, it poses poor convergence and diversity near the two extreme points. On benchmark function bi-objective LSMOP6, the advantage of CF-LEMO is more obvious. The population obtained by CF-LEMO can approximate PF as a

TABLE 1 IGD values of the five algorithms on benchmarks LSMOP1-LSMOP9 with 2- and 3-objectives.

MOPs	m	n	CF-LEMO	WOF	NSLS	CCGDE3	NSGA-III
LSMOP1	2	200	3.5721e-3 (6.26e-7)	4.0640e-1 (5.70e-2) –	2.8967e-2 (1.21e-2) –	2.9242e+0 (4.57e-1) –	3.5425e-1 (1.24e-1) –
	3	300	4.1363e-2 (2.62e-4)	1.9224e-1 (1.76e-2) –	4.4535e-2 (1.45e-3) –	6.4217e+0 (7.64e-1) –	2.1476e-1 (4.81e-2) –
LSMOP2	2	200	3.7525e-3 (2.64e-5)	2.2230e-2 (8.97e-4) –	4.2293e-2 (1.85e-3) –	1.4543e-1 (4.58e-3) –	3.9852e-2 (2.00e-3) –
	3	300	4.1704e-2 (3.04e-4)	6.6304e-2 (4.28e-3) –	6.5776e-2 (1.71e-3) –	9.7285e-2 (2.67e-3) –	4.7609e-2 (3.39e-4) –
LSMOP3	2	200	5.7079e-1 (6.99e-2)	6.4864e-1 (3.48e-2) –	5.1349e-1 (7.77e-2) +	1.5080e+1 (2.03e+0) –	8.8952e-1 (4.36e-2) –
	3	300	5.7489e-1 (3.45e-2)	4.4822e-1 (3.47e-2) +	6.8609e-1 (5.47e-2) –	1.5563e+1 (1.85e+0) –	5.5185e-1 (5.18e-2) +
LSMOP4	2	200	5.8247e-3 (4.32e-4)	6.4808e-2 (1.55e-3) –	4.8746e-2 (1.95e-3) –	1.9666e-1 (1.13e-2) –	5.9067e-2 (3.44e-3) –
	3	300	5.9655e-2 (4.28e-3)	1.4883e-1 (5.09e-3) –	9.3747e-2 (2.03e-3) –	2.9609e-1 (8.28e-3) –	9.1643e-2 (2.16e-3) –
LSMOP5	2	200	4.2236e-3 (4.72e-5)	1.1382e-1 (8.98e-2) –	1.7429e-1 (4.12e-2) –	6.4831e+0 (6.14e-1) –	3.4296e-1 (6.81e-4) –
	3	300	5.1746e-2 (1.54e-3)	4.6804e-1 (2.70e-2) –	1.4650e-1 (3.04e-2) –	7.9761e+0 (2.03e+0) –	3.1495e-1 (1.96e-2) –
LSMOP6	2	200	2.9515e-2 (6.80e-3)	5.3077e-1 (1.39e-1) –	6.2356e-1 (1.19e-1) –	9.2667e-1 (1.47e-2) –	5.9293e-1 (9.64e-2) –
	3	300	5.4758e-1 (6.66e-2)	1.2078e+0 (3.11e-3) –	1.6849e+0 (1.92e-1) –	7.6340e+3 (4.20e+3) –	1.2883e+0 (3.21e-1) –
LSMOP7	2	200	9.0669e-1 (1.50e-1)	1.0352e+0 (2.64e-1) –	1.9918e+0 (3.12e-1) –	1.2365e+4 (3.78e+3) –	1.0993e+0 (3.59e-1) –
	3	300	7.3720e-1 (1.07e-1)	8.6740e-1 (1.36e-2) –	9.3768e-1 (3.75e-2) –	1.5524e+0 (6.19e-2) –	9.3645e-1 (5.52e-2) –
LSMOP8	2	200	4.3096e-3 (1.98e-4)	1.3066e-1 (7.96e-2) –	1.1378e-1 (4.54e-2) –	5.8375e+0 (7.41e-1) –	3.4548e-1 (7.69e-4) –
	3	300	5.1299e-2 (1.07e-3)	1.3638e-1 (2.15e-2) –	1.2270e-1 (9.99e-3) –	8.6378e-1 (1.16e-1) –	3.4423e-1 (3.43e-2) –
LSMOP9	2	200	6.2032e-1 (2.76e-1)	8.1004e-1 (3.10e-16) –	1.5261e-1 (3.45e-2) +	1.4655e+1 (5.81e+0) –	8.1004e-1 (5.18e-16) –
	3	300	9.5934e-1 (3.22e-1)	1.1457e+0 (1.02e-3) –	3.5804e-1 (1.16e-1) +	4.3487e+1 (8.65e+0) –	1.2658e+0 (2.63e-1) –
– / + / ≈	—	—	—	17/1/0	15/3/0	18/0/0	17/1/0

TABLE 2 HV values of the five algorithms on solving TREE1-TREE6.

MOPs	m	n	CF-LEMO	WOF	NSLS	CCGDE3	NSGA-III
TREE1	2	3,000	8.5364e-1 (1.71e-4)	8.4862e-1 (3.70e-3) –	7.4950e-1 (1.89e-3) –	NaN (NaN) –	8.5376e-1 (5.57e-5) ≈
TREE2	2	3,000	8.5653e-1 (2.93e-5)	8.5596e-1 (2.59e-4) –	7.7696e-1 (1.11e-3) –	NaN (NaN) –	8.5305e-1 (1.11e-4) –
TREE3	2	6,000	8.8770e-1 (1.50e-5)	8.7725e-1 (6.39e-3) –	NaN (NaN) –	NaN (NaN) –	8.4309e-1 (8.84e-4) –
TREE4	2	6,000	9.6440e-1 (8.19e-5)	9.6296e-1 (1.18e-3) –	NaN (NaN) –	NaN (NaN) –	9.0754e-1 (1.25e-3) –
TREE5	2	6,000	9.3871e-1 (6.52e-5)	9.2726e-1 (8.28e-3) –	NaN (NaN) –	NaN (NaN) –	9.3207e-1 (4.13e-4) –
– / + / ≈	—	—	—	5/0/0	5/0/0	5/0/0	4/0/1

whole, while comparison algorithms WOF, NSLS, and NSGA-III only converge to a tiny part of the PF. On LSMOP8 with a concave PF, the CF-LEMO outputs a set of superior-quality of solutions, followed by NSLS and WOF, with CCGDE3 worest.

3.3 Comparison on ratio error estimation of voltage transformers

To further study the performance of the proposal and four comaprison MOEAs on a real-world application of time-varying ratio error estimation (TREE) in voltage transformers (He et al., 2020). We choose five LSMOPs with large-scale decision variables and multiple conflicting objectives, termed TREE1 to TREE6. To be specific, TREE1 and TREE2 have two objectives and 3,000 decision variables, TREE3-TREE5 have two objectives and 6,000 decision variables. We set the maximum number of fitness evaluations as 3×10^6 and 6×10^6 for TREE1-TREE2 and TREE3-TREE5, respectively.

Table 2 illustrates the statistics of HV results produced by the five algorithms. The reason for the NaN results is that no feasiable solutions are obtained by the corresponding MOEAs. It is clear that the proposed CF-LEMO significantly outperforms all the four competitors by obtaining the highest HV values in 4 out of the 5 application cases. Based on the experimental results on TREE1-TREE6, it exhibits that the proposed CF-LEMO is superior over baselines for resolving LSMOPs on ratio error estimation of voltage transformers.

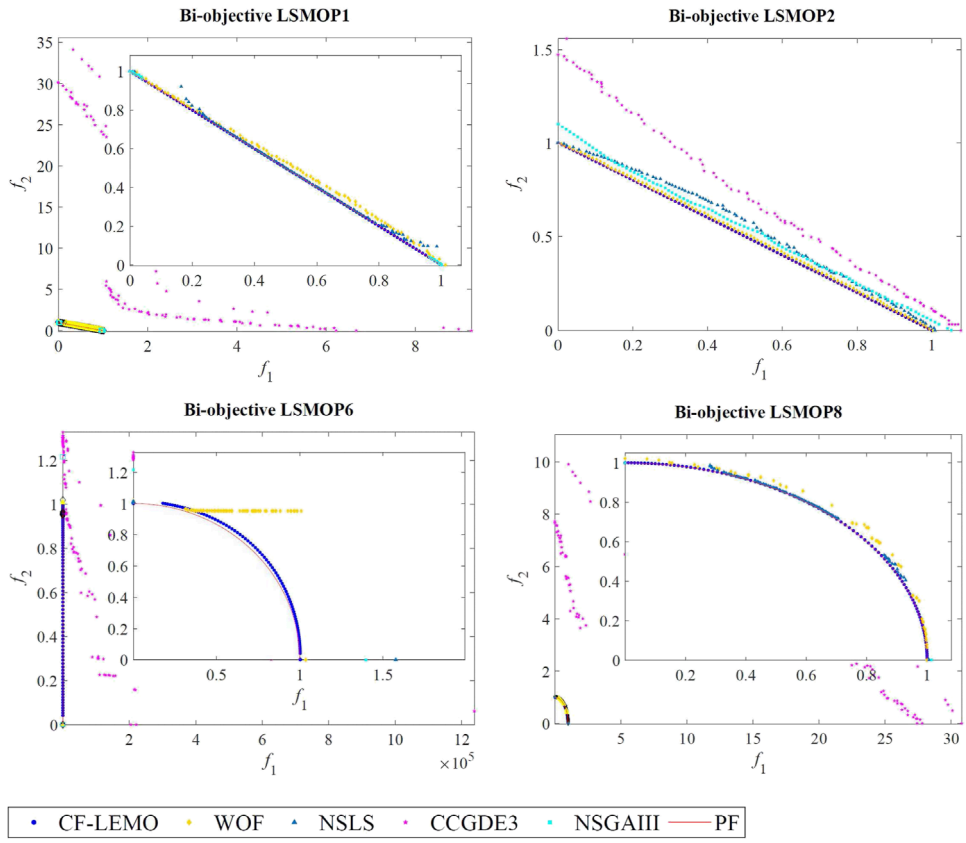

FIGURE 2
Output populations of CF-LEMO, WOF, NSLS, CCGDE3, and NSGA-III on bi-objective LSMOP1, LSMOP2, LSMOP6, and LSMOP8.

4 Conclusion

In this paper, we design a coarse-to-fine evolutionary search to handle large-scale multi-objective optimization problems, which are common in various fileds, such as condition monitoring for renewable energy systems, and cloud workflow scheduling. In the coarse search phase, the proposal leverages the problem transformation technique to simplify the complex original LSMOPs into small-scale multi-objective weight optimization problems, resulting in the rapid convergence of the population towards the Pareto-optimal fronts. Meanwhile, an archive equipped with a diversity maintenance mechanism is employed to perserve a set of well-diversified solutions. In the fine search phase, the proposal employs traditional MOEAs, such as local search and decomposition based MOEAs, to further push the solutions in the population and archive to well approximate the Pareto-optimal fronts. Finally, we conduct numerical experiments on a challenging benchmark test suite and multi-objective ratio error estimation problems for voltage transformers to verify the superior performance of the proposed CF-LEMO in resolving multi-objective problems with large-scale decision variables.

The problem transformation approaches are fundamental for the population to quickly approach the Pareto-optimal fronts of LSMOPs. But, the coarse search stage of the proposed CF-LEMO directly employs an existing problem transformation approach. Then, designing more powerful transformation approaches is our future research direction. Besides, many real-world multi-objective optimization problems often involve complex constraints and dynamic environments, which are tough tasks for evolutionary optimization. Thus, designing problem-specific strategies to handle these tasks deserves further research.

Data availability statement

Publicly available datasets were analyzed in this study. This data can be found here: https://github.com/BIMK/PlatEMO.

Author contributions

JL: investigation, methodology, writing-original draft preparation. KZ: experiments, review, and editing. LX: conceptualization, review, and supervision.

Funding

This research work is supported by the National Social Science Fund of China (Grand No. 18BTQ055), and the Special Project in Major Fields of Guangdong Universities (Grand No. 2021ZDZX1019).

Conflict of interest

The authors declare that the research was conducted in the absence of any commercial or financial relationships that could be construed as a potential conflict of interest.

Publisher's note

All claims expressed in this article are solely those of the authors and do not necessarily represent those of their affiliated organizations, or those of the publisher, the editors and the reviewers. Any product that may be evaluated in this article, or claim that may be made by its manufacturer, is not guaranteed or endorsed by the publisher.

References

Abdel-Basset, M., Mohamed, R., and Mirjalili, S. (2021). A novel whale optimization algorithm integrated with Nelder–Mead simplex for multi-objective optimization problems. *Knowledge-Based Syst.* 212, 106619. doi:10.1016/j.knosys.2020.106619

Antonio, L. M., and Coello, C. A. C. (2013). "Use of cooperative coevolution for solving large scale multiobjective optimization problems," in IEEE Congress on Evolutionary Computation (Cancun, Mexico: IEEE), 2758–2765.

Belgacem, A., and Beghdad-Bey, K. (2022). Multi-objective workflow scheduling in cloud computing: Trade-off between makespan and cost. *Clust. Comput.* 25, 579–595. doi:10.1007/s10586-021-03432-y

Chen, B., Zeng, W., Lin, Y., and Zhang, D. (2015). A new local search-based multiobjective optimization algorithm. *IEEE Trans. Evol. Comput.* 19, 50–73. doi:10.1109/tevc.2014.2301794

Chen, H., Cheng, R., Wen, J., Li, H., and Weng, J. (2020). Solving large-scale many-objective optimization problems by covariance matrix adaptation evolution strategy with scalable small subpopulations. *Inf. Sci.* 509, 457–469. doi:10.1016/j.ins.2018.10.007

Chen, H., Tian, Y., Pedrycz, W., Wu, G., Wang, R., and Wang, L. (2019). Hyperplane assisted evolutionary algorithm for many-objective optimization problems. *IEEE Trans. Cybern.* 50, 3367–3380. doi:10.1109/tcyb.2019.2899225

Chen, H., Zhu, X., Liu, G., and Pedrycz, W. (2021). Uncertainty-aware online scheduling for real-time workflows in cloud service environment. *IEEE Trans. Serv. Comput.* 14, 1167–1178. doi:10.1109/tsc.2018.2866421

Cheng, R., Jin, Y., Olhofer, M., and sendhoff, B. (2017). Test problems for large-scale multiobjective and many-objective optimization. *IEEE Trans. Cybern.* 47, 4108–4121. doi:10.1109/tcyb.2016.2600577

Deb, K., and Jain, H. (2014). An evolutionary many-objective optimization algorithm using reference-point-based nondominated sorting approach, part I: Solving problems with box constraints. *IEEE Trans. Evol. Comput.* 18, 577–601. doi:10.1109/tevc.2013.2281535

Fadaee, M., and Radzi, M. (2012). Multi-objective optimization of a stand-alone hybrid renewable energy system by using evolutionary algorithms: A review. *Renew. Sustain. Energy Rev.* 16, 3364–3369. doi:10.1016/j.rser.2012.02.071

Feng, Y., Feng, L., Kwong, S., and Tan, K. C. (2021). A multi-variation multifactorial evolutionary algorithm for large-scale multi-objective optimization. *IEEE Trans. Evol. Comput.* 26, 248–262. doi:10.1109/tevc.2021.3119933

Ghorbanpour, S., Pamulapati, T., Mallipeddi, R., and Lee, M. (2021). Energy disaggregation considering least square error and temporal sparsity: A multi-objective evolutionary approach. *Swarm Evol. Comput.* 64, 100909. doi:10.1016/j.swevo.2021.100909

He, C., Cheng, R., Zhang, C., Tian, Y., Chen, Q., and Yao, X. (2020). Evolutionary large-scale multiobjective optimization for ratio error estimation of voltage transformers. *IEEE Trans. Evol. Comput.* 24, 868–881. doi:10.1109/tevc.2020.2967501

He, C., Li, L., Tian, Y., Zhang, X., Cheng, R., Jin, Y., et al. (2019). Accelerating large-scale multiobjective optimization via problem reformulation. *IEEE Trans. Evol. Comput.* 23, 949–961. doi:10.1109/tevc.2019.2896002

Hong, H., Ye, K., Jiang, M., Cao, D., and Tan, K. C. (2022). Solving large-scale multiobjective optimization via the probabilistic prediction model. *Memet. Comput.* 14, 165–177. doi:10.1007/s12293-022-00358-9

Hong, W.-J., Yang, P., and Tang, K. (2021). Evolutionary computation for large-scale multi-objective optimization: A decade of progresses. *Int. J. Autom. Comput.* 18, 155–169. doi:10.1007/s11633-020-1253-0

Huang, C., Li, L., He, C., Cheng, R., and Yao, X. (2021). "Operator-adapted evolutionary large-scale multiobjective optimization for voltage transformer ratio error estimation," in International Conference on Evolutionary Multi-Criterion Optimization (Berlin, Germany: Springer), 672–683.

Ishibuchi, H., Pang, L. M., and Shang, K. (2022). Difficulties in fair performance comparison of multi-objective evolutionary algorithms [research frontier]. *IEEE Comput. Intell. Mag.* 17, 86–101. doi:10.1109/mci.2021.3129961

Jiang, Z.-Z., Feng, G., Yi, Z., and Guo, X. (2021). Service-oriented manufacturing: A literature review and future research directions. *Front. Eng. Manag.* 9, 71–88. doi:10.1007/s42524-021-0171-3

Kropp, I., Nejadhashemi, A. P., and Deb, K. (2022). Benefits of sparse population sampling in multi-objective evolutionary computing for large-scale sparse optimization problems. *Swarm Evol. Comput.* 69, 101025. doi:10.1016/j.swevo.2021.101025

Li, L., He, C., Cheng, R., and Pan, L. (2021a). "Large-scale multiobjective optimization via problem decomposition and reformulation," in IEEE Congress on Evolutionary Computation (Kraków, Poland: IEEE), 2149–2155.

Li, S., Gong, W., Wang, L., and Gu, Q. (2022). Multi-objective optimal power flow with stochastic wind and solar power. *Appl. Soft Comput.* 114, 108045. doi:10.1016/j.asoc.2021.108045

Li, T., Tao, S., He, K., Lu, M., Xie, B., Yang, B., et al. (2021b). V2G multi-objective dispatching optimization strategy based on user behavior model. *Front. Energy Res.* 494. doi:10.3389/fenrg.2021.739527

Liao, Z., and Li, S. (2022). Solving nonlinear equations systems with an enhanced reinforcement learning based differential evolution. *Complex Syst. Model. Simul.* 2, 78–95. doi:10.23919/csms.2022.0003

Lin, A., Yu, P., Cheng, S., and Xing, L. (2022). One-to-one ensemble mechanism for decomposition-based multi-objective optimization. *Swarm Evol. Comput.* 68, 101007. doi:10.1016/j.swevo.2021.101007

Liu, R., Liu, J., Li, Y., and Liu, J. (2020). A random dynamic grouping based weight optimization framework for large-scale multi-objective optimization problems. *Swarm Evol. Comput.* 55, 100684. doi:10.1016/j.swevo.2020.100684

Liu, S., Li, J., Lin, Q., Tian, Y., and Tan, K. C. (2022). Learning to accelerate evolutionary search for large-scale multiobjective optimization. *IEEE Trans. Evol. Comput.* 2022, 1. doi:10.1109/tevc.2022.3155593

Ma, X., Liu, F., Qi, Y., Wang, X., Li, L., Jiao, L., et al. (2016). A multiobjective evolutionary algorithm based on decision variable analyses for multiobjective optimization problems with large-scale variables. *IEEE Trans. Evol. Comput.* 20, 275–298. doi:10.1109/tevc.2015.2455812

Omidvar, M. N., Li, X., and Yao, X. (2021). "A review of population-based metaheuristics for large-scale black-box global optimization: Part A," in IEEE Transactions on Evolutionary Computation. doi:10.1109/TEVC.2021.3130838

Omidvar, M. N., Yang, M., Mei, Y., Li, X., and Yao, X. (2017). DG2: A faster and more accurate differential grouping for large-scale black-box optimization. *IEEE Trans. Evol. Comput.* 21, 929–942. doi:10.1109/tevc.2017.2694221

Pang, L. M., Ishibuchi, H., and Shang, K. (2022). Counterintuitive experimental results in evolutionary large-scale multi-objective optimization. *IEEE Trans. Evol. Comput.* 2022, 1. doi:10.1109/tevc.2022.3161363

Qin, S., Sun, C., Jin, Y., Tan, Y., and Fieldsend, J. (2021). Large-scale evolutionary multiobjective optimization assisted by directed sampling. *IEEE Trans. Evol. Comput.* 25, 724–738. doi:10.1109/tevc.2021.3063606

Rizk-Allah, R. M., Hassanien, A. E., and Slowik, A. (2020). Multi-objective orthogonal opposition-based crow search algorithm for large-scale multi-objective optimization. *Neural comput. Appl.* 32, 13715–13746. doi:10.1007/s00521-020-04779-w

Sander, F., Zille, H., and Mostaghim, S. (2018). "Transfer strategies from single- to multi-objective grouping mechanisms," in Proceedings of the Genetic and Evolutionary Computation (New York, NY, USA: ACM), 729–736.

Tian, Y., Si, L., Zhang, X., Cheng, R., He, C., Tan, K. C., et al. (2021). Evolutionary large-scale multi-objective optimization: A survey. *ACM Comput. Surv.* 54, 1–34. doi:10.1145/3470971

Tseng, L.-Y., and Chen, C. (2009). "Multiple trajectory search for unconstrained/constrained multi-objective optimization," in IEEE Congress on Evolutionary Computation (Trondheim, Norway: IEEE), 1951–1958.

Wang, L., Pan, Z., and Wang, J. (2021). A review of reinforcement learning based intelligent optimization for manufacturing scheduling. *Complex Syst. Model. Simul.* 1, 257–270. doi:10.23919/csms.2021.0027

Wang, Z., Ong, Y.-S., Sun, J., Gupta, A., and Zhang, Q. (2019). A generator for multiobjective test problems with difficult-to-approximate pareto front boundaries. *IEEE Trans. Evol. Comput.* 23, 556–571. doi:10.1109/tevc.2018.2872453

While, L., Hingston, P., Barone, L., and Huband, S. (2006). A faster algorithm for calculating hypervolume. *IEEE Trans. Evol. Comput.* 10, 29–38. doi:10.1109/tevc.2005.851275

Yang, R., Qi, Y., Lei, J., Ma, X., and Zhang, H. (2022). A parallel multi-objective optimization algorithm based on coarse-to-fine decomposition for real-time large-scale reservoir flood control operation. *Water Resour. manage.* 36, 3207–3219. doi:10.1007/s11269-022-03196-z

Yang, X., Zou, J., Yang, S., Zheng, J., and Liu, Y. (2021). A fuzzy decision variables framework for large-scale multiobjective optimization. *IEEE Trans. Evol. Comput.* 2021, 1. doi:10.1109/tevc.2021.3118593

Yang, Z., Tang, K., and Yao, X. (2008). Large scale evolutionary optimization using cooperative coevolution. *Inf. Sci.* 178, 2985–2999. doi:10.1016/j.ins.2008.02.017

Yi, J.-H., Xing, L.-N., Wang, G.-G., Dong, J., Vasilakos, A. V., Alavi, A. H., et al. (2020). Behavior of crossover operators in NSGA-III for large-scale optimization problems. *Inf. Sci.* 509, 470–487. doi:10.1016/j.ins.2018.10.005

Zhang, X., Tian, Y., Cheng, R., and Jin, Y. (2018). A decision variable clustering-based evolutionary algorithm for large-scale many-objective optimization. *IEEE Trans. Evol. Comput.* 22, 97–112. doi:10.1109/tevc.2016.2600642

Zille, H., Ishibuchi, H., Mostaghim, S., and Nojima, Y. (2018). A framework for large-scale multiobjective optimization based on problem transformation. *IEEE Trans. Evol. Comput.* 22, 260–275. doi:10.1109/tevc.2017.2704782

Zitzler, E., Thiele, L., Laumanns, M., Fonseca, C. M., and Da Fonseca, V. G. (2003). Performance assessment of multiobjective optimizers: An analysis and review. *IEEE Trans. Evol. Comput.* 7, 117–132. doi:10.1109/tevc.2003.810758

Zong, X., Yuan, Y., and Wu, H. (2022). Multi-objective optimization of multi-energy flow coupling system with carbon emission target oriented. *Front. Energy Res.* 10, 451. doi:10.3389/fenrg.2022.877700

frontiers | Frontiers in Energy Research

TYPE Original Research
PUBLISHED 27 September 2022
DOI 10.3389/fenrg.2022.1014983

OPEN ACCESS

EDITED BY
Yusen He,
The University of Iowa, United States

REVIEWED BY
Dongwhi Choi,
Kyung Hee University, South Korea
Xiang Zhu,
Huazhong University of Science and Technology, China
Jingxi Liu,
Huazhong University of Science and Technology, China

*CORRESPONDENCE
Dapeng Zhang,
zhangdapeng@gdou.edu.cn

SPECIALTY SECTION
This article was submitted to Smart Grids,
a section of the journal
Frontiers in Energy Research

RECEIVED 09 August 2022
ACCEPTED 14 September 2022
PUBLISHED 27 September 2022

CITATION
Yan J, Mei N, Zhang D and Zhong Y (2022), Design of a soft-contact triboelectric nanogenerator for vibrational energy collection and its output performance.
Front. Energy Res. 10:1014983.
doi: 10.3389/fenrg.2022.1014983

Design of a soft-contact triboelectric nanogenerator for vibrational energy collection and its output performance

Jin Yan[1,2], Naerduo Mei[1], Dapeng Zhang[1]* and Yinghao Zhong[1]

[1]Guangdong Ocean University, Zhanjiang, China, [2]Shenzhen Research Institute of Guangdong Ocean University, Shenzhen, China

Finding renewable energy sources to lower carbon emissions has emerged as a challenge the world faces in the wake of global warming and energy crises. Vibration is a type of mechanical motion common in daily life, and one popular research topic in this regard is how to gather vibrational energy and transform it into electricity. Vibration energy can be collected using triboelectric nanogenerators whose working mechanism is based on contact electrification and electrostatic induction. The COMSOL software is used to simulate the relationship between the voltage across electrodes, transferred charge, and the electrode moving distance (*V-Q-X*) of triboelectric nanogenerator. Theoretical analysis of the simulation result is offered, along with a brief description of the simulation procedure. When wool is glued to the inner core aluminum foil, TENG's output performance is significantly improved, with a maximum open-circuit voltage of 160 V. In addition, TENG's output performance improves linearly as the vibration frequency and amplitude increase. Specifically, when the vibration frequency rises from 1 to 2.5 Hz, the open-circuit voltage rises from 43 to 100 V, the short-circuit current increases from 0.45 to 1.5 μA, and the peak transfer charge grows from 23 to 46 nC; when the vibration amplitude increases from 30 to 60 mm, the maximum open-circuit voltage increases from 50 to 110 V, the maximum short-circuit current increases from 0.3 to 1.5 μA, and the maximum charge transfer increases from 21 to 54 nC. Durability tests of TENG shows that the soft-contact TENG with wool adhesives is exceptionally durable, with decreased mechanical wear on the contact surface and extended service life. The present work is expected to provide some insight into the working mechanism of low-loss and high-performance TENGs and facilitate their wider adoption.

KEYWORDS

TENG, wool, horizontal sliding, improved durability, vibration energy

1 Introduction

Demand for energy has been growing with the fast advances of the modern world (Lin et al., 2016; Cheng et al., 2019; Lin et al., 2020). Despite the many conventional energy sources developed in the past (Chen et al., 2015; Bera, 2016; Liu et al., 2021a), the development process suffers such problems as expensive raw materials, limited resources, and threats to environmental pollution (Cao et al., 2016; Liu et al., 2021b; Wang, 2021), making it an urgent need to develop energy sources that are both economical and environmentally-friendly. To meet this need, researchers are now shifting to natural energy sources to produce electricity through friction.

The friction nanogenerator (TENG), which can effectively convert mechanical energy into electrical energy and output (Yu et al., 2012; Jing et al., 2014; Yang et al., 2014; Guo et al., 2017; Wang et al., 2017; Xu et al., 2018; Wu et al., 2019; Zhao et al., 2019; LIANG et al., 2020; Xia et al., 2020; Zhang et al., 2020) it as an electrical signal through frictional initiating effect and electrostatic induction coupling, was first proposed by Prof. Zhonglin Wang's team in 2012. The triboelectric nanogenerator (TENG), which is now witnessing quick development and updating (Zhang et al., 2019a; Khandelwal et al., 2020; Long et al., 2021), has been intelligently coupled with various energy sources including wave energy (Xu et al., 2018; Rodrigues et al., 2020), wind energy (Li et al., 2021a; Li et al., 2021b; Liu et al., 2021c; Li, 2022a; Li, 2022b), solar energy (Zheng et al., 2022), vibration energy (Yang et al., 2013; Quan et al., 2015; Chen and Wang, 2017; Wu et al., 2017), body movement energy (Xia et al., 2018; Zhang et al., 2019a; Xia et al., 2019), Liquid-solid interactions (Jang et al., 2020; Jang et al., 2022; Yoo et al., 2022), just to name a few. And to make better use of these energies, researchers are making unremitting efforts to enhance the electrical output performance of TENG in terms of material surfaces (Chen et al., 2020; Zhou et al., 2020), structure optimization (Niu et al., 2014; Feng et al., 2021; Nurmakanov et al., 2021; Yun et al., 2021), and management circuits (Qin et al., 2018). Meanwhile, a number of TENGs have been developed and used to portable electronics (Zhang et al., 2019b), sensors (Wang et al., 2015), and biomedical systems (Zheng et al., 2017) to meet the demand for energy and environmental adaptability in many domains. The closeness of the contact between the frictional electrodes determines a TENG's output performance. A higher friction between frictional surfaces can result in material degradation and reduced durability of the device, but closer contact can generate more frictional charge and better output performance. Therefore, it is crucial to find ways to improve the TENG's stability, decrease wear, and increase durability without sacrificing output performance. Zhang et al. (Zhang et al., 2020) designed a non-contact cylindrical rotating TENG to recover mechanical energy from hydraulic systems, and its operating mechanism is based on the non-contact free rotation of a flexible nanowire (NW) structure and a copper foil curve, or more specifically, the rotation of a flexible nanowire (NW) structure of a fluorinated ethylene-propylene (FEP) polymer sheet in non-contact with a bent copper foil, though the TENG's output performance is still constrained by the TENG's limited contact area and charge. Li et al. (Li et al., 2021c) have presented a polyester fur-reinforced rotating triboelectric nanogenerator (PFR-TENG) with ultra-stable high voltage output, where a soft polyester fur layer is introduced as a charge pump and charge emitter to form partial soft-contact and non-contact based on the proper work function and electronegativity. Though the non-contact TENG has less losses in the friction layer, its output is not stable and its structure is complicated. To reduce the loss, Li et al. (Long et al., 2021) presented a floating self-excited sliding TENG (FSS-TENG) with a floating mode and a non-contact TENG air breakdown model. The FSS-TENG achieves a self-increased charge density by self-excited amplification between the rotor and stator; the minimum of transmitted charge, however, remains a significant issue. These studies offer helpful suggestions for enhancing the TENG's output performance, stability, and wear resistance during extended periods of operation.

2 Experiment

2.1 Design and modelling of the TENG

Figure 1A depicts a perspective view of the interior and an external model of the TENG. As PTFE is more electronegative than other materials due to its different position in the frictional electric sequence, PTFE is more likely to lose electrons than other materials and as a result has a higher capacity for charge transfer and higher output performance. The main structure of the TENG is made up of a shell with aluminum foil and PTFE film attached to the inner surface in sequence. For this reason, the upper electrode and dielectric are made of aluminum foil and PTFE, respectively. As the lower electrode, an aluminum foil is put to the outside surface of the core, and wool is then attached on top of the foil as an additional material. Wool is a more ideal additional material since it is more readily available, more electronegative, and softer than other materials. The two friction layers of the TENG become electrically charged when it moves horizontally, with the PTFE foil being electronegative and the wool being electrically positive. The TENG's operating signals, which are high voltage and low current, can be gathered.

A fundamental model of a TENG with a horizontal sliding structure is created (Figure 1), which successfully separates the two friction layers under various external stresses, as shown in Figure 1A. The proposed TENG comprises of a cylindrical structure inside the shell connected to a hollowed inner rectangular core. A steel spring is installed to the top and bottom of the cylindrical structure, giving the inner core more strength so it can rub more thoroughly. This pillar

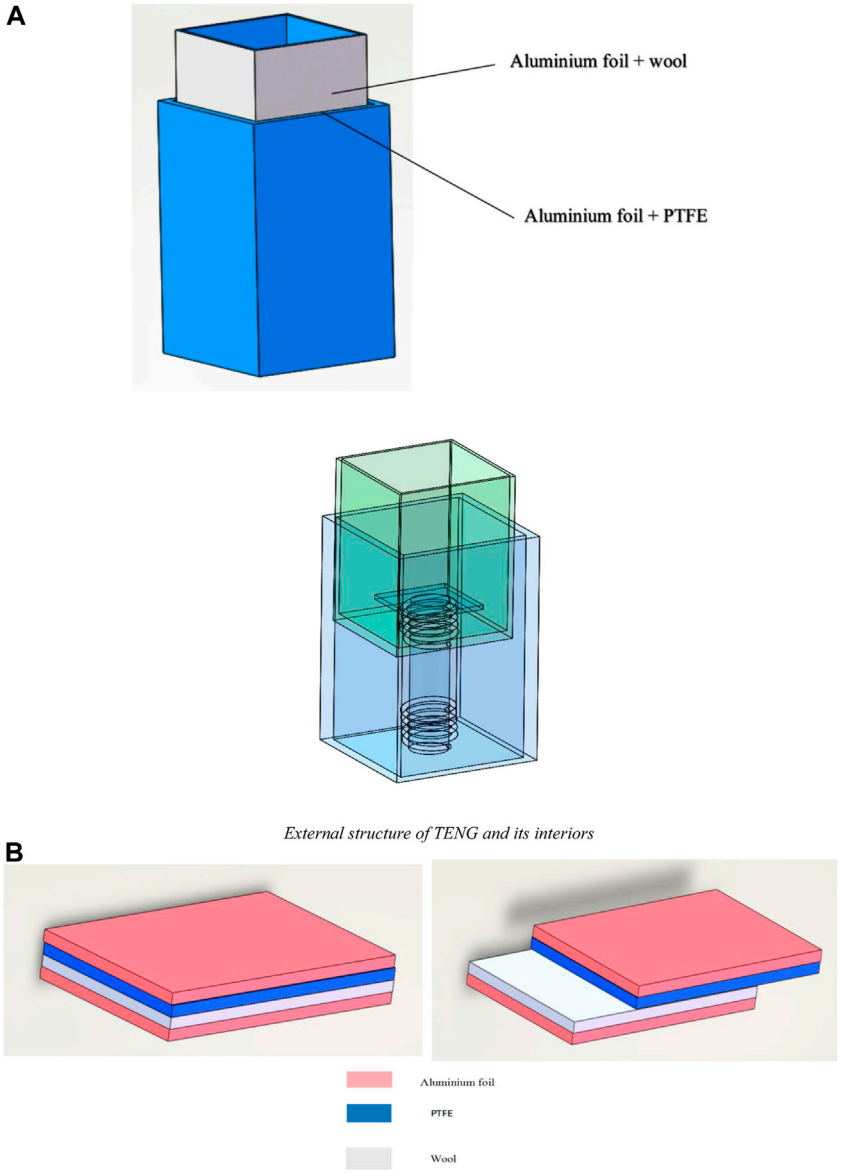

FIGURE 1
Structure and internal coating of the TENG. **(A)** External structure of TENG and its interiors. **(B)** Internal coating of TENG.

system passes through a circular hole at the bottom of the core connected to the shell. To prevent the core from ejecting from the shell when force is applied and to limit the movement of the core to the top of the cylindrical structure, an acrylic sheet is glued to the top of the cylinder after the cylindrical structure and the inner core are linked. Figure 1 2) shows the internal coating of the Teng. The aluminum foil and the PTFE film, which serve as the upper electrode and dielectric, are bonded on the interior surface of the shell; as the bottom electrode, the aluminum foil is laminated onto the outer surface of the inner core, and wool is added as a support material on the outside of the electrode. The high voltage and low current produced during operation are collected by the TENG.

2.2 TENG test platform

Figure 2 shows the test rig for TENG's output performance. First, the linear motor is connected and fixed

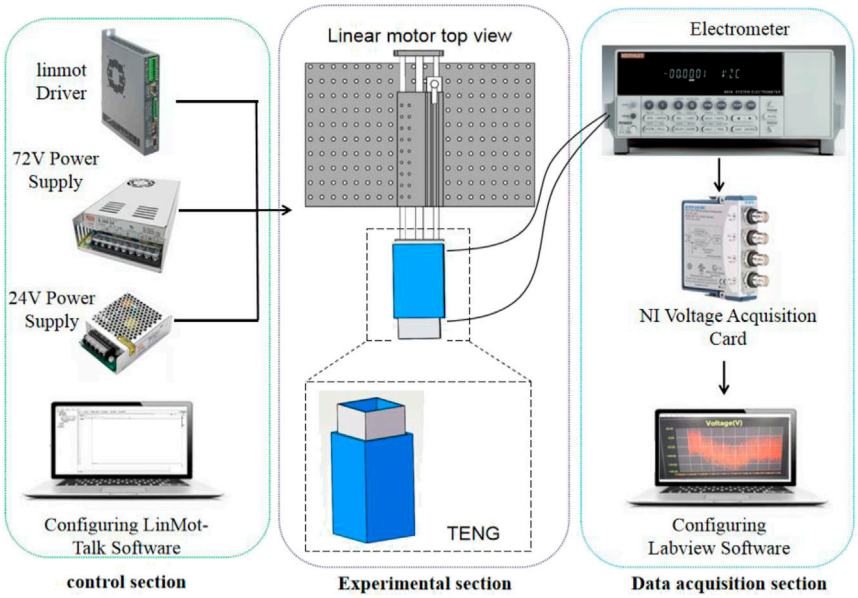

FIGURE 2
Schematic diagram of the TENG output performance test rig.

to the optical plate; next, the TENG is connected to the linear motor and fixed to the linear motor push plate before controlling the linear motor *via* the computer. The linear motor software LinMot-Talk can only set the acceleration, speed, and displacement, so the linear motion formula needs to be derived to calculate the displacement and acceleration at different frequencies and amplitudes. For data collection, the acceleration and displacement parameters are configured to control the linear motor; meanwhile, the positive and negative electrodes are connected by two wires to the positive and negative contacts on the Keithley 6,514 electrostatic meter, which converts the received digital signals such as voltage, current, and charge into analogue signals and then transmits them to the NI voltage acquisition card. The sampling frequency is set to 500 by the LabView software for data storage, and then the collected data are processed and analyzed to obtain the experiment results.

1) Keithley 6,514 electrostatics meter: input impedance up to 200TΩ, high sampling rate, dynamic current, voltage, and charge acquisition in real time, combined with high-speed voltage acquisition card and system software makes the acquisition signal can reach a maximum speed of 50,000 points per second, with voltage measurement ranges of 10 μV-200V, and current measurement ranges of 1fA-20mA. Friction nanogenerators' high output voltage and low output current electrical output features.
2) Data acquisition equipment: A voltage acquisition card, model NI-9215, with four simultaneous acquisition channels, a 100 kS/S acquisition rate per channel, a 16-bit resolution, built-in signal conditioning, and a USB connection to the PC without an external power source is used for data acquisition. The voltage acquisition card receives the electrostatic meter's converted analogue signal during the data acquisition process, which then displays the signal on the PC hooked up to the card to display the measurement results.
3) Linear motor: In the experiment, a linear motor is used to replicate the motion of the wave. The LinMot-E1200-RS type, with a top speed of 3.2 m/s, a top thrust of 163 N, and a stroke of 360 mm, was selected for the linear motor. The output current can also be used to control different thrust sizes. The requirements of this experiment are entirely satisfied by the linear motor, which satisfies the wave's low frequency and low amplitude properties.
4) 3D printer: UItinaker three model, a professional-grade 3D printer with a dual printhead design, long uptime, water-soluble support, quick nozzle swapping, sticky 3D printing ecosystem, and interconnected cohesiveness. The print medium is PLA (Polylactic Acid), which has a wire diameter tolerance of 0.03 mm and a tensile strength of 250 kg/cm^2, a melting point of 160–165°C and a wire diameter tolerance of 0.03 mm. SOLIDWORKS was used to create the inner and exterior boat structure, which was then imported into CURA for slicing and manufactured using a 3D printer.

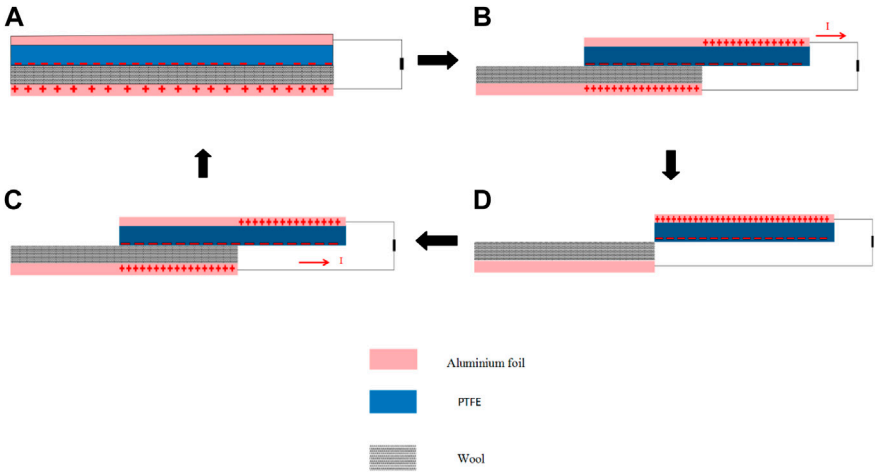

FIGURE 3
Schematic diagram of an operation cycle of TENG.

3 Theoretical analysis

3.1 Principle of operation

Figure 3 shows one complete cycle of the TENG in operation, and Figure 3A describes the state at which no mechanical forces are applied and there is no relative displacement of the fleece-bonded aluminum foil from the PTFE film. Since the frictional charge is distributed only on the surface layer of the polymer that is well insulated, no charge leakage occurs during one cycle. At the initial position, the distance between the positively and negatively charged surfaces is negligible, so there is hardly any potential difference between the two electrodes. As shown in Figure 3B, once the positively charged upper electrode plate starts to slide outwards, the contact area between the two plates decreases, resulting in separation of charges on the plane and hence a higher potential of the upper plate. In this case, electrons flow from the upper electrode to the lower electrode to offset the potential difference created by the frictional charge. Ideally, the vertical distance between the electrode layer and the friction charge surface is negligible compared to the lateral separation distance of the charges, so the amount of transferred charge at the electrode is approximately equal to the amount of charge separated at any sliding position. Therefore, as the sliding process proceeds, the charge will continue to flow so that the separated charge increases, until the upper plate slides completely away from the lower plate and the frictional charge surfaces are completely separated, as shown in Figure 3C, where the test value of the current is determined by the sliding speed of the two plates. Subsequently, when the upper plate slides back in, as shown in Figure 3D, the separated charges are again in contact with each other but not annihilated due to the insulating nature of the polymer material. As the contact area increases, the excess of the electrode transfer charge is induced to flow from the lower electrode back to the upper electrode *via* an external load to maintain electrostatic equilibrium. This process is the second half of the sliding process. When the two plates return to the overlapping position, the charged surfaces are again in full contact with each other. At this point, there is no remaining transfer charge at the electrodes and the device returns to the state shown in Figure 3A. Throughout the cycle, the outward and inward sliding processes are symmetrical and therefore a symmetrical pair of AC current peaks will be obtained.

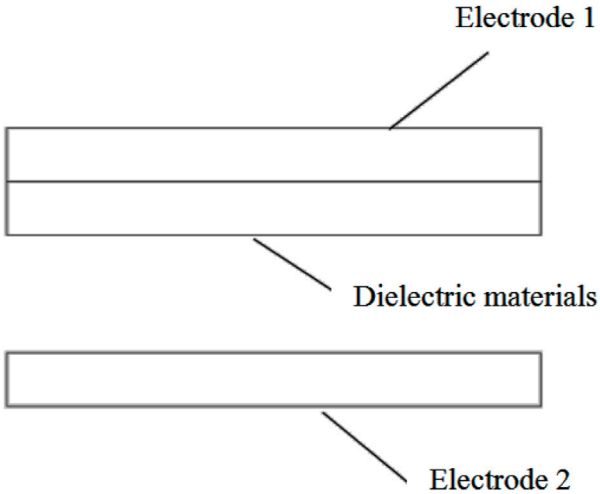

FIGURE 4
TENG geometric model.

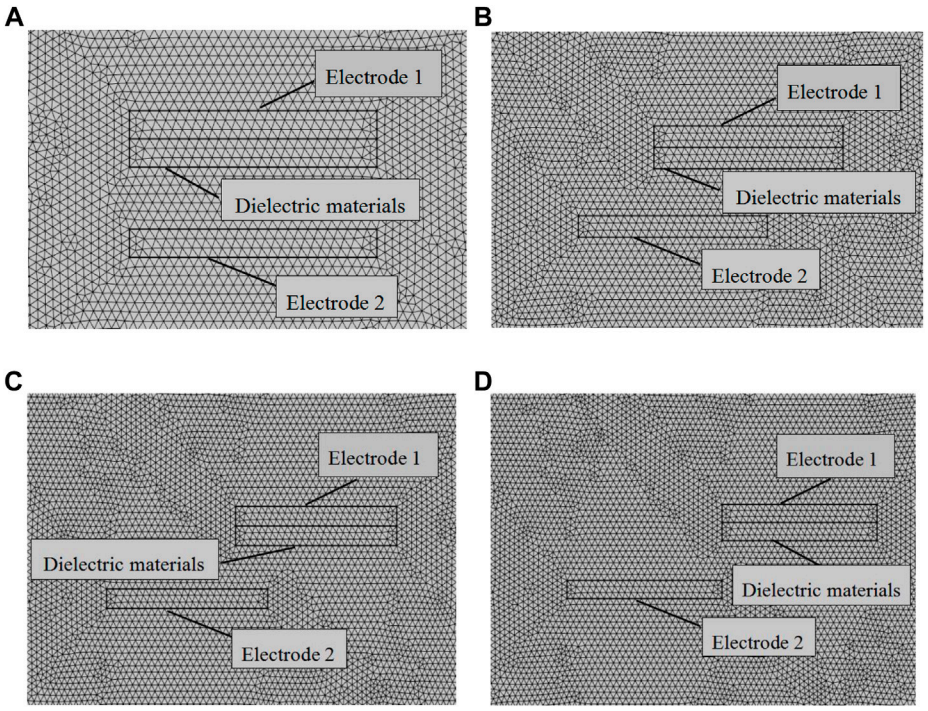

FIGURE 5
Geometric meshing of TENG.

3.2 Electrical performance simulation by comsol multiphysics

To describe the operating principle of the double-layer soft-contact TENG, the COMSOL simulation software, which specializes in multi-physics field coupling, was used to model, mesh and simulate the potential distribution of the friction material under different conditions.

First, a two-dimensional geometric model of the TENG was created using COMSOL (Figure 4), and different materials were added to the material library for different geometries, with the dielectric material set as PTFE, the thickness set to 1 mm and the Poisson's ratio set to 0.3. The surface metal of the inner and outer structures and the two electrodes were set as aluminum, and the width of both electrodes was set to 1 mm. To simplify computation, the simulation was set to a steady-state calculation. To obtain the trend in the potential, the charge density on the PTFE surface was set to $-0.02\ \mu C/m^2$ and the total charge density on the aluminum surface was set to $0.01\ \mu C/m^2$.

Next, after the geometric model was built and material settings were completed, the geometry was meshed, as shown in Figure 5, The mesh was predefined and set to "finer". For all materials, a free triangular mesh is selected, and the air-domain mesh was set to "very fine" with a maximum cell size of 0.4 mm and a minimum cell size of 5×10^{-3} mm, since air has a small effect on the induced potential distribution in this geometry. For the electrodes, separate metals and dielectric materials in contact with each other, the mesh was set to "superfine" with a maximum cell size of 0.04 mm and a minimum cell size of 3×10^{-4} mm. As Figure 5 shows, the mesh size for the air gap is larger, and the mesh is finer as it gets closer to the electrodes, the separate metals, and the dielectric materials that are the contact parts.

Finally, using Maxwell's control equations, the potential distribution between the two electrodes at different spacings can be calculated using finite element simulations, as shown in Figure 6, which clearly shows the potential difference between the two electrodes. At the initial state, the aluminum electrode is in full contact with the PTFE (Figure 6A) and charge transfer occurs between the two. As the two begin to move away from each other (Figure 6B), an electric field is formed between the electrodes and the air gap, creating an electric potential difference between the upper and lower electrodes and, as can be seen from the potential cloud, the potential difference between the two electrode surfaces increases with the increasing horizontal displacement. This is consistent with the linear variation of the potential difference with the separation distance, as previously mentioned. When the separation distance reaches a maximum (Figure 6D), the potential difference is at its maximum. As the separation distance decreases from the maximum (Figure 6C), the potential difference decreases as

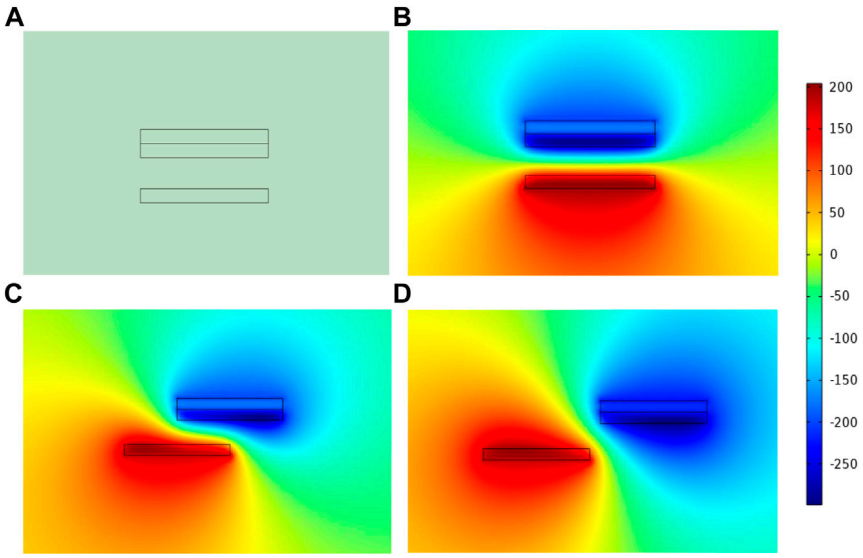

FIGURE 6
TENG simulation potential distribution.

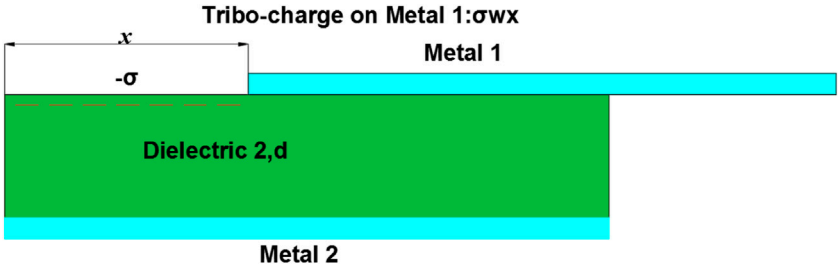

FIGURE 7
TENG Theoretical models.

well. It should be noted that the separation distance should not be set too large during simulation; otherwise, the edge effect will have a significant impact and make the electric field line become approximately an electric field line between two point charges, rather than a uniform electric field. The simulation result shows that the trend of the potential distribution is consistent with the working principle of TENG.

3.3 Theoretical foundations

In the present work, a horizontal sliding TENG *V-Q-X* model is developed, as shown in Figure 7. Under ideal conditions, the length and width of the dielectric are much greater than its thickness, so that edge effects are negligible. The metal plate one is not only the top friction layer, but also the top electrode itself. When the metal plate one is separated from the dielectric 2, a frictional charge with a charge density of $-\sigma$ is uniformly distributed on the top surface of the separated area of the dielectric two due to the frictional start effect, while an equal amount of negative frictional charge is distributed on the surface of the metal plate 1. Thus, under open-circuit conditions (where the charge reference state can reach a minimum), the total charge at the bottom electrode is 0. To facilitate understanding, the frictional charge in the overlap region of the dielectric surface can be regarded as the portion of the top metal layer with a charge density of σ. The total amount of anti-signal frictional charge of $\sigma w(l-x)$ is removed.

In general, it is impossible to derive an analytical equation for the sliding TENG with attached electrodes, but a rigorous theoretical analysis based on numerical calculations is

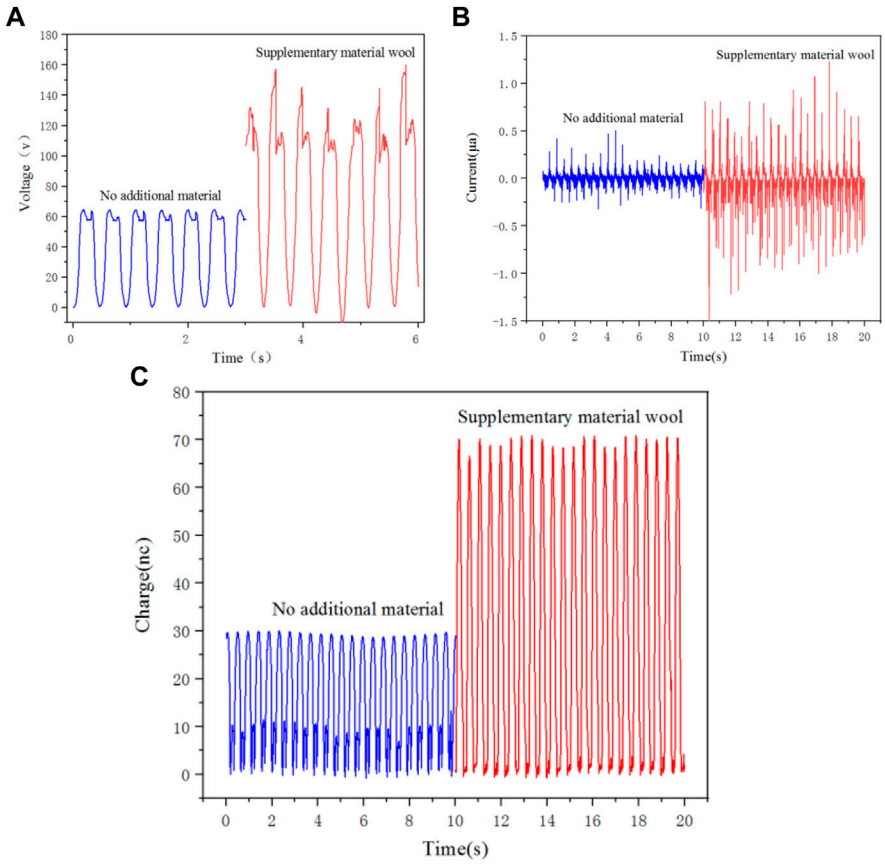

FIGURE 8
Output performance of TENG with and without supplementary materials. **(A)**Open-circuit voltage; **(B)** Short-circuit current; **(C)**Transfer of charge.

feasible. In practice, the lateral separation distance x is always less than 0.91 L, considering that l is always far larger than d_1 and d_2, and that it is difficult to align the two dielectric surfaces precisely again after complete separation of the two dielectrics. First, the intrinsic capacitance C is derived, and since the thickness of the dielectric is much smaller than its length, the total capacitance is determined by the capacitance between the overlapping regions as long as the two dielectrics do not reach a complete separation. Therefore, using the parallel plate capacitor model, the total capacitance C can be estimated by the following equation:

$$C = \frac{\varepsilon_0 w(l-x)}{d_0} \tag{1}$$

where d_0 is the effective thickness constant.

The value of V_{oc} is then estimated from the charge distribution. Since the length of the dielectric is much larger than its thickness, it can be assumed that in each region, the metal electrodes are infinitely large flat plates. By this approximation, the charge in each region is uniformly distributed and the electric field inside the dielectric is uniformly distributed along the y-axis. This conclusion can also be verified by the result of finite element calculations. Thus, in the ideal case, the absolute value of charge density on the surface of the non-overlapping region is σ. While the charge density in the overlapping region is still uniformly distributed, the charge density in the overlapping region can be calculated by taking the total charge on each electrode as 0 in the open-circuit condition. The ideal charge distribution under open-circuit conditions (where the charge reference state can reach the minimum) can be approximated by the following equations:

For the un-overlapped area of the bottom electrode, the charge density is:

$$p = \sigma \tag{2}$$

For the overlapping area of the bottom electrode:

$$p = -\frac{\sigma x}{l-x} \tag{3}$$

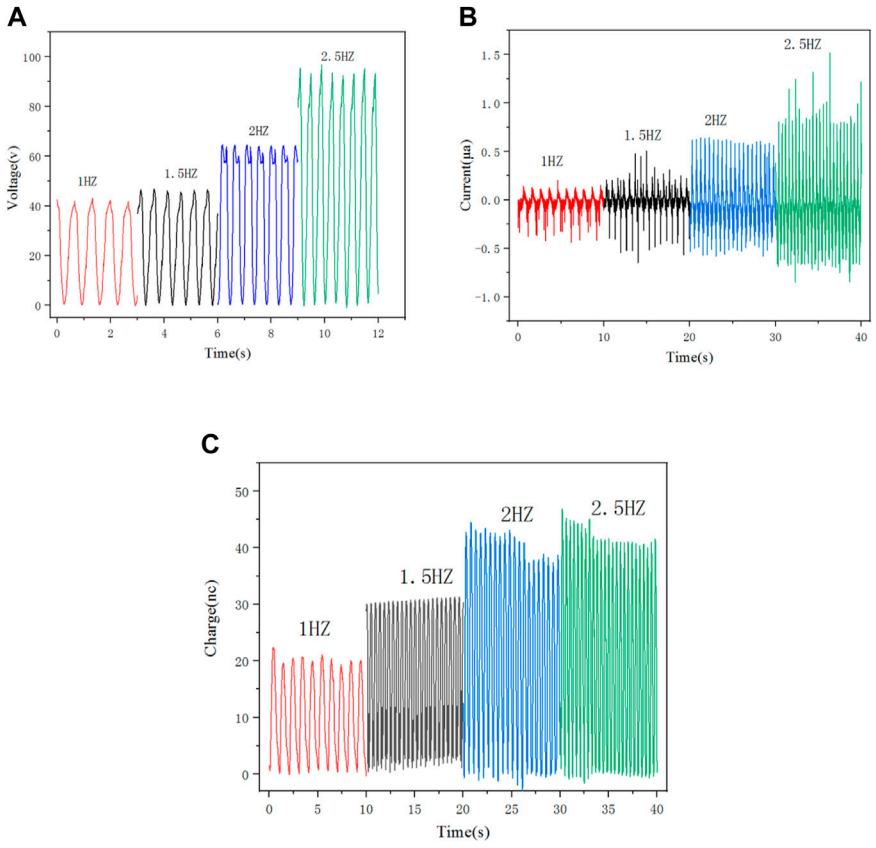

FIGURE 9
Output performance at the same amplitude and different frequencies. **(A)** Open-circuit voltage; **(B)** Short-circuit current; **(C)** Transfer of charge.

For the un-overlapped area of the top electrode:

$$p = -\sigma \tag{4}$$

For the overlapping area of the top electrode:

$$p = \frac{\sigma x}{l - x} \tag{5}$$

Using the above charge distribution law and the Gauss theorem, the analytical expression for the open-circuit voltage V_{oc} can be estimated:

$$V_{OC} = \frac{\sigma x d_0}{\varepsilon_0 (l - x)} \tag{6}$$

Thus, when the edge effect is neglected, the *V-Q-X* relationship for the sliding TENG with attached electrodes is:

$$V = -\frac{1}{C}Q + V_{oc} = -\frac{d_0}{w\varepsilon_0 (l - x)}Q + \frac{\sigma d_0 x}{\varepsilon_0 (l - x)} \tag{7}$$

4 Discussion of experimental results

4.1 Comparison of output performance of TENG with and without supplementary materials

Figure 8 shows a comparison of the performance of the TENG with and without the supplementary material wool. Two types of cores were chosen for the test: one with wool on the outer aluminum foil, and one without. The output performance of the TENG with wool is much higher than that of the TENG without, as shown in Figures 8A–C. Specifically, the TENG with wool as the supplementary material achieves an open-circuit voltage and peak transfer charge two times higher than that without, reaching a maximum open-circuit voltage of 160 V and a peak charge of 72 nC. The peak short-circuit current is more than three times higher, reaching 1.5 μA. This is because in the TENG without wool, there is no contact between the core and the shell.

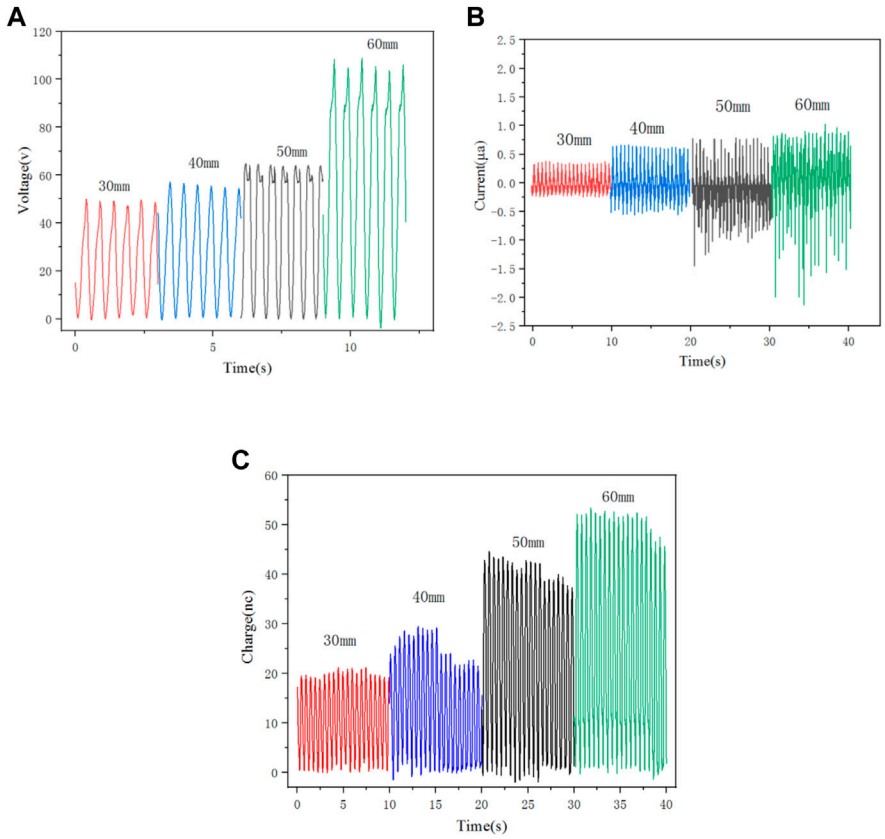

FIGURE 10
Output performance at the same frequency and different amplitudes. **(A)** Open-circuit voltage; **(B)** Short-circuit current; **(C)** Transfer of charge.

4.2 Effect of frequency on TENG output performance

The TENG output performance was investigated within the frequency range of 1–2.5 Hz and at a fixed amplitude of 50 mm, with the internal structural conditions kept constant, i.e., a wool-glued inner core was selected and PTFE of 0.3 mm thickness was used as a dielectric film.

Figure 9 shows the experiment result. The open-circuit voltage increases from 43 to 100 V and the short-circuit current increases from 0.45 to 1.5 μA when the TENG frequency increases from 1 to 2.5 Hz, while the peak transfer charge increases from 23 to 46 nC. This trend can be considered as a linear growth, ignoring the effect of experimental errors. Increase the frequency of the linear motor's movement stroke in the case of constant amplitude, which increases the motor's movement speed. According to formula 6 in the second chapter, open circuit voltage and transfer charge are proportional to d_0, or the separation distance per unit of time. Here, in the case of constant amplitude, the increase in frequency side reflects the TENG device's movement speed at the same time, increasing the voltage and transfer charge. The increase in frequency per unit of time leads to a rise in the current when the same amount of charge is transferred; at the same time, as the frequency increases, the times of contact between the TENG inner core and the shell rise, hence a rise in the amount of transferred charge.

4.3 Effect of amplitude on TENG output performance

The effect of amplitude on THE TENG's output performance was then investigated. Amplitude refers to the maximum distance between the inner core and the outer shell at each contact separation in a TENG device. Four values of amplitude — 30 mm, 40 mm, 50 mm and 60 mm, were selected in the present work. In analysis of the impact of amplitude on the output performance, other factors were controlled to be constant for controlled experiments. In this case, the acceleration and motion of the linear motor were controlled, and the frequency was adjusted to the same value for each test on the four different amplitudes. Specifically, the frequency was set at 2 Hz, and 0.3-mm-thick PTFE was used as the dielectric film.

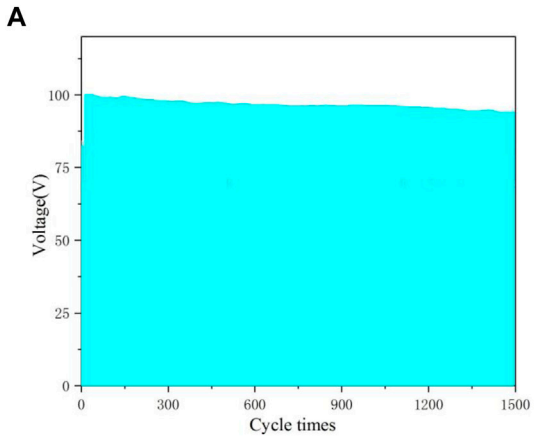

FIGURE 11
TENG durability test results. **(A)** Wool friction layer TENG open circuit voltage cycle test results. **(B)** TENG open circuit voltage test results for aluminium foil friction layer.

Figure 10 shows the experiment result. At the four amplitudes, the maximum open-circuit voltage is 50 V, 60 V, 70 V and 110 V, respectively; the maximum short circuit current is 0.3, 0.75, 1.1 and 1.5 μA, respectively; and the maximum transferred charge is 21 nC, 30 nC, 45 nC, and 54 nC, respectively. The open-circuit voltage, short-circuit current and transferred charge all increase significantly as the amplitude rises. Here, at a constant frequency, the increase in amplitude is accompanied by an increase in the speed of motion of the TENG device, so both the open-circuit voltage and the transferred charge increase. As the speed of movement increases, the wool adhering to the PTFE film comes into closer frictional contact with the aluminum foil, which also increases the electrical output after horizontal sliding.

4.4 Durability of TENG

The durability of the TENG was tested and Figure 11 shows the test result. The linear motor parameters were set, with the frequency set to 2.5 Hz and the amplitude to 50 mm. The wool friction layer TENG's open-circuit voltage started out at about 100 V, as indicated in Figure 11. The open-circuit voltage dropped to 95 with only a small 5% decline after 1,500 rounds of durability testing. After 1,500 cycles of durability testing, the friction layer without wool as an additional material had an open circuit voltage of 76 and a 24% drop in voltage. This suggests that the wool friction layer is more stable over time, which is good for vibration energy gathering.

5 Conclusion

In the present work, a soft-contact triboelectric nanogenerator (TENG) for capturing vibrational energy is designed, and its output performance is examined using the concepts of friction-generated electricity and electrostatic induction. The COMSOL software is used to simulate the horizontal sliding TENG. A brief description of the simulation procedure is given, and the findings are theoretically examined. The effect of wool as the supplementary material on the TENG's performance is then investigated. The findings indicate that using a friction layer with wool improves output performance and mechanical durability compared to using a friction layer without wool. Then, the effect of the frequency on the TENG's performance is examined, and it is found that the performance improves linearly with the increasing frequency. The higher the frequency, the higher the open circuit voltage, short circuit current and peak transfer charge will be. Experiments that measure the impact of vibration amplitude on the TENG's performance reveal that increased amplitude leads to better performance. The higher the amplitude, the higher the open circuit voltage, short circuit current and peak transfer charge will be. Durability tests indicate that the soft-contact TENG with wool adhesives is found to be exceptionally durable, boasting decreased mechanical wear on the contact surfaces and extended service life. These findings are expected to offer some insights into the working mechanism of TENGs and widen the adoption of low-loss and high-performance TENGs.

Data availability statement

The original contributions presented in the study are included in the article/Supplementary Material, further inquiries can be directed to the corresponding author.

Author contributions

JY proposed the conception, wrote, and edited the manuscript. NM drafted the manuscript and figures. DZ

participated in drafting and editing the manuscript as well as checking references. YZ performed electrical performance simulations. All authors listed in the paper have made a substantial, direct, and intellectual contribution to the work and approved of its publication.

Funding

The authors gratefully acknowledge the support from National Nature Science Foundation of China (51979045), Natural Science Foundation of Guangdong Province (2022A1515011562) and Guangdong Provincial Special Fund for promoting high quality economic development [GDNRC (2021)56, Yuerong Office Letter (2020)161].

Conflict of interest

The authors declare that the research was conducted in the absence of any commercial or financial relationships that could be construed as a potential conflict of interest.

Publisher's note

All claims expressed in this article are solely those of the authors and do not necessarily represent those of their affiliated organizations, or those of the publisher, the editors and the reviewers. Any product that may be evaluated in this article, or claim that may be made by its manufacturer, is not guaranteed or endorsed by the publisher.

References

Bera, B. (2016). Literature review on triboelectric nanogenerator[J]. *Imperial J. Interdiscip. Res. (IJIR)* 2 (10), 1263–1271.

Cao, X., Jie, Y., Wang, N., and Wang, Z. L. (2016). Triboelectric nanogenerators driven self-powered electrochemical processes for energy and environmental science. *Adv. Energy Mat.* 6 (23), 1600665. doi:10.1002/aenm.201600665

Chen, A., Zhang, C., Zhu, G., and Wang, Z. L. (2020). Polymer materials for high-performance triboelectric nanogenerators. *Adv. Sci. (Weinh).* 7 (14), 2000186. doi:10.1002/advs.202000186

Chen, J., and Wang, Z. L. (2017). Reviving vibration energy harvesting and self-powered sensing by a triboelectric nanogenerator. *Joule* 1 (3), 480–521. doi:10.1016/j.joule.2017.09.004

Chen, J., Yang, J., Guo, H., Li, Z., Zheng, L., Su, Y., et al. (2015). Automatic mode transition enabled robust triboelectric nanogenerators. *ACS Nano* 9 (12), 12334–12343. doi:10.1021/acsnano.5b05618

Cheng, T., Gao, Q., and Wang, Z. L. (2019). The current development and future outlook of triboelectric nanogenerators: A survey of literature. *Adv. Mat. Technol.* 4 (3), 1800588. doi:10.1002/admt.201800588

Feng, P. Y., Xia, Z., Sun, B., Jing, X., Li, H., Tao, X., et al. (2021). Enhancing the performance of fabric-based triboelectric nanogenerators by structural and chemical modification. *ACS Appl. Mat. Interfaces* 13 (14), 16916–16927. doi:10.1021/acsami.1c02815

Guo, Hengyu, Zi, Yunlong, Wen, Zhen, Chen, J., Liu, G., Hu, C., et al. (2017). Ultralight cut-paper-based self-charging power unit for self-powered portable electronic and medical systems. *ACS Nano* 11 (5), 4475–4482. doi:10.1021/acsnano.7b00866

Jang, S., Joung, Y., Kim, H., Cho, S., Ra, Y., Kim, M., et al. (2022). Charge transfer accelerating strategy for improving sensitivity of droplet based triboelectric sensors via heterogeneous wettability. *Nano Energy* 97, 107213. doi:10.1016/j.nanoen.2022.107213

Jang, S., La, M., Cho, S., Yun, Y., Choi, J. H., Ra, Y., et al. (2020). Monocharged electret based liquid-solid interacting triboelectric nanogenerator for its boosted electrical output performance. *Nano Energy* 70, 104541. doi:10.1016/j.nanoen.2020.104541

Jing, Qingshen, Zhu, Guang, Bai, Peng, Xie, Y., Chen, J., Han, R. P. S., et al. (2014). Case-encapsulated triboelectric nanogenerator for harvesting energy from reciprocating sliding motion. *Acs Nano* 8 (4), 3836–3842. doi:10.1021/nn500694y

Khandelwal, G., Raj, N. P. M. J., and Kim, S. J. (2020). Triboelectric nanogenerator for healthcare and biomedical applications. *Nano Today* 33, 100882. doi:10.1016/j.nantod.2020.100882

Li, H., Deng, J., Feng, P., Pu, C., Arachchige, D. D. K., and Cheng, Q. (2021). Short-term nacelle orientation forecasting using bilinear transformation and ICEEMDAN framework. *Front. Energy Res.* 9, 780928. doi:10.3389/fenrg.2021.780928

Li, H., Deng, J., Yuan, S., Feng, P., and Arachchige, D. D. K. (2021). Monitoring and identifying wind turbine generator bearing faults using deep belief network and EWMA control charts. *Front. Energy Res.* 9, 799039. doi:10.3389/fenrg.2021.799039

Li, H. (2022). SCADA data based wind power interval prediction using LUBE-based deep residual networks. *Front. Energy Res.* 10, 920837. doi:10.3389/fenrg.2022.920837

Li, H. (2022). Short-term wind power prediction via spatial temporal analysis and deep residual networks. *Front. Energy Res.* 10, 920407. doi:10.3389/fenrg.2022.920407

Li, Q., Liu, W., Yang, H., He, W., Long, L., Wu, M., et al. (2021). Ultra-stability high-voltage triboelectric nanogenerator designed by ternary dielectric triboelectrification with partial soft-contact and non-contact mode. *Nano Energy* 90, 106585. doi:10.1016/j.nanoen.2021.106585

Liang, Xi, Jiang, Tao, Liu, Guoxu, Feng, Y., Zhang, C., and Wang, Z. L. (2020). Spherical triboelectric nanogenerator integrated with power management module for harvesting multidirectional water wave energy. *Energy Environ. Sci.* 13 (1), 277–285. doi:10.1039/c9ee03258d

Lin, Z., Chen, J., and Yang, J. (2016). Recent progress in triboelectric nanogenerators as a renewable and sustainable power source. *J. Nanomater.* 2016, 1–24. doi:10.1155/2016/5651613

Lin, Z., Zhang, B., Zou, H., Wu, Z., Guo, H., Zhang, Y., et al. (2020). Rationally designed rotation triboelectric nanogenerators with much extended lifetime and durability. *Nano Energy* 68, 104378. doi:10.1016/j.nanoen.2019.104378

Liu, S., Li, X., Wang, Y., Yang, Y., Meng, L., Cheng, T., et al. (2021). Magnetic switch structured triboelectric nanogenerator for continuous and regular harvesting of wind energy. *Nano Energy* 83, 105851. doi:10.1016/j.nanoen.2021.105851

Liu, W., Wang, Z., and Hu, C. (2021). Advanced designs for output improvement of triboelectric nanogenerator system. *Mater. Today* 45, 93–119. doi:10.1016/j.mattod.2020.11.012

Liu, Y., Ping, J., and Ying, Y. (2021). Recent progress in 2D-nanomaterial-based triboelectric nanogenerators. *Adv. Funct. Mat.* 31 (17), 2009994. doi:10.1002/adfm.202009994

Long, L., Liu, W., Wang, Z., Wencong, H., Gui, L., Qian, T., et al. (2021). High performance floating self-excited sliding triboelectric nanogenerator for micro mechanical energy harvesting[J]. *Nat. Commun.* 12 (1), 1–10.

Niu, S., Liu, Y., Wang, S., Lin, L., Zhou, Y. S., Hu, Y., et al. (2014). Theoretical investigation and structural optimization of single-electrode triboelectric nanogenerators. *Adv. Funct. Mat.* 24 (22), 3332–3340. doi:10.1002/adfm.201303799

Nurmakanov, Y., Kalimuldina, G., Nauryzbayev, G., Adair, D., and Bakenov, Z. (2021). Structural and chemical modifications towards high-performance of triboelectric nanogenerators. *Nanoscale Res. Lett.* 16 (1), 122–127. doi:10.1186/s11671-021-03578-z

Qin, H., Cheng, G., Zi, Y., Gu, G., Zhang, B., Shang, W., et al. (2018). High energy storage efficiency triboelectric nanogenerators with unidirectional switches and passive power management circuits. *Adv. Funct. Mat.* 28 (51), 1805216. doi:10.1002/adfm.201805216

Quan, T., Wu, Y., and Yang, Y. (2015). Hybrid electromagnetic–triboelectric nanogenerator for harvesting vibration energy. *Nano Res.* 8 (10), 3272–3280. doi:10.1007/s12274-015-0827-6

Rodrigues, C., Nunes, D., Clemente, D., Mathias, N., Correia, J. M., Rosa-Santos, P., et al. (2020). Emerging triboelectric nanogenerators for ocean wave energy harvesting: State of the art and future perspectives. *Energy Environ. Sci.* 13 (9), 2657–2683. doi:10.1039/d0ee01258k

Wang, S., Lin, L., and Wang, Z. L. (2015). Triboelectric nanogenerators as self-powered active sensors. *Nano Energy* 11, 436–462. doi:10.1016/j.nanoen.2014.10.034

Wang, Xiaofeng, Niu, Simiao, Yin, Yajiang, Hao, C., Zhang, Y., et al. (2017). Harvesting ambient vibration energy over a wide frequency range for self-powered electronics. *ACS Nano* 11 (2), 1728–1735. doi:10.1021/acsnano.6b07633

Wang, Z. L. (2021). From contact electrification to triboelectric nanogenerators. *Rep. Prog. Phys.* 84 (9), 096502. doi:10.1088/1361-6633/ac0a50

Wu, C., Liu, R., Wang, J., Zi, Y., Lin, L., and Wang, Z. L. (2017). A spring-based resonance coupling for hugely enhancing the performance of triboelectric nanogenerators for harvesting low-frequency vibration energy. *Nano Energy* 32, 287–293. doi:10.1016/j.nanoen.2016.12.061

Wu, Yesheng, Qi, Liu, Cao, Jie, Li, K., Cheng, G. G., Zhang, Z. Q., et al. (2019). Design and output performance of vibration energy harvesting triboelectric nanogenerator. *Acta Phys. Sin.* 68 (19), 190201. doi:10.7498/aps.68.20190806

Xia, K., Zhu, Z., Zhang, H., Du, C., Fu, J., and Xu, Z. (2019). Milk-based triboelectric nanogenerator on paper for harvesting energy from human body motion. *Nano Energy* 56, 400–410. doi:10.1016/j.nanoen.2018.11.071

Xia, K., Zhu, Z., Zhang, H., Du, C., Xu, Z., and Wang, R. (2018). Painting a high-output triboelectric nanogenerator on paper for harvesting energy from human body motion. *Nano Energy* 50, 571–580. doi:10.1016/j.nanoen.2018.06.019

Xia, Kequan, Fu, Jiangming, and Xu, Zhiwei (2020). Multiple-frequency high-output triboelectric nanogenerator based on a water balloon for all-weather water wave energy harvesting. *Adv. Energy Mat.* 10 (28), 2000426. doi:10.1002/aenm.202000426

Xu, Liang, Jiang, Tao, Shao, Jiajia, He, C., Zhong, W., Chen, X. Y., et al. (2018). Coupled triboelectric nanogenerator networks for efficient water wave energy harvesting. *ACS Nano* 12 (2), 1849–1858. doi:10.1021/acsnano.7b08674

Yang, W., Chen, J., Zhu, G., Wen, X., Bai, P., Su, Y., et al. (2013). Harvesting vibration energy by a triple-cantilever based triboelectric nanogenerator. *Nano Res.* 6 (12), 880–886. doi:10.1007/s12274-013-0364-0

Yang, Weiqing, Chen, Jun, Wang, Zhonglin, Jing, Q., Yang, J., Su, Y., et al. (2014). Triboelectrification based motion sensor for human-machine interfacing. *ACS Appl. Mat. Interfaces* 6 (10), 7479–7484. doi:10.1021/am500864t

Yoo, D., Kim, S. J., Joung, Y., Jang, S., and Choi, D. (2022). Lotus leaf-inspired droplet-based electricity generator with low-adhesive superhydrophobicity for a wide operational droplet volume range and boosted electricity output. *Nano Energy* 99, 107361. doi:10.1016/j.nanoen.2022.107361

Yu, Aifang, Jiang, Peng, Wang, Zhonglin, et al. (2012). Nanogenerator as self-powered vibration sensor[J]. *Nano Energy* 1 (3), 418–423.

Yun, Y., La, M., Cho, S., Jang, S., Choi, J. H., Ra, Y., et al. (2021). High quality electret based triboelectric nanogenerator for boosted and reliable electrical output performance. *Int. J. Precis. Eng. Manuf. -Green. Tech.* 8 (1), 125–137. doi:10.1007/s40684-020-00245-z

Zhang, Nan, Cheng, Qin, Jun, Li, Yang, Z., Sun, X., Liang, E., et al. (2020). Non-contact cylindrical rotating triboelectric nanogenerator for harvesting kinetic energy from hydraulics. *Nano Res.* 13 (7), 1903–1907. doi:10.1007/s12274-020-2654-7

Zhang, Q., Zhang, Z., Liang, Q., Gao, F., Yi, F., Ma, M., et al. (2019). Green hybrid power system based on triboelectric nanogenerator for wearable/portable electronics. *Nano Energy* 55, 151–163. doi:10.1016/j.nanoen.2018.10.078

Zhang, R., Hummelgård, M., Örtegren, J., Olsen, M., Andersson, H., and Olin, H. (2019). Interaction of the human body with triboelectric nanogenerators. *Nano Energy* 57, 279–292. doi:10.1016/j.nanoen.2018.12.059

Zhao, Hongfa, Xiao, Xiu, Xu, Peng, Zhao, T., Song, L., Pan, X., et al. (2019). Dual-tube helmholtz resonator-based triboelectric nanogenerator for highly efficient harvesting of acoustic energy. *Adv. Energy Mat.* 9 (46), 1902824. doi:10.1002/aenm.201902824

Zheng, Q., Shi, B., Li, Z., and Wang, Z. L. (2017). Recent progress on piezoelectric and triboelectric energy harvesters in biomedical systems. *Adv. Sci. (Weinh).* 4 (7), 1700029. doi:10.1002/advs.201700029

Zheng, Y., Liu, T., Wu, J., Xu, T., Wang, X., Han, X., et al. (2022). Energy conversion analysis of multilayered triboelectric nanogenerators for synergistic rain and solar energy harvesting. *Adv. Mater.* 34, 2202238. doi:10.1002/adma.202202238

Zhou, Y., Deng, W., Xu, J., and Chen, J. (2020). Engineering materials at the nanoscale for triboelectric nanogenerators. *Cell Rep. Phys. Sci.* 1 (8), 100142. doi:10.1016/j.xcrp.2020.100142

frontiers | Frontiers in Energy Research

TYPE Brief Research Report
PUBLISHED 09 January 2023
DOI 10.3389/fenrg.2022.1033099

OPEN ACCESS

EDITED BY
Xun Shen,
Tokyo Institute of Technology, Japan

REVIEWED BY
Haoyun Shi,
Great Wall Motor, China
Kai Zhao,
Zhito Technology Co., Ltd., China

*CORRESPONDENCE
Zhi Zhang,
zhangzhi6881@163.com

SPECIALTY SECTION
This article was submitted to Smart Grids,
a section of the journal
Frontiers in Energy Research

RECEIVED 31 August 2022
ACCEPTED 14 September 2022
PUBLISHED 09 January 2023

CITATION
Zhang Z, Xu G and Yang N (2023), Research on security-constrained unit commitment based on an improved ordinal optimization algorithm.
Front. Energy Res. 10:1033099.
doi: 10.3389/fenrg.2022.1033099

Research on security-constrained unit commitment based on an improved ordinal optimization algorithm

Zhi Zhang[1]*, Guobin Xu[2] and Nan Yang[2]

[1]Tsinghua University, Beijing, China, [2]New Energy Micro-grid Collaborative Innovation Center of Hubei Province, China Three Gorges University, Yichang, China

It is of great significance for the development of intermittent renewable energy and the marketization of electricity to study an efficient and accurate algorithm for solving the unit commitment problem with security constraints. Based on the existing constrained ordinal optimization (COO) algorithm, an improved ordinal optimization (OO) algorithm is proposed, which can be applied to solve SCUC problems. In order to solve the rough model and the accurate model, the discrete variable identification strategy and the effective safety constraint reduction strategy are adopted, respectively. Compared with the traditional object-oriented algorithm, the improved object-oriented algorithm not only gives full play to the computational efficiency of the traditional object-oriented algorithm but also further improves the compactness and reduces the computational redundancy. IEEE 118 simulation results verify the correctness and effectiveness of the algorithm.

KEYWORDS

constrained ordinal optimization, invalid security constraint identification, discrete variable identification, security-constrained unit commitment, wind power

Introduction

Under the background of large-scale wind power integration, SCUC considering the uncertainty of wind power has become not only the main basis for making a day-ahead generation schedule but also an important basis for day-ahead power market decision-making (Shi et al., 2016). On the one hand, SCUC is a large-scale mixed-integer planning problem with constraints and nonlinearity in math (Zhang et al., 2013). On the other hand, it is a typical non-deterministic polynomial hard problem in solving. With the scale of a power grid being increasingly enlarged and more intermittent renewable energy integration, the difficulty of solving SCUC problems has been increasing daily (Yang et al., 2022a). Therefore, how to solve the SCUC problems with the uncertainty of wind power quickly and effectively has become a research focus (Nan et al., 2018).

For solving the uncertain SCUC models, the recent mainstream method is based on Benders decomposition (BD). With the help of BD, the SCUC model can be decomposed

into two subproblems which are unit commitment and network security constraint check. Then, the Lagrangian relaxation method (Zhang et al., 2012), dynamic programming method (Chen et al., 2015), branch and bound method (Hussin and Hassan, 2014), and different kinds of intelligent optimization algorithms (Lee and Lin, 2012; Chen et al., 2021; Li et al., 2021; Ma et al., 2021; Yang et al., 2022b; Yang et al., 2022c; Wang et al., 2022; Zhou et al., 2022; Zhu et al., 2022) can be used to solve each subproblem. The first three methods have a strict mathematical model, but the Lagrangian relaxation method is affected by the sensitivity of the unit to the Lagrangian multiplier, and the oscillation phenomenon is easy to occur in the iterative process of the algorithm. The dynamic programming method is easy to cause a "dimension disaster" problem; if the bound estimation of the branch and bound method is wrong, it is no different from an exhaustive search in extreme cases. The intelligent optimization algorithm is used for uncertain optimization problems with complex constraints, and an iterative calculation is used to deal with constraint subproblems in various scenarios, which requires a lot of calculation time. In short, the solving efficiency has been difficult to meet the needs of engineers (Lee and Lin, 2012).

In recent years, as one of the efficient methods which can solve complicated optimization problems, the theory of OO (Jia, 2006) has attracted more and more attention. In Wu and Shahidehpour (2014), this method was first introduced into the field of solving uncertain SCUC problems. Considering the situation of actual engineering, OO abandons any attempt to find the optimal solutions but seeks for good enough solutions. Compared with traditional BD, this method has successfully increased the solving efficiency by nearly 30 times, which proves the advantages of the OO theory in the field of solving uncertain SCUC problems. From the existing research, OO has been proved that it is a kind of efficient method to solve uncertain SCUC problems. However, the traditional OO theory starts from the solution space, reducing the scale of model feasible regions by constructing several rough models, which makes the redundant information of the model itself to be ignored and eliminated. Therefore, in the aspect of solving efficiency, the OO theory still has much need for improvement and advancement. It is mainly shown in the following paragraph. In this study, an improved adaptive Prony method is proposed to accurately describe the changes in electrical parameters when power system faults occur. The variable step size strategy is used to search the points of the subsegment, and MSRFE is used as the criterion. The simulation results on a given fault signal show that the improved Prony algorithm has higher accuracy and efficiency than the traditional method.

Step 1: although the SCUC model is solved by OO, a rough model should be constructed at first, which could select the feasible solution space of startup/shutdown states. Nonetheless, there are many units in large-scale power systems. If the feasible solution of the startup/shutdown states is selected for all units, the efficiency of the rough model will be greatly affected. For the actual large-scale power grid, the maximum load usually reaches more than 70% of the installed capacity, which means that some units are in a normally open circuit or shutdown state. Thus, there is no need to do state combinations for all units (Gao et al., 2008) if the normally open or stopped units could be first identified in the OO rough model, which will effectively improve the solving efficiency of it.

Step 2: the computational complexity of network security constraint checking and calculation is the largest calculation amount in solving SCUC problems. In Wu and Shahidehpour (2014), the strategy is to check all lines one by one in an accurate OO-based model because the number of nodes and lines which need to be checked will increase rapidly with the expansion of the grid scale. Therefore, the calculation efficiency of OO will be seriously affected by this strategy. In Mogo and Kamwa (2019), the research illustrates that there is only a little part of numerous network security constraints that could restrict the feasible regions. A fast identification method for identifying invalid security constraints is proposed, which successfully reduces the invalid security constraints by more than 85% without affecting the calculation accuracy of the model. Introducing the identification method of invalid security constraints into the COO-based exact model can effectively reduce the redundancy of the exact model and improve the computational efficiency.

In order to solve SCUC problems with wind power fast and effectively, an improved stochastic COO method is proposed in this study. The main contributions of this method are as follows.

A discrete variable identification strategy is proposed and introduced into the rough model, which lays a foundation for constructing a rough model based on COO. This improvement reduces the scale of solution space of a rough model and improves the compactness and solving efficiency of the rough model.

The non-effective security constraint reduction strategy in Wu and Shahidehpour (2014) is introduced into the accurate model, which forms the basis of building the accurate OO-based model for continuous variables. This improvement could greatly reduce the number of security constraints in the OO-based model, which will promote the efficiency of the solution effectively. The correctness and effectiveness of the proposed method can be verified by numerical experiments on an IEEE 118-bus system.

The structure of this study is shown in the following sections. A mathematical model of SCUC is introduced in chapter 2. The improved COO algorithm is shown in chapter 3. The numerical test and simulation results are set in chapter 4. The conclusion is in chapter 5.

Uncertain unit commitment model considering security constraints

In the security-constrained unit commitment problem considering wind power uncertainty, not only the

constraints of system power balance, generator capacity, and network security should be considered but also the risk constraints of positive and negative rotation should be considered. In this study, the opportunity constraint is used to characterize the rotation risk constraint, and the model is established with the objective function of minimizing the total operating cost.

Objective function and conventional constraints

The SCUC problem of the wind power-integrated power system usually includes two parts (Gao et al., 2008): first, considering the uncertainty of the wind power output and second, to ensure the safe and stable operation of the system. In that proposition, the total operation costs should be minimized. The objective function of this model can be abstracted as follows:

$$\min F_{Gt} = \sum_{t=1}^{24}\sum_{i=1}^{M}[U_{Git}Y_{it}(P_{Git}) + U_{Git}(1-U_{Git-1})S_{Git}], \quad (1)$$

where F_{Gt} is the total operation cost. P_{Git}, t is time and i is the number of units. U_{Git} are the active power output and startup/shutdown status. $Y_{it}(P_{Git})$ is the operation cost of unit, and $S_{it}(\tau_i)$ is the startup/shutdown cost of the unit.

The operation cost of the unit and startup/shutdown cost of the unit can be represented as follows:

$$Y_{it}(P_{Git}) = \alpha_i + \beta_i P_{Git} + \gamma_i P_{Git}^2, \quad (2)$$

$$S_{it}(\tau_i) = S_{0i} + S_{1i}\left(1 - e^{\tau_i/\omega_i}\right), \quad (3)$$

where α_i,β_i,$\gamma_i$are the operation cost parameters of units and ω_i is the parameter of the startup/shutdown cost.

The constraint condition of decision variables in an SCUC model is the key to ensure the safe and reliable operation of the system.

i) The system power balance constraint is defined as follows:

$$\sum_{i=1}^{M} U_{Git}P_{Git} + P_{Wt} = P_{Lt} + P_{Dt}, \quad (4)$$

where P_{Dt} is the active load of the system at time t. P_{Lt} is the network active power loss at time t. P_{Wt} is the active output power of the wind turbine at time t.

ii) The capacity constraints of generators can be expressed as follows:

$$P_{Gi\min} \le P_{Git} \le P_{Gi\max}, \quad (5)$$

where P_{Gimin} and P_{Gimax} are the upper limit and lower limit of active power generation of unit i at time interval t, respectively.

iii) Minimum up and down time constraints are defined as follows:

$$\sum_{t=1}^{24}|U_{Git} - U_{Git-1}| \le n_i, \quad (6)$$

where ni is the maximum startup/shutdown times of unit i in a scheduling cycle.

iv) Minimum startup/shutdown time constraints are as follows:

$$(U_{Git-1} - U_{Git})\left(X_{Git}^{on} - T_{Git}^{on}\right) \ge 0, \quad (7)$$

$$(U_{Git} - U_{Git-1})\left(X_{Git}^{off} - T_{Git}^{off}\right) \ge 0, \quad (8)$$

where X_{Git}^{on} and X_{Git}^{off} are the startup and shutdown time of unit i at time interval t, respectively. T_{Git}^{on} and T_{Git}^{off} are the minimum startup/shutdown time available.

v) Ramping up and down constraints are as follows:

$$-\Delta P_{Gi}^{down} \le P_{Gi} - P_{Git-1} \le \Delta P_{Gi}^{up}, \quad (9)$$

where ΔP_{Gi}^{up} and ΔP_{Gi}^{down} are the maximum ramping up/down limits of unit i in an hour, respectively.

vi) Network security constraints are defined as follows:

$$A \cdot P_t \le B_t, \quad (10)$$

among which

$$A = \begin{pmatrix} T \times K_p \\ -T \times K_p \end{pmatrix}, \quad (11)$$

$$B_t = \begin{pmatrix} P_{L\max} + T \times K_D \times D_t \\ P_{L\max} - T \times K_D \times D_t \end{pmatrix}, \quad (12)$$

where P_t is the unit active output power matrix at time t. T is the shift factor matrix. K_p is the node-generator correlation matrix. K_D is the bus-load correlation matrix, and D_t is the load matrix at time t. P_{Lmax} is the transmission capacity of the line L.

Risk constraints of positive and negative rotation

The chance-constrained method (Wang et al., 2012) is adopted to appropriately add the uncertainty factors caused by wind power to the SCUC model in this study.

Considering the random UC of wind power, if the deterministic method is used to obtain the spinning reserve, the influence of wind power uncertainty on the system cannot be measured accurately (Wu et al., 2016; Roald et al., 2017). Therefore, based on the opportunity constraint theory, an index reflecting the system operation risk is constructed. The deterministic constraint of a traditional rotating reserve is transformed into the uncertainty constraint, considering the

operation risk, and the UC model, considering the uncertainty of wind power generation, is constructed.

System positive and negative rotation reserve risk indicators should be established as follows.

$$Q_{dt} = q\left\{P_{Wt}\middle|P_{Wt} < \bar{P}_{Wt}\&R_{Gp} < \bar{P}_{Wt} - P_{Wt} + R_{Lp}\right\}, \quad (13)$$

$$Q_{ut} = q\{P_{Wt}|P_{Wt} > \bar{P}_{Wt}\&R_{Gn} < P_{Wt} - \bar{P}_{Wt} + R_{Ln}\}, \quad (14)$$

where Q_{dt} and Q_{ut} are the probability of positive and negative rotation reserve of the system at time t. q(PW) is the probability density function of wind power. $\bar{P}_{Wt}$ is the average wind power output at time t. R_{Gp} and R_{Gn} are provided by the positive and negative rotation standby systems, respectively. R_{Lp} and R_{Ln} are positive and negative spinning reserve demands for conventional units, respectively.

Using the chance constraint theory in an uncertain environment, the rotation reserve of wind power integration is changed from the deterministic inequality constraint to the uncertain inequality constraint. It is necessary to ensure that the probability of shortage of the positive and negative spinning reserve capacity is less than a certain risk threshold. Therefore, (13) and (14) can be transformed as follows:

$$Q_{dt}\left(R_{Gp}\right) = \int_{-\infty}^{P_{Wt}+R_{Lp}-R_{Gp}} q\left(P_{Wt}\right)dP_{Wt} \le \lambda, \quad (15)$$

$$Q_{u}\left(R_{Gn}\right) = \int_{\bar{P}_{W}+R_{Gn}-R_{Ln}}^{+\infty} q\left(P_{W}\right)dP_{W} \le \lambda. \quad (16)$$

This study assumes that the probability of the short-term wind speed follows normal distribution (Bian et al., 2018). The derivation processes of relations (13–16) and the introduction of the wind power uncertainty in the model are described in Appendix. The effectiveness of using the chance-constrained method to describe the uncertainty of wind power generation in a power dispatching problem has been used for Yang et al. (2013).

SCUC model solved by an improved COO algorithm

Ordered optimization (OO) is compared with the traditional optimization method; the OO method is not to find the global optimal solution but to find the "good enough" solution to meet the project requirements. The process called target softening (Ho et al., 1992) has good efficiency and compatibility and can be combined with other optimization methods.

Since the SCUC model is a mixed-integer programming problem with relatively independent decision variables, a rough model and accurate model are, respectively, constructed for the discrete decision variable U_{Git} and continuous decision variable P_{Git}, which can be decoupled during the ordinal comparison process.

The general framework of the improved COO algorithm

The improvement is based on the existing COO algorithm, which is as follows.

i) By adding discrete variable identification to the rough model, the normally open/normally closed elements in the discrete space can be identified. Then, the remaining elements are filtered by the rough model to reduce the calculation dimension of the rough model and improve the efficiency of the rough model.

ii) Adding non-effective security constraints to the accurate model can reduce the network security constraints in the accurate model and eliminate the invalid security constraints. It can reduce the number of network security constraints that need to be identified, thus reducing the complexity of solving.

The following three steps of implementing the algorithm are as follows.

Step 1: a rough model is established, and N feasible solutions are preselected from the unit startup/shutdown solution space according to the normal distribution. The number of these N feasible solutions is closely related to the size of the solution space and constitutes a feature set Ω. When the size of the solution space is less than 108, N is usually set to 1000.

Step 2: s solutions from Ω are selected, and specific rules are used to form a set s that contains at least k solutions good enough with a probability of α%. Blind selection (BP) (Lau and Ho, 1997) is used to determine the selected collection s. Its mathematical model is as follows.

$$P\left(|G \cap S| \ge k\right) = \sum_{j=k}^{\min\left(g,s\right)} \sum_{i=0}^{s-j} \frac{C_g^j C_{N-g}^{s-i-j}}{C_N^{s-i}} C_s^i q^{s-i}\left(1-q\right)^i \ge \eta, \quad (17)$$

where $P(\cdot)$ is the alignment probability. g is the size of feasible solutions in set G. s is the number of solutions in the selected set S. k represents the alignment level that is measured by counting how many good enough solutions exist in the set S. η is the probability criteria, representing that it contains at least k good enough solutions in the selected set S. η is usually set as 0.95. q is the probability that an observed feasible decision is truly feasible.

Step 3:an accurate model is created to obtain the continuous P_{Git} variable. Minimizing the total cost of ownership with performance constraints considered is the goal of the model. Then, according to the state of each unit, the operation cost and output of each unit are calculated according to the selected quantity s. Finally, the solutions of the selected set are sorted to obtain the optimal solution.

The construction of the rough models

Discrete variable identification model

The feasible region space is reduced by using the rough model to perform prescreening; this may reduce the

computational complexity of an accurate model. Considering the time scale of the late dispatch being short, in this period, there are always some units that are normally open/stopped, owing to the impact of the load level and the scale of the install generations. Therefore, if the normally open/stopped units can be identified before prescreening the rough model, the scale of the SCUC solution space can be efficiently reduced so that it may increase the calculation efficiency.

A quadratic optimization model for identifying normally open/stopped units is first constructed in this study. Assuming the units of the system are all open in the model and then considering the main constraints which are related to the output of generators, the minimum operating cost is considered as the optimization objective; the mathematical model is shown as follows:

$$\begin{cases} \sum_{i=1}^{M} Y_{it}\left(P_{Git}\right) \\ \min F_{Gt} = \sum_{t=1}^{24} s.t. \sum_{i=1}^{M} P_{Git} + P_{Wt} = P_{Dt} + R \\ A \cdot P_t \le B_t \\ 0 \le P_{Git} \le P_{Gi\max} \\ -\Delta P_{Gi}^{down} \le P_{Git} - P_{Git-1} \le \Delta P_{Gi}^{up}. \end{cases} \tag{18}$$

According to the solution result of the model, for all time period t = 1, 2, 3,...., T. If P_{Git} satisfies $P_{Git} > P_{Gi\min}$, the unit i is a normally open unit. If P_{Git} satisfies $P_{Git} < \delta P_{Gi\min}$, the unit i is a normally stopped unit, and δ is the identification parameter which is set at 0.05.

The normally open/stop generators can be effectively identified by the model, and the main reason is as follows.

The power generation rights, equal opportunity, and free competition ideas are integrated into the design of the model, which may give all units the opportunity of opening. Then, the operation cost is used as the target to perform optimal calculation. If the unit output power in the whole scheduling period is in the low level, which means the units cannot obtain the share of electricity by competition in the previous load level. Therefore, they can be treated as normally stopped units. On the contrary, if the unit output is higher than the minimum output in the entire scheduling period, it can be considered that the units can always get more power in the competition. Thus, they can be considered as normally open units.

Although the optimization model with constraints belonging to the quadratic optimization model and the solution is complex, it only needs to be solved once. It is very effective in reducing the dimensions of the solution space. Overall, adding that model into the rough COO model can improve the overall computational efficiency.

The construction of a COO-based rough model

In order to realize the decoupling process of discrete and continuous variables in solution, according to the startup/shutdown state of the constraints, the rough model is built and the solution space of unit commitment is screened out. These are power balance constraints, ramping up constraints, and minimum up and down constraints. The mathematical description is as follows.

$$\begin{cases} \sum_{i=1}^{M} U_{Git} P_{Gi\max} + P_{Wt} \ge P_{Dt} + R_{Dp}, \\ \sum_{i=1}^{M} U_{Git} P_{Gi\min} + P_{Wt} \le P_{Dt} - R_{Dn}, \\ \sum_{i=1}^{M} \left[U_{Git}\Delta P_{Gi}^{up} + P_{Gi\min}\left(U_{Git} - U_{Git-1}\right)\right] \ge \left|P_{Dt} - P_{Dt-1}\right|, \\ \sum_{i=1}^{M} \left[U_{Git}\Delta P_{Gi}^{down} + P_{Gi\min}\left(U_{Git} - U_{Git-1}\right)\right] \ge \left|P_{Dt} - P_{Dt-1}\right|, \\ \sum_{t=1}^{24} \left|U_{Git} - U_{Git-1}\right| \le N_i. \end{cases} \tag{19}$$

The parameters in the aforementioned formula are mentioned previously and will not be repeated here.

The solution of the rough model

The solving ideas of this study used a discrete variable to identify the normally open/stopped units and to optimize those in the model. After that, the COO-based rough model is used to perform the prescreening for optimizing units, which may form the solution space. The pseudo-code is shown as follows.

The discrete variable identification model is constructed and solved; t=1; s=1; i=1; while $i \le M$do:

if $t \in [1, 24]$, $P_{Git} > P_{G\min}$; then, optimization normally open units;

else if $t \in [1, 24]$, $P_{Git} < \delta P_{G\min}$; then, optimization normally stopped units;

else add to the set of units that are not optimized, i=i+1;

end if

while $s \le N$do:

Randomly generating one-time unit startup/shutdown plan that the constraint is not optimized. Formula (19) is the constraint, and the branch and bound method is used to solve the unit startup/shutdown state matrix of the following time;

s=s+1

end if

End algorithm

The construction of an accurate model

Non-effective security constraint reduction

A modern power system has a large scale and many nodes. Therefore, the solution of a power flow equation and checking of network security constraints are the two most time-consuming steps in solving SCUC problems. However, research shows that only a small part of network constraints is effective and can limit the formation of feasible regions (Gao et al., 2008). Therefore, if ineffective constraints can be identified quickly, the model will

greatly enhance the compactness and reduce the difficulty of solving.

In this study, the definition of non-effective security constraints is that if a constraint is removed, the feasible region of the model is the same as the previous one. The constraint is a non-effective constraint. According to the definition, the necessary and sufficient conditions for the identification of non-effective security constraints, which are the non-effective constraint and feasible regions, do not have any intersection or the intersection is just a vertex of the simple form. According to the sufficient and necessary conditions mentioned previously, constructing the feasible region optimization model after cutting security constraint condition $A^{\{j\}}(P_{G1t}, P_{G2t}, \cdots P_{GMt})^T \le B_t^{\{j\}}$ is shown as follows.

Using Eq. 20, it can identify the non-effective security constraints precisely. Due to the requirement of solving a constrained optimization model, the calculation is much more complex. Therefore, the constraints of Eq. 20 can be relaxed to construct a sufficient rather than a necessary condition for identifying ineffective security constraints.

$$\begin{cases} Z_2 = \max \sum_{i=1}^{M} a_{ji} P_{Git}, \\ s.t. 0 \le P_{Git} \le P_{Gi\max}, \\ \sum_{i=1}^{M} P_{Git} + P_{Wt} = P_{Dt} + R. \end{cases} \tag{20}$$

Due to the fact that $Z_1 \le Z_2$, it can be considered that when $Z_2 \le B_{j,t}$, the constraint $A^{-\{j\}}(P_{G1t}, P_{G2t}, \cdots P_{GMt})^T \le B_t^{-\{j\}}$ is a non-effective one. In order to carry out further simplification of the calculation, formula (20) is solved analytically. Thus, the abandoned solution model can be proposed; the sufficient but not necessary condition used the known parameters to identify the non-effective constraints, which are shown as follows.

$$\begin{cases} \sum_{i=1}^{k-1} \bar{P}_i \le D_t - P_{w,t} \le \sum_{i=1}^{k} \bar{P}_i, \\ \sum_{m=1}^{k-1} \left(a_{j,i_m} - a_{j,i_k}\right) \bar{P}_{i_m} + a_{j,i_k}(P_{Dt} - P_{Wt}) \le B_{j,t}. \end{cases} \tag{21}$$

Accurate model construction

A model based on exact COO can accurately sort the solutions in the selected set while ensuring that all solutions satisfy the model constraints. Identifying and reducing invalid security constraints is the foundation. An accurate COO-based model is constructed based on the objective function of the SCUC model and the constraints associated with continuous variables P_{Git}, which is shown as follows:

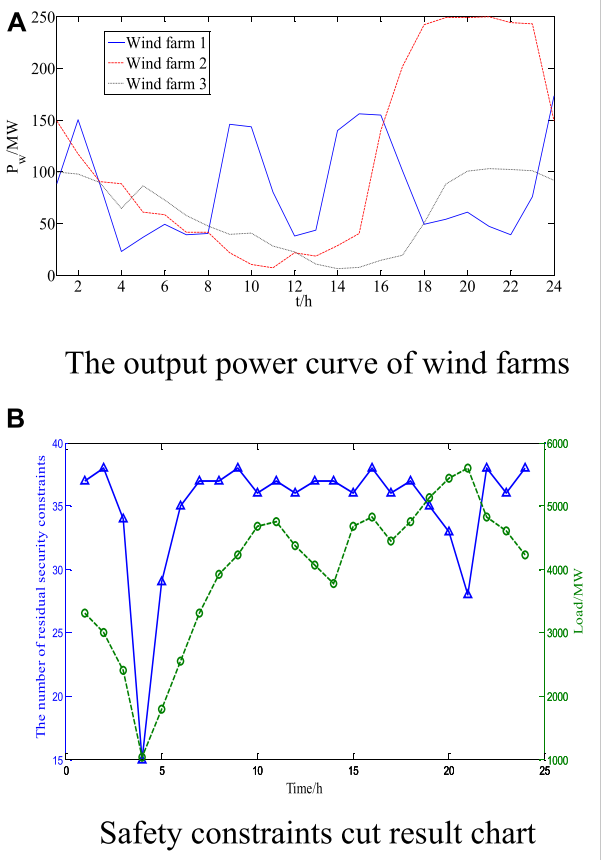

FIGURE 1
(A) The output power curve of wind farms and **(B)** Safety constraints cut result chart.

$$\begin{cases} \min F_{Gt} = \sum_{t=1}^{24} \sum_{i=1}^{M} Y_{it}(P_{Git}) \\ s.t, \\ A \cdot P_t \le B_t, \\ P_{Gi\min} \le P_{Git} \le P_{Gi\max}, \\ \sum_{i=1}^{M} U_{Git} P_{Git} + P_{Wt} = P_{Dt}. \end{cases} \tag{22}$$

The parameters in the aforementioned formula are mentioned previously and will not be repeated here.

Numerical simulation

The numerical tests were conducted on a modified IEEE 118-bus system consisting of 54 thermal generators, 91 demand sides, and three wind farms. Wind farms with a rated power of 100 MW, 200 MW, and 250 MW are located at buses 144, 54, and 95, respectively, and their active power curves are shown in Figure 1A. The positive rotating standby of traditional units accounts for 8% of the maximum load of the system, the negative

TABLE 1A Spinning reserve of each wind farm (MW).

Reserve	Wind farm 1	Wind farm 2	Wind farm 3	Spinning reserve for the system	Total reserve
Positive spinning reserve	10	19	24	480	533
Negative spinning reserve	10	19	24	44	97

TABLE 1B Result of discrete variable identification.

	Unit number	
	Discrete variable identification model	BD
Normally open units	11, 27, and 39	4, 5, 10, 11, 20, 27, 29, 35, 36, 39, 40, 43, and 45
Normally stopped units	1, 2, 3, 6, 8, 9, 13, 15, 17, 18, 31, and 32 33, 38, 41, 42, 46, 49, 50, and 52	1–3, 6–9, 12–19, 22–24, and 26 31–33, 38, 41, 42, 44, and 46–52

rotating standby accounts for 2% of the minimum load of the system, and the risk index of the rotating standby is 0.01. The network structure, generator parameters, and loads can be obtained with reference to Chen et al. (2015). The numerical test is realized on the computer by MATLAB 8.0 and the optimizer CPLEX 12.5. First, the rough model is established by MATLAB programming and then solved by CPLEX. The MATPOWER toolbox is used to solve nonlinear programming problems in exact models.

The opportunity-constrained method is used to obtain the system rotational standby. The wind farm is shown in Table 1A. In order to verify the validity of a discrete identification model, it is used to identify unit commitment states, and the results are compared with the final results that are based on traditional BD. The results are shown in Table 1B.

By comparing the results, in 20 normally open units, the discrete variable identification model has identified three; the recognition rate is 15%. However, in the 31 normally stopped units, the model identifies 20; the identification rate is 64.5%. There are no identification errors that occurred during the whole recognition process.

The comparison shows that the discrete variable recognition model proposed in this study not only has the high rate of identifying normally stopped units but also has high recognition accuracy. When it is incorporated into the COO-based rough model, the computational dimension of the rough model can be reduced, and the solving efficiency can be improved.

In order to verify the validity of the proposed security constraint reduction strategies, formula (22) is used to cut the non-effective security constraints. The remaining security constraints after cutting are shown in Figure 1B.

Figure 1B shows that the IEEE 118 system in each period has 372 security constraints, so there are 8928 security constraints in 24 h. Through the non-effective security constrained cut model, there are 8090 non-effective security constraints that have been cut in a total of 24 h. The cutting proportion reached above 90%. The aforementioned results show that there is a large amount of redundant information in the security constraints of the existing SCUC model, and the non-effective security constraint reduction strategy can effectively eliminate them.

From each time interval, the number of remaining security constraints is between 15 and 38. The trend of variation is related to the load change. The reason is that when the load is heavy, the safety margin of the whole system will drop. Thus, there are more lines that need to be checked, which may produce much more effective security constraints. On the contrary, if the load is light, the number of effective security constraints will reduce.

To verify the validity of the ineffective security constraints introduced in the COO-based accurate model, each start/close scenario for the selected set S is solved using the improved COO-based accurate model and the traditional COO-based model. The operating time is shown in Table 2B. It is necessary to point out that the simulation is carried out on the basis of the improved COO-based rough model proposed in this study.

TABLE 2A Rough model performance.

	Time of identifying model(s)	Total time(s)
Before improvement	—	153.18
After improvement	2.89	113.33

TABLE 2B Accurate model performance.

	Time of identifying model(s)	Total time(s)
Before improvement	—	203.89
After improvement	0.09	161.46

TABLE 3A Start–stop scheme.

Total cost = 1,461,876.48$

Unit	Time (1–24 h)
10	111111111111111111111110
14	000000000000000111111111
16	111111111111111111111000
19	111111111111111111111000
21	111111111111111111111000
23	111111111111111111111000
25	111111111111111111111100
47	000000001111111111111111
1–3, 6, 8, 9, 13, 15, and 17 18, 22, 24, 26, 31–33, 36, 38, and 39 41, 42, 46, 49, and 50–52	000000000000000000000000
4, 5, 7, 11, 12, 20, 27–30, and 34–35 37, 40, 43–45, 48, and 53–54	111111111111111111111111

It is necessary to point out that the simulation is carried out on the basis of the improved COO-based rough model proposed in Table 2A, which shows that the time to solve the rough model is increased by 40 s after the discrete variable identification strategy is added to the COO-based rough model. Although the discrete variable recognition model requires 2.89 s, the whole dimension of the rough model is decreased. Therefore, as a result, the solving efficiency of the improved COO-based rough model has been improved.

Table 2B also shows the non-effective security constraint reduction strategy in this study can effectively identify non-effective security constraints. The whole calculation process takes only 0.09 s, and the total time is reduced by nearly 42.43 s. It can be seen that incorporating an ineffective security constraint reduction strategy into an accurate COO-based model can effectively improve the computational efficiency.

The correctness and validity of the whole algorithm

In this study, the improved COO algorithm is used to solve the SCUC model to verify the correctness and effectiveness of the proposed method. The cost of the optimal solution and the start–stop state of the conventional unit are shown in Table 3A.

TABLE 3B Performance tables of each algorithm.

	CPU running time(s)	Total fee($)
Method 1	338.64	1,460,620.21
Method 2	2857.00	1,467,256.55
This study	274.79	1,461,876.48

To compare the validity and correctness of the proposed methods, we use the following two methods to solve SCUC problems.

Method 1 is a sequential optimization algorithm of a document (Lee and Lin, 2012).

Method 2 is a mixed-integer programming based on BD.

The calculation results and computation time of the three methods are shown in Table 3B.

As shown in Table 3B, compared with the Benders decomposition method, the COO method has obvious advantages both in calculating the efficiency and accuracy. Compared with the method in Wu and Shahidehpour (2014), the improved COO algorithm reduces the total cost by about 0.45% but increases the computational efficiency by nearly 18.85%.

There are some reasons for the solving efficiency of the improved COO algorithms being increased. The COO-based rough model uses a discrete variable identification strategy, which reduces the dimension of the solution. An ineffective security constraint reduction strategy is introduced in the exact model based on collaborative work, eliminating the ineffective security constraints in the exact model. The aforementioned improvements improve the compactness of the algorithm and further improve the efficiency of the algorithm.

Summary

In order to reach the goal of solving the uncertain SCUC problems with wind power fast and effectively. Based on the traditional COO theory, this model introduces discrete variable identification and ineffective security constraint reduction strategies. This study proposes an improved stochastic COO method. The simulation results based on standard examples show some advantages of this method.

i) Although solving the discrete variable identification model needs some time, it can reduce the dimension of rough model's solution space. Therefore, as a result, introducing the discrete variable identification strategy can improve the calculation efficiency of the COO-based rough model.

ii) The invalid security constraint reduction strategy can identify more than 90% of invalid security constraints in the short term. Introducing it into the precise model based on COO can effectively reduce the computational redundancy and improve the computational efficiency.

iii) The improvement strategy in this study has improved the compactness of the COO algorithm. Compared with the traditional COO algorithm, the improved random COO algorithm improves the solving efficiency greatly. At the same time, compared with other methods, it has obvious advantages both in accuracy and efficiency.

A discrete variable recognition strategy is proposed and incorporated into the rough model, which is the foundation of building a COO-based rough model. This improvement reduces the scale of solution space of the rough model, which could promote the compactness of the rough model and the efficiency of the solution. The non-effective security constraint reduction strategy [12] is introduced into the accurate model, which is the base of building the accurate OO-based model for continuous variables. This improvement could greatly reduce the number of security constraints in the OO-based model, which will promote the efficiency of the solution effectively. The correctness and effectiveness of the proposed method in this study can be tested from the numerical test on the IEEE 118-bus system.

Data availability statement

The original contributions presented in the study are included in the article/Supplementary Material; further inquiries can be directed to the corresponding author.

Author contributions

ZZ put forward the main research points; GX completed manuscript writing , revision and simulation research; NY collected relevant background information and revised grammar and expression. All authors contributed to manuscript revision, read, and approved the submitted version.

Conflict of interest

The authors declare that the research was conducted in the absence of any commercial or financial relationships that could be construed as a potential conflict of interest.

Publisher's note

All claims expressed in this article are solely those of the authors and do not necessarily represent those of their affiliated organizations, or those of the publisher, the editors, and the reviewers. Any product that may be evaluated in this article, or claim that may be made by its manufacturer, is not guaranteed or endorsed by the publisher.

References

Bian, Q. Y., Qiu, Y. T., Wu, W. L., Xin, H. H., and Fu, X. H. (2018). Generation dispatch method based on maximum entropy principle for power systems with high penetration of wind power. *J. Mod. Power Syst. Clean. Energy* 6 (6), 1213–1222. doi:10.1007/s40565-018-0419-z

Chen, Z., Wu, L., and Shahidehpour, M. (2015). Effective load carrying capability evaluation of renewable energy via stochastic long-term hourly based SCUC. *IEEE Trans. Sustain. Energy* 6 (1), 188–197. doi:10.1109/tste.2014.2362291

Chen, J. J., Qi, B. X., Rong, Z. K., Peng, K., Zhao, Y., and Zhang, X. (2021). Multi-energy coordinated microgrid scheduling with integrated demand response for flexibility improvement. *Energy* 217, 119387. doi:10.1016/j.energy.2020.119387

Gao, Z., Gen, J., and Zhang, X. (2008). Monthly unit commitment and security assessment algorithm for large-scale power system[J]. *Automation Electr. Power Syst.* 32 (23), 28–30. doi:10.3321/j.issn:1000-1026.2008.23.007

Ho, Y., and Michael, E. (1995). Ordinal optimization approach to rare event probability problems. *Discrete Event Dyn. Syst.* 5 (2-3), 281–301. doi:10.1007/bf01439043

Ho, Y. C., Serenivas, R. S., and Vkaili, P. (1992). Ordinal optimization of DEDS. *Discret. Event Dyn. Syst.* 2 (2), 61–88. doi:10.1007/bf01797280

Hussin, S. M., and Hassan, M. Y. (2014). "Coordination of short-term maintenance scheduling with hourly security-constrained unit commitment[C]," in Proceedings of the 2014 IEEE 8th International Power Engineering and Optimization Conference (PEOCO), MALAYSIA, 73–78.

Jia, Q. (2006). *Enhanced ordinal OPtimization: A theoretical study and applications [D]*. Beijing: Tsinghua University.

Lau, T. W. E., and Ho, Y. C. (1997). Universal alignment probabilities and subset selection for ordinal optimization. *J. Optim. Theory Appl.* 93 (3), 455–489. doi:10.1023/a:1022614327007

Lee, G., and Lin, G. (2012). Unit commitment with security assessment using chaotic pso algorithm[J]. *J. Circuits Syst. Comput.* 20 (7), 1357–1376.

Li, Z., Yu, C., Abu-Siada, A., Li, Z., and Zhang, T. (2021). An online correction system for electronic voltage transformers. *Int. J. Electr. Power & Energy Syst.* 126, 106611. doi:10.1016/j.ijepes.2020.106611

Ma, H., Zheng, K., Jiang, H., and Yin, H. (2021). A family of dual-boost bridgeless five-level rectifiers with common-core inductors. *IEEE Trans. Power Electron.* 36 (11), 12565–12578. doi:10.1109/tpel.2021.3078533

Mogo, J. B., and Kamwa, I. (2019). Improved deterministic reserve allocation method for multi-area unit scheduling and dispatch under wind uncertainty. *J. Mod. Power Syst. Clean. Energy* 7 (5), 1142–1154. doi:10.1007/s40565-019-0499-4

Nan, Y., Di, Y., Zhou, Z., Jiazhan, C., Daojun, C., and Xiaoming, W. (2018). Research on modelling and solution of stochastic SCUC under AC power flow constraints. *IET Gener. Transm. &amp. Distrib.* 12 (15), 3618–3625. doi:10.1049/iet-gtd.2017.1845

Roald, L., Misra, S., Krause, T., et al. (2017). Corrective control to handle forecast uncertainty: A chance constrained optimal power flow[J]. *IEEE Trans. Power Syst.* 32 (2), 1626–1637.

Shi, T., Gao, S., and Zhang, N. (2016). Two-stage stochastic model of unit commitment with wind farm and an improved algorithm [J]. *Trans. China Electrotech. Soc.* 31 (16), 172–180.

Wang, Q., Guan, Y., and Wang, J. (2012). A chance-constrained two-stage stochastic program for unit commitment with uncertain wind power output. *IEEE Trans. Power Syst.* 27 (1), 206–215. doi:10.1109/tpwrs.2011.2159522

Wang, C., Chu, S., Ying, Y., Wang, A., Chen, R., Xu, H., et al. (2022). Underfrequency load shedding scheme for islanded microgrids considering objective and subjective weight of loads. *IEEE Trans. Smart Grid*, 1. doi:10.1109/TSG.2022.3203172

Wu, H., and Shahidehpour, M. (2014). Stochastic SCUC solution with variable wind energy using constrained ordinal optimization. *IEEE Trans. Sustain. Energy* 5 (2), 379–388. doi:10.1109/tste.2013.2289853

Wu, Z., Zeng, P., Zhang, X. P., and Zhou, Q. (2016). A solution to the chance-constrained two-stage stochastic program for unit commitment with wind energy integration. *IEEE Trans. Power Syst.* 31 (6), 4185–4196. doi:10.1109/tpwrs.2015.2513395

Yang, N., Wang, B., and Liu, D. (2013). Large-scale wind power stochastic optimization scheduling method considering flexible load peaking[J]. *Trans. China Electrotech. Soc.* 28 (11), 231–238.

Yang, N., Yang, C., Wu, L., Shen, X., Jia, J., Li, Z., et al. (2022). Intelligent data-driven decision-making method for dynamic multisequence: An E-Seq2Seq-based SCUC expert system. *IEEE Trans. Ind. Inf.* 18 (5), 3126–3137. doi:10.1109/tii.2021.3107406

Yang, N., Dong, Z., Wu, L., Zhang, L., Shen, X., Chen, D., et al. (2022). A comprehensive review of security-constrained unit commitment. *J. Mod. Power Syst. Clean Energy* 10 (3), 562–576. doi:10.35833/mpce.2021.000255

Yang, N., Yang, C., Xing, C., Ye, D., Jia, J., Chen, D., et al. (2022). Deep learning-based SCUC decision-making: An intelligent data-driven approach with self-learning capabilities. *IET Generation Trans. Dist.* 16 (4), 629–640. doi:10.1049/gtd2.12315

Zhang, N., Gao, S., and Zhao, X. (2012). A fast Lagrangian relaxation method for unit commitment[J]. *Power Syst. Prot. Control* 40 (19), 47–53.

Zhang, N., Gao, S., and Zhao, X. (2013). An unit commitment model and algorithm with randomness of wind power[J]. *Trans. China Electrotech. Soc.* 28 (05), 22–29.

Zhou, Y., Zhai, Q., and Wu, L. (2022). Optimal operation of regional microgrids with renewable and energy storage: solution robustness and nonanticipativity against uncertainties. *IEEE Trans. Smart Grid*, 1. doi:10.1109/TSG.2022.3185231

Zhu, B., Wang, H., Zhang, Y., and Chen, S. (2022). Buck-based active-clamp circuit for current-fed isolated DC–DC converters. *IEEE Trans. Power Electron.* 37 (4), 4337–4345. doi:10.1109/tpel.2021.3121704

frontiers | Frontiers in Energy Research

TYPE Brief Research Report
PUBLISHED 11 January 2023
DOI 10.3389/fenrg.2022.989221

OPEN ACCESS

EDITED BY
Yusen He,
The University of Iowa, United States

REVIEWED BY
Haoyun Shi,
Great Wall Motor, China
Yahui Zhang,
Sophia University, Japan

*CORRESPONDENCE
Jizheng Xue,
xuchaobb1985@163.com

SPECIALTY SECTION
This article was submitted to Smart Grids, a section of the journal Frontiers in Energy Research

RECEIVED 08 July 2022
ACCEPTED 19 August 2022
PUBLISHED 11 January 2023

CITATION
Xue J, Xu Y and Yang Y (2023), Power enterprises-oriented carbon footprint verification system using edge computing and blockchain.
Front. Energy Res. 10:989221.
doi: 10.3389/fenrg.2022.989221

Power enterprises-oriented carbon footprint verification system using edge computing and blockchain

Jizheng Xue[1]*, YouRui Xu[2] and Yun Yang[3]

[1]Tellhow Software Co. Ltd, Xi'an, China, [2]State Grid Qinghai Electric Power Company Haixi Power Supply Company, Qinghai, China, [3]Tellhow Software Co. Ltd, Shanghai, China

The purpose is to study the Carbon Footprint (CF) verification system of power enterprises, promote the Low-Carbon Economy (LCE) in the power industry, and improve resource utilization during Energy Conservation and Emission Reduction (ECER). The Carbon Dioxide Emission (CDE) of power enterprises is explored based on the CF. First, Edge Computing (EC) is adopted to calculate the direct Carbon Dioxide Emission (CDE) of the Chinese power industry from 2005 to 2020 based on energy input. The direct CDE and the changing trend are analyzed. On this basis, Blockchain Technology (BCT) is employed to quantify the indirect CDEs of power enterprises' energy consumption. A comprehensive analysis is made of the changing trend and circulation of the total CF of power enterprises based on the direct and indirect CDEs. The data show that the proportion of direct and indirect CDEs in total CF gradually decreases and increases. The results show that the power industry should increase the proportion of clean power in the power industry, control the CDEs from the source, and improve energy utilization to optimize the CF verification.

KEYWORDS

edge computing, blockchain, power enterprises, carbon footprint, carbon footprint verification

1 Introduction

China's energy demand has been increasing with the rapid economic development in recent years. Many have realized that China's dependence on crude oil has exceeded the international warning line. It is now urgent for China to focus on the efficient use of energy, reduce energy consumption, reduce air pollution, and achieve Energy Conservation and Emission Reduction (ECER). Especially since the Reform and opening-up, China's economy has seen decades of economic boom. However, the cost of resource consumption and environmental destruction is overwhelming. The uncontrolled development and utilization of resources have led to the deterioration of the environment and seriously affected China's sustainable development (Sonmez et al., 2018). Therefore, the emergence of ECER technology-driven Low-Carbon Economy (LCE) offers a possible development path, targeting greenhouse gas emission reduction. LCE has changed people's lifestyles and brought structural transformation. It is reshaping

the development concepts and becoming a new direction for China's economic development. Because of the current situation of China's economic development, there is a need to take corresponding measures to promote LCE's rapid development vigorously.

In 2007, the term Carbon Footprint (CF) was proposed as one of the key quantitative parameters in the ECER process. CF measures the greenhouse gas emissions in production and consumption, including direct and indirect emissions. Indirect carbon emissions are greenhouse gas emissions from using purchased power or heat. CF is generally divided into personal, product, enterprise, and national urban CF. Of these, personal CF estimates carbon emissions in daily life. The enterprise CF is the sum of the carbon emissions generated by the overall enterprise activities. It includes the carbon emissions from non-production activities to the product CF. The urban CF mainly includes the various greenhouse gas emissions. At present, the exploration of CF in China has just begun without any in-depth achievements, and more industrial practices are urgently needed to promote CF development (Premsankar et al., 2018). The lagging and high regional power grid emission factors will make the carbon emission results of non-emission control enterprises distorted and large. There are potential disadvantages that damage the competitiveness of enterprises. China's accounting guidelines specify that the regional power grid emission factors published in the latest year should be used to account for indirect electric power emissions. The accounting guidelines are also applicable to non-emission-controlled enterprises. However, the regional power grid emission factors have not been updated. Thus, it is understood that the national, provincial, and pilot carbon-market emission factors are often used for non-emission-controlled enterprises. Adopting the grid emission factor more in line with the actual situation as a supplementary means can play certain positive roles. Nevertheless, doing so will lead to poor comparability of accounting results and great reference difficulty. Hence, it is not conducive to the benchmarking evaluation and decision-making of enterprises, the public, and investors (Wiche et al., 2022). According to the research review in China and overseas, the current indirect Carbon Dioxide Emission (CDE) calculation methods mainly include the input-output method, life cycle method, and Intergovernmental -Panel on Climate Change (IPCC) method (Osorio et al., 2022). Firstly, the input-output method is based on the division of different departments. It cannot reflect the differences in CFs of different products within the department. This leads to a large deviation in the results. At the same time, the CF of specific industries or departments obtained by the input-output method cannot be applied to calculating other products, with a limited applicational range (Schmitt et al., 2022). The life cycle method involves many links in the production process. The data collection is often incomplete, or the data collection is often distributed on multiple links. The final results fail to reflect the CF of the product genuinely. Lastly, although the IPCC method is widely used, it only considers the direct CF within the region and does not consider the indirect CF caused by the linkage between the outside and the inside of the region. Therefore, it has high requirements for the research object and applies to the CF calculation within the closed system.

In this work, the total CF of the power industry is obtained through the direct and indirect emissions of carbon dioxide in the power industry and its change trend. Further, the indirect CDE of power enterprises is quantified using Blockchain Technology (BCT) based on specific data. The trend and cycle of total CF of power enterprises are analyzed from the direct and indirect CDEs. The innovation of this work is to analyze the direct and indirect CDEs and their change trends in the power industry using Edge Computing (EC) and BCT. Consequently, the flow of the total CF of the power industry is obtained. This work aims to provide an important reference for improving energy efficiency and optimizing CF verification of power enterprises. Chapter 1 describes the purpose and background. Chapter 2 analyzes the relevant research on EC and BCT and combines the two to verify the CF. Chapter 3 gives the experimental results. The research results can provide suggestions and references for the follow-up ECER work and the CF verification work of power enterprises. At the same time, it lays a foundation for optimizing the CF verification system of power enterprises from the emission source and breaks down the obstacles that hinder the development of LCE. It is of great significance to Chinese power enterprises' economic growth and ECER.

2 Materials and method

2.1 Edge computing

Multi-access EC is proposed by European Telecommunication Standards Association (ETSA). It provides computing, storage, and other infrastructure for the Internet of Things (IoT) devices at the network edge close to users. MEC is defined as mobile EC in the narrow sense and multi-access EC in the broad sense. EC supplements the performance of current cloud computing and exerts a more positive impact on the development of the IoT (Li et al., 2021a; Li et al., 2021b).

EC has unique advantages over Cloud Computing. EC performs on widely distributed nodes compared to the centralized nodes of Cloud Computing. EC can provide computing services for the network edge close to the data source, meet the needs of IoT applications, and can give a better solution. It has six basic characteristics: wide distribution, low delay, edge devices-based computing, edge intelligence, secured user privacy, and reduced traffic (Krestinskaya et al., 2019; Li, 2022a; Li, 2022b). Based on this, the edge node must have certain computing ability, network transmission, storage capacity, and compatibility with multiple protocols. The IoT terminal devices interact with the cloud center through the edge nodes in EC. Offline computing of many businesses can be directly implemented on the edge side in an EC ecosystem. There is no need to upload to the cloud, making the business processing faster and more efficient, relieving the traffic pressure,

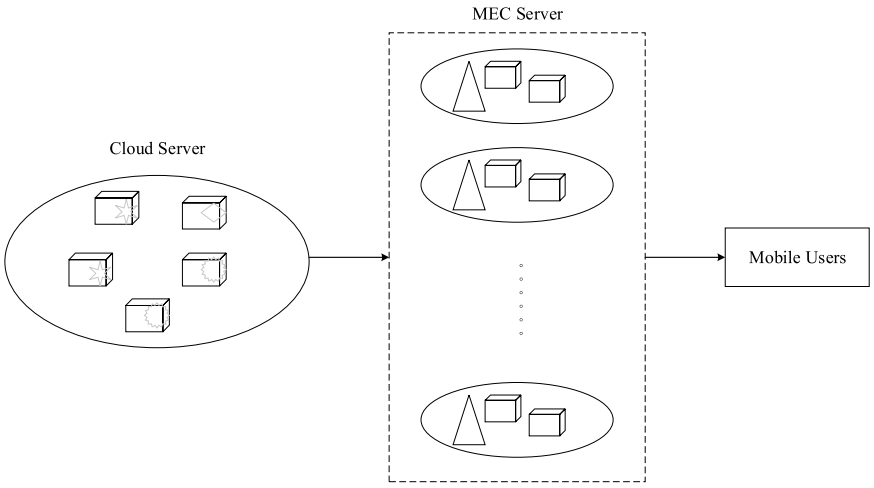

FIGURE 1
MEC system architecture.

and increasing private data security (Porambage et al., 2018; Yousefpour et al., 2019). Figure 1 displays the system architecture of EC, which consists of three layers: cloud server layer, MEC server layer, and mobile terminal layer from top to bottom.

EC can shorten the data processing distance and enhance real-time performance. However, the security issues in the data processing and analysis steps still need further research. Meanwhile, with the development of IoT technology, BCT has become a research hotspot in many fields with its strong data security storage capacity. Therefore, further research on BCT is needed.

2.2 Blockchain

BCT is a crucial technological innovation. Its basic structure includes six application, contract, incentive, consensus, network, and data layers. This structure is distributed from top to bottom, reflecting the function allocation from concrete to abstract. Each of these six layers has its function and can cooperate. A reasonable blockchain includes at least these six layers. Figure 2 presents the specific structure. Each layer should be designed according to its functional requirements (Sabella et al., 2019; Sodhro et al., 2019).

2.2.1 Data layer

The data layer is a physical expression of BCT, the basic and core structure in the whole structure. It is characterized by no-tampering and full backup.

2.2.2 Network layer

The network layer controls the communication of the whole system. It can improve data transmission efficiency in each stage when sending, receiving, and sharing data. The most crucial part of the blockchain network is Point to Point (P2P) transmission, which is adapted to complete a distributed network. Thereby, blockchain is essentially a P2P network structure with an automatic networking mechanism. At each node, information can be received and generated. Any node in the network can maintain the communication between them when the same growing blockchain structure is maintained. Moreover, the network layer also has many functions, such as data dissemination and verification, which are the most basic (Sittón-Candanedo et al., 2019).

2.2.3 Consensus layer

The consensus layer encapsulates a consensus mechanism algorithm on each node to control the authentication and identification of data in P2P mode. Dispersed nodes must reach a consensus through the consensus layer in the decentralized network structure to safeguard data validity. The consensus mechanism guarantees system security and reliability and is one of the core technologies of blockchain structure.

2.2.4 Incentive layer

There are many incentive mechanisms in the incentive layer, and the nodes in each blockchain participate in verifying new blocks.

2.2.5 Smart contract layer

The smart contract layer is the basis for the blockchain to program and de-trust. It systematically specifies the transaction method and specific process, including all kinds of scripts and codes, which can be executed automatically and cannot be tampered with at will.

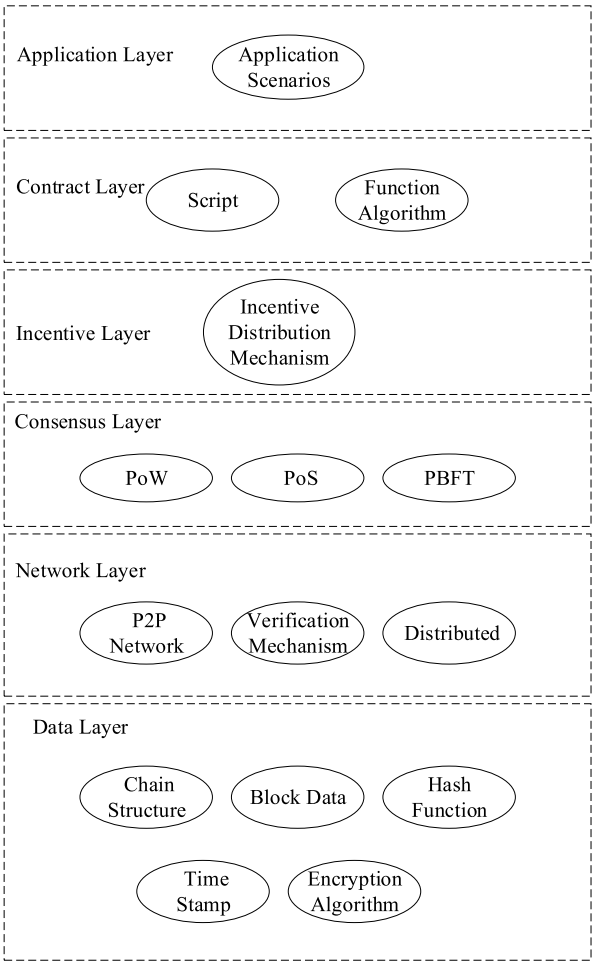

FIGURE 2
Infrastructure of blockchain.

2.2.6 Application layer

The application layer undertakes the docking with various application scenarios, and the entities in each application scenario will participate in it and formulate the overall rules according to the intelligent contract, making the whole business logic more complete (Roman et al., 2018).

2.3 Carbon footprint verification based on edge computing and blockchain technology

CF verification is a metric of the product life cycle level, a bottom-up carbon accounting system. It is the carbon emission of products or services in the life cycle. For example, the CF of a book considers all carbon emissions generated in the process of paper making, printing, transportation, sales, disposal, and natural decomposition. The British Standards Institute issued the CF calculation standard and elaborated CF's calculation methods and principles. CF calculation can let consumers know the greenhouse gas emissions during the whole life cycle of commodities and encourage consumers to choose low-carbon commodities. In addition, calculating CF can help manufacturers fully understand the carbon emissions of goods in production, transportation, and consumption. It helps explore improvements to guide the reduction of energy consumption and costs (Ray et al., 2019). In short, it is the total amount of greenhouse gases released by products or services in the life cycle. With the continuous improvement of the international market's understanding of the product CF, CF verification is a key condition for obtaining orders from multinational companies. CF can be verified through the enterprise CF of the whole company or the product CF, including the complete life cycle of a specific product or service, the supply chain, and pollutant emission control technology (Monrat et al., 2019).

At the same time, the blockchain can be divided into public, private, and alliance chains according to the range distribution of blockchain nodes. The public chain is entirely open to the public, which anyone can directly access without authorization. A private chain is established by an organization and accessible to only specific authorized users. An alliance chain is a mixture of public and private chains visited by users who join the alliance. The public chain has reliability and privacy security problems, and the alliance chain is difficult to deploy due to its large scale. Thus, this work selects a private blockchain with a small scale to record and store relevant event information, such as CF verification of power enterprises. Also, the private blockchain is deployed on the local platform, so the initial blockchain is safe and reliable. EC processes data at the network's edge or near the data source. According to the research data, the deployed edge node computing and processing capacity can meet the processing requirements of the equipment used for CF verification of power enterprises (Gao et al., 2022). Based on this, this work further analyzes the CF verification of power enterprises by fusing EC and BCT.

2.4 Calculation of total carbon footprint

The CF verification system of power enterprises is studied. The specific calculation method is as follows:

2.4.1 Calculation method of direct carbon dioxide emission

The direct CDE is calculated based on EC by Eq. 1:

$$C_{dir} = \sum_{ij} CO_{2ij} = \sum_{ij} \left(E_{ij} \times CF_j \times \left(1 - S_j\right) \times CC_j \times COF_j \times 44/22 \right) \quad (1)$$

In Eq. 1, C_{dir} is the total amount of carbon dioxide emitted by fossil fuel consumption; E_{ij} represents the consumption of

fuel j in sector i; CF_j represents the average low calorific value of the fuel j; S_j represents the proportion of the j-th fuel that is not used for combustion but used as raw material in the product. CC_j represents the carbon emission coefficient of the j-th fuel, which is the carbon emission per unit heat of the j-th fuel; COF_j represents the oxidation factor of the j-th fuel, and represents the oxidation rate level of the fuel; 44/22 is the conversion coefficient of carbon atom mass to carbon dioxide molecular mass; i is the source consumer sector; j is the type of fuel (Belotti et al., 2019).

2.4.2 Calculation of indirect carbon dioxide emission

Consuming the products or services of other sectors will emit carbon dioxide, which is the indirect CDEs. The carbon emission coefficient should be calculated as follows (Efanov and Roschin, 2018):

a. Calculation of indirect carbon dioxide emission coefficient

$$d_j = f_j \times \left(\sum_{i=1}^{n} e_i \times b_{ij} \right) \tag{2}$$

d_j is the indirect CDE coefficient of sector j, with the unit of t CO_2/10000 RMB; f_j is the CDE coefficient per unit of energy in sector j, with the unit of t CO_2/tce; e_i is the energy intensity of sector I, with the unit of tce/10,000 RMB; b_{ij} is the complete consumption coefficient, which is the total consumption of j sector to i sector; $\sum_{i=1}^{n} e_i \times b_{ij}$ is the indirect energy consumption of all n intermediate products per unit product of j department (Gatteschi et al., 2018).

b. Calculation of indirect carbon dioxide emission

The following equation calculates the indirect emissions of each sector after the coefficient calculation.

$$C_{indj} = d_j \times X_j \tag{3}$$

X_j is the total output of sector j (Halaburda, 2018).

According to the input-output method, the cost of power input and the amount of carbon dioxide indirectly emitted by the power enterprise is calculated by Eq. 4:

$$\mathrm{R} = \mathrm{K}/\mathrm{IN} \tag{4}$$

Here, R is the proportion of input. K denotes the total investment amount. IN represents the sum of output added value.

(3) This research cites foreign scholars' definitions of direct and indirect CDEs. It calls the CDEs related to the direct combustion of fossil energy the direct CDEs of power enterprises, namely, the CDEs generated by the direct combustion of coal, oil, and other energy sources in the power industry's production. Indirect CDEs are the CDEs of non-energy products or services in their life cycle. That is, the energy consumption of other industrial sectors of the national economy and the CDEs generated to maintain the production needs of consumers in the power sector (Reyna et al., 2018; Al-Jaroodi and Mohamed, 2019).

The direct CDE of power enterprises is mainly due to the excessive consumption of thermal power generation and electric heating energy. The indirect CDE is mainly the services consumed by the thermal power sector. CDEs of the product refer to the CDEs of commodities in the whole life cycle of exploitation, production, power and heat distribution, consumption, and recycling of raw materials (Andoni et al., 2019).

The sum of direct and indirect CDEs is the total CF (Salah et al., 2019) that is:

$$C = C_{dir} + C_{ind} \tag{5}$$

TABLE 1 Information for data settings.

Model	BCT	EC	EC and BCT
The amount of data	600		
Type of data	Economy	Sports	Education
Evaluation method	Accuracy	Calculation rate	—

2.5 Data setting

This work mainly uses the method of data set to evaluate the model of EC and BCT, to explore the comprehensive performance of this model. The used dataset is the Dash dataset, which is a Python data visualization library for building web applications. It is based on the Python web framework Flask and the Javascript drawing library Plotly.js and the Javascript library React.js for building user interfaces, so it is very suitable for building web pages with Flask-based backend and front-end data visualization. The Dash application consists of two parts. The first part is the layout, which describes the design style of the application, and it is used to display data and guide users; the second part describes the interactivity of the application. The specific settings for evaluating the models are illustrated in Table 1.

As portrayed in Table 1, experimental evaluations of three models are set up, and the models are evaluated from different perspectives, making the evaluation results more valuable.

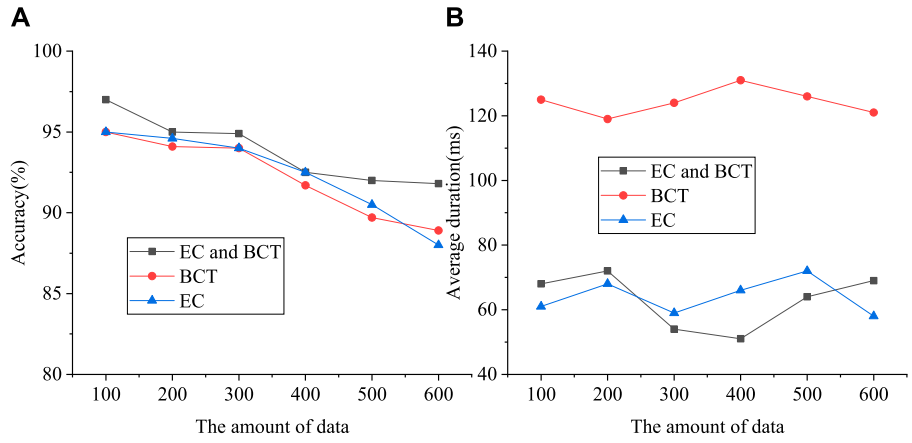

FIGURE 3
Performance evaluation of EC and BCT **(A)** refers to the accuracy of data processing, **(B)** stands for the duration of data processing).

3 Results and discussion

3.1 Performance evaluation of edge computing and blockchain technology

Based on the progress of science and technology, data processing has become a key requirement of the current society for various technologies. The development of EC technology and BCT can not only satisfy the demands of data processing efficiency but also meet the requirements of data security. Therefore, this vision is fulfilled by the design of EC and BCT. Figure 3 demonstrates the performance evaluation results of the EC and BCT model.

In Figure 3, the design uses EC and BCT to analyze the CF of power enterprises, and the designed model can well meet this requirement. The accuracy rate of the designed model is more than 92%, which is almost the same as the data processing effect of EC and BCT, but the data processing rate of this work far exceeds that of blockchain technology, and the duration of data processing is about 70 ms. It means that the designed model not only has good data processing effect but also has security and efficiency. In addition, the work also evaluates the model under 100 experiments with different types of data. Table 2 presents the average accuracies of the models evaluated using different types of data. Table 2 Denotes that the accuracy rates of the three models are basically the same in different types of data processing. Therefore, it can be found that the designed model of EC and BCT is relatively successful.

TABLE 2 Evaluation of different performances of the models.

Type of data	BTC	EC	EC and BCT
Economy	90.8%	91.7%	91.4%
Sports	91.6%	89.7%	92.1%
Education	91.1%	88.5%	90.5%

3.2 Analysis of carbon footprint of power enterprises

The total CF is the sum of the total amount of carbon dioxide emitted directly and indirectly. Direct CDE is obtained through EC, and indirect CDE accounting is based on input-output analysis and BCT. On this basis, the change and characteristic structure of direct and indirect CDE of China's power enterprises in 2005, 2010, 2015, and 2020 are studied by using the data of power enterprises from 2005 to 2020. Then, the BCT is used to quantitatively analyze the influencing factors of direct CDEs from thermal power consumption (Niranjanamurthy et al., 2019).

The total CF of the power industry in 2005, 2010, 2015, and 2020 is obtained by the sum of direct CDEs and indirect CDEs in the above 4 years. Tables 3; Figure 4 are the calculation results. Table 3 shows that power enterprises' total CF has rapidly increased in the past 20 years.

The comprehensive analysis of the data in Figure 4 reveals the following results.

a. Regarding the total amount of CDEs in 2005, the direct CDEs were 2,363,908,700 tons, and the indirect CDEs were 405,530,900 tons. By 2020, the direct CDEs had reached 15,685,676,900 tons, and the indirect CDEs had reached 770,912,080 tons. It suggests that the total CF of China's power industry is growing rapidly. Regarding the structure, direct CDEs account for a large proportion of the total CF. Proportion of direct CDE in 2005, 2010,

TABLE 3 Direct CDEs and growth rate of the power industry.

Time	Direct CDEs (10,000 tons)	Growth rate (%)	Direct CDEs (10,000 tons)	Growth rate (%)
2005	236390.87	—	40553.09	—
2010	406454.97	0.72	56606.64	0.39
2015	616208.73	0.52	70669.788	0.25
2020	1568567.69	1.55	77091.208	0.091

The direct and indirect CDEs, and their proportion in power enterprises are shown in Figure 4.

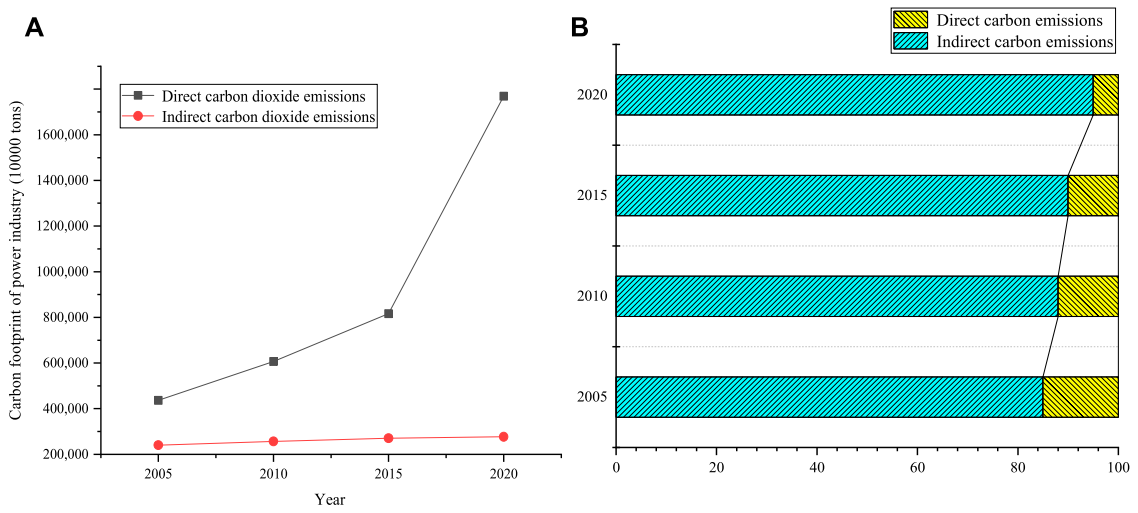

FIGURE 4
Direct and indirect CDEs and emission ratio of power enterprises. **(A)** Direct and indirect CDEs from power enterprises; **(B)** Proportion of direct and indirect CDEs in power enterprises.

2015 and 2020 was 85%, 88%, 90% and 95%. The proportion of direct CDE is rising yearly, while the proportion of indirect CDE is declining yearly. In the final analysis, the power industry and other related industries are gradually decoupling due to the continuous improvement of technology levels. The investment in intermediate technology is added, resulting in a substantial increase in indirect CDEs.

b. China's energy demand for industrial, civil, and heating has proliferated from 2005 to 2020, resulting in an obvious upward trend in power and heat production. Both energy input and direct CDE have an obvious upward trend. The CDE of the power industry is the main contributor to China's CDE growth. The main factors affecting the emission reduction effect of China's power industry are the input structure of energy, the structure of power sources, the technology in the power generation process, and the scale of the industry.

c. The power industry CF has risen from 2005 to 2020, with direct CDE and indirect CDE accounting for 95% and 5%, respectively. It reveals that the direct CDEs are very large, accounting for a significant proportion of power enterprises' total CF. In the indirect CDEs, thermal power production is closely related to heavy manufacturing, mining, transportation, warehousing, postal, and other service industries. Service industries consume the intermediate services and products of other industries and greatly impact the CDEs of these industries.

4 Conclusion

The CDE of the power industry is analyzed from the perspective of CF verification. The results reveal that the power industry needs to focus on adjusting the power supply structure and expanding the proportion of clean power in electric power production. Clean power generation using wind, nuclear, and other low-carbon technologies should be encouraged. The investment structure of power generation and heating energy should be adjusted accordingly to control the growth of CDEs from the source

and optimize CF verification. The energy intensity of China's power industry may continue to decline. Its effect on ECER will gradually appear. Hence, power enterprises must improve energy utilization to implement CF verification and control the production's power consumption and heat loss.

The research deficiency is that no specific industry-oriented CF research is explored. Currently, China's CF verification research is in the demonstration and promotion stage. CF analysis is very crucial for enterprise CF verification systems. Enterprises should contain the CDE within the international standard and constantly improve the CF verification indexes in the future. This work hopes enterprises can focus on the full use of energy and better verify the CF. It is expected to help power enterprises control the power consumption index and heat loss in production, thereby achieving ECER.

Data availability statement

The original contributions presented in the study are included in the article/supplementary material, further inquiries can be directed to the corresponding author.

Author contributions

Each author made significant individual contributions to this manuscript. JX: writing and performing surgeries; YX: article review and intellectual concept of the article; YY: data analysis and performing surgeries.

Conflict of interest

Author JX was employed by Tellhow Software Co. Ltd.

Author YX was employed by State Grid Qinghai Electric Power Company Haixi Power Supply Company.

Author YY was employed by Tellhow Software Co. Ltd.

Publisher's note

All claims expressed in this article are solely those of the authors and do not necessarily represent those of their affiliated organizations, or those of the publisher, the editors and the reviewers. Any product that may be evaluated in this article, or claim that may be made by its manufacturer, is not guaranteed or endorsed by the publisher.

References

Al-Jaroodi, J., and Mohamed, N. (2019). Blockchain in industries: A survey. *IEEE Access* 7, 36500–36515. doi:10.1109/access.2019.2903554

Andoni, M., Robu, V., Flynn, D., Abram, S., Geach, D., Jenkins, D., et al. (2019). Blockchain technology in the energy sector: A systematic review of challenges and opportunities. *Renew. Sustain. Energy Rev.* 100, 143–174. doi:10.1016/j.rser.2018.10.014

Belotti, M., Božić, N., Pujolle, G., and Secci, S. (2019). A vademecum on blockchain technologies: When, which, and how. *IEEE Commun. Surv. Tutorials* 21 (4), 3796–3838. doi:10.1109/comst.2019.2928178

Efanov, D., and Roschin, P. (2018). The all-pervasiveness of the blockchain technology. *Procedia Comput. Sci.* 123, 116–121. doi:10.1016/j.procs.2018.01.019

Gao, T., Jin, P., Song, D., and Chen, B. (2022). Tracking the carbon footprint of China's coal-fired power system. *Resour. Conserv. Recycl.* 177, 105964. doi:10.1016/j.resconrec.2021.105964

Gatteschi, V., Lamberti, F., Demartini, C., Pranteda, C., and Santamaria, V. (2018). To blockchain or not to blockchain: That is the question. *IT Prof.* 20 (2), 62–74. doi:10.1109/mitp.2018.021921652

Halaburda, H. (2018). Blockchain revolution without the blockchain?[J]. *Commun. ACM* 61 (7), 27–29. doi:10.1145/3225619

Krestinskaya, O., James, A. P., and Chua, L. O. (2019). Neuromemristive circuits for edge computing: A review. *IEEE Trans. Neural Netw. Learn. Syst.* 31 (1), 4–23. doi:10.1109/tnnls.2019.2899262

Li, H., Deng, J., Feng, P., Pu, C., Arachchige, D. D., and Cheng, Q. (2021). Short-term nacelle orientation forecasting using bilinear transformation and ICEEMDAN framework. *Front. Energy Res.* 697. doi:10.3389/fenrg.2021.780928

Li, H., Deng, J., Yuan, S., Feng, P., and Arachchige, D. D. (2021). Monitoring and identifying wind turbine generator bearing faults using deep belief network and EWMA control charts. *Front. Energy Res.* 770. doi:10.3389/fenrg.2021.799039

Li, H. (2022). SCADA data based wind power interval prediction using LUBE-based deep residual networks. *Front. Energy Res.* 10, 920837. doi:10.3389/fenrg.2022.920837

Li, H. (2022). Short-term wind power prediction via spatial temporal analysis and deep residual networks. *Front. Energy Res.* 10, 920407. doi:10.3389/fenrg.2022.920407

Monrat, A. A., Schelén, O., and Andersson, K. (2019). A survey of blockchain from the perspectives of applications, challenges, and opportunities. *IEEE Access* 7, 117134–117151. doi:10.1109/access.2019.2936094

Niranjanamurthy, M., Nithya, B. N., and Jagannatha, S. (2019). Analysis of blockchain technology: Pros, cons and SWOT. *Clust. Comput.* 22 (6), 14743–14757. doi:10.1007/s10586-018-2387-5

Osorio, A. M., Úsuga, L. F., Vásquez, R. E., Nieto-Londono, C., Rinaudo, M. E., Martinez, J. A., et al. (2022). Towards carbon neutrality in higher education institutions: Case of two private universities in Colombia. *Sustainability* 14 (3), 1774. doi:10.3390/su14031774

Porambage, P., Okwuibe, J., Liyanage, M., Ylianttila, M., and Taleb, T. (2018). Survey on multi-access edge computing for Internet of Things realization. *IEEE Commun. Surv. Tutorials* 20 (4), 2961–2991. doi:10.1109/comst.2018.2849509

Premsankar, G., Di Francesco, M., and Taleb, T. (2018). Edge computing for the Internet of Things: A case study. *IEEE Internet Things J.* 5 (2), 1275–1284. doi:10.1109/jiot.2018.2805263

Ray, P. P., Dash, D., and De, D. (2019). Edge computing for Internet of Things: A survey, e-healthcare case study and future direction. *J. Netw. Comput. Appl.* 140, 1–22. doi:10.1016/j.jnca.2019.05.005

Reyna, A., Martín, C., Chen, J., Soler, E., and Diaz, M. (2018). On blockchain and its integration with IoT. Challenges and opportunities. *Future gener. Comput. Syst.* 88, 173–190. doi:10.1016/j.future.2018.05.046

Roman, R., Lopez, J., and Mambo, M. (2018). Mobile edge computing, fog et al.: A survey and analysis of security threats and challenges. *Future Gener. Comput. Syst.* 78, 680–698. doi:10.1016/j.future.2016.11.009

Sabella, D., Sukhomlinov, V., Trang, L., Kekki, S., Paglierani, P., Rossbach, R., et al. (2019). Developing software for multi-access edge computing. *ETSI white Pap.* 20, 1–38. doi:10.1007/978-3-030-79618-1_9

Salah, K., Rehman, M. H. U., Nizamuddin, N., and Al-Fuqaha, A. (2019). Blockchain for AI: Review and open research challenges. *IEEE Access* 7, 10127–10149. doi:10.1109/access.2018.2890507

Schmitt, L., Jeong, J., Potier, J. M., Izoret, L., Mai-Nhu, J., Decousser, N., et al. (2022). Using an analysis of concrete and cement epd: Verification, selection, assessment, benchmarking and target setting. *Acta Polytech. CTU Proc.* 33, 546–551. doi:10.14311/app.2022.33.0546

Sittón-Candanedo, I., Alonso, R. S., Corchado, J. M., Rodriguez-Gonzalez, S., and Casado-Vara, R. (2019). A review of edge computing reference architectures and a new global edge proposal. *Future Gener. Comput. Syst.* 99, 278–294. doi:10.1016/j.future.2019.04.016

Sodhro, A. H., Pirbhulal, S., and De Albuquerque, V. H. C. (2019). Artificial intelligence-driven mechanism for edge computing-based industrial applications. *IEEE Trans. Ind. Inf.* 15 (7), 4235–4243. doi:10.1109/tii.2019.2902878

Sonmez, C., Ozgovde, A., and Ersoy, C. (2018). EdgeCloudSim: An environment for performance evaluation of edge computing systems. *Trans. Emerg. Tel. Tech.* 29 (11), e3493. doi:10.1002/ett.3493

Wiche, P., Droguett, B. R., and Granato, D. (2022). Challenges to quantify the life cycle carbon footprint of buildings in Chile. *E3S Web Conf.* 349, 04005. doi:10.1051/e3sconf/202234904005

Yousefpour, A., Fung, C., Nguyen, T., Kadiyala, K., Jalali, F., Niakanlahiji, A., et al. (2019). All one needs to know about fog computing and related edge computing paradigms: A complete survey. *J. Syst. Archit.* 98, 289–330. doi:10.1016/j.sysarc.2019.02.009

frontiers | Frontiers in Energy Research

TYPE Original Research
PUBLISHED 12 January 2023
DOI 10.3389/fenrg.2022.1019464

OPEN ACCESS

EDITED BY
Yusen He,
The University of Iowa, United States

REVIEWED BY
Huajin Li,
Chengdu University, China
Omveer Singh,
Gautam Buddha University, India
Amil Daraz,
Nazarbayev University, Kazakhstan
Lichun Zhang,
The University of Iowa, United States

*CORRESPONDENCE
Xin Ma,
pengbo20@sdjzu.edu.cn

SPECIALTY SECTION
This article was submitted to Smart Grids,
a section of the journal
Frontiers in Energy Research

RECEIVED 15 August 2022
ACCEPTED 30 September 2022
PUBLISHED 12 January 2023

CITATION
Peng B, Ma X, Ma X, Tian C and Sun Y (2023), Coordinated AGC control strategy for an interconnected multi-source power system based on distributed model predictive control algorithm.
Front. Energy Res. 10:1019464.
doi: 10.3389/fenrg.2022.1019464

Coordinated AGC control strategy for an interconnected multi-source power system based on distributed model predictive control algorithm

Bo Peng[1], Xin Ma[1]*, Xiangxue Ma[1], Changbin Tian[1] and Yuqiong Sun[2]

[1]Shandong Key Laboratory of Intelligent Buildings Technology, School of Information and Electrical Engineering, Shandong Jianzhu University, Jinan, China, [2]Jinan Yuny Technology Co., Ltd., National Offshore Innovation and Entrepreneurship Base for Overseas Professionals, Jinan, China

The erratic and random characteristics of wind power and wind-thermal replacement significantly degrade the performance of AGC in an interconnected, multi-source power system. For the lack of cooperation between wind power and thermal plants in AGC of interconnected power system as well as the heavy computational burden and inflexible information interaction of centralized AGC architecture, a novel coordinated AGC control strategy for an interconnected multi-source power system based on distributed model predictive control (DMPC) algorithm is proposed in this research. Under the DMPC architecture, the dimension of centralized AGC problem is reduced in each subsystem, and the overall AGC performance can be enhanced through inter-area communication between subsystems. In the meantime, based on the proposed coordinated control strategy, the active AGC response capability of wind farms and energy storage in the interconnected system is exploited to realize the dynamic cooperation between the wind generation and thermal AGC plants, and the overall AGC control performance can be further improved. In this paper, local DMPC controllers are deployed in each subsystem to address the drawbacks of a centralized control architecture by exchanging forecast and state measurement information with neighboring subsystems. In addition, considering the current operating status of multiple kinds of energy sources with different features, a fuzzy-based coordinated control strategy is designed for the purpose of dynamically allocating the AGC demand inside the wind-storage system, and the wind farm's reliability for AGC response in diverse operation scenarios can be guaranteed. Finally, comparative analysis with existing works has been conducted on a three-area power system, and numerical results demonstrate that the proposed coordinated AGC control strategy has better performance in AGC performance and the dynamic cooperation can be achieved between wind power and thermal plants in AGC response through the designed wind-storage system and coordinated DMPC AGC control strategy.

KEYWORDS

AGC, multi-area, frequency response, DMPC, fuzzy algorithm

1 Introduction

With the increasing need of energy consumption, the scale of interconnected power systems around the world is continuously expanding. Currently, large power systems are generally composed of several interconnected subsystems or control areas through interregional tie-lines. All the thermal plants in each subsystem are responsible for balancing their own power demand. However, once a sudden power fluctuation event occurs, it will cause a significant impact on the power balance in each subsystem, and leading the whole interconnected grid into an unstable operation state with frequency and tie-line power fluctuations. Therefore, AGC has been widely applied for maintaining the active power balance of the interconnected power systems. Many types of controllers have been designed for improving the AGC dynamic performance, such as proportional-integral-derivative (PID) control (Debbarma et al., 2013; Hasanien and El-Fergany, 2019), robust control (Shayeghi et al., 2007; Zhang et al., 2013; Xiong et al., 2018), event-triggered load frequency control (Wen et al., 2015; Lv et al., 2020; Yuan et al., 2020), neural fuzzy-based intelligent control (Kocaarslan and Çam, 2005; Yousef et al., 2014; Aziz et al., 2019), and model prediction schemes (Venkat et al., 2008; Ma et al., 2014; Shiroei and Ranjbar, 2014). In addition, advanced soft computing techniques are also applied in AGC controller to deal with the uncertainties and variation of operating points. In (Abd-Elazim and Ehab, 2018), genetic and firefly optimal algorithm are applied in the load frequency controller of a two-area system composing of PV grid and thermal generators. In (Mohanty et al., 2014), Differential evolution algorithm is adopted for AGC control of an interconnected power systems with non-linearity. Moreover, fuzzy logic algorithm has been applied in (Kocaarslan and Çam, 2005; Aziz et al., 2019) for scheduling the gains of the AGC controller dynamically of two-area interconnected power systems. In (Arya, 2017), fuzzy-based fractional order controller is designed for diminishing the frequency and tie-lie power deviations efficiently. The above-mentioned literatures have improved the dynamic AGC performance of interconnected power systems by means of complex controllers or advanced optimization algorithms. However, control strategies of the mentioned works are built on a centralized architecture, which is unsuitable for large-scale power grids due to the calculation complexity, communication delays, and resilience risks. Therefore, a distributed control architecture has more adaptability for interconnected system, and due to the robust control performance and efficient information communication features, DMPC algorithm has been acknowledged as an efficient method for improving the frequency stability of the interconnected system. A DMPC-based load frequency controller is designed in (Ma et al., 2017) for a deregulated three-area power system considering the effect of bilateral contracts of load demands. In (Jain et al., 2018), a DMPC AGC architecture is proposed for wide-area control of power system oscillations under communication and actuation constraints. In (Chen et al., 2018) an extended DMPC controller is designed for frequency regulation of a two-area power system under uncertain system condition and parameters. In addition, considering environmental pressure and market competition pressure, a distributed economic MPC for LFC of multi-area power system with wind power plants is proposed in (Zhang et al., 2021), but the dynamic features of wind plants and potential for active AGC response has not been discussed.

Nevertheless, besides the centralized control framework, another factor for weakening the AGC performance is the increasing penetration rate of renewable energy (e.g., wind energy) and the lack of coordination between multiple energy sources. With the increase of wind power integration capacity, more researchers are attracted into fields like wind power forecasting (Li et al., 2021a; Li, 2022a; Li, 2022b), wind turbines (WT) fault detection and wind farm's flexible operation (Li et al., 2021b), and it has been testified that the active AGC response capability of WT can be exploited by advanced control strategy. Therefore, it is essential to exploit the potential of WTs for AGC response. A coordinated control framework and an adaptive PID control scheme has been designed for wind farms in (Magdy et al., 2018). Moreover, an interconnected power system with enhanced load frequency management is proposed in (Chang-Chien et al., 2013), and WTs are included into the AGC model of entire system. It should be noted that the WT operation state is significantly affected by the wind speed, which in turn affects the interconnected system's capacity to provide a reliable frequency response. In previous studies (Wu et al., 2017; Abazari et al., 2019; Peng et al., 2019), reliable active power reserve for WT's frequency response can be acquired through the de-loading operation, and when WT is incapable of participating the frequency regulation process, energy storage (ES) units with rapid responding characteristics are deployed to manage the power shortages in frequency response. However, in most literature cited above, the AGC control techniques are employed in scenarios with a constant windspeed rather than scenarios with varying ones, which might impair the strategies' reliability and efficiency. Moreover, in an interconnected power system with multiple power sources like wind energy, conventional thermal plants and ES unit, because of the slow ramp rate of thermal plants and the large "wind-thermal replacement", the thermal plants cannot meet the AGC demand of each subsystem alone, and the frequency will suffer more severe fluctuations if the current windspeed is not sufficient to support WT's participation in AGC, which is detrimental to the frequency stability of the whole multi-area power system. Therefore, it is critical that WTs must be able to dynamically collaborate with the ES for obtaining a reliable and active AGC response ability in various operation conditions, and it is also important for WTs to cooperate with thermal plants to make up for the operation constraints of the thermal power.

It is apparent from the previous works that the AGC performance of interconnected power system with multiple kinds of power sources largely depends on the control strategy architecture and the coordination between power sources. Therefore, a coordinated AGC control strategy based on DMPC algorithm is proposed to enhance the AGC performance of a multi-source interconnected power system with high-level wind power penetration rate. In the proposed coordinated control strategy, to deal with the drawbacks mentioned under the centralized framework, the dimension of centralized AGC problem is reduced in each subsystem under the DMPC architecture. Then, local DMPC controller of each subarea communicates with adjacent areas exchange their states and prediction information to improve the AGC performance of the whole system with better stability and reliability. Moreover, ES units are deployed in the windfarms as a combined wind-storage system (CWES) to let the WTs participate in AGC response actively through cooperation with the ES. Taking current operation states of CWESs and thermal plants into consideration, a fuzzy-based controller is designed for active frequency response inside the CWES system and realizing a dynamic cooperation between wind farm and thermal generators in each subsystem. Therefore, the CWES system is ensured with better adaptability and reliability for AGC support under fluctuating windspeeds and the features of renewable generation and conventional thermal plants can be coordinated flexibly, and the overall AGC dynamic performance of the multi-source interconnected power system can be effectively improved.

The main contributions of this paper are as follows:

1) Based on a DMPC algorithm, a novel AGC model of a multi-source interconnected power system is designed. In each subsystem, a synthesised AGC state-space model composed of a combined wind-energy storage system and thermal generators is designed to let the local WTs participate in the AGC process. Then, through communication of the control and prediction information between local DMPC controllers, the AGC response potential of the WTs is fully exploited, and the AGC performance of multi-area power system is improved effectively.
2) A novel coordinated control strategy for multiple kinds of power sources with different operational features is designed based on the fuzzy logic algorithm. Considering current operation trajectories of the combined wind turbine and energy storage units, a fuzzy controller is designed to realize an active AGC response of the CWES system dynamically. Under the proposed control strategy, flexible coordinated operation between WTs and ES is achieved. Therefore, adaptability and performance of the CWES system for multi-area AGC active response under multi-scenarios are both enhanced.
3) Through the proposed control strategy, the active AGC response capability of the CWES and conventional thermal generators inside multi-area grid can be fully exploited, and the ramping rate issue of conventional plants can be well alleviated through the quick power response feature of CWES in the beginning stage of AGC. As a result, the frequency stability weakened by the wind-thermal replacement is ameliorated.

The remainder of this paper is organized as follows. The system structure and modelling theories are introduced in Section 2. The DMPC algorithm and dynamic cooperation strategy for a CWES system in frequency support are introduced in Section 3, and case studies are given in Section 4. Finally, conclusions are summarized in Section 5.

2 System framework

The framework of multi-area power grid studied in this paper is demonstrated in Figure 1, there are three subsystems inside the interconnected system, and power flows among these adjacent areas through tie-lines. It can be observed that there exists a conventional generator model and a CWES model as the power source in each area. In addition, an MPC-based AGC controller is deployed in each area for local AGC response.

2.1 Modelling of an interconnected system

From Figure 1, the dynamic relationships among every block in the overall multi-area AGC system can be represented by differential equations, and the dynamic balance between the power variation and the frequency fluctuation $\Delta\omega_i$ in subarea 1 can be expressed as

$$\Delta\dot{\omega}_i = -\left(\frac{D_i}{2H_i}\right)\Delta\omega_i + \left(\frac{1}{2H_i}\right)\Delta P_{mi} + \left(\frac{1}{2H_i}\right)\Delta P_{CWESi} - \left(\frac{1}{2H_i}\right)\Delta P_{Li} - \left(\frac{1}{2H_i}\right)\Delta P_{tiei} \quad (1)$$

where $\Delta\omega_i$ is the frequency variation in the *ith* subarea system; D_i and H_i are the system damping constant and inertia constant, respectively; and ΔP_{mi} and ΔP_{CWESi} are the active power variations from the thermal unit and the CWES system, respectively. ΔP_{Li} is the load fluctuation, which is also the disturbance in the AGC response model, and ΔP_{tiei} is active power interaction of the tie-line in this area.

The differential equation of the thermal plant's turbine in i^{th} area can be expressed as

$$\Delta\dot{P}_{mi} = -\frac{1}{T_{Ti}}\Delta P_{mi} + \frac{1}{T_{Ti}}\Delta P_{vi} \quad (2)$$

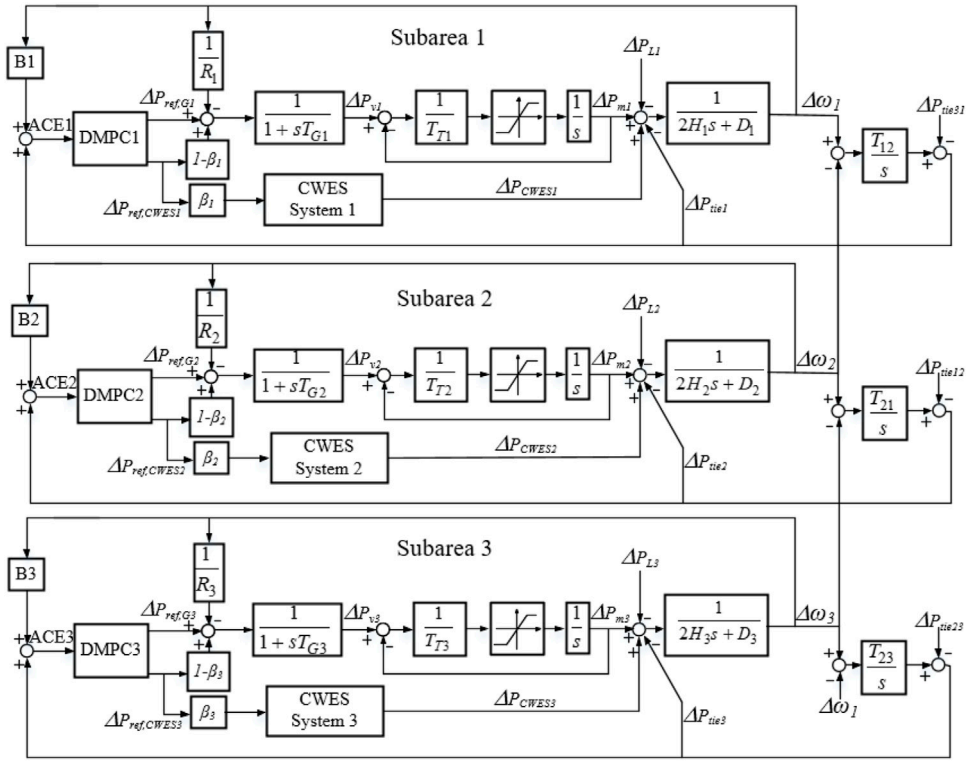

FIGURE 1
Framework of multi-area power system with CWES.

where ΔP_{vi} is the governor valve adjustment of the conventional generation unit and T_{Ti} is the time constant of the steam turbine.

The differential equation of the thermal plant's governor in area i is given as

$$\Delta \dot{P}_{vi} = -\frac{1}{R_i T_{Gi}} \Delta \omega_i - \frac{1}{T_{Gi}} \Delta P_{vi} + \frac{1}{T_{Gi}} \Delta P_{ref,Gi} \tag{3}$$

where T_{Gi} is the time coefficient of the governor valve adjustment, R_i is the system's primary frequency response coefficient, and $\Delta P_{ref,G}$ is the AGC reference command of the DMPC controller for the thermal power unit in this area.

Moreover, the active power exchanged between the i^{th} area and its adjacent area can be expressed as

$$\Delta \dot{P}_{tiei} = \sum_{\substack{j=1 \\ j \neq i}}^{M} T_{ij} \Delta \omega_i - \sum_{\substack{j=1 \\ j \neq i}}^{M} T_{ij} \Delta \omega_j \tag{4}$$

where T_{ij} is the power exchange factor between the i^{th} area and the j^{th} area, M is the number of subareas contained in the multi-area grid, and $M = 3$ in this paper.

2.2 AGC response model of a subarea integrated with a CWES system

As shown in Figure 1, the previous section introduced the structure of the interconnected power system and the dynamic relationships of the thermal plants in the AGC process. Since each subarea in the interconnected system has a high penetration rate of wind generation and the power output of wind farm accounts for approximately 30% of the total active power generation in each subarea, the "wind-thermal" substitution effect of the entire multi-area power system is obvious. Therefore, this section jointly models the AGC process of the thermal plants and WTs in the same area so that cooperation of these two kinds of energy sources in the AGC process can be achieved. Moreover, the adjustment burden and the slow response problem of thermal plants in AGC can be alleviated, and the AGC response capability of the interconnected system is improved.

The simplified WT model applied in the multi-area system in this study is displayed in Figure 2. Here, $P_{ref,W}$ and P_W are the active power output reference and actual power output of WT, and k_{wp} and k_{wi} are the proportional and integral gain coefficients of the PI block of the rotor-side converter, respectively. The constant T_{fl} is the filter coefficient of the power outer loop. i_{rd} is the d-axis component of the rotor current, and s_g is the generator

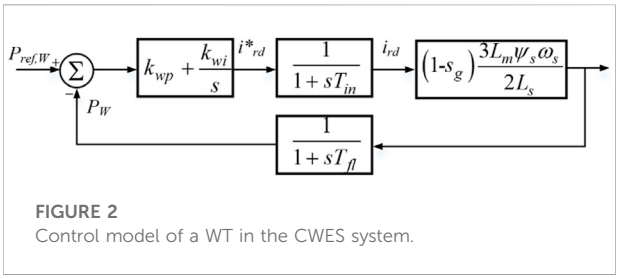

FIGURE 2
Control model of a WT in the CWES system.

slip. K_{RSC} is defined as the gain coefficient of the rotor-side converter. According to the above control block diagram, the mathematical models of the WT are as follows:

$$\Delta\dot{P}_W = -\frac{1}{T_{fl}}\Delta P_W + K_{RSC}\Delta i_{rd} \tag{5}$$

$$\Delta\dot{P}_{err} = -\Delta P_W + \Delta P_{ref,W} \tag{6}$$

$$\Delta\dot{i}_{rd} = -\frac{k_{wp}}{T_{in}}\Delta P_W + \frac{k_{wi}}{T_{in}}\Delta P_{err} - \frac{1}{T_{in}}\Delta i_{rd} + \frac{k_{wp}}{T_{in}}\Delta P_{ref,W} \tag{7}$$

$$K_{RSC} = \left(1 - s_g\right)\frac{3L_m\psi_s\omega_s}{2L_s} \tag{8}$$

In the CWES system proposed in this paper, the energy storage unit mainly assists the WTs in participating in the AGC process of the interconnected system. The ES output is mainly determined according to the operating state and active power reference value of the WTs, so the subarea AGC controller does not determine this output. Therefore, the active power reference value $P_{ref,W}$ delivered to the WTs in the subarea is equal to the reference value $P_{ref,\ CWES}$ of the CWES system.

During the AGC response, the output characteristics of AGC resources should be fully utilized in this area. The CWES is mainly responsible for addressing the slow power ramping problem of thermal plants in the initial stage of AGC response. As the AGC process progresses, the power generation of thermal plants gradually matches the AGC demand. For that scenario, the CWES system should gradually reduce the output, transfer the main task back to thermal plants, and provide a reliable active power reserve for the next AGC demand to make up for the "wind-thermal replacement" effect. In this paper, according to the AGC response process and real-time frequency variation, the wind power is integrated into the AGC process of each area by dynamically modifying the control parameters of local DMPC controller. Then, the active AGC response capability of CWES and conventional thermal generators inside multi-area grid can be fully utilized, and the ramping rate issue of conventional plants can be well alleviated.

The power reference modifications of CWES and thermal plant in the i^{th} area can be expressed in Eq. 9:

$$\begin{cases} \Delta P'_{ref,CWESi} = \beta_i \cdot \Delta P_{ref,CWESi} \\ \Delta P'_{ref,Gi} = \Delta P_{ref,Gi} + \left(1-\beta_i\right)\cdot \Delta P_{ref,CWESi} \end{cases} \tag{9}$$

where $\Delta P'_{ref,CWESi}$ and $\Delta P'_{ref,Gi}$ are the modified control variables of the CWES system and thermal plants in subarea i, respectively, and β is the modification factor, and it represents the frequency response process. Based on fuzzy theory, β is dynamically determined by frequency deviation $\Delta\omega$ and frequency change rate $\mathrm{d}\omega/\mathrm{d}t$ of the i^{th} area, and it will be explained in Section 3.1.

In summary, based on Eqs 1–9, the dynamic relationship between the WTs and the thermal plants in the AGC response model of subarea i can be expressed, from which a state-space model of the AGC response process in this subarea can also be obtained, as shown in Eq. 10:

$$\begin{cases} \dot{x}_i(t) = A_{ii}x_i(t) + B_{ii}u_i(t) + E_{ii}w_i(t) + \sum_{j\neq i}\left(A_{ij}x_j(t) + B_{ij}u_j(t)\right) \\ y_i(t) = C_{ii}x_i(t) \end{cases} \tag{10}$$

The parameters of the AGC state-space model of area i are as follows:

$$A_{ii} = \begin{bmatrix} -\frac{D_i}{2H_i} & \frac{1}{2H_i} & 0 & -\frac{1}{2H_1} & -\frac{1}{2H_1} & 0 & 0 \\ 0 & -\frac{1}{T_{Ti}} & \frac{1}{T_{Ti}} & 0 & 0 & 0 & 0 \\ -\frac{1}{R_iT_{Ti}} & 0 & -\frac{1}{T_{Ti}} & 0 & 0 & 0 & 0 \\ \sum_{\substack{j=1 \\ j\neq i}}^{M} T_{ij} & 0 & 0 & 0 & 0 & 0 & 0 \\ 0 & 0 & 0 & 0 & -\frac{1}{T_{fl}} & 0 & K_{RSC} \\ 0 & 0 & 0 & 0 & -1 & 0 & 0 \\ 0 & 0 & 0 & 0 & -\frac{k_{wp}}{T_{in}} & \frac{k_{wi}}{T_{in}} & -\frac{1}{T_{in}} \end{bmatrix}$$

$$B_{ii} = \begin{bmatrix} 0 & 0 \\ 0 & 0 \\ \frac{1}{T_{Gi}} & \frac{1-\beta_i}{T_{Gi}} \\ 0 & 0 \\ 0 & 0 \\ 0 & 1 \\ 0 & \frac{k_{wp}}{T_{in}} \end{bmatrix} \quad E_{ii} = \begin{bmatrix} -\frac{1}{2H_i} \\ 0 \\ 0 \\ 0 \\ 0 \\ 0 \\ 0 \end{bmatrix}$$

$$C_{ii} = \begin{bmatrix} B_i & 0 & 0 & 1 & 0 & 0 & 0 \end{bmatrix} x_i$$

$$= \begin{bmatrix} \Delta\omega_i & \Delta P_{mi} & \Delta P_{vi} & \Delta P_{tiei} & \Delta P_{CWESi} & \Delta P_{erri} & \Delta i_{rdi} \end{bmatrix}^T$$

$$u_i = \begin{bmatrix} \Delta P_{ref,Gi} & \Delta P_{ref,CWESi} \end{bmatrix}^T w_i = \Delta P_{Li}$$

$$A_{ij} = \begin{bmatrix} 0 & \cdots & 0 \\ \sum_{\substack{j=1 \\ j \neq i}}^{M} T_{ij} & \ddots & \vdots \\ 0 & \cdots & 0 \end{bmatrix} B_{ij} = [0]$$

In Eq. 10, x_i is the state variable of the state-space model and contains the main state indicators of each block in the AGC process of the i^{th} area; u_i is the input variable. The DMPC controller in this area modifies u_i according to the operating state of the system, thereby adjusting the output of the thermal plants and the CWES system to improve the AGC performance. A_{ij} and B_{ij} are the state variable and control variable coefficient matrixes of area i and its adjacent area j, respectively. In this paper, by adding the state information and control information of adjacent areas to the local state-space expression, coordinated communication between the controllers of each area is realized. w_i is the system disturbance variable. In this paper, the active load fluctuation is set as the disturbance variable in each subarea. y_i is the output variable of the state-space model of the i^{th} area. In this paper, the area control error ACE_i is set as the controller's output.

This section integrates the CWES in each subarea with traditional thermal power units into a unified AGC response model, and the wind power is integrated into the AGC process of each area by dynamically modifying the control parameters of local DMPC controller. As a result, the active AGC response capability of the CWES and conventional thermal generators inside multi-area grid can be fully utilized, and the ramping rate issue of conventional plants can be well alleviated.

3 Design of the DMPC algorithm and CWES cooperation strategy

3.1 Application of DMPC algorithm in interconnected power system

MPC is also known as rolling-horizon optimal control. The optimal closed-loop control sequence can be achieved by solving the optimal control problem at each control period, and only the initial step of the control sequence is applied. In the next time interval, a new optimization problem is established and solved based on the new measurement results. The application of MPC algorithms in interconnected power systems can be mainly divided into centralized MPC and distributed MPC (DMPC), but the centralized control architecture has the drawbacks of inflexible information communication and stability issues for large-scale interconnected systems with extensive geographic distribution scales and significant number of subsystems. Moreover, the computational burden of the upper-level controllers is always heavy. However, the DMPC algorithm transforms the large-scale constrained optimization problem into multiple small-scale local problems, and focusing on the

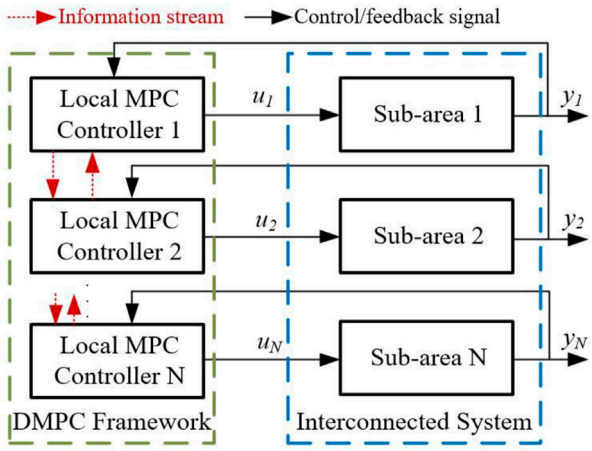

FIGURE 3
Framework of DMPC algorithm.

association among subsystems, the optimization decision of subsystems, and the information exchange to ensure a global stability of the interconnected system. In addition, each local MPC controller cooperates through iteration and coordination to meet the global control objectives set by the system, and the DMPC algorithm can achieve the same performance as the centralized MPC algorithm with reduced computation time. Moreover, the DMPC algorithm is able to ensure a closed-loop stability by satisfying the iteration's termination constraints. Considering that the modern interconnected power systems integrated with wind and thermal power units are typically geographically dispersed and complex systems with multiple interconnection areas, so the traditional centralized MPC models are complex with high dimensions and physical operation constraints. Therefore, under the DMPC control framework, the AGC of each sub-area is controlled by its local MPC controller without going through the upper-level controller, and the coordination of each subarea's AGC process at the system level can be achieved through information communication between local controllers, which can reduce the computational burden and improve the overall AGC control performance effectively.

The framework of DMPC algorithm is designed by dividing the entire interconnected system into several subsystems, and each of which has its own independent local MPC controller. The local controller solves the local optimization problem while considering the state and control variables of its neighbouring subsystems, including the constraints, objectives, disturbances, and interactions between the subsystems. In addition, each local controller achieves optimal control based on local information and improves the overall performance by sharing information with other controllers to achieve a global optimization goal of the interconnected system through the coordinated strategy. The

framework of DMPC is demonstrated in Figure 3. In this study, the AGC optimal control problem of a interconnected power system with combined wind-storage system is solved using a DMPC method.

1) Prediction model and objective function

At each control interval, the local DMPC controllers of each area will exchange prediction and operation information with its neighbour subareas. The discretization of AGC state-space model of multi-area power system can be transformed into:

$$\begin{cases} x_i(k+1) = A_{ii}x_i(k) + B_{ii}u_i(k) + E_{ii}w_i(k) + \sum_{j\neq i}\left(A_{ij}x_j(k) + B_{ij}u_j(k)\right) \\ y_i(k) = C_{ii}x_i(k) \end{cases} \tag{11}$$

Define the prediction variable $z_i(k)$, and its relationship with the state variable $x_i(k)$, disturbance variable $w_i(k)$ and control variable $u_i(k)$ is shown in Eq. 12:

$$z_i(k) = C_2x_i(k) + D_2w_i(k) + D_3u_i(k) \tag{12}$$

In summary, the objective function of the i^{th} subarea is shown in Eq. 17:

$$\min_{u_i'\theta} J_i\left(x_i'(t), u_i'\theta\right) \tag{13}$$

By substituting Eq. 12 into Eq. 13, the optimization target J_i can be expressed in Eq. 14:

$$J_i\left(x_i'(t), u_i'\theta\right) = \sum_{j=0}^{N_m} z_i'T(k+j|k)\Gamma(j)z_i'(k+j|k) \tag{14}$$

$$\begin{aligned} &\sum_{j=1}^{N_m} z_i'T(k+j|k)\Gamma(j)z_i'(k+j|k) \\ &= \sum_{j=1}^{N_p} x_i'T(k+j|k)Q_ix_i'(k+j|k) + \sum_{j=1}^{N_c} u_i'T(k+j|k)R_iu_i'(k+j|k) \end{aligned} \tag{15}$$

In the above equations, N_p and N_c are the prediction and control steps of each optimization interval, respectively. $x'_i(k+j|k)$ and $u'_i(k+j|k)$ are the AGC response model's prediction trajectories of the state variable and control variable in period T_p, respectively, and both trajectories' starting point is k. Q_i and R_i are the weighted positive definite matrixes in the i^{th} subarea and are used as weight matrixes in the optimization function to affect the optimization result. Q_i mainly affects the process of the state variable trending to the reference value, and R_i affects the control variable's variation range in each optimization interval. The weighted matrixes in Eq. 15 are set as $Q_1 = Q_2 = Q_3 =$ diag (100,0,0,0,0,100,100) and $R_1 = R_2 = R_3 =$ diag (1,0).

According to the discrete state-space model and the states of the model at k, the states in the future period N_p can be predicted. The prediction model based on the state variables and control variables of subarea i and its adjacent area j at time k can be expressed as follows:

$$\begin{aligned} x_i'\left(k+N_p|k\right) = {} & A_{ii}^{N_p}x_i(k) + \sum_{p=1}^{N_p} A_{ii}^{p-1}B_{ii}u_i\left(k+N_P-p\right) \\ & + \sum_{p=1}^{N_p} A_{ii}^{N_p-1}E_{ii}w_i\left(k+N_P-p\right) \\ & + \sum_{j\neq i}\left(A_{ij}^{N_p}x_j(k) + \sum_{p=1}^{N_p} A_{ij}^{p-1}B_{ij}u_j\left(k+N_P-p\right)\right) \end{aligned} \tag{16}$$

$$\begin{aligned} z_i'\left(k+N_p|k\right) = {} & C_2x_i'\left(k+N_p|k\right) + D_2w_i\left(k+N_p\right) + D_3u_i\left(k+N_p\right) \\ & + \sum_{j\neq i} x_j'\left(k+N_p|k\right) \end{aligned} \tag{17}$$

The prediction vectors z_i^*, u_i^* and w_i^* are defined as:

$$z_i^* = \begin{bmatrix} z_i'(k|k) \\ z_i'(k+1|k) \\ \vdots \\ z_i'\left(k+N_p|k\right) \end{bmatrix} u_i^* = \begin{bmatrix} u_i(k|k) \\ u_i(k+1|k) \\ \vdots \\ u_i\left(k+N_p|k\right) \end{bmatrix}$$

$$w_i^* = \begin{bmatrix} w_i(k|k) \\ w_i(k+1|k) \\ \vdots \\ w_i\left(k+N_p|k\right) \end{bmatrix}$$

The prediction vectors are substituted into Eq. 17, and the result is transformed into the following prediction vector form:

$$\begin{aligned} z_i^*(k) &= C_2^*x_i(k) + D_2^*w_i^*(k) + D_3^*u_i^*(k) + C_3^*\sum_{j\neq i} x_j(k) \\ &= p_i^*(k) + D_3^*u_i^*(k) \end{aligned} \tag{18}$$

By substituting the above equation into Eq. 15, the optimization objective function can be rewritten as:

$$\begin{cases} J_i\left(x_i'(t), u_i'\theta\right) = z_i^{*T}(k)\Gamma'(j)z_i^*(k) \\ \Gamma'(j) = \mathrm{diag}\left(\Gamma(0), \Gamma(1), \cdots, \Gamma\left(N_p-1\right)\right) \end{cases} \tag{19}$$

$$\begin{aligned} J_i\left(x_i', u_i'\right) &= u_i^{*T}(k)D_3^{*T}\Gamma'D_3^*u_i^*(k) + 2u_i^{*T}(k)D_3^{*T}\Gamma'p_i^*(k) + p_i^{*T}(k)\Gamma'p_i^*(k) \\ &= \frac{1}{2}u_i^{*T}(k)Hu_i^*(k) + u_i^{*T}(k)f(k) + c(k) \end{aligned} \tag{20}$$

In Eq. 20, $f(k)$ and $c(k)$ are functions of state variables and system disturbances at time k, respectively, which are known values, and H is a constant coefficient. By converting the objective function into a quadratic function form with $u_i^*(k)$ as the pending variable, the optimization functions for each control interval are:

$$\min_{u_i^*}\left(\frac{1}{2}u_i^{*T}Hu_i^* + u_i^{*T}f + c\right) \tag{21}$$

$$\begin{cases} H = 2D_3^{*T}\Gamma' D_3^* \\ f(k) = 2D_3^{*T}\Gamma' p_i^*(k) \\ c(k) = p_i^{*T}(k)\Gamma' p_i^*(k) \end{cases} \tag{22}$$

The transformation relationships between the main coefficient matrixes in the optimization model and the coefficient matrixes in the state-space model are as follows:

$$C_2^* = \begin{bmatrix} C_2 \\ C_2A_{ii} \\ C_2A_{ii}^2 \\ \vdots \\ C_2A_{ii}^{N_p} \end{bmatrix} D_2^* = \begin{bmatrix} D_2 & 0 & \cdots & 0 & 0 \\ C_2E_{ii} & D_2 & \cdots & 0 & 0 \\ C_2A_{ii}E_{ii} & C_2E_{ii} & \ddots & \vdots & \vdots \\ \vdots & \vdots & \ddots & D_2 & 0 \\ C_2A_{ii}^{N_p-1}E_{ii} & C_2A_{ii}^{N_p-2}E_{ii} & \cdots & C_2E_{ii} & D_2 \end{bmatrix}$$

$$C_3^* = \begin{bmatrix} C_2 \\ C_2A_{ij} \\ C_2A_{ij}^2 \\ \vdots \\ C_2A_{ij}^{N_p} \end{bmatrix} D_3^* = \begin{bmatrix} D_3 & 0 & \cdots & 0 & 0 \\ C_2B_{ii} & D_3 & \cdots & 0 & 0 \\ C_2A_{ii}B_{ii} & C_2B_{ii} & \ddots & \vdots & \vdots \\ \vdots & \vdots & \ddots & D_3 & 0 \\ C_2A_{ii}^{N_p-1}B_{ii} & C_2A_{ii}^{N_p-2}B_{ii} & \cdots & C_2B_{ii} & D_3 \end{bmatrix}$$

2) Constraints

According to (Ma et al., 2014), a typical value of the GRC (generation rate constraint, GRC) for a conventional synchronous generator is taken as 8%–10% per minute, and the power deviation rate of the conventional plant in the i^{th} area can be restricted to

$$|\Delta P_{mi}| = \left|\frac{\Delta P_{vi} - \Delta P_{mi}}{T_{Ti}}\right| \le 0.002 p.u. \tag{23}$$

The power increment constraints of both conventional generator and wind turbine can be expressed as

$$\begin{cases} |\Delta P_{ref,gi}| = \le 0.3 p.u. \\ |\Delta P_{ref,wtesi}| = \le 0.2 p.u. \end{cases} \tag{24}$$

Based on the above constraints and the expression of the state-space model of the multi-area power system, the constraints of the state variable and control variable in the objective function can be summarized as inequalities Eqs 25–27:

$$\left|\frac{x_{i3}(\delta) - x_{i2}(\delta)}{T_{Ti}}\right| \le 0.0034,\ \delta \in \left[t, t + T_p\right] \tag{25}$$

$$\left|u_i'(\delta)\right| \le 0.3,\ \delta \in \left[t, t + T_p\right] \tag{26}$$

$$\left|\frac{du_{i2}'(\delta)}{d\delta}\right| \le 0.0102, \delta \in \left[t, t + T_p\right] \tag{27}$$

In this section, according to the AGC regulation demand and the operating states of WTs and ES, fuzzy-based controllers FLC1 and FLC2 are designed for dynamic modification of u_i and cooperation inside the CWES system. Considering the physical constraints of the generation units in a subarea, by solving the DMPC-based optimal control objective function of each subarea, the WTs can take active part in the AGC response of each area to enhance the interconnected system's AGC performance.

3.2 Coordinated operation strategy of the CWES system in subarea i

Due to the output characteristics of WTs, it cannot be guaranteed that wind farms in multi-source interconnected power system are capable of acting AGC response under scenarios with fluctuating wind speed. However, in the early stage of the frequency response process of the multi-area power system, WTs may not be able to increase their power due to the wind speed. Because of the slow ramp rate of thermal plants and the large "wind-thermal replacement", the thermal plants alone cannot meet the AGC demand of this subarea, and there will be greater frequency fluctuations in this area, which will affect the frequency stability of the whole multi-area system. Therefore, to deal with the reliability problem in AGC response of wind farm, a coordinated control strategy of the CWES is proposed based on fuzzy theory. The Coordinated control and dynamic modification diagram of the CWES is demonstrated in Figure 4. This control diagram is composed of a DMPC parameter correction block and a CWES coordinated control block, which are introduced as follows:

1) Dynamic modification of DMPC

Each area's DMPC output are modified by β, and β (0–1) can be dynamically achieved through FLC1 as shown in Figure 4. The input variables Frequency deviation and frequency change rate are chosen as FLC1's input, and the data range can be found in reference (Peng et al., 2019). The fuzzy membership of FLC1 is depicted in Figure 5. The states of the input and output variables of FLC1 are described by five variables, and the reasoning rule of FLC1 is defined as: if frequency variation value or the absolute value of frequency change rate of local area is large, then DMPC modification coefficient β should be large; if frequency variation value is small and frequency change rate is nearly 0, then β should be small. The fuzzy reasoning rule of FLC1 is demonstrated in Table 1.

2) Coordinated operation strategy of the CWES system

By FLC1 and the fuzzy membership introduced above, the modified CWES active power for AGC response $\Delta P'_{ref,CWESi}$ can be calculated. Hereafter, in order to participate in AGC response under scenarios with varying wind speed, a fuzzy controller FLC2 is designed for the CWES as depicted in Figure 6. In FLC2, real-time wind speed data and state of charge (SOC) value are chosen as inputs of FLC2 to represent current operation states of CWES. Furthermore,

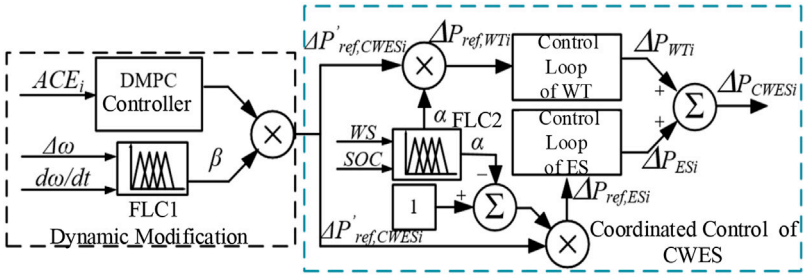

FIGURE 4
Coordinated control and dynamic modification diagram of CWES.

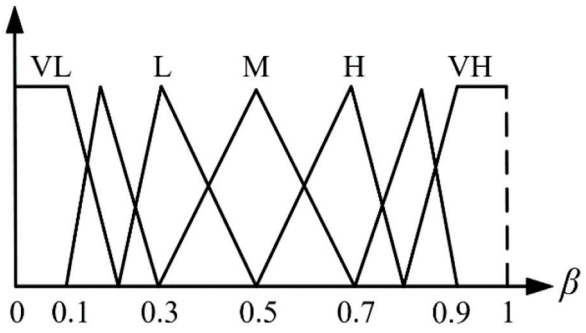

FIGURE 5
Fuzzy membership of FLC1 output.

TABLE 1 Reasoning rules of FLC1.

$d\omega/dt$	$\Delta\omega$						
	VL	ML	L	M	S	MS	VS
NL	VL	VL	VL	VL	VL	ML	L
NM	VL	VL	VL	VL	ML	L	L
NS	VL	VL	VL	ML	L	L	M
Z	VL	ML	ML	L	L	M	S
PS	ML	L	L	M	M	S	MS
PM	L	L	M	M	S	S	MS
PL	L	M	M	S	S	MS	VS

considering the AGC response demand and fluctuating wind scenario, reasoning rules of FLC2 are designed and the AGC cooperation factor α_t can be calculated. Finally, by deploying FLC2 in the active power control block of the CWES, then a dynamic AGC demand allocation between the WTs and ES can be realized, and the flexible cooperation inside the CWES can be expressed as Eq. 28:

$$\begin{cases} \Delta P_{ref,WTi} = \alpha_t \cdot \Delta P'_{ref,CWESi} \\ \Delta P_{ref,ESi} = (1-\alpha_t) \cdot \Delta P'_{ref,CWESi} \end{cases} \tag{28}$$

where $\Delta P_{ref,\ ES}$ and $\Delta P_{ref,\ WT}$ are the active power output reference of the wind turbine and energy storage unit, respectively. The sum of these two variables are the output of the CWES system, and the allocation of AGC response demand is adjusted by α_t.

The fuzzy linguistic variables defined in FLC2 are similar with FLC1. The fuzzy membership of FLC2 is depicted in Figure 6. It can be observed in Figure 6A, when SOC_t is below 0.2, which means there is little energy left in the ES, and the membership value can be set as VL. In addition, the membership which represents the level of wind speed is depicted in Figure 6B, according to operation characteristics of WTs studied in (Li et al., 2021a), the range of wind speed is defined from 0 to 17 m/s. Finally, as demonstrated in Figure 6C, α_t is set to [0, 1].

In this paper, the scenario of a sudden load increase in the interconnected system is used as an example for analysis. Based on this scenario, the basic fuzzy logic rules of the controller are designed as follows:

When the active power generation in the power system cannot meet its load, then the ES device will turn into discharge state, and the WTs will increase their power output to support the system frequency in rising back to the rated value. When the capacity of the ES is fixed, a higher SOC_t value indicates that the ES has sufficient electrical energy reserves for frequency support. Correspondingly, at that time, the active power reserve of WTs in the CWES system can be smaller. Moreover, when the WS_t value is low, the active power backup of WTs at this time can only meet some part of the AGC regulation order, so the frequency regulation capability of WTs at this time is weak. In summary, if the SOC_t value is high and the WS_t value is low, then the dynamic allocation coefficient α_t will take a higher value, which means that the ES will bear more AGC demand. If the SOC_t value is low and the WS_t value is high, then α_t will take a lower value in this scenario, indicating that the CWES system will

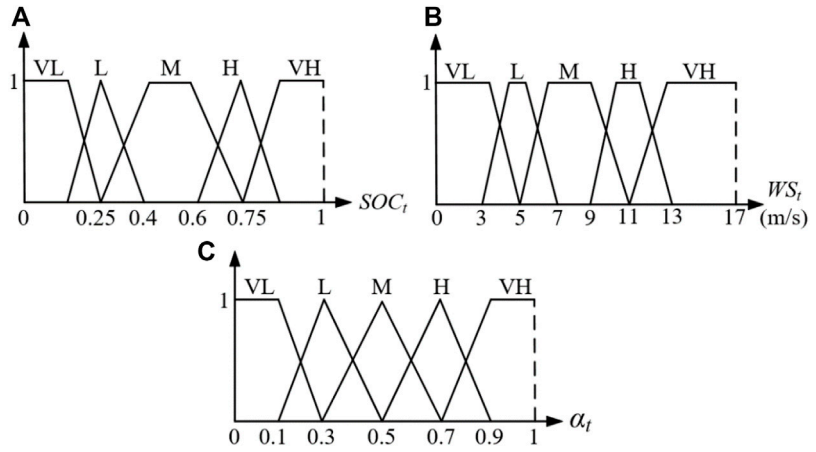

FIGURE 6
Fuzzy membership of FLC2. **(A)** Fuzzy membership of SOC **(B)** Fuzzy membership of wind speed **(C)** Fuzzy membership of FLC2's output.

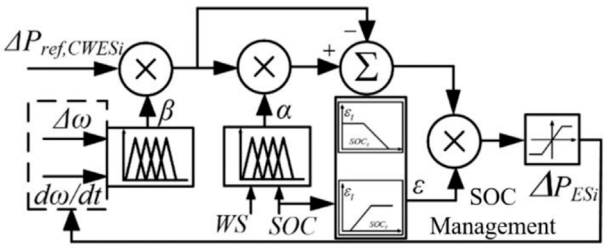

FIGURE 7
Control block of ES in subarea.

mainly use the active power reserve of WTs in response to the current AGC demand.

In the i^{th} area, the control block framework of energy storage units is depicted in Figure 7.

To fully utilize the limited ES capacity and avoid overcharging/discharging events during the subarea's AGC process, this section designs an output modification diagram for the ES control loop. According to the SOC of the ES, the ES output is flexibly modified to realize dynamic cooperation between the ES and WTs and a smooth power output as expressed as Eq. 29. In addition, the proposed SOC management strategy is improved based on former works. Moreover, a piecewise function is constructed to establish a linear relationship between ε_t and SOC_t to avoid a step change in ε_t with varying SOC. The relationship between ε_t and SOC_t is shown in Eqs 30, 31.

$$\Delta P_{ESi,t} = \varepsilon_t \cdot \Delta P_{ref,ESi,t} \tag{29}$$

$$\underset{\mu_t=1}{\varepsilon_t} = \begin{cases} 1 & 0 < SOC_t \le 0.75 \\ 1 - 5(SOC_t - 0.75) & 0.75 < SOC_t \le 0.95 \\ 0 & 0.75 < SOC_t \end{cases} \tag{30}$$

$$\underset{\mu_t=0}{\varepsilon_t} = \begin{cases} 1 & 0 < SOC_t \le 0.75 \\ 1 - 5(SOC_t - 0.75) & 0.75 < SOC_t \le 0.95 \\ 0 & 0.75 < SOC_t \end{cases} \tag{31}$$

Where ε_t is the correction factor of the ES output. When the ES is charging, μ_t equals 1, and μ_t will be set to 0 when the ES is discharging.

Based on the fuzzy logic algorithm, FLC1 and FLC2 are designed in this section to realize the unified AGC response of the CWES and conventional generator in each subarea, and dynamic cooperation inside the CWES system can also be achieved. Moreover, by applying the fuzzy-based FLC2 in the control loop of the CWES, the WTs are enabled to take active part in the AGC regulation of the multi-area power system reliably under scenarios with fluctuating wind speed, and the limited ES capacity can be fully exploited under the improved SOC management strategy. Then, by solving the optimal control objective function of the DMPC algorithm and considering the physical constraints of the thermal plants and CWES system in the subarea, the AGC performance can be improved at the level of whole multi-area power system.

3.3 Implementation steps of the DMPC algorithm in the interconnected multi-area system with CWES systems

The application steps of the proposed DMPC-CWES algorithm are demonstrated in Figure 8, and the entire control process can be divided into three parts: the initialization part (red

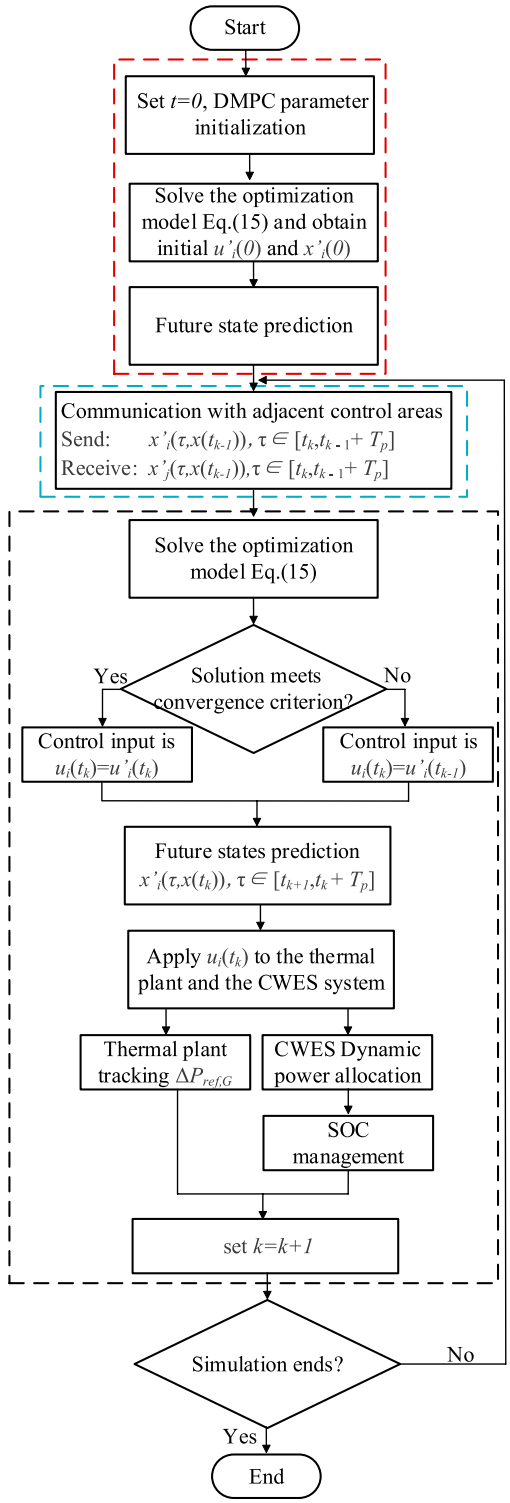

FIGURE 8
Flow chart of the proposed DMPC algorithm.

dashed box), the communication part (blue dashed box), and the MPC part (black dashed box). Each part is specifically introduced as follows:

Algorithm initialization part:

a) Initialize the DMPC algorithm and the interconnected system.
b) Solve the optimization model in Eq. 15, and obtain the first solutions of the control input $u_i^{'}(0)$ and state $x_i^{'}(0)$ under the initial conditions.
c) The first prediction will proceed with the initial state variable and control variable of the system to obtain future states.

Information communication part:

Information exchange between control areas. At time instant t_k, subarea i will send its previous predictions $x_i^{'}(\delta, x(t_{k-1}))$, $\delta \in [t_k, t_{k-1} + T_p]$ to the adjacent control areas and receive prediction and control information $x_j^{'}(\delta, x(t_{k-1}))$, $\delta \in [t_k, t_{k-1} + T_p]$ from other controllers.

MPC part:

a) Optimization: Solve the optimization model in Eq. 15.
b) If the solutions meet the convergence criterion, then the control input is $u_i(t_k) = u_i^{'}(t_k)$; otherwise, $u_i(t_k) = u_i^{'}(t_{k-1})$.
c) Predict the future states $x_i^{'}(\delta, x(t_k))$, $\delta \in [t_{k+1}, t_k + T_p]$.
d) Apply the control input to the thermal plants and the CWES system. Then, the thermal plants will track the reference generation setpoint $\Delta P_{ref,G}$. After the reference power of the CWES $\Delta P_{ref,CWES}$ is decided by the DMPC controller, the power demand will be dynamically allocated between the WT and ES units according to their operating states. The WTs can participate in the AGC with auxiliary support from ES under various wind conditions, and the ES life can be prolonged by the SOC management strategy.
e) Set k = k + 1. If the simulation is not complete, then return to the communication part.

4 Simulation and case study

4.1 Parameter settings

To verify the AGC response performance of the proposed control strategy, a 3-area test model is designed on the MATLAB/Simulink platform, as depicted in Figure 1. The test model consists of three interconnected power systems, and each sub-power system has its own CWES system with an equivalent 15 MW wind turbine model and a 2 MW/1 MWh energy storage unit. The installed capacity of the conventional thermal generators in each subarea is 20 MW. In order to verify the dynamic AGC response performance of the multi-area system under different control strategies, a sudden 0.1 p.u. load step increase is set at 6 s in area 1 and area 2. The sampling time of the

TABLE 2 Parameters applied in the simulation test.

sUBAREA	$D(Pu/Hz)$	H$(pu\,s)$	$R(Hz/pu)$	$B(pu/Hz)$	$T_G(s)$	$T_T(s)$
Area 1	2	2.5	1.2	1.5	0.08	0.4
Area 2	2.5	2.15	1.2	1.5	0.08	0.45
Area 3	2	2.2	1.2	1.5	0.1	0.4

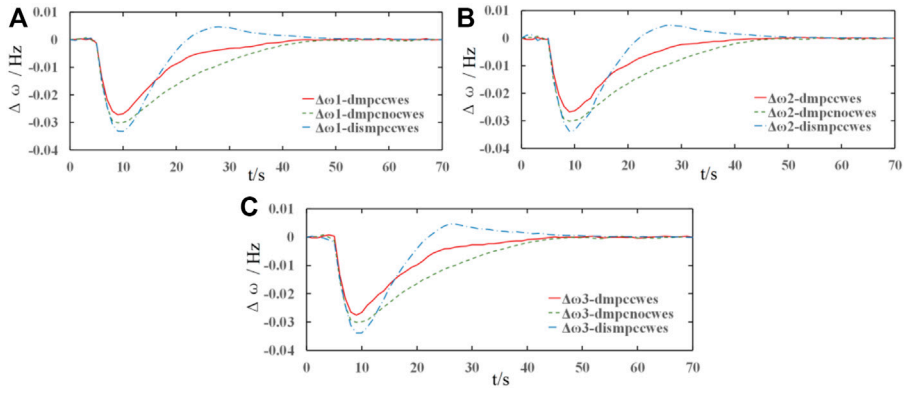

FIGURE 9
AGC response performance of multi-area power system. **(A)** AGC response performance in the 1st area; **(B)** AGC response performance in the 2nd area; **(C)** AGC response performance in the 3rd area.

TABLE 3 Test results in case A.

Control strategy	DMPC-CWES	DMPC	DISMPC-CWES
$\Delta f_{\max}(Hz)$	0.027	0.029	0.034
$t_{\text{stable}}(s)$	43	45	54

simulation scenarios is T_s = 1 s, and the prediction horizon T_p and control horizon T_c of the MPC algorithm are set as 10 s and 5 s, respectively. The parameters of the interconnected areas in the simulation are demonstrated in Table 2.

4.2 Simulation results and analysis

4.2.1 Case A

In this case, the multi-area simulation system is tested with fixed wind speed. Three kinds of control methods including the proposed DMPC-CWES strategy have been tested and compared in this case. The test results of this case are depicted in Figures 9–14.

The AGC performance of each subarea is shown in Figure 9. The red solid curves represent the simulation results under the proposed DMPC strategy with CWES auxiliary support; the green dotted lines show the response results under the DMPC strategy without the CWES system, and the blue dashed curves display the response performance of the distributed MPC algorithm. The test data results in case A are listed in Table 3, and Δf_{max} is the maximum average value of frequency fluctuation and t_{stable} is the average period for frequency to recover to stable state.

From Figures 9A–C, it is apparent that the frequency maximum variation and the frequency recovery time and the steady-state stability under the proposed DMPC algorithm with CWES demonstrate better performance than those of the other control strategies. Figures 9A is taken for further analysis because the frequency response performance is similar in each subarea. Comparing both DMPC algorithm results shown in Figures 9A, the algorithm with auxiliary frequency support from the CWES system shows better response performance than the control strategy without the CWES system. During the frequency response process, the CWES takes an active part in the AGC process. Moreover, both the WT and ES units have better power order tracking features than conventional thermal plants; therefore, when the load step occurs, the CWES system responds to the power imbalance immediately by injecting active power into the interconnected system, so the red curve exhibits smaller frequency variation than the green curve without the CWES system. Owing to the GRC constraints on the thermal

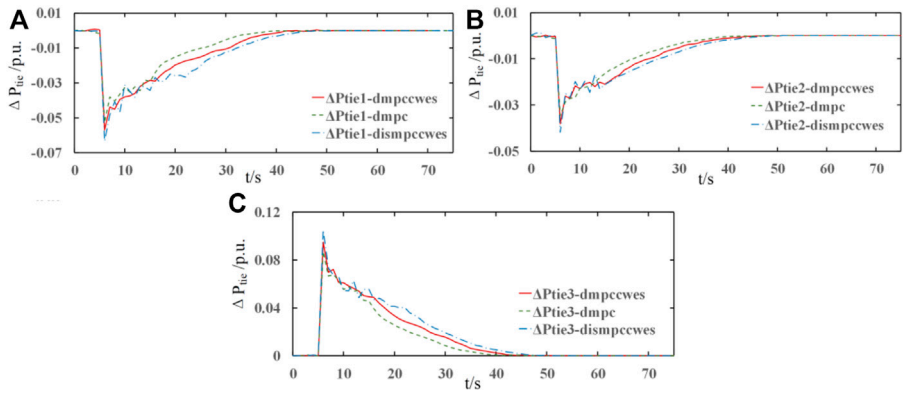

FIGURE 10
Power exchange of tie-lines between the adjacent areas. **(A)** active power exchange in the 1st area; **(B)** active power exchange in the 2nd area; **(C)** active power exchange in the 3rd area.

plants, the green curves take more time to return to steady state. It can be observed that in all three images in Figure 9, the control performance under the distributed MPC algorithm has the largest frequency variation and fluctuation during the AGC response process. In the distributed MPC control algorithm, the frequency of the interconnected power system may eventually return to the normal value. However, due to the lack of prediction and control information exchange between subareas during the AGC control process, the sub-MPC controllers focus more on their local control targets than on coordination from an interconnected system perspective, leading to a less satisfactory simulation result.

The connections between subareas are maintained by tie-lines, and the active power exchange during the AGC process is also realized through them. The tie-line active power exchange in each subarea under different control methodologies is displayed in Figures 10A–C, and the appearances of the curves are the same as those in Figure 1. As can be observed in Figures 10A, the ΔP_{tie} curves under the DMPC algorithm are smoother than the control performance under the distributed MPC strategy. Owing to the lack of information communication with other sub-MPC controllers, there are more power fluctuations in the tie-line power change process. Moreover, it can also be observed that the dotted green curves are slightly closer to zero than the solid red curves, which means that more power is exchanged through the tie-lines under the DMPC mode with CWES auxiliary support. According to the curves shown in Figure 9, the frequency is restored to the normal value quicker than in the strategy without CWES support. Although the blue curves may show that more energy is exchanged *via* the tie-lines than in the other two situations during certain periods, the negative influences of tie-line power fluctuations under the distributed MPC mode are much larger than those under the DMPC mode. Moreover, because the load step occurs in area 1 and area 2, as displayed in Figure 10, active power is injected into these two areas through the tie-lines to support the power imbalance in these two areas. In contrast, the power flows from area 3 to the other areas, and this also demonstrates that the AGC control target of the whole system is achieved through coordination among subareas inside the interconnected system. Therefore, in the design process of the AGC controller, the control and prediction information communication between subareas should be fully considered like that in the proposed DMPC algorithm, and the control performance has been clearly improved, as shown in Figures 9, 10.

In the interconnected multi-area system, the AGC response is mainly realized by the generation units, and most of them are conventional thermal units. The power output variation simulation results ΔPm of the conventional thermal plants in each subarea are shown in Figure 11. It is apparent that the simulation curves in Figures 11A,B have similar trends, and it is reasonable to choose Figures 10A for the control performance analysis of the 1st and 2nd area. As depicted in Figure 11A, ΔP_m under the proposed DMPC strategy with CWES reaches its steady output state at t = 38 s, and the steady-state time of ΔP_m under DMPC without CWES is 42 s. Although the results of the DMPC methods share similar times for reaching the steady state, ΔP_m of the DMPC algorithm with CWES auxiliary support has a faster response speed, and the fast response ability is realized by coordinated operation between the WT and ES units inside the CWES system. Therefore, the frequency support performance under this control strategy is better than that of the other two methods. Moreover, the simulation results under the distributed MPC algorithm show more fluctuation features than those under the DMPC algorithm, and the time when steady state is reached is t = 44 s, which is longer than that of the former control methods. Figure 11C demonstrates the simulation results of the active power variation of the thermal plants in area 3, and it can be clearly observed that ΔP_m in area 3 returns to 0 after reaching the steady state. Area 3 mainly

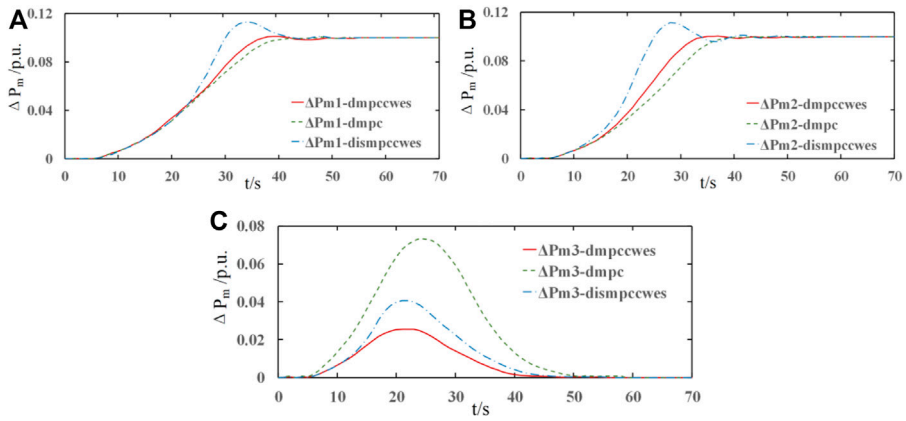

FIGURE 11
Active power output variation of the conventional generators in the interconnected areas. **(A)** Active power trajectory in the 1st area; **(B)** active power trajectory in the 2nd area; **(C)** active power trajectory in the 3rd area.

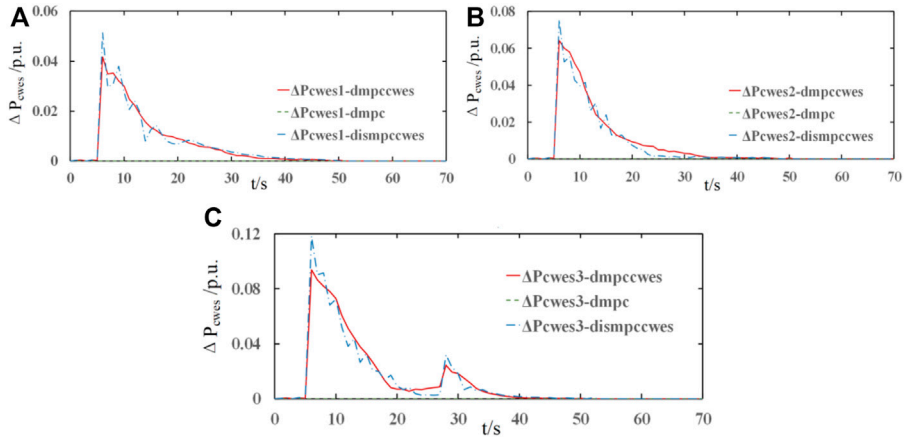

FIGURE 12
Active power output variation of the CWES systems in each subarea in the AGC response process: **(A)** active power variation of the CWES in the 1st area; **(B)** active power variation of the CWES in 2nd area; **(C)** active power variation of the CWES in the 3rd area.

provides active power support for the other two areas in the AGC process, and there is no load step in this area. Therefore, ΔP_m in area 3 is 0 at steady state, and ΔP_m is 0.1 p. u. MW in both the area 1 and area 2 to make up for the energy imbalance generated by the load steps.

Notably, the power variation curves under DMPC without the CWES system are higher than those curves of the other two strategies. This means that without the auxiliary AGC support of the CWES system, the power generation burden of thermal power plants in area 3 to provide power support for area 1 and area 2 is much heavier than that of the control strategy with the CWES system.

Figure 12 illustrates the simulation results of the power output variation of the CWES systems in the three interconnected areas, and the results under different control algorithms are displayed in different colours for comparison. Notably, in all three images in Figure 12, the power variation under the DMPC algorithm without the CWES system is zero; therefore, only the test results under the proposed DMPC-CWES control framework and the distributed MPC algorithm are compared and displayed in Figure 12.

As demonstrated in Figures 12A,B, all the CWES power variation curves step up at t = 6 s to respond to the active power load steps in area 1 and area 2. Due to the generation rate

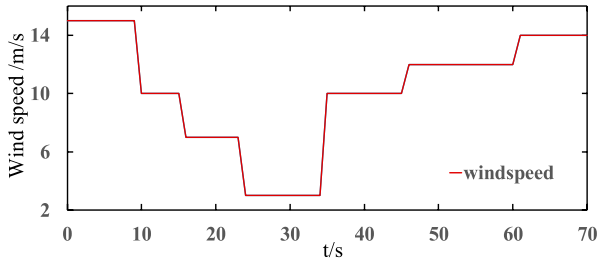

FIGURE 13
Varying wind speed for testing the CWES in the multi-area power system.

constraints of conventional thermal plants in the interconnected power system, the active power imbalance cannot be compensated immediately. Therefore, during the early stages of the power imbalance, the CWES system assumes the main role of frequency support and makes a quick response to the AGC requirements to prevent the system frequency from falling to a lower level. Moreover, with the auxiliary energy from the CWES, the AGC burden of the conventional thermal plants can be effectively alleviated. Then, as the AGC process proceeds, the main AGC responsibility gradually shifts from the CWES systems to the thermal plants in the interconnected system because the long-term AGC power generation matches the features of the thermal plants. Although the CWES system can provide auxiliary frequency support under both control algorithms, in terms of control performance, it can be clearly observed that there are more fluctuations in the distributed MPC algorithm than in the proposed control strategy. Due to the absence of control information exchange between sub-MPC controllers in each area, the power generated from the WTs and ES changes more frequently, leading to unsatisfactory control performance compared with that of the proposed DMPC algorithm with information sharing.

Notably, as shown in Figure 12C, there is another generation step up at t = 28 s for frequency support with a smaller margin than that at t = 6 s. As shown in Figure 11C, ΔP_m of the thermal plants in area 3 begins gradually decreasing to 0; however, the AGC process is still ongoing, so the power outputs of the CWES system increase again to alleviate the AGC burden on the thermal plants.

4.2.2 Case B

Considering the wind speed in practical scenarios is fluctuating, therefore it is essential to test the control performance of the proposed control strategy under a varying wind condition. The range of the test wind speed fluctuates from 3 m/s to 14 m/s, which covers the most operation states of the WT. The wind speed trajectory is depicted in Figure 13.

TABLE 4 Test results in case B.

Control strategy	$\Delta f_{15s}\,(Hz)$	$\Delta f_{22s}\,(Hz)$	$t_{\text{stable}}\,(s)$
DMPC-CWES	0	0.001	43
DMPC-WT	0.003	0.01	54

In case B, the AGC response capability of the WT and ES is fully utilized through fuzzy controller FLC1, FLC2, and SOC management. The test results data under fluctuating wind speed are listed in Table 4. Δf_{15s} and Δf_{22s} are the frequency drops caused by the wind speed changes at t = 15 s and 22 s, respectively; $t_{stable}(s)$ is the period when the frequency recovers to stable state.

The test results are depicted in Figure 14A. The simulation results in Figure 14A are obtained under the same DMPC algorithm, except that the red curve represents auxiliary support from the CWES system and the green curve indicates without that support. The curves show similar control performance until the wind speed drops from 10 m/s to 7 m/s at t = 15 s. When the WT operates under a wind speed higher than 10 m/s, it achieves the rated power output. However, when the wind speed drops below 10 m/s, the WT has to change into the MPPT mode, in which it adjusts its power output according to the wind speed; therefore, the power for AGC support is restrained by the current wind conditions. When there is no ES unit to compensate for the insufficient power that should be generated by the WT, the mode with only the WT exhibits a second frequency drop at t = 15 s, as shown by the green dashed curve in Figure 14A. Moreover, at t = 22 s, a greater decrease occurs in the wind speed, which drops by 3 m/s. In this wind condition, the WT will stop generating power, and the AGC support process will be suspended. As demonstrated from Figures 14A–C, after t = 22 s, there is no power from the WTs for AGC support, and the frequency drops again due to the sudden power imbalance caused by the stopping of the WTs. In contrast, under the proposed DPMC-CWES control algorithm, the negative influences on the control performance caused by the varying wind conditions are much smaller than those without the CWES system. In Figure 14A, the frequency fluctuations in the red curve at t = 15 s and t = 22 s are obviously smaller than those in the green curve. As shown in Figure 14B, after t = 22 s, the green curve reaches 0, which means that the WTs stop supporting the AGC process, while the power from the CWES system still responds to the AGC demand until the frequency returns to a normal value. As shown in Figure 14C, in spite of its lower power output as wind speed decreases, the WT still can respond to AGC regulation demand effectively, and the ES generates additional power to make up for the power imbalance caused by WT's exit. Figure 14D demonstrates the ES power output inside the CWES system during the AGC process. When the wind speed drops and the power from WTs decreases,

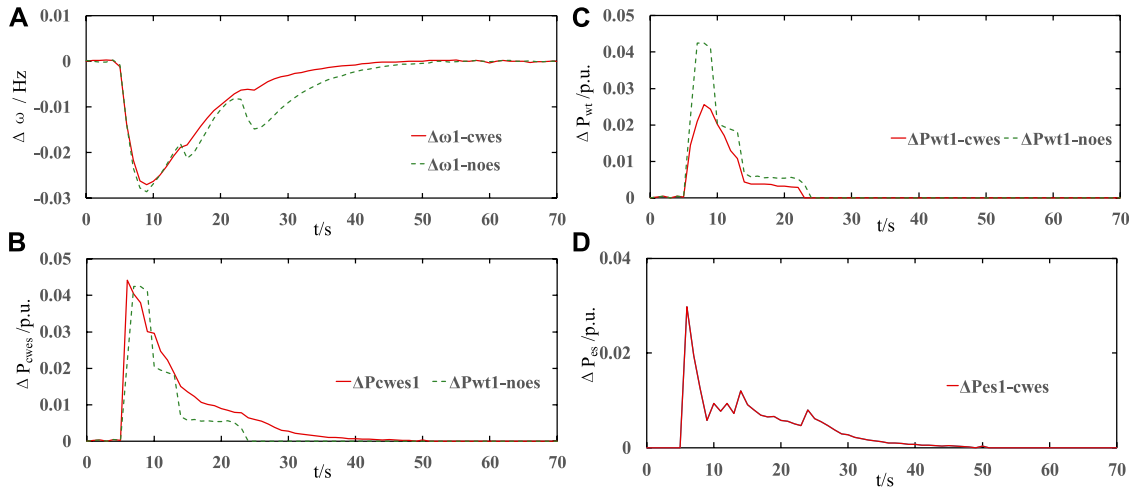

FIGURE 14
Test results under fluctuating wind speed: **(A)** frequency simulation trajectory under the DMPC-CWES and no-ES strategy in the 1st area, **(B)** active power of the wind farm under the DMPC-CWES and no-ES strategy in the 1st area, **(C)** active power of the CWES under the DMPC-CWES and no-ES strategy in the 1st area, and **(D)** active power output curve of the ES.

TABLE 5 Test results of AGC performance under different control strategies.

Control strategy type	Average frequency settling time (s)		1st Δ_ω Nadir ($\times10^{-2}$Hz)			2nd Δ_ω Nadir ($\times10^{-2}$Hz)		
	First drop	Second drop	$\Delta_{\omega1}$	$\Delta_{\omega2}$	$\Delta_{\omega3}$	$\Delta_{\omega1}$	$\Delta_{\omega2}$	$\Delta_{\omega3}$
GAPI (Abd-Elazim and Ehab, 2018)	41	20	−4.6	−4.7	−4.7	−2.9	−2.8	−2.9
FPID (Aziz et al., 2019)	38	17	−3.4	−3.4	−3.5	−2.0	−2.1	−2.0
DEPID (Mohanty et al., 2014)	41	18	−4.0	−3.9	−3.9	−2.3	−2.3	−2.2
FOFPID (Arya, 2017)	37	16	−2.9	−2.9	−3.0	−1.6	−1.6	−1.5
CENTMPC (Shiroei and Ranjbar, 2014)	38	14	−3.0	−3.1	−3.1	−1.2	−1.2	−1.2
DMPC	31	8	−2.8	−2.9	−2.8	−0.8	−0.8	−0.8

the ES power will ramp up to meet the AGC demand for the CWES system to ensure that the CWES system can exhibit adaptability and reliability for operating in varying wind conditions.

This case demonstrates that the proposed DMPC-CWES coordinated operation strategy is capable of adapting operation scenarios with fluctuating wind speed, and the AGC response performance of the multi-area power system can also be assured.

4.2.3 Comparison with other AGC control strategies

In this section, the AGC control performance of control strategies applied this paper and other research works on the AGC problem of the interconnected power system are compared. The comparison tests are conducted on the same simulation system of Section 4.1, a sudden 0.1 p.u. load step increase is set at 6 s in area 1 and area 2. In addition, a wind speed fluctuation event is set at 46 s in order to compare the reliability of different AGC control strategies under varying wind speed. The comparison results are listed in Table 5, and the simulation result is demonstrated in Figures 15, 16.

Besides the proposed DMPC-based AGC control strategy, five other AGC control strategies are tested in this section, including the GAPI (Genetic algorithm-based PI controller), FPID (Fuzzy algorithm-based PID), DEPID (differential evolution algorithm based PID), FOFPID (fractional order fuzzy PID), and CENTMPC (centralized MPC). As demonstrated in Figure 15, the DMPC, CENTMPC and FOFPID have better performance in lifting the frequency

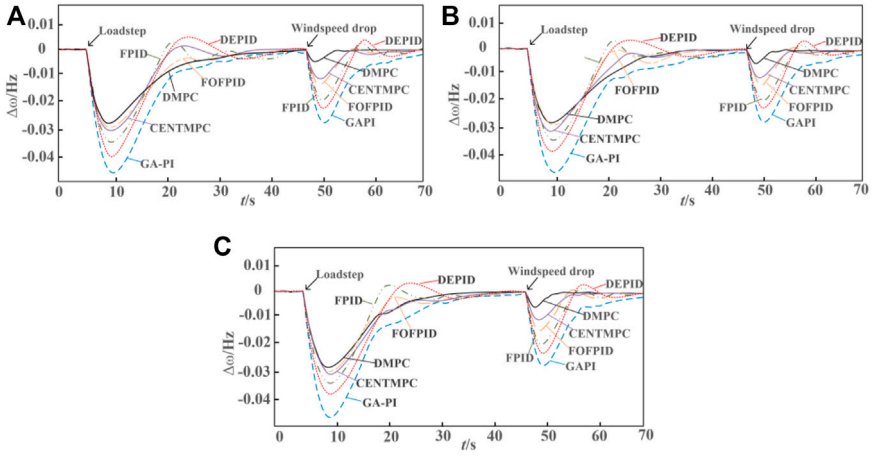

FIGURE 15
AGC response performance of multi-area power system under different control strategies. **(A)** AGC response performance in the 1st area; **(B)** AGC response performance in the 2nd area; **(C)** AGC response performance in the 3rd area.

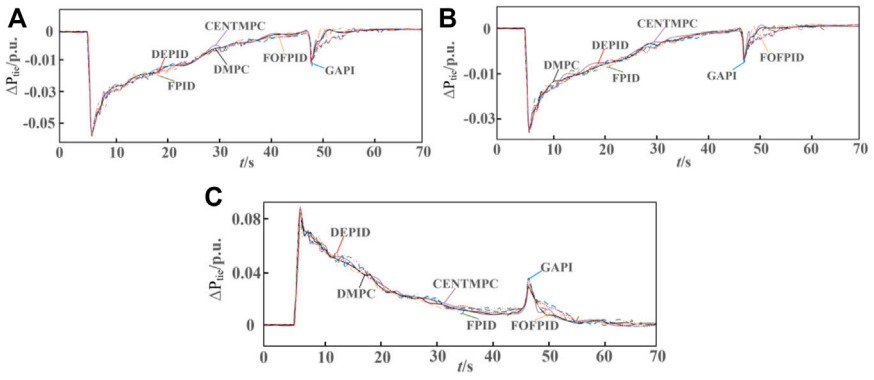

FIGURE 16
Power exchange of tie-lines between the adjacent areas under different control strategies. **(A)** active power exchange in the 1st area; **(B)** active power exchange in the 2nd area; **(C)** active power exchange in the 3rd area.

nadir caused by sudden load step than the other three strategies, and average frequency variation settling time of the proposed DMPC-based strategy in the first frequency drop event is 38 s, which is the shortest of all the AGC strategies in the comparison test. After windspeed fluctuation at t = 46 s, there is a second frequency drop, and the frequency nadir is -0.8×10^{-2} Hz under the proposed strategy and it outperforms the other AGC strategies due to the coordinated operation between windfarm and thermal plants as well as the active AGC response from the combined wind and energy storage system. In addition, as can be observed in Figure 16, due to the coordinated multi-source operation and the effective information communication between local MPC controllers in each control step, there is less fluctuations and power overshoots in the exchanged tie-line power under the proposed AGC strategy than the other strategies under a centralized and uncoordinated control framework.

4.3 Discussion

Three simulation scenarios are designed to validate the proposed AGC control strategy. In Case A, the combined wind-storage systems inside the multi-area power system operate under fixed wind speed to validate the effectiveness of the proposed coordinated AGC strategy. In Case B, a varying windspeed has been added to the test system to test the

adaptability and reliability of the proposed strategy under practical complex operation scenarios. Finally, in Section 4.3, comparisons among other AGC control strategies in existing works have been made to validate the outstanding performance of the proposed control strategy for the interconnected power system with high wind power integration.

From the numerical results in Section 4.2, it demonstrates that during the frequency response process, by exchanging the prediction and state information with adjacent subsystems in the distributed MPC control framework, the power fluctuations of tie-lines can be apparently depressed than the other control strategies. Moreover, through the coordinated operation strategy for multi-sources inside the interconnected power system, the combined wind-storage system can take an active part in the AGC process, and the AGC response burden of conventional thermal plants can be alleviated significantly. Specially in Section 4.2.3, comparisons with other AGC control strategies also demonstrates the effectiveness and the adaptability of the proposed control strategy for the specified interconnected power system with multiple energy sources and high wind power penetration rate. Although other AGC control strategies in existing works both have outstanding control performance for interconnected power system, there still exist a performance gap compared to the proposed coordinated control strategy due to the lack of coordination between fluctuating wind energy, thermal plants with physical constraints and features of energy storage units. In conclusion, the overall AGC performance of an interconnected multi-source power system can be effectively improved through the DMPC-based coordinated AGC control strategy.

In this paper, the focus of the proposed control strategy lies on the coordinated operation of the combined wind-storage system and the complementary characteristics between wind turbine, energy storage units and traditional thermal plants to achieve the improvement of AGC performance. The authors assume that each area communicates through a dedicated AGC channel, and the time delay effect of the signal is ignored. However, with the increasing scale of grid interconnection, AGC needs to transmit wide-area control signals with the help of open communication networks, which may generate large time delays and negatively affect the control performance. Therefore, the impact of communication time delay on the AGC control performance in large-scale interconnected grids needs to be considered in future work to make further improvements and enhancements to the control strategy.

5 Conclusion

This paper designed a novel coordinated AGC control strategy for an interconnected multi-source power system based on distributed model predictive control algorithm. The multi-source interconnected power system is separated into three subsystems, and local DMPC controllers are deployed in each area to address the drawbacks of a centralized control architecture by exchanging forecast and state measurement information with adjacent areas. Additionally, in each subarea, the operation parameters of the CWES and local thermal generators are created into a synthetic state-space model that allows for a flexible cooperation between wind farm and thermal plants to enhance the AGC performance at the level of the interconnected system. In addition, taking into consideration the current operating points of the CWES, a fuzzy-based coordinated operation scheme is designed for the purpose of dynamically allocating the AGC power demand inside the CWES system. Consequently, dynamic collaboration between WTs and ES can be realized, and the CWES's reliability for AGC in diverse operation scenarios can be guaranteed. Finally, the effectiveness of the proposed DMPC-CWES AGC response strategy is validated by simulation tests on a three-area multi-source power system with high wind penetration, numerical results demonstrate that the proposed coordinated AGC control strategy has better performance in AGC performance and the dynamic cooperation can be achieved between wind power and thermal plants in AGC response through the designed wind-storage system and coordinated DMPC AGC control strategy.

Data availability statement

The original contributions presented in the study are included in the article/supplementary material, further inquiries can be directed to the corresponding author.

Author contributions

Conceptualization, BP and XM; methodology, BP; software, XXM; validation, BP, CT, and YS; formal analysis, YS; investigation, CT; data curation, BP; writing—original draft preparation, BP; writing—review and editing, BP; visualization, XM; supervision, BP; project administration, BP; funding acquisition, BP. All authors have read and agreed to the published version of the manuscript.

Funding

This work is supported in part by the Natural Science Youth Foundation of Shandong province under Grant ZR2021QE240, and in part by PhD Research Fund of Shandong Jianzhu University under Grant X21040Z.

Conflict of interest

Author YS was employed by Jinan Yuny Technology Co., Ltd.

The remaining authors declare that the research was conducted in the absence of any commercial or financial relationships that could be construed as potential conflict of interest.

Publisher's note

References

Abazari, Ahmadreza, Hassan, Monsef, and Wu, Bin (2019). Load frequency control by de-loaded wind farm using the optimal fuzzy-based PID droop controller. *IET Renew. Power Gener.* 131, 180–190. doi:10.1049/iet-rpg.2018.5392

Abd-Elazim, Sahar M., and Ehab, S. Ali. (2018). Load frequency controller design of a two-area system composing of PV grid and thermal generator via firefly algorithm. *Neural comput. Appl.* 302, 607–616. doi:10.1007/s00521-016-2668-y

Arya, Yogendra. (2017). AGC performance enrichment of multi-source hydrothermal gas power systems using new optimized FOFPID controller and redox flow batteries. *Energy* 127, 704–715. doi:10.1016/j.energy.2017.03.129

Aziz, S., Wang, H., Liu, Y., Peng, J., and Jiang, H. (2019). Variable universe fuzzy logic-based hybrid LFC control with real-time implementation. *IEEE Access* 7, 25535–25546. doi:10.1109/access.2019.2900047

Chang-Chien, L., Sun, C., and Yeh, Yu-Ju (2013). Modeling of wind farm participation in AGC. *IEEE Trans. Power Syst.* 293, 1204–1211.

Chen, Min-Rong, Zeng, Guo-Qiang, and Xie, Xiao-Qing (2018). Population extremal optimization-based extended distributed model predictive load frequency control of multi-area interconnected power systems. *J. Frankl. Inst.* 35517, 8266–8295. doi:10.1016/j.jfranklin.2018.08.020

Debbarma, S., Chandra Saikia, L., and Sinha, N. (2013). AGC of a multi-area thermal system under deregulated environment using a non-integer controller. *Electr. Power Syst. Res.* 95, 175–183. doi:10.1016/j.epsr.2012.09.008

Hasanien, H. M., and El-Fergany, A. A. (2019). Salp swarm algorithm-based optimal load frequency control of hybrid renewable power systems with communication delay and excitation cross-coupling effect. *Electr. Power Syst. Res.* 176, 105938. doi:10.1016/j.epsr.2019.105938

Jain, A., Chakrabortty, A., and Emrah, B. (2018). Distributed wide-area control of power system oscillations under communication and actuation constraints. *Control Eng. Pract.* 74, 132–143. doi:10.1016/j.conengprac.2018.03.003

Kocaarslan, Ilhan, and Çam, Ertuğrul (2005). Fuzzy logic controller in interconnected electrical power systems for load-frequency control. *Int. J. Electr. Power & Energy Syst.* 278, 542–549. doi:10.1016/j.ijepes.2005.06.003

Li, H., Deng, J., Feng, P., Pu, C., Arachchige, D. D. K., and Cheng, Q. (2021). Short-term nacelle orientation forecasting using bilinear transformation and ICEEMDAN framework. *Front. Energy Res.* 9, 780928. doi:10.3389/fenrg.2021.780928

Li, H. (2022), SCADA data based wind power interval prediction using LUBE-based deep residual networks. *Front. Energy Res.* 10, 920837. doi:10.3389/fenrg.2022.920837

Li, H., Deng, J., Yuan, S., Feng, P., and Arachchige, D. D. K. (2021). Monitoring and identifying wind turbine generator bearing faults using deep belief network and EWMA control charts. *Front. Energy Res.* 9, 799039. doi:10.3389/fenrg.2021.799039

Li, H. (2022). Short-term wind power prediction via spatial temporal analysis and deep residual networks. *Front. Energy Res.* 662. doi:10.3389/fenrg.2022.920407

Lv, X., Sun, Y., Wang, Y., and Dinavahi, V. (2020). Adaptive event-triggered load frequency control of multi-area power systems under networked environment via sliding mode control. *IEEE Access* 8, 86585–86594. doi:10.1109/access.2020.2992663

Ma, M., Chen, H., Liu, X., and Allgower, F. (2014). Distributed model predictive load frequency control of multi-area interconnected power system. *Int. J. Electr. Power & Energy Syst.* 62, 289–298. doi:10.1016/j.ijepes.2014.04.050

Ma, M., Zhang, C., Liu, X., and Chen, H. (2017). Distributed model predictive load frequency control of the multi-area power system After deregulation. *IEEE Trans. Ind. Electron.* 646, 5129–5139. doi:10.1109/tie.2016.2613923

Magdy, Gaber, Mohamed, E. A., Shabib, G., Elbaset, A. A., and Mitani, Y. (2018). SMES based a new PID controller for frequency stability of a real hybrid power system considering high wind power penetration. *IET Renew. Power Gener.* 1211, 1304–1313. doi:10.1049/iet-rpg.2018.5096

Mohanty, Banaja, Panda, Sidhartha, and Hota, P. K. (2014). Controller parameters tuning of differential evolution algorithm and its application to load frequency control of multi-source power system. *Int. J. Electr. power & energy Syst.* 54, 77–85. doi:10.1016/j.ijepes.2013.06.029

Peng, B., Zhang, F., Liang, J., Ding, L., Liang, Z., and Wu, Q. (2019). Coordinated control strategy for the short-term frequency response of a DFIG-ES system based on wind speed zone classification and fuzzy logic control. *Int. J. Electr. Power & Energy Syst.* 107, 363–378. doi:10.1016/j.ijepes.2018.11.010

Shayeghi, H., Shayanfar, H. A., and Malik, O. P. (2007). Robust decentralized neural networks based LFC in a deregulated power system. *Electr. Power Syst. Res.* 77, 3241–4251. doi:10.1016/j.epsr.2006.03.002

Shiroei, M., and Ranjbar, A. M. (2014). Supervisory predictive control of power system load frequency control. *Int. J. Electr. Power & Energy Syst.* 61, 70–80. doi:10.1016/j.ijepes.2014.03.020

Venkat, Aswin N., Hiskens, I., Rawlings, J., and Wright, S. (2008). Distributed MPC strategies with application to power system automatic generation control. *IEEE Trans. Control Syst. Technol.* 166, 1192–1206. doi:10.1109/tcst.2008.919414

Wen, S., Yu, X., Zeng, Z., and Wang, J. (2015). Event-triggering load frequency control for multiarea power systems with communication delays. *IEEE Trans. Ind. Electron.* 632, 1308–1317. doi:10.1109/tie.2015.2399394

Wu, Ziping, Gao, D. W., Zhang, H., Yan, S., and Wang, X. (2017). Coordinated control strategy of battery energy storage system and PMSG-WTG to enhance system frequency regulation capability. *IEEE Trans. Sustain. Energy* 83, 1330–1343. doi:10.1109/tste.2017.2679716

Xiong, L., Li, H., and Wang, J. (2018). LMI based robust load frequency control for time delayed power system via delay margin estimation. *Int. J. Electr. Power & Energy Syst.* 100, 91–103. doi:10.1016/j.ijepes.2018.02.027

Yousef, Hassan A., Al-Kharusi, K., Albadi, M. H., and Hosseinzadeh, N. (2014). Load frequency control of a multi-area power system: An adaptive fuzzy logic approach. *IEEE Trans. Power Syst.* 294, 1822–1830. doi:10.1109/tpwrs.2013.2297432

Yuan, Y., Zhang, P., Wang, Z., and Chen, Y. (2020). Noncooperative event-triggered control strategy design with round-robin protocol: Applications to load frequency control of circuit systems. *IEEE Trans. Ind. Electron.* 67 (3), 2155–2166. doi:10.1109/tie.2019.2903772

Zhang, C.-K., Jiang, L., Wu, Q. H., He, Y., and Wu, M. (2013). Delay-dependent robust load frequency control for time delay power systems. *IEEE Trans. Power Syst.* 283, 2192–2201. doi:10.1109/tpwrs.2012.2228281

Zhang, Chunyu, Wang, Shouxiang, and Zhao, Qianyu (2021). Distributed economic MPC for LFC of multi-area power system with wind power plants in power market environment. *Int. J. Electr. Power & Energy Syst.* 126 (2021), 106548. doi:10.1016/j.ijepes.2020.106548

Frontiers in
Energy Research

Advances and innovation in sustainable, reliable and affordable energy

Explores sustainable and environmental developments in energy. It focuses on technological advances supporting Sustainable Development Goal 7: access to affordable, reliable, sustainable and modern energy for all.

Discover the latest Research Topics

See more →

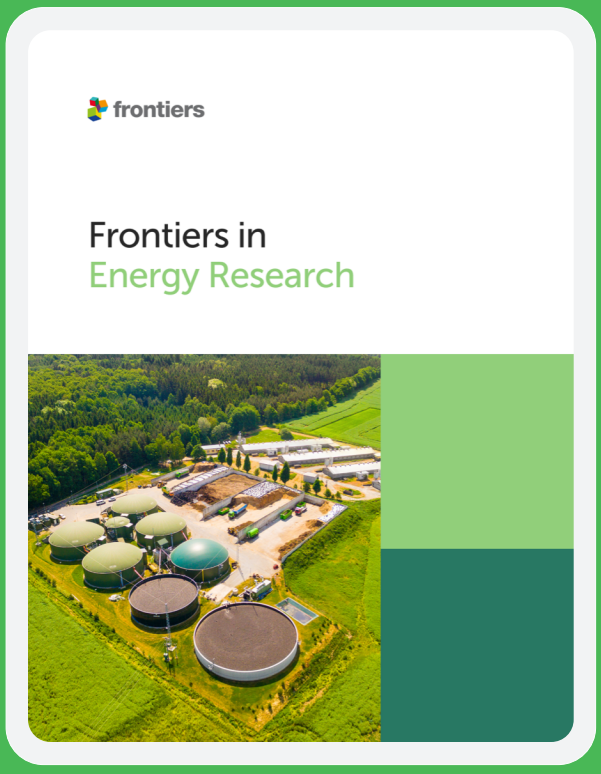

Frontiers

Avenue du Tribunal-Fédéral 34
1005 Lausanne, Switzerland
frontiersin.org

Contact us

+41 (0)21 510 17 00
frontiersin.org/about/contact